

Geophysical Monograph Series  
Including  
Maurice Ewing Volumes  
Mineral Physics Volumes

# GEOPHYSICAL MONOGRAPH SERIES

## GEOPHYSICAL MONOGRAPH VOLUMES

- 1 **Antarctica in the International Geophysical Year** *A. P. Crary, L. M. Gould, E. O. Hulbert, Hugh Odishaw, and Waldo E. Smith (Eds.)*
- 2 **Geophysics and the IGY** *Hugh Odishaw and Stanley Ruttenberg (Eds.)*
- 3 **Atmospheric Chemistry of Chlorine and Sulfur Compounds** *James P. Lodge, Jr. (Ed.)*
- 4 **Contemporary Geodesy** *Charles A. Whitten and Kenneth H. Drummond (Eds.)*
- 5 **Physics of Precipitation** *Helmut Weickmann (Ed.)*
- 6 **The Crust of the Pacific Basin** *Gordon A. Macdonald and Hisashi Kuno (Eds.)*
- 7 **Antarctic Research: The Matthew Fontaine Maury Memorial Symposium** *H. Wexler, M. J. Rubin, and J. E. Caskey, Jr. (Eds.)*
- 8 **Terrestrial Heat Flow** *William H. K. Lee (Ed.)*
- 9 **Gravity Anomalies: Unsurveyed Areas** *Hyman Orlin (Ed.)*
- 10 **The Earth Beneath the Continents: A Volume of Geophysical Studies in Honor of Merle A. Tuve** *John S Steinhardt and T. Jefferson Smith (Eds.)*
- 11 **Isotope Techniques in the Hydrologic Cycle** *Glenn E. Stout (Ed.)*
- 12 **The Crust and Upper Mantle of the Pacific Area** *Leon Knopoff, Charles L. Drake, and Pembroke J. Hart (Eds.)*
- 13 **The Earth's Crust and Upper Mantle** *Pembroke J. Hart (Ed.)*
- 14 **The Structure and Physical Properties of the Earth's Crust** *John G. Heacock (Ed.)*
- 15 **The Use of Artificial Satellites for Geodesy** *Soren W. Henriksen, Armando Mancini, and Bernard H. Chovitz (Eds.)*
- 16 **Flow and Fracture of Rocks** *H. C. Heard, I. Y. Borg, N. L. Carter, and C. B. Raleigh (Eds.)*
- 17 **Man-Made Lakes: Their Problems and Environmental Effects** *William C. Ackermann, Gilbert F. White, and E. B. Worthington (Eds.)*
- 18 **The Upper Atmosphere in Motion: A Selection of Papers With Annotation** *C. O. Hines and Colleagues*
- 19 **The Geophysics of the Pacific Ocean Basin and Its Margin: A Volume in Honor of George P. Woollard** *George H. Sutton, Murli H. Manghnani, and Ralph Moberly (Eds.)*
- 20 **The Earth's Crust: Its Nature and Physical Properties** *John G. Heacock (Ed.)*
- 21 **Quantitative Modeling of Magnetospheric Processes** *W. P. Olson (Ed.)*
- 22 **Derivation, Meaning, and Use of Geomagnetic Indices** *P. N. Mayaud*
- 23 **The Tectonic and Geologic Evolution of Southeast Asian Seas and Islands** *Dennis E. Hayes (Ed.)*
- 24 **Mechanical Behavior of Crustal Rocks: The Handin Volume** *N. L. Carter, M. Friedman, J. M. Logan, and D. W. Stearns (Eds.)*
- 25 **Physics of Auroral Arc Formation** *S.-I. Akasofu and J. R. Kan (Eds.)*
- 26 **Heterogeneous Atmospheric Chemistry** *David R. Schryer (Ed.)*
- 27 **The Tectonic and Geologic Evolution of Southeast Asian Seas and Islands: Part 2** *Dennis E. Hayes (Ed.)*
- 28 **Magnetospheric Currents** *Thomas A. Potemra (Ed.)*
- 29 **Climate Processes and Climate Sensitivity (Maurice Ewing Volume 5)** *James E. Hansen and Taro Takahashi (Eds.)*
- 30 **Magnetic Reconnection in Space and Laboratory Plasmas** *Edward W. Hones, Jr. (Ed.)*
- 31 **Point Defects in Minerals (Mineral Physics Volume 1)** *Robert N. Schrock (Ed.)*
- 32 **The Carbon Cycle and Atmospheric CO<sub>2</sub>: Natural Variations Archean to Present** *E. T. Sundquist and W. S. Broecker (Eds.)*
- 33 **Greenland Ice Core: Geophysics, Geochemistry, and the Environment** *C. C. Langway, Jr., H. Oeschger, and W. Dansgaard (Eds.)*
- 34 **Collisionless Shocks in the Heliosphere: A Tutorial Review** *Robert G. Stone and Bruce T. Tsurutani (Eds.)*
- 35 **Collisionless Shocks in the Heliosphere: Reviews of Current Research** *Bruce T. Tsurutani and Robert G. Stone (Eds.)*
- 36 **Mineral and Rock Deformation: Laboratory Studies—The Paterson Volume** *B. E. Hobbs and H. C. Heard (Eds.)*

## MAURICE EWING VOLUMES

- 1 **Island Arcs, Deep Sea Trenches, and Back-Arc Basins** *Manik Talwani and Walter C. Pitman III (Eds.)*
- 2 **Deep Drilling Results in the Atlantic Ocean: Ocean Crust** *Manik Talwani, Christopher G. Harrison, and Dennis E. Hayes (Eds.)*
- 3 **Deep Drilling Results in the Atlantic Ocean: Continental Margins and Paleoenvironment** *Manik Talwani, William Hay, and William B. F. Ryan (Eds.)*
- 4 **Earthquake Prediction—An International Review** *David W. Simpson and Paul G. Richards (Eds.)*
- 5 **Climate Processes and Climate Sensitivity** *James E. Hansen and Taro Takahashi (Eds.)*
- 6 **Earthquake Source Mechanics** *Shamita Das, John Boatwright, and Christopher H. Scholz (Eds.)*

## MINERAL PHYSICS VOLUMES

- 1 **Point Defects in Minerals** *Robert N. Schrock (Ed.)*

Geophysical Monograph 37  
Maurice Ewing Volume 6

# **Earthquake Source Mechanics**

Edited by

Shamita Das  
John Boatwright  
Christopher H. Scholz



American Geophysical Union  
Washington, D.C.  
1986

Published under the aegis of AGU Geophysical Monograph Board: Patrick Muffler, Chairman; Wolfgang Berger, Donald Forsyth, and Janet Luhmann, members.

**Library of Congress Cataloging-in-Publication Data**

Earthquake source mechanics.

(Geophysical monograph, ISSN 0065-8448 ; 37)  
(Maurice Ewing ; v. 6)  
1. Faults (Geology)—Congresses. 2. Earthquakes—  
Congresses. I. Das, Shamita. II. Series. III.  
Series: Maurice Ewing series ; 6.  
QE606.E17 1986 551.2'2 86-8074  
ISBN 0-87590-405-X  
ISSN 0065-8448

Copyright 1986 by the American Geophysical Union, 2000 Florida Avenue,  
NW, Washington, DC 20009

Figures, tables, and short excerpts may be reprinted in scientific books and journals if the source is properly cited.

Authorization to photocopy items for internal or personal use, or the internal or personal use of specific clients, is granted by the American Geophysical Union for libraries and other users registered with the Copyright Clearance Center (CCC) Transactional Reporting Service, provided that the base fee of \$1.00 per copy, plus \$0.10 per page is paid directly to CCC, 21 Congress Street, Salem, MA 01970. 0065-8448/86/\$01. + .10.

This consent does not extend to other kinds of copying, such as copying for creating new collective works or for resale. The reproduction of multiple copies and the use of full articles or the use of extracts, including figures and tables, for commercial purposes requires permission from AGU.

Printed in the United States of America.



## CONTENTS

Foreword *S. Das, J. Boatwright, and C. H. Scholz* vii

Preface: A Short Geophysical History of Westerly Granite *C. H. Scholz* ix

### LABORATORY STUDIES

On the Normal Stress Dependence of the Shear Fracture Energy *Teng-Fong Wong* 1

Dynamic Breakdown Processes and the Generating Mechanism for High-Frequency Elastic Radiation During Stick-Slip Instabilities *Mitiyasu Ohnaka, Yasuto Kuwahara, Kiyohiko Yamamoto, and Tomowo Hirasawa* 13

State Variable Fault Constitutive Relations for Dynamic Slip *Paul G. Okubo and James H. Dieterich* 25

A Model for the Nucleation of Earthquake Slip *James H. Dieterich* 37

Velocity-Dependent Behavior of Simulated Halite Shear Zones: An Analog for Silicates *Toshihiko Shimamoto and John M. Logan* 49

### THEORETICAL MODELING

On the Elastic Contact Modeling of Faults With Variable Stiffness *B. V. Kostrov and S. Das* 65

Rupture Processes in the Presence of Creep Zones *Victor C. Li and N. Fares* 71

Slip on an Impermeable Fault in a Fluid-Saturated Rock Mass *J. W. Rudnicki* 81

Fracture of a Single Asperity on a Finite Fault: A Model for Weak Earthquakes? *S. Das and B. V. Kostrov* 91

The Seismic Radiation From a 3-D Dynamic Model of a Complex Rupture Process. Part I: Confined Ruptures *John Boatwright and Howard Quin* 97

Effect of Transverse Isotropy on Strong Ground Motion Due to Strike Slip Faulting *J. D. Achenbach and M.-K. Kuo* 111

Fast Near Source Evaluation of Strong Ground Motion for Complex Source Models *V. Farra, P. Bernard, and R. Madariaga* 121

### OBSERVATIONS: THE FAULTING PROCESS

A Discussion of the Depth Extent of Rupture in Large Continental Earthquakes *Jurgen Strehlau* 131

The Fractal Geometry of Faults and Faulting *C. H. Scholz and C. A. Aviles* 147

Rupture Interaction With Fault Jogs *Richard H. Sibson* 157

Variations in the Geometry and Amount of Slip on the Haiyuan (Nanxiushan) Fault Zone, China and the Surface Rupture of the 1920 Haiyuan Earthquake *Deng Quidong, Chen Shefa, Song Fangmin, Zhu Shilong, Wang Yipeng, Zhang Weiqi, Jiao Decheng, B. C. Burchfiel, P. Molnar, L. Royden, and Zhang Peizhen* 169

Strain Accumulation and Rupture Processes in the Subduction Zone Along the Nankai-Suruga Trough in Western Japan *Kiyoo Mogi* 183

Seismic Slip, Aseismic Slip, and the Mechanics of Repeating Earthquakes on the Calaveras Fault, California *William H. Bakun, Geoffrey C. P. King, and Robert S. Cockerham* 195

## OBSERVATIONS: SOURCE PARAMETERS

Small and Large Earthquakes: The Effects of the Thickness of Seismogenic Layer and the Free Surface *Kunihiko Shimazaki* 209

Some Observations Indicating Complications in the Nature of Earthquake Scaling  
*A. McGarr* 217

Earthquake Repeat Time and Average Stress Drop *Hiroo Kanamori and Clarence R. Allen* 227

Low Stress-Drop Earthquakes in the Light of New Data From the Anza, California Telemetered Digital Array *James N. Brune, Joe Fletcher, Frank Vernon, Linda Haar, Tom Hanks, and Jon Berger* 237

Rupture of the Valparaiso (Chile) Gap From 1971 to 1985 *I. Korrat and R. Madariaga* 247

Objective Determination of Source Parameters and Similarity of Earthquakes of Different Size *D. J. Andrews* 259

On Simulating Large Earthquakes by Green's-Function Addition of Smaller Earthquakes *William B. Joyner and David M. Boore* 269

The Effect of Finite Bandwidth on Seismic Scaling Relationships *D. M. Boore* 275

## OBSERVATIONS: STRONG GROUND MOTION

Dense Seismograph Array Observations of Earthquake Rupture Dynamics *Paul Spudich and David Oppenheimer* 285

A Study of Strong Motions From Italy and Yugoslavia in Terms of Gross Source Properties *Ezio Faccioli* 297

Implication of Attenuation for Studies of the Earthquake Source *John G. Anderson* 311

Downhole Recordings of Seismic Radiation *Ralph J. Archuleta* 319

The Effects of Attenuation on the Scaling of Source Parameters for Earthquakes at Anza, California *J. B. Fletcher, L. C. Haar, F. L. Vernon, J. N. Brune, T. C. Hanks, and J. Berger* 331

Maurice Ewing V Symposium Participants 339

List of Reviewers 341

## FOREWORD

This volume contains papers presented at the Fifth Maurice Ewing Symposium, on the subject, "Earthquake Source Mechanics," held May 20-23, 1985, at Arden House, Harriman, New York.

Although the title of the symposium suggests a seismological viewpoint of the subject, the content of the papers contained in this volume reflects the fact that the study of the earthquake mechanism has become increasingly interdisciplinary. Thus although the observation of radiated seismic waves remains the primary tool for studying earthquakes, and has been increasingly focused on extracting the physical processes occurring in the "source," geological studies have also begun to play a more important role in understanding the faulting process, and defining the physical underpinnings for these phenomena has come to be an important subject in experimental and theoretical rock mechanics. While each of these specialties retains its particular flavor and outlook, the degree of interaction between them is amply evident in this volume.

The papers have been grouped according to discipline, although, as indicated above, the subject matter often strongly overlaps. The first two sections are on laboratory and theoretical studies. The first of these contains experimental studies of shear fracture and friction of rock that particularly emphasize understanding the instability that gives rise to dynamic slip. The theoretical papers in the section that follows employ the results of experimental studies to model phenomena applicable to large-scale processes. A number of these papers take up the role of asperities in the faulting process. The importance of heterogeneity in the faulting process, as reflected in these papers, presages the emphasis on the role of heterogeneity in many of the observational studies that follow; indeed, this was a major unifying thread throughout this meeting.

The following three sections contain observational studies. The first contains geological, or at least quasi-static, studies of faults and the faulting process. The second of these sections contains papers on seismological studies of earthquake source parameters. Although many of these deal with attempts at finding scaling laws for various parameters, the role of heterogeneity is still of considerable underlying importance. The final section is on strong ground motions produced by earthquakes, with emphasis on their dependence on source parameters, on heterogeneity, and on the propagation properties of the medium, particularly attenuation.

Acknowledgments. We would like to thank Linda Lee Murphy for coordinating our editorial efforts for this volume. The members of the Steering Committee, K. Aki, J. Boatwright, S. Das, A. McGarr, C. B. Raleigh, J. R. Rice, and C. H. Scholz, were responsible for the scientific organization of the meeting. Ellie Wellmon and Linda Lee Murphy capably handled the logistical organization, with the assistance of Greg Boatnott, Simon Cox, Craig Nicholson, and John Armbruster. The symposium was funded partially by the U.S. Geological Survey under grant USGS-14-08-0001-G-993 and was funded partially by the National Science Foundation under grant EAR84-12420. The U.S. Geological Survey grant also supported partial page charges for the papers in this volume.

S. Das  
J. Boatwright  
C. H. Scholz

Editors

PREFACE:  
A SHORT GEOPHYSICAL HISTORY OF WESTERLY GRANITE

C. H. Scholz

Lamont-Doherty Geological Observatory of Columbia University,  
Palisades, New York 10964

A number of rocks have achieved a kind of fame in geophysical circles because of their frequent use in experimental studies. The names Carrera marble, which has attained a far larger fame in its use for Italian sculpture and facades, Yule marble, and Solenhofen limestone come immediately to mind as experimentalists' rocks. None, however, can match the longevity and shear body of study devoted to them as that of the granite from Westerly, Rhode Island. It is because of the great attention that has been played upon this rock and because of the considerable difficulty one encounters in obtaining a sample of it (it has not been commercially quarried in over 25 years), that Westerly granite has achieved a sort of cult status among experimental geophysicists. It is ironic that many who use the well-worn quip "geophysicists think that the crust is made of Westerly granite" are probably unaware that Westerly granite was once designated by the U.S. Geological Survey and the Carnegie Institution as 'G-1', the type rock of the continental crust [Fairbairn et al., 1951].

Aside from geophysicists, only one other group has lavished such reverence on this rather ordinary looking granite, and those are long-time residents of the town of Westerly. This coastal community in southwestern Rhode Island owed its development and prosperity in the second half of the 19th century and the early part of the 20th to the quarrying of Westerly granite which was obtained in several small stocks in the vicinity. The granite is tight and very fine grained and comes in two varieties: the 'pink' and the 'blue', both of which are often of monumental or statuary grades. Westerly granite was much sought after when granite was extensively used as a construction material and the town enjoyed a boom. Several generations of Italian and Portuguese immigrants were attracted to Westerly as stoneworkers. The last commercial quarry closed in the mid-1950s: the only persisting operation is the Bonner Monument Company, which intermittently quarries a stock at Bradford, several miles away.

The first geophysicist to use Westerly granite for experimental studies was Frank Dawson Adams, a professor at McGill University who, beginning in the late 1890s and continuing for about 25 years, produced a very large body of experimental work on the mechanical properties of rock. He extensively used Westerly granite: the first published photomicrograph and color photograph of the rock are by Adams and Coker [1906]. Adams was one of the first to measure the strength of rock at elevated pressure, using a technique called 'Kick's method' in which confining pressure was produced by deforming the rock inside a steel tube. Adams was a close friend of James Furman Kemp, then a professor at Columbia and in about 1910 presented Kemp with a display collection of his apparatus and samples, both deformed and undeformed. This 'Adams Deformation Set', thought to be the only one of its kind, is now displayed in the Seismology Building at L-DGO.

In 1935, Francis Birch, then a student, later a professor at Harvard, went on an excursion to the Quincy, Massachusetts granite quarry. Birch was interested in finding a granite suitable for experimental work. From among the fine-grained commercial stones on exhibit at Quincy, Birch selected Westerly because of its homogeneous, fairly isotropic fabric and because he remembered that Adams had used it. Birch continued to use Westerly granite throughout his long career and its use was subsequently adopted by his students and colleagues at Harvard, M.I.T., and other institutions. There is so much data available for it that it is still used as a standard rock in many laboratories, particularly those in the northeastern USA.

References

- Adams, F. D., and E. G. Coker, An investigation into the elastic constants of rock, Carnegie Inst., Wash. Publ. 46, 69 pp., 1906.  
Fairbairn, H. W., et al., A cooperative investigation of precision and accuracy in chemical, spectrochemical and model analysis of silicate rocks, U.S. Geol. Soc. Bull. 980, 71 pp., 1951.

## ON THE NORMAL STRESS DEPENDENCE OF THE SHEAR FRACTURE ENERGY

Teng-fong Wong

Department of Earth and Space Sciences, State University of New York, Stony Brook, New York 11794

**Abstract.** The shear fracture energy  $G$  has been determined in the laboratory by biaxial tests using relatively large sawcut specimens or by triaxial tests using cm-sized sawcut or intact specimens. An approximate scheme was used to determine the expected slip-weakening behavior under constant normal stress condition from the post-failure deformation data of triaxial tests. When applied to new results on San Marcos gabbro together with published results on Fichtelbirge granite, this shows that the nominal value of the shear fracture energy calculated using triaxial data at constant confining pressure would be reduced by about a factor of 2 under constant normal stress condition. The data reduction scheme can also be applied to stick-slip data obtained in triaxial tests and lower and upper bounds on  $G$  were evaluated. The experimentally determined values of  $G$  are lower than the seismologically inferred values by orders of magnitude.

## Introduction

Laboratory studies on the fracture and frictional behavior of rock have provided insights on the mechanics of earthquake rupture. Stick-slip instability in the laboratory [Brace and Byerlee, 1966] is generally considered to be an analogue for crustal earthquake rupture. Earthquake ground motion is interpreted to be caused by a sudden drop in shear stress accompanied by unstable slip on a geological fault.

The conceptual model of shear fracture is basically of a strength degradation process during which the peak frictional resistance is overcome to initiate slip and the strength subsequently decays to a reduced level on well-slipped segments of the fault. The simplest model for such a breakdown process is probably the slip-weakening model for which the shear strength at a given location along the fault is assumed to be a decreasing function of the slip (Figure 1). The model was motivated by the cohesive zone models originally developed for tensile fracture by Barenblatt [1962], Dugdale [1960] and Bilby, et al., [1963]. The concept was generalized to the shear faulting problem by Ida [1972] and Palmer and Rice [1973].

The slip-weakening model provides a straightforward interpretation of the shear fracture energy  $G$  as defined in elastic crack mechanics: if the breakdown zone dimension is small relative to the fault length, then  $G$  is simply given by an integral under the slip-weakening curve (Figure 1). Since it is based on a physical description of the breakdown process in the evolution of fault instability and at the same time has such a simple connection with elastic crack mechanics, the slip-weakening model has been used extensively to tackle a wide range of fault mechanics problems [e.g., Ida, 1972; Andrews, 1976; Aki, 1979; Stuart and Mavko, 1979; Rudnicki, 1980; Day, 1982; Li and Rice, 1983; Papageorgiou and Aki, 1983].

The direct observation of the slip-weakening behavior at the tip of a propagating slip zone can only be made on a relatively large sample in the laboratory. The recent study by Okubo and Dieterich [1984] on a 2-m long frictional surface under biaxial loading has elucidated details of the slip-weakening behavior in a stick-slip instability. Their experiments were performed at normal stresses up to 4 MPa and measurements of the shear fracture energy range from 0.2 to 2.4 J/m<sup>2</sup>.  $G$  has been observed to increase as a function of the normal stress as well as the fault roughness. Okubo and Dieterich [1984] pointed out that a direct extrapolation of their data to the relatively high normal stresses typical of triaxial tests would predict  $G$  to be of the order of 400 J/m<sup>2</sup>.

Values of  $G$  have also been inferred from measurements of the post-failure force-displacement curves for cm-sized specimens loaded in a conventional triaxial configuration and under crustal conditions of pressure and temperature [Rice, 1980; Wong, 1982]. Such measurements are typically of the order 10<sup>4</sup> J/m<sup>2</sup>, about two orders of magnitude higher than those suggested by Okubo and Dieterich [1984].

A key difference between the two types of experiments is in the loading configuration. The normal stress steadily decreases during the slip-weakening process in a triaxial test but it is maintained constant in a biaxial test. Therefore the nominal stress drop is expected to be higher in a triaxial test resulting in an apparent

## 2 SHEAR FRACTURE ENERGY

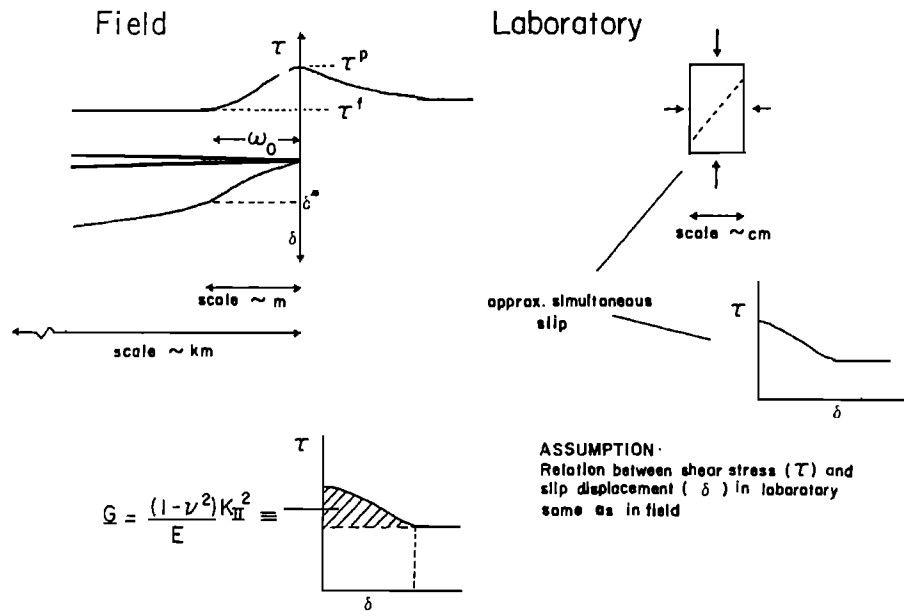


Fig. 1. Slip-weakening model as applied in the field and in the laboratory. The distribution of shear stress  $\tau$  and slip displacement  $\delta$  with respect to a fault in the field is shown.

enhancement of values of  $G$  calculated from the slip-weakening curve. Can the discrepancy among laboratory data be simply attributed to such differences in the loading path? The effect of loading path on the slip-weakening behavior can be analyzed theoretically, and an approximate scheme has been formulated by which the expected slip-weakening behavior under constant normal stress can be inferred from post-failure deformation data of triaxial tests [Rice, 1984]. We have recently completed a study on the pressure dependence of the post-failure behavior of San Marcos gabbro under triaxial loading [Wong and Biegel, 1985]. In addition, a few experiments were also performed in which the confining pressure was continually increased in proportion to the decrease in axial load so that the normal stress acting on the shear band remained constant throughout the post-failure stage. The new data on the gabbro provide a test on the validity of the theoretical analysis. We have also used the data reduction scheme to determine the shear fracture energy as a function of the normal stress for Fichtelbirge granite [Rummel et al., 1978] and for San Marcos gabbro.

Nearly all the triaxial data were obtained from fracture experiments performed on initially intact specimens, whereas the biaxial experiments were conducted on sawcut samples. To what extent is the discrepancy between the two types of measurements due to the difference between the slip-weakening behavior for an incipient fault of an initially intact sample and that for a sawcut frictional surface? The data reduction scheme can also be applied to triaxial data such as those of Byerlee [1970] for stick-slip instabilities along a

frictional surface. We have used measurements on Westerly granite obtained by Byerlee [1970] and Scholz et al. [1972] to determine bounds on the shear fracture energy as a function of normal stress.

Byerlee's [1970] experiments were conducted under relatively high normal stresses (ranging from 0.2 to 1.2 GPa), Scholz et al.'s [1972] biaxial tests were conducted in an intermediate range of normal stresses (from about 5 to 40 MPa), and Okubo and Dieterich's [1984] work covered the low end of the normal stress. The experiments were all performed on sawcut surfaces of comparable roughness. However, the dimension of the frictional surface ranges over two orders of magnitude. If a comparison of the three sets of data indicates that significant discrepancy exists, then one probably has to conclude that they are due to scale effects. Such a comparison should also have implications on the important problem concerning the scaling of laboratory measurements to tectonic settings.

## Theory

As a slip instability propagates along the fault, one would expect the shear stress ( $\tau$ ) at a fault segment to peak off at a value  $\tau_p$  and then decrease as a function of slip ( $\delta$ ) until it reaches a residual value  $\tau_f$  (Figures 1 and 2). It is assumed in the slip-weakening model that the frictional strength does not have a strong dependence on the slip rate, and hence one expects the shear stress  $\tau$  during the slip-weakening process to be generally given by:

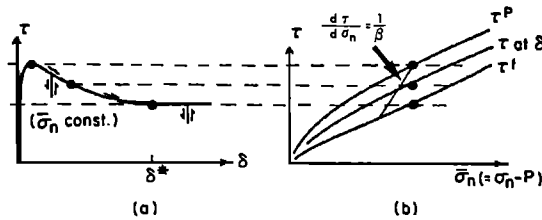


Fig. 2. (a) Slip-weakening stress versus slip relations for constant effective normal stress. Unloading and reloading branches shown. (b) Peak ( $\tau^P$ ), residual ( $\tau^f$ ), and intermediate strengths depend on effective normal stress, and also on temperature. Loading path for a triaxial test is also shown.

$$\tau = \tau(\sigma_n, \delta) \quad (1)$$

where  $\sigma_n$  is the normal stress acting on the fault. ( $\sigma_n$  should be replaced by  $\sigma_n - p$  for a rock mass which is saturated with fluid at pore pressure  $p$ ). The slip  $\delta$  is set to be zero at the initiation of the slip-weakening process and hence we have the peak strength  $\tau^P = \tau(\sigma_n, 0)$  and the residual strength  $\tau^f = \tau(\sigma_n, \infty)$ . The residual value will have been attained as the slip reaches a characteristic value  $\delta^*$  (Figure 1).

In a biaxial test with  $\sigma_n$  maintained constant, the reduction of  $\tau$  during the slip-weakening process is solely due to an accumulation of slip. On the other hand, both  $\sigma_n$  and  $\delta$  change during the slip-weakening process in a triaxial test. If the angle between the maximum compressive stress  $\sigma_1$  and the fault normal is denoted by  $\alpha$ , then the loading path is given by:

$$d\tau / d\sigma_n = \tan \alpha = 1/\beta$$

As indicated in Figure 2b, the nominal shear stress drop recorded in a triaxial test is expected to be higher than that for a biaxial test with normal stress maintained constant.

Given a set of triaxial data  $\tau = \tau(\sigma_n, \delta)$  for which the loading paths satisfy  $d\sigma_n/d\tau = \beta$ , we would like to determine  $\tau$  as a function of  $\delta$  for loading paths with  $d\sigma_n = 0$ . This problem was analyzed by J. R. Rice (unpublished notes, 1981) for the case when the normal stress dependence of both the peak strength and the residual strength are approximately linear:

$$\begin{aligned} \tau^P &= A \sigma_n + B \\ \tau^f &= a \sigma_n + b \end{aligned} \quad (2)$$

The linear approximations are not expected to hold over an extensive range of normal stress (say, up to 1 GPa). However, experimental results indicate that such linear relations are reasonable approximations for both fracture strength [e.g., Hoek and Brown, 1980] and frictional strength [e.g., Byerlee, 1970; Scholz et al., 1972] over a limited range of normal stress (up to several tens of MPa).

Over the same range of normal stress, one would expect the general slip-weakening function  $\tau(\sigma_n, \delta)$  to be approximated reasonably well by the one-term Taylor expansion:

$$\tau = m(\delta) \sigma_n + c(\delta) \quad (3)$$

such that  $m(0)=A$ ,  $c(0)=B$ ,  $m(\infty)=a$  and  $c(\infty)=b$ .

In a triaxial test, if slip initiates at a stress state on the peak strength envelope with shear stress  $\tau^P$ , then the subsequent loading will follow a path with  $d\sigma_n/d\tau = \beta$  until both the shear and the normal stresses reduce to values lying on the residual strength envelope. Hence, the slip-weakening behavior in a triaxial test is given by:

$$\tau = F(\tau^P, \delta)$$

$$= \tau^f(\tau^P) + (\tau^P - \tau^f) h(\tau^P, \delta) \quad (4)$$

with  $h(\tau^P, 0)=1$  and  $h(\tau^P, \infty)=0$ . The values of the shear fracture energy determined from post-failure deformation data in triaxial tests [Rice, 1980; Wong, 1982] using measurements of the nominal strength drop as a function of slip are therefore given by:

$$\begin{aligned} G_{\text{nom}}(\tau^P) &= \int_0^\infty (\tau - \tau^f) d\delta \quad (\text{triaxial loading}) \\ &= (\tau^P - \tau^f) \int_0^\infty h(\tau^P, \delta) d\delta \end{aligned} \quad (5)$$

Note that each increment of the slip does not make the same contribution towards the fracture energy. The total contribution is given by the weighted average below:

$$\langle \delta_{\text{nom}} \rangle = \int_0^\infty h(\tau^P, \delta) d\delta \quad (6)$$

As we discuss below, the experimental data indicate that both  $\langle \delta_{\text{nom}} \rangle$  and the weighting function  $h$  do not vary significantly for a range of normal stress over which the peak and residual strength envelopes are linear (2). For such cases, we can take  $h$  to be independent of  $\tau^P$ . It was shown by Rice (unpublished notes, 1981) after extensive algebra that if  $h = h(\delta)$  then:

$$\begin{aligned} m(\delta) - a &= (A-a) f(\delta) h(\delta) \\ c(\delta) - b &= (B-b) f(\delta) h(\delta) \end{aligned} \quad (7)$$

with  $f(\delta) = (1-\beta\delta)/[(1-\beta A) + \beta(A-a) h(\delta)]$ .

If we denote by  $G$  the shear fracture energy for a loading path with the normal stress  $\sigma_n$  maintained constant, then:

$$\begin{aligned} G &= \int_0^\infty (\tau - \tau^f) d\delta \\ &= [(A-a)\sigma_n + (B-b)] \int_0^\infty f(\delta) h(\delta) d\delta \end{aligned} \quad (8)$$

## 4 SHEAR FRACTURE ENERGY

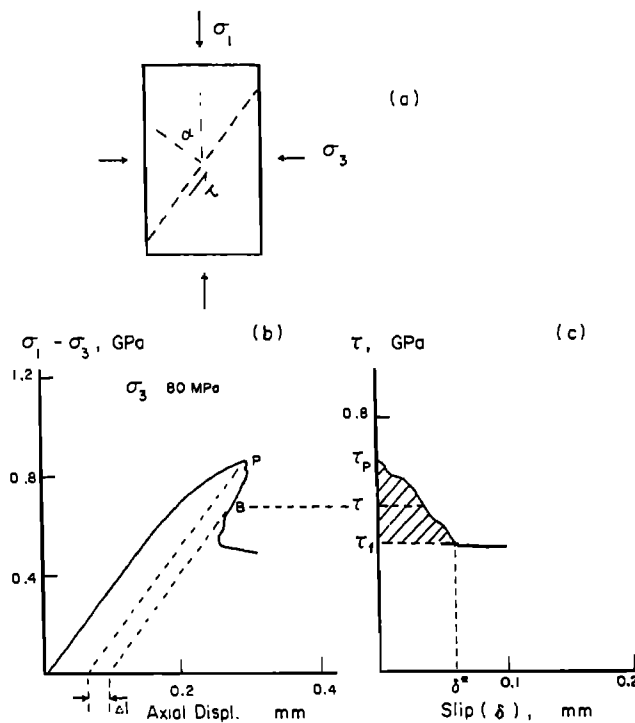


Fig. 3. (a) Loading of a sample with a shear band in a triaxial test (b) and (c) Transformation of postfailure data (of an initially intact sample of Westerly granite at 80 MPa confining pressure and room temperature) to infer shear stress versus relative slip relation used in slip-weakening model.

If the constants  $A$ ,  $B$ ,  $a$  and  $b$  in (2) have been determined from experimental data for a range of pressure, then  $G$  can be evaluated from measurements of  $h(\delta)$  in triaxial tests by evaluating the above integral numerically. Equation (8) also implies the following upper and lower bound on  $G$ :

$$(1-\beta a)/(1-\beta A) < G/[(A-a)\sigma_n + (B-b)]\langle\delta_{nom}\rangle < 1 \quad (9)$$

if  $(A-a)/(1-\beta A) < 0$ . The inequality signs would be reversed if  $(A-a)/(1-\beta A) > 0$ .

#### Experimental Results

##### Post-failure Behavior of San Marcos Gabbro

A series of experiments were performed to study the post-failure behavior of San Marcos gabbro. The deformation data and microstructural observations were given by Wong and Biegel [1985]. The samples were cylindrical with diameter 15.8 mm and length 38.1 mm. They were predried in vacuo, jacketed with polyurethane and deformed in a conventional triaxial configuration. All the

experiments were performed at room temperature. The confining pressures range from 250 MPa to 400 MPa. The postfailure behavior of San Marcos gabbro is relatively stable in comparison with those of other crystalline rocks previously investigated (e.g., Westerly granite and Frederick diabase). The stiffness of the test machine ( $0.25 \text{ GNm}^{-1}$ ) was sufficiently high that no post failure instability was observed in this study for confining pressures of 250 MPa and above.

The confining pressure was monitored with a Heise gauge, and maintained constant to within 1 MPa. The axial strain rate was  $10^{-5}/\text{s}$ . The axial load was measured with an external load cell with a probable error of 2%. The displacement was measured outside the pressure vessel with a differential transformer (DCDT) mounted between the moving piston and the fixed lower platen. Measurements were accurate to within 1%.

Several of the samples have conjugate faults and their data are not included here. Our measurements of the peak differential stresses are in good agreement with previous data (Figure 4). After each run, the sample was retrieved from the pressure vessel and the fault angle was measured with a protractor. The data reduction procedure was identical to the previous study [Wong, 1982]. If the angle between  $\sigma_1$  and the fault normal is  $a$ , then the shear traction is given by (Figure 3a):

$$\tau = (\sigma_1 - \sigma_3)/2 \sin 2a \quad (10a)$$

whereas the relative slip  $\delta$  at a point B in Figure 3b can be expressed in terms of the postfailure axial displacement  $\Delta l$  by:

$$\delta = \Delta l / \sin a \quad (10b)$$

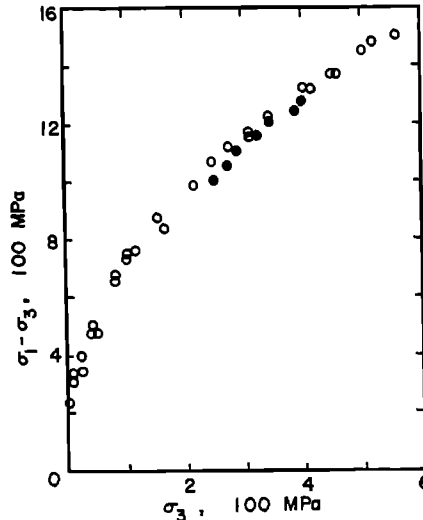


Fig. 4. Peak strength versus confining pressure for San Marcos gabbro at room temperature. The open circles are data compiled by Hadley [1973] and the dark circles are from this study.

TABLE 1. San Marcos Gabbro

Sample	Confining Pressure (MPa)	$\alpha$ (deg)	$G_{\text{nom}}$ ( $10^4 \text{ J/m}^2$ )	Peak Stresses $\tau_p^P$ (MPa)	$\sigma_n$	Residual Stresses $\tau_p^P$ (MPa)	$\sigma_n$	$\langle \delta_{\text{nom}} \rangle$ (mm)	$G$ ( $10^4 \text{ J/m}^2$ )
GF3	250	60	2.6	433	500	326	439	.25	1.7-1.8
GF24	277	57	2.6	481	588	377	523	.25	1.6-1.7
GF4	305	57	2.8	490	620	395	563	.30	1.8-1.9
GF25	325	58	2.1	505	640	417	586	.24	1.4-1.5
GF6	350	57	2.9	542	702	448	641	.31	1.7-1.8
GF28	396	59	1.9	548	725	459	672	.22	1.2-1.2
GF5	400	56	1.9	569	784	493	732	.26	1.2-1.3
GF17*	250	58		449	531	372	531	.28	2.1

\*Sample deformed with controlled increase in confining pressure so that  $\sigma_n$  remained constant in postfailure stage.

The calculation of  $\Delta l$  is based on the observation [Wawersik and Brace, 1971] that the unloading response is linear and can be approximated by the Young's modulus of the initial loading stage. After transforming the postfailure deformation data to a  $\tau-\delta$  plot, we performed a numerical integration under the slip-weakening curve as shown in Figure 3c to evaluate the nominal value of the shear fracture energy  $G_{\text{nom}}$  (4). The data are compiled in Table 1. The peak and residual strength are plotted against the normal stress in Figure 5.

Two additional experiments were performed with a controlled increase of confining pressure during the postfailure stage such that the normal stress acting on the fault plane remained constant. One sample (GF19) showed conjugate faulting and the data were discarded. The other sample (GF17) was loaded at a confining pressure of 250 MPa to the peak differential stress. In the postfailure stage, the confining pressure was manually controlled such that the ratio of the axial force  $F$  and the confining pressure  $P$  satisfies:

$$dF/dP = A_p [1 - A_s/(A_p \cos^2 \alpha)]$$

where  $A_s$  and  $A_p$  are the areas of the specimen and the loading piston respectively.  $\alpha$  was taken to be  $58^\circ$  which turned out to be almost identical to that measured after the experiment.

The shear traction can be calculated using (10a). To calculate the slip in this case, we need to determine the elastic component of the axial displacement which has to be subtracted from the total displacement to calculate  $\Delta l$  (10b). Since both the axial stress and the confining pressure changed during the slip-weakening process, values of the Young's modulus (for unloading) and bulk modulus (for pressure increase) have to be known. We measured the bulk modulus of San Marcos gabbro which had a constant value of 153 GPa at confining pressures up to 250 MPa. The porosity of the gabbro is negligible and hence this corresponds to the 'intrinsic' value

for a crack-free aggregate. The postfailure sample should have undergone extensive stress-induced microcracking and hence its bulk modulus is expected to be smaller than this 'intrinsic' value we used in the calculation. Our estimate of  $\Delta l$  and hence  $G$  should therefore be an overestimate. The data for GF17 is included in Table 1. The peak and residual strength for this sample are also plotted in Figure 5.

#### Evaluation of $G$ as a Function of Normal Stress from Postfailure Data of Triaxial-Tests

We have used the data reduction scheme outlined above to evaluate  $G$  as a function of the normal stress. In addition to San Marcos gabbro, we also considered Fichtelbirge granite a detailed study of which had been undertaken by Rummel et al., [1978].

It can be seen from Figure 5 that our data for both the peak and residual strength data of the

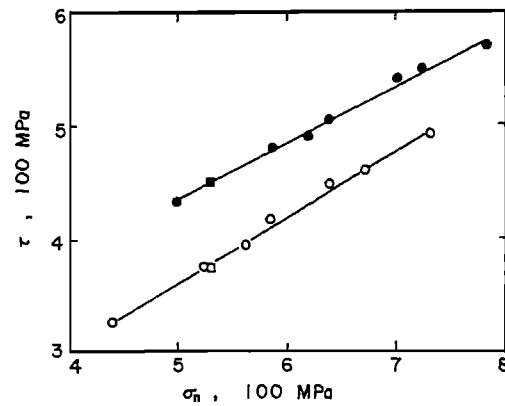


Fig. 5. The shear and normal stresses resolved on the fault plane (San Marcos gabbro). The dark symbols are for the peak values and the open symbols are for the residual values. The squares are for sample GF17 (see Table I).

## 6 SHEAR FRACTURE ENERGY

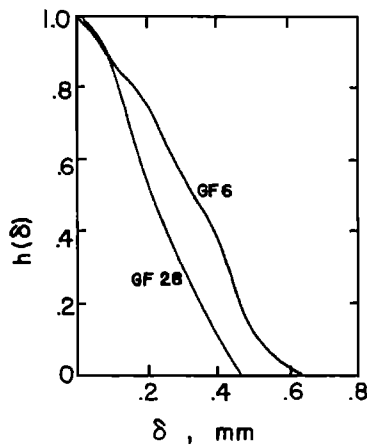


Fig. 6. The function  $h(\delta)$  for the samples GF28 and GF6 (see Table 1 and (3)).

gabbro show a linear dependence on the normal stress. The coefficients  $A$ ,  $B$ ,  $a$  and  $b$  (2) were determined by linear regression and the best-fit straight lines are given by:

$$\tau^P = .49\sigma_n + 189 \text{ (MPa)}$$

$$\tau^f = .57\sigma_n + 77 \text{ (MPa)}$$

$\langle\delta_{nom}\rangle$  ranges from 0.22 to 0.31 mm. The function  $h(\delta)$  (3) for the two samples with the minimum (GF28) and maximum (GF6) values of  $\langle\delta_{nom}\rangle$  are plotted in Figure 6. The variation in  $h(\delta)$  is more than that expected from experimental error. However, there is no systematic correlation with either the normal or the shear stresses (Table I). A comparable amount of scatter is also evident in Wawersik and Brace's [1971] post-failure data for 25 samples of Westerly granite loaded in uniaxial compression. Therefore it is unlikely that the observed variation for the function  $h$  is due to a stress dependence. Most probably it reflects a statistical variation in the slip-weakening behavior from sample to sample.

The value of  $(1-\beta)/(\beta A)$  is about 0.93 for all the gabbro samples and hence the upper and lower bounds given by (9) are very tight. We have evaluated these bounds on  $G$  using (9) for the value of  $\sigma_n$  which is the arithmetic mean of the peak and residual values of the normal stress in the postfailure stage. The results are shown in Figure 7.

A similar approach was taken in analyzing Rummel et al.'s [1978] experimental data for Fichtelbirge granite. Values of  $G_{nom}$  for three of the samples were evaluated by Rice [1980]. The data for the peak differential stress at confining pressures up to 300 MPa have been reproduced in Figure 8. If the room pressure value is not included, the data can be approximated quite well by a bilinear dependence on pressure. Rummel et al. [1978] reported an  $\alpha$  value of  $54^\circ$  for the samples deformed at the higher end of confining

pressures. It is expected that  $\alpha$  will increase somewhat as the confining pressure decreases [e.g., Mogi, 1966]. We assumed  $\alpha = 60^\circ$  for the samples deformed at confining pressures between 7.5 and 33 MPa. The results are not sensitive to the exact value of  $\alpha$  used. The calculated values for  $\tau^P$ ,  $\tau^f$ ,  $G_{nom}$ , and  $\langle\delta_{nom}\rangle$  are compiled in Table 2. The strength data are plotted in Figure 9. The following bilinear relations were obtained by linear regression analysis of the data:

$$\tau^P = 1.14\sigma_n + 26 \text{ (MPa)} \quad 100 \text{ MPa} < \sigma_n < 186 \text{ MPa}$$

$$\tau^P = .67\sigma_n + 92 \text{ (MPa)} \quad 243 \text{ MPa} < \sigma_n < 715 \text{ MPa}$$

$$\tau^f = 1.05\sigma_n + 12 \text{ (MPa)} \quad 56 \text{ MPa} < \sigma_n < 121 \text{ MPa}$$

$$\tau^f = .63\sigma_n + 39 \text{ (MPa)} \quad 136 \text{ MPa} < \sigma_n < 608 \text{ MPa}$$

It can be seen from the data in Table 2 that the decrease in slope of the strength envelope is accompanied by an increase in  $\langle\delta_{nom}\rangle$  of about a factor of 2. The scatter of  $\langle\delta_{nom}\rangle$  within each of

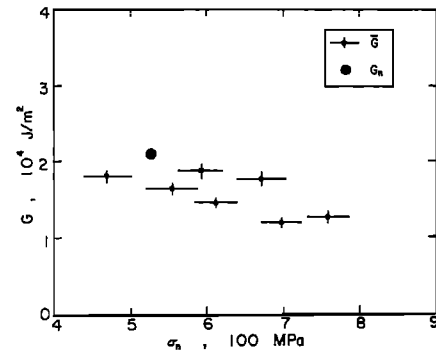
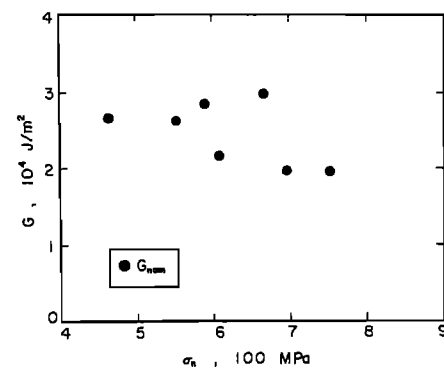


Fig. 7. (a)  $G_{nom}$  for San Marcos gabbro evaluated from nominal stress drop observed in triaxial tests. (b)  $G$  for San Marcos gabbro. The vertical bars indicate the range in  $G$  corresponding to the lower and upper bound according to (9). The horizontal bars represent the range of normal stress acting on the shear band during the postfailure stage. The dark circle is for sample GF17.

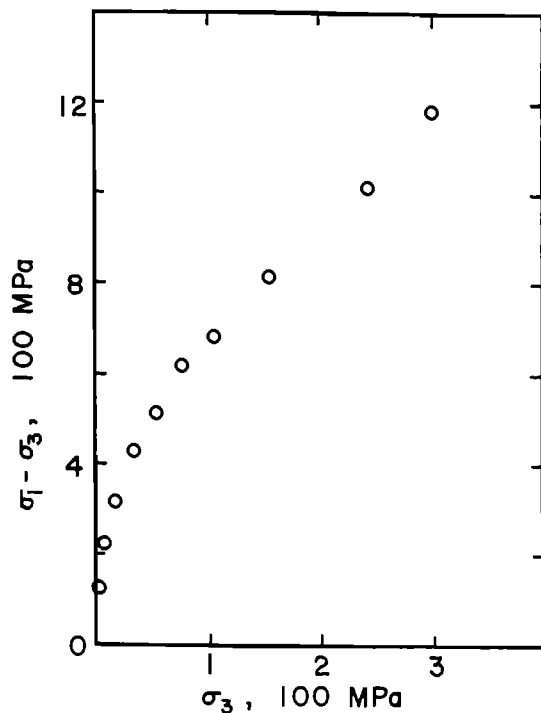


Fig. 8. Peak strength of Fichtelbirge granite versus confining pressure at room temperature. Data from Rummel et al. [1978].

the two normal stress groupings is comparable to that for San Marcos gabbro (Table 1).

$(1-\beta_a)/(1-\beta A)$  has a value of 1.14 for the three samples deformed at confining pressures up to 33 MPa, and a value of 1.06 for the high pressure samples. Again, (9) would imply that the lower and upper bounds on  $G$  are very tight. The calculated values for these bounds are shown in Figure 10 and Table 2.

#### Discussion

##### The Normal Stress Dependence of $G$ Determined from Post failure Behavior in Triaxial Tests

It can be seen from the analysis above that the values of  $G_{\text{nom}}$  inferred from the nominal strength drop versus slip data obtained during the post failure stage in triaxial tests are higher than the expected values of  $G$  for a biaxial test with normal stress maintained constant. The data for San Marcos gabbro (Table 1 and Figure 7) and for Fichtelbirge granite (Table 2 and Figure 10) show that the ratio of  $G_{\text{nom}}$  to  $G$  can be up to a factor of 2.  $G_{\text{nom}}$  previously determined from triaxial data [Rice, 1980; Wong, 1982] ought to be appropriately adjusted if the results are to be compared with biaxial data determined under comparable normal stress conditions.

The data reduction scheme is based on the explicit assumption that the strength envelopes

are piecewise linear. The data for GF-17 (obtained at a constant normal stress) is consistent with this assumption. We also assume that the function  $h(\delta)$  is not strongly stress-dependent (within a range of normal stress over which the strength envelopes are linear) but has a statistical variation from sample to sample. This is a physically plausible assumption, but hard to justify experimentally. The scatter of  $G_{\text{nom}}$  evident in Figures 7 and 10 is partly due to the variation in stress drop. The use of Mohr circle analysis in equation (2) assuming a stress-independent value for  $\langle \delta_{\text{nom}} \rangle$  basically smoothes out the statistical variation in the stress drop data.

The overall trend is for  $G$  to increase as a function of the normal stress  $\sigma_n$  in Fichtelbirge granite. The rate of increase is higher in the low normal stress end. A reversed trend is observed for San Marcos gabbro. The normal stress dependence is given by the difference  $A-a$  (8) which has a value of 0.04 for the granite (under high normal stress) and -0.08 for the gabbro. Taken into account the scatter in the data, one should probably not attach much significance to this difference in sign.

##### Bounds on $G$ for Stick-slip Instabilities in Westerly Granite

Rice [1980] evaluated  $G_{\text{nom}}$  for stick-slip instability from the data of Rummel et al. [1978] for Fichtelbirge granite using equation (5) above. We are not aware of any other measurements performed over a range of pressure from which  $G$  as a function of  $\sigma_n$  can be determined using the data reduction scheme above. However, Byerlee [1970] and Scholz et al. [1972] have performed careful studies on the normal stress dependence of shear stress drop for stick-slip events in Westerly

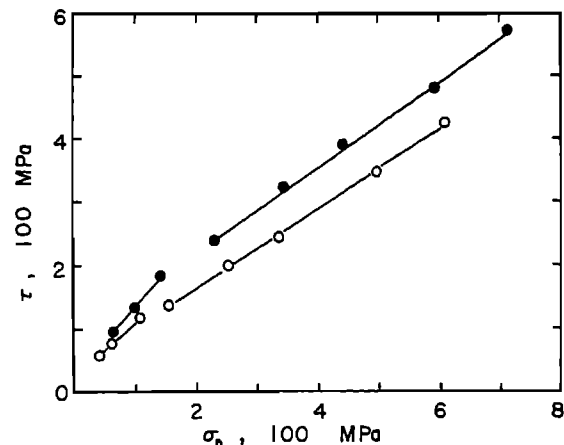


Fig. 9. Shear and normal stresses resolved on the fault plane (Fichtelbirge granite). The dark and open symbols are for the peak and residual values respectively.

## 8 SHEAR FRACTURE ENERGY

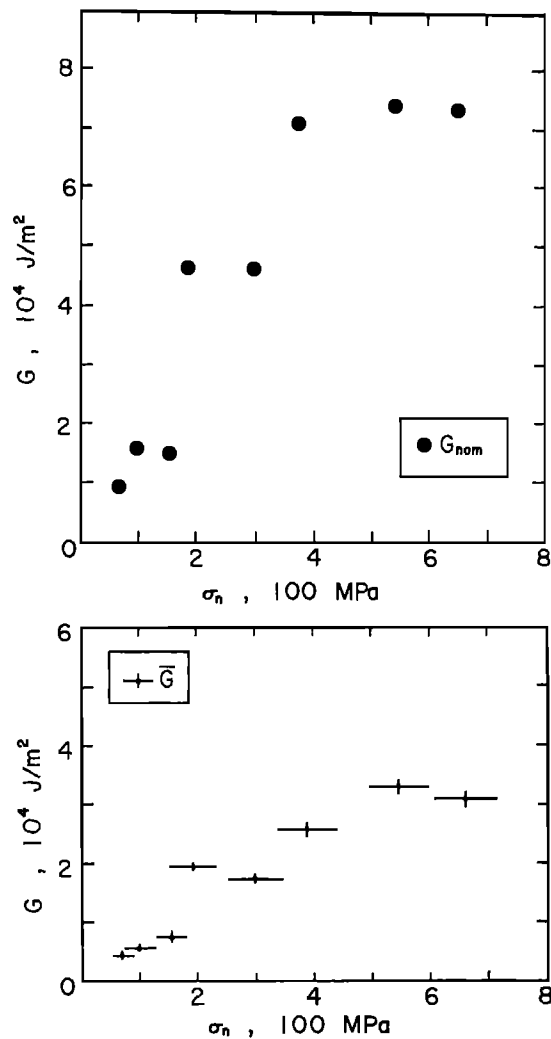


Fig. 10. (a)  $G_{\text{nom}}$  for Fichtelbirge granite evaluated from nominal stress drop observed in triaxial tests. (b)  $G$  for the granite. The vertical bars indicate the range in  $G$  corresponding to the lower and upper bound according to (9). The horizontal bars represent the range of normal stress acting on the shear band during the postfailure stage.

granite at room temperature.  $\langle \delta_{\text{nom}} \rangle$  for faulting in initially intact samples of Westerly granite was determined by Wong [1982] over a wide range of temperature and pressure. Detailed measurements of  $\delta^*$  (Figure 1) for frictional surfaces of different degrees of roughness (at a normal stress of 10 MPa) was made by Dieterich [1980, 1981]. We used these data which had been obtained in both biaxial [Scholz et al., 1972; Dieterich 1980, 1981] and triaxial [Byerlee, 1970; Wong, 1982] tests to determine bounds on  $G$  for frictional instabilities in Westerly granite.

Byerlee [1970] performed Mohr circle analysis on his stress drop data in triaxial tests to

determine the 'kinetic' coefficient of friction. The experiments were performed on sawcut samples 15.8 mm in diameter with  $\alpha = 45^\circ$  and  $60^\circ$ . His results imply an upper and a lower bound on the stress drops for stick-slip events:

$$0.05\sigma_n + 50 \text{ (MPa)} < \tau^P - \tau^f < .4\sigma_n + 50 \text{ (MPa)}$$

for  $\sigma_n$  between 0.2 and 1.2 GPa.

Byerlee's samples were described as 'finely-ground' and their roughness should be comparable to that of the samples of Scholz et al. [1972] which were polished with an 80-grit wheel. This latter set of experiments was conducted on slabs of dimension  $3 \times 10 \times 180$  cm with a sawcut inclined at  $30^\circ$  to the major face. The normal stress was not servo-controlled and hence was expected to vary somewhat in a stick-slip event. The data obtained by Scholz et al. [1972] (Figure 4) on shear stress drop ( $\tau^P - \tau^f$ ) as a function of  $\tau^P$  can be fitted reasonably well with a linear curve:

$$\tau^P - \tau^f = .2 \tau^P$$

$\tau^P$  is related to  $\sigma_n$  through the 'static' coefficient of friction which was reported to vary between 0.35 and 0.55. Hence the data for this intermediate range of normal stress ( $5 \text{ MPa} < \sigma_n < 40 \text{ MPa}$ ) imply the following upper and lower bound on the stress drop:

$$0.11 \sigma_n < \tau^P - \tau^f < 0.07 \sigma_n$$

In an analysis of this kind, it is sufficient to take  $G$  to be approximately given by  $[(A-a)\sigma_n + (B-b)] \langle \delta_{\text{nom}} \rangle$  (9). The above results of Byerlee [1970] and Scholz et al. [1972] provide upper and lower bounds on both of the coefficients  $A-a$  and  $B-b$ .

An estimate of  $\langle \delta_{\text{nom}} \rangle$  for a relatively smooth sawcut surface can be obtained from Dieterich's [1980] data obtained in quasi-static tests. He determined the quantity  $d_r$  which was the slip required for the frictional strength to reach a steady state, residual value following an order of magnitude change in slip velocity. Laboratory data have shown that  $d_r$  is a reasonable estimate of  $\delta^*$  (Figure 1) for the dynamic slip-weakening process accompanying a stick-slip event [Dieterich, 1980; Okubo and Dieterich, 1986]. For a smooth slip-weakening curve,  $\langle \delta_{\text{nom}} \rangle$  is approximately given by  $\delta^*/2$ .

Dieterich [1980] reported a  $d_r$  value of  $25 \mu\text{m}$  for frictional surface of Westerly granite (lapped using 60-90 grit abrasive) at a normal stress of 10 MPa. We infer that a  $\langle \delta_{\text{nom}} \rangle$  value of  $12.5 \mu\text{m}$  is probably appropriate for the intermediate normal stress range used by Scholz et al. [1972]. Wong's [1982] data for initially intact samples indicate an increase of  $\langle \delta_{\text{nom}} \rangle$  with normal stress. As long as  $\langle \delta_{\text{nom}} \rangle$  does not decrease significantly with normal stress, a lower bound on  $G$  in the high normal stress range can be similarly obtained using a  $\langle \delta_{\text{nom}} \rangle$  value of  $12.5 \mu\text{m}$  and Byerlee's

TABLE 2. Fichtelbirge Granite

Confining Pressure (MPa)	$\alpha^*$ (deg)	$G_{\text{nom}}$ ( $10^4$ J/m <sup>2</sup> )	Peak Stresses $\tau^p$ (MPa)	$\sigma_n$	Residual Stresses $\tau^p$ (MPa)	$\sigma_n$	$\langle \delta_{\text{nom}} \rangle$ (mm)	$G$ ( $10^4$ J/m <sup>2</sup> )
7.5	60	.9	65	100	40	56	.21	.4-.5
17	60	1.6	97	139	57	69	.23	.4-.6
33	60	1.5	141	186	103	121	.23	.7-.8
55	54	4.7	231	243	154	136	.44	1.9-2.0
108	54	4.6	323	343	200	253	.37	1.7-1.8
157	54	7.1	390	440	247	337	.50	2.5-2.6
300	54	7.3	571	715	423	608	.49	3.0-3.2

\*Fracture angles assumed.

The calculations are based on experimental data of Rummel et al. [1978].

[1970] stress drop data. The results are plotted in Figure 11.

An upper bound can be evaluated in an analogous manner. It has been generally observed [Byerlee, 1970; Ohnaka, 1973; Okubo and Dieterich, 1984] that if the fault surface roughness or the size of the gouge particles are increased, the stress drop would decrease. On the other hand, one expects  $\delta^*$  or  $\langle \delta_{\text{nom}} \rangle$  to increase as a function of the fault surface roughness and the gouge particle size. A limited amount of data obtained by Okubo and Dieterich [1984] indicate that the net result is for  $G$  to increase with the roughness. If one takes the stress drop value observed for a smooth sawcut surface and multiply it by  $\langle \delta_{\text{nom}} \rangle$  for a rough surface, the product represents an upper bound on  $G$  for surfaces spanning the range of roughness.

A reasonable estimate for  $\langle \delta_{\text{nom}} \rangle$  in the intermediate range of normal stresses can be determined from two different kinds of data. The slip-weakening process in the postfailure stage of triaxial tests of initially intact samples can probably be considered to occur over a very 'rough' surface. Wong's [1982] data for Westerly granite would imply  $\langle \delta_{\text{nom}} \rangle$  to be of order 70  $\mu\text{m}$  at room temperature. A second estimate can be obtained from Dieterich's [1981] data on  $d_r$  for slip on Westerly granite blocks (60-90 grit) sandwiched between a 0.5 mm layer of simulated gouge. The gouge was crushed Westerly granite with particle sizes between 125 and 250  $\mu\text{m}$  and the normal stress was 10 MPa.  $d_r$  was of the order 180  $\mu\text{m}$ . We simply used a value of 70  $\mu\text{m}$  for  $\langle \delta_{\text{nom}} \rangle$  in our calculation. For the high normal stress range corresponding to Byerlee's [1970] study, we have used a value of 200  $\mu\text{m}$  for  $\langle \delta_{\text{nom}} \rangle$  which was estimated from Wong's [1982] data. The results are plotted in Figure 11.

#### Comparison with Seismologically Inferred Values of G

Okubo and Dieterich [1984] observed the slip-weakening behavior at the tip of a propagating

slip zone and they evaluated  $G$  by directly integrating the slip-weakening curve. Their data are also included in Figure 11 for comparison. Their results were for a 2-m long frictional surface of Sierra white granite lapped using 30-grit abrasive. It can be seen that their data for the low normal stress range are quite consistent with the lower bound on  $G$  for the intermediate and the high normal stress regions. The average value of  $\delta^*$  reported by Okubo and Dieterich [1984] was 25  $\mu\text{m}$  which is the same value we used in calculating the lower bound on  $G$ . The type of agreement shown in Figure 11 simply reflects that on the question of the normal stress dependence of stress drop, there is no significant discrepancy among experimental data for polished sawcut surfaces which have been obtained over three orders of magnitude of normal stress and two orders of magnitude of specimen dimension.

We have only considered the effect of the physical characteristics of the frictional surface and the gouge layer on the magnitude of  $G$ . The composition and the thickness of the gouge layer can also affect the stress drop and the weakening displacement. Mineralogy and grain size of the country rock, temperature, and pore pressure may also be important. However, judging from the existing data, it seems unlikely that values of  $G$  determined in the kinds of setup currently in use in rock mechanics laboratory will be higher than the upper bound curve in Figure 11 by orders of magnitude.

Wong [1982] has compiled seismologically inferred values of  $G$  which were obtained by a variety of approaches. Except for anomalously low values which were evaluated using average stress drop and fault dimension inferred from corner frequency analysis [Husseini et al., 1976], all the estimates are of the order  $10^6$  J/m<sup>2</sup> and above. Similar results were recently obtained by Li and Rice [1983 in their study of rupture propagation of crustal scale earthquake instability and by Papageorgiou and Aki [1983] in their interpretation of strong motion data using a barrier model.

## 10 SHEAR FRACTURE ENERGY

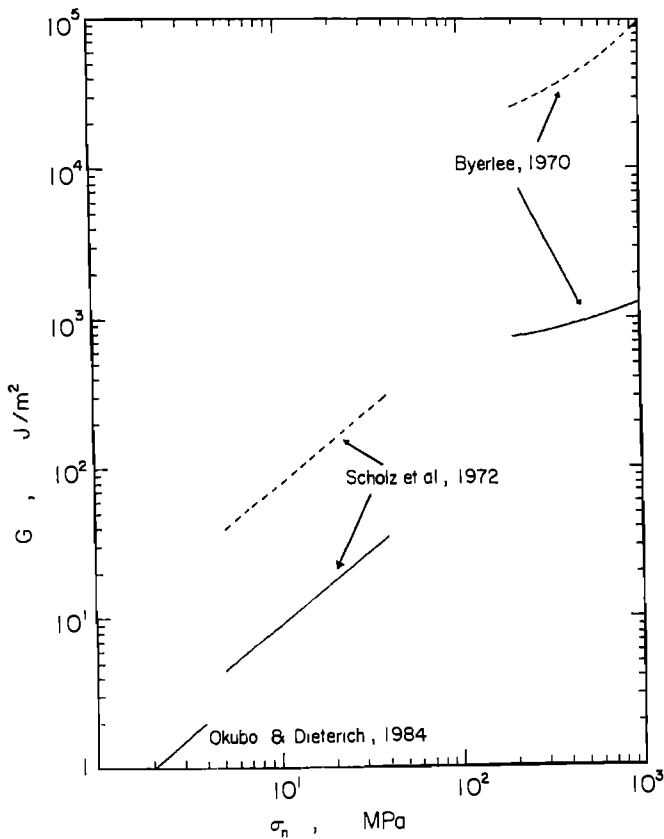


Fig. 11. Upper and lower bound on  $G$  for stick-slip instability in Westerly granite. The lower bound curves are calculated assuming a  $\langle \delta_{\text{nom}} \rangle$  value of 12.5  $\mu\text{m}$ . The upper bound curve in the intermediate normal stress range (corresponding to experiments of Scholz et al., 1972) is for  $\langle \delta_{\text{nom}} \rangle$  of 70  $\mu\text{m}$  and that in the high normal stress range (corresponding to Byerlee's [1970] experiment) is for  $\langle \delta_{\text{nom}} \rangle$  of 200  $\mu\text{m}$ . Okubo and Dieterich's [1984] measurements are also included for comparison.

Our analysis of the laboratory data above therefore indicates that experimentally determined values of  $G$  are lower than the seismologically inferred values. It is unlikely that laboratory measurements of the weakening slip will exceed hundreds of microns. There are, however, in-situ measurements on natural joints (of dimensions comparable to Okubo and Dieterich's [1984] apparatus) by Coulson [1972] and Pratt et al. [1974] which would indicate a  $\langle \delta_{\text{nom}} \rangle$  value of 2 to 5 mm. A number of recent reviews [Madariaga, 1983; Rice, 1983; Papageorgiou and Aki, 1983] have pointed out that the average weakening slip would have to be of the order of 10 cm or so to be agreeable with the seismological data.

There seem to be fundamental differences between geologic faults and sawcut surfaces prepared in the laboratory which result in a discrepancy of up to several orders of magnitude

in the weakening slip. Preliminary geometric arguments [e.g., Scholz and Aviles 1986] have been put forward to explain such a discrepancy. Further systematic in-situ tests on the frictional characteristics of 'natural' joints should also be useful in resolving this question.

Recent estimates of the 'local' stress drops [e.g., Aki, 1984; Boatwright, 1984] span over a narrow range of about 10 to 40 MPa. On the other hand, experimental measurements on sawcut samples tend to be somewhat higher and have more scatter. Not much has been done (in the laboratory or in-situ) to investigate systematically the effects of fault 'roughness' (whether it is due to the surface topography of the country rock or to the particle size distribution and thickness of the gouge layer) on the stress drop. Hence the coupling between the stress drop and the weakening slip is a question not well understood even in the laboratory context. These questions are of fundamental importance and deserve to be explored in more detail.

Acknowledgment. I am grateful to Jim Rice who kindly provided me with his unpublished analysis on the slip-weakening behavior in triaxial tests. I would like to thank Bill Brace for the use of his laboratory facilities. This research was supported by the National Science Foundation under grant EAR-8319914.

## References

- Aki, K. Characterization of barriers on an earthquake fault, *J. Geophys. Res.*, **84**, 6140-6148, 1979.
- Aki, K., Asperities, barriers, characteristic earthquakes and strong motion prediction, *J. Geophys. Res.*, **89**, 5867-5872, 1984.
- Andrews, D. J., Rupture propagation with finite stress in antiplane strain, *J. Geophys. Res.*, **81**, 3575-3582, 1976.
- Barenblatt, G. I., The mathematical theory of equilibrium cracks in brittle fracture, *Adv. Appl. Mech.*, **7**, 55-129, 1962.
- Bilby, B. A., A. H. Cottrell, and K. H. Swindon, The spread of plastic yield from a notch, *Proc. R. Soc. London, Ser. A* **272**, 304-314, 1963.
- Boatwright, J., Seismic estimates of stress release, *J. Geophys. Res.*, **89**, 6961-6968, 1984.
- Brace, W. F. and J. D. Byerlee, Stick-slip as a mechanism for earthquakes, *Science*, **153**, 990-992, 1966.
- Byerlee, J. D., Static and kinetic friction of granite at high normal stress, *Int. J. Rock Mech. Min. Sci.*, **7**, 577-582, 1970.
- Coulson, J. H., Shear strength of flat surfaces in rocks, *Proc. U.S. Symp. Rock. Mechanics*, **13**, 77-105, 1972.
- Day, S. M., Three-dimensional simulation of spontaneous rupture: the effect of nonuniform prestress, *Bull. Seismol. Soc. Am.*, **72**, 1881-1902, 1982.

- Dieterich, J. H., Experimental and model study of fault constitutive properties, in Solid Earth Geophysics and Geotechnology, AMD 42, edited by S. Nemat-Nasser, American Society Mechanical Engineers, NY., 1980.
- Dieterich, J. H., Constitutive properties of faults with simulated gouge, in Mechanical Behavior of Crustal Rocks edited by N. L. Carter, M. Friedman, J. M. Logan and D. W. Stearns, pp. 102-120, Monogr. Ser. monograph 24, AGU, Washington, D. C., 1981.
- Dugdale, D. S., Yielding of steel sheets containing slits, J. Mech. Phys. Solids, 8, 100-104, 1960.
- Hadley, K., Laboratory investigation of dilatancy and motion on fault surfaces at low confining pressures, in Proc. Conf. Tectonic Problems of the San Andraes Fault System edited by R. L. Kovach and A. Nur, pp. 427-435, 1973.
- Hoek, E., and E. T. Brown, Underground Excavation Engineering 527 pp, Institute of Mining and Metallurgy, London, 1980.
- Husseini, M. F., D. B. Jovanovich, M. J. Randall and L. B. Freund, The fracture energy of earthquakes, Geophys. J. R. Astron. Soc., 43, 367-385, 1975.
- Ida, Y., Cohesive force across the tip of a longitudinal shear crack and Griffith's specific surface energy, J. Geophys. Res., 77, 3796-3805, 1972.
- Li, V. C., and J. R. Rice, Preseismic rupture progression and great earthquake instabilities at plate boundaries, J. Geophys. Res., 88, 4231-4246, 1983.
- Madariaga, R., Earthquake source theory:a review, in Earthquakes: observation, theory and interpretation. edited by H. Kanamori and E. Boschi, pp. 1-44, North-Holland, Amsterdam, 1983.
- Mogi, K., Some precise measurements of fracture strength of rocks under uniform compressive stress, Felsmechanik und Ingen., 4, 41-55, 1966.
- Ohnaka, M., Experimental studies of stick-slip and their application to the earthquake source mechanism, J. Phys. Earth, 21, 285-303, 1973.
- Okubo, P. G., and J.H.Dieterich, Effects of physical fault properties on frictional instabilities produced on simulated faults, J. Geophys. Res., 89, 5817-5827, 1984.
- Okubo, P. G., and J. H. Dieterich, State variable fault constitutive relations for dynamic slip, this volume, 1986.
- Palmer A.C., and J.R.Rice, The growth of slip surfaces in the progressive failure of over-consolidated clay, Proc. R. Soc. London, Ser. A332, 527-548, 1973.
- Papageorgiou, A. S., and K. Aki, A specific barrier model for the quantitative description of inhomogeneous faulting and the prediction of strong ground motion, Bull. Seismol. Soc. Am., 73, 693-722, 1983.
- Pratt, H. R., A. D. Black, W. S. Brown, and W. F. Brace, A new technique for determining the deformation and frictional characteristics of in-situ rock, in Field Testing and Instrumentation of Rock, American Society for Testing and Materials, Philadelphia, Pa., STP 554, pp. 3-19, 1974.
- Rice, J. R., The mechanics of earthquake rupture, in Physics of the Earth's Interior edited by A. M. Dziewonski and E. Boschi, pp. 555-649, 1980.
- Rice, J. R., Constitutive relations for fault slip and earthquake instabilities, Pageoph, 121, 443-475, 1983.
- Rice, J. R., Shear instability in relation to the constitutive description of fault slip, in Rockbursts and Seismicity in Mines, edited by N. C. Gay and E. H. Wainwright, S. African Institute of Mining and Metallurgy, Johannesburg, pp. 57-62, 1984.
- Rudnicki, J. W., Fracture mechanics applied to the earth's crust, Ann. Rev. Earth Planet. Sci., 8, 489-525, 1980.
- Rummel, F., H. J. Alheid, and C. Frohn, Dilatancy and fracture-induced velocity changes in rock and their relation to frictional sliding, Pageoph, 116, 743-764, 1978.
- Scholz, C. H., and C. A. Aviles, The fractal geometry of faults and faulting, this volume, 1986.
- Scholz, C. H., P. Molnar, and T. Johnson, Detailed studies of frictional sliding of granite and implications for the earthquake mechanism, J. Geophys. Res., 77, 6392-6406, 1972.
- Stuart, W. D., and G. M. Mavko, Earthquake instability on a strike-slip fault, J. Geophys. Res., 84, 2153-2160, 1979.
- Wawersik, W. R., and W. F. Brace, Post-failure behavior of a granite and a diabase, Rock Mech., 3, 61-85, 1971.
- Wong, T.-f., Shear fracture energy of Westerly granite from post-failure behavior, J. Geophys. Res., 87, 990-1000, 1982.
- Wong, T.-f., and R. Biegel, Effects of pressure on the micromechanics of faulting in San Marcos gabbro, J. Structural Geol., 7, 737-749, 1985.

## DYNAMIC BREAKDOWN PROCESSES AND THE GENERATING MECHANISM FOR HIGH-FREQUENCY ELASTIC RADIATION DURING STICK-SLIP INSTABILITIES

Mitiyasu Ohnaka

Earthquake Research Institute, University of Tokyo, Bunkyo-ku, Tokyo 113

Yasuto Kuwahara, Kiyohiko Yamamoto, and Tomowo Hirasawa

Faculty of Science, Tohoku University, Sendai, Japan

**Abstract.** Local breakdown processes during stick-slip unstable shear failure have been examined to clarify the physical mechanism for generating high-frequency elastic radiation. Stick-slip was generated along a 40 cm long precut fault in Tsukuba granite samples using a servocontrolled biaxial loading apparatus. The displacement-time function or the slip velocity-time function depends upon an applied normal stress. The frequency content of the elastic waves depends on normal stress; higher-frequency components are generated during stick-slip failure at higher normal stress. A physical explanation for this is given in terms of asperities where sliding surfaces make contact. The cutoff frequency  $f_c$  originating from slip instability along the fault is related to  $v/\langle l_i \rangle$  ( $v$  rupture velocity,  $\langle l_i \rangle$  average distance between two adjacent asperities), and  $f_c$  can be estimated from the slip velocity power spectra. Interrelations between shear stress  $\tau$ , displacement and slip velocity  $V$  near a tip of the propagating slip zone were investigated to reveal dynamic breakdown processes, during which the strength can degrade regardless of  $V$ . Slip failure instability is promoted during the phase  $d\tau/dt < 0$  and  $dV/dt > 0$ , and stability during the phase  $dV/dt < 0$  regardless of  $d\tau/dt$ . At a high normal stress, a number of cycles of accelerating and decelerating phases are repeated during a slip failure, showing that the breakdown of local asperities on the slipping surfaces occurs successively during the slip failure.

### Introduction

It has been established that an earthquake source is a shear dislocation on the fault plane, and major earthquakes occur repeatedly along the same preexisting faults. This strongly suggests that stick-slip frictional instability is a plausible mechanism for shallow-focus earthquake failure [Brace and Byerlee, 1966]. Numerous studies have been conducted on various aspects of stick-slip frictional sliding [Scholz et al., 1972; Stesky et al., 1974;

Ohnaka, 1975; Scholz and Engelder, 1976; Dieterich, 1978, 1979; Okubo and Dieterich, 1981; Shimamoto and Logan, 1981a, b; Lockner and Okubo, 1983; Ohnaka et al., 1983], and in particular much attention has been focussed on studies of dynamic processes of stick-slip failure as seismic sources [Wu et al., 1972; Brune, 1973; Johnson et al., 1973; Ohnaka, 1973, 1978; Archuleta and Brune, 1975; Johnson and Scholz, 1976; Okubo and Dieterich, 1981, 1984].

In earthquake source failure, the fault strength must decrease with ongoing slip in the vicinity of the propagating tip of a slipping region [e.g. Rice, 1980]. In their stick-slip experiments, Okubo and Dieterich [1981] observed the degradation of the shear strength with ongoing slip near the tip of a propagating slip zone during stick-slip failure along a simulated fault in a large rock sample, and they showed, among other things, that the apparent fracture energy of stick-slip events increases with normal stress, and the critical slip-weakening displacement increases with increased roughness of slipping surfaces [Okubo and Dieterich, 1984]. This is basic information for understanding earthquake failure in terms of physics.

Stick-slip experiments in the laboratory can provide further basic physical information about the local breakdown process of earthquake failure. The generating mechanism for high-frequency seismic radiation has recently been of great concern among seismologists [e.g. Papageorgiou and Aki, 1983; Aki, 1984, 1986]. Dynamic breakdown processes during stick-slip unstable shear failure and the physical mechanism for generating high-frequency elastic radiation during the processes may give a clue to further understanding the mechanism for high-frequency seismic radiation from earthquake failure. We have been doing systematic experiments on stick-slip using large samples of granite (over four times larger than the breakdown zone size), and examined the dynamic breakdown process near a tip of the propagating slip zone and the subsequent slipping process during stick-slip instability on a simulated

## 14 DYNAMIC BREAKDOWN PROCESSES

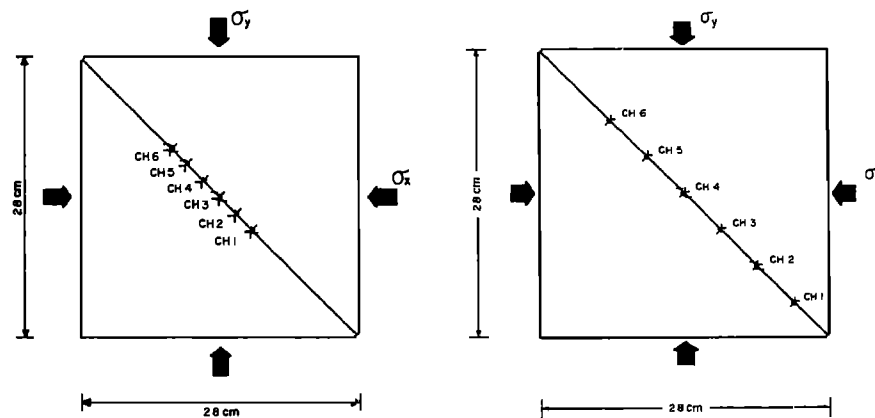


Fig. 1. Schematic diagrams showing sensor locations on the samples A (left) and B (right).

fault. In this paper, we first present our experimental data, and then discuss the breakdown process during a stick-slip failure and the generating mechanism for high-frequency elastic radiation from a physical viewpoint.

## Experimental Method

Stick-slip shear instability was generated along a simulated fault about 40 cm long in each of two samples (with different widths) of Tsukuba granite; one sample (A) has dimensions of 28 cm x 28 cm x 5 cm, and the other (B) 28 cm x 28 cm x 10 cm. Elastic wave velocities in this granite are  $v_p = 4.4$  km/s and  $v_s = 2.9$  km/s at room temperature and atmospheric pressure. The rigidity and Poisson's ratio of the granite are  $2 \times 10^4$  MPa and 0.12, respectively. The simulated fault in both samples is a through saw cut oriented at a 45° angle to the sides of the samples (cf. Figure 1). The length of simulated faults selected for the present studies is more than four times larger than the size (<10 cm) of the local breakdown zone where the shear strength degrades with ongoing slip. The breakdown zone size can be estimated both theoretically and experimentally, as will be shown later. The sliding surfaces and the sides of the samples were ground flat with a reciprocating surface grinder using a silicon carbide wheel, during which water was used to keep the surfaces cool. After cleaning and drying the samples, roughness and waviness of the sliding surfaces were measured with a profilometer. The maximum height roughness was of the order of 5  $\mu\text{m}$  for traverses about 2 cm long. Figure 2 shows a measured profile of slipping surfaces of sample A; note a cracklike shape of mating surfaces. This will result in a lower normal stress in central portion of the fault, which may be important in helping to confine slip initiation to interior of the block. A high-pass filtered (cutoff length 10 cm) output of waviness of lower slipping surface in Figure 2a is shown as an example in Figure 2b, where shorter wavelength components are accentuated.

A series of semiconductor strain gages (active

gage length 2 mm) were mounted at every 2.5 cm interval for sample A and 5 cm interval for sample B along each fault at positions 5 mm from the fault; matched gage pairs with mutually perpendicular orientations to monitor directly local shear strains (or stresses) parallel to the fault surface, gages oriented to monitor strains (or stresses) normal to the fault surface, and gages oriented to monitor longitudinal strains in the direction parallel to the fault. The high stiffness ( $5 \times 10^6$  N/cm) of the loading apparatus used enabled us to measure relative local displacements between two sides of the fault directly by metallic foil strain gages with the effective length of 2 mm (Figure 3).

Frequency characteristics of a strain gage sensor are determined from the frequency response of semiconductor or metal crystals, the cementing technique, and the relation between the gage length and the wavelength of signals. The theoretical limitation on the frequency response, say, of semiconductor crystals is on the order of 10<sup>5</sup> MHz or higher, and frequency range of signals of the present concern is less than 1 MHz; hence, there is no practical limitation on this. The cementing technique may be influential, and great care was taken to cement strain gages. Creep of  $\alpha$ -cyanoacrylate cement used is negligible. Thus, frequency

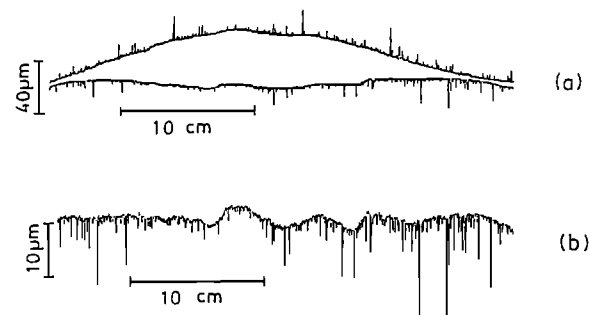


Fig. 2. (a) A profile of sliding surfaces (sample A). (b) A high-pass filtered output of waviness of sliding surface (cutoff length 10 cm).

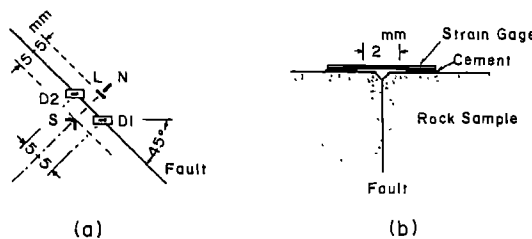


Fig. 3. (a) Schematic diagram showing the relation between semiconductor strain gages to monitor shear stress (S), normal stress (N), and longitudinal strain (L), and metallic foil strain gages to monitor relative displacement (D1, D2). (b) Schematic diagram of setup of strain gage sensor to monitor relative displacement.

characteristics  $f(\Delta X)$  of a strain gage sensor are practically determined only from the relation between the gage length and the wavelength of signals (Figure 4). The parameter  $\Delta X$  in Figure 4 is given in terms of the gage length  $L$ , the wavelength  $\lambda$  of signals as [Ohnaka et al., 1983]:

$$\Delta X = (L \cos \theta) / \lambda = (f L \cos \theta) / v \quad (1)$$

where  $\theta$  is the angle between the direction of the gage length and the direction of signal propagation,  $v$  the propagation velocity of the signal,  $f$  the frequency, and the signal has been assumed to be plane waves. In case the propagation direction of a signal is parallel to the direction of the gage length ( $\theta=0$ ), the frequency response is flat from DC to 450 kHz (0-1.4 dB) (Figure 4), if we assume  $v=3$  km/s and  $L=2$  mm.

Strain and displacement signals were amplified, filtered, and the resulting signals were A/D converted at a sampling rate of 1 MHz [resolution of 1/1024 (= about 0.1 %) for input-range full scale], and stored in digital buffer memories (memory length of 2048 words for each channel). The recording system was controlled by a computer (HP9826) through GP-IB interface bus (IEEE488\_1978 standard), and digital data transferred from the buffer memories were finally recorded on floppy discs. Overall response of the entire measuring and recording system was flat from DC to 200 kHz. Hence, recorded signals provide enough resolution for studies of the local breakdown process containing significantly high frequencies.

The experiments were conducted at normal stresses up to about 30 MPa and a constant strain rate of  $10^{-6}/\text{s}$ , using a servocontrolled biaxial loading apparatus. The press has a load capacity of  $4.9 \times 10^6$  N in the vertical direction and  $2.9 \times 10^6$  N in the lateral direction.

### Experimental Results

#### General

Figure 5 shows an example of original data on local shear stress and relative displacement signals

generated during a stick-slip shear failure on the fault in sample A at an average local normal stress of 2.33 MPa. Local normal stresses varied along the fault and they were lower at central portion of the fault than near both ends, as expected from the shape of mating surfaces of the sample. The slip velocity shown in the figure is the time derivative of the relative displacement smoothed by a simple moving average of 21 points. The shear stress was given by the shear strain multiplied by the rigidity of the granite sample used. The numbers of the left side of each figure give the transducer locations (Figure 1). The arrow marks in the figure indicate the time of onset of shear stress degradation, and both onset and termination of rapid drop in shear stresses. Figure 7a is the space-time view of the breakdown (or slip weakening) zone for the data shown in Figure 5. Stick-slip failure begins at a point A, from which the rupture propagates bilaterally toward both ends of the fault at an apparent velocity of a few hundreds m/s (no strain gage sensors were placed along the fault on the other side of the sample block to check orientation of 2-D rupture front). This is a nucleation process preceding unstable slip failure. Note that branching of the rupture propagation occurred at the point B, from which the rupture propagated at a high speed of about 2 km/s. There is a critical crack length  $L_c$  beyond which the energy released with further crack advance is greater than the fracture energy; with this energy surplus crack growth occurs dynamically [Andrews, 1976; Okubo and Dieterich, 1984]. This critical length  $L_c$  determined experimentally was about 10 cm (cf. Figure 7a).

Figure 6 shows an example of original data on local shear stress and relative displacement signals in the region where the rupture propagates steadily at the speed of about 2 km/s. The signals shown in Figure 6 were generated during a slip failure on the fault in sample A at an average normal stress of 6.48 MPa. The slip velocity in Figure 6 is the time derivative of the displacement smoothed by a moving average of 5 points. Rayleigh wave velocity  $v_R$  is theoretically given as  $v_R = 0.80v_s = 2.3$  km/s for the sample with Poisson's ratio of 0.12 and the shear wave velocity of 2.9 km/s. Thus, we find that the rupture velocity of about 2 km/s in the region of steady propagation is roughly equal to the

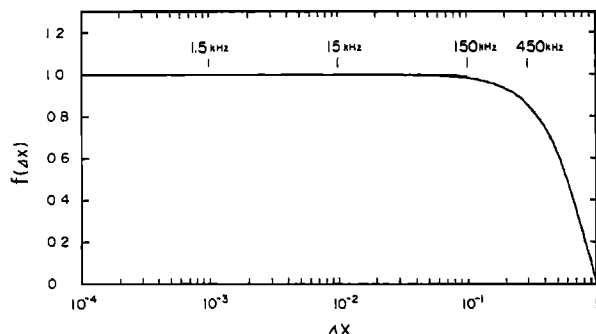


Fig. 4. Frequency response  $f(\Delta X)$  of a strain gage.

## 16 DYNAMIC BREAKDOWN PROCESSES

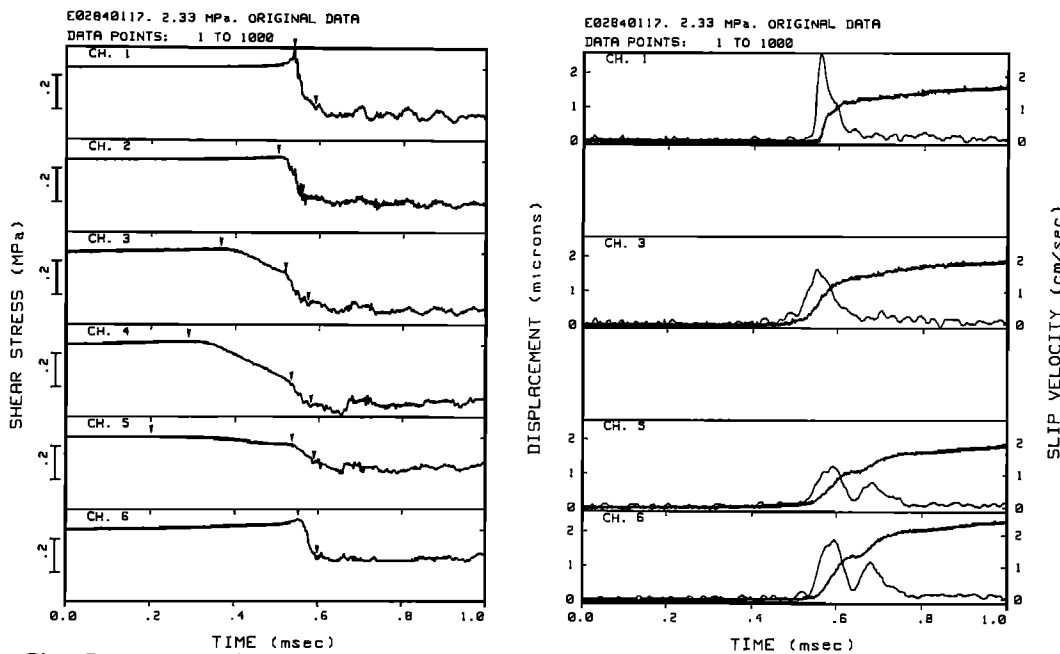


Fig. 5. An example of shear stress and displacement records in the region of failure nucleation (normal stress 2.33 MPa). The slip velocity is the time derivative of the displacement record.

Rayleigh wave velocity. Temporary stress drops ahead of permanent stress drop at the shear wave front appeared in the region of steady rupture propagation with the velocity of about 2 km/s. Propagation velocity of 2.8 km/s was obtained for

corresponding temporary stress drops connected by broken straight lines in the figure. This indicates that these temporary stress drops propagate at the shear wave velocity. Temporary stress drops at the shear wave front have been predicted theoretically

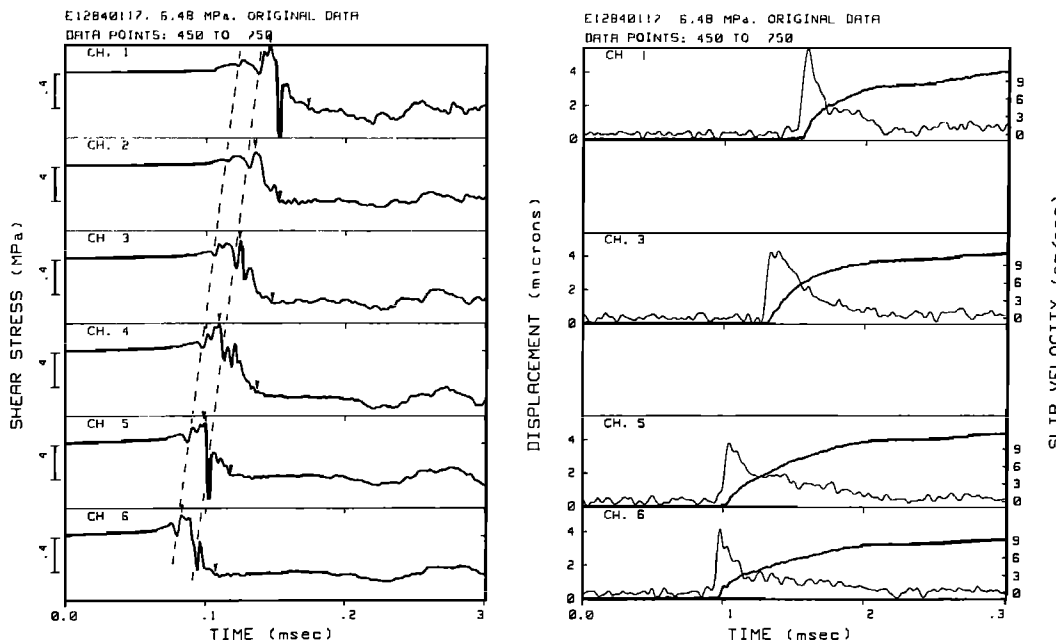


Fig. 6. An example of shear stress and displacement records in the region of steady rupture propagation (normal stress 6.48 MPa). The slip velocity is the time derivative of the displacement record.

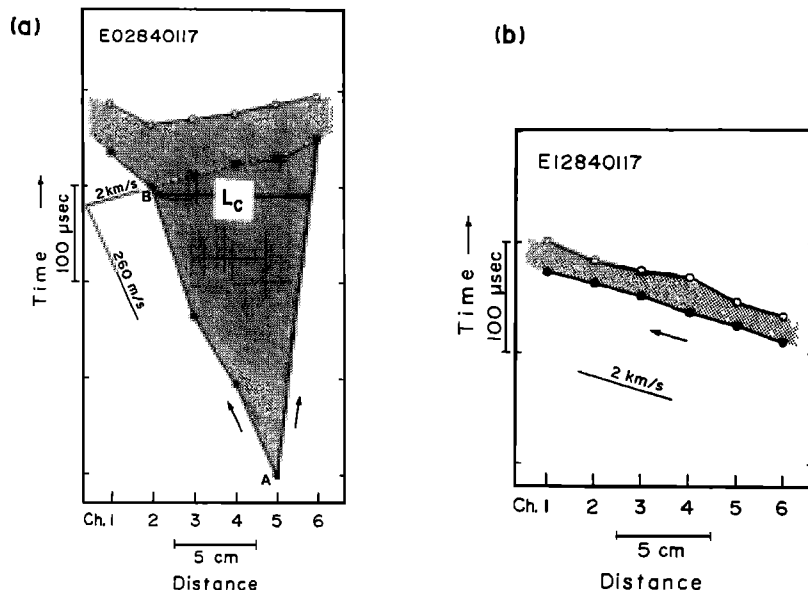


Fig. 7. (a) Space-time view of the breakdown zone in the nucleation region for the data shown in Figure 5. (b) Space-time view of the breakdown zone in the region of steady rupture propagation for the data shown in Figure 6. Black circles indicate the time when the shear stress takes a peak value on the verge of local slip failure at individual sensor locations, white circles indicate the time when the shear stress has just dropped to the sliding friction stress level, and triangles show the onset of rapid drop in shear stress due to branching of the rupture propagation. These correspond to the arrow marks in Figures 5 and 6.

by Andrews [1976], and our observation is experimental confirmation of his theoretical prediction. Figure 7b is the space-time view of the breakdown zone for the data shown in Figure 6. Dotted portions in Figure 7 indicate how the breakdown zone varies with time. The length of any straight line segment (parallel to the abscissa) touching both edges of the dotted portion in Figure 7b gives the breakdown zone size in the region of steady rupture propagation. Thus, we can experimentally evaluate the average size  $L$  of the breakdown zone and the time interval  $T$  required for the shear stress to drop, and from Figure 7b we have  $L = 5.3$  cm and  $T = 27 \mu\text{s}$  in the region of steady rupture propagation at the normal stress of 6.48 MPa. The size of the breakdown zone decreases with an increase in normal stress, and this has been pointed out by Okubo and Dieterich [1984]. The time interval  $T$  decreases with increasing rupture velocity [Ohnaka and Yamamoto, 1984].

#### Dynamic Breakdown and Sliding Processes

We focus attention on interrelations between shear stress, relative displacement, and slip velocity near a tip of the propagating slip zone to reveal dynamic breakdown and subsequent sliding processes. Figure 8 shows a typical example of the relation between shear stress, displacement, and slip velocity,

where the shear stress is normalized to the dynamic normal stress. The relation between shear stress and relative displacement is known as slip-weakening curve [Rice, 1980; Okubo and Dieterich, 1981, 1984]; the shear stress decreases with ongoing slip from the slip-failure peak stress to a residual sliding friction level near a tip of the slipping zone. In the region where rupture velocity is high, slip-weakening process is preceded by an increase in the shear stress ahead of a tip of the propagating rupture [Okubo and Dieterich, 1981, 1984]; however, there is no such stress increase in the nucleation region where the rupture is initiated. The critical energy release rate, or fracture energy, is estimated from the shear stress-displacement curve during slip-weakening process [Palmer and Rice, 1973; Rice, 1980]. The shear fracture energy estimated for the event shown in Figure 5 was  $6.2 \times 10^{-2} \text{ J/m}^2$  at the location CH5,  $12.8 \times 10^{-2} \text{ J/m}^2$  at CH3 and  $13.5 \times 10^{-2} \text{ J/m}^2$  at CH1. This indicates that the fracture energy is the lowest at a point of failure initiation, suggesting the general criterion for rupture initiation that the rupture begins at a point where the fracture energy is the lowest. This will be discussed further in detail in a later paper (Kuwahara et al., in preparation).

The relation between shear stress and slip velocity will be particularly important in understanding dynamic breakdown processes near a tip of the slipping zone during failure. In the breakdown and

## 18 DYNAMIC BREAKDOWN PROCESSES

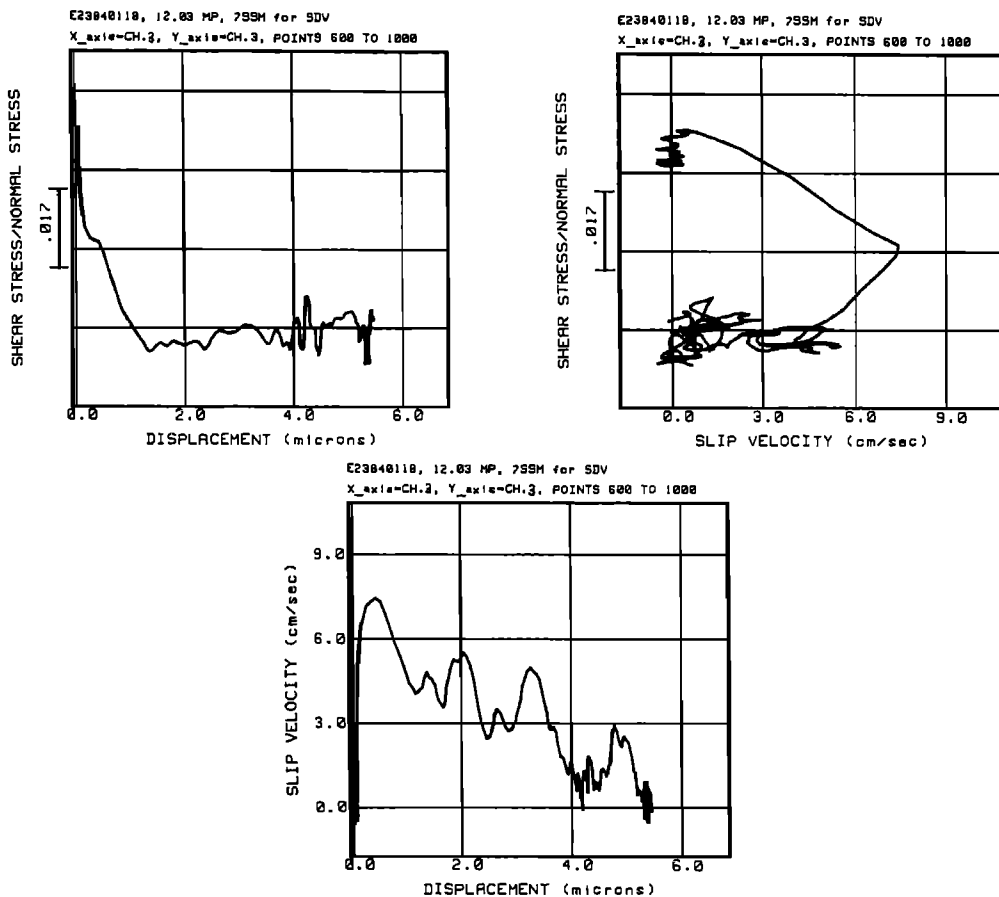


Fig. 8. A typical example of the relation between shear stress, displacement, and slip velocity. The shear stress is normalized to the dynamic normal stress.

subsequent sliding processes, in general, the shear stress drops from the peak stress (or the slip-failure strength) to a residual sliding friction level, while the slip velocity accelerates from zero to a maximum value, and finally decelerates to zero. Thus, the relation between shear stress and slip velocity is basically irreversible during one dynamic breakdown process, as shown in Figure 8. If the displacement  $U_v$  at which the slip velocity has a maximum value is smaller than the critical breakdown (or slip-weakening) displacement  $U_c$ , then the breakdown process is divided into accelerating and decelerating phases (Figure 8). If  $U_v \geq U_c$ , the breakdown process comprises only an accelerating phase, and subsequent decelerating phase is included in a residual frictional sliding process after breakdown. The slip velocity can have more than one maximum value during the entire breakdown and subsequent frictional sliding processes. Such a typical example is given in Figure 11, and in this case, more than one cycle of the accelerating and decelerating phases are repeated during the entire slipping process of one stick-slip event. This will be discussed later in relation to the mechanism for generating high-frequency elastic radiation.

#### High-Frequency Elastic Radiation

High-frequency elastic radiation from the fault rupture is directly related to the slip velocity-time function and the rupture velocity. Here, attention will be focussed on the effect of the slip velocity function. Figure 9a shows time-plots of local shear stress, longitudinal strain (in the direction parallel to the fault), and relative displacement data generated during a stick-slip failure along the fault in sample B at an average normal stress of 7.60 MPa, and these data were monitored at a location CH2 in the region of steady rupture propagation (rupture velocity being about 2 km/s). The slip velocity-time function (Figure 9a) is the time derivative of the displacement-time curve. Figure 9b shows similar data for a stick-slip event generated along the same fault at an average normal stress of 14.5 MPa, monitored at the same location CH2 during steady rupture propagation. Figure 9c indicates data for another event generated at an average higher normal stress of 19.1 MPa during steady rupture propagation (monitoring location being CH4 for this event). It is found from these figures that the displacement-time function or the slip velocity-time function

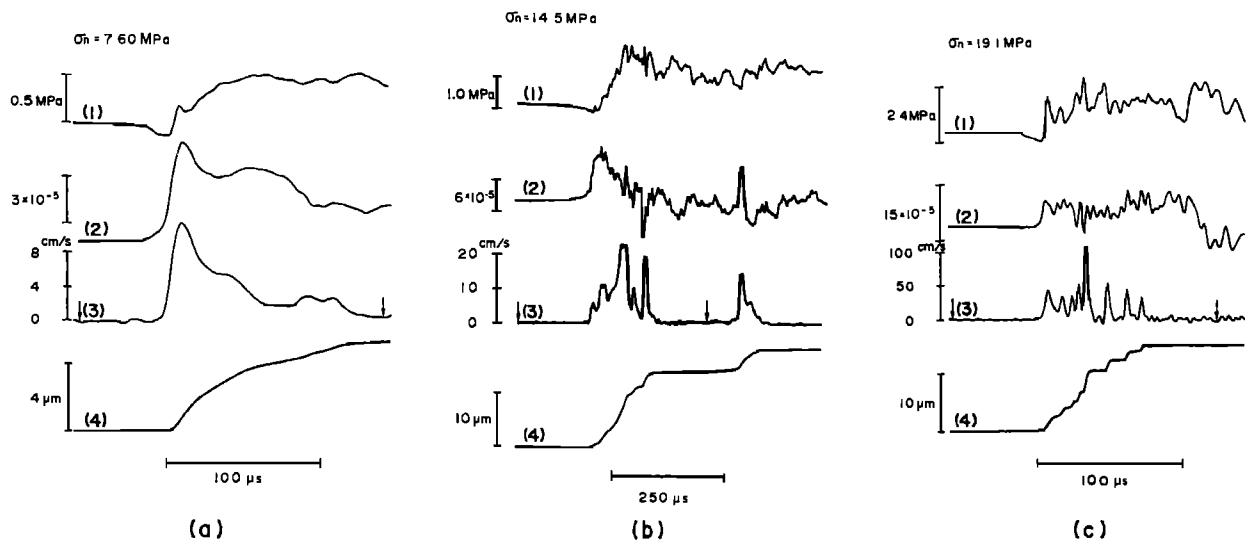
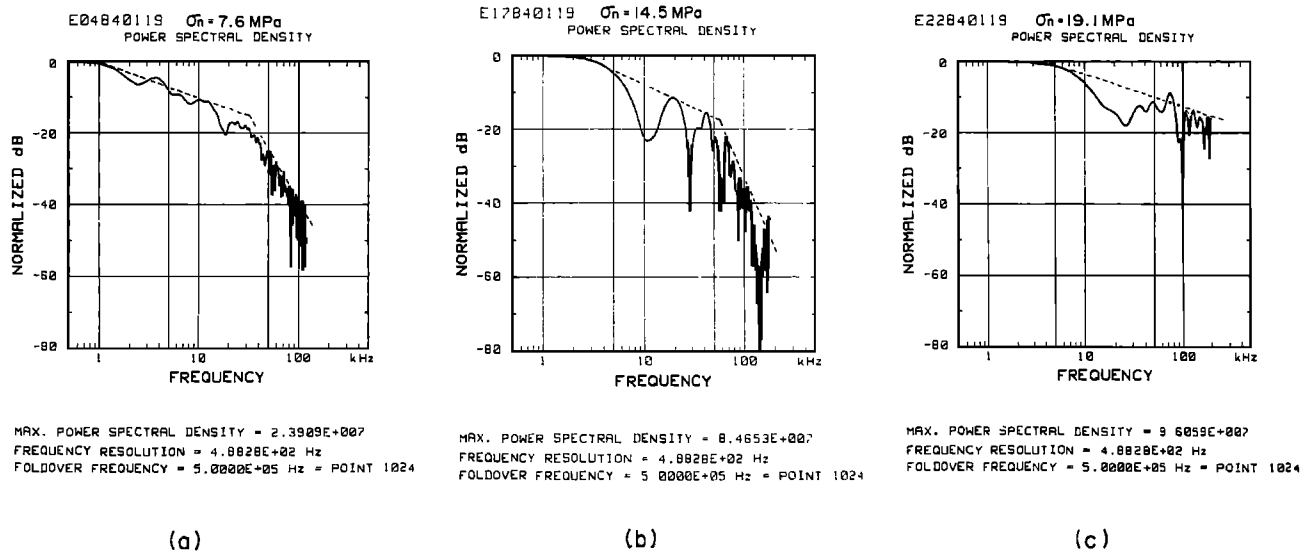


Fig. 9. (a) Shear stress (1), longitudinal strain (2), slip velocity (3) and displacement (4) records at the normal stress of 7.60 MPa (location CH2 in sample B). (b) Shear stress (1), longitudinal strain (2), slip velocity (3) and displacement (4) records at the normal stress of 14.5 MPa (location CH2 in sample B). (c) Shear stress (1), longitudinal strain (2), slip velocity (3) and displacement (4) records at the normal stress of 19.1 MPa (location CH4 in sample B).

depends upon an applied normal stress. At a low normal stress, the displacement-time curve is represented by rather single, smooth ramp form with a gradual increase in displacement at the termination of fault slip, and hence the slip velocity-time function is expressed by a gentle pulse form (Figure 9a). At a high normal stress, however, the displacement-time curve is an irregular superposition of subslip events, and the slip velocity function is expressed

by a sequence of clustered sharp pulses containing significantly high frequencies (Figure 9c). This shows that higher-frequency elastic waves are generated during a slip failure at a higher normal stress. A physical explanation for this will be given in the next section.

One may claim that the observed later pulses were due to reflections of elastic waves from the top and bottom free surfaces or from the sides of



Figs. 10. Power spectral densities of slip velocity function for the events shown in Figures 9a, b, and c, respectively.

## 20 DYNAMIC BREAKDOWN PROCESSES

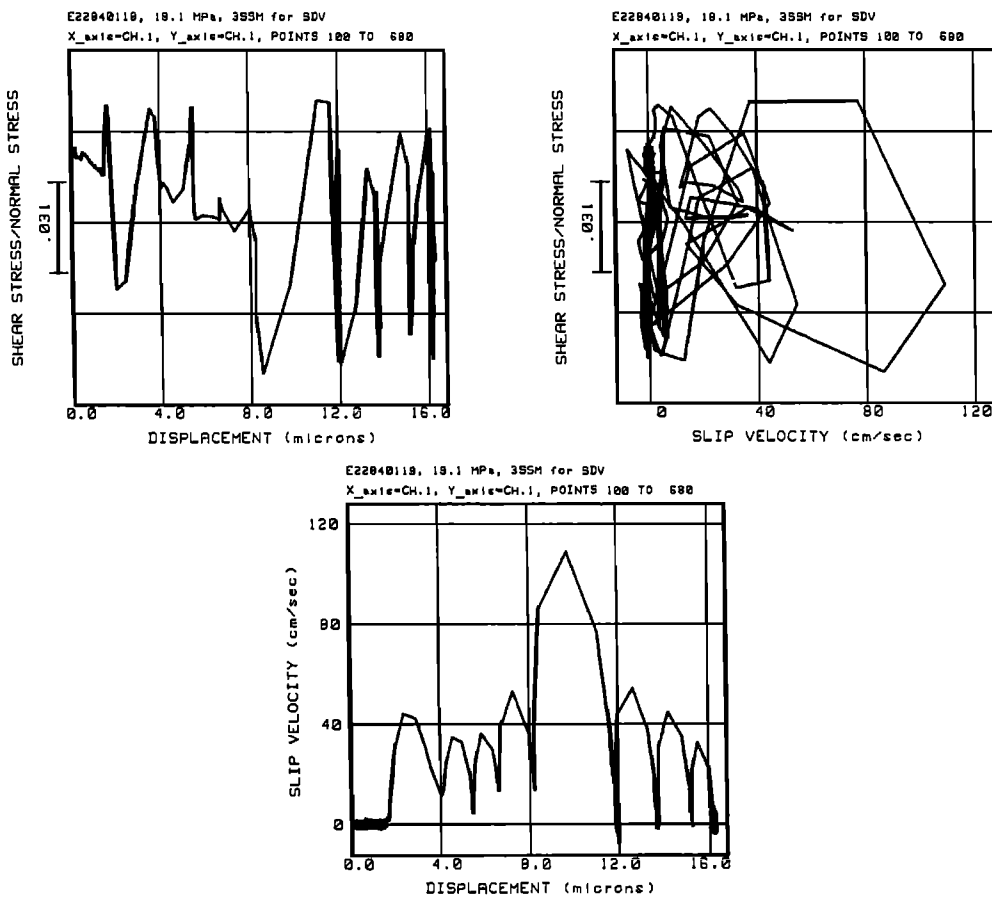


Fig. 11. Interrelation between shear stress, displacement, and slip velocity for the event shown in Figure 9c. The shear stress is normalized to the dynamic normal stress.

the sample. However, this is not the case. It is true that the reflected waves from the free surfaces or the sides of the sample are sensed by semiconductor strain gages with high sensitivity of  $10^{-6}$ , and these are observed as later phases of shear and longitudinal strain records (Figure 9). However, the displacement transducers, for which metal foil strain gages are used, do not have such high sensitivity as to sense the reflected elastic waves (strain sensitivity  $5 \times 10^{-5}$ ); they sense deformation only when local slip between the two blocks occurs at individual sensor locations, and remind that the slip velocity curves are the time derivative of those displacement records. If subslip is caused at displacement sensor locations by dynamic stress disturbances reflected from the top and bottom free surfaces or from the sides of the sample, then the resulting slip velocity pulse would appear in a later phase. However, the systematic difference in the three experiments at three different normal stresses (Figure 9) suggests that a sequence of clustered pulses in initial part of the slip velocity records are not due to reflections, but to fracture of local asperities.

Figures 10a, 10b, and 10c show power spectral

densities of the slip velocity-time curves shown in Figures 9a, 9b, and 9c, respectively (analyzed portions are indicated by arrows in each figure). The corner frequency  $f_o$ , found in each of Figures 10a, 10b, and 10c, was 1 kHz for the event at the average normal stress of 7.60 MPa, 2.5 kHz for the event at the normal stress of 14.5 MPa, and 4 kHz for the event at the normal stress of 19.1 MPa, and we find that  $f_o$  increases with an increase in normal stress. The corner frequency  $f_o$  corresponds to the overall time interval  $T_0(\sim 1/f_o)$  of a sequence of clustered pulses in the time domain. The higher corner frequency  $f_c$  gives the cutoff frequency of the power spectral density of the corresponding slip acceleration-time curve, and  $f_c$  in Figures 10a and 10b was found to be about 30 kHz for the event at the normal stress of 7.60 MPa, and 60 kHz for the event at the normal stress of 14.5 MPa. It is suggested from Figure 10c that  $f_c$  for the event at the normal stress of 19.1 MPa may be equal to 200 kHz or higher. Thus, it can be concluded that  $f_c$  also increases with an increase in normal stress. This is more clearly seen if we examine over wider range of the normal stress [Ohnaka et al., 1986]. In particular, if the average values of  $f_c$  determined

OHNAKA ET AL.

21

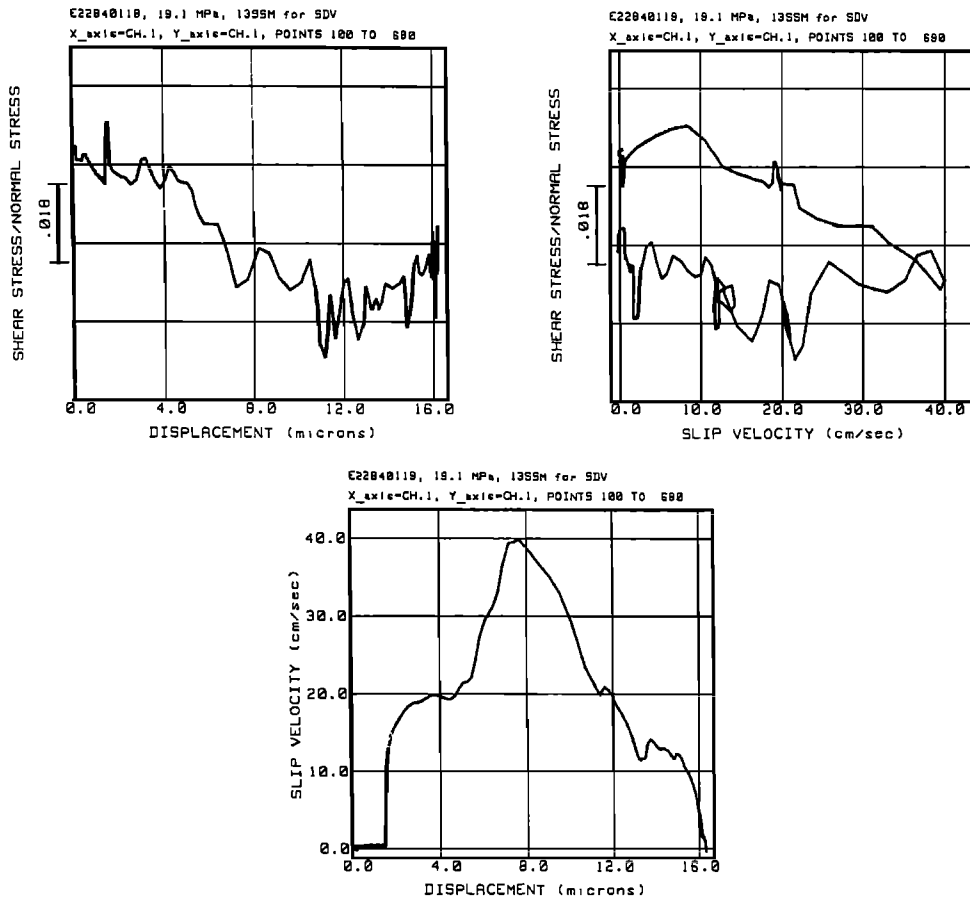


Fig. 12. Interrelation between shear stress, displacement, and slip velocity for a low-pass filtered output (cutoff frequency 30 kHz) of the data shown in Figure 11. The shear stress normal stress is normalized to the dynamic

from individual power spectral densities of local slip velocity-time records at different locations along the fault during a stick-slip failure are compared with the average local normal stresses, then we find that the average cutoff frequency is directly proportional to the average normal stress within the normal stress range less than 17 MPa [Ohnaka et al., 1986].

Figure 11 shows the interrelation between shear stress, slip velocity, and displacement for the data shown in Figure 9c. The relation between shear stress and slip velocity is so complicated in this case that it is difficult to discuss the dynamic breakdown process from the shear stress-slip velocity curve. We find for this event that the shear stress does not decrease monotonically with ongoing slip, but is a complicated function of the displacement. The slip velocity has multiple maximum values during slip, and many cycles of accelerating and decelerating phases are repeated. Note, however, that abrupt drops in shear stress concur with a rapid increase in slip velocity. This indicates that the breakdown of local asperities on the sliding surfaces occurs successively during the slipping process; in other words, (dynamic) friction can vary con-

siderably during slip, due to local asperities. The breakdown process for a stick-slip event at a high normal stress, thus, seems to be different from the process suggested by the simple slip-weakening instability model [Rice, 1980]. However, if high-frequency disturbances possibly caused by fracture of local asperities are neglected, the overall breakdown process conforms to the slip-weakening instability model. This is seen from Figure 12, showing the interrelation between shear stress, displacement, and slip velocity for a low-pass filtered output (cutoff frequency 30 kHz) of the data shown in Figure 11.

#### Discussion

In the foregoing section, we have evaluated from experimental data the size ( $L = 5.3$  cm) of breakdown zone during a stick-slip failure in the region of steady rupture propagation. The breakdown zone size may be estimated theoretically [Rice, 1980] as:

$$L = \frac{\pi}{4(1-\nu)} \frac{G U_c}{\Delta T} \quad (2)$$

## 22 DYNAMIC BREAKDOWN PROCESSES

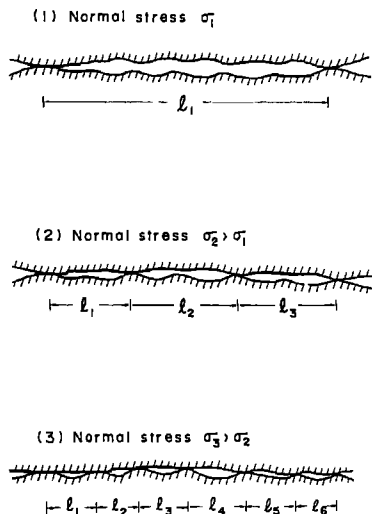


Fig. 13. Schematic representation of deformation of mating surfaces with increasing normal stresses.

where  $\nu$  is Poisson's ratio,  $G$  the rigidity, and  $\Delta T = T_p - T_f$  ( $T_p$  being the peak shear stress, and  $T_f$  the residual sliding friction stress). For the event shown in Figure 6,  $\Delta T/G = 38.6 \times 10^{-6}$  and  $U_c = 2 \mu\text{m}$  are estimated from the shear stress-displacement curves. Using these values, we have  $L = 4.6 \text{ cm}$  from equation (2), showing reasonable agreement between the experimental and theoretical estimates. The critical crack length  $L_c$  can also be estimated theoretically from the equation derived by Andrews [1976, p. 5680], and the theoretical estimate agrees with the experimental determination.

We have found that higher-frequency elastic wave components are generated during a stick-slip failure at a higher normal stress. The physical explanation for this can be given as follows. In general, the surface of a solid, even when best-prepared, is made up of asperities (for waviness on sliding surfaces of the sample used see Figure 2). When the two sliding surfaces of granite sample are pressed together, the sliding surfaces come into contact at these asperities. The strain distribution along the fault is prescribed by spatial distribution of the asperities that are in contact on the sliding surfaces. At a higher normal stress, larger deformation of the asperities that are in contact causes more asperities to get in contact, and this leads to a decrease in the average distance  $\langle l_i \rangle$  between two adjacent asperities (cf. Figure 13). This explains why the slip velocity function is expressed by a sequence of clustered sharp pulses at a high normal stress.

If gouge particles distribute over sliding surfaces and if the two surfaces get into contact at places where gouge particles exist, spatial distribution of the gouge particles will also prescribe the strain distribution. Hence, the discussion given above on the effect of asperities will also be applied for the effect of gouge particles.

We notice that initial part of the slip velocity

records is similar to that of the longitudinal strain records (cf. Figure 9). This similarity is expected if the rupture velocity is constant. When the rupture velocity  $v$  is constant, the slip velocity is directly proportional to longitudinal strain in the direction parallel to the fault. Let  $\langle T_c \rangle$  be the average time required for the rupture to propagate from one asperity to another adjacent asperity along the fault. The cutoff frequency  $f_c$  originating from asperity failures during a stick-slip instability may be given by

$$f_c = 1/\langle T_c \rangle = v/\langle l_i \rangle \quad (3)$$

As mentioned in the foregoing section, the average cutoff frequency was proportional to the average local normal stress within the lower normal stress range [Ohnaka et al., 1986]. Within that stress range, thus,  $\langle l_i \rangle$  varies inversely as the normal stress if the rupture velocity is constant. If we estimate  $\langle l_i \rangle$  from (3), we have  $\langle l_i \rangle = 6.6 \text{ cm}$  for the event shown in Figure 9a and  $\langle l_i \rangle = 3.3 \text{ cm}$  for the event in Figure 9b under the assumption of  $v = 2 \text{ km/s}$ . The rupture velocity for the event shown in Figure 9c was as high as  $4 \text{ km/s}$ , and hence we have  $\langle l_i \rangle \leq 2 \text{ cm}$  for this event by assuming that  $v = 4 \text{ km/s}$ .

We discuss below the breakdown (or weakening) and restrengthening (or healing) processes of stick-slip in terms of the shear stress  $T$  and the slip velocity  $V$ . If  $dT/dt < 0$  and  $dV/dt > 0$  during the entire breakdown process, slip failure instability is promoted during the process, and the slip movement is stabilized by subsequent sliding friction process during which  $dV/dt < 0$  and  $dT/dt = 0$ . One may argue that the irreversible relation between shear stress and slip velocity during the breakdown process can be explained by assuming that instantaneous strength (or shear resistance) of the slipping surface degrades irreversibly with an increase in slip velocity, or alternatively assuming that instantaneous condition of the slipping surface is prescribed by the slip velocity. As shown in the foregoing section, however, the breakdown process itself is divided into accelerating and decelerating phases in some stick-slip events. In this case, there is a phase where  $dV/dt < 0$  despite the fact that  $dT/dt < 0$ ; that is, the slip movement is decelerated in spite of strength degradation. In other words, the strength (or shear resistance) can degrade regardless of the slip velocity.

Slip instability and stability may be discussed in terms of  $T$  and  $V$ . In general, when  $V > 0$ , there are four possible phases during the entire breakdown and subsequent sliding friction processes for one stick-slip. Phase I is characterized by the strength degradation ( $dT/dt < 0$ ) and slip acceleration ( $dV/dt > 0$ ), II by  $dT/dt > 0$  and  $dV/dt > 0$ , III by  $dT/dt < 0$  and  $dV/dt < 0$ , and IV by  $dT/dt > 0$  and  $dV/dt < 0$ . Slip failure instability is promoted during phase I; stability is promoted during phases III and IV. Phase II can be observed in the initial process of slip instability, and such examples will be seen in

Figures 5 and 6 in our companion paper [1986]. Needless to say, actual breakdown and subsequent sliding processes during a slip failure may not necessarily comprise all these phases. Rice and Gu [1983] and Gu et al. [1984] have theoretically discussed these phases on the  $\tau$ - $V$  plane on the basis of a specific rate and evolving state constitutive description for frictional slip. When  $V = 0$ , mating surfaces are sticking to each other, and hence the shear strength along the fault increases or decreases along the  $\tau$ -axis on the  $\tau$ - $V$  plane according to an increase or decrease in normal stress. If an applied normal stress is raised, the shear strength increases; this is a restrengthening process during a stick period. In general, however, the restrengthening (or healing) is possible even at a constant normal stress [e.g. Dieterich, 1972, 1979; Ruina, 1983].

We have examined the relations between shear stress, slip velocity, and displacement near a tip of the propagating slipping zone during a stick-slip failure along simulated faults to reveal the local dynamic breakdown process and the mechanism for generating high-frequency elastic radiation. The finding and discussions given here may be useful in understanding the failure process of earthquake sources and the mechanism for generating high-frequency seismic radiation.

**Acknowledgment.** This work was subsidized in part by the Ministry of Education, Science and Culture of Japan (Project Number, 56020007).

#### References

- Aki, K., Asperities, barriers, characteristic earthquakes and strong motion prediction, *J. Geophys. Res.*, **89**, 5867-5872, 1984.
- Aki, K., Origin of  $f_{\max}$ , this issue, 1986.
- Andrews, D. J., Rupture velocity of plane strain shear cracks, *J. Geophys. Res.*, **81**, 5679-5687, 1976.
- Archuleta, R. J., and J. N. Brune, Surface strong motion associated with a stick-slip event in a foam rubber model of earthquakes, *Bull. Seismol. Soc. Am.*, **65**, 1059-1071, 1975.
- Brace, W. F., and J. D. Byerlee, Stick-slip as a mechanism for earthquakes, *Science*, **153**, 990-992, 1966.
- Brune, J. N., Earthquake modeling by stick-slip along precut surfaces in stressed foam rubber, *Bull. Seismol. Soc. Am.*, **63**, 2105-2119, 1973.
- Dieterich, J. H., Time-dependent friction in rocks, *J. Geophys. Res.*, **77**, 3690-3697, 1972.
- Dieterich, J. H., Preseismic fault slip and earthquake prediction, *J. Geophys. Res.*, **83**, 3940-3948, 1978.
- Dieterich, J. H., Modeling of rock friction. 1. Experimental results and constitutive equations, *J. Geophys. Res.*, **84**, 2161-2168, 1979.
- Gu, J.-C., J. R. Rice, A. L. Ruina, and S. T. Tse, Slip motion and stability of a single degree of freedom elastic system with rate and state dependent friction, *J. Mech. Phys. Solids*, **32**, 167-196, 1984.
- Johnson, T. L., and C. H. Scholz, Dynamic properties of stick-slip friction of rock, *J. Geophys. Res.*, **81**, 881-888, 1976.
- Johnson, T., F. T. Wu, and C. H. Scholz, Source parameters for stick-slip and for earthquakes, *Science*, **179**, 278-280, 1973.
- Lockner, D. A., and P. G. Okubo, Measurements of frictional heating in granite, *J. Geophys. Res.*, **88**, 4313-4320, 1983.
- Ohnaka, M., Experimental studies of stick-slip and their application to the earthquake source mechanism, *J. Phys. Earth*, **21**, 285-303, 1973.
- Ohnaka, M., Frictional characteristics of typical rocks, *J. Phys. Earth*, **23**, 87-112, 1975.
- Ohnaka, M., Application of some dynamic properties of stick-slip to earthquakes, *Geophys. J. R. Astron. Soc.*, **53**, 311-318, 1978.
- Ohnaka, M., and K. Yamamoto, Experimental studies of failure nucleation and propagation along simulated faults in rock. *Study on Short-Period Behavior in Fault Motion and Estimation of Input Seismic Motion* (in Japanese), Final Technical Report (Organizer R. Sato), No. A-59-3, pp. 11-46, 1984.
- Ohnaka, M., K. Yamamoto, Y. Kuwahara, and T. Hirasawa, Dynamic processes during slip of stick-slip as an earthquake fault model, *J. Seismol. Soc. Jpn.*, **36**, 53-62, 1983.
- Ohnaka, M., Y. Kuwahara, and K. Yamamoto, Constitutive relations between dynamic physical parameters near a tip of the propagating slip zone during stick-slip unstable shear failure, *Tectonophysics* (Special Issue on Earthquake Faulting), in press, 1986.
- Okubo, P. G., and J. H. Dieterich, Fracture energy of stick-slip events in a large scale biaxial experiment, *Geophys. Res. Lett.*, **8**, 887-890, 1981.
- Okubo, P. G., and J. H. Dieterich, Effects of physical fault properties on simulated faults, *J. Geophys. Res.*, **89**, 5817-5827, 1984.
- Palmer, A. C., and J. R. Rice, The growth of slip surfaces in the progressive failure of over-consolidated clay, *Proc. R. Soc. London, Ser. A.*, **332**, 527-548, 1973.
- Papageorgiou, A. S., and K. Aki, A specific barrier model for the quantitative description of inhomogeneous faulting and the prediction of strong ground motion. I. Description of the model, *Bull. Seismol. Soc. Am.*, **73**, 693-722, 1983.
- Rice, J. R., The mechanics of earthquake rupture, *Physics of the Earth's Interior, Proc. Int. Sch. Phys. Enrico Fermi*, pp. 555-649, North-Holland, Amsterdam, 1980.
- Rice, J. R., and J.-C. Gu, Earthquake aftereffects and triggered seismic phenomena, *Pure Appl. Geophys.*, **121**, 187-219, 1983.
- Ruina, A., Slip instability and state variable friction laws, *J. Geophys. Res.*, **88**, 10359-10370, 1983.
- Scholz, C. H., and J. T. Engelder, The role of asperity indentation and ploughing in rock friction-I. Asperity creep and stick-slip, *Int. J. Rock Mech. Min. Sci.*, **13**, 149-154, 1976.
- Scholz, C., P. Molnar, and T. Johnson, Detailed

## 24 DYNAMIC BREAKDOWN PROCESSES

- studies of frictional sliding of granite and implications for the earthquake mechanism, *J. Geophys. Res.*, 77, 6392-6406, 1972.
- Shimamoto, T., and J. M. Logan, Effects of simulated fault gouge on the sliding behavior of Tennessee sandstone: nonclay gouges, *J. Geophys. Res.*, 86, 2902-2914, 1981a.
- Shimamoto, T., and J. M. Logan, Effects of simulated clay gouges on the sliding behavior of Tennessee sandstone, *Tectonophysics*, 75, 243-255, 1981b.
- Stesky, R. M., W. F. Brace, D. K. Riley, and P.-Y. F. Robin, Friction in faulted rock at high temperature and pressure, *Tectonophysics*, 23, 177-203, 1974.
- Wu, F. T., K. C. Thomson, and H. Kuenzler, Stick-slip propagation velocity and seismic source mechanism, *Bull. Seismol. Soc. Am.*, 62, 1621-1628, 1972.

## STATE VARIABLE FAULT CONSTITUTIVE RELATIONS FOR DYNAMIC SLIP

Paul G. Okubo<sup>1</sup> and James H. Dieterich

U.S. Geological Survey, Menlo Park, California 94025

**Abstract.** Laboratory observations of quasistatic rock-on-rock frictional sliding have led to the development of fault constitutive relations which incorporate effects of slip rate and slip history, or state, on frictional resistance. These friction models can be constructed to predict sliding behavior which resembles slip weakening. Local, high-frequency records of fault displacements and shear stresses have been recorded during stick-slip failures on a simulated fault in a block of Sierra granite. These observations suggest that, despite the vastly different slip conditions which characterize quasistatic sliding and stick-slip, the same constitutive friction models might also adequately describe the frictional response of the simulated fault under dynamic, seismogenic slip conditions. The maximum observed slip speeds during stick-slip are roughly three or four orders of magnitude larger than speeds used in quasistatic tests. In addition, the velocity jumps observed during stick-slip are as much as six orders of magnitude larger than those which typify the quasistatic tests. Fault behavior which is slip weakening-like in appearance is observed during stick-slip. Immediately prior to the onset of stick-slip sliding, rapid increases in local shear stresses, from initial shear stress levels to peak shear stress levels, are observed. Following the onset of stick-slip sliding, shear stresses on the fault rapidly decrease from their peak levels to lower residual sliding stress levels. In general, the stress drops observed during stick-slip are approximately 10% of the average applied shear stresses. Stress changes are compared to calculations based on two specific constitutive friction models which are interchangeable at low slip rates but predict markedly different results for high rates of slip. Both quasistatic and dynamic fault slip behavior are accounted for by the rate- and state-dependent friction model, but the stick-slip data suggest that an appropriate fault constitutive relation must admit high-speed cutoffs to the velocity-dependent effects. The cutoffs impose bounds on the changes in fault frictional strength during unstable slip, with limiting shear stresses determined by normal

stress and fault loading history as well as friction model parameters. Finally, the existence of these cutoffs implies that fault weakening at the onset of stick-slip is essentially slip rate-independent so that the process resembles slip weakening.

## Introduction

Using the concept of a crack-tip cohesive zone introduced by Barenblatt [1959] for tensile cracks, Ida [1972] proposed that earthquake sources be modeled as dynamically supported shear cracks governed by a fault slip-weakening constitutive model. Ida [1972] notes that this modeling approach allows the use of physically motivated failure criteria for determining details related to the growth of the fault rupture surface without requiring that a priori assumptions with regard to the rupture history be made. Cohesive zone models are free of the problem of crack-tip stress singularities which characterize elastic-brittle crack solutions. Furthermore, Ida [1973] has used the slip weakening-type of cohesive zone model to determine seismic ground motion parameters and to demonstrate the effects of fault model parameters on ground motion.

Slip-weakening modeling has been extended to investigate shear rupture propagation behavior in 2-D [Andrews, 1976] and 3-D [Day, 1982] dynamic crack simulations using simple linear slip-weakening constitutive models for fault response in finite difference calculations. In particular, Day [1982] has investigated the effects of a non-uniform pre-stress distribution on the speed of rupture growth. Simulations of rupture processes based on specified rupture speeds clearly would not exhibit the effects of pre-stress on rupture velocity.

Advances in seismic strong ground motion recording capabilities have increasingly emphasized the importance of dynamic shear crack modeling. Archuleta [1984] used a kinematic forward modeling method to match details of the recorded strong ground motions from the 1979 Imperial Valley, California earthquake. He inferred a strong correlation between fault slip rate and fault rupture velocity as well as locally supersonic rupture extension. His modeling effort was not based on a dynamic crack formulation, but his results, including the possibility of supporting locally supersonic velocity depending on the distribution of fault

<sup>1</sup>also formerly at Department of Earth, Atmospheric and Planetary Sciences, Massachusetts Institute of Technology, Cambridge, Massachusetts 02139

## 26 STATE VARIABLE FAULT RELATIONS

prestress, are in qualitative agreement with Day's theoretical results for fully spontaneous dynamic shear crack propagation along a slip-weakening fault.

It has been previously noted, for example, by Dieterich [1979a] and Rice [1983], that fault constitutive relations of a slip weakening-type are not fully appropriate for characterizing repeated seismic slip along a given fault segment because no provision is made for restrengthening. Thus, seismicity would ultimately be expected to cease or give way to quasistatic fault slip as a means for accommodating fault motion. In addition, slip weakening models do not account for experimental observations of velocity-dependent frictional sliding behavior. Constitutive relations which incorporate rate- and state-dependent friction have been developed to overcome these limitations [Dieterich, 1978, 1979a, 1981; Ruina, 1983]. It has been demonstrated that the constitutive laws predict a wide range of frictional sliding behavior as well as describe laboratory observations of quasistatic sliding [e.g., Dieterich, 1979a, b, 1980, 1981; Ruina, 1983; Gu et al., 1984; Tullis and Weeks, unpublished manuscript, 1985].

In an earlier work [Okubo and Dieterich, 1984], we reported the occurrence of slip weakening-like behavior at the onset of stick-slip sliding. That behavior was found to be similar to that observed for quasistatic sliding when slip rate along the simulated fault is suddenly increased. Insofar as these observations are obtained on similarly prepared simulated fault surfaces, it might be expected that similar constitutive relations could be used for both quasistatic sliding and stick-slip sliding. In this report, following a discussion of rate- and state-dependent friction models, we explore this possibility by comparing model calculations based on two specific forms of the state variable friction law to stick-slip data.

#### State Variable Friction Models

Rate- and state-dependent rock friction models were developed to account for details of laboratory-observed quasistatic slip along simulated fault surfaces. Their development can be traced through Dieterich [1972, 1978, 1979a, 1981] and Ruina [1983]. The essential elements of the state variable rock friction model for sliding under constant normal stress are:

- (i) A direct velocity effect. When a sudden change in fault slip rate  $V$  is introduced, the frictional resistance changes in the same sense as that of the change in slip rate. That is, suddenly imposed increases in slip rate result in sudden increases in friction. Likewise, sudden decreases in slip rate are accompanied by sudden decreases in frictional resistance.
- (ii) A steady-state effect. For sliding at constant slip rate, friction tends toward a steady-state value which depends on that slip rate.
- (iii) Characteristic slip distances. The evolution of friction toward the steady-state value at a given slip rate is

controlled by an exponential decay over a characteristic or critical displacement. This critical displacement is related to fault roughness and is apparently insensitive to slip rate and normal stress.

The formulation for coefficient of friction  $\mu$  proposed by Dieterich [1979a] to account for these observed effects in the quasistatic experiments is:

$$\mu = C/F \quad (1)$$

where

$$C = c_1 + c_2 \log_{10}(c_3 \theta + 1)$$

and

$$F = f_1 + f_2 \log_{10}(f_3/V + 1) .$$

Coefficients  $c_1$ ,  $c_2$ ,  $c_3$ ,  $f_1$ ,  $f_2$ , and  $f_3$  are empirically determined constants. The empirical formulations for the evolution of the state variable  $\theta$ , typically contain an exponential decay of  $\theta$  as a function of fault slip.

Ruina [1983] elaborated on the interpretation of  $\theta$  as a state variable and proposed a simpler form for  $\mu$ . While Dieterich [1981] attempted to identify the variable  $\theta$  which appears in his formulation as an effective lifetime of contacting asperities, Ruina [1983] suggests that state variables need not be identified with specific physical quantities. From this perspective, the rate- and state-dependent friction models are viewed as phenomenological descriptions of the frictional sliding process and specific formulations can be adopted in order to closely match experimental observations. In order to account for his own experimental observations of quasistatic sliding [Ruina, 1983] and, later, to serve as a starting point for the analysis of the stability of a sliding system governed by a state variable friction law [e.g., Gu et al., 1984], Ruina proposed the following simplified form of the friction law proposed by Dieterich:

$$\mu = \mu_0 + A \ln(V/V^*) + \Theta \quad (2)$$

where we have normalized the terms in this relation by normal stress  $\sigma$ . The parameters  $\mu_0$  and  $A$  are empirical constants and  $\mu_0$  may be regarded as a nominal value of friction. Ruina's state variable is  $\Theta$  and  $V^*$  is an arbitrary reference slip rate. In this form, the evolution of  $\mu$  is separated from the direct velocity effect.

For the low slip rates which are characteristic of the quasistatic sliding experiments, the reduction of (1) to (2) is straightforward, but we present it in some detail here in order to clearly establish the relationship between these two formulations and to indicate how they would predict different behavior at high slip rates which are achieved during stick-slip. This is apparently the same reduction used by Mavko [unpublished manuscript, 1983] who assigned values to the parameters in (2) based on the empirically determined values presented in Dieterich [1981]

OKUBO AND DIETERICH 27

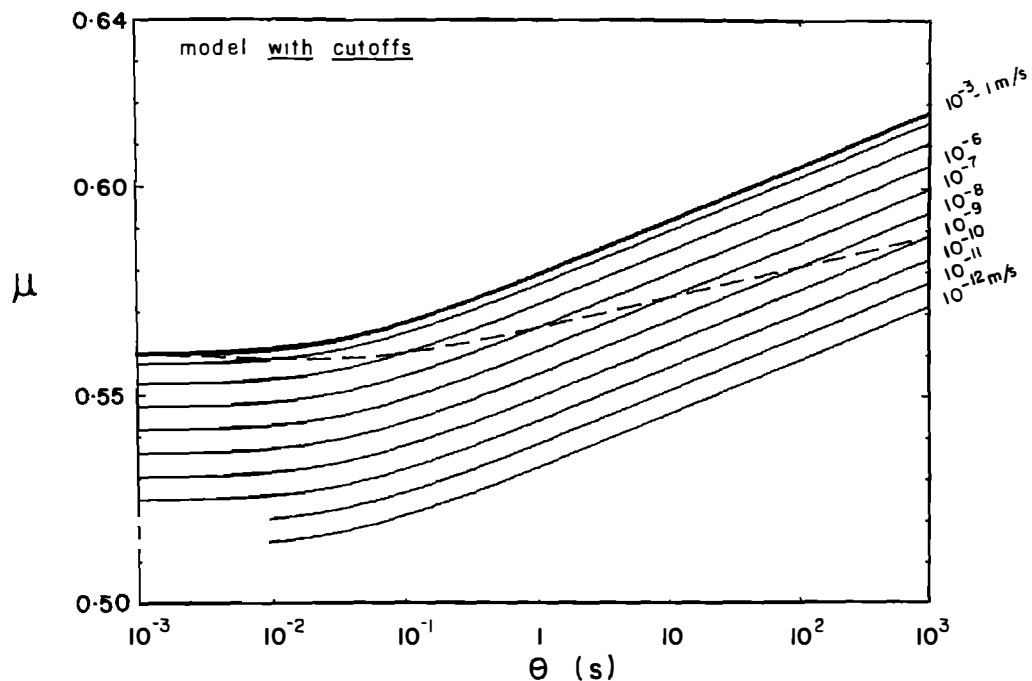


Fig. 1a.

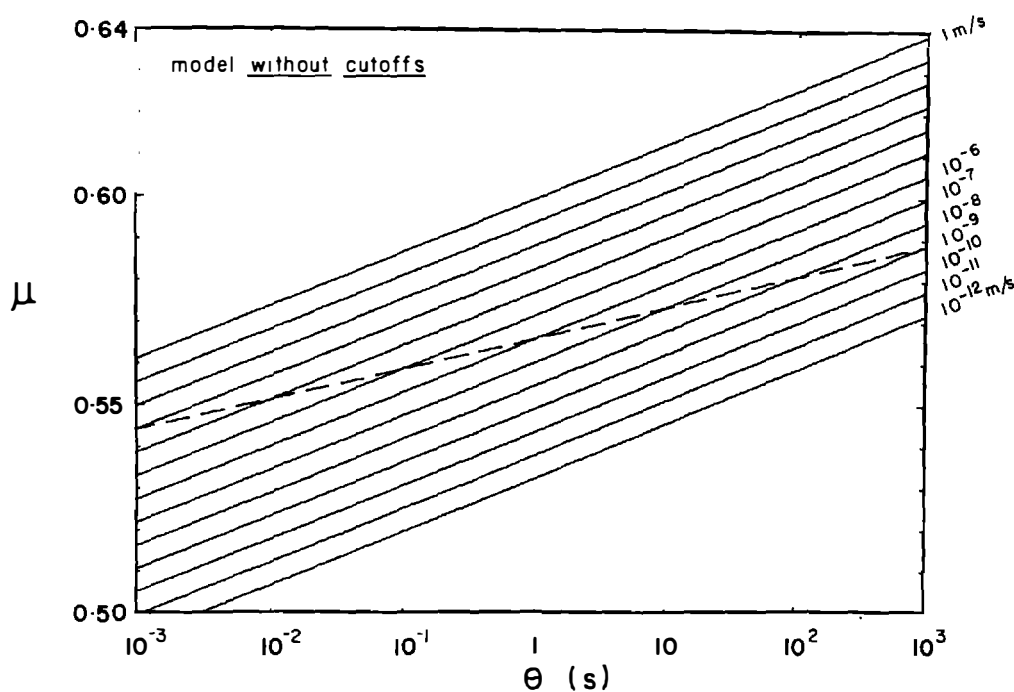


Fig. 1b.

Fig. 1. Calculated values of  $\mu$  as a function of  $\theta$  for different values of slip velocity.  $c_1 = 0.56$ ,  $c_2 = 0.013$ ,  $c_3 = 30/\text{s}$ ,  $f_1 = 1.0$ ,  $f_2 = 0.01$ ,  $f_3 = 200 \mu\text{m/s}$ . (a)  $\mu$  calculated from equation (6a), the friction model with cutoffs. (b)  $\mu$  calculated from equation (6b), the friction model without cutoffs. Dashed lines represent steady-state values of  $\mu$  where  $V = d_c/\theta$ .

## 28 STATE VARIABLE FAULT RELATIONS

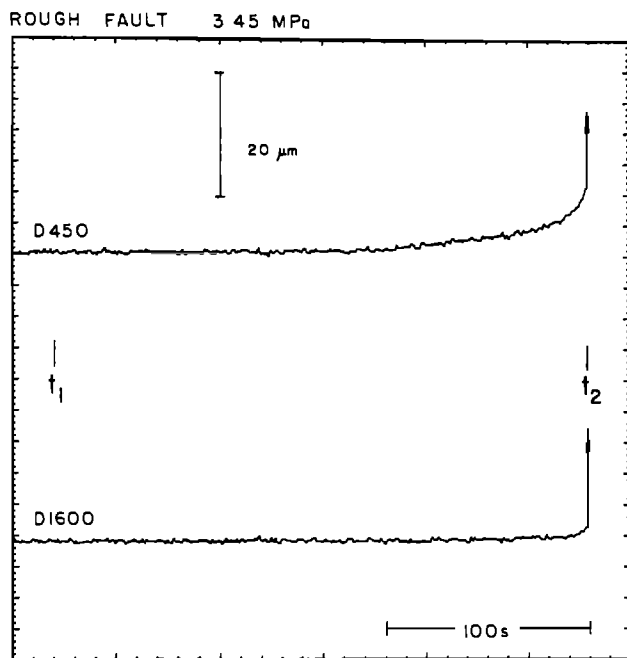


Fig. 2a.

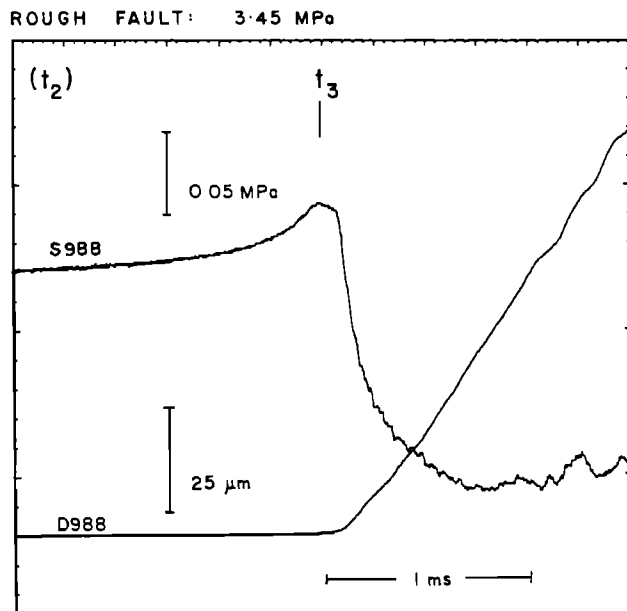


Fig. 2b.

Fig. 2. (a) Plots of quasistatic fault displacement history for stick-slip. (b) High-frequency shear stress and fault displacement. Times  $t_1$ ,  $t_2$ , and  $t_3$  signifying stages in the analysis are indicated in the figure.

and used a friction model of the same form as (2) for a large-scale simulation of fault creep.

In reference to the parameters appearing in (1), it is generally observed [Dieterich, 1980, 1981] that

$$c_1 \gg c_2, f_1 \gg f_2$$

and

$$c_1 \approx f_1, c_2 \approx f_2 .$$

For the values of model parameters presented in Dieterich [1981] it also follows that

$$c_1 \gg c_2 \log_{10}(c_3 \theta + 1)$$

and

$$f_1 \gg f_2 \log_{10}(f_3/V + 1) .$$
(3)

Using inequalities (3) and neglecting higher order terms, expression (1) can be rewritten as

$$\mu \approx \frac{c_1}{f_1} + \frac{c_2}{f_1} \log_{10}(c_3 \theta + 1) - \frac{c_1 f_2}{f_1^2} \log_{10}(f_3/V + 1) . \quad (4)$$

In (4) the direct velocity effect has been separated from the state-related effect. If  $\theta$  is interpreted as being related to an effective time of asperity contact for sliding at slip rate  $V$ , then  $\theta$  and  $V$  are inversely related. For low slip rate  $V$  which typifies the quasistatic sliding experiments,  $c_3 \theta$  is large so that (4) can be reduced to a form which is identical to (2), namely,

ROUGH FAULT 3.45 MPa

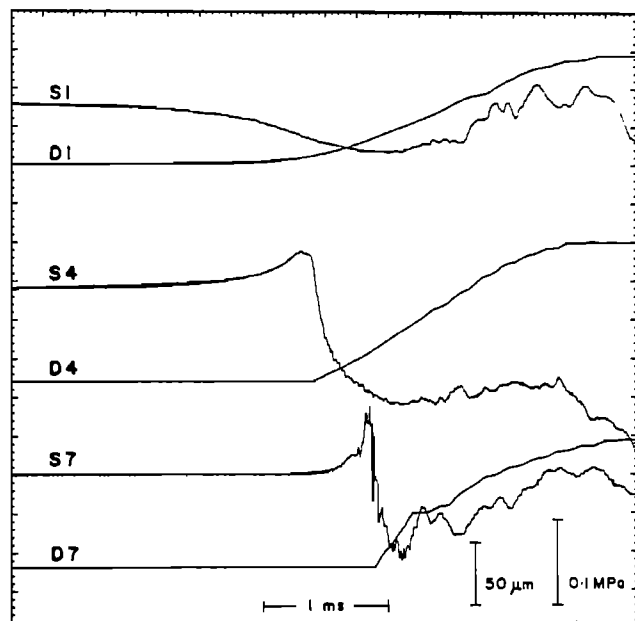


Fig. 3. Rough fault stick-slip data. Traces marked with S are fault shear stress; those marked with D are fault displacement.

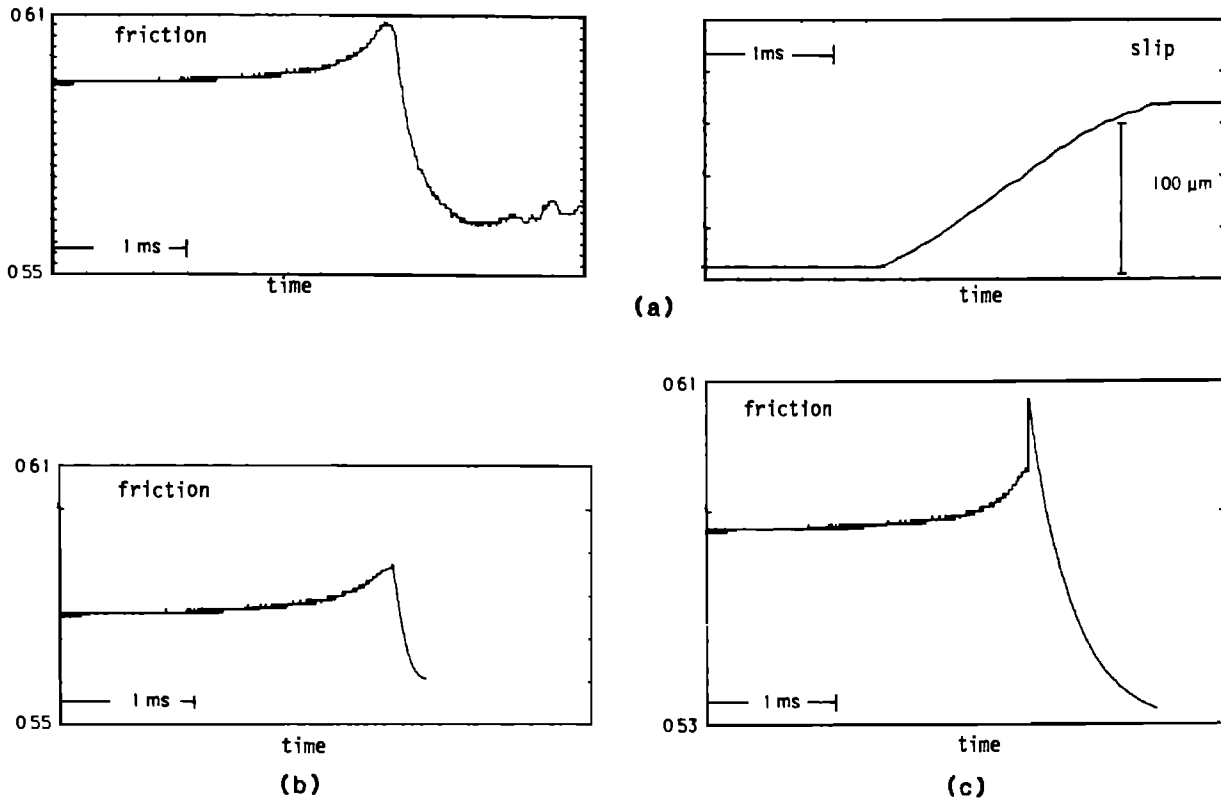


Fig. 4. Example of the fitting procedure to record 47-4 to determine values of high-speed cutoffs. (a) Normalized stress and fault displacement data. (b) Calculated  $\mu$  using equation (6a). (c) Calculated  $\mu$  using equation (6b). In all calculations  $c_1 = 0.56$ ,  $c_2 = 0.013$ ,  $c_3 = 0.5/\text{s}$ ,  $f_1 = 1.0$ ,  $f_2 = 0.01$ , and  $f_3 = 25 \mu\text{m}/\text{s}$ .

$$\mu \approx \mu_0 + A \ln(V/V^*) + \Theta ,$$

if

$$\begin{aligned} \mu_0 &= \frac{c_1}{f_1} + \frac{c_2}{f_1} \log_{10}(c_3) \\ A &\approx \frac{1}{2.303} \frac{c_1 f_2}{f_1^2} \\ V^* &= f_3 \\ \Theta &= \frac{c_2}{f_1} \log_{10}(\theta) . \end{aligned} \quad (5)$$

From this discussion, it is seen that, under conditions of low rates of slip which are characteristic of quasistatic experiments, formulations (1) and (2) converge and are fully equivalent. However, at large  $V$ , the additive constant terms in the logarithms dominate in (1). As  $V$  increases,  $\theta$  will decrease until  $c_3\theta \ll 1$  and  $f_3/V \ll 1$ . As a result, both the direct velocity effect and the state-related effects encounter cutoffs such that further increases in  $V$  or decreases in  $\theta$  do not affect  $\mu$ . Because no such cutoffs are present in (2), the constitutive laws could predict rather different results when  $V$  is large, possibly as during stick-slip.

In this study, we focus on two questions. First, are state variable constitutive laws compatible with dynamic observations of stick-slip? Second, if they are compatible, is the simpler form (2) adequate, or is it necessary to incorporate the high-speed cutoffs to the velocity- and state-related effects? We present model calculations based on a rate- and state-dependent friction model which includes velocity cutoffs,

$$\mu = \frac{c_1}{f_1} + \frac{c_2}{f_1} \log_{10}(c_3\theta + 1) - \frac{c_1 f_2}{f_1^2} \log_{10}(f_3/V + 1) \quad (6a)$$

or one which admits no cutoffs at high slip rate

$$\mu = \frac{c_1}{f_1} + \frac{c_2}{f_1} \log_{10}(c_3\theta) - \frac{c_1 f_2}{f_1^2} \log_{10}(f_3/V) . \quad (6b)$$

Note that (6a) is identical to relation (4) which is the first-order simplification of Dieterich's originally proposed friction law. If conditions (5) are met, then (6b) is identical to Ruina's friction law (2).

## 30 STATE VARIABLE FAULT RELATIONS

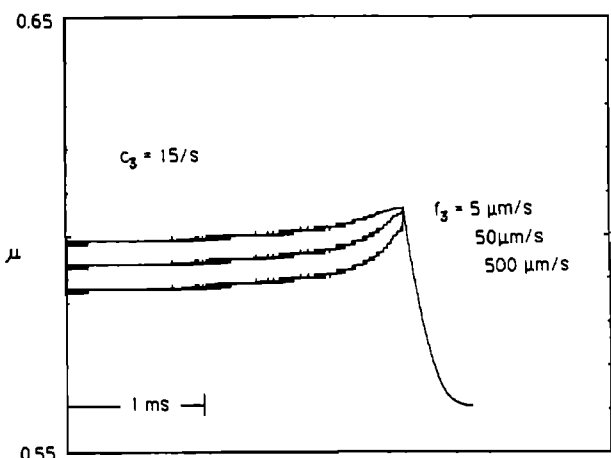


Fig. 5a.

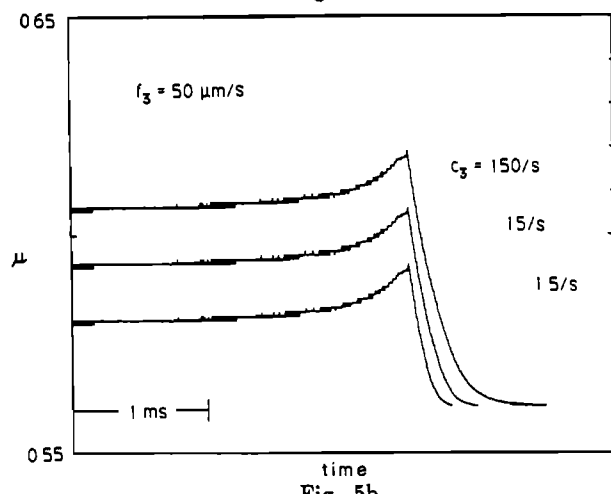


Fig. 5b.

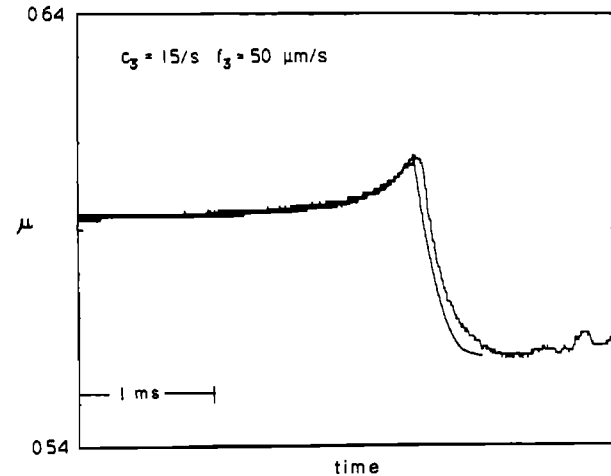


Fig. 5c.

Fig. 5. Effects of adjusting cutoff parameters  $c_3$  and  $f_3$  in equation (6a);  $c_1 = 0.56$ ,  $c_2 = 0.013$ ,  $f_1 = 1.0$ ,  $f_2 = 0.01$ . (a) Different  $f_3$ . (b) Different  $c_3$ . (c) Final choices of  $c_3$  and  $f_3$ .

Equations (6a) and (6b) for  $\mu$ , then, are the forms of the rate- and state-dependent friction constitutive model that we considered here. Both forms feature a constant term, which, given the relative magnitudes of the model parameters, can be regarded as a nominal value of frictional resistance. The state- and velocity-dependent terms in (6) are appropriately viewed as second-order terms in these models. The differences between (6a) and (6b) are readily seen in Figure 1. Figure 1a is a plot of  $\mu$  as a function of  $\theta$  according to equation (6a) for selected values of  $V$  ranging from  $10^{-12} \text{ m/s}$  to  $1 \text{ m/s}$ . Figure 1b is the same as 1a using (6b) instead of (6a). Looking first at Figure 1b, the linear relationship between  $\mu$  and  $\log_{10}(\theta)$  predicted by (6b) appears such that  $\mu$ -vs.- $\log_{10}(\theta)$  relations for different  $\log_{10}$  (velocity) plot as parallel straight lines for all  $V$  and  $\theta$ . For the friction model with cutoffs, represented by (6a), the lower right portion of Figure 1a for large  $\theta$  and/or small  $V$  shows a  $\mu$ -vs.- $\log_{10}(\theta)$  relationship which is identical to that in Figure 1b. That is, at low slip rate and large  $\theta$  the Dieterich and Ruina formulations are equivalent. In the case of sufficiently small  $\theta$ , this "low slip rate" equivalence of (6a) and (6b) breaks down, the additive constant "plus one term" dominates over the evolution of  $\theta$  and friction  $\mu$  is independent of  $\theta$ . The range of  $\theta$  over which the  $\theta$ -dependence of  $\mu$  flattens out is clearly related to the value of  $c_3$ . For large  $V$  the direct velocity term in (6a) is dominated by the "plus one" that appears there and the coefficient of friction is not affected by increases in slip rate. This cutoff is determined by the value of  $f_3$ . The dashed lines in this figure represent steady-state frictional resistance, and, in both cases, the particular choices of model parameters used here establish steady-state  $\mu$  which decreases for increasing slip rate.

## Data and Analysis

We consider the stick-slip data from which our earlier [Okubo and Dieterich, 1984] source parameter determinations were made. The laboratory apparatus and experimental procedures are described in that report and we mention details in this discussion only as they directly relate to the present study. Descriptions of the general features of stick-slip events are also given in the previous work.

The loading history that we use to generate stick-slip events is prescribed as a constant remote shear loading rate under constant normal stress. Our evaluation of the state variable friction models depends on being able to measure the slip rates quasistatically and dynamically and thus follow the evolution of the sliding state from an estimated initial value  $\theta_0$  through the course of the experiment. It is also important that the condition of constant normal stress is maintained through a given sliding history. The loading machine was designed so that stiffnesses in the two principal stress directions are roughly equal and the  $45^\circ$  orientation of the sliding surface with respect to these directions would ensure that normal load across the sliding surface remains constant during stick-slip [Goodman and Sundaram, 1978].

We noted that, in the series of experiments performed on

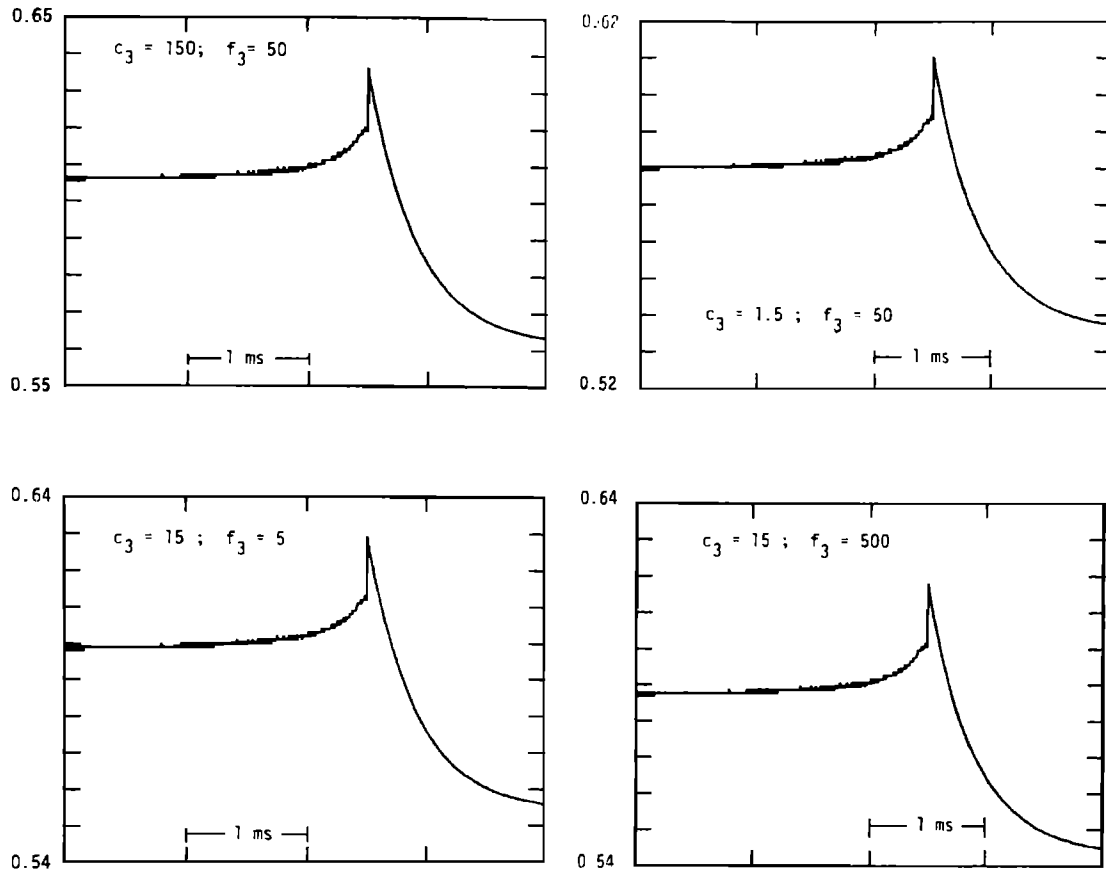
47-4 Calculated  $\mu$  vs time - no cutoffs

Fig. 6. Plots of  $\mu$  versus time for model without cutoffs, equation (6b);  $c_1 = 0.56$ ,  $c_2 = 0.013$ ,  $f_1 = 1.0$ ,  $f_2 = 0.01$ .  $c_3$  and  $f_3$  values indicated.

a smooth and a rough fault, stick-slip sliding on the smooth fault is preceded by relatively little measurable fault creep compared to the rough fault. On the rough fault, a long time interval of stable fault slip always preceded the stick-slip event, often to offsets comparable to the fault displacement associated with the dynamic slip. Because of the difficulty in measuring the small amounts of precursory creep on the smooth fault and thus in estimating the fault slip rate before the stick-slip event, we limit the present study to consideration of the rough fault data.

The procedure that we follow is discussed in connection with Figure 2. From DCDT displacement transducers which are digitally recorded at 1 Hz, we measure fault displacement  $d$  with respect to zero offset values. The displacement records are also differentiated once in the time domain to provide estimates of fault slip rate. An averaged value of slip rate is associated with locations not near a DCDT. From this information, the evolution of the state variable  $\theta$  is calculated according to an evolution law which we adopt from Dieterich [1979a],

$$\theta = \frac{d_c}{V} \left[ \theta_0 \frac{V}{d_c} \right]^{\exp \left[ \frac{d_0 - d}{d_c} \right]} \quad (7)$$

The parameter  $d_c$  controls the evolution of the state variable and gives rise to the characteristic slip distances mentioned previously.

We estimate an initial  $\theta_0$  value of 300 s to begin this first evolution calculation at times corresponding to time  $t_1$  in Figure 2. This value is adopted as a nominal time between stick-slip events. Departure of actual initial  $\theta_0$  values for each record from this uniform assumed initial value can be expected to introduce discrepancies between observed and calculated results. Because of the logarithmic dependence of  $\mu$  on  $\theta$ , or  $c_3\theta$ ,  $\theta_0 = 300$  s was selected as a reasonable representative value to associate with the time between stick-slip events. The stick-slip event appears in the 1 Hz displacement records as the step-like feature at time  $t_2$ . During each time step  $dt$ ,  $V$  is assumed to be constant and  $\theta$  is evolved through displacement increment

## 32 STATE VARIABLE FAULT RELATIONS

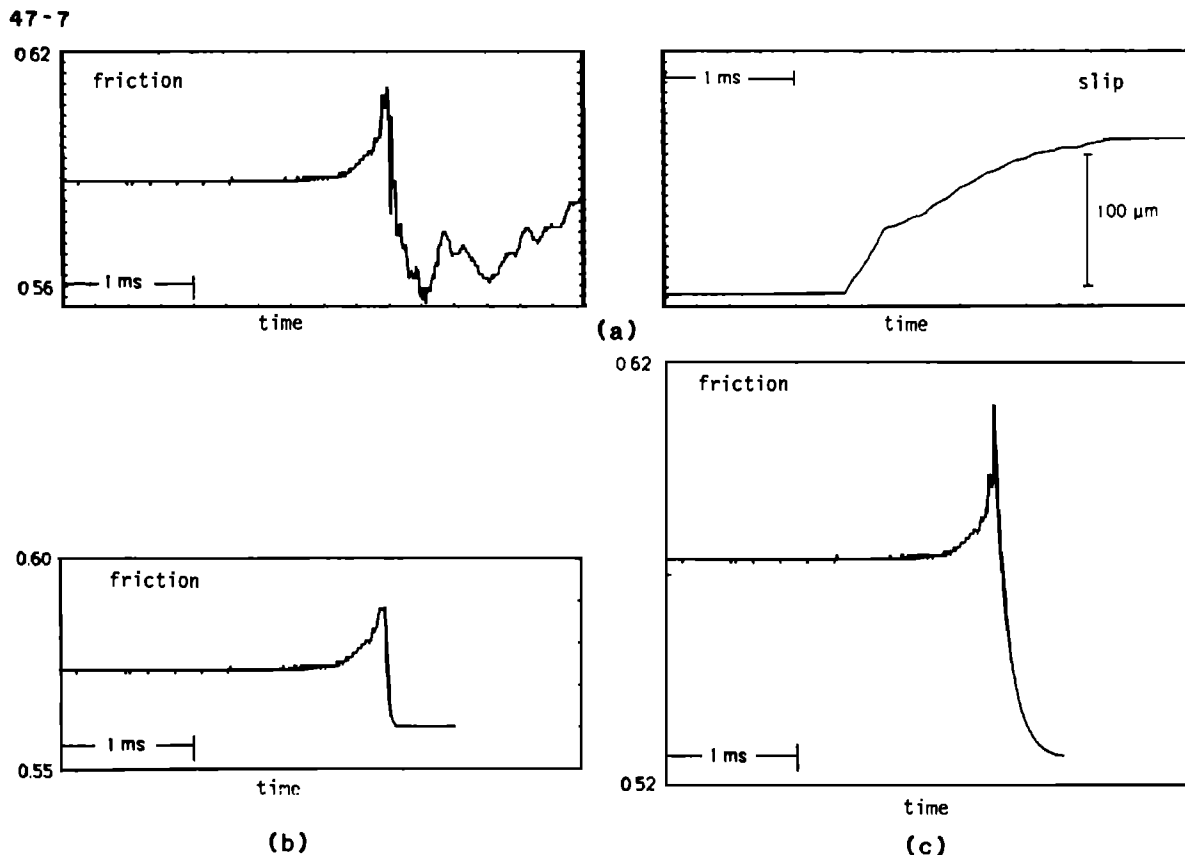


Fig. 7. Same as Figure 4, but for record 47-7.

$d - d_0 = V dt$ .  $\theta_0$  is updated to this new value of  $\theta$ , and the calculation using (7) for the next time step is repeated. We perform this calculation through the accelerating creep stage indicated in the sketch up to the time  $t_2$  of the step-like feature.

To make what might be the best estimate of the fault state at the onset of the stick-slip instability, rather than take the  $V$  and  $\theta$  values determined from this procedure at time  $t_2$  as the final pre-instability state values, we continue to estimate the fault state evolution up to the time of stick-slip using the high-frequency shear stress and fault slip data recorded at 200,000 Hz which are sketched in Figure 2b. The displacement records generally do not indicate measurable amounts of fault movement in the few milliseconds immediately prior to the stick-slip event, so that we do not use these displacement records as we used the DCDT records to estimate the fault state between times  $t_2$  and  $t_3$  in the high-frequency data. Instead, we assume that, because the offsets which can be achieved during these last fractions of a millisecond before a stick-slip are small compared to  $d_c$ , the changes in shear stress can be attributed primarily to the direct velocity effect and not to the evolution of the state variable. Thus, the fault slip rate  $V$  from  $t_2$  up to the time of stick-slip  $t_3$  is estimated from the recorded shear stress (normalized by normal stress  $\sigma$ ) by solving (6) for slip rate  $V$ . Once

stick-slip begins at time  $t_3$ , the fault slip rate is set to the measured values  $V_{s-s}$  and (6) and (7) are used to calculate the remainder of the friction-time history.

Stress and slip data from a stick-slip event are shown in Figure 3. Stress data are marked with an  $S$  and slip data with a  $D$ . This event began to rupture near one end of the fault and then propagated over the remainder of the fault surface. Near the nucleation area, from which the top traces are recorded, there is a relatively smooth acceleration from creep into stick-slip. Away from this part of the fault, the changes in slip rate are more pronounced so that the records at the lower part of the figure more closely reflect the conditions used in the quasistatic tests where the slip rate changes are suddenly introduced. In this study, we restrict our attention to those data for which there is the suggestion that the change in slip rate to stick-slip was achieved also in a very sudden manner. Such data resemble S4 and S7 in Figure 3.

## Results

This fitting procedure is illustrated with the stick-slip record which is pictured in Figure 4a. The model parameters that we use in the calculations are based on those presented in Dieterich [1980] for the clean, rough granite surfaces. They are:  $f_1 = 1.0$ ,  $f_2 = 0.010$ ,

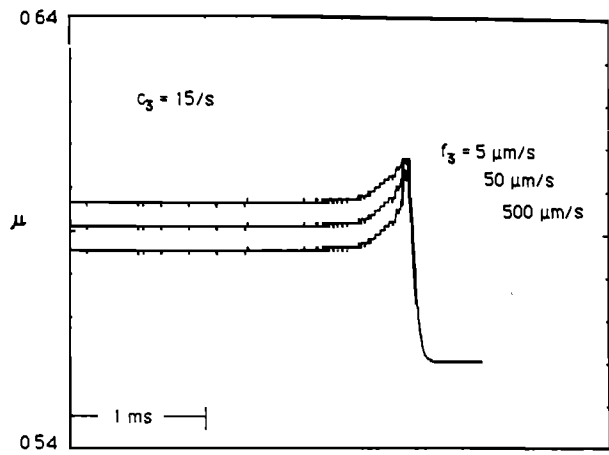


Fig. 8a.

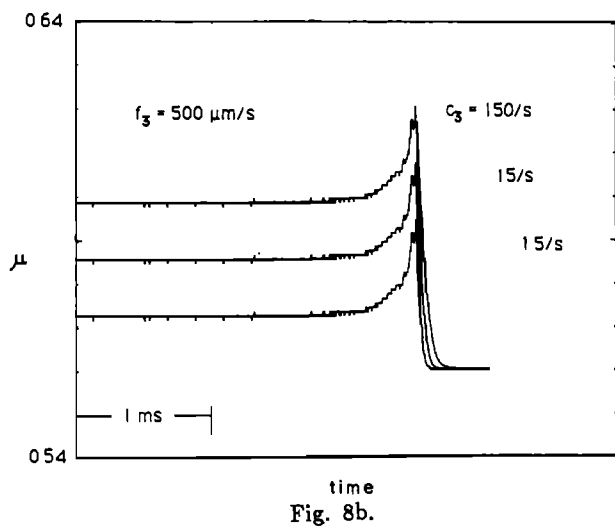


Fig. 8b.

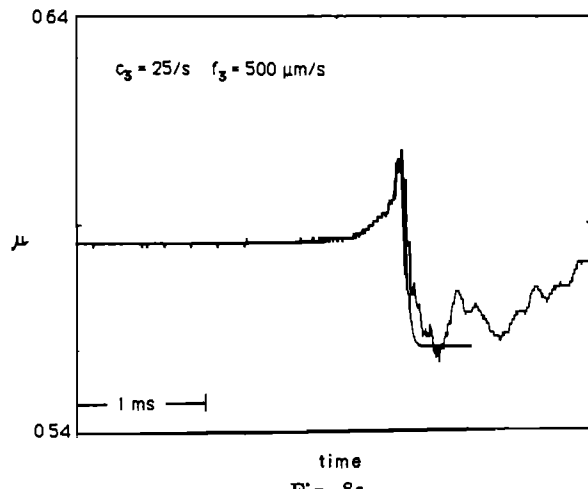


Fig. 8. Same as Figure 5, but for record 47-7.

$f_3 = 25.0 \mu\text{m/s}$ ,  $c_2 = 0.013$ , and  $c_3 = 0.5/\text{s}$ . For  $f_1 = 1.0$ , the parameter  $c_1$  can be interpreted as a nominal value for the friction coefficient at high slip rate and we determined this from the records used here to be  $c_1 = 0.56 \pm 0.07$ . Parameter  $d_c$  which controls the evolution of the state variable corresponds to observed "slip weakening" displacements of approximately 25  $\mu\text{m}$ . With these model parameters, the calculated friction history is shown in Figure 4b from model (6a) with cutoffs and in 4c from the model without cutoffs (6b). As might have been expected because of the cutoffs, the simulation employing (6a) is truncated with respect to the simulation employing (6b) and the data. On the other hand, the simulation with (6b) based on the Ruina approximation overpredicts the changes in  $\mu$ ; that is, it overpredicts the peak friction stress and underpredicts the residual sliding friction stress. Consequently, the important stress difference parameters (peak-initial) and (peak-residual) are correspondingly overpredicted.

The velocity cutoffs in (6a) introduce additional degrees of freedom to the fitting of the stick-slip data which are not available when using (6b). Because the cutoffs are felt under conditions where  $c_3 \theta \ll 1$  and  $f_3/V \ll 1$ , by varying the values of parameters  $c_3$  and  $f_3$ , the stress differences can be adjusted. Maintaining constant values for the parameters  $c_1$ ,  $c_2$ ,  $f_1$ , and  $f_2$ , the effects of changing the values of  $c_3$  and  $f_3$  are shown in Figures 5a and 5b, respectively, in the model calculations of  $\mu$  using the formulation with cutoffs (6a). As seen in this figure, increasing the direct velocity cutoff  $f_3$  allows the peak initial stress difference to increase. Similarly, increasing  $c_3$  allows the peak-residual stress difference to increase. In Figure 5c, data and a good-fitting calculation using  $c_3 = 15/\text{s}$  and  $f_3 = 50 \mu\text{m/s}$  are shown. Calculations using (6b), the friction model without high-speed cutoffs, are illustrated in Figure 6. Varying the values of  $c_3$  and  $f_3$  does not affect the shapes of the calculated friction histories and the friction changes are consistently overestimated. The fitting to another record from the same stick-slip event using (6a) is shown in Figures 7 and 8, and the estimates of cutoff parameters resulting from this fitting procedure for all of the records used here are given in Table 1. Again, note that only the parameters  $c_3$  and  $f_3$  are allowed to vary in these calculations. The other model parameters and starting value of  $\theta$  are identical for each of these calculations.

#### Discussion and Summary

Observations of dynamic stick-slip frictional instabilities can be matched by model calculations based on a rate- and state-dependent friction constitutive relation of the form proposed by Dieterich [1979a] for observations of quasistatic sliding of simulated fault surfaces. Besides the introduction of a state memory which evolves with fault displacement, important features of this frictional constitutive relation are cutoffs at high slip rates to both the rate- and state-related effects. With the exception of

## 34 STATE VARIABLE FAULT RELATIONS

TABLE 1. Estimates of Velocity Cutoff Parameters and Friction Changes.

record	$V_o$ (μm/s)	$V_{s-s}$ (cm/s)	$\mu_p - \mu_0$ observed	calculated		calculated		$v_{sta}$ (μm/s)	$c_3$ (/s)	$f_3$ (μm/s)	
				(6a)	(6b)	(6a)	(6b)				
44-4	0.33	5.48	0.0116	0.0117	0.0292	0.0507	0.0507	0.0682	26	100	40
44-7	0.33	15.50	0.0275	0.0273	0.0318	0.0493	0.0493	0.0750	$1.1 \times 10^4$	65	$2.5 \times 10^4$
45-7	0.04	7.54	0.0304	0.0302	0.0351	0.0464	0.0462	0.0774	$1.2 \times 10^4$	12	$1 \times 10^4$
46-7	0.02	1.90	0.0294	0.0294	0.0335	0.0417	0.0413	0.0697	474	5	3500
47-4	0.17	6.15	0.0138	0.0138	0.0311	0.0457	0.0462	0.0750	54	15	50
47-7	0.06	18.54	0.0221	0.0220	0.0363	0.0482	0.0475	0.0825	98	15	500
48-4	0.42	6.76	0.0055	0.0062	0.0292	0.0397	0.0403	0.0719	2.5	10	5
48-7	0.22	8.02	0.0209	0.0209	0.0311	0.0397	0.0402	0.0756	70	6	1200
49-4	0.14	7.93	0.0122	0.0121	0.0322	0.0496	0.0495	0.0768	16	25	20
49-7	0.06	18.83	0.0218	0.0220	0.0364	0.0479	0.0475	0.0826	43	15	500
50-1	0.31	4.33	0.0058	0.0069	0.0288	0.0471	0.0471	0.0661	0.7	60	5
57-1	0.42	11.87	0.0210	0.0211	0.0305	0.0747	0.0747	0.0771	1040	3100	2500
57-4	0.25	5.98	0.0058	0.0074	0.0301	0.0450	0.0462	0.0749	1.3	15	5

$v_{sta}$  is last value of slip rate calculated by matching  $\mu$  with direct velocity effect before setting slip rate to  $V_{s-s}$  for unstable slip.  $c_1 = 0.56$ ,  $c_2 = 0.013$ ,  $f_1 = 1.0$ ,  $f_2 = 0.01$  [Dieterich, 1981]. Friction changes are calculated using equations (6a) and (6b).

average  $\log f_3 = (2.29 \pm 1.38) \Rightarrow f_3 \approx 200 \text{ } \mu\text{m/s}$ ,

average  $\log c_3 = (1.44 \pm 0.73) \Rightarrow c_3 \approx 30/\text{s}$ .

the cutoff parameters  $c_3$  and  $f_3$ , identical numerical values of friction model parameters can be used to fit both the quasistatic and dynamic observations.

Previous attempts to measure  $c_3$  and  $f_3$  [Dieterich, 1978, 1979a] were limited by the minimum  $\theta$  and maximum slip speed  $V$  that could be controlled in the quasistatic tests. The results obtained in this study from the dynamic tests are compatible with those previously established limits but show large variation. The fitting procedure that is used in this study assumes that all of the variation within a friction history is due to the level of slip rate at which the effects of the cutoffs are felt, and, indeed, adjusting the values of the cutoff parameters is sufficient to approximately fit the observed friction history to the constitutive law. The variability of  $c_3$  and  $f_3$  estimates obtained here is possibly an artifact of the use of a uniform  $\theta_0$  value in all of the data reductions. Departures of actual values of  $\theta_0$  from the assumed value of  $\theta_0 = 300 \text{ s}$  would trade off with the resultant  $c_3$  and  $f_3$  estimates. Irrespective of the variation in the determination of  $c_3$  and  $f_3$ , the slip rates during stick-slip are large enough to clearly establish a cutoff at the high speeds.

While the formulations proposed by Dieterich [1979a] and Ruina [1983] are equivalent for describing frictional slip at low slip rates, at which the cutoff parameters are not important, frictional sliding at high slip rates associated with dynamic shear instabilities appears to be best described by a state variable friction model which includes the high-speed cutoffs. With these high-speed cutoffs, the changes in fault strength at the onset of stick-slip and the residual frictional strength are rate-independent at very

high slip rates. Consequently, a fault slip weakening constitutive relation, although not applicable over the entire range of slip rates nor strictly appropriate for describing more than one episode of dynamic slip, is indeed capable of describing a stick-slip frictional instability.

Acknowledgments. We would like to acknowledge helpful discussions with J. Andrews, J. R. Rice, and S. Tse.

## References

- Andrews, D. J., Rupture velocity of plane-strain shear cracks, *J. Geophys. Res.*, 81, 5679–5687, 1976.
- Archuleta, R. J., A faulting model for the 1979 Imperial Valley earthquake, *J. Geophys. Res.*, 89, 4559–4585, 1984.
- Barenblatt, G. I., The formation of equilibrium cracks during brittle fracture. General ideas and hypotheses: Axially symmetric cracks, *Appl. Math. Mech.*, 23, 622–636, 1959.
- Day, S. M., Three-dimensional simulation of spontaneous rupture: the effect of nonuniform prestress, *Bull. Seismol. Soc. Am.*, 72, 1881–1902, 1982.
- Dieterich, J. H., Time-dependent friction in rocks, *J. Geophys. Res.*, 77, 3690–3697, 1972.
- Dieterich, J. H., Time-dependent friction and the mechanics of stick-slip, *Pageoph.*, 116, 790–806, 1978.
- Dieterich, J. H., Modeling of rock friction 1. Experimental results and constitutive equations, *J. Geophys. Res.*, 84, 2161–2168, 1979a.

- Dieterich, J. H., Modeling of rock friction 2. Simulation of preseismic slip, *J. Geophys. Res.*, **84**, 2169–2175, 1979b.
- Dieterich, J. H., Experimental and model study of fault constitutive properties, in Solid Earth Geophysics and Geomechanics, edited by S. Nemat-Nasser, *Appl. Mech. Div.*, **42**, A.S.M.E., 21–30, 1980.
- Dieterich, J. H., Constitutive properties of faults with simulated gouge, in Mechanical Behavior of Crustal Rocks, edited by N. L. Carter, M. Friedman, J. M. Logan and D. W. Stearns, *Geophys. Monogr. Ser.*, **24**, AGU, Washington, D.C., 103–120, 1981.
- Goodman, R. E., and P. N. Sundaram, The influence of system stiffness and test mode on phenomena accompanying stick-slip on fault surfaces, *Pageoph.*, **116**, 873–887, 1978.
- Gu, J.-C., J. R. Rice, A. L. Ruina, and S. T. Tse, Slip motion and stability of a single degree of freedom elastic system with rate and state dependent friction, *J. Mech. Phys. Solids*, **32**, 167–196, 1984.
- Ida, Y., Cohesive force across the tip of a longitudinal shear crack and Griffith's specific surface energy, *J. Geophys. Res.*, **77**, 3796–3805, 1972.
- Ida, Y., The maximum acceleration of seismic ground motion, *Bull. Seismol. Soc. Am.*, **63**, 959–968, 1973.
- Okubo, P. G., and J. H. Dieterich, Effects of physical fault properties on frictional instabilities produced on simulated faults, *J. Geophys. Res.*, **89**, 5815–5827, 1984.
- Rice, J. R., Constitutive relations for fault slip and earthquake instabilities, *Pageoph.*, **121**, 443–475, 1983.
- Ruina, A. L., Slip instability and state variable friction laws, *J. Geophys. Res.*, **88**, 10359–10370, 1983.
- Stesky, R. M., Mechanisms of high temperature frictional sliding in Westerly granite, *Can. J. Earth Sci.*, **15**, 361–375, 1978.
- Tullis, T. E., and J. D. Weeks, Constitutive behavior and stability of frictional sliding on granite, oral presentation at 5th Ewing Symposium on Earthquake Mechanics, 1985.

## A MODEL FOR THE NUCLEATION OF EARTHQUAKE SLIP

James H. Dieterich

U.S. Geological Survey, Menlo Park, California 94025

**Abstract.** The nucleation of unstable slip on faults with state variable constitutive properties has the following characteristics. First, unstable slip may initiate only on patches exceeding a critical radius,  $r_c$ . Below the critical radius slip is always stable. The critical radius is a function of normal stress, loading conditions and constitutive parameters which include  $D_c$ , the characteristic slip distance. Second, for a patch larger than the critical radius, slip accelerates to instability if the normalized stress,  $\mu$ , exceeds the steady-state friction  $\mu_s$ . Over a wide range of conditions, following application of the initial stress, the logarithm of the time to instability linearly decreases as the difference  $\mu - \mu_s$  increases. Using laboratory derived constitutive parameters extrapolated to the time intervals characteristic of earthquake faulting ( $10^7$  seconds or longer) the time delay from the application of  $\mu$  to the time of instability varies from seconds to times on the order of the interevent time. It is speculated that this delayed failure may be an important process in controlling the timing of a mainshock following a foreshock, or in controlling aftershock sequences. The familiar  $1/t$  decay in rate of aftershock occurrence is satisfied by this model assuming a uniform distribution of initial stresses,  $\mu - \mu_s$ , on the population of nucleation patches for the aftershocks. Displacements during the accelerating slip that leads to instability are proportional to  $D_c$ . Unless  $D_c$  for earthquake faults is significantly greater than that observed on simulated faults, premonitory displacements prior to earthquakes may be too small to detect using current strain observation methods.

## Introduction

Slip instability on faults with rate and rate-history constitutive properties has been the subject of analyses by Dieterich [1979a, 1981]; Ruina [1980, 1983]; Rice and Ruina [1983]; Rice [1983]; Gu et al. [1984]; and Weeks and Tullis [1985]. A result these studies have in common is that slip instability does not occur instantaneously at some threshold stress—an interval of accelerating slip always precedes instability. This paper discusses the possible

sequence of events that must occur to satisfy the conditions necessary for instability on faults with these constitutive properties and then examines the characteristics of the interval of accelerating slip that precedes the instability. The results are believed relevant to understanding the scaling of possible earthquake premonitory phenomena and in explaining some of the temporal characteristics of earthquake occurrence. Of particular interest for the latter are the mechanisms causing foreshocks and aftershocks. Because the intent is to explore the importance of the fault constitutive properties in controlling the characteristics of earthquake occurrence, other aspects of fault interactions have been simplified to the maximum extent considered reasonable.

## Constitutive Law for Faulting

Laboratory study of slip on simulated faults has demonstrated the existence of time-, velocity- and history-dependent processes that perturb fault strength [e.g., Dieterich, 1978a, 1981; Scholz and Engelder, 1976; Ruina, 1980, 1983; Weeks and Tullis, 1985]. Other features of the laboratory observations include: displacement weakening, over a distance that scales by the parameter  $D_c$ , at the onset of slip if the fault is previously stationary; and time-dependent recovery of fault strength following an episode of rapid fault slip [Dieterich, 1972, 1981]. The displacement scaling parameter  $D_c$ , varies from a few microns for semipolished surfaces [Dieterich, 1978a; Ruina, 1980] to about 50 microns for roughened surfaces separated by a thin layer of crushed rock [Dieterich, 1981]. Throughout this paper fault displacements,  $d$ , and slip velocity,  $v$ , are normalized by the characteristic slip distance  $D_c$ , and are indicated by capitalized letters:

$$D = d/D_c, \quad V = v/D_c \quad (1)$$

The experimental observations may be represented by constitutive laws that incorporate slip rate and rate-history effects [Dieterich, 1979a, 1981; Ruina, 1980, 1983; Rice, 1983; Gu et al. 1984]. In this approach, sliding history

## 38 NUCLEATION OF EARTHQUAKE SLIP

effects are represented by a state variable that evolves with displacement toward a steady state value that is governed by the instantaneous slip speed. Several specific forms for the constitutive laws have been employed in the studies cited above. The various constitutive formulations differ in detail, depending largely on approximations employed, but all share the same approach and provide very similar representations of the data. For example, useful simplifying approximations to the relations employed by Dieterich [1979a, 1981] are introduced by Ruina [1980, 1983] by not representing the saturation of the slip rate and history effects at high slip velocity. The results of Ruina [1980] and Weeks and Tullis [1985] suggest that under some conditions the data are better represented by more than one state variable. Some relationships between constitutive laws and comparison of data from dynamic slip events are discussed by Okubo and Dieterich [1986].

In the following discussion, the coefficient of friction,  $\mu$ , is defined:

$$\mu = \tau / \sigma \quad (2)$$

where  $\tau$  is the shear stress acting across the fault and  $\sigma$  is the normal stress. Throughout this work,  $\sigma$  is considered to be constant during slip and multiplication of  $\mu$  by  $\sigma$  is implied when reference is made to fault shear stress. The following single state variable constitutive law for  $\mu$  has been employed for the study reported here [see Okubo and Dieterich, 1986]:

$$\mu = \mu_0 + B_1 \ln(B_2 \theta + 1) - A_1 \ln[(A_2/V) + 1] \quad (3)$$

where  $\mu_0$ ,  $A_1$ ,  $A_2$ ,  $B_1$ , and  $B_2$  are experimentally determined parameters,  $V$  is the normalized slip speed and  $\theta$  is the state variable that depends on slip history. The state variable is discussed further below. It is noted that (3) is equivalent to that of Dieterich [1979, 1981] with the distinction that the earlier forms employ somewhat awkward quotients that are well represented by expansion to (3). The summing of  $B_2\theta$  and  $A_2/V$  with 1 is done to represent the saturation of the rate and rate-history effects at high slip speeds. See Okubo and Dieterich [1986] for a discussion of the rate limits. At  $V$  and  $\theta$  well removed from the rate limits (i.e.,  $B_2\theta \gg 1$ ,  $A_2/V \gg 1$ ) equation (3) is exactly equivalent to that employed by Ruina [1980] and later by several other investigators. That is:

$$\mu = \mu'_0 + \Theta + A_1 \ln V \quad (4)$$

where:  $\Theta = B_1 \ln \theta$  and  $\mu'_0 = \mu_0 + B_1 \ln B_2 - A_1 \ln A_2$ .

The variable  $\theta$  represents sliding history effects and consequently incorporates displacement dependence.  $\theta$  has been interpreted [Dieterich, 1979a; Dieterich and Conrad,

1984] as the average age of the load supporting contacts between the sliding surfaces. A number of equations for the evolution of  $\theta$  have been employed in studies reported in the literature, with similar results. The following evolution law discussed by Ruina [1980] and employed by Dieterich [1981] is used here:

$$d\theta/dt = 1 - \theta V \quad (5)$$

Hence, at steady state slip, where slip speed is constant for large displacements:

$$d\theta/dt = 0, \quad \theta = 1/V \quad (6)$$

For a nominally stationary fault in which the contacts are not disturbed by displacement,  $d\theta/dt = 1$  and  $\theta$  increases with the time of stationary contact. Consequently, for conditions of periodic earthquake slip separated by long intervals of nominally stationary fault contact,  $\theta$  is approximately the time since the last slip event. In practice this is only an upper limit for  $\theta$  because some amount of creep always occurs in simulations of the interevent period that tends to reduce  $\theta$ . Below, initial values of  $\theta$  in the range  $10^5$ – $10^9$  s are employed for calculations of the processes leading to slip instability. The larger values of  $\theta$  are considered representative of the conditions on a fault prior to earthquake recurrence. Under conditions of constant velocity (5) can be solved for  $\theta$  using the chain rule to replace  $d\theta/dt$  with  $d\theta/V dD$  yielding:

$$\theta = 1/V + (\theta_0 - 1/V)e^{-D} \quad (7)$$

where  $\theta_0$  is the value of  $\theta$  at  $D = 0$ . Below, use is made of (7) in numerical computations by treating slip as a series of small constant velocity steps.

#### Conditions for Slip Instability

It is assumed for the remainder of the paper that conditions are well removed from the effects of the saturation of  $\theta$  that occurs at small contact times (i.e., it is assumed that  $B_2\theta \gg 1$ ). This assumption is reasonable because the experiments indicate that  $B_2 > 1$ . For the conditions of interest recall that  $\theta$  is greater than the time since the last fault slip. Therefore,  $\theta \gg 1$ . Hence, in the following the term  $(B_2\theta + 1)$  of (3) is replaced by  $\theta$ , with a suitable change in the constant  $\mu_0$  as given above.

Some characteristics of the constitutive relations are useful for discussing the nucleation of unstable fault slip. Note first that the maximum limit of the frictional strength,  $\mu_{\max}$ , occurs when  $V \gg A_2$  with the result that (3) becomes:

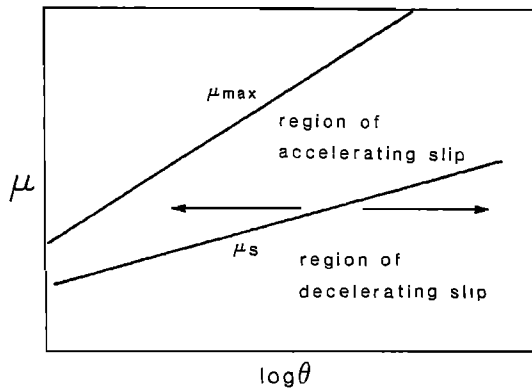


Fig. 1. Plot of maximum friction,  $\mu_{\max}$ , and steady state friction,  $\mu_s$ , against state variable  $\theta$ . This plot assumes that  $B_2\theta \gg 1$ . Under conditions of constant stress,  $\mu$ , slip velocity and  $\theta$  will remain constant only at  $\mu = \mu_s$ . Under conditions of  $\mu > \mu_s$  and constant stress, velocity increases and  $\theta$  decreases with time until  $\mu = \mu_{\max}$ , at which time instability occurs. At  $\mu < \mu_s$ , under conditions of constant stress, velocity decreases and  $\theta$  increases. The arrows indicate the direction in which  $\theta$  evolves away from  $\mu_s$ .

$$\mu_{\max} = \mu_0 + B_1 \ln \theta \quad (8)$$

As  $\mu$  approaches  $\mu_{\max}$ ,  $V$  approaches infinity. Also note that in general, frictional strength,  $\mu$  is uniquely defined only if both  $\theta$  and  $V$  are known. However, at steady state slip,  $\theta = 1/V$ , which yields the steady-state friction

$$\mu_s = \mu_0 - B_1 \ln V - A_1 \ln(A_2/V + 1) \quad (9a)$$

or equivalently:

$$\mu_s = \mu_0 + B_1 \ln \theta - A_1 \ln(A_2\theta + 1) \quad (9b)$$

A dynamic slip instability occurs when the frictional strength decreases at a rate that exceeds the capability of the applied stress to follow (i.e., the applied load exceeds the frictional resistance). Below  $\mu_{\max}$ , if the friction is less than the applied load, then the system needs only to slide at a higher rate to balance the friction to the applied load and stabilize the slip. This is because of the direct velocity-dependent term in the constitutive relation. Therefore, under quasi-static conditions, instability can only occur at the instant the applied stress reaches the limiting strength  $\mu_{\max}$ . Unless the stress state steps instantaneously to  $\mu_{\max}$  there is an interval of accelerating slip rate immediately prior to the onset of instability as the friction approaches

$\mu_{\max}$ . Additionally, for an instability to occur, the stiffness of the system loading the fault at the point of instability must be less than a critical value. At stiffnesses greater than the critical stiffness the displacements that occur during accelerating slip decrease the applied stress at a rate that is sufficient to move the applied stress away from  $\mu_{\max}$  which terminates the acceleration.

Under conditions of constant  $\mu$  (corresponding to zero stiffness) in the range  $\mu_s < \mu < \mu_{\max}$ , the state variable  $\theta$  will continuously decrease with displacement resulting in accelerating slip. The decrease of  $\theta$  with displacement may be seen by noting that: when  $\mu > \mu_s$ , then  $V > 1/\theta$  (equations (3) and (9)) and consequently from (5)  $d\theta/dt < 1$ . Because  $\mu_s$  and  $\mu_{\max}$  depend upon  $\theta$  (equations (8) and (9)), the accelerating slip continues until either  $\mu$  equals  $\mu_s$  or  $\mu_{\max}$  at which point the slip will become either steady state slip or unstable, respectively (Figure 1). Note from Figure 1 that at  $\mu > \mu_s$ , slip will always accelerate to instability when  $B_1 > A_1$ . This result was noted by Dieterich [1979a] and proved by Ruina [1980]. From this it is seen that  $\mu_s$  and  $\mu_{\max}$  define the range of frictional stresses in which slip may accelerate to instability. Below  $\mu_s$ , slip rates decelerate under conditions of constant or decreasing stress and sliding is intrinsically stable.

A general result of investigations of the stability of simple spring and slider systems [e.g., Dieterich 1979a, 1981; Ruina, 1983; Rice and Ruina, 1983; Gu et al., 1984] is that slip will accelerate to instability if the stiffness of the spring,  $k$ , is less than a critical value,  $k_c$ , given by:

$$k_c = \xi \sigma / D_c \quad (10)$$

Where  $\xi$  is parameter that depends on the constitutive parameters and the conditions of the experiment. For steady state slip at  $\mu = \mu_s$ , Ruina [1980, 1983] shows that perturbations will grow to instability at stiffness less than a critical value. For the constitutive relations (3) and (5) the Ruina result is:

$$\xi = (B_1 - A_1) \quad (11)$$

for steady state sliding removed from the saturation of the  $\theta$  and  $V$  dependence (i.e.,  $B_2\theta \gg 1$ ,  $A_2/V \gg 1$ ). Note from (11) that for systems with finite positive stiffness, instabilities growing from perturbations about  $\mu_s$  can occur only when  $B_1 > A_1$ . For sliding above the steady state friction ( $\mu > \mu_s$ ) equation (11) is the lower bound for the critical system stiffness. Gu et al. [1984] examine the conditions for instability with  $\mu > \mu_s$  under various loading conditions.

The results for a spring slider system may be applied to approximately determine the conditions for stability of a fault patch embedded in an elastic media. We consider the simple case of slip on a circular fault patch of radius,

## 40 NUCLEATION OF EARTHQUAKE SLIP

$\theta$ , subject to a uniform change of shear stress,  $\Delta\tau$ . The displacement at the center of the patch due to  $\Delta\tau$  is greater than any other point on the patch and is given by:

$$d = \frac{24\Delta\tau r}{7\pi G} \quad (12)$$

where  $G$  is the shear modulus, [Chinnery, 1969]. The effective stiffness of every point on the patch is  $\Delta\tau$  divided by the local displacement. Because the displacement is maximum at the center point, the effective stiffness of the center is less than any other point. Below it is demonstrated that a low stiffness system tends to reach instability before a higher stiffness system under equivalent initial conditions. Consequently, the center point is assumed to control the onset of instability for the entire patch. From (12) the effective stiffness of the center of the patch:

$$k = \frac{7\pi G}{24r} \quad (13)$$

Combining (10) and (13) yields an approximate relationship for the minimum critical crack radius for unstable fault slip:

$$r_c = \frac{7\pi G D_c}{24\sigma\xi} \quad (14)$$

Similar approaches for displacement weakening cracks are given by Andrews [1976] and Day [1982] and for displacement weakening arising from rate and state dependence by Dieterich [1979a].

The result of equation (14) indicates an interval of premonitory stable fault slip will occur on faults with heterogeneity that is independent of the premonitory slip seen in the single degree of freedom spring-slider systems. For example, consider a fault with uniform frictional properties and heterogeneous shear stress. The constitutive relation (3) indicates that every point on the fault will slip at some velocity depending upon  $\theta$  and the applied stress. However, because the coefficient  $A_1$  is small, very large variation in slip rates arise from small variations in stress. Therefore in terms of the stress state and relative displacement rates we treat some sections of a fault as being essentially locked while others are slipping. Patches with stress at or above  $\mu_s$  will slide stably as long as  $r < r_c$ . A patch will enlarge as the stress at the edge of the patch increases due to increasing tectonic stress and stress redistribution from slip on the patch. This slip is intrinsically stable until  $r > r_c$ . At that point the slip may accelerate to instability if  $\mu > \mu_s$  without further increase of the stress on the fault.

These considerations suggest that two distinct phases of stable slip can be identified leading to confined unstable

slip on a laterally varying fault. The first is associated with the growth of the slipping patch to a radius exceeding some critical radius. Until the radius is reached, slip is intrinsically stable and is largely externally driven. The second phase consists of the interval of accelerating slip that may begin on the patch only if  $r > r_c$  and  $\mu > \mu_s$ . These patches with  $r > r_c$  and  $\mu > \mu_s$  are the sites at which unstable slip can eventually nucleate. The large stress drop that occurs at the time of the instability on the nucleating fault patch may subsequently drive the instability to dimensions in excess of the dimensions of  $r_c$ .

Stable slip on a fault patch has been observed experimentally [Dieterich, 1978b; Dieterich et al., 1978] and has been analyzed, in part, with a 2-D numerical model [Dieterich, 1979b]. Those studies show the existence of two readily distinguished phases of premonitory slip. The first phase is associated with the growth of a stably sliding fault patch. The growth of the patch is controlled by the magnitude of the stress/strength variations on the surface and by the rate of loading on the fault. In situations where the dimensions of the minimum nucleation zone exceed the dimensions of the experimental fault, the second phase always begins after slip has propagated along the entire fault [Dieterich, 1979b]. In this case the experimental apparatus and the fault behave approximately as a spring slider system with the stiffness,  $K$ , determined by the machine stiffness. In large scale tests on a 2-m fault, the expected minimum size for the nucleation zone is less than the dimensions of the fault. In this case rapidly accelerating slip may begin before the growing patch reaches the ends of the sample and often the slip instability does not rupture to the ends of the fault [Dieterich et al., 1978]. Where the embedded creeping patch nucleates unstable slip, the stiffness of the system is given by the parameters of the slipping patch (as in (13)) and not by the apparatus.

The interval of accelerating slip on a patch with  $r > r_c$  is now considered in more detail. Unlike previous studies cited above which emphasize stability criteria, the following treatment emphasizes: 1) the scaling of the magnitude and form of the premonitory displacements that occur during the interval of accelerating fault slip, and 2) the factors that control the duration of the period of accelerating slip. The former is of interest in attempting to assess the potential utilization of premonitory fault slip for earthquake prediction. The latter may be of interest for illuminating some factors that control the timing of earthquakes, particularly following a perturbation of stress on the nucleating patch. Each of these is discussed below.

## Numerical Model

The model is represented as a single slider attached to spring with a constant stiffness,  $k$ . The fault obeys the constitutive law (3) and the evolution law of (5). Follow-

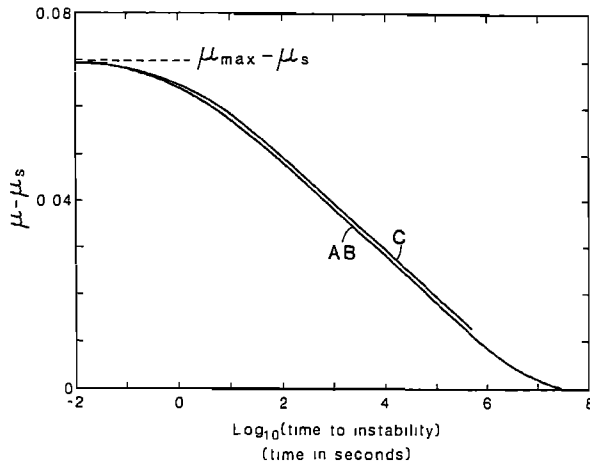


Fig. 2. Time to instability following a step in applied stress to an initial level given by  $\mu - \mu_s$ , for a fixed loading point ( $V_l = 0$ ). This plot is generated from a series of numerical solutions, in which the initial stress for the computation was incremented through the range of initial stress from  $\mu_s$  to  $\mu_{\max}$ . The constitutive parameters for these simulations were chosen to be representative of the experimental results:  $B_1 = .015/2.3$ ,  $A_1 = .010/2.3$ ,  $A_2 = 1.0$ . At the beginning of each simulation  $\theta = 10^7$  seconds. The normalized stiffnesses are  $K = 0$ ,  $K_c/10$ ,  $K_c/1.1$  for curves A, B and C, respectively.  $K_c$  is the normalized critical stiffness for instability arising from perturbation of steady state slip.

ing the discussion of (12)–(14) it is argued that this model provides a simple treatment for slip stability on a confined fault patch, assuming the zone of slip does not expand during the period covered by the computations and that the stress is uniform over the fault patch. The computations employ normalized displacements and velocity for the slider,  $D$  and  $V$ , respectively. Displacements and velocity of the load point attached to the spring,  $D_l$  and  $V_l$ , respectively are also normalized by  $D_c$ . Stress acting perpendicular to the sliding surface,  $\sigma$ , is constant during slip permitting the shear stress acting on the surface and fault frictional strength to be normalized by  $\sigma$ . The focus of interest for these calculations is the factors that control the duration and characteristics of the long interval of slow fault creep that precedes slip instability. Therefore, we assume quasi-static motions and the applied stress equals the friction at all times. The change in normalized shear stress,  $\Delta\mu$ , caused by displacement of the load point and slider is:

$$\Delta\mu = \frac{kD_c(D_l - D)}{\sigma} \quad (15)$$

or:

$$\Delta\mu = K(D_l - D) \quad (16)$$

where  $K$  is the normalized spring stiffness:

$$K = kD_c/\sigma \quad (17)$$

The stiffness employed for the computations described below are expressed as a factor of the critical stiffness for steady state sliding,  $K_c$ , which is obtained from (10).

The computations employ a time marching procedure to follow the slip on the patch. Slip is treated as a series of constant velocity time steps utilizing the evolution law of (7). A numerical integration is performed to assure that the average frictional resistance is equal to the average stress applied by the spring during each time step. An instability occurs when the applied elastic stress exceeds  $\mu_{\max}$ .

Only stiffnesses less than the critical stiffness have been examined. In some cases it is expected that the radius of the patch may equal  $r_c$  when the stress is still well below  $\mu_s$ , the minimum stress for self-driven acceleration to instability. In such cases growth of the patch will in all likelihood continue to increase and be greater than  $r_c$  by the time  $\mu = \mu_s$ . Also during the interval of accelerating slip the displacements on the patch will presumably drive additional growth of the patch. The interest here is in illuminating controlling processes, therefore crack radius and consequently stiffness are held constant during a computation. Below, several different stiffnesses have been examined to evaluate the possible effect of variable crack radius on the process.

For the purpose of this study the loading of the patch on the fault is treated as the sum of a constant rate of displacement of the loading point and discrete jumps in applied load. The former may be viewed as the model equivalent of the large-scale background tectonic loading rate of a fault. The latter corresponds to strain events that alter the strain field on the nucleating patch. An obvious example of a deformation event would be the occurrence of an earthquake at some other location on the fault, i.e., a foreshock or a mainshock. Another common source of a load step might be the rapid intrusion of magma in a volcanic region. Of particular interest below are the form and magnitude of displacements during accelerating slip under various loading conditions and alteration of the time to instability caused by a load step.

## Results

Figure 2 gives the times to instability from a series of simulations in which the loading point was stepped to apply an initial stress,  $\mu$ , in the interval  $\mu_s < \mu < \mu_{\max}$ . The stress step is plotted as  $\mu - \mu_s$ . Following application of the stress step the loading point is held fixed. The state variable  $\theta$  in these simulations is set initially at

## 42 NUCLEATION OF EARTHQUAKE SLIP

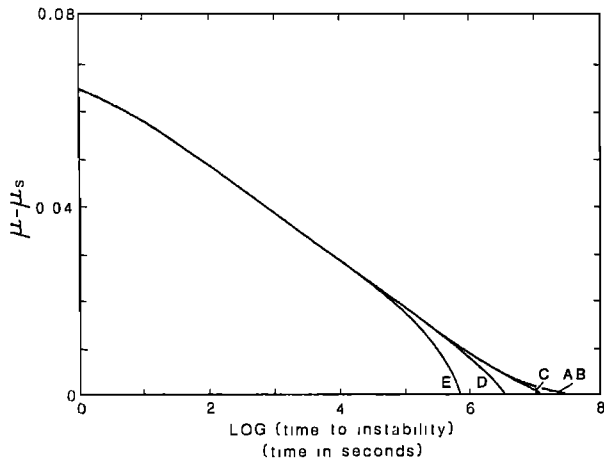


Fig. 3. Time to instability following a step in applied stress to an initial level given by  $\mu - \mu_s$ , for different loading point velocities. The constitutive parameters and initial value of  $\theta$  are the same as that of Figure 2. The stiffness is  $K = K_c/10$ . The loading point velocities are  $V_l = 0, 10^{-7}, 10^{-6}, 10^{-5}, 10^{-4}$ , for the curves labeled A, B, C, D and E, respectively. For the initial value of  $\theta = 10^7$  the steady state slip velocity is  $10^{-7}$ .

$10^7$  s at the beginning of each simulation. This choice of  $\theta$  is arbitrary. The value of  $\theta$  is large to simulate the large interevent times for earthquake faults. Below, results are given showing the effect of  $\theta$  on the time to instability. Constitutive parameters for the simulations are representative of the laboratory results reported by Dieterich [1981] with  $\mu_0 = 0.6$ ,  $2.3B_1 = 0.015$ ,  $2.3A_1 = 0.010$ ,  $A_2 = 1.0$ . (Note this value of  $A_2$  is arbitrary. The effect of  $A_2$  on these results is to shift the time at which the curves bend to become asymptotic to  $\mu_{\max}$ .) Several features of the simulations of Figure 2 are of note. First, although the necessary conditions for the instability are satisfied when  $\mu$  exceeds  $\mu_s$ , and  $K < K_c$ , the instability process is time-delayed. The time to instability is strongly dependent on the amplitude of the initial stress step. The time to instability goes to zero asymptotically as  $\mu$  goes to  $\mu_{\max}$  and the time to instability becomes very large, presumably approaching infinity, as  $\mu$  approaches  $\mu_s$ . Over a wide range of initial stresses the logarithm of the time to instability is proportional to the amplitude of the stress step  $\mu - \mu_s$ . Second, in the interval  $\mu_s < \mu < \mu_{\max}$  the system may accelerate monotonically to instability without the necessity of further displacement of the load point—the acceleration to instability is self-driven. For small stress steps as  $K$  approaches  $K_c$  an instability does not occur. Third, similar results are obtained for the time to instability over the entire range of stiffnesses from  $K = K_c$  to  $K = 0$ , with the exception that the time to instability increases slightly as  $K$  approaches  $K_c$ . This insensitivity of the time to instability indicates that patch radius does not

exert a strong influence on the details of the acceleration to instability.

Figure 3 gives the time to instability for simulations in which the loading point attached to the slider was subjected to a uniform velocity,  $V_l$ , following the initial load step. The stiffness in this series of simulations was set at  $K_c/10$ . For comparison the zero-load rate result of Figure 2 is included. The effect of moving the loading point at a uniform velocity is to reduce the time to instability for the smaller initial loading steps. At loading rates  $V_l < 10/\theta$  the time to instability is little affected by the motion of the loading point. Results from simulations with lower spring stiffnesses are similar, but the effect of loading point velocity is reduced. With stiffness approaching  $K_c$  and small initial stress steps, slip does not accelerate monotonically to instability. Instead, motion of the loading point causes slip to progress through a series of stable oscillations of increasing amplitude before reaching instability. The narrow range of conditions yielding oscillations has not been considered in the current study.

In the range of initial stress and loading conditions which yield an approximately linear relation between initial stress and logarithm of the time to instability, the results are found to scale by:

$$\mu - \mu_s = C + A_1 \ln \theta_0/t \quad (18)$$

where  $t$  is the time to instability following the stress step ( $\mu - \mu_s$ ),  $C$  is a constant that depends on  $K$  and  $A_2$  and  $\theta_0$  is the value of  $\theta$  at the time of the stress step. This result is illustrated by the series of simulations of Figure 4 and Figure 5. The simulations of Figure 4 employ different values for  $A_1$  while using otherwise identical constitutive parameters and model conditions. For the computations of Figure 5 only  $\theta$  has been varied. From earlier discussion recall that  $\theta$  is approximately the time since the last rapid slip event. The result of (18) also agrees with a recently obtained analytic solution for this problem. It is noted that as  $A_1$  goes to zero the time to instability also goes to zero. In this case  $\mu_s$  equals  $\mu_{\max}$  and becomes the threshold stress for instability. This result is evident from (8) and (9) for  $\mu_{\max}$  and  $\mu_s$ .

Figure 6 plots displacement against time showing the interval that includes the final 50 hr before the onset of instability. The constitutive parameters for these simulations are those of the simulations of Figure 2 and are considered representative of the experimental measurements. The velocity of the loading point,  $V_l$ ; stiffness; initial stress; and  $\theta$  are at the indicated values. Note that the form and magnitude of the displacements in the 50 hr before the instability are essentially the same in all cases. The curves are offset because of differing durations of slip before the 50-hour cutoff of the plots. However, the slip rates are initially very low, with the

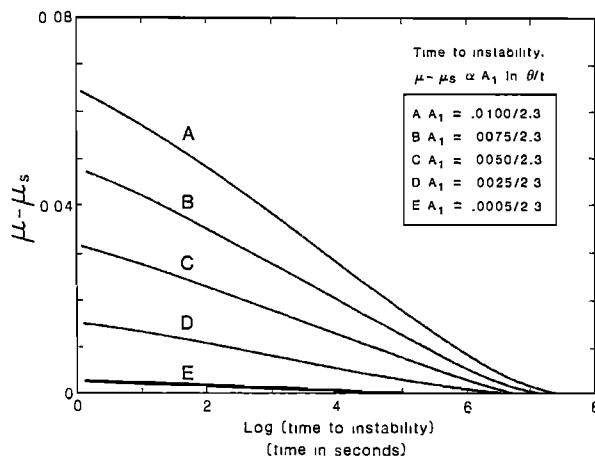


Fig. 4. Time to instability following a step in applied stress to an initial level given by  $\mu - \mu_s$ , for different values of  $A_1$ . In each series of computations the loading point is held fixed, the initial value of  $\theta$  is  $10^7$ , and  $K = 0$ ,  $B_1 = .015/2.3$ ,  $A_2 = 1.0$ . The parameter  $A_1$  is  $.010/2.3$ ,  $.0075/2.3$ ,  $.005/2.3$ ,  $.0025/2.3$ , and  $.0005/2.3$  for the curves A, B, C, D, and E, respectively. Plotted against  $\log_{10} t$  the slopes of the linear portions of the curves are  $-0.10$ ,  $-0.0075$ ,  $-0.0050$ ,  $-0.0025$ ,  $-0.0005$  for A, B, C, D, and E, respectively. When plotted against the natural log of  $t$  the slopes are equal to  $-A_1$ .

result that most of the slip occurs in the final stages of the accelerating slip and the total amount of slip is also less sensitive to the duration of slip.

Of possible practical interest is the possibility of recording premonitory displacements for the purpose of earthquake prediction. From that perspective these results indicate that expected displacement rates in the early stages of the accelerating slip rates are very low and would be difficult to detect. Somewhat arbitrarily the interval 10 days to 10 min has been taken as the interval of practical interest for earthquake prediction. For simulations with these constitutive parameters, having an interval of slip of 10 days or more, the amount of stable slip in the interval from 10 days to 10 min is always about  $d = 5D_c$ . This result is discussed below.

#### Discussion and Conclusions

We have outlined some aspects of the processes leading to unstable fault slip that may be inferred from laboratory observations of fault constitutive properties. The applicability of the laboratory results to faulting in the earth, of necessity, involves extrapolation to conditions not yet examined in the laboratory. In the absence of observations to the contrary, it is assumed that the structure of rate- and state-dependent constitutive relations as employed for the laboratory results is valid for the interevent times, slip

rates and temperature conditions for shallow earthquake-active faults. The wide range of slip phenomena observed in the laboratory and the obvious parallels between phenomena observed on simulated faults and active faulting in nature give some support for this assumption.

On faults with rate- and state-dependent constitutive properties unstable fault slip does not begin spontaneously at some threshold stress on a previously locked fault except if  $\mu$  jumps instantaneously to  $\mu_{\max}$ . In general, stress will increase continuously or in small increments, and unstable slip will be preceded by an interval of stable accelerating slip. This result leads to the notion of a nucleation phase for unstable slip. The principal condition for unstable slip is that accelerating slip must take place on a patch that exceeds a minimum radius,  $r_c$ , given approximately by (14). Slipping portions of a fault with  $r > r_c$  which may be slipping very slowly until a short time prior to instability are therefore the locations of interest for the nucleation of unstable fault slip. Once unstable slip begins, the large stress drops associated with the instability may permit the instability to propagate well beyond the dimensions of the nucleation patch.

The creation of nucleation patches on faults in nature is presumably controlled by the processes stressing the fault and by heterogeneity of fault stresses and fault constitutive properties. Stresses at the edge of a patch will increase because of remote tectonic stressing and because of slip on the patch. If slip begins on a patch that is of subcritical size the dimensions of the patch will tend to increase to the critical size with time as the stresses at the edges of the patch increase. This process of stable patch growth to

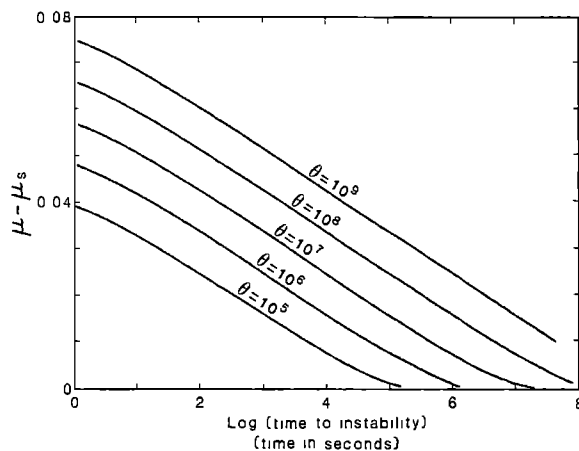


Fig. 5. Time to instability following a step in applied stress to an initial level given by  $\mu - \mu_s$ , showing the effect of different initial values of  $\tau$ . For these computations the loading point was held fixed,  $K = 0$  and the constitutive parameters are those of Figure 2. The initial values of  $\theta$  are indicated on the plot. Note that the time to instability following a stress step is proportional to  $\theta$ .

## 44 NUCLEATION OF EARTHQUAKE SLIP

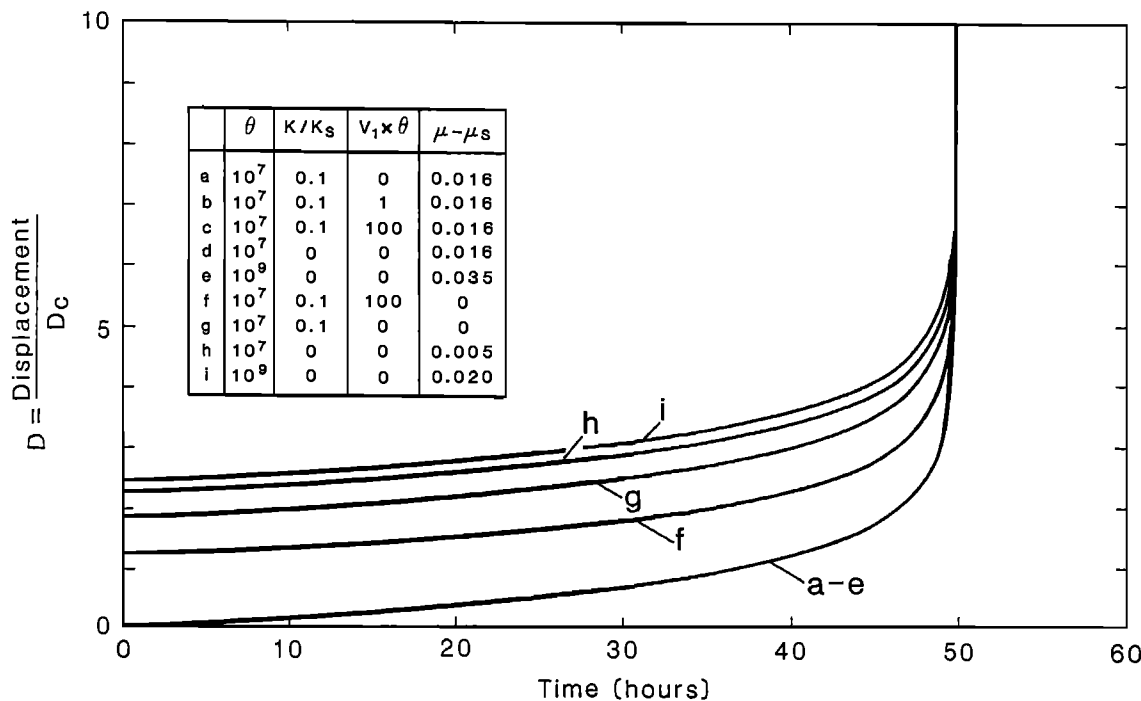


Fig. 6. Displacements plotted against time beginning 50 hr before instability for a variety of conditions and model parameters. The constitutive parameters are those of Figure 2.

create the nucleation patches is therefore associated with intrinsically stable fault slip.

On patches exceeding a critical size, slip will begin to accelerate to instability when the applied stress exceeds the steady-state friction,  $\mu_s$ , for the patch. The results of Figures 2 through 6 outline some characteristics of the interval of accelerating slip on the nucleation patch. An interesting feature of the results is that the time to instability and the form of the premonitory displacements are relatively insensitive to stiffness (i.e., patch radius) and loading rates over a wide range of conditions. This suggests that the model assumption of constant patch size during accelerating slip and the approximation of (14) which reduces a 3-D problem to one with a single dimension parameter may not severely affect the quantitative results for time to instability and premonitory displacements. At  $\mu > \mu_s$ , the time to instability is very sensitive to the magnitude of the stress step. Over a wide range of conditions the logarithm of time to instability following a stress step decreases linearly with the amplitude of the stress step.

It appears plausible that the frequency versus time relationships of aftershock sequences and of mainshocks following foreshocks arise from the strong dependence of the time to instability of the magnitude of a loading step. Specifically, we propose that mainshocks or foreshocks cause a stress step on nearby nucleation patches that advance the onset time of subsequent earthquakes originating on those

patches. For example, in the case of aftershock sequences the mainshock provides the loading step to the population of nucleation patches of the aftershocks. It follows then, that the time of occurrence of earthquakes in a population is determined by the population distribution of stresses on the nucleation patches following the stress step. We assume the initial stresses,  $\mu - \mu_s$ , on the population of nucleation patches, affected by the earthquake does not vary significantly from a uniform distribution:

$$N = N_0 - R(\mu - \mu_s), \quad \mu < \mu_{\max} \quad (19)$$

where  $N$  is the cumulative number of patches with initial stress in the interval from  $\mu$  to  $\mu_s$ , following an earthquake-related step in stress. The magnitude of the parameter  $R$  gives a measure of the size of the stress step and the area affected by the stress step. Combining (18) and (19) and differentiating yields the familiar result for aftershock rates:

$$\frac{dN}{dt} = \frac{RA_1}{t} \quad (20)$$

Similar frequency versus time relationships are found for foreshock-mainshock pairs [Jones and Molnar, 1979; Jones, 1984] suggesting similar mechanisms for foreshocks and aftershocks.

It is also noted that the explanation presented here

Table 1. Premonitory Displacement and Minimum Nucleation Patch Radius

$D_c$	Premonitory Slip 10 Days to 10 Min Before Stability	Minimum Radius of Nucleation Patch ( $\sigma = 100$ MPa)	Moment of Premonitory Slip ( $\sigma = 100$ MPa, $r = r_c$ )
50 mm	250 mm	5.3 km	$5.5 \times 10^{17}$ N-m
5 mm	25 mm	0.53 km	$5.5 \times 10^{14}$ N-m
0.5 mm	2.5 mm	53 m	$5.5 \times 10^{11}$ N-m
50 $\mu\text{m}^*$	0.25 mm	5.3 m	$5.5 \times 10^8$ N-m
5 $\mu\text{m}$	25 $\mu\text{m}$	0.53 m	$5.5 \times 10^5$ N-m

\* Upper limit of  $D_c$  observed in experiments.

for aftershocks at least qualitatively explains observations of the spatial characteristics of aftershocks. Commonly, aftershocks cluster at the edges of the mainshock rupture and spread to progressively greater distances from the rupture with increasing time. The spatial clustering may be explained as arising from the stress concentration at the ends of the rupture. The high stress steps at the rupture edges would give rise to the greatest number of nucleation patches with stresses in excess of  $\mu_s$ , and the greatest number of patches at the upper end of the stress range. The earliest and the greatest numbers of aftershocks would therefore tend to arise at the rupture edges. At progressively greater distances from the rupture, the stress step will be smaller and consequently the times to aftershock instability will be longer.

The results of Figure 6 show that premonitory displacements are insensitive to patch size and loading conditions. This permits some generalizations independent of assumptions for specific models. At long times before instability the slip rates are low, but slip rapidly accelerates as the time of instability approaches. Consequently, the largest premonitory displacements occur in the final stages of the stable slip interval. Using constitutive parameters representative of the laboratory results, the displacements in the interval from 10 days to 10 min before instability are found to be approximately  $5D_c$ .

Table 1 gives premonitory displacement, minimum critical patch radius and minimum moment,  $M_0$ , of premonitory strain for a range of possible values for  $D_c$ . In Table 1, equation (14) has been used with the criteria for instability at steady-state slip  $\xi = B_1 - A_1 = 0.0022$ ,  $G = 2.5 \times 10^4$  MPa and a normal stress of 100 MPa. Direct measurements of  $D_c$  for prepared laboratory faults fall in the range 1–50  $\mu\text{m}$ , yielding 5–250  $\mu\text{m}$  of premonitory slip if extrapolated to the large  $\theta$  for earthquake interevent times—a result that is not particularly encouraging for use of premonitory slip as a practical means for earthquake prediction. However, the magnitude of  $D_c$  for natural faults is an open question at this time.

The laboratory observations of  $D_c$  indicate that this parameter is sensitive to surface roughness and gouge

particle dimensions. Because natural faults are much rougher than laboratory faults and also have much larger and more heterogeneous gouge fragments it is plausible to expect that  $D_c$  for natural faults may be substantially greater than any of the laboratory measurements. Upper limits for  $D_c$  can be approximately established from earthquake source parameters by assuming the earthquake instability does not propagate beyond the nucleation patch. Equation (14) can then be employed to find a limiting maximum value for  $D_c$  by taking the critical patch radius to be equal to the earthquake rupture radius.

These considerations suggest two very different limiting hypotheses for the characteristics of  $D_c$  of faults in nature. The first hypothesis is for  $D_c$  to be the same everywhere. In this case, the smallest earthquakes occurring on a fault are those with a source radius equal to the critical radius of the nucleation patches. Larger earthquakes occur only when the earthquake rupture is able to propagate beyond the nucleation zone. Under these conditions, the magnitude of premonitory displacements of earthquakes of all sizes would be the same. The smallest recorded earthquakes in many regions appear to have a source radius on the order of 100 m or possibly much less. Using  $r_c = 100$  m,  $A_1 = 0.010/2.3$ ,  $B_1 = 0.015/2.3$ ,  $G = 2.5/10^4$  MPa, and  $\sigma = 100$  MPa in (14) yields a maximum  $D_c$  of 1 mm. At  $\sigma = 10$  MPa,  $D_c$  is 0.1 mm. If this hypothesis is correct, it is evident that accelerating premonitory displacements would be difficult to detect in most situations.

Recently Johnston et al. [1986] reported on a number of high quality strain records obtained for the few hours immediately preceding several moderate earthquakes. At the resolution of these records, there is no evidence for premonitory strains for any of the events studied. For the different earthquakes Johnston et al. [1986] have calculated the maximum possible moments for premonitory strain at the source that could have escaped detection by falling below the limit of strain resolution on the records. The maximum possible moments fall in the range  $1.5 \times 10^{12}$  N-m to  $3.3 \times 10^{17}$  N-m. When applied to the results of the present study those maximum moments provide an upper limit to  $D_c$  in the nucleation zone. Assuming,

## 46 NUCLEATION OF EARTHQUAKE SLIP

$\sigma = 100$  MPa,  $G = 2.5 \times 10^4$  MPa, and  $\xi = 0.0022$  in (14) the maximum values of  $D_c$  are 0.9 mm and 200 mm, respectively for the end-member moments of  $1.5 \times 10^{12}$  N-m and  $3.3 \times 10^{17}$  N-m, respectively.

The second limiting hypothesis calls for scaling of the dimensions of earthquake ruptures by the dimensions of the nucleation zone:

$$r_c = r/F \quad (21)$$

where  $r$  is the rupture radius and  $F$  is a constant equal to or greater than 1. This hypothesis implies a heterogeneity of nucleation patch dimensions. Consequently, from (14) and (21)  $D_c$  would have variability comparable to the size-frequency statistics of earthquakes. This hypothesis might obtain if heterogeneity of fault-strength to fault stress is great enough to inhibit rupture propagation much beyond the nucleation zone. Premonitory displacements would scale by rupture dimensions and large earthquakes could have very sizable premonitory displacements.

Available evidence is very limited, but possibly favors the second hypothesis or some intermediate case. The intermediate case would consist of heterogeneous  $D_c$  with the radius of some ruptures scaling by  $r_c$ , but with many others resulting from runaway propagation from small nucleation patches. Faults in nature appear extremely inhomogeneous compared to the prepared sawcuts generally used to simulate faults in the laboratory, perhaps suggesting large and spatially variable values for  $D_c$ . Estimates of fracture energy for earthquakes are often large and require breakdown displacements (i.e.,  $D_c$ ) on the order of centimeters or tens of centimeters. Because small earthquakes cannot originate on faults with such large  $D_c$  values the occurrence of small earthquakes elsewhere on a fault implies great heterogeneity of  $D_c$ . Conversely, the small earthquakes might be evidence of problems with fracture energy determinations. The occurrence of large premonitory displacements, as we have seen, also indicate large values for  $D_c$  in the nucleation region. The failure to observe evidence for premonitory creep for many moderate earthquakes in well monitored locations may be interpreted as rupture propagation well beyond a small nucleation patch.

Acknowledgments. During the course of this study several discussions with P. Segall were especially useful. P. Segall, P. Okubo, and B. Hobbs are thanked for reviews and comments.

## References

- Andrews, D. J., Rupture velocity of plane strain shear cracks, *J. Geophys. Res.*, 81, 5679–5687, 1976.
- Chinnery, M. A., Theoretical fault models, Symp. Processes in the Focal Region, Publ. Dominion Observatory, Ottawa, 37, 211–223, 1967.
- Day, S. M., Three-dimensional simulation of spontaneous rupture: The effect of non-uniform prestress, *Bull. Seismol. Soc. Am.*, 72, 1881–1902, 1982.
- Dieterich, J. H., Time-dependent friction in rocks, *J. Geophys. Res.*, 77, 3690–3697, 1972.
- Dieterich, J. H., Time-dependent friction and the mechanics of stick-slip, *Pure Appl. Geophys.*, 116, 790–806, 1978a.
- Dieterich, J. H., Preseismic fault slip and earthquake prediction, *J. Geophys. Res.*, 83, 3940–3948, 1978b.
- Dieterich, J. H., Modeling of rock friction: 1. Experimental results and constitutive equations, *J. Geophys. Res.*, 84, 2161–2168, 1979a.
- Dieterich, J. H., Modeling of rock friction: 2. Simulation of preseismic slip, *J. Geophys. Res.*, 84, 2169–2175, 1979b.
- Dieterich, J. H., Constitutive properties of faults with simulated gouge, in *Mechanical Behavior of Crustal Rocks*, Geophysical Monograph 24, 103–120, AGU, Washington, D.C., 1981.
- Dieterich, J. H., and G. Conrad, Effect of humidity on time- and velocity-dependent friction, *J. Geophys. Res.*, 89, 4196–4202, 1984.
- Dieterich, J. H., D. W. Barber, G. Conrad, and Q. W. Gordon, Preseismic slip in a large scale friction experiment, Proc. U.S. Rock Mech. Symp., 19th, 110–117, 1978.
- Gu, J.-C., J. R. Rice, A. L. Ruina, and S. T. Tse, Slip motion and stability of a single degree of freedom elastic system with rate and state dependent friction, *J. Mech. Phys. Solids*, 32(3), 167–196, 1984.
- Johnston, M. J. S., A. T. Linde, and M. T. Gladwin, Fault failure with moderate earthquakes, *Tectonophysics*, in press, 1986.
- Jones, 1984.
- Jones, L. M., Foresights and time-dependent earthquake hazard assessment in southern California, *Bull. Seismol. Soc. Amer.*, in press, 1985.
- Jones, L. M., and P. Molnar, Some characteristics of foreshocks and their possible relation to earthquake prediction and premonitory slip, *J. Geophys. Res.*, 84, 5709–5723, 1979.
- Okubo, P. G., and J. H. Dieterich, State variable fault constitutive relations for dynamic slip, this volume, 1986.
- Rice, J. R., Constitutive relations for fault slip and earthquake instabilities, *Pure Appl. Geophys.*, 121, 443–475, 1983.
- Rice, J. R., and A. L. Ruina, Stability of steady frictional slipping, *J. Appl. Mech.*, 50, 343–349, 1983.
- Ruina, A. L., Friction laws and instabilities: a quasi-static analysis of some dry friction behaviour, Ph.D. dissertation, Brown University, Providence, R.I., November 1980.
- Ruina, A. L., Slip instability and state variable friction laws, *J. Geophys. Res.*, 88, 10359–10370, 1983.
- Scholz, C. H., and J. T. Engelder, The role of asperity

indentation and ploughing in rock friction, I. Asperity  
creep and stick-slip, (abstract), *Int. J. Rock Mech. Min.*  
*Sci. Geomech.*, 149–154, 1976.

Weeks, J. D., and T. E. Tullis, Frictional sliding in dolomite:  
a variation in constitutive behavior, *J. Geophys. Res.*, 90,  
7821–7826, 1985.

## VELOCITY-DEPENDENT BEHAVIOR OF SIMULATED HALITE SHEAR ZONES: AN ANALOG FOR SILICATES

Toshihiko Shimamoto<sup>1</sup> and John M. Logan

Center for Tectonophysics, Texas A &amp; M University, College Station, Texas 77843

**Abstract.** A complete transition between frictional slip and ductile shearing flow has been reported recently for halite, thereby linking the fault behavior in the brittle field and the ductile shearing deformation in the pressure-insensitive flow regime. Halite is selected as an analog for natural intrafault materials because it provides a wide spectrum of mechanical behavior at tractable laboratory conditions. This paper reports more comprehensive mechanical data and results from observations of deformed halite. Triaxial experiments are performed on dry cylindrical specimens of Tennessee sandstone with 0.3 - 1.0 mm thick layer of halite along a 35° pre-cut at room temperatures, with slip rates along the pre-cut ranging from 300 $\mu\text{m/s}$  down to 0.003 $\mu\text{m/s}$  ( $< 10 \text{ cm/yr}$ ), and confining pressures to 250 MPa. Important results are: (1) Negative velocity dependency of steady-state friction is present at confining pressures below 100 MPa (frictional regime). This changes to a positive dependency with increasing velocity (high-speed frictional regime). With increasing confining pressure, frictional and high-speed frictional regimes shrink and expand, respectively, and the frictional-velocity relationship changes into one for ductile shearing flow. (2) Deformation of halite is brittle or semibrittle at pressures below about 50 MPa, and halite is in the pressure-insensitive flow regime at 250 MPa pressure. At the intermediate range of pressures, deformation of halite is ductile in texture but its shear resistance is pressure-dependent (semiductile regime). (3) Stick-slip occurs only in the frictional regime with a negative velocity dependence, consistent with the theoretical prediction of Rice and Ruina. Potentially seismogenic behavior is extended well into the semiductile regime. This, coupled with the fact that most large earthquakes initiate at deep portions of seismogenic depths, strongly suggests

the semiductile regime as the primary area of interest in future studies. In view of the well-developed foliation of halite in the semiductile field, mylonites should receive renewed attention with the view that at least some zones could well be associated with seismogenic fault motion. (4) Slip behavior of simulated faults change from flow-type to potentially unstable friction-type behavior with increasing shear strain, approximately when the homogeneous deformation within the shear zone changes to a heterogeneous one. Thus, the potentially unstable motion is associated with the localized deformation within the shear zone. The critical shear strain for the strain localization markedly increases with increasing pressure.

## Introduction

Stick-slip along existing fault zones, including plate boundaries, is now generally accepted as the most likely mechanism for most of the shallow destructive earthquakes [Bridgeman, 1951; Brace and Byerlee, 1966]. Since the pioneering work on fault constitutive properties by Dieterich [1979a, 1981] and Ruina [1983], one of the major strategies of earthquake prediction efforts is to utilize theoretical models for a better understanding of the earthquake phenomena [Dieterich, 1979b, 1985; Rice, 1983; Rice and Gu, 1983; Rice and Ruina, 1983]. An essential component of such theoretical efforts is to establish fault constitutive relations for intrafault materials under geologically realistic conditions, the elucidation of which is an active part of present experimental efforts.

Because of: (1) the uncertainty in extending existing constitutive relations to longer periods of time [Shimamoto and Logan, 1984]; (2) the suggestion that semibrittle, rather than the brittle regime is more appropriate to characterize the rocks at seismogenic depths [Carter and Kirby, 1978; Sibson, 1983; Tse and Rice, 1986; Shimamoto, 1985b; Logan and Teufel, 1986]; and (3) the paucity of existing data in this domain [e.g., Stesky, 1978], this research addresses these specific topics.

Ideally, one would like to work directly with

---

<sup>1</sup>Present address: Institute of Geology and Mineralogy, Faculty of Science, Hiroshima University, Hiroshima 730, Japan.

## 50 SIMULATED HALITE SHEAR ZONES

those minerals and rocks that are presumed to be major components of fault zones, namely quartz, feldspars and other silicates. However, these are difficult to investigate in the semibrittle and ductile fields of behavior in the laboratory, because maintaining necessary high temperatures and pressures for long periods of time is technically demanding. Additionally, the large total displacements that are required for collecting meaningful data on the velocity-dependent behavior of faults [Dieterich, 1981] are difficult to attain in existing high pressure and temperature apparatuses. Thus, one would like an analog material, which is substantially similar in behavior, but which shows the spectrum of mechanical response under more tractable laboratory conditions. Halite is especially suitable since the entire spectrum of deformation mechanisms may be produced at room or very low temperatures and at relatively low pressures. Importantly, there are no known major differences in the deformation mechanisms or mechanical behavior between it and silicates (e.g., Carter and Hansen [1983]; Handin et al. [1985], among many others). Thus, it should serve as an ideal analog for many natural intrafault materials.

## Experimental Procedures

Triaxial experiments were conducted in which cylindrical specimens of Tennessee sandstone, cored normal to the bedding, with a layer of compacted halite grains along a precut at an angle of 35° to the cylinder axis were deformed dry at room temperature in an apparatus described by Handin et al. [1972]. Stiffness and inertial properties of this machine are reported in Shimamoto et al. [1980]. The confining pressure and the velocity ranges, respectively, from 10 MPa to 250 MPa and from 300  $\mu\text{m/s}$  down to 0.003  $\mu\text{m/s}$  ( $\approx 10 \text{ cm/yr}$ ). Smaller specimens were used at higher confining pressures; that is, length = 9 - 11 cm and diameter = 4.8 cm at pressures below 200 MPa, and length = 6 - 7 cm and diameter = 3.8 cm at pressures above 200 MPa. Specimen ends and the precut surfaces were ground with an 80-grit silicon-carbide grinding wheel. Polyolefin shrink fit-tubes of 3 mm in total thickness were used as jackets. Corrections for apparatus distortion, contact-area change, and jacket strength were all employed in determining stress values and the amount of slip [Shimamoto, 1977].

Synthetic halite (reagent-class pure NaCl; about 0.1 mm in grain size) and natural halite of unknown origin (iodized cooking salt; 0.2 - 0.3 mm in grain size) were used in the halite layer, whose average thickness was estimated from its weight assuming zero porosity. The thickness of halite layers varied from 0.3 - 1.0 mm to examine the effect of average shear strain. The halite layer was precompacted either by leaving the specimen under a confining pressure of 200 MPa and a differential stress of about 100 MPa for 15 - 30 minutes or by applying a  $P_c$ -reduction

treatment [Shimamoto, 1985a]. The latter procedure was employed in most of our experiments. Velocity-stepping tests were made, similar to other workers [e.g., Dieterich, 1979a; Tullis and Weeks, 1986] to investigate the velocity dependent behavior.

## Mechanical Data

Table 1 summarizes 20 experiments reported. In two tests, H17 and H20, the precut surfaces appear to have been locally in direct contact, since these specimens exhibited 15 - 20% higher frictional strength and notably more unstable behavior than did other specimens under similar conditions. Hence their mechanical data are not used, although their deformation textures are included.

## General Slip Behaviors

Dieterich [1981] recognized that velocity-dependence of friction changes during an early stage of a test; that is, the velocity dependence is positive initially and becomes negative only after a certain displacement (positive and negative dependencies: increasing and decreasing steady-state friction with increasing velocity, respectively). A point on a fault or on a plate boundary should experience earthquakes a great many times, so that frictional properties after some critical displacement are much more significant than those during the initial transient portion. Thus, the early change in frictional properties with displacement has to be scrutinized when trying to collect meaningful data. Unfortunately, this important point was overlooked in most previous experiments, thus making it difficult to interpret some data on the velocity dependence, especially those at high temperatures.

The contrasting behaviors upon a step change in velocity will be summarized first: friction type [Dieterich, 1979a, 1981; Ruina, 1983] for which a fault exhibits an instantaneous viscous like response followed by a gradual change within a critical displacement toward the steady-state value, and steady-state friction is inversely proportional to the logarithm of velocity (negative velocity dependency), and (2) flow type [Shimamoto, 1985b, 1986] for which shear resistance changes gradually and monotonically toward its steady-state value, and the steady-state shear resistance increases with increasing velocity.

Only flow-type behavior is observed for a thicker layer of halite deformed at a confining pressure of 150 MPa (Figure 1a), whereas a thinner layer of halite exhibits friction-type behavior at the velocities of 0.3-3  $\mu\text{m/s}$  (between R3 and R4 in Figure 1b). It appears that the behavior changes approximately when a broad maximum in the stress-shortening curve is reached. The average shear strain of gouge at

TABLE 1. Summary of Experiments at Room Temperature

Test Number	Halite	Confining Pressure (MPa)	Average Thickness of Halite Layer (mm)	Type of Precompaction <sup>1)</sup>	$\gamma_{av}^2)$	$\theta_{av}^3)$	$R_{av}^4)$
H01	natural	70	0.7	P-red.	31	1.9	940
H02	natural	150	1.0	P & $\sigma$	14	4.0	200
H03	natural	100	1.0	P & $\sigma$	14	4.0	200
H04	natural	100	0.3	P & $\sigma$	45	1.3	2,000
H05	natural	150	0.3	P & $\sigma$	45	1.3	2,100
H06	natural	70	0.3	P & $\sigma$	47	1.2	2,200
H07	natural	35	0.3	P & $\sigma$	54	1.1	3,000
H08*	synthetic	70	0.3	P-red.	62	0.9	3,800
H09*	synthetic	35	0.3	P-red.	115	0.5	13,000
H10	synthetic	100	0.3	P-red.	63	0.9	4,000
H11	synthetic	150	0.3	P-red.	65	0.9	4,200
H12	synthetic	10	0.3	P-red.	65	0.9	4,300
H13	synthetic	50	0.3	P-red.	56	1.0	3,200
H14	synthetic	200	0.3	P-red.	44	1.3	1,900
H15	synthetic	250	0.3	P-red.	41	1.4	1,700
H16	natural	250	0.3	P-red.	39	1.5	1,500
H17**	natural	200	0.3	P-red.	45	1.3	2,100
H18	natural	50	0.3	P-red.	62	0.9	3,800
H19	natural	100	0.3	P-red.	61	0.9	3,700
H20**	natural	150	0.3	P-red.	56	1.0	3,100

1) P-red.: The halite layer was precompacted by applying a  $P_c$ -reduction treatment [Shimamoto, 1985a].

P &  $\sigma$ : The halite layer was precompacted by leaving the specimen under a confining pressure of 200 MPa and a differential stress of about 100 MPa for 15–30 minutes.

2)  $\gamma_{av}$ : Average shear strain of halite layer which is equal to the total displacement divided by the average thickness of the layer (homogeneous simple shear is assumed).

3)  $\theta_{av}$ : Angle between the orientation of the maximum elongation (the major axis of the strain ellipse) and the rock-halite boundary, calculated from the average shear strain.

4)  $R_{av}$ : Axial ratio of the strain ellipse corresponding to  $\gamma_{av}$ .

\*): The second run on the specimen deformed in H08.

\*\*): The country rock might have been in contact very locally in these runs.

this peak is about the same for thick and thin layers (Figure 1). For velocities faster than 70  $\mu\text{m/s}$ , the simulated fault exhibits only positive dependence of friction and no instantaneous responses to a step change in velocity even after the broad peak is reached, but it shows a clear peak in friction following the resumption of slip after the fault was at rest for several minutes (Figure 1b). These are characteristic of the high-speed frictional regime of Shimamoto [1986].

Similar behaviors are observed at lower pressures (Figures 2 and 3). Note that well-defined stick-slip occurs at confining pressure of 70 MPa. The broad peak in the stress-shortening curve tends to be reached earlier at a lower pressure; that is, the shear strain at this peak is about 3, 4 and 4–5 at pressures of 70, 100 and 150 MPa, respectively (Figures 1, 2 and 3b).  $P_c$ -reduction treatment [Shimamoto, 1985a] reduces this critical strain (cf. Figures 3a and

3b). Thus, a thin layer of halite with  $P_c$ -reduction treatment must be used in order to collect mechanical data of interest within the allowable displacement (15–20 mm) in our experiments. All later tests, H08–H20, were made on such layers of halite.

#### Pressure Dependence of Shear Resistance

The shear stress sustainable by halite is slightly lower than that for many rocks compiled by Byerlee [1978], but it deviates markedly from his relationship at higher pressures (Figure 4). No clear velocity dependence of friction can be seen in Figure 4a for thick layers and for thin layers without  $P_c$ -reduction treatment. For thin layers with  $P_c$ -reduction treatment, friction is high at slower velocities at a low pressure and opposite at high pressures (Figure 4b). More extensive results, very similar to Figure 4b, are

## 52 SIMULATED HALITE SHEAR ZONES

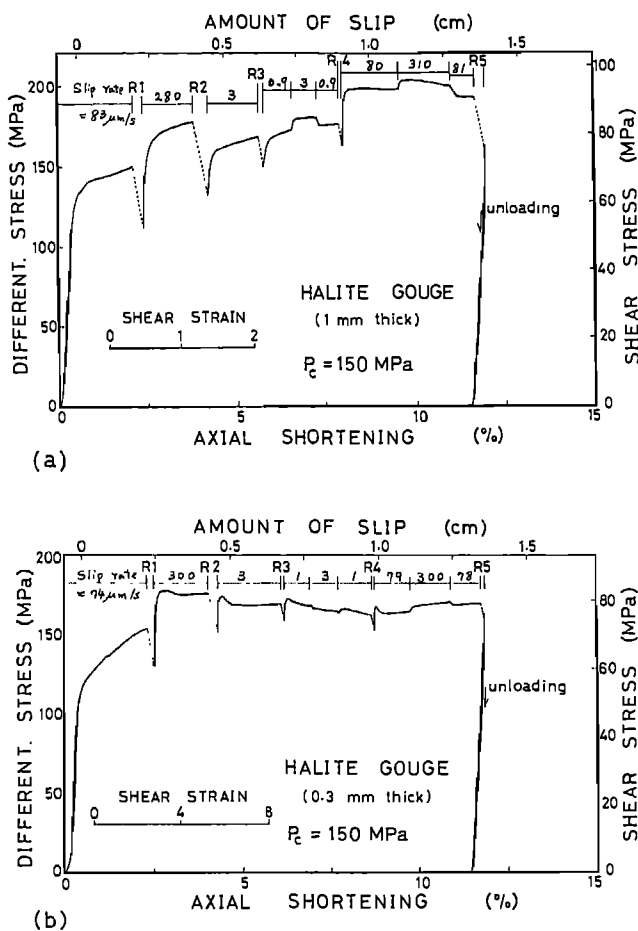


Fig. 1. Differential stress versus axial shortening curves for two specimens of Tennessee sandstone with (a) 1 mm thick and (b) 0.3 mm thick layers of natural halite along a 35° pre-cut, deformed at room temperature and at a confining pressure of 150 MPa (run numbers = H02 and H05). In this and the next two figures, the slip rate along the pre-cut, which was changed either abruptly or after several minute pause in the loading, is shown in  $\mu\text{m/s}$  near the top of each diagram. Short dashed lines beneath R0-R5 in these diagrams indicate stress relaxation just after the loading motor was turned off.

obtained for synthetic halite [see Shimamoto, 1985b, Fig. 8]. The shear resistance is nearly independent of the normal stress at pressures above about 100 MPa at slow velocities and above about 250 MPa at fast slip rates.

#### Velocity Dependence of Steady-State Friction

A variety of changes in the velocity dependence can be seen in the relationship between the steady-state friction and the velocity (Figures 5 and 6; see also Shimamoto [1985b; 1986]). The resistance to slip is expressed in terms of the

shear stress rather than the frictional coefficient, for the latter varies substantially with the normal stress at high pressures (examine Figure 4). A number of observations are notable.

(1) At pressures below 100 MPa, a negative velocity dependence is present at intermediate velocities. Well-defined stick-slip is observed at and below 35 MPa confining pressure for synthetic halite and at and below 70 MPa for natural halite. Stick-slip has been recognized only at velocities showing negative dependence, consistent with the theoretical prediction of Rice and Ruina [1983].

(2) The negative velocity dependence changes to a positive dependence at slow slip rates. This is accompanied by a change in sliding mode; stick-slip changes to episodic slip and then to stable sliding. These occur when the shear resistance becomes nearly equal to that in the pressure-insensitive flow regime at 250 MPa [Shimamoto, 1986]. Those changes, although

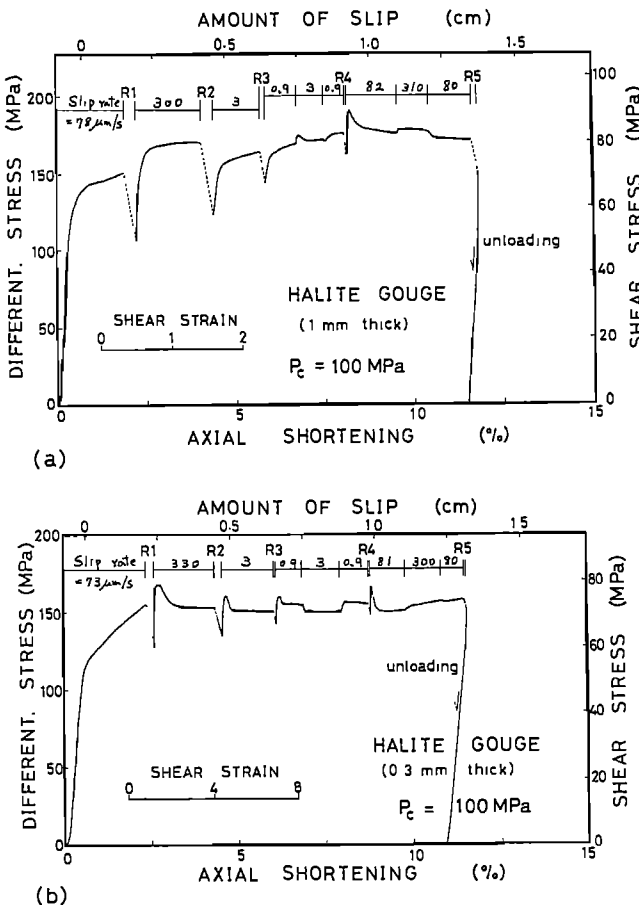


Fig. 2. Stress-shortening curves for two specimens of Tennessee sandstone with (a) 1 mm thick and (b) 0.3 mm thick layers of natural halite, deformed at room temperature and at a confining pressure of 100 MPa (run numbers = H03 and H04).

suggested by the previous theoretical model of Higgs [1981] and from experimental considerations by Logan [1978], have not been documented to date, to our knowledge. Such a transition is not reached in the test at 10 MPa confining pressure (Figure 5).

(3) Another transition from negative to positive velocity dependence occurs with increasing velocity; i.e. the transition from frictional regime to high-speed frictional regime [Shimamoto, 1986]. This change is accompanied also by a transition in sliding mode from stick-slip to stable slip. The abrupt slip events associated with stick-slip were not audible and were rela-

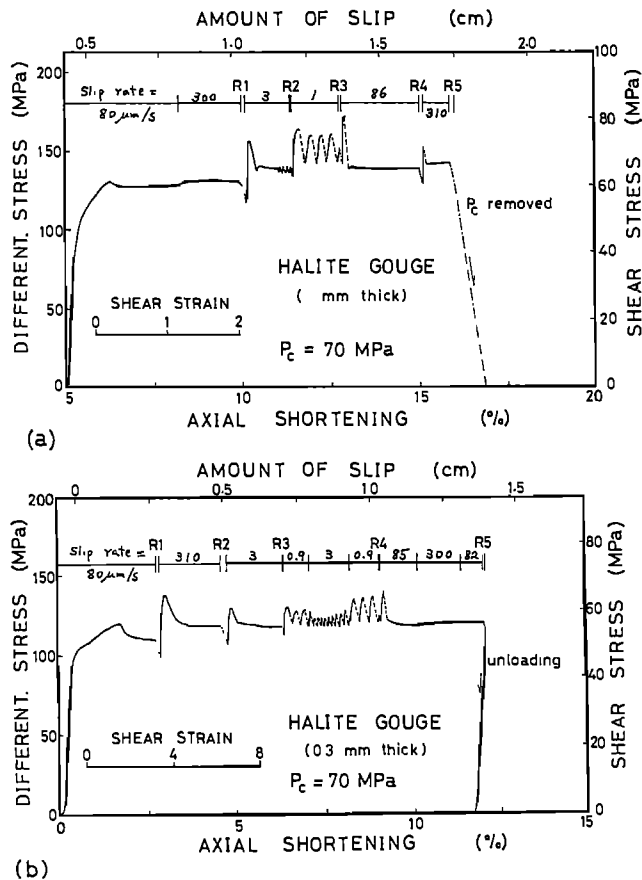


Fig. 3. Stress-shortening curves for two specimens of Tennessee sandstone with (a) 0.7 mm thick and (b) 0.3 mm thick layers of natural halite, deformed at room temperature and at a confining pressure of 70 MPa (run numbers = H01 and H06). Long dashed lines indicate abrupt slip events during stick-slip. Halite layer was precompacted by a  $P_c$ -reduction treatment for the run shown in (a), whereas in the other runs shown in Figures 1-3 halite was precompacted by leaving the specimen under a confining pressure of 200 MPa and a differential stress of 100 MPa for 15-20 minutes.

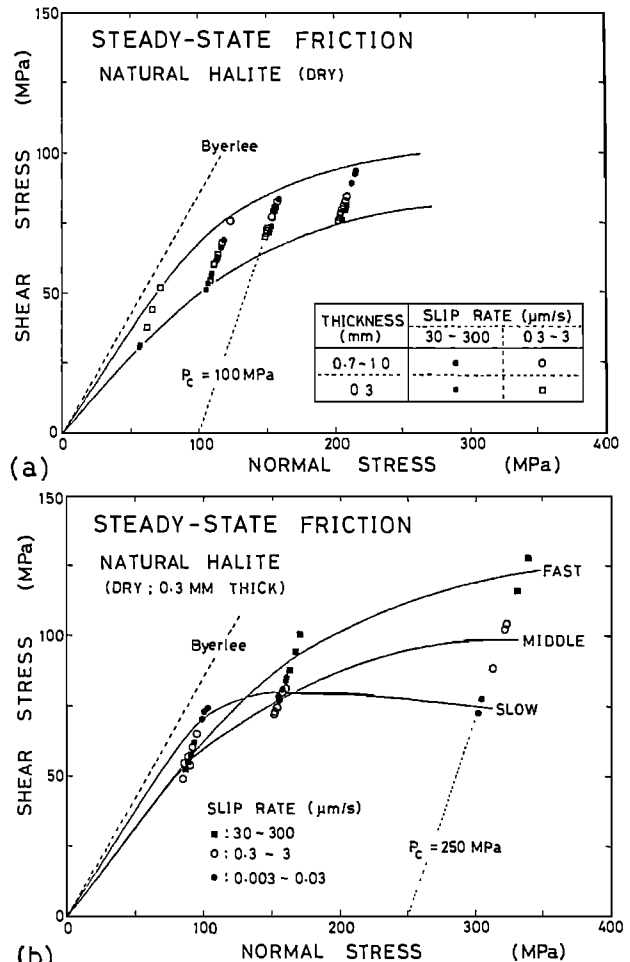


Fig. 4. Shear stress versus normal stress on the precut at steady-state or nearly steady-state sliding for specimens of Tennessee sandstone with natural halite: (a) 0.7-1.0 mm thick layer of halite (run numbers = H01-H03) and 0.3 mm thick layer of halite without  $P_c$ -reduction treatment (run number = H04-H07), (b) 0.3 mm thick layer of halite with  $P_c$ -reduction treatment (run numbers = H16, H18 and H19). When stick-slip occurred, a regular stick-slip portion was selected and the peak in the stress was plotted. The intercept of a straight line through each group of data with the abscissa gives the confining pressure. The long dashed lines indicate the frictional strength for most rocks compiled by Byerlee (1978).

tively slow phenomena, presumably due to this velocity barrier against slip acceleration. While Dieterich [1978] showed a change to no velocity dependency in a granite, and Weeks and Tullis [1984] suggested the presence of a positive dependency in dolomite at faster rates, this is also the first clear documentation of a complete transition for rocks that we are aware

## 54 SIMULATED HALITE SHEAR ZONES

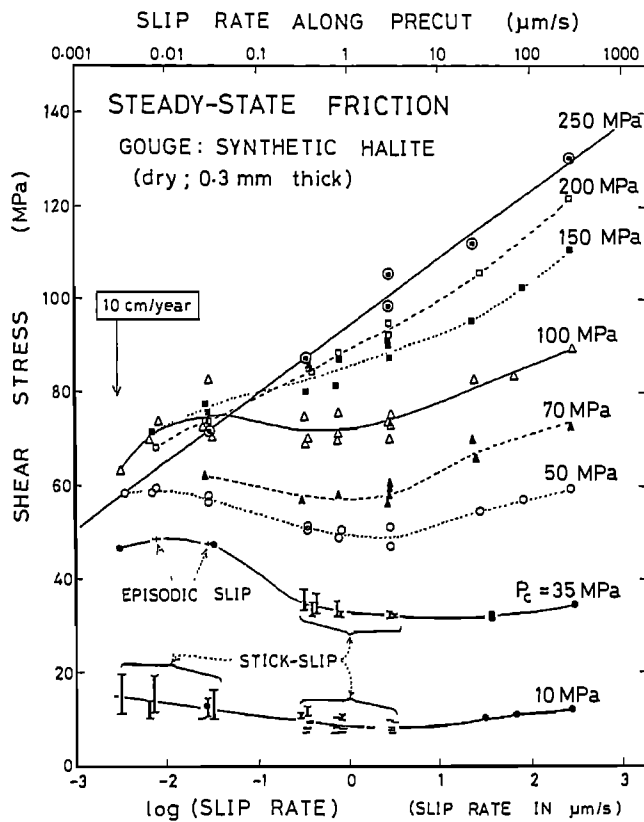


Fig. 5. Steady-state or nearly steady-state shear resistance of synthetic halite (0.3 mm thick) plotted against the logarithm of slip rate along the pre-cut (run numbers = H08-H15; from Shimamoto, 1985b). The shear resistance is expressed as the shear stress on the pre-cut. Plotted are the results from 8 runs at confining pressures as shown on each curve. When stick-slip occurs, a regular stick-slip portion is selected and the shear stresses at the onset and at the stop of abrupt slip events are tied with a thick vertical bar in the diagram. The run at a confining pressure of 35 MPa is the second run that was performed on the same specimen deformed at 70 MPa, also shown in the figure, after the displacement had been reset. All other runs in this and next figures are on initially undeformed specimens.

of. The slope in the high-speed frictional regime is reduced with decreasing pressure, and the friction-velocity curve approaches that typical of brittle behavior (cf. the curve at 10 MPa in Figure 5, and Figure 1 in Dieterich [1978]).

(4) There is a change at intermediate velocities from negative to positive dependency at pressures around 100 MPa. Such a behavior had been implied from previous experimental results [Brace and Byerlee, 1970; Higgs and Logan, 1977; Stesky, 1978; Higgs, 1981] but not documented in a systematic fashion. With this change is an

increase in the slope of the positive dependency in the high-speed frictional regime and expansion of this domain (Figure 5). At 250 MPa confining pressure, friction-velocity curves change into that for pressure-insensitive shearing flow (see also Shimamoto [1986] Figure 4).

#### Microscopic Observations

Microscopic observations were made on polished specimens with a polarized microscope under reflected light to examine the physical processes involved in the various mechanical behaviors of simulated faults. The country rock shows no evidence of permanent deformation and textures of halite only will be described. Specimens were polished by standard procedures using benzine which turned out to be much more effective than alcohol in preventing the dissolution of halite. The final polish was made with a diamond paste (1  $\mu\text{m}$  in size), and this was essential for producing good polished surfaces. Grain boundaries were etched by putting a small amount of saliva over the polished surfaces and wiping it off quickly. Observations on thin sections were not effective in revealing fine textures. Observations of dislocations on polished surfaces not on cleaved surfaces, following the procedures of Mendelson [1961] were not successful.

Because we mounted uncompacted halite grains on the pre-cut surfaces before the tests, the halite layer tends to be slightly thicker toward the lower leading edge of the pre-cut specimen. In all photomicrographs reported, the shear strain,  $\gamma$ , was computed from the measured displacement using the thickness of halite at the location of each photomicrograph. Thus,  $\gamma$  is the average shear strain at that location, whereas  $\gamma_{av}$  in Table 1 is the average shear strain of the halite layer as a whole.

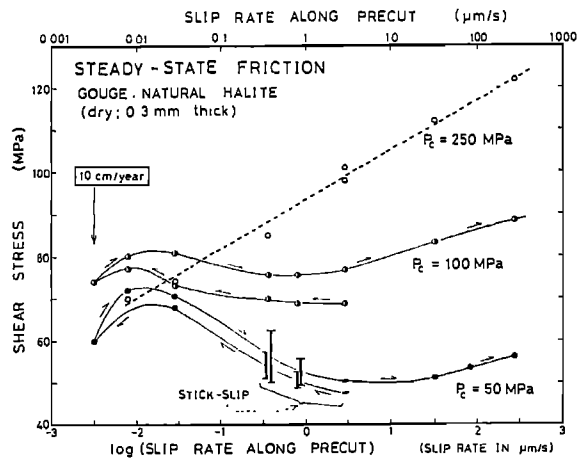
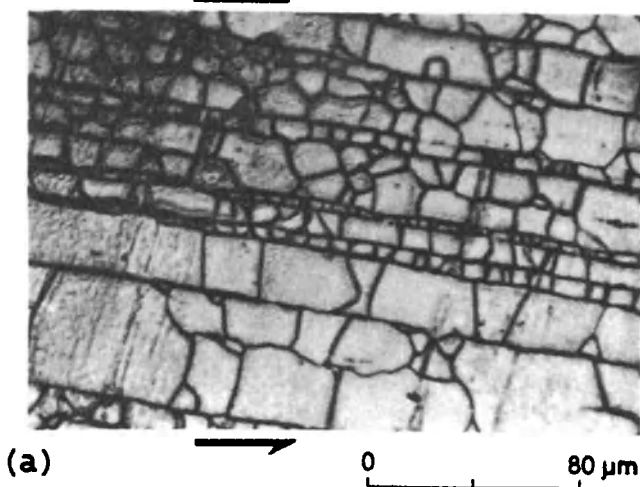


Fig. 6. The same as Figure 5 for natural halite (0.3 mm thick) from three tests (run numbers = H16, H18 and H19; from Shimamoto, 1985b). Arrows point toward a later stage of each test.

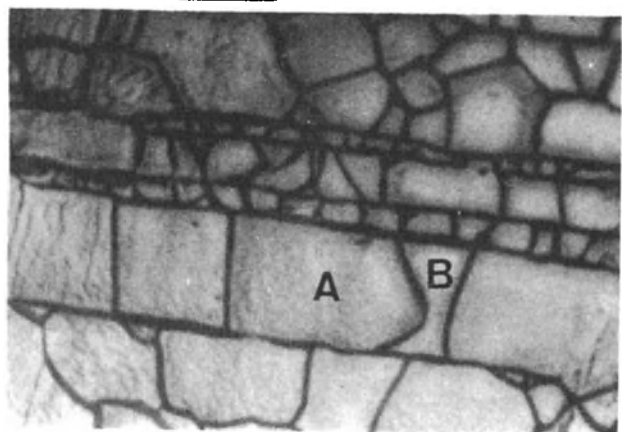
Recrystallized Grains and Foliation

Well-defined foliation, characteristic of only natural halite, is manifest by the straight and very continuous alignment of grain boundaries (Figure 7). Because of these straight boundaries, the grains tend to be rectangular in shape. Such foliation is absent in the synthetic-halite shear zones where most grains are equant

$P_c = 70 \text{ MPa}$ ,  $\gamma = 30.3$



(a)  $0$   $80 \mu\text{m}$

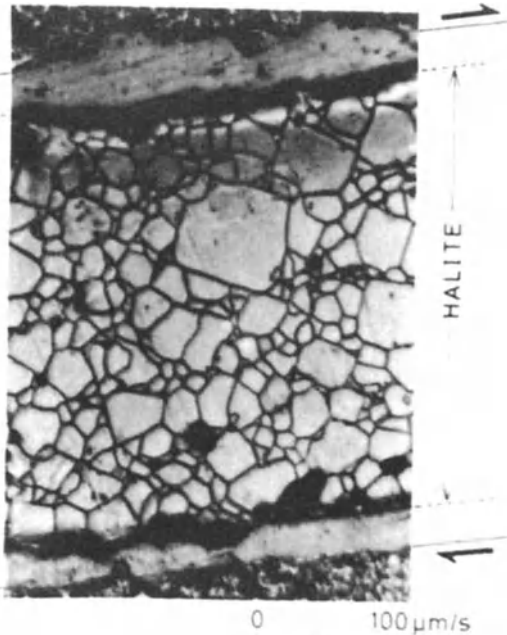


(b)  $0$   $40 \mu\text{m}$

Fig. 7. Photomicrographs showing well-developed foliation in natural halite sheared along a  $35^\circ$  precut of Tennessee sandstone at room temperature and at a confining pressure of 70 MPa (reflected light; run number = H01). (b) is a close-up of the central part of (a). In this and subsequent photomicrographs,  $\gamma$  denotes the shear strain at the end of each run and the sense of shear is shown with a pair of arrows.

## SYNTHETIC HALITE

$P_c = 250 \text{ MPa}$ ,  $\gamma = 38.5$



$0$   $100 \mu\text{m/s}$

Fig. 8. Photomicrograph of recrystallized grains of synthetic halite sheared at room temperature and at a confining pressure of 250 MPa (reflected light; run number = H15). The halite and country rock was separated upon the removal of pressure.

and display typical recrystallized textures (Figure 8).

From his experiments, for which  $\gamma_{av}$  is less than 16, Knapp [1983] reports textural evidences indicating that these grains formed by recrystallization from fine-grained deformed halite. In our high-strain experiments for which  $\gamma_{av}$  varies from 14 to 115, recrystallization is more complete and the textures showing recrystallized euhedral neoblasts in the fine-grained matrix are seen only locally. Grain-boundary geometry often implies that grain-boundary migration took place; e.g., the boundary between A and B in Figure 7b seems to have migrated rightward resulting in the growth of grain A.

It is not perfectly clear at this time whether these grains formed during shearing deformation of halite (dynamic or syntectonic recrystallization) or after the termination of the experiments (static or annealing recrystallization). Our attempt to observe dislocations to resolve this problem has been unsuccessful so far. The following evidence, however, strongly suggests that a considerable fraction of these grains formed or grew after the deformation. (1) The textures occasionally changed substantially, especially on humid days during our observations;

## 56 SIMULATED HALITE SHEAR ZONES

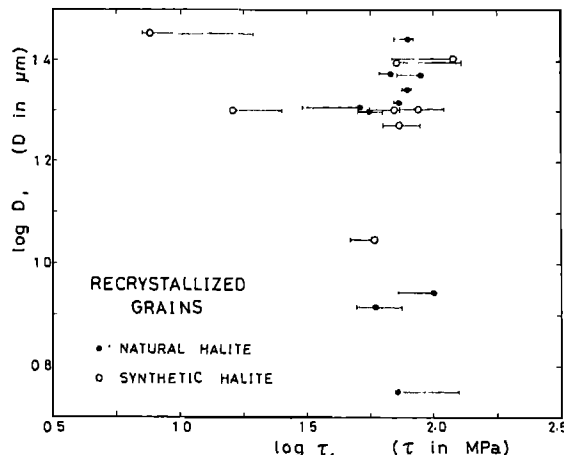


Fig. 9. Plot of log grain size,  $D$ , versus log shear stress,  $\tau$ , for recrystallized grains of natural (closed) and synthetic (open) halite, sheared at room temperature and at confining pressures to 250 MPa (run numbers = H01-H16, H18 and H19). Grain sizes were measured by use of an intercept method (Smith and Guttman, 1953; see also, Christie and Ord, 1980).

in some cases, the fine grains disappeared almost completely to form an aggregate of coarse-grained neoblasts. (2) Deformed halite exhibits no clear relationship between the grain size and stress (Figure 9). This implies either that such relationships [e.g., Carter et al., 1982] do not hold in the pressure-dependent semibrittle and semiductile fields or that the original grain sizes were altered by later grain growth. (3) Grain sizes in our halite shear zones are much larger than those expected for the shear stress in our experiments from previously established relationships (cf. Figure 9, and Figure 3 in Carter et al. [1982]). Moreover, our early tests (H01 - H07) had been done on the same cooking salt in 1981, about 2 years before the later tests (H16 - H20) were made. The grain sizes for H01 - H07 all fall on the upper right corner of Figure 9 and are distinctly more coarse-grained than those for later tests which plot on the lower right corner. This might imply that some grain growth took place during that time interval.

Highly deformed halite grains are very unstable, and this may not be surprising if one thinks of the internal energy stored in the grains during the deformation for which the axial ratio of the strain ellipse amounts to a few hundreds to as much as several thousands (Table 1). We conclude that the textures in the halite shear zones do not necessarily reflect the processes of deformation.

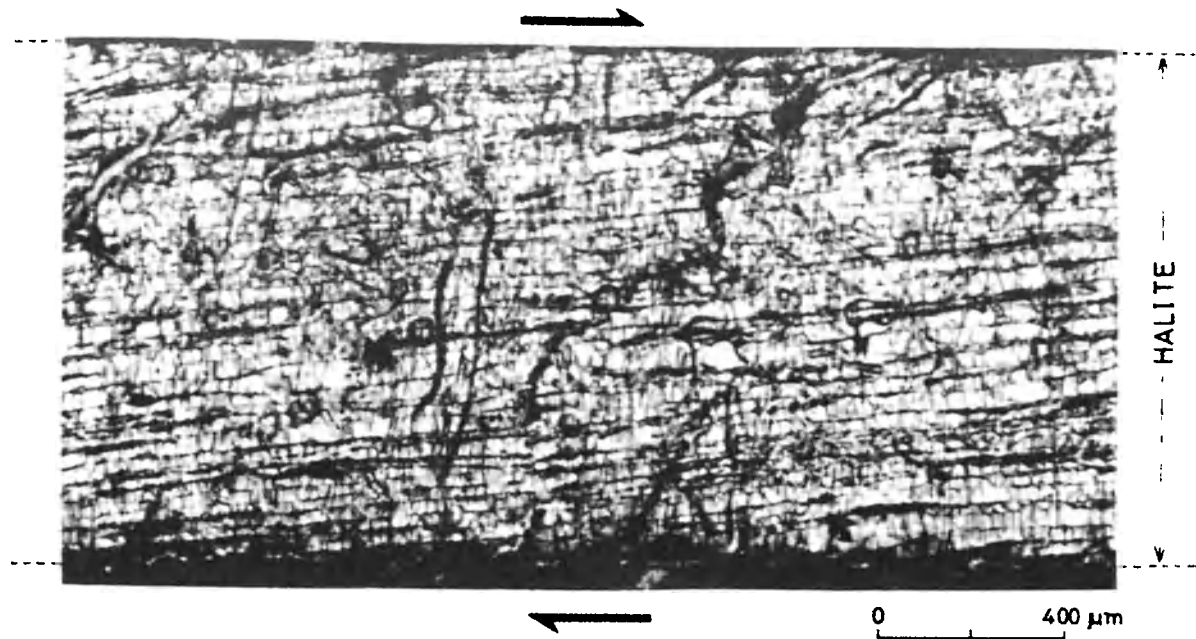
#### Origin of Foliation

The most conspicuous texture we have observed is the foliation and its pattern within the halite shear zones. Indeed, it appears to be the

only structure that convincingly reflects the deformation processes in halite. Figure 10 displays uniform and well-developed foliation in natural halite deformed at 150 MPa pressure. The measured angle,  $\theta_{\text{obs}}$ , between the foliation and rock-halite boundary is  $4.3^\circ \pm 0.5^\circ$ , the error being one standard deviation of 8 measurements at different locations on the same polished specimen (19 mm long). Assuming homogeneous simple shear for the deformation of halite, the average shear strain at this location is estimated from the total displacement and the thickness of the shear zone as 13.2. The angle,  $\theta_{\text{cal}}$ , between the orientation of maximum elongation (i.e., the major axis of the strain ellipse) and the shear-zone boundary agrees closely with  $\theta_{\text{obs}}$ . Such a uniform and pervasive foliation was observed in specimen H16 for which the agreement was very good; that is  $\theta_{\text{obs}} = 1.8^\circ \pm 0.8^\circ$  and  $\theta_{\text{cal}} = 2.17^\circ$ .

The starting material compacted only by a confining pressure of 200 MPa and a differential stress of 100 MPa is a structureless aggregate of halite clasts and granulated material [Hiraga and Shimamoto, 1986; see also Knapp, 1983, Figure 11]. This, together with the above, indicate (1) that the foliation is formed parallel to the direction of the maximum elongation of halite grains and (2) that the foliation preserves its original orientation despite the likely post-deformational recrystallization. Friedman and Higgs [1981] and Knapp [1983] observed foliations in calcite and halite shear zones, respectively, and showed that their orientation also can be predicted based on homogeneous simple shear. Foliation in our specimens is somewhat different from those described by them. Halite grains in Figures 7 and 10 are not elongated, different from calcite grains deformed at temperatures of 250°C to around 600°C. Moreover, we could not observe any clear ghost structures on polished surfaces, such as those developed in calcite deformed at temperatures above 600°C and in halite deformed at room temperature and at 70 MPa pressure.

The remarkably straight and continuous grain boundaries (Figure 7) have not been recognized in either synthetic-halite shear zones (Figure 8) or in the zones consisting of crushed natural halite [Knapp, 1983], although they are characteristic of the shear zones composed of cooking salt. The origin of the foliation, although not perfectly clear, appears to be related to the various nutrients that are added to iodized cooking salt and that salt grains should contain impurities near their surfaces. Recall that the axial ratio of the strain ellipse in our experiments is as large as a few hundreds to several thousands (Table 1). When salt grains are deformed uniformly to such an extreme degree, the original grain surfaces should become very straight and planar in the direction parallel to the maximum grain elongation. Diffusion of the impurities should be very slow at room temperature, and hence the impurities should be distributed along the straight and continuous planes which were



$$P_c = 150 \text{ MPa}, \quad \gamma = 13.2, \quad \theta_{\text{cal}} = 4.29^\circ, \quad \theta_{\text{obs}} = 4.3^\circ \pm 0.5^\circ$$

Fig. 10. Photomicrograph showing uniformly and well-developed foliation across the entire layer of natural halite, sheared at room temperature and at a confining pressure of 150 MPa (reflected light; run number = H02). The observed angle,  $\theta_{\text{obs}}$ , between the foliation and the rock-halite interface agrees quite closely with the calculated angle,  $\theta_{\text{cal}}$ , from the measured displacement and the thickness of halite layer assuming homogeneous simple shear of the halite layer.

original surfaces of salt grains. We believe that these straight and continuous grain boundaries with impurities are immobile even during dynamic or static recrystallization, resulting in the development of foliation. Thus, the presence of impurities near the original grain surfaces seem to be an essential factor in the foliation formation, although this is yet to be tested by experiments.

#### Localization of Deformation

Despite textural differences, uniformly developed foliation such as that in Figure 10 has been recognized in halite shear zones deformed at room temperature and at 70-MPa confining pressure [Knapp, 1983]. Also, halite had been shown to exhibit stick-slip and negative velocity dependence under similar conditions [Shimamoto, 1982]. The enigma is how homogeneously shearing halite yields unstable behavior. Indeed, homogeneously deforming materials rarely exhibit negative strain-rate dependency [R.A. Schapery, personal communication, 1984]. Thus, this was a motivation of our further observations.

Upon closer examination, the deformation is found to be far from homogeneous. In an example of slightly heterogeneous deformation (Figure 11), foliation is pervasive and nearly continuous

but is wavy-shaped and seems to be discontinuous across AB and CD. In other examples, Figures 12 and 13, the foliation (solid lines in the sketches) exhibits complex patterns which are discontinuous. The patterns of the dotted portions are not very clear but perhaps can be correlated with that of Riedel shears, particularly  $R_1$  and Y shears [e.g., Bartlett et al., 1981]. This may imply that brittle deformation is overlapped on the ductile deformation associated with the formation of foliation. However, the dotted portions consist of an aggregate of relatively equigranular and equant grains, displaying a classic recrystallization texture, and is virtually free from microfractures (Figure 14).

For halite deformed at 150 MPa pressure, deformation is homogeneous when the shear strain,  $\gamma$ , is 13.2 (Figure 10) but is heterogeneous when  $\gamma$  is 27.2 (Figure 12). Our halite deformed at 70 MPa pressure exhibits heterogeneous deformation (Figure 13), but halite deformed less at the same pressure shows homogeneous deformation [Knapp, 1983]. Thus, deformation is homogeneous initially and appears to become heterogeneous only after the shear strain reaches a critical value,  $\gamma_{\text{cr}}$ . The effect of slip rate on this critical shear strain is not clear from our data, since the velocity was varied during the test. The shear

## 58 SIMULATED HALITE SHEAR ZONES

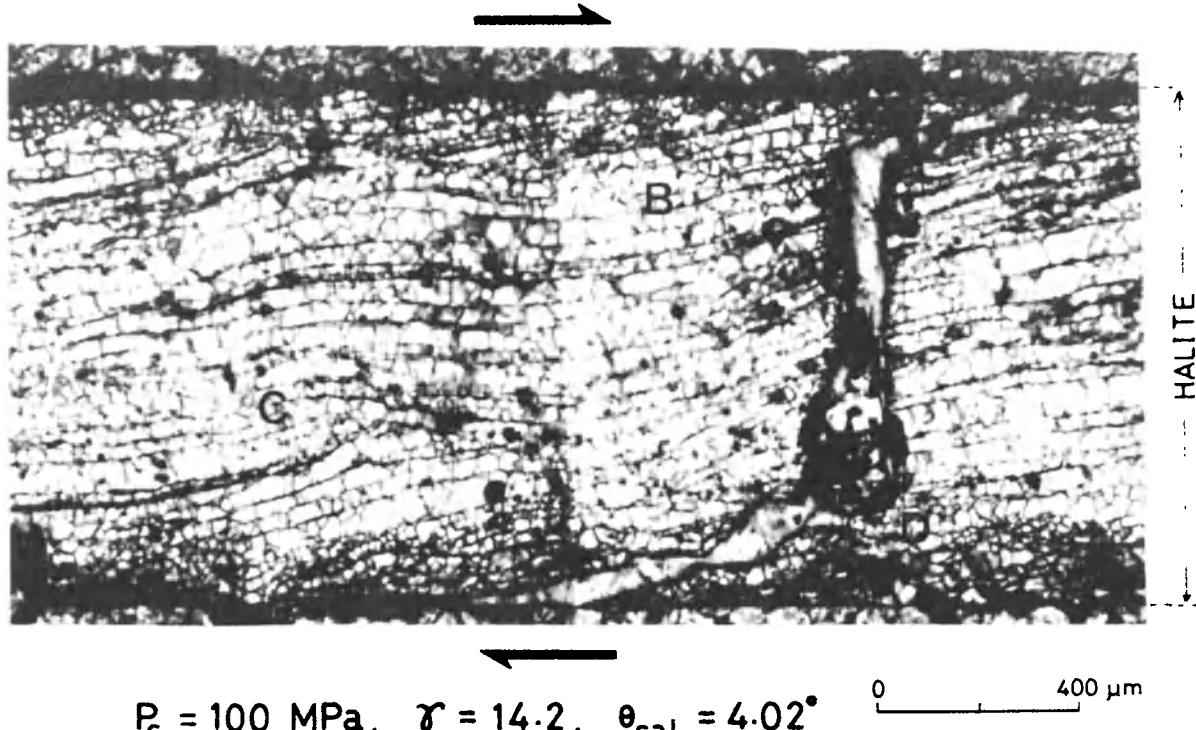


Fig. 11. Photomicrograph showing somewhat heterogeneous deformation of natural halite at room temperature and a confining pressure of 100 MPa (reflected light; run number = H03). Foliation is wavy shaped and seems to be discontinuous across AB and CD.

strain for halite in Figure 11 deformed at 100 MPa pressure is about the same as that for halite in Figure 10 deformed at a higher pressure, but the deformation is heterogeneous in the former, so the critical shear strain for the strain localization seems to increase with increasing pressure.

#### Synthesis of Mechanical and Observational Data

Deformation thus changes from homogeneous to heterogeneous with progressive shearing. It has been revealed also that the mechanical behavior changes from flow type to friction type with increasing displacement. Figure 15 summarizes the comparison of the observational and mechanical data in confining pressure versus shear-strain space.

Deformation of halite is divided roughly into (1) homogeneous deformation which is characterized by a uniformly and well-developed foliation with good agreement between  $\theta_{\text{obs}}$  and  $\theta_{\text{cal}}$  (Figure 10); (2) heterogeneous deformation which is represented in Figures 11-13, and; (3) very heterogeneous deformation which displays a more complex pattern of foliation than those in Figures 11-13. The observational data are plotted using the average shear strain at the location of the polished specimen.

Differences in flow-type and friction-type behaviors can be recognized best at the interme-

diate range of velocity ( $0.3\text{-}3 \mu\text{m/s}$ ), because this range is characterized by the negative velocity dependence of friction over a wide range of confining pressures (Figures 5 and 6). Thus, the mechanical behaviors of simulated faults at intermediate velocities are divided into (1) flow type and (2) friction type based on their characteristics. The ranges of shear strain for which these behaviors are identified on the stress-shortening curves, are plotted in Figure 15. The shear strain in this case is the average shear strain,  $\gamma_{\text{av}}$ , for the entire shear zone, i.e., displacement divided by the average thickness of the zone.

Although our data are not exhaustive at high pressures and at low shear strains, Figure 15 indicates (1) that the change in mechanical behavior roughly coincides with the onset of heterogeneous deformation, as shown by the dashed line, and (2) that this critical shear strain markedly increases with increasing confining pressure. Potentially seismogenic friction-type behavior is thus associated with the strain localization within halite shear zones.

#### Discussion and Conclusions

Although our analyses of the data are still preliminary, there are a number of implications. These should be viewed, as argued earlier, not

NATURAL HALITE :  $P_c = 150 \text{ MPa}$ ,  $\tau = 27.2$ ,  $\theta_{\text{cal}} = 2.1^\circ$

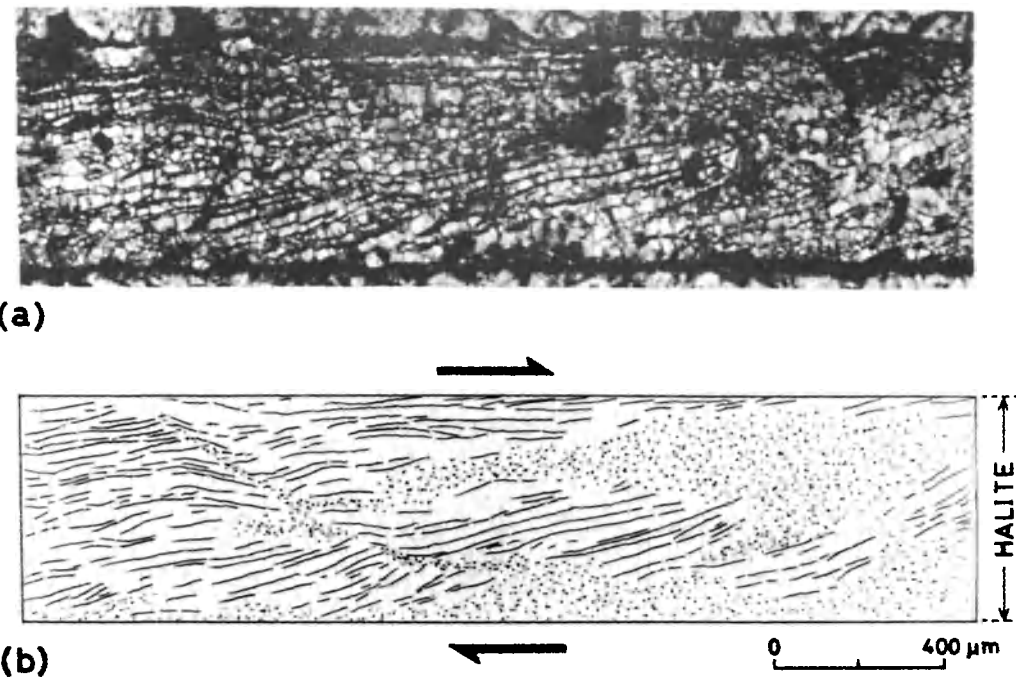


Fig. 12. (a) Photomicrograph under reflected light and (b) its sketch showing heterogeneous deformation of halite at room temperature and at a confining pressure of 150 MPa (run number = H05). Foliation is discontinuous across the dotted portions in (b).

just in the context of halite but as an analog for more representative intrafault materials.

(1) Steady-state friction of a simulated fault with halite is slightly lower than the frictional strength for many rocks compiled by Byerlee [1978] at confining pressures less than about 50 MPa, but deviates markedly from Byerlee's relationship at pressures above about 100 MPa, the departure being greater at slow slip rates (Figure 4). The shear resistance becomes nearly independent of the normal stress at confining pressures above about 250 MPa at fast slip rates and above 100 MPa at slow slip rates [Figure 4b; see also Shimamoto, 1985b, 1986].

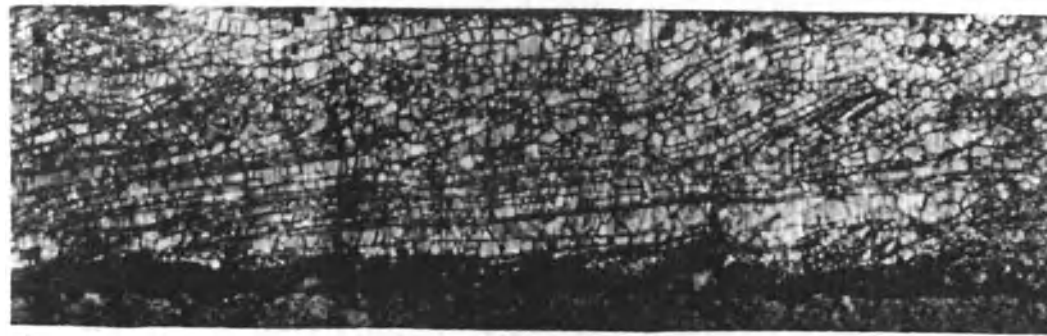
(2) Foliation, defined by parallel alignment of straight and continuous grain boundaries, is well-developed in the shear zones consisting of natural halite deformed at pressures at and above 50 MPa (Figure 10). When foliation is uniform throughout the shear zone, its orientation can be predicted based on homogeneous simple shear. Formation of such a pervasive foliation suggests that the original grains were elongated extensively and uniformly primarily by intracrystalline gliding, although the elongated grains are replaced by recrystallized grains. Notable is that the deformation in this pressure-dependent regime (50–200 MPa confining pressure) is very similar in texture to that developed in the pressure-insensitive flow regime at 250 MPa

pressure. Such an apparently ductile but pressure-dependent deformation will be called "semiductile". Deformation appears to be predominantly brittle at pressures below 10 MPa and semibrittle roughly at 30–50 MPa pressures. Shear zones consisting of synthetic halite are structureless and their textures cannot be used to infer the deformation processes.

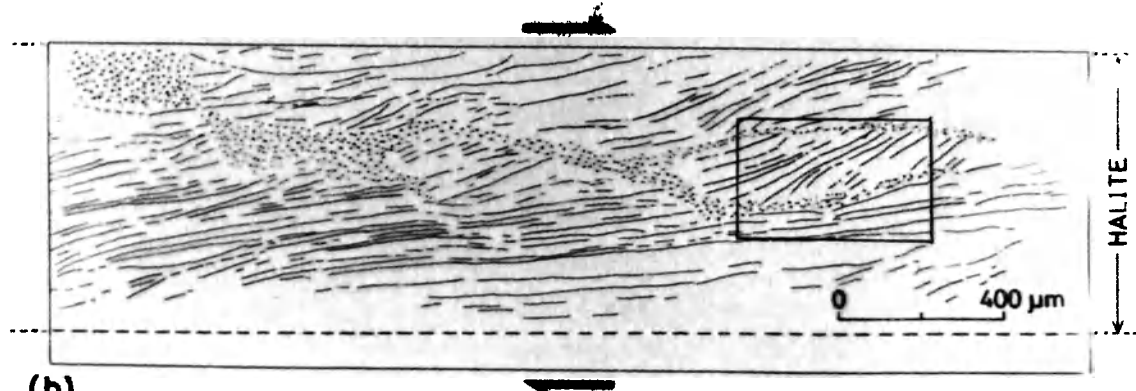
(3) Two contrasting behaviors upon step-changes in velocity are recognized (Figures 1–3): (i) flow type characterized by monotonic and gradual change in shear resistance toward a new steady-state value without showing any instantaneous response and by positive velocity dependency of steady-state shear resistance, and (ii) friction type [e.g., Dieterich, 1979a], which shows an instantaneous viscous like response, followed by a gradual change within a characteristic displacement toward a new steady-state value, and a negative velocity dependency of steady-state friction. Behavior at fast slip rates (high-speed frictional regime) is somewhat different from these.

(4) The behavior changes from flow type to friction type with increasing shear strain of halite or with increasing displacement along a simulated fault (Figures 1–3). This coincides with a change from homogeneous shearing deformation (Figure 10) to heterogeneous deformation (Figures 11–13), and the critical

NATURAL HALITE:  $P_c = 70 \text{ MPa}$ ,  $\gamma = 30.3$ ,  $\theta_{cal} = 1.9^\circ$



(a)



(b)

Fig. 13. (a) Photomicrograph under reflected light and (b) its sketch showing heterogeneous deformation of natural halite at room temperature and at a confining pressure of 70 MPa (run number = H01). Foliation, shown in solid lines in (b), are discontinuous across the dotted portions in the same sketch.

shear strain for these changes increases markedly with increasing confining pressure (Figure 15). Potentially seismogenic friction-type behavior is associated with a localization of deformation with the shear zone.

(5) Stick-slip is recognized only when the velocity dependence of steady-state friction is negative (Figures 5 and 6), consistent with the theoretical prediction by Rice and Ruina [1983]. Synthetic halite exhibits stick-slip at pressures to 35 MPa (Figure 5), whereas well-defined stick-slip is recognized for natural halite to 70 MPa (Figures 3 and 6). Presumably, impurities in halite destabilizes fault motion.

(6) A transition between frictional slip and ductile shearing flow is observed for the first time, thereby linking the friction-velocity relationship in the brittle regime [Dieterich, 1978, Figure 1] and that in the pressure-insensitive flow regime (Figures 5 and 6). Friction-type behavior changes with decreasing velocity into flow-type behavior when friction becomes nearly equal to the flow stress in the pressure-

insensitive flow regime (see Shimamoto [1986] for a criterion for this transition). The friction-type behavior changes with increasing velocity into stable behavior in the high-speed frictional regime. With increasing confining pressure, the frictional regime shrinks and the high-speed frictional regime expands, and the friction-velocity relationship changes to a flow law in the pressure-insensitive regime.

While, results 5 and 6 (already reported in Shimamoto, 1985b, 1986) are the principal mechanical findings of this study, this paper intends to seek the physical processes responsible for the various behaviors through the observation of deformed halite. For the imminent prediction of earthquakes, it would be essential to understand the processes leading to the rupture initiation of large or great earthquakes. Because the frictional strength increases with increasing depth and therefore the deeper part of a fault should resist slip until the last moment, the majority of large earthquakes nucleate near the base of the seismogenic layer [Das and Scholz,

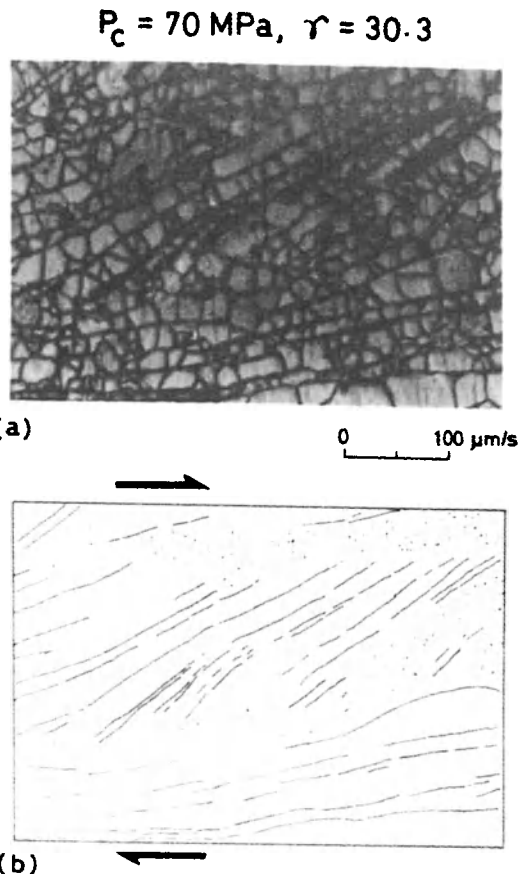


Fig. 14. Close-up of the framed portion on the right side of Figure 12, (b). Foliation (solid lines) is discontinuous across the dotted portions which consist of an aggregate of more or less equigranular halite grains.

1983]. It is important in this regard that the domain of stick-slip or potentially-unstable frictional slip with a negative velocity dependency is extended well into the semiductile field of deformation (results 2, 5, and 6). Thus, the fault constitutive properties in the semiductile field emerges as the primary area of interest. Determination of constitutive parameters describing the wide spectrum of behavior of halite and modeling of fault motion based on them will be an important step toward realistic modeling of large earthquakes.

Another interesting aspect is that the foliation developed in natural halite in the semiductile regime is similar to the planar structures in mylonites and that the semiductile field occupies a considerable range of pressure dependence (results 1 and 2). Thus, mylonites should receive renewed attention with the view that seismic fault motion could well be associated with at least some of these zones.

As for the mechanisms responsible for poten-

tially seismogenic fault motion in the semiductile field, the most significant finding is that its onset nearly coincides with the strain localization within the halite shear zone (result 4). Such a coincidence might have been expected but has not been documented previously. The prediction of the onset of this localization is an interesting future problem. However, the potentially unstable fault motion is a post-localization phenomenon and hence this prediction in itself will not lead to understanding of the underlying processes. Textures of halite in Figures 11-13 suggest that deformation of a brittle nature is superposed on the ductile deformation after the localization. But the exact nature of this heterogeneous deformation is not clear. Although closer observations of deformed halite are now in progress, it is recrystallized so completely that it is perhaps not suitable for close examination of the deformation processes during slip. It may be necessary in the future to seek another material that preserves deformation textures better, even under extreme strain, or to attempt an observation during deformation.

Knapp [1983] suggests recrystallization waves [see McQueen and Jonas, 1975] as a likely mechanism of stick-slip observed for halite in the semiductile regime. However, the close association of stick-slip with the strain localization

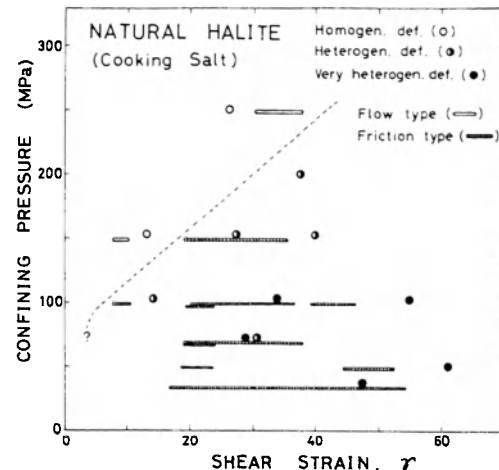


Fig. 15. Summary diagram showing the nature of deformation and the type of mechanical behavior of natural halite, undergoing large shearing deformation at room temperature, in the confining-pressure versus shear-strain space. Nature of deformation is roughly classified into homogeneous, heterogeneous and very heterogeneous deformations, as shown by different circular symbols. Mechanical behavior during the sliding with the intermediate slip rates ( $0.3-3 \mu\text{m/s}$ ) is divided into flow and friction types based on the stress-shortening curves. See text for more explanation of the figure.

## 62 SIMULATED HALITE SHEAR ZONES

indicates that such a mechanism, which does not require the strain localization, is not solely responsible for the unstable behavior. Dieterich [1979a] offers an explanation of frictional properties in the brittle field based on time-dependent interactions of asperities in contact and the changes in the asperity population. His physical model is attractive, but its applicability to semiductile deformation is still uncertain. The pressure is high enough in the semiductile field for individual grains to deform more or less uniformly (Figure 10), so that the intergranular phenomena should be much less significant than in the brittle field. Relative contributions of intergranular and intragranular phenomena after the strain localization are presently unknown, and the underlying processes leading to the unstable fault motion in the semiductile regime are still in the realm of speculation.

The significance of semibrittle deformation with respect to the earthquake problem has been emphasized by Carter and Kirby [1978] and other workers. But it should be kept in mind that the data from deformation of intact specimens are severely restricted in their applications to repeated earthquakes along existing faults and plate boundaries, for the critical shear strain for the strain localization is most likely to be well beyond that reached in those experiments. Even during shearing experiments such as those reported herein, the total displacement often is not sufficient to reach the total displacement required for collecting meaningful data. In our view, this large total displacement is one of the severest limiting factors in performing high-temperature and high-pressure friction experiments in semibrittle and semiductile fields, and many previous data on the velocity dependence of friction cannot be interpreted properly.

The critical strain for strain localization seems to be around 40-50 at 250 MPa pressure where halite is in the pressure-insensitive flow regime (Figure 15). Moreover, specimen H16 deformed at 250 MPa exhibits heterogeneous deformation very locally. Thus, there still exists a possibility that if halite is deformed still further, deformation becomes localized even in the ductile regime to exhibit friction-type behavior. In this regard, our data in Figures 5 and 6 have to be used with caution since these friction-velocity relationships are established for different degrees of heterogeneous deformation in the shear zones at different pressures. There is, of course, no guarantee that the degree of strain heterogeneity along natural faults changes with increasing depth in the same manner as in our experiments. Friction experiments with even larger displacements need to be done to examine the large-strain behavior more completely.

Halite data have implications for the long-term behavior of faults. All friction laws are

established on an empirical basis mostly from short-term laboratory tests and they are applicable to slow motion of natural faults only if the long-term behavior can be predicted by these laws [Shimamoto and Logan, 1984]. Halite data at very slow rates (down to 10 cm/yr) are encouraging in this respect, since no peculiar long-term behaviors are observed. For instance, the logarithmic law for steady-state friction [Dieterich, 1978] holds for halite shear zones until the friction-velocity curves hit that for the pressure-insensitive flow regime. Friction laws have perhaps wide applicabilities to the natural faults, although scale-effects on the laws are uncertain at present.

**Acknowledgements.** We thank J.H. Dieterich, J.W. Handin, J. Rice, T. Tullis, and F. Chester for many stimulating discussions and suggestions. This work was supported by the U.S. Geological Survey, Grants 14-18-0001-19293 and 14-0001-21181.

## References

- Bartlett, W. L., M. Friedman, and J. M. Logan, Experimental folding and faulting of rocks under confining pressure, Part IX. Wrench faults in limestone layers, *Tectonophysics*, **79**, 255-277, 1981.
- Brace, W. F., and J. D. Byerlee, Stick-slip as a mechanism for earthquakes, *Science*, **153**, 990-992, 1966.
- Brace, W. F., and J. D. Byerlee, California earthquakes - why only shallow focus? *Science*, **168**, 1573-1575, 1970.
- Bridgeman, P. W., Some implications for geophysics of high-pressure phenomena, *Geol. Soc. Am. Bull.*, **62**, 533-536, 1951.
- Byerlee, J. D., Friction of rocks, *Pure Appl. Geophys.*, **116**, 615-626, 1978.
- Carter, N. L., and F. D. Hansen, Creep of rocksalt, *Tectonophysics*, **92**, 275-333, 1983.
- Carter, N. L., and S. H. Kirby, Transient creep and semibrittle behavior of crystalline rocks, *Pure Appl. Geophys.*, **166**, 807-839, 1978.
- Carter, N. L., F. D. Hansen, and P. E. Senseny, Stress magnitudes in natural rock salt, *J. Geophys. Res.*, **87**, 9289-9300, 1982.
- Christie, J. M., and A. Ord, Flow stress from microstructures of mylonites: example and current assessment, *J. Geophys. Res.*, **85**, 6253-6262, 1980.
- Das, S., and C. H. Scholz, Why large earthquakes do not nucleate at shallow depths? *Nature*, **305**, 621-623, 1983.
- Dieterich, J. H., Time-dependent friction and the mechanics of stick-slip, *Pure Appl. Geophys.*, **116**, 790-806, 1978.
- Dieterich, J. H., Modeling of rock friction, 1, Experimental results and constitutive equations, *J. Geophys. Res.*, **84**, 2161-2168, 1979a.
- Dieterich, J. H., Modeling of rock friction, 2,

- Simulation of preseismic slip, *J. Geophys. Res.*, 84, 2161-2168, 1979b.
- Dieterich, J. H., Constitutive properties of faults with simulated gouge, *Geophys. Monogr. Ser.*, AGU, Washington, D. C., 24, 103-120, 1981.
- Dieterich, J. H., Nucleation and triggering of earthquake slip (abstract), *IASPEI, 23rd General Assembly, Tokyo*, 2, 389, 1985.
- Friedman, M., Mechanical properties of rocks affecting earthquake prediction and control, 2nd Semi-Annual Progress Report to U. S. Geol. Survey, 22 pp., 1975.
- Friedman, M., and N. G. Higgs, Calcite fabrics in experimental shear zones, *Geophys. Monogr. Ser.*, AGU, Washington, D. C., 24, 11-27, 1981.
- Handin, J. W., M. Friedman, J. M. Logan, L. J. Pattison, and H. S. Swolfs, Experimental folding of rocks under confining pressure: buckling of single-layer beams. *Geophys. Monogr. Ser.*, AGU, Washington, D. C., 16, 1-28, 1972.
- Handin, J., J. E. Russell, and N. L. Carter, Experimental deformation of rocksalt, *Geophys. Monogr. Ser.*, AGU, Washington, D. C., 36, 1986.
- Higgs, N. G., Mechanical properties of ultrafine quartz, chlorite and bentonite in environments appropriate to upper-crustal earthquakes, Ph. D. thesis, 267 pp., Texas A&M Univ., College Station, TX, 1981.
- Higgs, N. G., and J. M. Logan, Effects of temperature on gouge deformation in sliding friction experiments (abstract), *EOS Trans. AGU*, 58, 1228, 1977.
- Hiraga, H. and T. Shimamoto, Textures of sheared halite and their implications to seismogenic slip of deep faults, *Tectonophysics*, in press, 1986.
- Knapp, S. T., Gliding flow and recrystallization of halite gouge in experimental shear zones, M. S. thesis, 78 pp., Texas A&M Univ., College Station, TX, 1983.
- Logan, J. M., Creep, stable sliding, and premonitory slip, *Pure Appl. Geophys.*, 116, 773-789, 1978.
- Logan, J. M., and L. W. Teufel, The effect of normal stress on the real area of contact during frictional sliding of rocks, *Pure Appl. Geophys.*, in press, 1986.
- McQueen, H. J., and J. J. Jonas, Recovery and recrystallization during high temperature deformation, in *Treatise on Materials Science and Technology*, Academic, New York, 6, 393-493, 1975.
- Mendelson, S., Dislocation etch pit formation in sodium chloride, *J. Appl. Phys.*, 32, 1579-1583, 1961.
- Rice, J. R., Constitutive relations for fault slip and earthquake instabilities, *Pure Appl. Geophys.*, 121, 443-476, 1983.
- Rice, J. R., and J.-C. Gu, Earthquake after-effects and triggered seismic phenomena, *Pure Appl. Geophys.*, 121, 187-220, 1983.
- Rice, J. R., and A. L. Ruina, Stability of steady frictional sliding, *J. Appl. Mech.*, 50, 343-349, 1983.
- Ruina, A. L., Slip instability and state variable friction laws, *J. Geophys. Res.*, 88, 10359-10370, 1983.
- Shimamoto, T., Effect of fault gouge on frictional properties of rocks: an experimental study, Ph. D. thesis, 198 pp., Texas A&M Univ., College Station, TX, 1977.
- Shimamoto, T., Mechanisms of shallow and intermediate-depth earthquakes in subduction zones: an insight from rock-mechanics (abstract), *Seismol. Soc. Japan Ann. Mtg.*, 2, 189, 1982.
- Shimamoto, T., Confining pressure reduction experiments: a new method for measuring frictional strength over a wide range of normal stress, *Int. J. Rock Mech. Min. Sci. Geomech. Abst.*, 22, 227-236, 1985a.
- Shimamoto, T., The origin of large or great thrust-type earthquakes along subducting plate boundaries, *Tectonophysics*, 119, 37-65, 1985b.
- Shimamoto, T., A transition between frictional slip and ductile flow undergoing large shearing deformation at room temperature, *Science*, 231, 711-714, 1986.
- Shimamoto, T., and J. M. Logan, Laboratory friction experiments and natural earthquakes: an argument for long-term tests, *Tectonophysics*, 109, 165-175, 1984.
- Shimamoto, T., J. W. Handin, and J. M. Logan, Specimen-apparatus interaction during stick-slip in a triaxial compression machine: a decoupled two-degree-of-freedom model, *Tectonophysics*, 67, 175-205, 1980.
- Sibson, R. H., Continental fault structure and shallow earthquake source, *J. Geol. Soc. London*, 140, 741-767, 1983.
- Smith, C. S., and L. Guttman, Measurement of internal boundaries in three-dimensional structure by random sectioning, *Trans. Am. Inst. Min. Metall. Pet. Eng.*, 197, 81-87, 1953.
- Stesky, R. M., Mechanisms of high temperature frictional sliding in Westerly granite, *Can. J. Earth Sci.*, 15, 361-375, 1978.
- Tse, S. T., and J. R. Rice, Crustal earthquake instability in relation to the depth variation of frictional slip properties, *Pure Appl. Geophys.*, in press, 1986.
- Tullis, T. E., and J. D. Weeks, Constitutive behavior and stability of frictional sliding of granite, *Pure Appl. Geophys.*, in press, 1985.
- Weeks, J. D., and T. E. Tullis, Frictional behavior of dolomite (abstract), *EOS, AGU Trans.*, 65, 1077, 1984.

## ON THE ELASTIC CONTACT MODELING OF FAULTS WITH VARIABLE STIFFNESS

B. V. Kostrov

Institute of Physics of the Earth, Moscow, USSR

S. Das

Lamont-Doherty Geological Observatory of Columbia University, Palisades, New York 10964

**Abstract.** A method for determining the slip and stress distribution along a fault with variable stiffness, which is constant outside a finite part of the fault, is presented. An integral equation is developed relating the slip  $\delta(x)$  on the fault to its stiffness  $k(x)$ . The fault stiffness is defined as the ratio of thickness averaged shear stress  $\sigma$  to the average fault slip  $\delta$ ,  $\sigma = k\delta$ . The integral equation is of Fredholm-type with logarithmic singularity, which permits easy numerical solution. To illustrate the method, some particular cases are presented. These range from the case of stress free cracks in a stiff and in a weak environment to the cases of stiff and weak gaps in a weak environment. The two former cases may be regarded as models for creeping portions of faults surrounded by slip-resistant portions, the two latter cases as models for seismic gaps or barriers on a fault.

## Introduction

Recently, heterogeneous fault models with 'asperities' and 'barriers' have received much attention and have been used in the analysis of seismic radiation from heterogeneous faults [e.g., Das and Aki, 1977; Madariaga, 1977; Day, 1982; Das and Kostrov, 1983, 1985] and in the determination of the slip and stress distribution along tectonic faults [e.g., Kostrov and Das, 1982; Li and Rice, 1983a,b; Tse et al., 1985]. Tse et al. [1985] propose an approximate mechanical model of a strike-slip fault in the lithosphere with locked patches (asperities). In their model, the lithosphere is represented by a thin plate under plane stress conditions and thickness averages of slip  $\delta$  and shear stress  $\sigma$  on the fault were related by  $\sigma = k\delta$ , where the fault stiffness  $k$  [Walsh and Grossenbaugh, 1979] is determined by the asperity distribution, and, in general, depends on the position on the fault.

In this paper, the same problem as Tse et al. [1985] addressed is considered but without some a priori assumptions used by them on the nature of the solution, in order to improve the method of

numerical solution. The geometry of the problem is shown in Figure 1. The problem consists of determining slip  $\delta$  and shear stress  $\sigma$  on the fault  $y = 0$ , with shear stress  $\sigma^\infty$  applied at infinity. The fault stiffness is assumed to be constant ( $k = k^\infty$ ) outside the interval  $-L \leq x \leq L$ , within which it is a given function  $k(x)$ .

We now briefly summarize the approach of Tse et al. [1985]. The shear stress distribution along the  $x$ -axis can be expressed in terms of a dislocation density which is equal to  $d\delta/dx$  by [e.g., Li and Rice, 1983a; Tse et al., 1985]

$$\sigma(x) = \sigma^\infty - \frac{\mu(1+\nu)}{2\pi} \text{V.P.} \int_{-\infty}^{\infty} \frac{\delta'(x_1) dx_1}{x-x_1} \quad (1)$$

where V.P. denotes the principal value of the integral,  $\mu$  is the rigidity and  $\nu$  the Poisson's ratio. Here, and in what follows, primes denote differentiation. Using the relation  $\sigma(x) = k(x)\delta(x)$ , one obtains the singular integro-differential equation

$$k(x)\delta(x) = k^\infty\delta^\infty - \frac{\mu(1+\nu)}{2\pi} \text{V.P.} \int_{-\infty}^{\infty} \frac{\delta'(x_1) dx_1}{x-x_1} \quad (2)$$

where  $\delta^\infty$  is the slip at  $x = \infty$ . This equation cannot be solved easily as the integration limits are infinite. To overcome this difficulty, Tse et al. [1985] assume that the slip  $\delta$  is 'effectively' constant outside the interval  $(-L', L')$  when  $L'$  is chosen large enough ( $L' \gg L$ ), and add concentrated dislocations at the ends of the interval  $(-L', L')$  to obtain

$$k(x)\delta(x) + \frac{\mu(1+\nu)}{2\pi} \text{V.P.} \int_{-L'}^{L'} \frac{\delta'(x_1) dx_1}{x-x_1} = \sigma^\infty \left[ 1 + \frac{\mu(1+\nu)}{\pi k^\infty} \frac{L'}{L'^2 - x^2} \right] \quad (3)$$

## 66 ELASTIC CONTACT MODELING

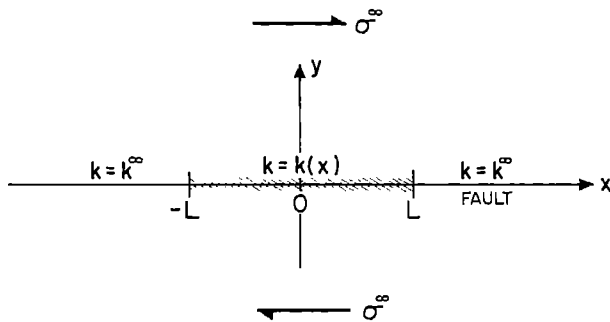


Fig. 1. The geometry of the problem. The fault is the  $x$ -axis, looking down at the plate.

However, in (2), if one assumes  $\delta$  to be effectively constant outside  $(-L', L')$ , then  $\delta'(x) = 0$  outside  $(-L', L')$  and one immediately gets from (2)

$$\sigma(x) = \sigma^\infty - \frac{\mu(1+\nu)}{2\pi} V.P. \int_{-L'}^{L'} \frac{\delta'(x_1) dx_1}{x-x_1} \quad (4)$$

which does not have any dislocation term. It is not clear whether (3) or (4) is better suited for numerical calculations. Moreover, the numerical solution of singular equations requires rather small grid sizes.

#### Method of Solution

In this section, another method to reduce (1) to an integral equation within finite limits is proposed. This method is based on the assumption that  $k(x)$  is constant for  $|x| > L$  alone, and is more economical than using (3) or (4).

We start from the expression (1) for  $\sigma(x)$  on the fault, i.e.,

$$\sigma(x) = \sigma^\infty + \frac{\mu(1+\nu)}{2\pi} V.P. \int_{-\infty}^{\infty} \frac{\delta'(x_1) dx_1}{x_1 - x}$$

The integral term on the right-hand side of this equation can be easily recognized as the imaginary part of the boundary value of an analytic function derivative, i.e.,

$$-\frac{\mu(1+\nu)}{2\pi} V.P. \int_{-\infty}^{\infty} \frac{\delta'(x_1) dx_1}{x_1 - x} = \text{Im } \phi'(x+i0)$$

where

$$\phi(z) = \frac{\mu(1+\nu)}{2\pi i} \int_{-\infty}^{\infty} \frac{(\delta(x_1) - \delta^\infty) dx_1}{x_1 - z}$$

is the Muskhelishvili potential, which is regular in the upper half-plane of  $z = x+iy$ . Obviously,

$$\text{Re } \phi(x+i0) = \frac{\mu(1+\nu)}{2} (\delta(x) - \delta^\infty) \quad (5)$$

The boundary condition  $\sigma = k\delta$  may be expressed in terms of  $\phi$ , as follows

$$\sigma^\infty - \text{Im } \phi'^+(x) = k(x) \left( \frac{2}{\mu(1+\nu)} \text{Re } \phi^+ + \delta^\infty \right)$$

where superscript '+' denotes the boundary value at  $x+i0$ . Our aim now is to express  $\phi(z)$  in terms of the distribution of  $\delta(x)$  within the interval  $-L < x < L$ . To do this, we rewrite the last equation as follows:

$$\text{Im } \phi'^+ + \left( \frac{2ik^\infty}{\mu(1+\nu)} \phi \right)^+ = k^\infty \left( 1 - \frac{k(x)}{k^\infty} \right) \delta(x)$$

where again the relation  $\sigma = k\delta$ , and in particular,  $\sigma^\infty = k^\infty \delta^\infty$  is used. The right-hand side of this equation vanishes for  $|x| > L$ . It is convenient to denote

$$\alpha = \frac{2ik^\infty}{\mu(1+\nu)}$$

and

$$\lambda(x) = 1 - \frac{k(x)}{k^\infty}$$

Using Schwartz's integral, we obtain

$$\phi'^+(z) + i\alpha \phi(z) = \frac{k^\infty}{\pi} \int_{-L}^L \lambda(x) \delta(x) \frac{dx}{x-z}, \quad \text{Im } z > 0$$

Next, we have to eliminate the derivative on the left-hand side of this equation. Using the condition that  $\phi(z)$  must vanish at infinity, this linear differential equation is easily solved to obtain

$$\phi(z) = \frac{k^\infty}{\pi} \int_{-L}^L \lambda(x) \delta(x) \int_{i\infty}^z \frac{e^{i\alpha(\zeta-z)}}{x-\zeta} d\zeta dx$$

Or, substituting  $\alpha(\zeta-z)$  by  $(it)$ , we get

$$\phi(z) = \frac{k^\infty}{\pi} \int_{-L}^L \lambda(x) \delta(x) \int_0^\infty \frac{e^{-t} dt}{t - i\alpha(z-x)} dx$$

Taking the boundary value at  $z = x+i0$ , we obtain

$$\phi^+(x) = \frac{k^\infty}{\pi} \int_{-L}^L \lambda(x_1) \delta(x_1) F(\alpha(x-x_1)) dx_1$$

where

$$F(z) = \int_0^\infty \frac{e^{-t} dt}{t - iz}$$

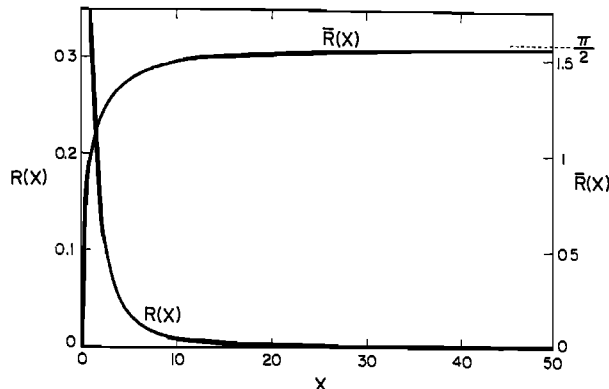


Fig. 2. The functions  $R(x)$  and  $\bar{R}(x)$ , as a function of  $x$ . Note that  $R(x)$  has a logarithmic singularity at  $x = 0$ .

The required integral equation is obtained taking the real part of  $\phi^+$  and using equation (5), which gives

$$\delta(x) = \frac{\alpha}{\pi} \int_{-L}^L \ell(x_1) R(\alpha(x-x_1)) \delta(x_1) dx_1$$

where

$$R(x) = \operatorname{Re} F(z) = \int_0^\infty \frac{e^{-xt}}{t^2+x^2} dt. \quad (6)$$

Representations of  $R(x)$  convenient for numerical calculations, are given in the appendix. Since  $\delta(x)$  is unknown, (6) comprises an integral equation for  $-L < x < L$ . At the same time, it may be used to evaluate  $\delta(x)$  and  $\sigma(x) = k(x)\delta(x)$  outside this interval.

To solve (6) numerically, the interval  $(-L, L)$  is divided into  $n$  equal grids of length  $h$  in each of which  $\ell(x)$  and  $\delta(x)$  are assumed constant and equal to their values at the center of the grid. The integration over each grid is performed analytically (appendix). This reduces the integral equation (6) to the set of simultaneous linear equations

$$\delta_k - \sum_{k=1}^n \ell_k R_{jk} \delta_j = \delta^\infty \quad (7)$$

where

$$R_{jk} = \frac{\alpha}{\pi} \int_{x_j-h/2}^{x_k+h/2} R(\alpha_k(x_j-x')) dx' \quad (8)$$

and  $x_k$  is the position of the center of the  $k$ th grid. Plots of  $R(x)$  and its integral  $\bar{R}(x) = \int_0^x R(x) dx$  are shown in Figure 2.

To calculate  $\delta(x)$  and  $\sigma(x)$  outside the interval  $(-L, L)$  the discrete form of (6), i.e. (7) is used. When  $\ell(x)$  is discontinuous and  $x$  is not the center of the grid, numerical oscillations appear. To eliminate such spurious oscillations, we replace the discontinuity by a ramp function with finite slope. It was found that  $n > 30$  gives sufficient accuracy in such cases, in contrast to 200 or 300 used by Tse et al. [1985].

In the next section, some examples of applications of this method are discussed.

### Examples

To test and illustrate the method we consider six cases and present the results here. These six cases are not to be considered as models for any particular real fault. Though our method can be used to interpret geophysical observations for a particular fault such comparisons are beyond the scope of the present paper. All lengths in the examples are scaled by the half-length of the interval and all stresses by  $\sigma^\infty$ . The interval under consideration is then  $(-1, 1)$ .

We start with the case of a very weak interval ( $k = 0$ ) surrounded by a very stiff environment ( $\alpha L = 500$ ). The slip (dots) and shear stress (crosses) versus the position along the fault, are plotted in Figure 3, with slip normalized by its value at  $x = 0$ . Slip and stress in only one half of the interval  $(-1, 1)$  are plotted, the slip and stress in the other half being symmetric about  $x = 0$ . The results show that the slip is mainly confined to the  $(-1, 1)$  interval, the slip outside this interval being negligible and that the stress is concentrated at  $x/L = \pm 1$ , and asymptotically approaches its value  $\sigma^\infty$  far from the interval. As a test of our results, we plot, using continuous lines, the slip and stress due

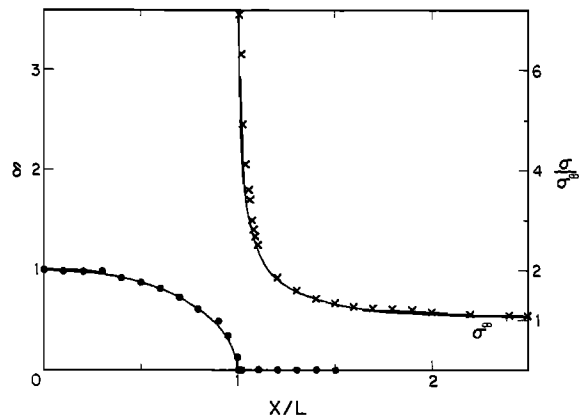


Fig. 3. The normalized slip (dots) and normalized stress (crosses) on the fault, averaged over the plate thickness for the case of a stress-free interval in a stiff environment. The continuous lines give the in-plane shear crack solution for a crack occupying the region  $(-1, 1)$ .

## 68 ELASTIC CONTACT MODELING

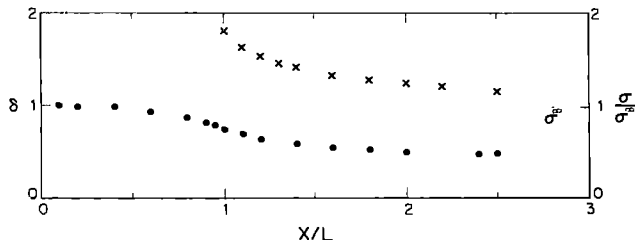


Fig. 4. Same as Figure 3 but for a stress-free interval in a weak environment.

to an inplane stress-free shear crack in a continuous plane occupying the interval  $(-1,1)$ . The results compare very well except near  $x = \pm 1$ . The slip in the crack solution is confined to the  $(-1,1)$  whereas in our model, some negligible slip occurs outside  $(-1,1)$ . The stress concentration at  $x = \pm 1$  in the crack problem is infinite while in our case it is finite and is found to be about 72 times the applied stress  $\sigma^\infty$ . These differences are quite expected and the comparison provides a test of our numerical results.

We next consider the case of a stress-free interval in an environment that is much weaker than in the previous case but nonetheless resistant to slip. This case may be considered as a model of a creeping section of a fault, surrounded by stiffer regions. The slip (dots) and stress (crosses) along the fault are shown in Figure 4. The slip and stress are plotted on the same scale. In contrast to the previous case, it is seen that the slip is much less confined to the stress-free interval and that the stress is much less concentrated at  $x = \pm 1$  now being less than twice the applied stress.

Next, we consider two examples of a fault section that is stiffer than its environment. This may be considered as a model for a seismic gap in a fault. The gap could be an unbroken barrier left on a fault after a recent large earthquake and in such a case it would have a very large stiffness compared to the surrounding weak portions which have recently slipped (stiff gap in a weak environment). Or, it could be a 'seismic gap' between two large earthquakes, which has been accumulating stress for a long time and has not slipped recently. In this case the contrast in stiffness would be expected to be less drastic and we may model it as a weaker gap in a weak environment. This is a more or less complementary 'exterior' problem to the first case studied above. We take,  $\alpha L = 1$  and  $L = -499$ , i.e., the interval  $(-1,1)$  is 500 times stiffer than the region  $|x| > 1$ . In this case, it was found that it is necessary to modify the discontinuity in  $\ell$  by a ramp to eliminate spurious oscillations. The length of the ramp we take is 20% of the interval half-length at each end and  $\ell$  is plotted at the top of Figure 5.

The slip normalized by  $\delta^\infty$  and the stress are shown in Figure 5. Large stress concentration is seen near  $x = \pm 1$  and slip is mainly confined to the regions outside this interval, the slip near  $x = 0$  being only about 3% of the slip far from the gap. The results can be compared to that for a single asperity on a stress-free fault under in-plane shear, which are shown by continuous lines in Figure 5. The stress closely follows the stress for the single asperity case in regions far from the gap edge. The slip outside the gap  $(-1,1)$  for the asperity problem is given by the relation  $\delta(x) = \log(x + \sqrt{x^2 + 1})$ . The difference between our slip and the pure asperity slip is large since in our case the region outside the gap has finite stiffness while the fault outside the asperity is stress free (i.e., has zero stiffness).

The second example of a seismic gap that we consider is that of a weak gap in a weak environment. We take  $\alpha = 1$ ,  $\ell = -4$  (i.e., the gap is now only 5 times stiffer than its environment) and  $\ell$  is modified by a ramp as in the previous case (Figure 5). The slip and stress are shown in Figure 6. The stress concentration is now much smaller than in the previous case and the displacement inside the gap is appreciable and increases towards the ends of the gap.

In both cases of seismic gaps studied above, due to foreshocks, aftershocks, post-seismic slip, or other time-dependent effects, the length of the gap could be expected to decrease and the difference in slip and stress distributions between the original gap and a shortened gap may provide precursory information on the fracture of this gap. We study the cases when the gaps studied above are shortened by 20% of their length from both ends, and the situation, along with  $\ell$  modified by the ramp is plotted at the top of Figure 7. The behavior of the stress concen-

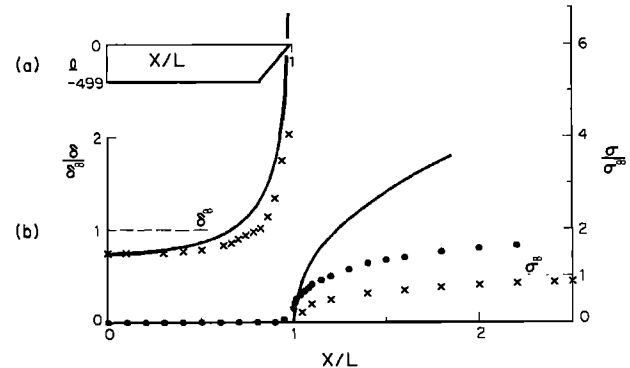


Fig. 5. (a) The function  $\ell(x)$ , as a function of  $x$ , showing the ramp at the edges. (b) Normalized slip (dots) and normalized stress (crosses) on the fault due to a stiff gap in a weak environment. The continuous lines give the solution for an asperity occupying the region  $(-1,1)$  under in-plane shear stress.

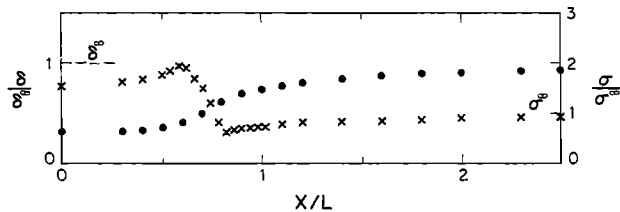


Fig. 6. Same as Figure 5b but for a weak gap in a weak environment.

tration and slip for the shortened stiff gap in a weak environment are similar to those shown in Figure 5 for the unshortened gap, but the interval  $(-1, 1)$  is now 'squeezed' into the interval  $(-0.8, 0.8)$ . Figure 8 shows the slip and stress for a shortened weak gap in a weak environment. Again, comparing the results with Figure 6 for an unshortened weak gap we find that the slip at the centre of the gap and the stress concentration at the ends are of the same magnitude for the shortened and unshortened gaps, with the same 'squeezing' effect seen for the stiff gap.

#### Conclusions

We have presented an integral equation method and solved it numerically, to determine the slip and stress fields due to a fault that has an interval with a different stiffness than the remainder of the fault. Our results for very simple cases are compared with known solutions for an in-plane crack and asperity to test the accuracy. Situations in which there is a stress-free interval in a stiff or weak environment or of a stiff or weak gap in a weak environment are studied as possible cases of models of creeping portions of faults, of seismic gaps and of barriers on a fault.

#### Appendix

##### Evaluation of $R(x)$

The representation

$$R(x) = \int_0^\infty e^{-t} \frac{t dt}{t^2 + x^2} \quad (A1)$$

is not convenient for numerical calculations. So we develop two different representations of  $R(x)$ , convenient for two different ranges of values  $x$ . The integral in (A1) may be expressed in closed form in terms of special functions [Gradshteyn and Ryzhik, 1965] as follows:

$$R(x) = -\text{si}(x)\sin x - \text{ci}(x)\cos x$$

where the sine and cosine integrals  $\text{si}(x)$  and  $\text{ci}(x)$  are given by

$$\text{si}(x) = - \int_x^\infty \frac{\sin x}{x} dx = -\frac{\pi}{2} + \int_0^x \frac{\sin x}{x} dx$$

and

$$\text{ci}(x) = - \int_x^\infty \frac{\cos x}{x} dx = C + \ln x + \int_0^x \frac{\cos x}{x} dx$$

To evaluate  $\text{si}(x)$  and  $\text{ci}(x)$ , we use their series representations

$$\text{si}(x) = -\frac{\pi}{2} + \sum_{k=1}^{\infty} \frac{(-1)^{k+1} x^{2k-1}}{(2k-1)(2k-1)!}$$

$$\text{ci}(x) = C + \ln(x) + \sum_{k=1}^{\infty} \frac{(-1)^k x^{2k}}{2k(2k)!}$$

Substituting these in  $R(x)$ , we find a series representation for  $R(x)$ , which only has a logarithmic singularity at  $x = 0$ , and can be easily evaluated for moderate values of  $x$ . For large values of  $x$ , an asymptotic series convenient for numerical use is obtained by expanding the quantity  $t/(t^2+x^2)$  in (A1) in power series of  $(1/x^2)$  and obtaining

$$R(x) = \sum_{k=0}^{\infty} \frac{(-1)^k (2k+1)!}{x^{2k+2}} \quad (A2)$$

For the discrete form of the integral equation (i.e., (7)), we need to obtain the indefinite integral of  $R(x)$ . It can be easily shown that

$$\bar{R}(x) = \int_0^x R(x) dx = -\sin x \text{ ci}(x) + \cos x \text{ si}(x) \quad (A3)$$

This expression is convenient for moderate values

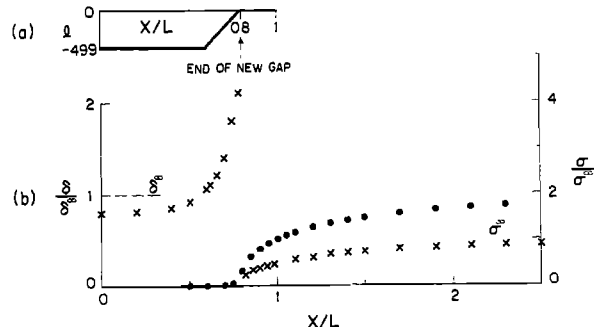


Fig. 7. (a) The function  $f(x)$  for a shortened gap. (b) Same as Figure 5 but with the length of the gap shortened by 20%.

## 70 ELASTIC CONTACT MODELING

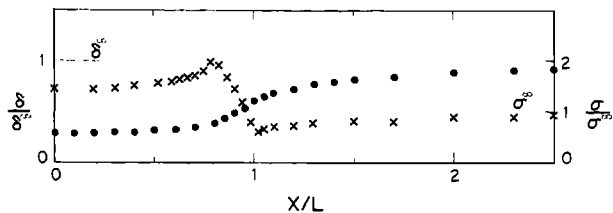


Fig. 8. Same as Figure 6 but with the length of the gap shortened by 20%.

of  $x$ , and using the power series expansions of  $\text{ci}(x)$  and  $\text{si}(x)$ ,  $R(x)$  can be obtained. For large values of  $x$ , we obtain  $R(x)$  by integrating the expression for  $R(x)$  term by term as follows:

$$\int_0^x R(x)dx = \int_{-\infty}^x R(x)dx + \int_0^{\infty} R(x)dx$$

The last term in the right-hand side is equal to  $\pi/2$  so that

$$\bar{R}(x) = \frac{\pi}{2} - \sum_{k=0}^{\infty} (-1)^k \frac{(2k)!}{x^{2k+1}} \quad (\text{A4})$$

(A2) and (A4) are divergent series and the sums over  $k$  are taken up to that value of  $k$  where the term is minimum. In Figure 2, we used the asymptotic series (A2) and (A4) for  $x > 20$  to plot  $R(x)$  and  $\bar{R}(x)$ . (It was found, in fact, that for  $20 \leq x \leq 30$ ,  $R(x)$  and  $\bar{R}(x)$  calculated using the asymptotic series and the expressions for moderate  $x$ , coincide to 4 decimal places.)

**Acknowledgments.** This work is part of a joint program in earthquake prediction under Area IX of the U.S.-U.S.S.R. Agreement in the Field of Environmental Protection. The work was done while B. V. Kostrov was visiting Lamont-Doherty. The Lamont-Doherty reviewers were C. Scholz and A. Lerner-Lam and we thank them for their comments. J. Rice of Harvard University also pro-

vided useful comments and we are grateful to him for this. This work was supported by the U.S. Geological Survey under contract USGS 14-08-0001-G-947. Lamont-Doherty Geological Observatory contribution number 3968.

## References

- Das, S., and K. Aki, Fault plane with barriers: A versatile earthquake model, *J. Geophys. Res.*, **82**, 5658-5670, 1977.
- Das, S., and B. V. Kostrov, Breaking of a single asperity: Rupture process and seismic radiation, *J. Geophys. Res.*, **88**, 4277-4288, 1983.
- Das, S., and B. V. Kostrov, An elliptical asperity in shear: Fracture process and seismic radiation, *Geophys. J. R. Astron. Soc.*, **80**, 725-742, 1985.
- Day, S., Three dimensional simulation of spontaneous rupture: The effect of non-uniform pre-stress, *Bull. Seismol. Soc. Am.*, **72**, 1881-1902, 1982.
- Gradstejn, I. S., and Ryzhik, I. M., *Tables of Integrals, Series and Products*, Academic New York, 1965.
- Kostrov, B. V., and S. Das, Idealized models of fault behavior prior to dynamic rupture, *Bull. Seismol. Soc. Am.*, **72**, 679-703, 1982.
- Li, V. C., and J. R. Rice, Preseismic rupture progression and great earthquake instabilities at plate boundaries, *J. Geophys. Res.*, **88**, 4231-4246, 1983a.
- Li, V. C., and J. R. Rice, Precursory surface deformation in great plate boundary earthquake segments, *Bull. Seismol. Soc. Am.*, **73**, 1415-1434, 1983b.
- Madariaga, R., High frequency radiation from crack (stress drop) models of earthquake faulting, *Geophys. J. R. Astron. Soc.*, **51**, 625-651, 1977.
- Tse, S. T., R. Dmowska, and J. R. Rice, Stressing of locked patches along a creeping fault, *Bull. Seismol. Soc. Am.*, **75**, 709-736, 1985.
- Walsh, J. B., and M. A. Grossenbaugh, A new model for analyzing the effect of fractures on compressibility, *J. Geophys. Res.*, **84**, 3532-3537, 1979.

## RUPTURE PROCESSES IN THE PRESENCE OF CREEP ZONES

Victor C. Li and N. Fares

Department of Civil Engineering, Massachusetts Institute of Technology, Cambridge, Massachusetts, 02139

**Abstract.** This paper describes a model of stress and slip distribution on a strike-slip fault with strength heterogeneity depthwise and along strike. The 3-D problem is analyzed by means of a "line-spring" procedure which is numerically implemented in an Indirect Boundary Element Program. The model is applied to study the effect of a creep zone on the stressing of the adjacent fault segments. Results include the thickness averaged slip rate in the creep zone, and stressing rate and slip zone penetration in the adjacent segments. Temporal and spatial variation of surface strain rate profiles are also computed. Order of magnitude comparisons of these and other parameters with geodetic measurements on the San Andreas fault in central California suggests that the model may be fine tuned for future site-specific studies. Simplification in boundary conditions, however, are expected to limit the model accuracy in the preseismic period. The 'line-spring' procedure itself is known to become inadequate in the limit when strength heterogeneities vary with wavelengths less than a plate thickness.

## Introduction

The resistance to rupture along plate boundaries may be regarded as heterogeneous, either due to changes in material rheology along strike or presence of tectonic features (such as fault segmentation). Two types of heterogeneities, generally termed asperities and barriers are recognized. Asperities are patches of plate boundary surface which have stronger resistance to slip movements. They are therefore focal points of stress accumulation and their eventual rupture often forms the site of large and great earthquakes [Kanamori and Stewart, 1978; Dmowska and Li, 1982]. In contrast, Aki [1984] defines barriers as areas which a seismic event 'skips' over. They are therefore likely locations of aftershocks. Thus the breaking of asperities may be seen as a smoothing process, while the creation of barriers may be seen as a roughening process of the fault surface. By virtue of these concepts, the preseismic and rupture initiation processes are controlled by asperities while the seismic and possibly postseismic processes are controlled by barriers on the fault.

In contrast to strong asperities, there are 'weak' segments of plate boundaries where continual creep is evident. In such zones, little or no stress is accumulated. However, this would imply high stress concentration at the adjacent fault segments. Perhaps the best known plate boundary where such behavior is observed is on the San Andreas fault in central California. Figure 1 shows the contemporary surface slip rate varying from close to zero to a maximum of 35 mm/yr along the length of the creep zone (as compiled by Tse et al., [1985]). Figure 2 [after Wesson et al., 1977; Burford and Harsh, 1980] shows the dense concentration of background seismicity reflecting the stress concentration and local slip failures adjacent to the creep segment. The Sargent and Calavaras faults near Hollister may also be manifestations of the higher local stress field related to the creep zone to their south. Furthermore the short cycle (~21 years) Parkfield earthquakes may be viewed as local

unstable slip in the breakdown zone of a loaded crack (the creep zone) in preparation for a major 1857-like rupture. The suggestion is that the continuous creep in central California acts as a stress transfer mechanism, focusing stress which will lead to eventual ruptures north and south of the creep segment. The objective of this paper is to study the mechanics of such stress transfer by means of an analytic model. The model is constructed in a more general context of slip interactions between fault segments with different strength characteristics. Although the present focus is on the behavior of creep zones and the adjacent fault segments, the general model can deal with fault bends and branch or subparallel faults, and asperities of various sizes and depth. These results will be described in future works.

In this paper we describe a 3-D model of tectonic scale earthquake rupture in a strike-slip environment. Fault surface 'strength' variation is described by a preassigned critical fracture energy release rate. Fault loading is due to a uniform tectonic stress which may be interpreted as the stress on a non-slipping fault associated with relative plate motion. Results of the numerical analyses include the spatial progression of the slip front evolving with time during an earthquake cycle, the accompanying fault stressing variation along-strike, the associated surface deformation pattern and other quantities important in understanding the physical processes leading to an earthquake instability. These analyses are meant to provide a basis to conduct further site-specific studies. Discussion of numerical results and their physical implications will be made with some reference to observed field data in California. While simulated fault behavior prior to an instability or the earthquake rupture are described, it is important to recognize major limitations of the results due to simplifying assumptions in the model. For example, the present model ignores viscoelastic coupling of the elastic lithosphere to the asthenosphere. Such coupling, however, is known to stabilize the fault and prolong the precursory stage as discussed by Li and Rice [1983a, b]. The instability described in this paper should therefore be regarded as a first instability under the fully decoupled condition. After first instability, viscosity resistance from the asthenosphere interacts with rapid fault slip, and cannot be ignored in a rigorous analysis of precursory deformations.

Geodetic measurements on the San Andreas fault [Thatcher, 1983] suggest a long-term strain-rate decay over the earthquake cycle. Such time transients have been variously attributed to deep aseismic slip below the locked crust and to relaxation of the asthenosphere. The latter mechanism has been studied as a means of tectonic scale stress transfer along plate margins [Lehner et al., 1981] and as a time-dependent tectonic loading on a given fault segment [Li and Kisslinger, 1984/5; Dmowska et al., 1985]. While the present calculations do not explicitly account for viscoelastic coupling between the lithosphere and asthenosphere, the long-term time transients described above may be incorporated into the present model through a variable tectonic loading rate. The results presented here should provide a good approximation of the rupture

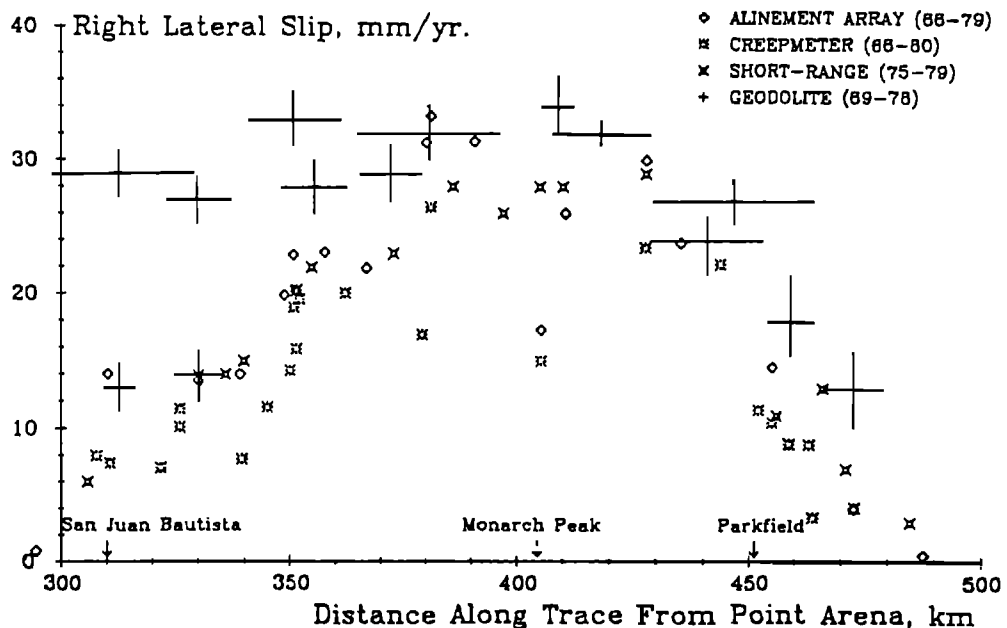


Fig. 1. Distribution of slip rate along the creep segment of the San Andreas [after Tse et al., 1985].

progression process, at least up to the first instability, under uniform (in time) tectonic loading. The emphasis is in the effect of strength heterogeneities, depthwise and along-strike, on the stress and slip distributions, and the associated time and spatial variation of ground surface deformation. The 3-D geometry of the problem requires special numerical treatment. Details of the modeling procedure are described below.

#### The Modeling Procedure

Referring to Figure 3, the elastic lithospheric plate is treated as undergoing plane-stress deformation so that all quantities such as displacements  $u$ , slip  $\delta$ , and stress  $\sigma$  are averaged over the thickness of the lithosphere  $H$ . This 2-D description of the plate deformation is appropriate if stresses and displacements are approximately uniform through the thickness and this is presumably so in the interior of the plate remote from the plate margin. We shall use this plate model to account for loading associated with relative tectonic plate movements, and also to account for loading at a particular fault segment due to slip relaxation at other segments. Such load transfers are especially important when strength heterogeneities (either material based or geometric such as fault steps) occur along a plate margin or when nonlinear features have to be taken into account (such as fault bends, subparallel or branch faults). Also, when a particular fault segment approaches instability, stress redistribution with adjacent segments could be an important factor in controlling precursory spatial seismicity and surface deformation patterns.

For the plate model, the stress (thickness averaged) at any point  $P$  may be written in terms of the applied tectonic load  $\sigma_\infty$  and the effect of fault slip  $\delta$ ,

$$\sigma(P) = \sigma_\infty(P) - f_S G(P,P') [\partial\delta(P)/\partial s] ds \quad (1)$$

where  $s$  denotes the arc distance along any line of displacement discontinuities  $S$ , over which the principal value integral is carried out.

In (1), the Green's function  $G(P,P')$  is the fundamental elastic shear edge dislocation solution (see, for example, Hirth and Lothe [1968]) and has the general form of 1/distance dependence. It should be pointed out that the fault slip  $\delta$  is generally non-zero during the earthquake cycle since it is a thickness averaged quantity which accounts for the continuous deep aseismic slip, in spite of a usually locked seismogenic layer between earthquakes.

At the plate margin, strong variations in mechanical properties of the fault zone with depth exist due to changes in temperature and pressure. Indeed, microseismicity and focal depths of major earthquakes on the San Andreas fault delineate a transition boundary between a strong brittle seismogenic zone of about 12 km deep below which stable sliding is often assumed to occur. Sibson [1982] described this transition as a change from frictional to quasi-plastic behavior. This depthwise variation of mechanical properties in the fault zone renders the 2-D plate model inadequate, especially in studying the surface deformation within a few plate thicknesses from the fault where most geodetic measurements are made. To overcome this problem, we introduce a plate-margin model shown in Figure 4. This plate-margin model represents the deformation behavior of a local cross-sectional slice across the fault. Each such slice (a short segment) is assumed to be loaded and deforms uniformly in the  $x$ -direction (along strike). We shall assemble a series of such slices to make up the fault, which is embedded in the plate model described earlier. This is the essence of the 'line-spring procedure' first proposed by Rice [1972] in treating 3-D part-through crack problems in plates and shells subject to in-plane and bending loads.

As a special version of the plate-margin model, we choose to represent the fault zone as an edge-crack in an elastic strip under anti-plane strain deformation (Figure 4), as did Turcotte and Spence [1974]. The justification of such a model is discussed in V.C. Li and J.R. Rice [unpublished manuscript, 1986]. This plate-margin model will be used to compute the surface strain rate profiles.

Upward progression of the shear zone and penetration of the seismogenic layer is modeled by crack advances in response to stressing

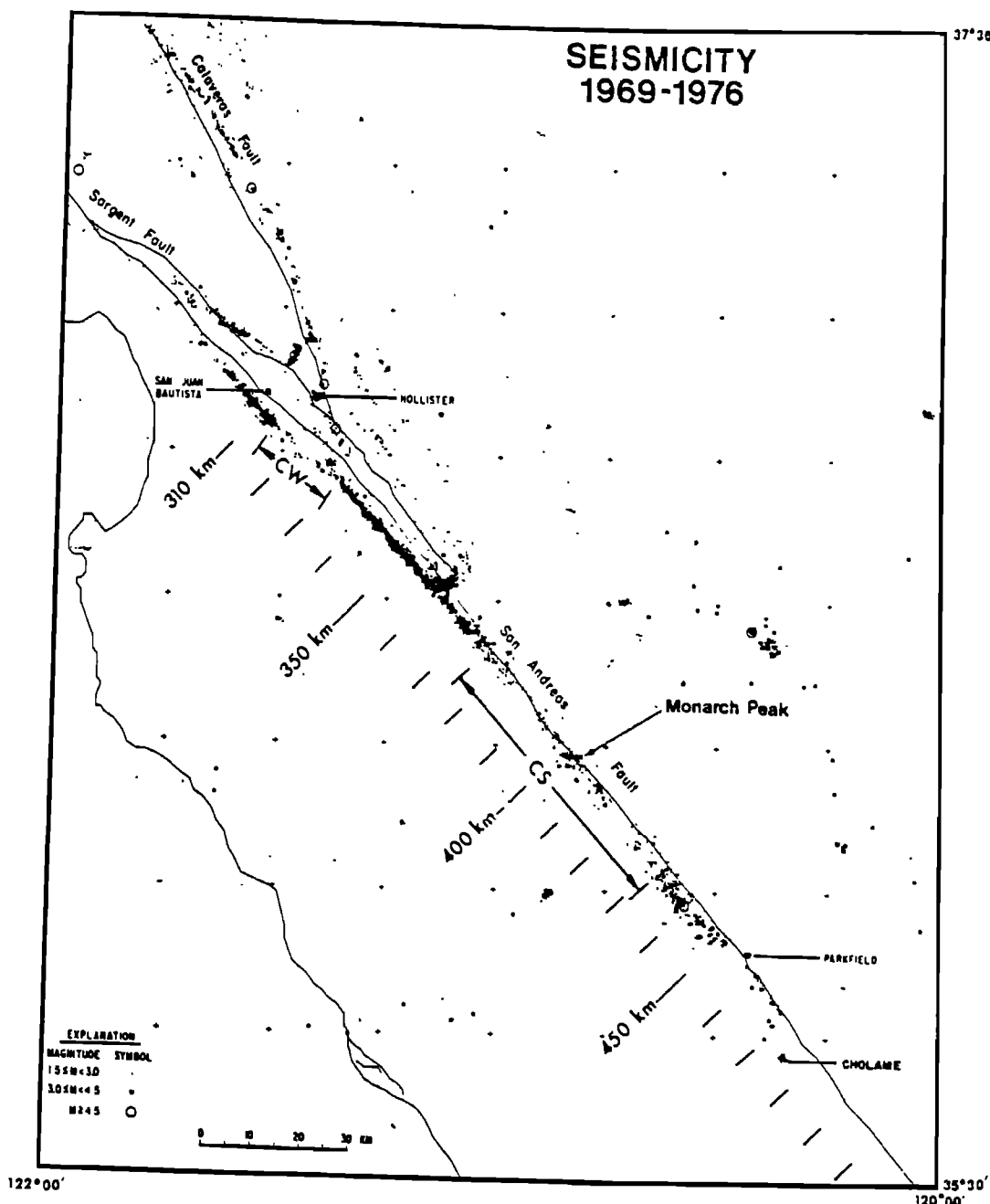


Fig. 2. Seismicity concentration along the fault segments adjacent to the creep zone on the San Andreas [after Wesson et al., 1977 and Burford and Harsh, 1980].

local to that fault segment, and based on the well known linear elastic fracture criteria. A distribution of fracture resistance (in the form of a critical energy release rate  $G_c$ ) varying with depth  $Z$  is imposed. Note that  $G_c(z) = G_c(H-A)$ . The adopted depthwise Gaussian variation shown in Figure 5 is meant to approximate the strength changes with depth, and has an origin in the assumed frictional resistance variation by Stuart [1979]. The peak value of  $G_c$  has been located at near typical focal

depths, while the broadness (determined by  $b$ ) can be chosen to represent the size of the seismogenic zone. All the parameters ( $G_c, Z_o, b$ ) can be adjusted to simulate particular situations in site-specific studies.

The general spatial Gaussian distribution of fracture energy shown in Figure 5 is also supported by physical considerations of increase in temperature (e.g., consideration of geotherm on the San Andreas by Lachenbruch and Sass [1973]) and lithostatic pressure with depth and by

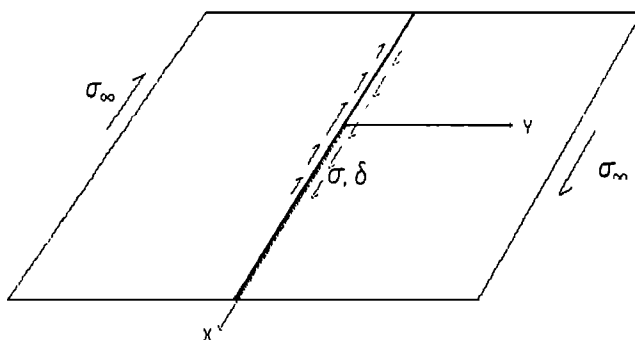


Fig. 3. Elastic plate model of the lithosphere loaded by tectonic stresses  $\sigma_\infty$  associated with relative plate movements. A varying stress  $\sigma$  and slip  $\delta$  distribution due to strength heterogeneities is indicated at the plate margin.

experimental evidence of fracture property changes with normal stress and temperature. Wong [1986] reported that the fracture energy exhibited an increasing trend up to 500 MPa normal stress (corresponding to roughly 15 km depth, for the case of no fluid pressure) for a series of triaxial tests on Fichtelberg granite and a slow decay of  $G_c$  with  $\sigma_n$  for another series of triaxial tests on San Marcos gabbro at high normal stress (>400 MPa). Both series were conducted at room temperature. Also, triaxial test results by Wong [1982] on the variation of fracture and frictional strength of Westerly granite at constant normal stress indicate that stress drop decreases monotonically with temperature, implying that the fracture energy must vanish at some depth (corresponding to quasi-plastic behavior). The composite trend that could be drawn from such laboratory tests suggests an initially increasing  $G_c$ , in response to increase of lithostatic pressure with depth, possibly reaching a peak at seismogenic depths and then decreasing in response to temperature (and perhaps also to pressure). At any rate, the Gaussian distribution of  $G_c$  is sufficiently general to account for such laboratory observations under relevant ranges of crustal temperature and pressures.

The crack model described above, together with the fracture energy description, allows the analysis of the upward propagation of a narrow shear zone during an earthquake cycle. The deformation in the shear zone is thus regarded as plastic flow under essentially constant stress. The criterion for slip front progression is that the local energy release rate reaches the level prescribed by the  $G_c$  curve. The stability of its upward penetration is governed by the contrast in local stiffness of the plate margin to the stiffness of the surrounding medium through which the tectonic load is transmitted.

For the edge-crack strip shown in Figure 4, Li and Rice [1983a] derived the equations

$$\sigma = [G G_c(A)/H \tan(\pi A/2H)]^{1/2} \quad (2)$$

$$\delta = (4H/\pi G) [G G_c(A)/H \tan(\pi A/2H)]^{1/2} \ln[1/\cos(\pi A/2H)]$$

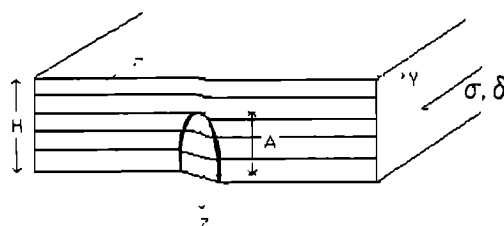


Fig. 4. Plate margin model of local cross-sectional slice of fault, with slip zone penetration  $A$  in lithosphere of thickness  $H$ .

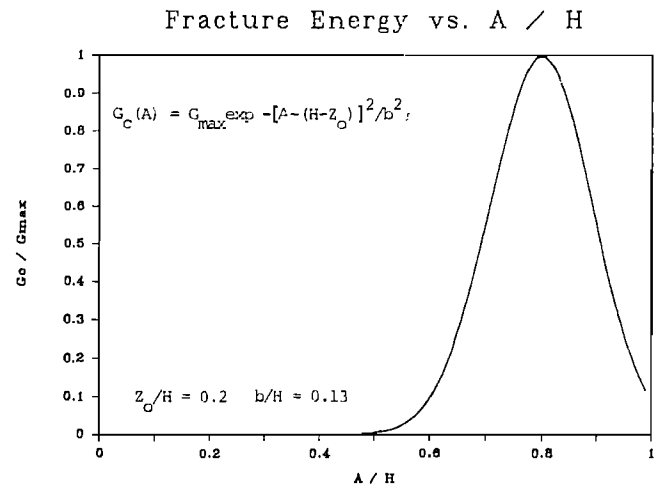


Fig. 5. Assumed fracture energy variation with depth in fault zone.

where  $G$  is the shear modulus and  $H$  is the lithospheric thickness. Equation (2) describes the parametric relationship of a non-linear spring (generalized spring force  $\sigma$  and spring extension  $\delta$ ) with spring constant  $k$  given by

$$k = (\pi G / 4H) / \ln[1/\cos(\pi A / 2H)] \quad (3)$$

The non-linear stiffness is associated with the changing crack depth  $A$ . Note that the effect of  $G_c$  on the spring constant  $k$  comes in through the crack depth or the slip penetration depth  $A$ , as can be observed from (2). Figure 6 illustrates typical  $\sigma$  versus  $\delta$  relationships for various choices of the  $G_c$  variation. These different  $\sigma$  versus  $\delta$  relationships may represent the inhomogeneous mechanical conditions along-strike. Typically, those with higher peaks may be associated with asperity zones requiring higher

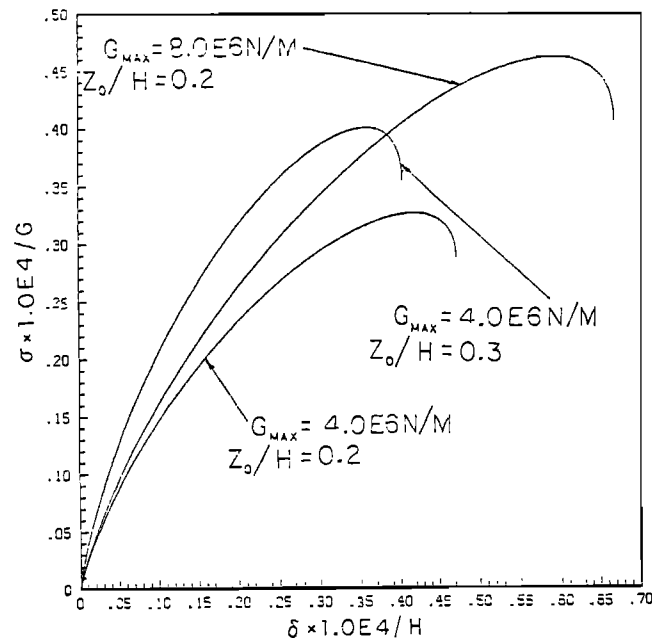


Fig. 6. 'Spring' laws derived based on the elastic crack plate-margin model and different distributions of fracture energy  $G_c$ .

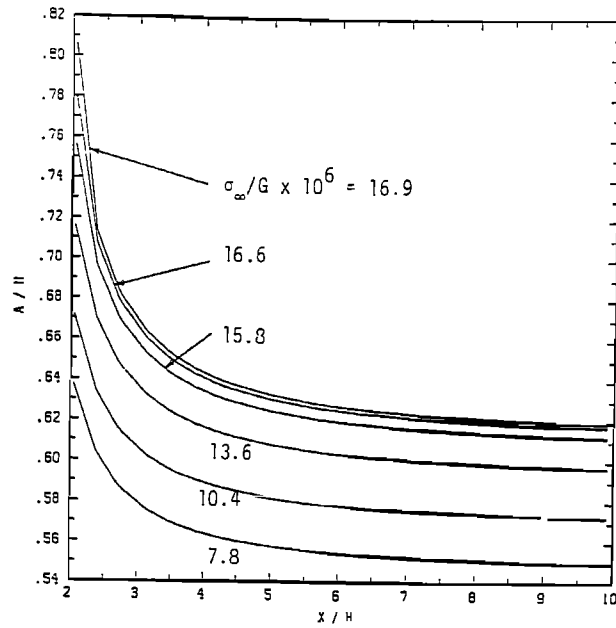


Fig. 7a.

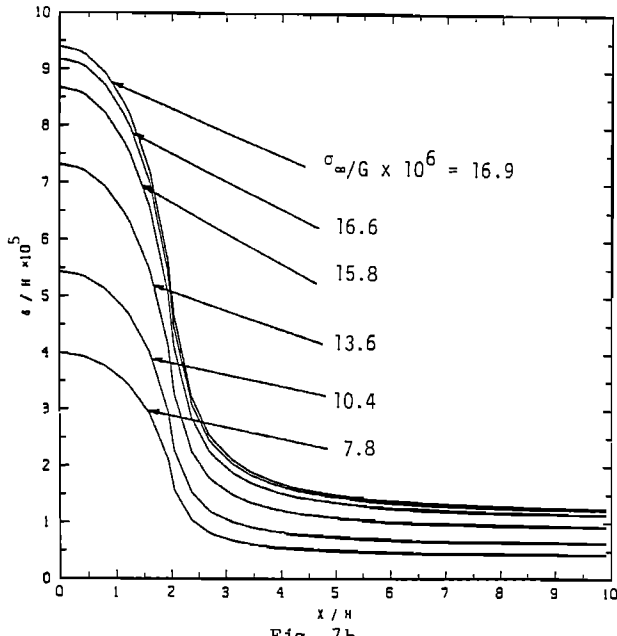


Fig. 7b.

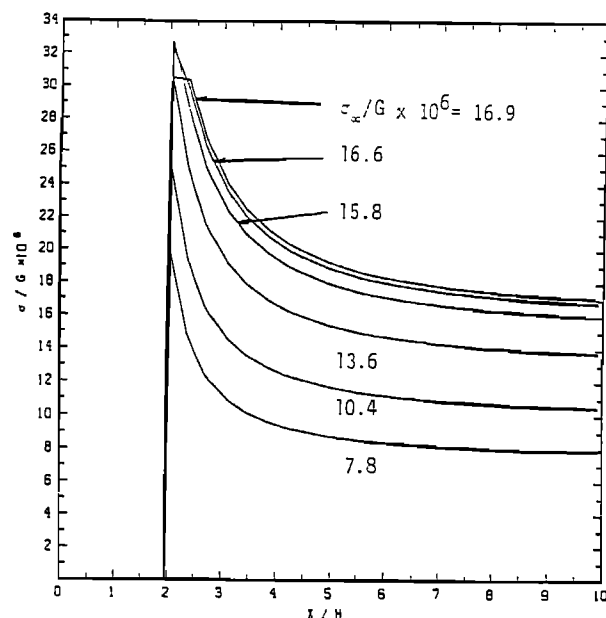


Fig. 7c.

Fig. 7. (a) Progression of slip front. Note rapid penetration at the edge of the creep zone ( $X=2H$ ). (b) Slip distribution. Note the almost parabolic shape of slip distribution inside the creep segment and the smooth transition to outside the creep zone. (c) Stress concentration at the edge of a creep segment, eventually leading to failure at this location. The last two time steps shown indicate softening just outside the creep zone. The stress decays to the remote level at large  $X$ .

energy concentration to penetrate through. It is also possible to simulate the depth variation of the transition zone from brittle to quasi-plastic behavior, which Sibson [1982] suggested based on variations of the maximum depth of microseismicity on the San Andreas fault. Locations with deep transition zones may be represented by a  $\sigma$  versus  $\delta$  relationship with larger  $Z_0$  value, which results in a higher peak value for

$\sigma$  occurring at a lower  $\delta$  as shown in Figure 6. This suggests that such "deep asperities" are particularly effective in resisting slip penetration without being stronger (in the  $G_c$  sense) than adjacent fault segments, and may act as locations for rupture nucleation.

The numerical implementation of the line-spring procedure involves solving (1) for  $\sigma(P)$ ,  $\delta(P)$ . If the point P lies on a fault trace, the stress

## 76 RUPTURE PROCESS IN CREEP ZONES

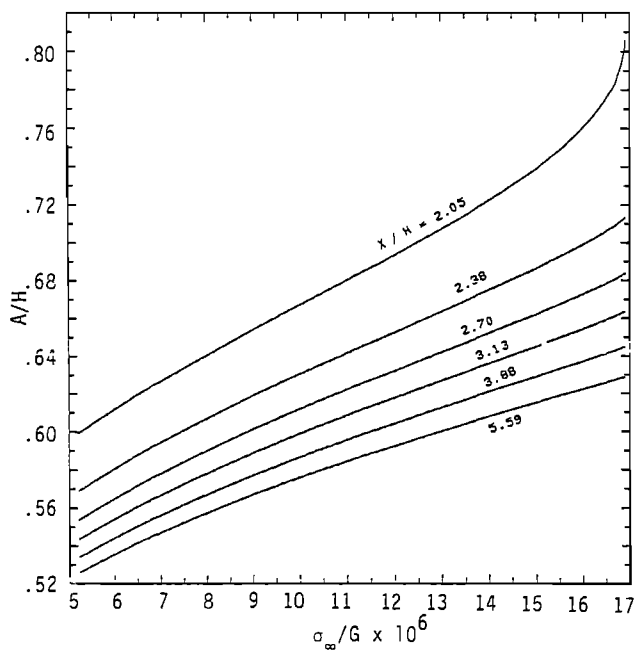


Fig. 8a.

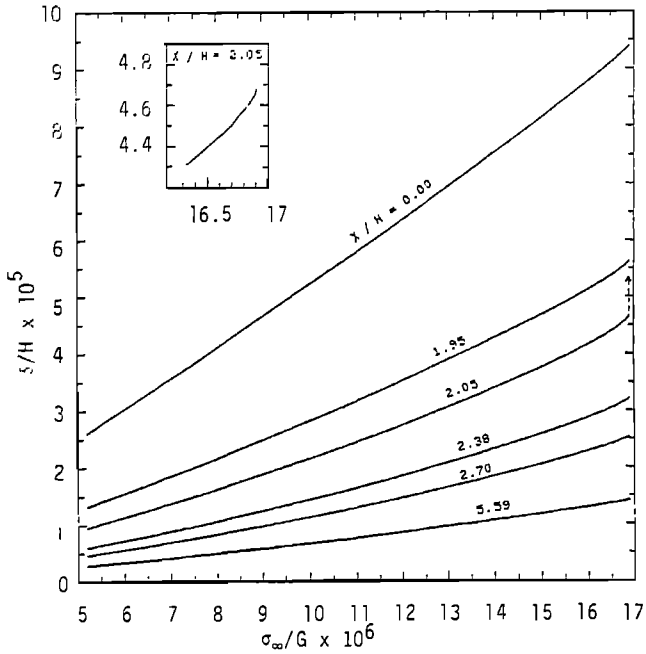


Fig. 8b.

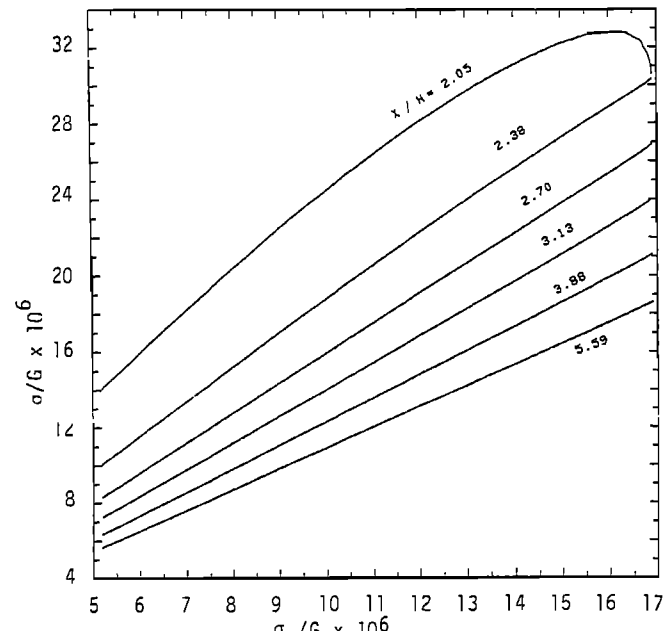


Fig. 8c.

Fig. 8. (a) Slip front penetration as a function of time. (b) Slip magnitude as a function of time. The insert is an enlargement of the slip at  $X = 2.05H$  approaching instability. (c) Stress accumulation versus time. Note the slip front acceleration accompanied by stress unloading at  $X = 2.05H$  near instability.

$\sigma$  may be written in terms of the slip  $\delta$  through a spring constant  $k(P)$ , i.e.

$$\sigma(P) = k(P)\delta(P) \quad (4)$$

where  $k$  is described by (3). Equations (1) with (4) forms a singular

integral equation which may be solved numerically. (If the point  $P$  is not on the fault, then  $\delta(P) = 0$  and  $\sigma(P)$  can be obtained by directly evaluating the right hand side of eqn (1).) In expectation of future development in accounting for fault geometry complexities, we have developed a versatile Indirect Boundary Element program [Fares and Li, 1986] to effectively handle this type of problems. Once  $\sigma(P)$ ,  $\delta(P)$  are solved, (2) may be

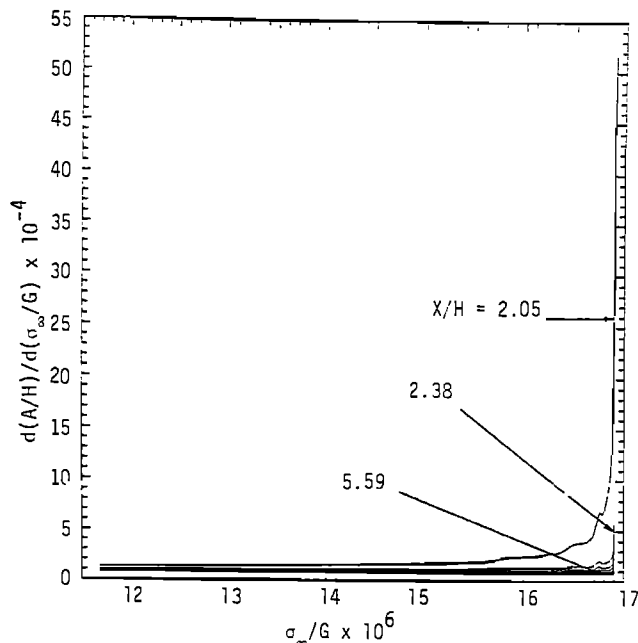


Fig. 9a.

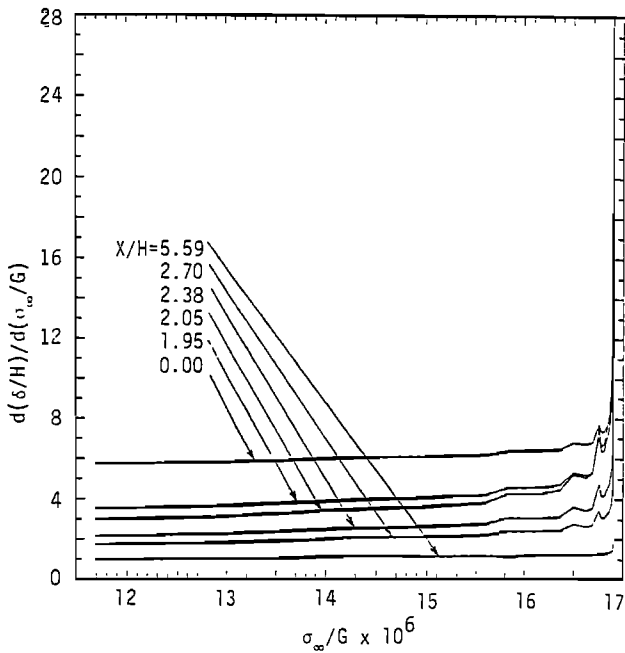


Fig. 9b.

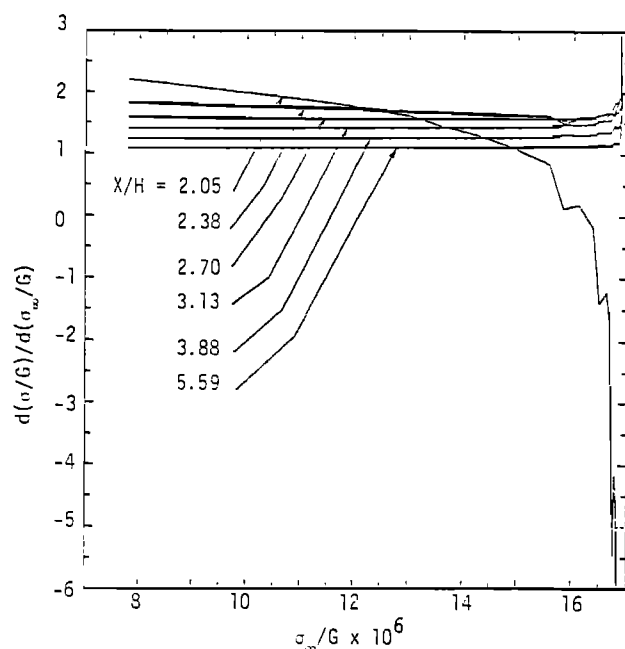


Fig. 9c.

Fig. 9. (a) Slip front penetration rate. (b) Slip rate and (c) stressing rate as a function of time. Instability point is marked by the rapid acceleration of slip front penetration and slip rate at  $X = 2.05H$ , accompanied by rapid stress deceleration. The unlabeled curves in 9(a) are associated with locations  $X = 2.7H$ ,  $3.13H$ , and  $3.88H$ .

used to invert for the slip penetration  $A(P)$ . In addition, the surface strains may be calculated using the expression

$$\gamma(X, Y) = \frac{\sigma(X, Y=0)}{G} \left[ \frac{\cosh(\pi Y/2H)}{[\sinh^2(\pi Y/2H) + \cos^2(\pi A/2H)]^{1/2}} \right] + \frac{\sigma(X, Y)}{G} \quad (5)$$

The surface strain rates are then obtained by numerical time differentiation of the surface strain values. Equation (5) merges the inner (anti-plane crack model) solution with the outer (plate model) solution so that the surface strain rate thus calculated should be accurate at any distance from the fault.

It should be emphasized that the modeling procedure described above

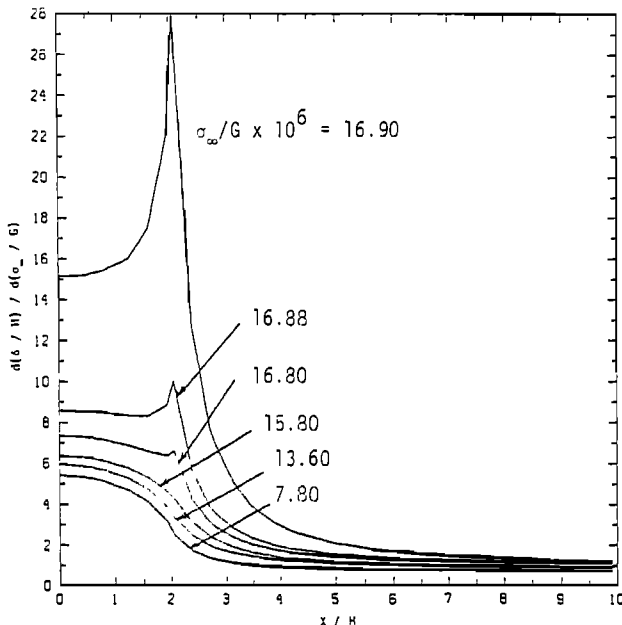


Fig. 10. Distribution of slip rates at various times. Compare the general features of this Figure with that of Figure 2 for  $\sigma_\infty/G < 15.8 \times 10^{-6}$ . The parabolic shape, however, is disturbed by the slip acceleration at the edge of the creep zone towards the later part of the earthquake cycle.

takes explicit account of depthwise variation of stresses and displacements at the plate margin and the strain profiles calculated by (5) are thus true surface quantities and not thickness averaged quantities, even though  $\sigma$  and  $\delta$  are.

#### Slip Zone Progression in a Fault Segment Containing a Creep Zone

As a special case of strength heterogeneity along-strike, we study a case where an otherwise uniform strength plate margin is interrupted by a creep segment. In this simulation the creep segment is four times the plate thickness, and is assumed to be sliding stably under essentially constant stress. In the computation this stress is taken to be the zero reference level. We represent the fracture strength variation along-strike and with depth in the form

$$G_c(X, A) = G_{\max} \exp\{-[A - (H - Z_0)]^2/b^2\} f(x) \quad (6)$$

where  $f(X) = 1 - [U(X+2H) - U(X-2H)]$  and  $U$  is the Heaviside function. Outside the creep zone, we have simulated uniform fault strength extending to infinity on both ends. This is achieved approximately by placing a 'cohesion zone' element ( $\delta > 0$  and  $\sigma \rightarrow \sigma_\infty$  smoothly) at  $X = \pm H$  in the numerical analysis.

The first of equations (2) indicates that earthquake stress drop magnitudes scale with the square-root of  $G_{\max}$ . Based on tectonic scale instability models and constrained by observed normal stress-drops and slip offsets, Rudnicki [1980] and Li and Rice [1983b] argued that  $G_{\max}$  should be of the order  $4.0 \times 10^6 \text{ J m}^{-2}$ . This is the value we have used for the results presented below. For the adopted value of  $b$  and  $Z_0$  shown in Figure 5, and if the lithosphere is assumed to have a thickness  $H$  of 30 to 50 km, the peak strength would be occurring at 6 to 10 km below ground and the seismogenic zone would have an approximate width of  $(2\sqrt{2}b) = 9$  to 15 km.

In the following and in connection with Figures 7 to 11, we shall present computational results on slip penetration  $A$ , thickness averaged slip  $\delta$ , thickness averaged stress  $\sigma$ , and the rates of  $A$ ,  $\delta$ , and  $\sigma$ , as a

function of position and time. Profiles of ground surface shear strain rates will also be presented. For numerical comparisons to field observations along the San Andreas in central California, we choose  $H = 35 \text{ km}$ ,  $G = 3.85 \times 10^{10} \text{ Pa}$ ,  $\sigma_\infty = 0.05 \text{ bar/yr}$ . The appropriateness of the choice of these parameters is debatable, but their values are consistent with various published findings. Because these parameters and the length of the creep zone have not been fine tuned, and because of idealizations in the model, all comparisons with field observations discussed below should be considered as order of magnitude comparisons.

As may be expected, the creep zone focuses stress at the adjacent fault segment, forcing the slip penetration to proceed more rapidly at this location. The slip front, the fault slip and the fault stress are shown in Figure 7 for various stages of the earthquake cycle. The highest load level indicated represents those just prior to instability, which occurs at the fault segment adjacent to the creep zone. Notice that the stress at failure is of the order  $30.0 \times 10^{-6} \text{ G}$  (almost doubling the remote load) which translates to a stress drop of about 12 bars. The tectonic load at failure is  $16.9 \times 10^{-6} \text{ G}$ . For the above assumed value of  $G$  and loading rate  $\sigma_\infty$ , an estimate of the earthquake cycle would be approximately 130 years.

The time evolution of slip penetration, fault slip and fault stress at specific locations are shown in Figure 8. The location adjacent to the creep section ( $X = 2.05H$ ) shows a clear acceleration in slip penetration and fault slip as instability is approached, accompanied by slip softening (unloading). It is seen in Figure 8a that when a fault segment softens, the adjacent segments (e.g. at  $X = 2.38H$ ) pick up the load. The time period of softening at location  $X = 2.05H$  is estimated to be ( $\sim 0.8 \times 10^{-6} \text{ G}/\sigma_\infty \approx 6 \text{ years}$ ).

Actually, the best way to study the approach to instability is to look at the rates of  $A$ ,  $\delta$ , and  $\sigma$ , rather than these quantities themselves. Figure 9 shows these rate changes as a function of time. The slip rate and penetration rate approach infinity at instability at all positions indicated, but particularly at the location adjacent to the creep zone, again indicating that this would be the site of nucleation of a great rupture. In Figure 9c, the stressing rate at this location is shown to decrease with time, while the other locations show the opposite trend. This may be understood by referring to Figure 7a, and recalling that the slip penetration  $A$  is always most advanced at the (eventual) failure location. While this location carries the highest load until softening occurs prior to instability, the stress rate must necessarily decrease due to the strong relaxation effect of slip penetration or 'unzipping'. The small wriggles near instability in Figure 9 are due to numerical inaccuracy and should be disregarded.

It is interesting to consider the slip rate evolution in space and time, since creepmeters and other instruments located in central California provide contemporary slip rate distributions (see Figure 1). In Figure 10, the slip rates along strike are shown for several time steps. As expected, the slip rate has a close to parabolic distribution in the creep section (for the three earlier times shown). At 80% cycle time ( $\sigma_\infty = 15.8 \times 10^{-6} \text{ G}$ ) the maximum slip rate (or creep rate at  $X = 0.0$ ) may be estimated to be 3 cm/yr. This compares favorably to the contemporary creep rate of 3.4 cm/yr at Monarch Peak. Note that the computed creep rate remains relatively constant up to 90% cycle time (Figure 9b). Close to instability, the slip rate just outside the creep zone accelerates, and eventually exceeds that at the middle of the creep section. While it is tempting to associate this phenomenon as a possible earthquake precursor, the precursor time cannot be accurately predicted here without accounting for the coupling effects of the lithosphere to the asthenosphere.

The surface strain rates are useful for comparison to field data from geodetic measurements. Figure 11 shows the normalized shear strain rate profiles at five locations, and in three time windows, corresponding to 35%, 80% and 98% of cycle time. The strain rates are much higher at the edge of the creep zone ( $X = 2.05H$ ). For example at  $\sigma_\infty = 16.64 \times 10^{-6} \text{ G}$ , the near fault shear strain rate at  $X = 2.05H$  is more than three times

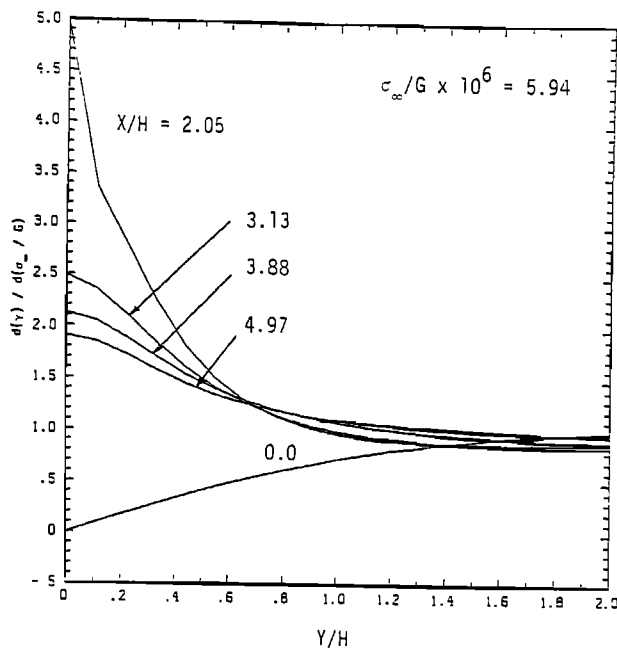


Fig. 11a.

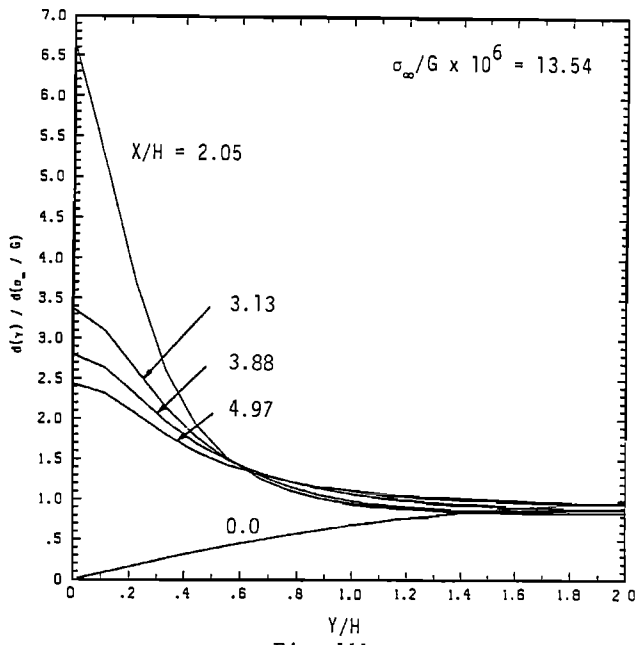


Fig. 11b.

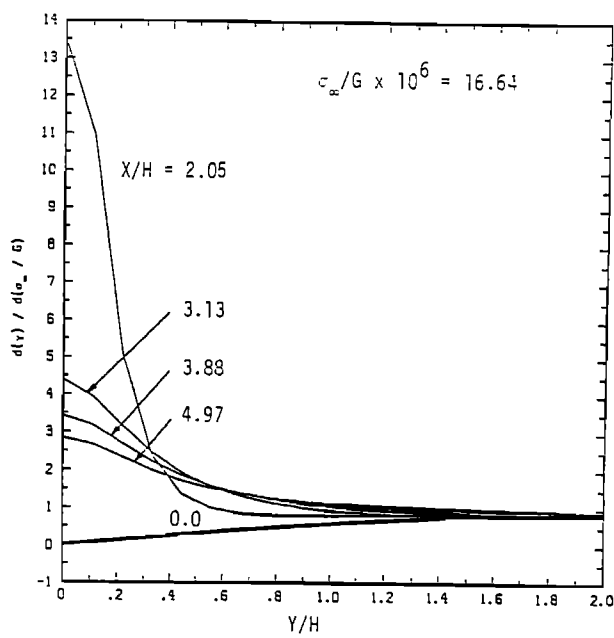


Fig. 11c.

Fig. 11. Surface shear strain rate profiles at five locations and at three time frames.

higher than at the location  $X = 4.97H$ . This is due to the presence of the creep zone and slip penetration, and such spatial effects along strike could not have been captured by 2-D models with uniform fault strength along-strike. Taking contemporary time as approximately at 80% of the earthquake cycle (Figure 11b) and assuming that Carrizo Plain and San Luis lies between  $X = 2.05H$  to  $4.97H$  (origin centered at Monarch Peak, exact placement of location is difficult because of presence of shallow creep not modeled here), then the normalized on-fault shear strain rate is predicted to be between 2.4 and 6.6, or 0.44 to 0.85  $\mu\text{strain}/\text{yr}$ . The slip front associated with this fault section at this time is at 10 km to 13 km

depth according to Figure 7a. Geodetic data from King (private communication, 1985) indicates a strain rate approximately 0.6  $\text{mstrain}/\text{yr}$  at Carrizo Plain and 0.72  $\mu\text{strain}/\text{yr}$  at San Luis.

#### Concluding Discussion

This paper describes a procedure for modeling deformation behavior at strike slip plate margins. The time and spatial evolution of fault slip, fault stress, and surface strain, and rates of these quantities are studied in an earthquake cycle in relation to slip penetration into the seismogenic

## 80 RUPTURE PROCESS IN CREEP ZONES

zone leading to an earthquake instability. We applied the procedure to study a fault containing a segment with a weak zone of creeping material. The analysis provide reasonable estimates of cycle time, slip rate distribution in the creep zone, and surface strain rate profiles which are comparable with observed field data from the San Andreas fault in central California. Strong limitations in interpretation of numerical results may be expected due to negligence of coupling of the lithosphere to the asthenosphere which was shown to be particularly important at near instability by Li and Rice [1983a, b]. Furthermore, interpretations of rates of slip, stress, and surface strain depend on the tectonic loading rate, here assumed to be constant at 0.05 bar/yr but is more likely influenced by viscoelastic relaxation effects of the asthenosphere [Li and Kisslinger, 1984/5]. Thus the present model calculations are most appropriate when the asthenosphere is essentially relaxed and this may mean well into an earthquake cycle but before instability (prior to the next earthquake) sets in. This is perhaps the time stage at which the 1906 and the 1857 ruptured fault segments of the San Andreas fault stand at the present time. Another limitation in the present model is associated with an intrinsic inadequacy in the 'line-spring' procedure when the strength variation along-strike occurs with wavelengths less than a plate thickness. The model should therefore be most appropriate when applied to tectonic size-scale features, such as the long creep zone in central California and the long asperity zones in southern California [Stuart, 1984/5].

The present work may be extended to studying the spatial variations in slip penetration and focal points of nucleating instabilities in long asperity zones, and in the study of apparent strengthening in a fault segment due to deep asperities. The present formulation is also capable of accounting for the geometrical changes in the fault trace, such as the big bend and branch faults on the San Andreas fault. In this case, the stress redistribution due to spacially differential slippage includes a normal across-the-fault component and such normal stress changes have been suggested as responsible for seismicity rate changes on the San Andreas fault. Coupling between the lithosphere and the asthenosphere could be incorporated in the model by generalization of the Green's function  $G(P,P')$  in (1) to include temporal dependence, although the expression is rather unwieldy [Lehner et al., 1981]. Time integration would then be necessary in the Boundary Element Method to account for the memory effects. The creep zone modeling discussed in this paper may be improved by incorporating an end zone of shallow creep with a submerged locked seismogenic layer, such as that discussed by Tse et al [1985] in connection with stressing in the Parkfield region. Unlike their model, however, the present model can simulate the progressive failure process leading to an instability.

**Acknowledgement.** The authors would like to thank J.R. Rice and T.F. Wong for many useful discussions. This work has been supported by the National Science Foundation under grant EAR-8412313 and by the U.S. Geological Survey under grant 14-08-0001-22043 to MIT.

## References

- Aki, K., Asperities, barriers and characteristic earthquakes, *J. Geophys. Res.*, **89**, 5867-5872, 1984.
- Burford, R.O., and P.W. Harsh, Slip on the San Andrews fault in central California from alignment array surveys, *Bull. Seismol. Soc. Am.*, **70**, 1233-1261, 1980.
- Dmowska, R., and V.C. Li, A mechanical model of precursory source processes for some large earthquakes, *Geophys. Res. Lett.*, **9**, No. 4, 393-396, 1982.
- Dmowska, R., V.C. Li, and J.R. Rice, Nonuniform stressing in the Parkfield region from interactions between adjacent creeping and locked fault zones, *EOS, Trans. Amer. Geophys. Union*, **66**, 985, 1985.
- Fares, N., and V.C. Li, An indirect boundary element method for 2-D finite/infinite regions with multiple displacement discontinuities, *I. Eng. Fracture Mech.*, in press, 1986.
- Hirth, J.P., and J. Lothe, *Theory of dislocations*, pp. 780, McGraw-Hill, New York, 1968.
- Kanamori, H., and G.S. Stewart, Seismological aspects of the Guatemala earthquake of February 4, 1976, *J. Geophys. Res.*, **83**, 3427-3434, 1978.
- Lachenbruch, A.H., and J.H. Sass, Thermo-mechanical aspects of the San Andreas, in *Proceedings, Conference on the Tectonic Problems of the San Andreas Fault System*, edited by R.L. Kovach and A. Nur, pp.192-205, *Stanford University Pub. Geol. Sci.*, **13**, 1973.
- Lehner, F.K., Li, V.C., and J.R. Rice, Stress diffusion along rupturing plate boundaries, *J. Geophys. Res.*, **86**, 6155-6169, 1981.
- Li, V.C., and C. Kisslinger, Stress transfer and nonlinear stress accumulation at subduction-type plate boundaries—Applications to the Aleutians, Special Issue on Earthquake Prediction, edited by K. Shimazaki and W. Stuart, pp.812-830, *PAGEOPH*, **122**, 1984/5.
- Li, V.C., and J.R. Rice, Preseismic rupture progression and great earthquake instabilities at plate boundaries, *J. Geophys. Res.*, **88**, 4231-4246, 1983a.
- Li, V.C. and J.R. Rice, Precursory surface deformation in great plate boundary earthquake sequences, *Bull. Seismol. Soc. Am.*, **73**, 1415-1434, 1983b.
- Rice, J.R., The line spring model for surface flaws, in *The Surface Crack: Physical Problems and Computational Solutions*, edited by J.L. Swedlow, pp.171-185, American Society of Mechanical Engineers, New York, 1972.
- Sibson, R.H., Fault Zone Models, heat flow, and the depth distribution of earthquakes in the continental crust of the United States, *Bull. Seismol. Soc. Am.*, **72**, 151-163, 1982.
- Stuart, W.D., Strain softening prior to two-dimensional strike-slip earthquake, *J. Geophys. Res.*, **84**, 1063-1070, 1979.
- Stuart, W.D., Instability model for recurring large and great earthquakes in southern California, *Pure Appl. Geophys.*, **122**, 793-811, 1984/5.
- Stuart, W.D., and G.M. Mavko, Earthquake instability on a strike-slip fault, *J. Geophys. Res.*, **84**, B5, 2153-2160, 1979.
- Thatcher, W., Nonlinear strain buildup and the earthquake cycle on the San Andreas fault, *J. Geophys. Res.*, **88**, 5893-5902, 1983.
- Tse, S.T., R. Dmowska, and J.R. Rice, Stressing of locked patches along a creeping fault, *Bull. Seismol. Soc. Am.*, **75**, 709-736, 1985.
- Turcotte, D.L., and D.A. Spence, An analysis of strain accumulation on a strike slip fault, *J. Geophys. Res.*, **79**, 4407-4412, 1974.
- Wesson, R.L., R. Robinson, C.G. Buse, W.L. Ellsworth, J.H. Pfluke, J.A. Steppe, and L.C. Seekins, Search for seismic forerunners to earthquakes in central California, *Tectonophysics*, **42**, 111-126, 1977.
- Wong, T.F., Shear fracture energy of Westerly granite from post-failure behavior, *J. Geophys. Res.*, **87**, 990-1000, 1982.
- Wong, T.F., On the normal stress dependence of the shear fracture energy, *Earthquake Source Mechanics*, this volume, 1986.

## SLIP ON AN IMPERMEABLE FAULT IN A FLUID-SATURATED ROCK MASS

J.W. Rudnicki

Department of Civil Engineering Northwestern University Evanston, Illinois 60201

**Abstract.** Previous solutions for slip in elastic fluid-saturated rock masses are appropriate for permeable faults because they assume no change in pore fluid pressure on the fault (slip) plane. Faults *in situ* are, however, often barriers to fluid flow, possibly because they contain much clay or very fine-grained gouge material. Here, the solution for a dislocation suddenly emplaced on an impermeable fault is used to analyze coupled deformation diffusion effects for impermeable faults. In contrast to predictions for the permeable fault, the shear stress induced by sudden slip on an impermeable fault does not decay monotonically in time from the undrained (instantaneous) value to the drained (long-time) value, but instead, first rises to a peak in excess of the undrained value by about 20% of the difference between the drained and undrained values. This rise in shear stress suggests that coupling between deformation and diffusion is initially destabilizing. Using two opposite signed dislocations to simulate a finite length fault suggests that the rise in shear stress occurs for 1.5 to 15 days for a fault 4 km in length and diffusivities of  $0.1 \text{ m}^2/\text{s}$  to  $1.0 \text{ m}^2/\text{s}$ . A characteristic time, defined as the time needed for the shear stress on the fault to decay to one-half of its long-time value, is  $a^2/4c$  for the impermeable fault compared with  $a^2/16c$  for the permeable fault where  $a$  is half the fault length and  $c$  is the diffusivity. Consequently, diffusive reloading of the fault, suggested as a contributor to aftershocks, does not begin immediately and occurs much more slowly for the impermeable fault. The pore pressure change on the impermeable fault is not zero as for the permeable fault, but is discontinuous and the values are opposite in sign on different sides of the fault. For the permeable fault, the position of the maximum pore pressure change moves away from the fault with time, but the maximum pore pressure change for the impermeable fault is always located at the dislocation.

## Introduction

The diffusion of pore fluid induced by slip on a fault can introduce time-dependence into the

response of the material surrounding the fault. This time-dependence has been suggested as playing a role in several processes associated with faulting: generation and migration of aftershocks [Nur and Booker, 1972; Booker, 1974], stability of precursory slip [Rudnicki, 1979], fault creep [Rice and Simons, 1976], earthquake swarms [Johnson, 1979] and response of water-wells to propagating creep events [Roeloffs and Rudnicki, 1985]. The solutions that have been used to analyze the coupling between fluid diffusion and fault slip and to interpret relevant field observations are appropriate for permeable faults. There is, however, considerable geological evidence that faults *in situ* can act as barriers to fluid flow possibly because the fault zones contain much fine-grained material or clay gouge [Wang and Lin, 1978; Wu et al., 1975]. In such cases it is more appropriate to model the fault as impermeable. This paper describes the solution for a shear dislocation suddenly introduced on an impermeable fault plane in a linear elastic, fluid-infiltrated solid. This solution is obviously a crude model for fault slip in the earth's crust. Nevertheless, comparison of this solution with that obtained for a permeable fault [Booker, 1974; Rice and Cleary, 1976] suggests differences in coupled deformation-diffusion effects for permeable and impermeable faults. These differences may be important in assessing the significance of coupled deformation-diffusion effects in fault processes and in designing proper strategies for their observation. Of course a more elaborate model is necessary for detailed analysis of the fault processes that have been mentioned, i.e., slip stability, aftershocks, etc. Such models can, however, be constructed by superposition of the dislocation solution.

This paper does not describe the details of the solution method, but instead concentrates on the results for two quantities of primary interest in fault problems: the shear stress induced on the fault plane and the pore fluid pressure. Differences with the corresponding quantities for the permeable fault are emphasized and the implications of these differences for fault processes are discussed.

## 82 SLIP ON AN IMPERMEABLE FAULT

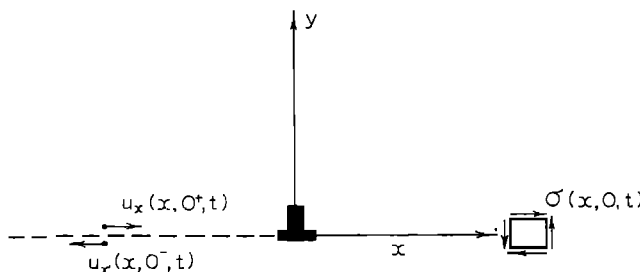


Fig. 1. Geometry of a plane strain shear dislocation. The dislocation corresponds to sudden introduction of a discontinuity in the  $x$ -direction displacement on the negative  $x$ -axis.

## Governing Equations

The governing equations for plane strain deformation (in  $xy$  plane) of a linear, fluid-infiltrated, porous elastic material can be written in terms of the stresses  $\sigma_{xx}$ ,  $\sigma_{xy}$ , and  $\sigma_{yy}$  and the pore fluid pressure  $p$  as follows:

$$\frac{\partial \sigma_{xx}}{\partial x} + \frac{\partial \sigma_{xy}}{\partial y} = 0 \quad (1)$$

$$\frac{\partial \sigma_{xy}}{\partial x} + \frac{\partial \sigma_{yy}}{\partial y} = 0 \quad (2)$$

$$\nabla^2(\sigma_{xx} + \sigma_{yy} + 2n p) = 0 \quad (3)$$

$$(c \nabla^2 - \partial/\partial t) [\sigma_{xx} + \sigma_{yy} + (2n/\mu)p] = 0 \quad (4)$$

where  $c$  is a diffusivity,  $\mu = (v_u - v)/(1 - v)$ , and  $n = 3(v_u - v)/2B(1 + v_u)(1 - v_u)$ . The Poisson's ratios  $v$  and  $v_u$  govern drained (slow) and undrained (rapid) deformation, respectively, and  $B$  is the ratio of pore fluid pressure to mean normal compression induced during an increment of undrained response. The first two equations express equilibrium in the absence of body forces and the third compatibility of strains. The diffusion equation (4) results from combining Darcy's law and conservation of fluid mass and using (3). The quantity in square brackets is proportional to the fluid mass content per unit volume of porous solid. Rice and Cleary [1976] have given a full discussion of these equations and have tabulated values of the material constants (also, see Rudnicki [1985]). These equations were originally derived in a different form by Biot [1941] and are equivalent to those studied by Booker [1974], although he chooses to express them in terms of displacements and restricts consideration to incompressible constituents. This restriction corresponds to  $v_u = 1/2$  and  $B = 1$ .

<sup>u</sup> The introduction of a shear dislocation at the origin corresponds to slitting the negative  $x$ -axis and creating a discontinuity in the  $x$ -direction

displacement  $u_x$  (Figure 1). Let  $\delta(x, t)$  be the displacement discontinuity defined by

$$\delta(x, t) = u_x(x, 0^+, t) - u_x(x, 0^-, t) \quad (5)$$

where the notation is intended to indicate that  $u_x$  is to be evaluated on the positive and negative sides of the  $x$ -axis. For the sudden introduction of a shear dislocation of magnitude  $b$  at the origin

$$\delta(x, t) = b H(-x) H(t) \quad (6)$$

where  $H(\dots)$  is the unit step function. Because the problem is antisymmetric about the  $x$ -axis, it is possible to restrict consideration to the upper half-plane  $y > 0$  with boundary conditions applied to  $y = 0$ . Thus, (5) can be expressed as

$$\delta(x, t) = 2u(x, 0^+, t) \quad (7)$$

Because of antisymmetry and continuity of tractions across  $y = 0$ ,  $\sigma_{yy}$  is zero on the fault plane:

$$\sigma_{yy}(x, 0, t) = 0 \quad (8)$$

Darcy's law states that the fluid mass flux is proportional to the gradient of pore fluid pressure. Consequently, for an impermeable fault plane the pore pressure satisfies the following condition:

$$\frac{\partial p}{\partial y}(x, 0, t) = 0 \quad (9)$$

In the previous solutions due to Booker [1974] and Rice and Cleary [1976], the pore pressure was assumed to be continuous across the fault plane. Because of antisymmetry, the value of  $p$  on the fault plane is then required to be zero. Obviously,  $\partial p/\partial y$  will not be zero on the fault plane in this case, corresponding to fluid flow across the fault plane. Hence, these solutions are appropriate for a permeable fault. For an impermeable fault, the pore pressure need not be continuous across the fault, but by antisymmetry the values on opposite sides of the fault are still required to be equal in magnitude and opposite in sign.

The governing equations (1), (2), (3), and (4) are expressed in terms of the stresses and pore fluid pressures. Consequently, it is convenient to convert (6) and (7) to conditions on the stresses. The constitutive relation for the strains of the solid matrix  $\epsilon_{\alpha\beta}$  in terms

of the stresses and pore fluid pressure is as follows:

$$2G\epsilon_{\alpha\beta} = \sigma_{\alpha\beta} - v(\sigma_{xx} + \sigma_{yy})\delta_{\alpha\beta} + 2n(1-v)p\delta_{\alpha\beta} \quad (10)$$

where  $\alpha, \beta = x, y$  and  $\delta_{\alpha\beta}$  is the Kronecker delta. The strains are related to the displacements by

$$\epsilon_{\alpha\beta} = \frac{1}{2} (\partial u_{\alpha}/\partial x_{\beta} + \partial u_{\beta}/\partial x_{\alpha}) \quad (11)$$

Substituting (11) into (10) and evaluating on  $y = 0$  for  $\alpha = \beta = x$  yields

$$G \frac{\partial \delta}{\partial x}(x, t) = \sigma_{xx}(1 - v) + 2n(1 - v)p \quad (12)$$

where (7) and (8) have been used. Differentiating (6), substituting into (12) and solving for  $\sigma_{xx}$  yields

$$\sigma_{xx}(x, 0, t) = -\frac{G b}{(1 - v)} \delta_{\text{DIRAC}}(x) H(t) - 2n p(x, 0, t) \quad (13)$$

where  $\delta_{\text{DIRAC}}$  is the Dirac delta function. The details of the solution method will not be given here but the general approach was to use the Laplace transform on time and the Fourier transform on  $x$ . Expressions for the complete stress and pore pressure fields have been obtained, but these are cumbersome and will not be displayed. Two quantities of most interest, the pore fluid pressure and the induced shear stress on the fault plane, are, however, given by relatively simple expressions and these are discussed in the following sections.

#### Shear Stress on the Fault Plane

The shear stress on the fault plane ( $y = 0$ ) due to sudden introduction of a unit dislocation at the origin corresponding to left-lateral slip is given by

$$\sigma_{xy}(x, 0, t) = \frac{G b}{2\pi(1 - v_u)x} F[x^2/(4ct)] \quad (14)$$

The time dependence of the solution is expressed by the function  $F$ :

$$F[\xi] = 1 - \mu [2e^{-\xi} - \xi^{-1}(1 - e^{-\xi})] \quad (15)$$

where  $\mu = (v_u - v) / (1 - v)$ . At  $t = 0^+$ , immediately after the introduction of the dislocation,  $\xi = \infty$ ,  $F = 1$  and (14) reduces to the usual elasticity expression based on the undrained

Poisson's ratio. At long times,  $t \rightarrow \infty$ ,  $\xi$  approaches zero and  $F[0] = (1 - v_u) / (1 - v)$ . Thus, (14) reduces to the usual elasticity expression based on the drained value of Poisson's ratio. This behavior is identical to that for the dislocation introduced on the permeable fault. The time dependence at intermediate times is, however, much different. For comparison, the function expressing the time dependence of the induced shear stress for a dislocation on a permeable fault is given by [Rice and Cleary, 1976]

$$F_p[\xi] = 1 - \mu \xi^{-1}(1 - e^{-\xi}) \quad (16)$$

where the subscript  $p$  denotes the permeable fault. Figure 2 plots the following quantity

$$\frac{\sigma_{xy}(x, 0, t) - \sigma_{xy}(x, 0, \infty)}{\sigma_{xy}(x, 0, 0) - \sigma_{xy}(x, 0, \infty)} \quad (17)$$

against  $4ct/x^2$  for the permeable and impermeable fault; this is the same as a plot of  $F$  and  $F_p$  against the reciprocal of their arguments. As shown, the induced shear stress for the permeable fault decays monotonically with time whereas that for the impermeable fault first rises above the undrained value before decaying to the drained value. The height of the peak above the undrained value is about 20% of the difference between undrained and drained values. To estimate the time scale of the changes in shear stress, two dislocations of opposite sign can be used to simulate a finite length fault. Rice [1980] suggests placing the dislocations at the centroids  $x = \pm 2a/\pi$  of the slip distribution caused by a uniform stress drop on a fault of length  $2a$ . The time-dependent stress drop is then given approximately by

$$\Delta\tau \approx (\Delta\tau)_{t=0} + F[a^2/\pi^2 ct] \quad (18)$$

Figure 3 plots the stress drops in nondimensional form for both the permeable and impermeable faults against  $ct/a^2$ . As expected from Figure 2, the stress drop for the impermeable fault continues to decrease for a time after the imposition of the slip, but then increases and eventually reaches the drained value. The minimum in the stress drop for the impermeable fault occurs at  $ct/a^2 \approx 0.0325$ . For a fault length  $2a = 4$  km and a diffusivity  $c = 0.1 \text{ m}^2/\text{s}$ , a value suggested by Rice and Simons [1976] as representative of field conditions,  $t \approx 15$  days. If the diffusivity  $c = 1.0 \text{ m}^2/\text{s}$ , then  $t \approx 1.5$  days. The stress drop for the permeable fault reaches half of its long-time value when  $ct/a^2 \approx 0.0625$  whereas the stress drop for the impermeable fault does not reach half its long time value until  $ct/a^2 \approx 0.2425$ . For a  $2a = 4$  km and  $c = 0.1 \text{ m}^2/\text{s}$  these values correspond to approximately 30 days and 112 days.

## 84 SLIP ON AN IMPERMEABLE FAULT

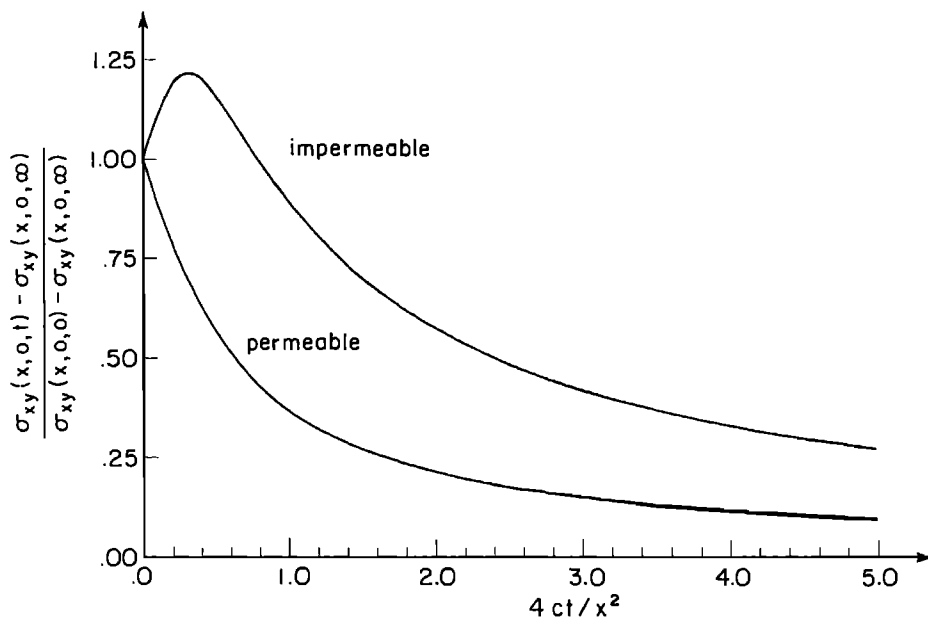


Fig. 2. Time dependence of the shear stress at a fixed position on the x-axis as a function of the nondimensional time  $ct/x^2$  where  $c$  is the diffusivity.

The differences in the fault-plane shear stress solutions for the permeable and impermeable faults have implications for several fault processes. First consider that the slip modelled by the dislocations is emplaced seismically. The solution for the permeable fault states that the shear stress induced on the fault plane has its highest value, the undrained value, immediately after slip occurs ( $t = 0^+$ ), and then decays monotonically to

the drained value. On the other hand, the solution for the impermeable fault indicates that the induced shear stress will rise from its value immediately after slip is emplaced for a period on the order of days. This means that the effect of coupling between deformation and diffusion is initially destabilizing for the impermeable fault. It is possible that this increase could trigger additional slip. Also, although the shear stress

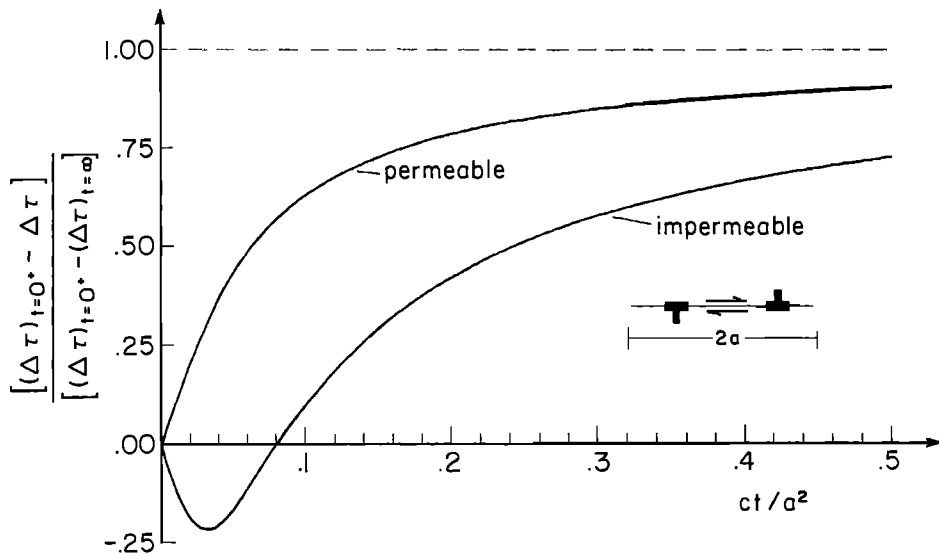


Fig. 3. Stress drop versus time divided by the diffusion time  $a^2/c$  for a fault of length  $2a$ . Two dislocations of opposite sign are used to simulate a finite length fault. The increase of the stress drop with time is accompanied by diffusive reloading of the fault.

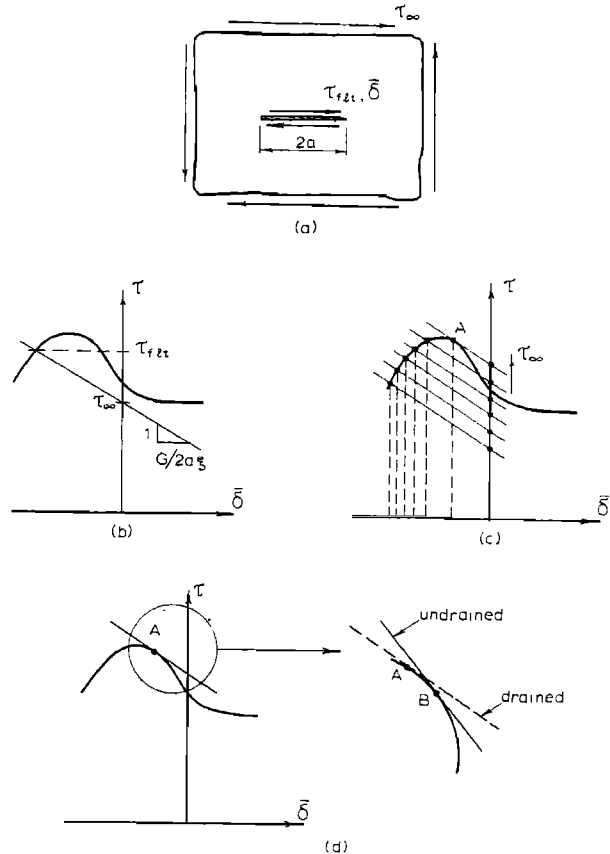


Fig. 4. Graphical construction originated by Rice [1979] for illustrating fault slip instability. (a) Fault of length  $2a$  sustains a shear stress  $\tau_{f\text{lt}}$  and average slip  $\bar{\delta}$ . The fault is loaded by far-field stresses  $\tau_\infty$ . (b) The solution for  $\tau_{f\text{lt}}$  and  $\bar{\delta}$  corresponding to a value of  $\tau_\infty$  is given by the intersection of the  $\tau_{f\text{lt}}$  versus  $\bar{\delta}$  static relation and a straight line representing the effective unloading stiffness of the surrounding material. The slope of this line is minus  $G/2a\xi$  where  $\xi$  depends on the geometry (e.g. plane strain versus axisymmetry) and the Poisson's ratio of the surrounding material. (c) At point A further increase in  $\tau_\infty$  cannot be accommodated by quasi-static response. Note that the increments in  $\bar{\delta}$  corresponding to equal increments of  $\tau_\infty$  increase as point A is approached. (d) Delay of instability by coupled deformation-fluid diffusion. Because the unloading stiffness of the material surrounding the fault is greater for more rapid deformation, instability is delayed until B.

on the impermeable fault ultimately decays with time, it remains higher than the shear stress on the permeable fault at any finite, non-zero time.

The differences between the solution for the permeable fault and that for the impermeable fault also require some reassessment of inferences by Nur and Booker [1972] and Booker [1974] (also,

discussed by Rice and Cleary [1976] and Rice [1980]) on the possible effects of coupled deformation and diffusion on aftershock processes. These authors noted that the solution for the permeable fault implies that the stress drop accompanying imposition of a fixed amount of slip decreases in time within the slipped region but increases outside of it. Consequently, the total shear stress increases in time within the slipped region but decreases outside it. As explained by Rice [1980], this is consistent with aftershock activity that is confined to the slipped region rather than the presumably more highly stressed surrounding region and is controlled by a time-dependence shown in Figure 3. Because the stress drop for the impermeable fault initially continues to drop after introduction of the dislocation and then rises more slowly than for the permeable fault, one would expect reloading of an impermeable fault to occur more slowly than for a permeable fault. If the time at which the shear stress drop reaches half its long-time value is regarded as characteristic of the duration of aftershock activity, then this time scale is approximately four times as long for the impermeable fault although no aftershock activity would be expected in the period during which stress drop is decreasing for the impermeable fault.

The solution also suggests that predictions of coupled deformation-diffusion effects on precursory slip may be different for permeable and impermeable faults. Figure 4 shows the graphical construction originated by Rice [1979] and used by Rudnicki [1979] to discuss the stabilizing effects due to coupled deformation-diffusion in the material surrounding a permeable fault. Initially, the material surrounding the fault responds in drained fashion because slip occurs slowly, by comparison to the diffusion time, under the action of increasing tectonic stress  $\tau_\infty$  (Figure 4b, c). As instability, predicted on the basis of the drained response, is approached (point A in Figure 4c, 4d), the accelerating fault slip induces the shorter time response of the material surrounding the fault. Because this response is stiffer than the drained response, instability is delayed. The response to instantaneous slip is undrained and, hence, instability occurs when the slope of the  $\tau_{f\text{lt}}$  versus  $\bar{\delta}$  curves equals the undrained unloading stiffness of the surrounding material (B in Figure 4d). Because of the differences in the time dependence of fault stress for the permeable and impermeable faults, the transition from drained to undrained behavior will be different. Rudnicki's [1979] analysis of the permeable fault predicted that the delay in the onset of fault instability due to coupled deformation-fluid diffusion effects occurred over such a short-time period that detection would be difficult. Whether the different time-dependent response of the impermeable fault gives rise to a longer precursory period is unclear.

## 86 SLIP ON AN IMPERMEABLE FAULT

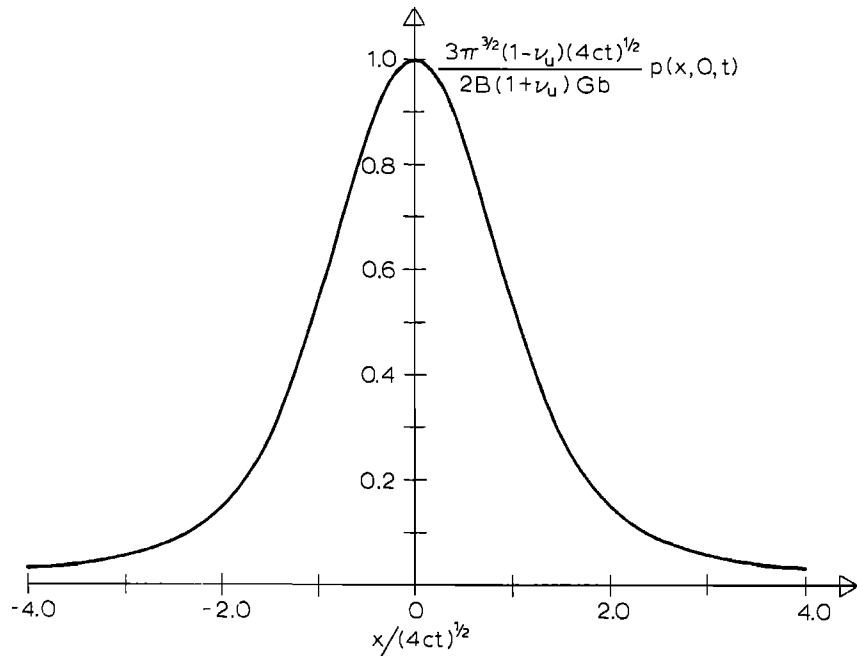


Fig. 5. Pore pressure, in nondimensional form, induced on the positive side ( $y = 0^+$ ) by a sudden dislocation of an impermeable fault. The pore pressure induced on the other side of the fault ( $y = 0^-$ ) is equal in magnitude and opposite in sign to that shown here.

## Pore Fluid Pressure

For the impermeable fault the induced pore fluid pressure is given by

$$p(x, y, t) = \frac{B(1 + v_u)}{3\pi(1 - v_u)} \left\{ \left( \frac{y}{r^2} \right) \text{erf} \left[ \frac{y}{(4ct)^{1/2}} \right] + \left( 2x/\pi^{1/2} r^2 \right) e^{-y^2/4ct} \text{Daw} \left[ \frac{x}{(4ct)^{1/2}} \right] \right\} \quad (19)$$

where  $r^2 = x^2 + y^2$ ,  $\text{erf}(\xi)$ , is the error function defined [Abramowitz and Stegun, 1964, 7.1.1] as

$$\text{erf}(\xi) = (2/\pi^{1/2}) \int_0^\xi e^{-\alpha^2} d\alpha \quad (20)$$

and  $\text{Daw}(\xi)$ , is Dawson's integral, defined as [Abramowitz and Stegun, 1964]

$$\text{Daw}(\xi) = e^{-\xi^2} \int_0^\xi e^{\alpha^2} d\alpha \quad (21)$$

Equation (19) gives the pore pressure in the half-plane  $y > 0$ ; the values in the lower half-plane  $y < 0$  are the negative of those in (19).

Figure 5 plots the non-dimensional pore pressure  $P$

$$P = \frac{3\pi^{3/2}(1 - v_u)(4ct)^{1/2}}{2B(1 + v_u) Gb} p \quad (22)$$

on the positive side of the fault plane ( $y = 0^+$ ) for a fixed time  $t > 0$ . Because the fault plane is impermeable, the pore pressure is discontinuous and the values on the lower side of the fault plane,  $y = 0^-$ , are the negative of those shown in Figure 5. Increases in pore pressure decrease the effective compressive stress on the fault, that is, the total compressive stress minus the pore fluid pressure and promote further slip. Consequently, a measure of the tendency of the induced stress changes to promote slip is

$$\psi(x, t) = \frac{2\pi(1 - v_u)}{Gb} [\sigma_{xy}(x, 0, t) + \phi p(x, 0, t)] \quad (23)$$

where  $\phi$  is a friction coefficient (because of (8), the normal stress on the fault is constant). This quantity is plotted against  $x/(4ct)^{1/2}$  in Figure 6 for the positive side of the fault ( $y = 0^+$ ). The dashed curve shows the shear stress only. The values of  $\psi$  on  $y = 0^+$  lie above it. This suggests that slip is promoted on the side of the fault with positive pore pressure and inhibited on the side with negative pore pressure.

For a finite length fault there will be positive and negative contributions to the pore

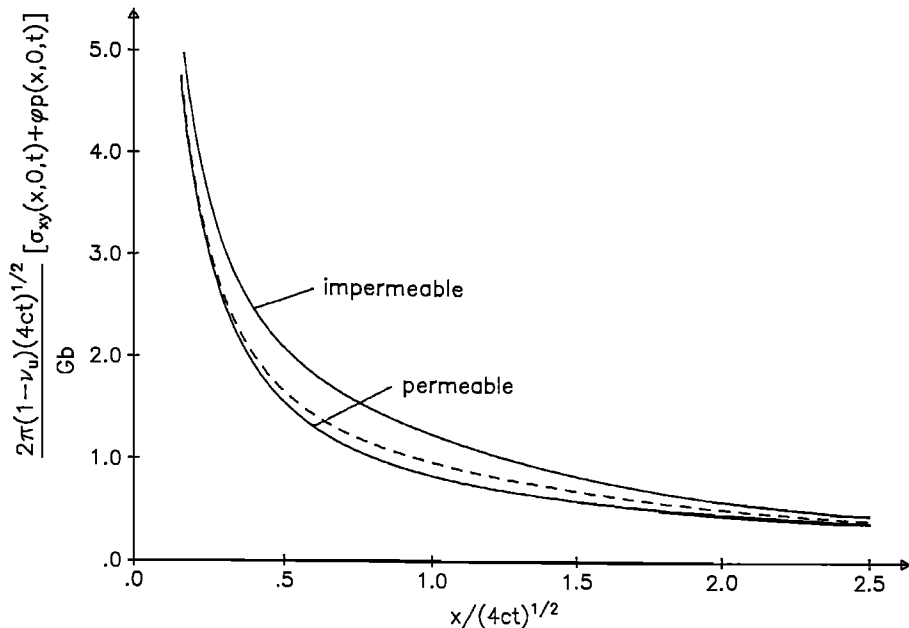


Fig. 6. Combined effect of the shear stress  $\sigma_{xy}(x, 0, t)$  and pore fluid pressure  $p(x, 0, t)$  induced on the positive side ( $y = 0^+$ ) of an impermeable fault. The dashed curve shows  $\sigma_{xy}(x, 0, t)$  in nondimensional form for the impermeable fault. Because the pore pressure is zero on the permeable fault the curve labeled "permeable" is  $\sigma_{xy}(x, 0, t)$  in nondimensional form. The plot is for  $\phi = 0.6$ .

pressure on each side of the fault. If the fault is modelled simply as two dislocations of opposite sign, the largest pore pressure changes will occur at the dislocations, near the ends of the fault, and be of opposite sign at the two ends on the same side of the fault. As a specific example, consider a finite length fault with the left lateral slip geometry shown in Figure 1; the pore pressure will increase on  $y = 0^+$  near the right end and on  $y = 0^-$  near the left end. A manifestation of this prediction might be the presence of transverse subsidiary faults in the regions of pore pressure increase, but not in the regions of decrease. Note, however, that the uncoupled elasticity solution predicts an increase in compressive mean stress, in the regions of pore pressure increase.

The curve labeled "permeable" in Figure 6 is the shear stress on the permeable fault; because the pore pressure is zero on the permeable fault,  $\psi$  is equal to the shear stress. As shown, the shear stress ahead of the dislocation is greater for the impermeable fault.

Figure 7 shows contours (solid lines) of the nondimensional pore pressure (22) for  $y > 0$  at a fixed time  $t > 0$ . As required by the condition of no flow across the fault, the contours of constant pore pressure intersect the fault at right angles. Because flow occurs in directions of decreasing pore fluid pressure, the flow near the fault is away from the origin. For comparison the pore pressure induced by sudden introduction of a dis-

location on a permeable fault is [Rice and Cleary, 1976]

$$p = \frac{B(1 + \nu_u)}{3\pi(1 - \nu_u)} G \frac{y}{r^2} [1 - \exp(-r^2/4ct)] \quad (24)$$

Contours of this pore pressure in the same non-dimensional form are shown as dashed lines in Figure 7. As noted by Booker [1974], the maximum pore pressure change occurs at a position that diffuses away from the fault with time. In contrast, the maximum pore pressure change for the impermeable fault occurs at the edge of the slip zone and remains there. The contours for the two cases merge away from the fault, but are different near the fault because of the different boundary conditions. In particular, note that the pore pressure changes are much greater near the impermeable fault.

Nur and Booker [1972] have noted that pore pressure changes induced off the fault plane could reduce the effective confining stress and contribute to the occurrence of aftershocks. A proper evaluation of this suggestion would need to consider, in addition, the stress changes at different orientations off the fault plane. Nevertheless, the pore pressure distribution near the fault seems sufficiently different for permeable and impermeable faults that differences in aftershock distribution might be anticipated if

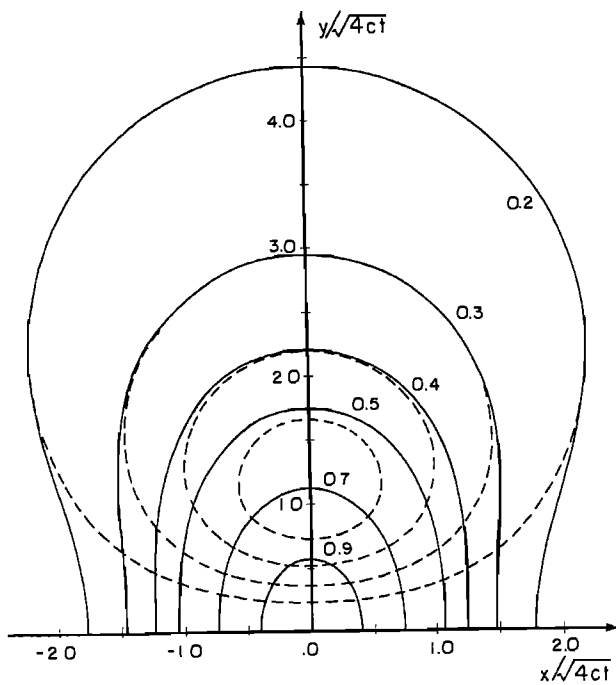


Fig. 7. Comparison of the contours of the non-dimensional pore pressure (22) for permeable (dashed) and impermeable (solid) faults. Plot is for a fixed time not equal to zero.

indeed coupled deformation diffusion effects play a prominent role.

#### Concluding Discussion

This paper has presented the solution for the shear stress on the fault plane and the pore fluid pressure induced by the sudden introduction of a shear dislocation at the origin. These results have been contrasted with those previously obtained by Booker [1974] and Rice and Cleary [1976] for a permeable fault. The most notable of the differences in the solutions are the larger pore pressure changes near the fault and the increase of the fault plane shear stress over the undrained value for the impermeable fault. A full assessment of the effects of these differences on fault processes, such as aftershocks and slip stability, must await study of fault models more realistic than the suddenly introduced dislocation. Nevertheless, the differences seem great enough that they should be considered in observational as well as theoretical studies of coupled deformation-fluid diffusion effects.

Some preliminary results have also been obtained for the pore pressure induced by a dislocation steadily propagating on an impermeable fault [Roeloffs and Rudnicki, 1984]. As for the stationary dislocation, the results substantially differ from those for the permeable fault [Roeloffs and Rudnicki, 1985]. Specifically, the pore pressure at a fixed distance from the impermeable fault rises more sharply than for the

permeable fault and then falls quickly to zero as the dislocation passes, but does not reverse sign, as for the permeable fault. These results are relevant to predictions of the change of water well levels in response to creep events [Wesson, 1981; Lippincott et al., 1985].

A question to be answered is whether coupled deformation-diffusion effects can stabilize propagating slip on an impermeable fault as predicted by Rice and Simons [1976] for a shear crack propagating on a permeable fault. An important feature of their solution is that the neighborhood of the edge of the slip zone always responds in drained fashion because the pore pressure on the fault plane is zero. For the impermeable fault, the pore pressure on the fault plane will not be zero and the effect on stabilization is unknown. One possibility for a destabilizing effect, suggested by the solutions for both the moving and the suddenly introduced dislocations, is that the pore pressure on one side of the fault ahead of the slipping region is increased tending to promote further slip there.

Acknowledgments. I thank J. Rice for suggesting some time ago that I look at this problem and E. Roeloffs for many helpful discussions.

This work was supported by the National Science Foundation and the U.S. Geological Survey.

#### References

- Abramowitz, M. and I.A. Stegun, (Eds.), Handbook of Mathematical Functions, Appl. Math. Ser. 55, National Bureau of Standards, Washington, D.C., 1964.
- Biot, M.A., General theory of three-dimensional consolidation, J. Appl. Phys., 12, 155-164, 1941.
- Booker, J.R., Time-dependent strain following faulting of a porous medium, J. Geophys. Res., 79, 2037-2044, 1974.
- Johnson, C.E., I. CEDAR - an approach to the computer automation of short period local seismic networks; II. Seismotectonics of the Imperial Valley of Southern California, Ph.D. thesis, 332 pp., California Institute of Technology, 1979.
- Lippincott, D.K., J.D. Bredehoeft, and W.R. Moyle, Jr., Recent movement on the Garlock fault as suggested by water level fluctuations in a well in Fremont Valley, California, J. Geophys. Res., 90, 1911-1924, 1985.
- Nur, A., and J.R. Booker, Aftershocks caused by fluid flow?, Science, 175, 885-887, 1972.
- Rice, J.R., Theory of precursory processes in the inception of earthquake rupture, Gelands Beitr. Geophys., 81, 91-127, 1979.
- Rice, J.R., The mechanics of earthquake rupture, in Physics of the Earth's Interior, Proc. Int'l. School of Physics "Enrico Fermi," edited by A.M. Dziewonski and E. Boschi, pp. 555-649, North Holland, Amsterdam, 1980.
- Rice, J.R., and M.P. Cleary, Some basic stress-diffusion solutions for fluid-saturated elastic porous media with compressible constituents, Rev. Geophys. Space Phys., 14, 227-241, 1976.
- Rice, J.R., and D.A. Simons, The stabilization of

- spreading shear faults by coupled deformation-diffusion effects in fluid-infiltrated porous solids, J. Geophys. Res., 81, 5322-5334, 1976.
- Roeloffs, E., and J.W. Rudnicki, Coupled deformation-pore fluid diffusion effects on fault rupture, Final Technical Report on Contract No. 21818, 30 pp. U.S. Geol. Sur., October, 1984.
- Roeloffs, E., and J.W. Rudnicki, Coupled deformation-diffusion effects on water level changes due to propagating creep events, Pure Appl. Geophys., 122, 560-582, 1985.
- Rudnicki, J.W., Stabilization of slip on a narrow weakening fault zone by coupled deformation - pore fluid diffusion, Bull. Seismol. Soc. Am., 69, 1011-1026, 1979.
- Rudnicki, J.W., Effects of pore fluid diffusion on deformation and failure of rock, in Mechanics of Geomaterials, Proc. IUTAM William Prager Symposium on Mechanics of Geomaterials: Rocks, Concrete, Soils, edited by Z.P. Bazant, pp. 315-347, John Wiley and Sons, New York, 1985.
- Wang, C-Y, and W. Lin, Constitution of the San Andreas fault zone at depth, Geophys. Res. Lett., 5, 741-744, 1978.
- Wesson, R.L., Interpretation of changes in water level accompanying fault creep and implications for earthquake prediction, J. Geophys. Res., 86, 9259-9267, 1981.
- Wu, F.T., L. Blatter, and H. Roberson, Clay gouges in the San Andreas fault system and their possible implications, Pure Appl. Geophys., 113, 87-95, 1975.

## FRACTURE OF A SINGLE ASPERITY ON A FINITE FAULT: A MODEL FOR WEAK EARTHQUAKES?

S. Das

Lamont-Doherty Geological Observatory of Columbia University, Palisades, New York 10964

B. V. Kostrov

Institute of Physics of the Earth USSR Academy of Sciences, Moscow

**Abstract.** Dynamic rupture of a single asperity on a finite, three dimensional, stress-free fault is suggested as one possible model of low-magnitude, large moment, long duration ('slow' or 'weak') earthquakes. Using the assumption of constant stress drop and the conventional schematic representation of the displacement spectral density, relations between seismic moments and corner frequencies of dislocation (crack) and asperity models are obtained for earthquakes of equal magnitude. It is shown that an earthquake due to asperity failure has a  $(R/r)^2$  larger seismic moment and  $(r/R)$  lower corner frequency than a 'normal' dislocation earthquake of the same magnitude, where  $r$  and  $R$  are the dimensions of the asperity and surrounding crack, respectively.

## Introduction

The 3-D problem of dynamic fracture of a single asperity on a infinite stress-free fault under remote displacement conditions was studied by Das and Kostrov [1983, 1985]. It was shown that the far-field P and S displacement pulses for this problem rise from zero to a final permanent level. This is in contrast to the conventional dislocation (crack) models in which the displacement rises from zero to a maximum and then decreases again to zero. In the earlier studies of Das and Kostrov [1983, 1985], the finiteness of the fault surrounding the asperity was ignored and this led to the final permanent non-zero offset. In this paper, we take into account the finiteness of the fault around the asperity and determine the resulting far-field displacement pulse shapes. Our results show that such earthquakes must have anomalously large moment and duration for a given magnitude and suggest one possible explanation for such 'slow' or 'weak' earthquakes which have been observed [e.g., Kanamori and Cipar, 1974; Kuznetsova et al., 1976; Shebalin, 1985].

This proposed model is only one possible explanation for such earthquakes, another possi-

ble model being that of a very low stress drop crack (dislocation). Essentially, these two models are equivalent from the point of view that the average stress drop on the crack is low in both cases, the asperity simply acting as a concentrator of this low stress drop onto a small area, and results in both cases in the slip rate on the fault being low. It is not possible to consider one of these two physical models to be more realistic than the other and our proposed model simply represents one possibility.

## Pulse Shapes Due to Asperity Failure on Infinite and Finite Faults

The geometry of the dynamic problem investigated here is shown in Figure 1. A circular asperity (unbroken region of the fault) of radius  $r$  is situated at the centre of a circular crack (broken region) of radius  $R$ . The stress on the broken region is assumed to be at the dynamic frictional level so that when the central asperity breaks, this region exhibits no dynamic stress drop and also has no resistance to slip (similar to the situation in Das and Kostrov [1983, 1985]). The slip distribution on the crack due to the fracture of the central asperity is calculated using the numerical boundary-integral method of Das [1980]. For the numerical simulation,  $r/R = .1$  and the central asperity is taken as a single spatial grid. The fracture of the asperity is allowed to occur instantaneously (in 1 time step) and the ensuing slip is determined. Since the annular region surrounding the asperity has no resistance to slip, points on it start slipping as soon as the first P-wave from the fracture of the central asperity arrives there. On close examination of the numerical results it is found, however, that though the slip at any point in the annular region is initiated by the arrival of the P-wave, the slip becomes appreciable only after the arrival of the S-wave. Thus, though the slip front propagates at the P-wave velocity, the main slip propagates

## 92 A MODEL FOR WEAK EARTHQUAKES

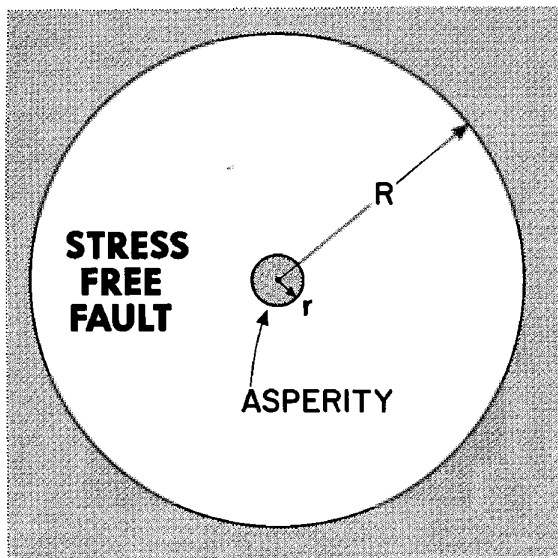


Fig. 1. Geometry of the problem.

at approximately the S-wave velocity over the annulus. The far-field displacement pulse shape is calculated by summing particle velocity over the fault surface [cf. Aki and Richards, 1980]. P and S pulse shapes in the far-field for different directions are calculated. The normalized S-wave displacement pulse shape looking down at the fault along the normal as a function of normalized time  $\alpha t/\Delta x$ , is shown in Figure 2, as a representative example, where  $\alpha$  is the P-wave velocity of the medium,  $t$  is time and  $\Delta x$  is the spatial grid length. The normalization factor for the displacement is  $\Delta x \alpha / 3\mu$ , where  $\Delta \sigma$  is the average stress drop on the asperity and  $\mu$  is the modulus of rigidity. It is found that the pulse shape immediately reaches its maximum value and

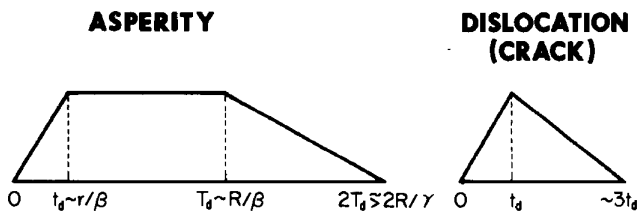


Fig. 3. Schematic representation of far-field displacement pulse shapes for asperity and dislocation (crack problems).

remains flat until the first diffracted waves from the crack edge arrive at the observer at relative time  $T_d \approx R/\beta$  (measured from first S-arrival), where  $\beta$  is the shear wave speed of the medium. The displacement then starts decreasing and finally reaches zero at  $\approx 2T_d$  ( $\approx 2R/\gamma$ ), where  $\gamma$  is the Raleigh wave velocity. Minor oscillations following this, due to our allowing back-slip on the fault, are ignored in this figure. The duration of the flat part of the pulse is thus controlled by the size of the large crack surrounding the asperity. Since the asperity fracture in this problem was allowed to occur instantaneously, this picture does not represent the initial rising part of the pulse correctly. But this was calculated by Das and Kostrov [1983] for several cases and using the previous results and adjusting the time scale, the pulse shape in the stippled region in the figure can be given as shown on the inset of Figure 2. The rise time in the case of fracture of a single asperity was shown to be controlled by the asperity size and given approximately by  $t_d \approx r/\beta$ .

Neglecting the details of the pulse shapes shown in Figure 2, since these details depend on particular parameters (say, crack and asperity

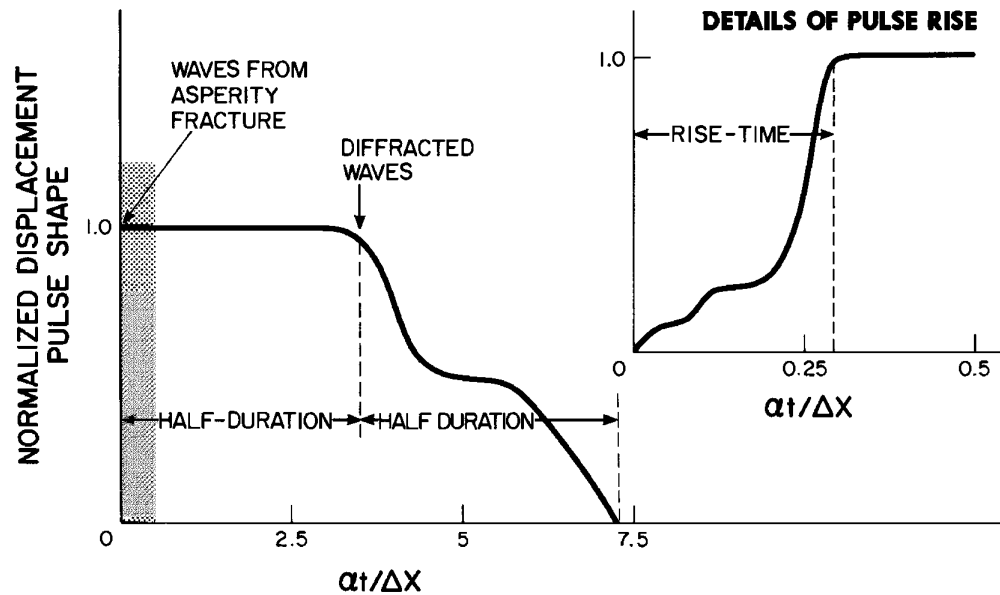


Fig. 2. Far-field displacement pulse shape for asperity failure on a finite fault. Inset shows details of pulse shape in stippled region from Das and Kostrov [1983].

size and shape, grid size, fracture velocity, etc.), one may construct a schematic representation of the pulse shape due to the fracture of a single asperity on a finite fault. This is given in Figure 3.

The main features of the asperity pulse are a steeply rising part followed by a flat portion of long duration and then a gradually decreasing portion. The schematic representation of the main features of the far-field pulse shape due to a crack (dislocation) model is also shown in Figure 3. If the crack in the crack model is taken to be of the same size as the asperity, then the pulse shape has approximately the same rise time as the asperity model, but then starts decreasing immediately and reaches zero in about twice the rise time [cf. Madariaga, 1976].

Thus the major differences between the pulses due to asperity fracture on a finite fault and a crack of radius  $r$  are the anomalously long pulse duration and the anomalously large seismic moment (area under the pulse) of the asperity problem. Such earthquakes are sometimes called 'slow' [Kanamori and Cipar, 1974] or 'weak' earthquakes [Kuznetsova et al., 1976; Shebalin, 1985].

The spectrum of the pulse in Figure 2 was determined numerically and it was found that the envelope of the spectrum has the same general form as for the conventional dislocation model, its corner frequency being determined by the pulse duration, its maximum (at  $\omega = 0$ ) by the area under the pulse and it was found to have a  $\omega^{-2}$  decay at frequencies higher than the corner frequency. This last result may appear to be somewhat surprising since the asperity pulse in Figure 2 and Figure 3 may appear to resemble a Heavyside function, which is known to have an  $\omega^{-1}$  fall-off at high frequencies. Note however that this pulse is not exactly a Heavyside pulse, but a Heavyside pulse modified by some other function (similar to a cosine-tapered pulse). Doing a numerical fast Fourier transform (FFT), we were unable to find a  $\omega^{-1}$  portion in the spectral fall-off. Thus, for the case where  $R = 10r$ , no  $\omega^{-1}$  portion is visible, though for a much larger crack or a much smaller asperity, it may appear. Moreover, if a  $\omega^{-1}$  spectral fall-off is not detectable even in such an idealized situation, it is even less likely to be observationally detectable and for all practical purposes, the spectral fall-off of the asperity pulse can sensibly be taken to be  $\omega^{-2}$ .

It should be pointed out here that more complicated distributions of stress-drop on the fault can be easily imagined. The classical 'crack' model and the 'asperity' model considered in this paper are only the simplest possible limiting cases.

#### Comparison of the Seismic Moments and Corner Frequencies for the Two Models

Seismic moment is determined by

$$M_o = \mu \int_s [u] ds, \quad (1)$$

in terms of the slip  $[u]$  on the fault surface  $s$ . For a circular crack of radius  $R$  with average stress drop  $\Delta\sigma$ ,  $M_o^d$  is given by [Brune, 1970]

$$M_o^d = \frac{16}{7} \bar{\Delta\sigma} R^3 \quad (2)$$

for a Poisson solid. For comparison, we need a corresponding expression for the seismic moment due to asperity fracturing on a finite fault. Following Aki [1967], we assume that the stress drop has the same value for all conventional (dislocation) earthquakes. This implies that the initial slip distribution on the stress-free fault would correspond to the same stress drop  $\Delta\sigma$ , if the asperity were absent. At the site of the asperity, this slip is given by the static crack solution [Eshelby, 1957]

$$[u_o] = \frac{24}{7\pi} \frac{\bar{\Delta\sigma}}{\mu} R. \quad (3)$$

Assuming that the asperity radius  $r \ll R$ , the stress distribution  $\Delta\sigma(\rho)$  on the asperity will be, according to St. Venant's principle, approximately the same as for an asperity on an infinite fault loaded by the same amount of remote slip [Mindlin, 1949; Das and Kostrov, 1983]

$$\Delta\sigma(\rho) = \frac{8}{7\pi} \frac{\mu [u_o]}{\sqrt{r^2 - \rho^2}} \quad (4)$$

where  $\rho$  is the distance from the center of the asperity. The average stress drop  $\Delta\sigma$  on the asperity is then found (integrating (4) over the asperity) to be

$$\frac{\Delta\sigma}{\Delta\sigma} = \frac{0.8}{R} \frac{R}{r} \approx \frac{R}{r} \quad (5)$$

Thus, the average stress drop on the asperity is increased by the ratio  $(R/r)$  over the average stress drop on the annular crack area. Applying Betti's theorem to the asperity problem under consideration and to the problem of a single crack of radius  $R$  with uniform stress drop  $\bar{\Delta\sigma}$ , we obtain

$$\bar{\Delta\sigma} \int_s^a [u] ds = [u_o] \int_s^a \Delta\sigma(\rho) ds \quad (6)$$

where  $[u^a]$  denotes the slip due to asperity failure and  $s$  is the total fault area. Substituting (3) and (4) into (6), we get

$$M_o^a = \frac{16}{7} \bar{\Delta\sigma} R^3 \cdot \frac{r}{R} \cdot \left( \frac{24}{7\pi} \right)^2 \quad (7)$$

where  $M_o^a$  is the seismic moment of the asperity problem considered in this paper. The ratio  $(24/7\pi)^2$  is equal to 1.19 and for estimation purposes may be replaced by unity. Using (2), we get

## 94 A MODEL FOR WEAK EARTHQUAKES

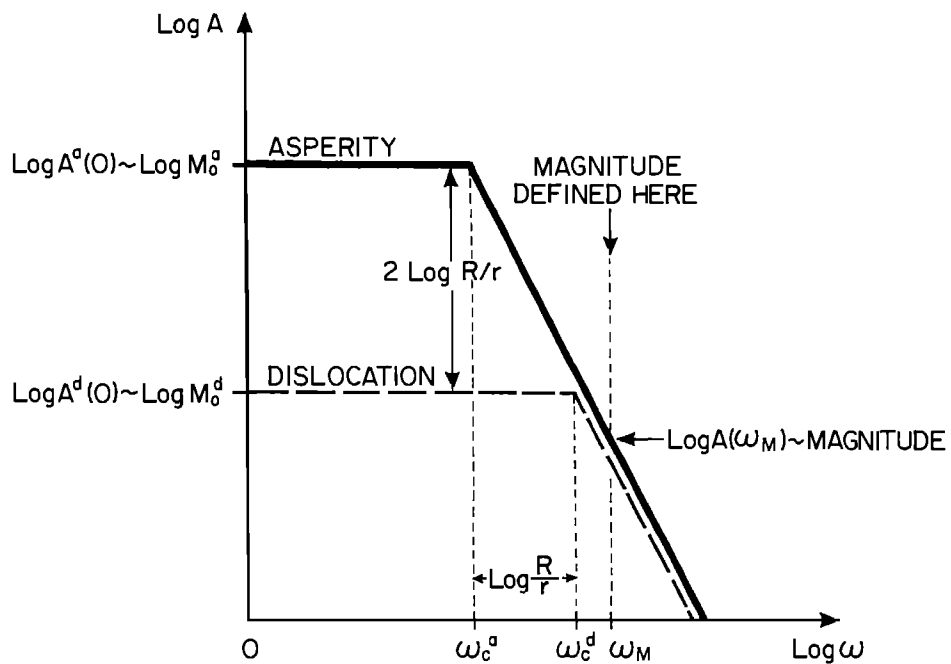


Fig. 4. Far-field displacement spectra for asperity and dislocation problem showing relation between seismic moment and corner frequency for the two problems at a given magnitude.

$$\frac{M_o^a}{M_o^d} = \left(\frac{r}{R}\right)^2 \quad (8)$$

i.e.,  $M_o^a \approx rR^2$ . Thus, the seismic moment due to fracture of a single asperity of radius  $r$  on a finite stress-free fault of radius  $R$  is  $(r/R)$  times smaller than the seismic moment due to a circular fault of radius  $R$  with uniform stress drop but  $(R/r)^2$  larger than the seismic moment due to a fault of radius  $r$  with uniform stress drop.

The above consideration is an alternative formulation of some results of McGarr [1981], which were derived on the assumption of the similarity between the solution of shear and tensile cracks in 3-D.

To illustrate these results, let us suppose that the stress-free fault was created by a large earthquake and the asperity corresponded to a 'barrier' [Das and Aki, 1977], then the seismic moment of an aftershock due to the breaking of this barrier of radius  $r$  is less than the moment of the main shock of radius  $R$  by the factor  $(r/R)$ , but larger than the moment of a dislocational aftershock of radius  $r$  by the factor  $(R/r)^2$ . Two such situations have been reported in the literature. The first was by Kuznetsova et al. [1976] for the aftershocks of the May 14, 1970 Dagestan earthquake ( $M_s = 6.6$ ). They observed that aftershocks near the central part of the faulted zone had anomalously low ratio of seismic moment whereas the aftershocks near the peripheral part had 'normal' values of this

ratio. A similar behavior was found by Shebalin [1985] for the March 14, 1983 Kum-Dagh, Turkmenia ( $M_s = 5.6$ ) earthquake.

The result of (8) is in contrast with the results of Rudnicki and Kanamori [1981]. The reason for this discrepancy (also noted by McGarr [1981]) is that these authors solved a 2-D problem whereas our problem is 3-D. In 2-D, the problem of an asperity on a stress-free fault is of non-St. Venant's type [Cherpanov, 1979] and the approach used by us in this section is not applicable.

As another example, suppose that our large crack corresponds to an active fault area sufficiently damaged during the preseismic period, and we consider a foreshock due to the fracture of one of a few remaining asperities, then the moment of such a foreshock will be amplified by the square of the ratio of the impending earthquake fault size to the asperity size. This might explain the observations of 'low-frequency, low stress drop' events near the center of the faulted region for two earthquakes in Garm, U.S.S.R. [Martynov, 1983], which are discussed in more detail later in this paper.

To recognize such 'slow' or 'weak' earthquakes in practice, it is necessary to compare seismic moments and corner frequencies for conventional (dislocational) and asperity models for earthquakes of equal magnitude.

Following Aki [1967], we assume that the magnitude  $M$  is proportional to the logarithm of the displacement spectral density at a fixed fre-

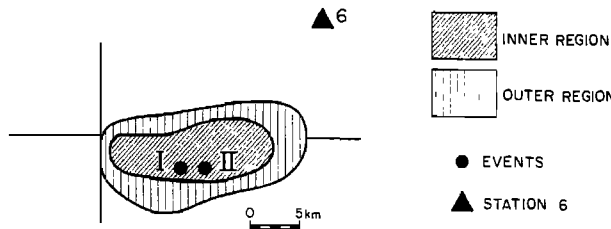


Fig. 5a. Fault geometry and station location for two earthquakes near Garm, USSR after Martynov [1983]. The faulted area, the location of the two earthquakes and the 'inner' and 'outer' areas of the fault where many smaller shocks occur are indicated. The earthquake marked I occurred on September 3, 1976 ( $m_h \approx 5.0$ ) and the earthquake marked II occurred on December 25, 1977 ( $m_h \approx 5.0$ ). The station marked '6' is the station at which the S-wave corner-frequency observations shown in Figure 5b were made. The smaller events had magnitude  $m_p \approx 2.3$ .

quency  $\omega_M$ , (where  $\omega_M/2\pi = 1$  Hz for body wave magnitudes and corresponds to 20 s period waves for surface wave magnitudes). For the sake of brevity, we confine our discussion to the simplest case when  $\omega_M$  is greater than any corner frequency involved. Then, with the conventional parameterization of the displacement spectral density envelope [Aki, 1967], we have

$$M = \log M_0 - 2 \log \omega_M + 2 \log \omega_c + c \quad (9)$$

where  $c$  is a constant and  $\omega_c$  is the corner frequency. Taking logarithm of (2) and/or (8), we obtain

$$\log M_0 = -3 \log \omega_c + \log \alpha + c_1 \quad (10)$$

where  $\alpha = 1$  for dislocation (crack) models,  $\alpha = (r/R)$  for the asperity model and  $\omega_c$  is taken proportional to  $1/R$  in both cases. The constants  $c$  and  $c_1$  are essentially the same for both models.

Using (9) and (10) for the two models at a given magnitude  $M$ , we obtain

$$\log M_o = \log M_0 - 2 \log(r/R)$$

$$\log \omega_c^a = \log \omega_c^d + \log(r/R)$$

or

$$M_o^a = M_o^d \left( \frac{R^2}{r^2} \right)$$

and

$$\omega_c^a = \omega_c^d \left( \frac{r}{R} \right) \quad (11)$$

Thus, an earthquake due to asperity failure has  $(R/r)^2$  larger seismic moment and  $(r/R)$  lower corner frequency than the conventional (dislocational) earthquake of the same magnitude. This is illustrated by Figure 4.

The interpretation by Martynov [1983] of some events occurring near the center of the faulted area for two earthquakes in Garm, U.S.S.R. as being 'low-frequency, low stress-drop' events, was, in fact, based on the decrease of observed S-wave corner frequencies. The plot of these corner frequencies versus time as well as the fault geometry are reproduced from Martynov [1983] in Figures 5a and 5b. The fault geometry and the station location (marked "6") are shown in Figure 5a. The 'inner' and 'outer' regions of the faulted area are indicated as well as the locations of the two earthquakes marked I and II. The S-wave corner frequencies versus time are plotted for events in the inner (solid line) and outer zone (dotted line) in Figure 5b. Each data point (solid and open circle for inner and outer regions, respectively) represents the average of several events and the standard deviations are indicated by bars. A significant decrease in corner frequency is seen for events in the inner zone before earthquake I and a less clear decrease is seen before earthquake II. The magnitudes of these small events did not change appreciably during this time period. A small increase in the corner frequency is also seen for events in the outer zone before earthquake I but this is somewhat ambiguous. The decrease in S-wave corner frequencies, observed before earthquake I, is much larger than the standard deviations indicated in the figure and persisted for more than a year prior to and for a short time following the occurrence of I. Based on our model and discussions related to Figure 4, we may suggest that for events prior to I, at first 'normal' (crack/dislocation) foreshocks occurred. As the time of occurrence of I approached, preslip may have taken place on regions of the fault close to the hypocenter (inner zone), so that the foreshocks occurring a year before I may represent events due to asperity failure. The events in the outer region are close to the edge of the fault and are better modelled as cracks. The events following I may

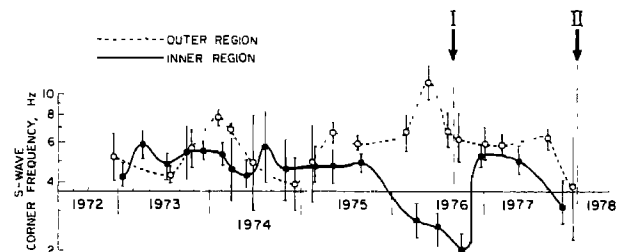


Fig. 5b. Plot of average observed S-wave corner frequency versus time for events occurring within the faulted areas of earthquakes I and II.

## 96 A MODEL FOR WEAK EARTHQUAKES

be considered as aftershocks of I or foreshocks of II but in either case, are still events due to asperity failure.

## Conclusion

The dynamic fracture of a single asperity surrounded by a finite, relatively much weaker fault is studied and the resulting far-field displacement pulse shape is calculated. It is found that such earthquakes have anomalously large seismic moment and duration for a given magnitude and suggest that this may be a possible model for so-called 'slow' earthquakes.

If one has reliable plots of corner frequency and/or seismic moment versus magnitude for conventional (normal) earthquakes, then, for an earthquake of a given magnitude one can read off the expected values of  $\omega_c^d$  and/or  $M_o^d$  from the plots. If, then, the observed values of  $\omega_c^a$  and/or  $M_o^a$  fall off these curves beyond a few standard deviations, one may conclude that the earthquake is a 'slow' one. Then, assuming the asperity model, the ratio of the dimension of the asperity  $r$  and the whole fault  $R$  would be given by

$$\frac{r}{R} = \frac{\omega_c^d}{\omega_c^a}$$

or,

$$\frac{r}{R} = \frac{\omega_c^a}{\omega_c^d}$$

from equation (11).

The relations between moment and magnitude for the 'dislocation' (crack) and 'asperity' models provide a comparison between the long-period (moment) and short-period (magnitude) radiation characteristics for the two source models.

Acknowledgments. This work is part of a joint program in earthquake prediction under Area IX of the U.S.-U.S.S.R. Agreement in the Field of Environmental Protection. This work was done while B. V. Kostrov was visiting Lamont-Doherty. The Lamont reviewers were C. H. Scholz and A. Lerner-Lam, and we thank them for their comments. The work was supported by the U.S. Geological Survey under contract USGS 14-08-0001-947 and the National Science Foundation under grant EAR83-18935. Lamont-Doherty Geological Observatory Contribution Number 3960.

## References

Aki, K., Scaling law of seismic spectrum, *J. Geophys. Res.*, 72, 1217-1231, 1967.

- Aki, K., and P. G. Richards, Quantitative Seismology: Theory and Methods, 932 pp., W. H. Freeman and Company, San Francisco, Calif., 1980.
- Brune, J. N., Tectonic stress and spectra of seismic shear waves from earthquakes, *J. Geophys. Res.*, 75, 4997-5009, 1970 (Correction, *J. Geophys. Res.*, 76, 5002, 1971).
- Cherpanov, G. P., Mechanics of Brittle Fracture, McGraw-Hill, New York, 1979.
- Das, S., A numerical method for determination of source time functions for general three-dimensional rupture propagation, *Geophys. J. R. Astron. Soc.*, 62, 591-604, 1980.
- Das, S., and K. Aki, Fault plane with barriers: A versatile earthquake model, *J. Geophys. Res.*, 82(36), 5658-5670, 1977.
- Das, S., and B. V. Kostrov, Breaking of a single asperity: Rupture process and seismic radiation, *J. Geophys. Res.*, 88(B5), 4277-4288, 1983.
- Das, S., and B. V. Kostrov, An elliptical asperity in shear: Fracture process and seismic radiation, *Geophys. J. R. Astron. Soc.*, 80, 725-742, 1985.
- Eshelby, J. D., The determination of the elastic field of an ellipsoidal inclusion, and related problems, *Proc. R. Soc. London, Ser. A*, 241, 376-396, 1957.
- Kanamori, H., and J. J. Cipar, Focal processes of the great Chilean earthquake May 22, 1960, *Phys. Earth Planet. Inter.*, 9, 128-136, 1974.
- Kuznetsova, K. I., Z. Y. Aptekman, N. V. Shebalin, and V. V. Shteynberg, Aftershocks of relaxation and aftershocks due to fracture growth of the Dagestan earthquake, in *Issledovaniya po fizike zemletryasenij* (Investigations in Earthquake Physics), (in Russian), Nauka, 1976.
- Madariaga, R., Dynamics of an expanding circular fault, *Bull. Seismol. Soc. Am.*, 66(3), 639-666, 1976.
- Martynov, V. G., Spectra of S-waves for small local earthquakes, possibilities for their use in seismic prediction, *Experimental Seismol.*, (in Russian), Nauka, p. 128-143, 1983.
- McGarr, A., Analysis of peak ground motion in terms of a model of inhomogeneous faulting, *J. Geophys. Res.*, 86, 3901-3912, 1981.
- Mindlin, R. D., Compliance of elastic bodies in contact, *J. Appl. Mech.*, 16, 259-268, 1949.
- Rudnicki, J. W., and H. Kanamori, Effects of fault interaction on moment, stress drop and strain energy release, *J. Geophys. Res.*, 86, 1785-1793, 1981.
- Shebalin, N. V., Kum-Dagh, Turkmenia, March 14, 1983 and the third Gazli, Kyzilkum, March 19, 1984, earthquakes, *Abstracts, International Association Seismology and Physics of the Earth's Interior*, Vol. 2, pp. 603, Aug. 19-30, 1985, Tokyo, Japan, 1985.

## THE SEISMIC RADIATION FROM A 3-D DYNAMIC MODEL OF A COMPLEX RUPTURE PROCESS. PART I: CONFINED RUPTURES

John Boatwright

U. S. Geological Survey, Menlo Park, California 94025

Howard Quin

Lamont-Doherty Geological Observatory and Department of Geological Sciences  
Columbia University, Palisades, New York 10964

**Abstract.** We have analyzed a class of rupture models with spontaneous rupture growth and spatially variable stress and strength using a computationally rapid solution of the 3-D boundary integral equation for dynamic rupture on a planar fault. The distributions of initial stress and strength are assumed to be self-similar; their spectral variation is assumed to be inversely proportional to wavenumber raised to three-halves power. The initial stress and strength are weakly correlated. The ruptures are confined by a fixed (*i.e.*, high-strength) rupture perimeter. This unphysical confinement allows both an optimal use of the limited computational duration of the model and direct comparison with results obtained from kinematic models. The significant parameters of the dynamic models are the *rms* normalized strength,  $\langle S \rangle$ , and the relative variation of the initial stress and strength. The average rupture velocity is controlled by the normalized strength; to distinguish ruptures with transonic and subsonic rupture velocities, we consider  $\langle S \rangle = 1.0$  and 1.5, respectively. The complexity of the rupture process is proportional to the variation of the initial stress and strength. In general, the complex ruptures exhibit significant variations of rupture velocity, and the rupture fronts are irregular in shape. The body-waves radiated by these models are calculated from the far-field terms of the Green's function. The radiated energy flux is calculated by integrating the velocity power spectrum. These integrals and the body-wave acceleration spectra are averaged over the focal sphere. For these confined ruptures, the radiation efficiency and the *rms* S-wave spectrum depend on the average rupture velocity but do not depend on the complexity of the rupture process. As the ruptures become more complex, the amplitude of the stopping phases decreases while the number of phases radiated from the interior of the rupture area increases. The ruptures with transonic rupture velocities radiate more energy than the subsonic ruptures.

### Introduction

The rupture process of crustal earthquakes is essentially complex; within the frequency band of the

strong ground motion observed in moderate and large earthquakes, the seismic radiation exhibits complexity at all frequencies higher than the corner frequency. Previously, the relationship between source complexity and seismic radiation has been analyzed using kinematic models of rupture in which the amplitude and timing of the slip velocity are randomized from a smooth distribution [Boore and Joyner, 1978], or where the slip velocity of the rupture is obtained by isolating a section from a stochastic realization of slip velocity generated in a larger volume of space-time [Andrews, 1981]. Because these models are kinematic, however, the complexity of the rupture process depends only on the model assumptions and is independent of the dynamics of the faulting process.

Few dynamic models of rupture with stochastic initial conditions have been thoroughly analyzed. Mikumo and Miyatake [1978, and 1979] analyzed dynamic models of unconfined ruptures with uniform stress drop and stochastic distributions of fracture strength; they found that the models with variable strength exhibited complex rupture growth, and that the high-frequency radiation from these ruptures was enhanced relative to the radiation from ruptures with uniform distributions of fracture strength. Zuercher and Smith [1984] used a 3-D finite element code developed by Archuleta [1976] to examine the effect of rupture propagation through a self-similar field of random fracture strength. The rupture propagation in his models was considerably more regular than the fields of stress and strength. This result may be conditioned, however, by Zuercher's method of calculating the stress intensity at the crack tip. Neither of these papers systematically analyzed the body waves radiated by the dynamic rupture models.

The object of this research is to analyze the waveforms, spectra, and energy flux radiated by dynamic rupture as a function of the average overall strength and the variability of the stress and strength. The initial conditions for these ruptures are obtained by modifying the self-similar stochastic analysis of Andrews [1980]. The initial stress and strength are generated from

## 98 CONFINED RUPTURES

positive, independent distributions for the stress drop and for the excess of the strength over the initial stress; the dynamic frictional stress is assumed to be constant. The dynamic nucleation, propagation, and stopping of the rupture are calculated from a rapid hybrid solution of the 3-D boundary integral description of rupture developed by Das [1980]. This hybrid solution calculates the spatial convolutions of stresses and Green's functions partly in the space domain and partly in the wavenumber domain. The ruptures propagate within a fixed perimeter; the finite size of the spatial grid in the model requires incorporating this unphysical confinement. The fixed perimeter also permits the radiation from these models to be directly compared with the radiation from many kinematic rupture models.

Although these ruptures are confined in a physically unrealistic manner, they represent a significant improvement in modeling seismic rupture processes. The stochastic nature of the distributions of stress and strength on faults is a fundamental characteristic of earthquake faulting which controls the frequency-magnitude statistics of earthquakes, the distribution of earthquake stress drops, and the spatial distribution of aftershocks. Incorporating this stochastic character into the initial conditions for dynamic rupture significantly effects the rupture growth, and consequently, the seismic radiation from the dynamic models.

#### *Distributions of Stress and Strength*

In general, the stress field which produces an earthquake contains contributions from two distinct sources: the long wavelengths are determined by the tectonic loading, while the short wavelengths are determined by the interaction of the stress field with a spatially variable strength. We assume the strength variation to be chiefly associated with previous failures. Any distribution of initial stress and strength used for modeling rupture processes must necessarily include the effects of previous failures of all spatial scales.

Following the argument presented by Andrews [1980], we assume that a fault of area  $\Sigma$  has a self-similar distribution of irregularities of various sizes on it. Then the number of irregularities having rupture area greater than  $A$  and centroids within  $\Sigma$  is  $N = K\Sigma/A$ , where  $K$  is a constant. Assume that the inhomogeneities may be represented by a self-similar distribution of circular regions, and consider a circular inhomogeneity of radius  $a$ . The stress function can be written as  $\tau(r; a) = \sigma(a)g(r/a)$  where  $g$  is a shape function and  $\sigma(a)$  is a stress drop function. If  $\sigma(a)$  is to have a self-similar form, it must be a power-law function, say  $\sigma(a) = a^\delta$ . Then the 2-D Fourier transform of the stress change function has the form  $\tau(k, a) = a^\delta a^2 f(ka)$ , where  $f(ka)$  is the transform of the shape function. Because the inhomogeneities are distributed at random, the transforms have random phases, and their squares are additive. The square of the total stress spectrum is  $|\tau^2(k)| = \int |\tau^2(k, a)| dN$ .

Because  $N = K\Sigma/\pi a^2$ ,  $dN = -2K\Sigma da/\pi a^3$ . Using

this result to evaluate the square of the total stress spectrum gives

$$\begin{aligned} |\tau^2(k)| &= -2K\Sigma/\pi \int a^4 a^{2\delta} |f^2(ka)| a^{-3} da \\ &= k^{-2\delta-2} (-2K\Sigma/\pi) \int x^{-2\delta+1} |f^2(x)| dx \\ &\propto k^{-2\delta-2} \end{aligned} \quad (1)$$

Andrews [1980] concludes his derivation by stating that "if stress changes in earthquakes reflect spatial fluctuations of the initial stress state, then stress spectral amplitudes proportional to  $k^{-\delta-1}$  will produce earthquakes with stress drops which vary as  $a^\delta$ ." This result provides the principal constraint on the stress distribution assumed in this analysis.

Equation (1) gives the functional form for the amplitude spectrum of the stress field transform. The phase is a random function with a uniform distribution between 0 and  $2\pi$ . To determine the initial conditions for the rupture models, however, it is not sufficient to generate an initial stress field from the stochastic distribution described above. Rather, three stress fields, the initial stress,  $\tau_o$ , the frictional stress,  $\tau_f$ , and the yield stress (or strength),  $\tau_u$ , must be generated under the constraints,

$$\Delta\tau = \tau_u - \tau_o > 0 \quad (2a)$$

$$\Delta\sigma = \tau_o - \tau_f \geq 0. \quad (2b)$$

defined locally on the fault surface. The first constraint is stronger than the second; as initial conditions for the Das and Aki [1977a] rupture model, the initial stress cannot equal the yield stress. It is physically possible, however, for the initial stress to fall below the frictional stress. In addition to this purely local description of stress and strength, the normalized strength,

$$S = (\tau_u - \tau_o)/\langle\Delta\sigma\rangle \quad (3)$$

is defined in a mixed local/global fashion, where  $\langle\Delta\sigma\rangle$  is the *rms* dynamic stress drop.

Rather than using a stochastic distribution for the frictional stress, we assume that the frictional stress,  $\tau_f$ , is a constant. This assumption conditions the healing of the rupture models but does not significantly modify the high-frequency radiation. The initial stress is obtained by adding a positive random variable, the stress drop,  $\Delta\sigma(x)$ , to the frictional stress. The distribution of stress drop could be generalized to include negative stress drops; the effect on the seismic radiation would be slight, however. The yield stress, or the strength, is obtained by adding a second positive random variable,  $\Delta\tau(x)$ , to the initial stress. We call this second random variable

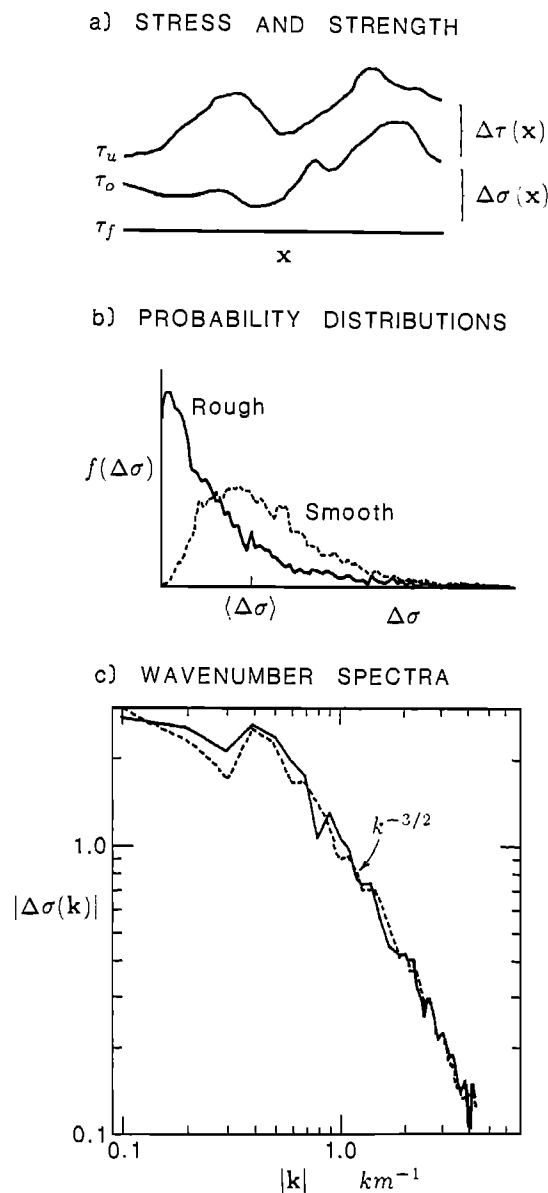


Fig. 1 (a). Schematic diagram showing the relation of the stress drop,  $\Delta\sigma(x)$ , and the strength excess,  $\Delta\tau(x)$ , to the dynamic frictional stress,  $\tau_f$ , the initial stress,  $\tau_o$ , and the yield stress, or strength,  $\tau_u$ . (b) Realizations of the rough (solid line) and smooth (dotted line) distributions for the stress drop. (c) Wavenumber amplitude spectra of the rough and smooth distributions of the stress drop.

the strength excess. The relationship between the two positive random variables and the distributions of the frictional stress, the initial stress, and the strength is shown in Figure 1a. These distributions have been designed to model brittle fault behavior. To model a ductile rheology at depth, Tse and Rice's [1986] model

for the cyclic behavior of a strike-slip fault incorporates a slip strengthening behavior at depth. In the scheme outlined above, slip strengthening could be obtained by specifying a negative stress drop and a negligible strength excess.

We have generated distributions of positive random variables for the stress drop and the strength excess by first generating two independent fields of random variables (say  $x_1$  and  $x_2$ ) with identical zero-mean Gaussian distributions and amplitude spectra which fall off as  $k^\delta$ . The composite random variable,  $y = x_1^2 + x_2^2$ , is then exponentially distributed; its spectrum also falls off as  $k^\delta$ . For the rough models, both the stress drop and the strength excess are exponentially distributed. For the smooth models, the stress drop and the strength excess are generated with a gamma distribution of order  $r = 3$ , obtained by summing three independent random variables with identical exponential distributions. The rough and the smooth distributions are normalized so that  $\langle \Delta\sigma(x) \rangle = 1.0$  and  $\langle \Delta\tau(x) \rangle = \langle S \rangle$ , where the brackets indicate root mean squares. Realizations of the two distributions are plotted in Figure 1b.

To generate the stochastic initial conditions for the rupture models, we have assumed  $\delta = 1.5$ , which gives a smoother distribution of stress than the value of  $\delta = 1.0$  endorsed by Andrews [1980, 1981]. The analysis presented in the beginning of this section indicates that such a distribution of stress would produce a slight increase of stress drop with increasing source size (*i.e.*, the average stress drop would be proportional to the square root of the source radius). This slight dependence is well within observational constraints on the distribution of stress drops in earthquakes [Hanks and Boore, 1984]. For considering the effect of rupture complexity on seismic radiation, however, the actual value of this falloff is not particularly important. The rough initial conditions obtained assuming  $\delta = 1.5$  produce sufficient rupture complexity to comprise a reasonable extremum. Figure 2 shows a set of contour plots of stress and strength for the rough and smooth distributions, as ellipsoidal inclusions within the high-strength perimeters.

Because the strength field is determined from the stress field by adding a positive random variable (*i.e.*, the strength excess), the stress and strength are weakly correlated. This correlation is clearly stronger for the smooth faults. The variance of the strength distribution is  $\langle \Delta\sigma \rangle^2 (1 + \langle S \rangle^2)$ , so that the composite strength function has a larger variance than the initial stress, but less variation relative to the rms strength than the variation of the initial stress relative to the rms stress.

#### *Calculation of Dynamic Rupture Growth*

The computational program used to calculate the fault slip is described in detail in Quin [1986]; the hybrid algorithm which Quin developed solves the 3-D integral boundary equation proposed and solved by Das [1981]. Instead of performing the required convolutions

## 100 CONFINED RUPTURES

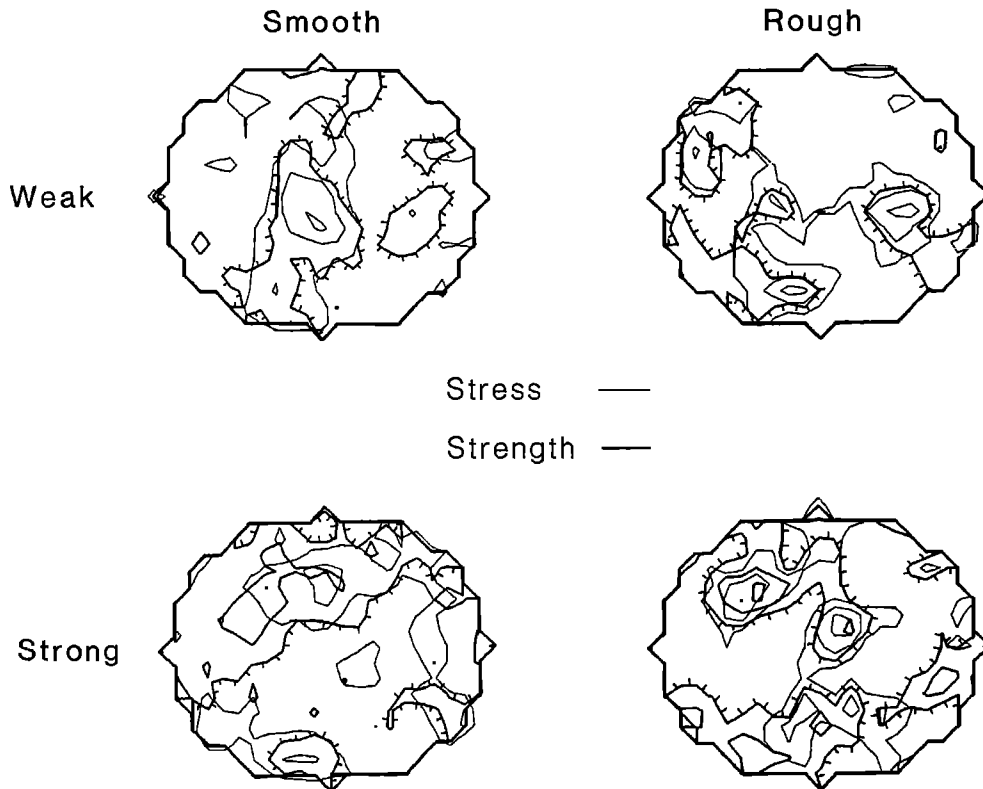


Fig. 2. Distributions of the initial stress and strength for four realizations of the stochastic model. The light lines show the contours of the initial stress in units of  $\langle \Delta\sigma \rangle$ , while the dark lines show the contours of the strength in units of  $2\langle \Delta\sigma \rangle$ . Where possible, the tick marks indicate the areas where the strength is less than  $2\langle \Delta\sigma \rangle$ . The rms stress drop is the same in all the models. The rough fault models have the larger variation of stress and strength; the strong models have the larger average strength.

of the Green's functions and the stress changes entirely in the space domain as in Das [1981], however, Quin [1986] performs the convolutions partly in the space domain and partly in the wavenumber domain, resulting in a substantial saving of computer time. The models were run on spatial grids of  $64 \times 64$  points at a time sampling of  $dt = dx/2\alpha$ . The computational model becomes inaccurate when the Green's functions grow beyond the size of the grid; because the ruptures nucleate at the center of the grid, the computational duration of the rupture model is constrained to 64 time points. The rupture perimeter ( $22 \times 18$  gnd points) is chosen to optimally use this finite duration. The perimeter is not centered on the nucleation point, however, so that the rupture area of the models is somewhat asymmetric.

The dynamic ruptures grow according to a fixed constitutive relation. When the load at a grid point exceeds the yield stress, the grid point begins to slip. The frictional traction resisting slip decreases (weakens) linearly with increasing slip. When the slip exceeds the slip weakening displacement,  $d_o$ , the traction remains at the dynamic frictional level until the component of slip velocity parallel to the traction decreases to zero. If the load decreases further, the slip is fixed, and the traction

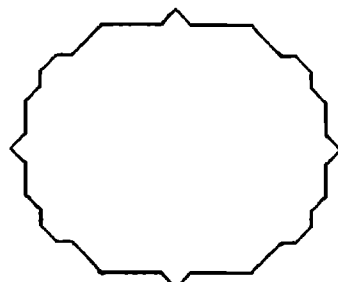
decreases. If the load subsequently increases so that the traction would exceed the dynamic frictional level, the traction is fixed at the dynamic frictional level, and the grid point resumes slipping. A slip weakening algorithm derived by Andrews (written communication, 1985) for a mixed-mode 2-D rupture was used without modification in the 3-D formulation.

For the rupture models analyzed in this research, we used a value of  $d_o$  approximately one third of the least value which inhibits spontaneous rupture growth from the cross of points on which rupture is initiated. This value of  $d_o$  provides some initial high-frequency damping without severely slowing the nucleation of the rupture. Once the ruptures of the uniform models are greater than 9 grid points across, however, the slip at the crack tip exceeds the slip weakening distance as soon as the grid point yields. The effect of the slip weakening on the seismic radiation is probably minimal.

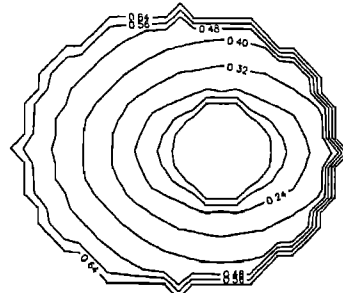
#### *Characteristics of the Rupture Process*

Graphical descriptions of the rupture process of a uniform model and a rough model of a weak fault are plotted in Figure 3 using contours of the stress and

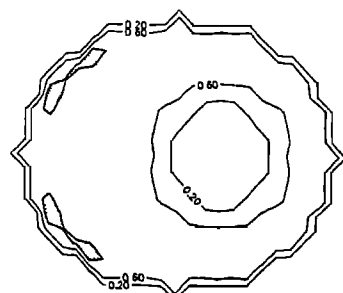
## MODEL 10



stress &amp; strength

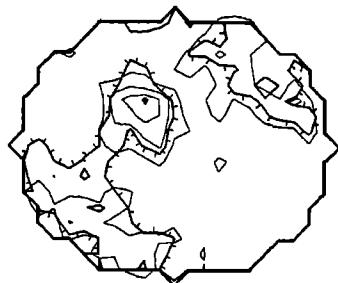


rupture times

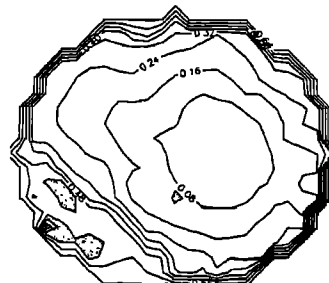


rupture velocity

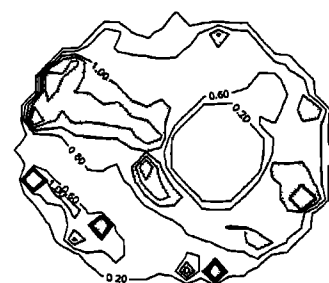
## MODEL 12A



stress &amp; strength



rupture times



rupture velocity

Fig. 3. Comparison of the rupture process of a uniform and a rough model for a weak fault. The contours of stress and strength are explained in Figure 2. The rupture fronts are contoured at 0.08 s intervals; the stippled areas indicate disjoint ruptures. The distribution of rupture velocity is contoured in  $0.20\beta$  intervals, where  $\beta$  is the shear wave velocity; the stippled areas indicate regions where the rupture velocity is transonic (*i.e.*, greater than the shear wave velocity). Note how the asperity near the center of the rupture area accelerates the rupture growth towards the upper left.

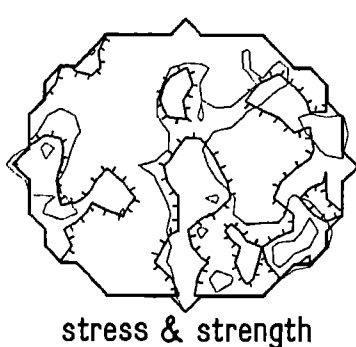
strength distributions, of the rupture fronts, and of the rupture velocity. The stress and strength distributions for the uniform model have no contours. For the rough model, the darker contours of the strength approximately follow the lighter contours of the stress; note the stress concentration in the left center of the rupture area. In the uniform model, the rupture propagation accelerates gradually and symmetrically; for the first 0.25 s, the rupture accelerates faster in the in-plane direction than in the anti-plane direction. In contrast, the rupture propagation in the rough model immediately accelerates to  $v > .6\beta$ ; as it ruptures through the asperity, the rupture growth becomes transonic. Once beyond the asperity, the rupture continues to grow at or near the P-wave velocity until it reaches the fixed perimeter of the rupture area. Just below this area of rapid rupture growth, the rupture front slows for  $\approx 0.20$  s before rupturing through a region of higher strength.

The contour plots of the rupture velocity and the rupture fronts demonstrate the important differences between the uniform and rough models. In the models with uniform loading, the rupture velocity changes gradually

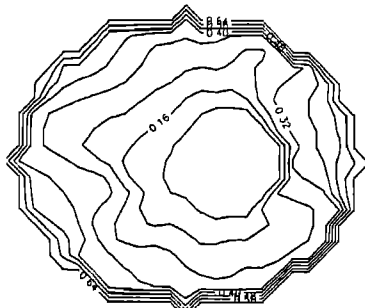
and the rupture fronts are smooth; in the models with stochastic distributions of stress and strength, the rupture velocity changes abruptly and the rupture fronts are irregular. In the rough models, the rupture velocity in any direction can change abruptly; the rupture fronts radiate energy throughout the rupture growth, not just when they reach the rupture perimeter. The irregularity of the rupture fronts in the rough models is a distinguishing characteristic of the stochastic distributions of stress and strength. Because there is no physical justification for assuming rupture fronts to be smooth (*i.e.*, differentiable), it is reasonable to assume that the rupture fronts are continuous, but not generally smooth, during the rupture of real materials. In contrast to the irregularity of the rupture fronts, Figure 3 shows that although there are small disjoint rupture areas in the rough model, the rupture is simply connected for the most part. The "jumping" of rupture barriers predicted by Das and Aki [1977b] from their 2-D models appears to be a minor component of these stochastic 3-D ruptures. Note that this aspect of the rupture models is partly determined by the choice of  $\delta$  used to generate the initial conditions.

## 102 CONFINED RUPTURES

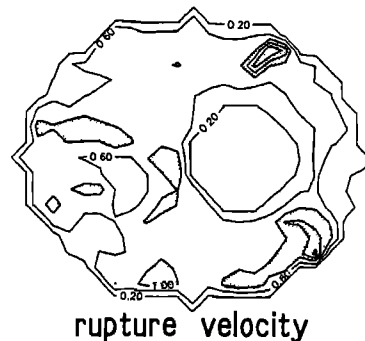
## MODEL 11B



stress &amp; strength

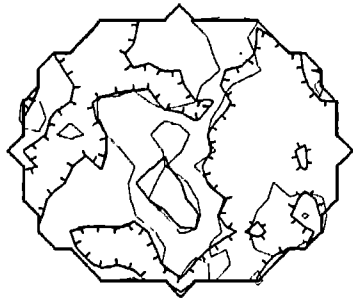


rupture times

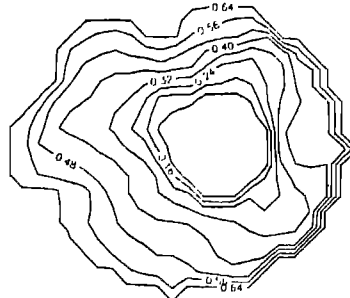


rupture velocity

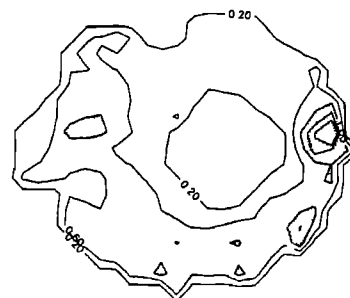
## MODEL 21B



stress &amp; strength



rupture times



rupture velocity

Fig. 4. The rupture processes of two smooth models. The contours are described in Figure 3. The rupture processes of both these events are relatively simple and circular; in detail, however, the rupture growth is unsteady and asymmetric. Although there are no disconnected rupture areas, the rupture velocity in the weak fault model (Model 11B) exhibits significant variation. The strong fault model only ruptures 90% of the area within the rupture perimeter.

The rupture process of two of the smooth models, shown in Figure 4, reiterates the importance of using stochastic distributions for the initial stress and the strength. In the smooth models, the initial stress and strength have a smaller variation over the fault surface. The rupture fronts are still irregular, but not as markedly deformed as in the rough model shown in Figure 3. Overall, the rupture growth is relatively simple and circular. In detail, however, the rupture process is unsteady and asymmetric; at any time, the rupture front is comprised of both salients and embayments. In the weak fault model, the rupture accelerates, decelerates, and accelerates again before reaching the fixed perimeter at the left of the rupture area. To the right of the nucleation area, the rupture delays for  $\approx 0.20$  seconds before rupturing to the perimeter.

The set of ruptures which have been analyzed are differentiated as weak and strong ( $\langle S \rangle = 1.0$  and 1.5,

respectively) and as functions of the complexity of the distribution of the initial stress, or the stress drop. This complexity is quantified as

$$c = (\text{var}(\Delta\sigma(x)))^{1/2} / \overline{\Delta\sigma} \quad (4)$$

where  $\overline{\Delta\sigma}$  is the mean stress drop. The rms stress drop is fixed in the models. The uniform distribution of stress drop in the uniform models gives  $c \equiv 0$ ; in the smooth models,  $0.50 < c < 0.65$ , and in the rough models,  $0.80 < c < 1.25$ . Note that this complexity only describes the distribution of the initial stress, not the distribution of the strength.

The average rupture velocities of the 11 rupture models are plotted as a function of complexity in Figure 5. The weak and strong faults are plotted separately; the rupture velocity averaged over the fault area is plotted with error bars showing one standard deviation. The diamonds

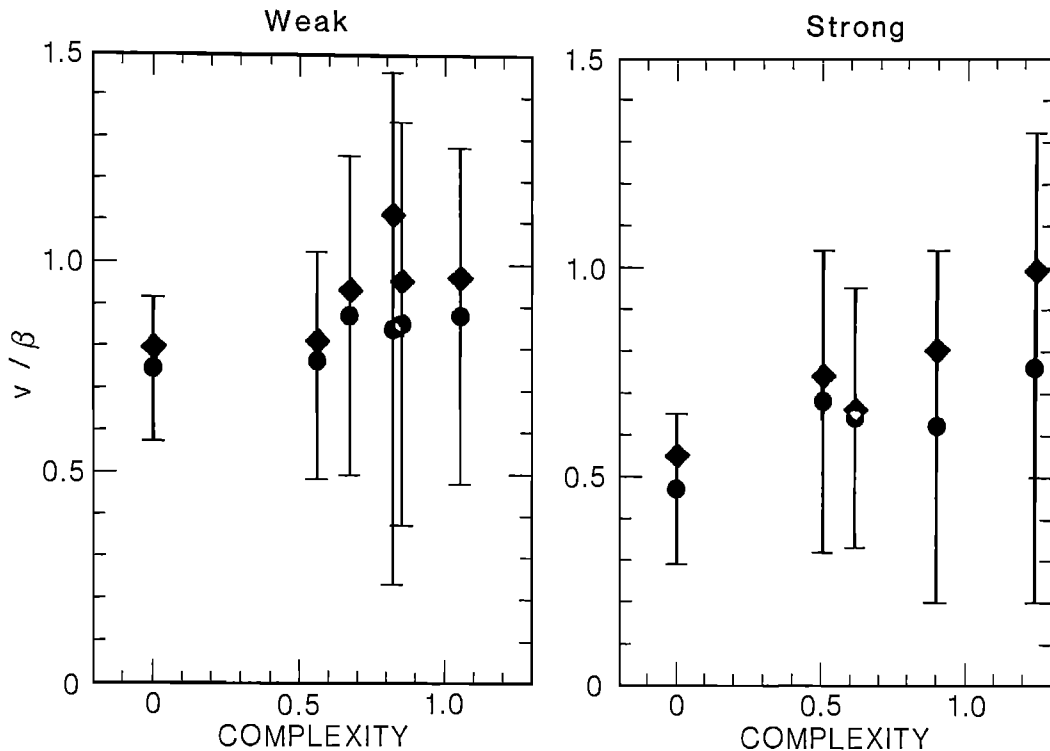


Fig. 5. The rupture velocity plotted against the complexity of the models. The circles and error bars show the mean rupture velocity,  $\bar{v}$ , and the 85 percentile of the rupture velocity distribution. The diamonds show the radiative rupture velocity,  $\langle v \rangle$ , defined in (5), which are assumed to better represent the rupture velocity associated with the radiation of seismic energy. Five of the models, i.e., four weak fault models and one strong fault model, have a significant amount of transonic rupture growth.

show the rupture velocity averaged over the fault area, weighted by the change of the rupture velocity:

$$\langle v \rangle = \sum_i |v_i| |\nabla v_i| / \sum_i |\nabla v_i| \quad (5)$$

Because this weighted average better represents the rupture velocity associated with the radiation of seismic energy, we call it the radiative rupture velocity. The brackets are used because the radiative rupture velocities are approximately the same as the rms rupture velocities. Boatwright [1982] compared the P and S-wave acceleration spectral levels radiated by 10 small earthquakes in Monticello, S.C., to determine an estimate of the "average change of rupture velocity" of  $\Delta v = 0.80\beta$ . If this quantity is equivalent to the radiative rupture velocity, Figure 5 indicates that either the strong fault models with  $c \geq 0.6$  or the weak fault models with  $c \leq 0.6$  are appropriate models for the Monticello earthquakes.

Overall, the variable stress and strength in the rough and smooth models appears to slightly weaken the faults; the ruptures nucleate more rapidly than in the uniform models. The uniform models have the slowest average rupture velocity and the narrowest

distributions of rupture velocity; the weak fault models exhibit faster rupture velocities and generally wider distributions of rupture velocity than the strong fault models. As the complexity of the stress distribution increases, the variability of the rupture velocity increases. The distribution of rupture velocity is  $0.35\beta$  wide in the uniform models,  $0.55\beta$  to  $0.80\beta$  wide in the smooth models and  $0.85\beta$  to  $1.10\beta$  wide in the rough models. Figure 5 shows that the partly transonic rupture growth of these models is an important component of the overall variability of the rupture velocity: if the rupture velocity were entirely subsonic (i.e., less than the S-wave velocity), the width of the resulting distribution of rupture velocity could not easily exceed  $0.6\beta$ .

Figure 6 shows the distributions of rupture velocity compiled separately for the weak and strong fault models. To isolate the difference between the rupture velocity in the in-plane and anti-plane directions, the sampling is restricted to rupture directions within narrow cones ( $\pm 15^\circ$ ) around these directions. The range of anti-plane rupture velocities slightly exceeds the S-wave velocity, while the range of in-plane rupture velocities slightly exceeds the P-wave velocity. The (locally) supersonic rupture velocities are the result of the complexity of the rupture pro-

## 104 CONFINED RUPTURES

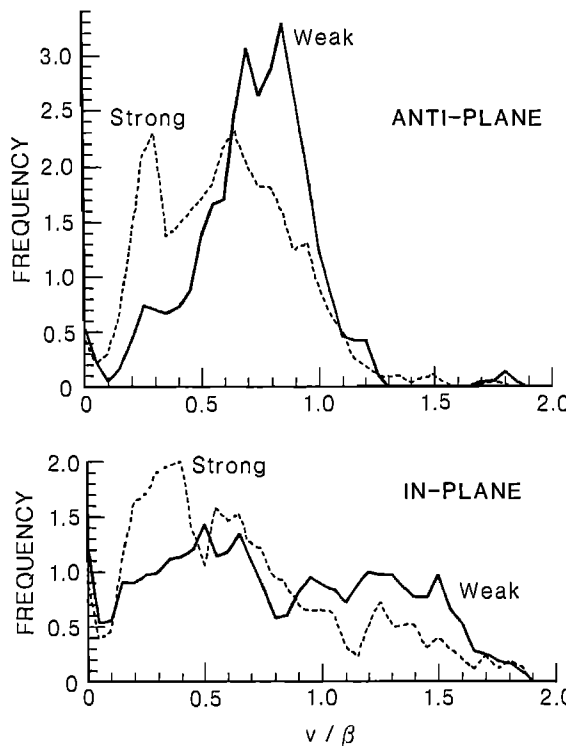


Fig. 6. The distribution of rupture velocities for the weak and strong fault models, differentiated into the in-plane and anti-plane directions. The weak models have the faster rupture velocities, as expected. The transonic rupture velocities comprise approximately 35% and 15% of the in-plane rupture velocity distributions, for the weak and strong models, respectively.

cess; they do not occur in the uniform rupture models. The partially transonic rupture of the stochastic models, particularly the weak fault models, is more important than the small amount of supersonic rupture, however. The prevalence of the transonic rupture enriches the complexity of the rupture process, and consequently, the complexity of the radiated waveforms.

#### *Radiated Waveforms and rms Spectra*

Every acceleration or deceleration of the rupture front radiates seismic energy. Because the initial conditions of these models are determined from self-similar functions, the variations from a uniform rupture growth occur at all spatial and temporal scales smaller than the extent and duration of the rupture process. The most marked differences between the stochastic and uniform ruptures will occur at high frequencies, however. It is natural, then, to analyze the radiated acceleration field for differences between the stochastic and the uniform ruptures.

The body-wave displacements radiated by these models were calculated using the far-field terms of the Green's function and the usual radiation patterns [Aki and Rich-

ards, 1980]. The P and S-wave displacement, velocity, and acceleration waveforms radiated at a single take-off angle by one of the smooth rupture models depicted in Figure 4 are plotted on the left hand side of Figure 7. The velocity and acceleration waveforms have been smoothed by using difference operators of 0.05 and 0.03 s length for the two differentiations. The displacement waveforms are approximately trapezoidal; the acceleration waveforms are dense in pulses. There is a stopping phase evident in the P waveforms at  $\approx 0.30$  s, but it is not much stronger than the high-frequency pulses which follow it. The corresponding phase in the S waveform, arriving at  $\approx 0.26$  s, appears somewhat obscured. The third column in Figure 7 shows the S waveforms radiated by the uniform rupture model depicted in Figure 3. The acceleration waveform is dominated by the stopping phase radiated from the nearest rupture perimeter, arriving at  $\approx 0.32$  s. Because the rupture growth is uniform, the pulses arriving between the strong stopping phase and the stopping phase radiated from the furthest rupture perimeter, arriving at  $\approx 0.73$  s, are not associated with changes of rupture velocity and indicate the level of noise in the radiated acceleration.

Although the displacement waveforms radiated by relatively simple stochastic models cannot be distinguished from those radiated by similar uniform models, Figure 7 shows that the acceleration waveforms are significantly different. Specifically, the acceleration waveforms radiated by uniform models are sparse in acceleration pulses, while the waveforms radiated by the stochastic models are relatively dense in acceleration pulses, although these pulses are weaker than the stopping phases radiated by the uniform models. We note that this difference does not represent a simple enrichment or depletion of high frequencies; the waveforms radiated by stochastic models cannot be filtered to approximate the waveforms radiated by uniform models. The complexity of the acceleration waveforms radiated by the stochastic models matches the observed complexity, or "random" character, of recorded accelerograms.

Because of the stochastic initial conditions, the fast rupture velocities, and the asymmetrical rupture areas of the models, the acceleration waveforms radiated by the stochastic models vary strongly with model, wave-type, and takeoff angle. To directly compare the body-waves radiated by these models, we calculated the rms acceleration spectra by averaging the acceleration power spectra sampled at 52 points distributed in 4 concentric rings (at  $\vartheta = 20^\circ, 40^\circ, 60^\circ$ , and  $80^\circ$  from the normal to the fault plane); the fault plane is a plane of symmetry for body-wave radiation. The acceleration spectra were low-pass filtered at 8 Hz before averaging.

The rms P and S-wave acceleration spectra are plotted in Figure 8, separated into the strong and weak fault models. The acceleration spectral levels are apparently independent of the rupture complexity, as predicted by Boatwright [1982] who showed that the acceleration spectral level is proportional to  $\langle \Delta\sigma \rangle A^{1/2}$ , where  $A$  is the rupture area. Note that the peak stress drops of the

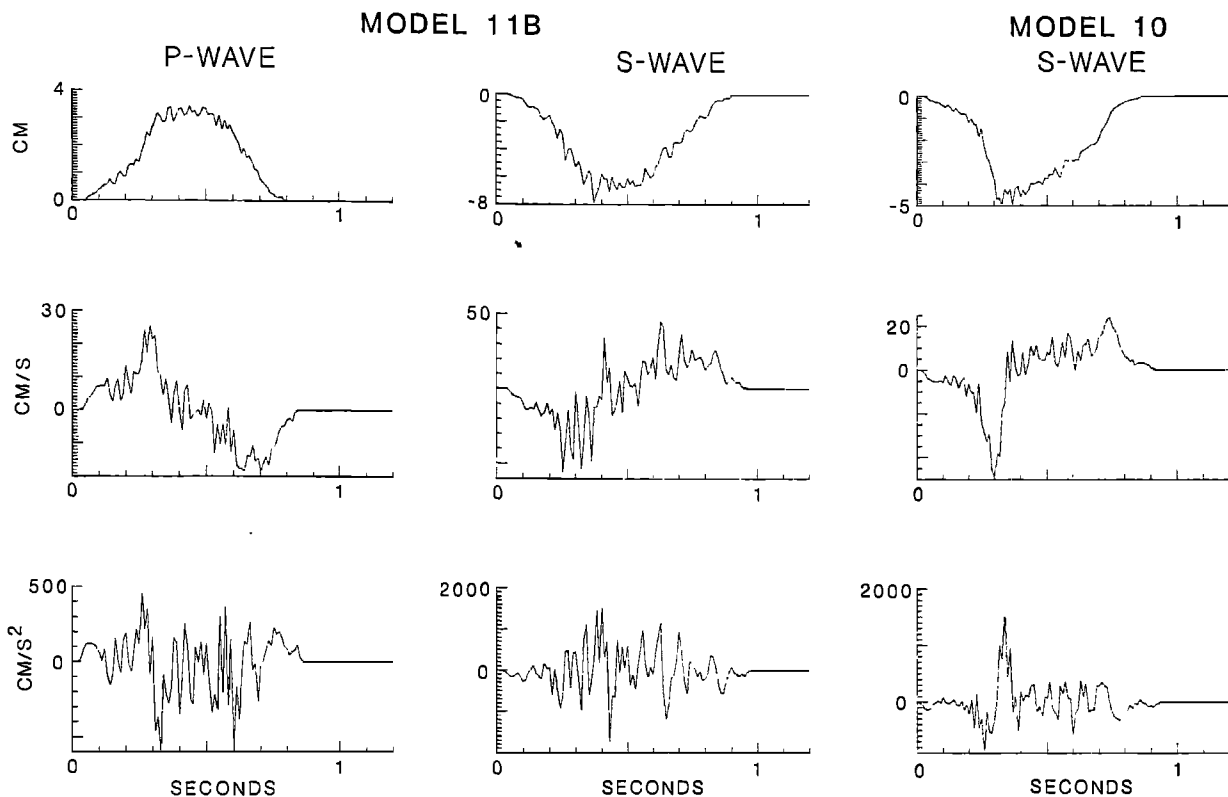


Fig. 7. Displacement, velocity and acceleration waveforms radiated by two of the rupture models. The P and S-waves radiated at  $\vartheta = 35^\circ$ ,  $\varphi = 230^\circ$  by Model 11B are plotted in the first two columns. The S-waves radiated at  $\vartheta = 50^\circ$ ,  $\varphi = 60^\circ$  by Model 10 are plotted in the third column.  $\varphi$  is measured clockwise from left in Figures 3 and 4. Strong stopping phases can be discerned in the P-wave from Model 11B, arriving at 0.30 s, and the S-wave from Model 10, arriving at 0.32 s.

rough fault models are 3 to 4 times the rms stress drop, and therefore, 3 to 4 times the peak stress drop of the uniform models. This difference is not evident in the rms spectra. The offset of the P and S-wave acceleration levels corresponds to a factor of 5 to 6, somewhat larger than the ratio,  $4.8 \pm 0.6$ , determined observationally by Boatwright [1982].

Remarkably, the shapes of the rms S-wave spectra for the different models are nearly identical. Above the corner frequency, the S-wave spectra increase approximately as frequency raised to the one-half power. This behavior is equivalent to a falloff of  $\omega^{-1.5}$  in the rms displacement spectra and represents an "intermediate" spectral trend first identified by Savage [1974]. Boatwright [1980] showed that the intermediate spectral trend results from the focussing of the rupture phase (i.e., the phase radiated by the rupture growth) as the rupture velocity approaches the phase velocity of the radiated waves. The trend is strongest in the S-waves radiated along the plane of the fault. Because the S-wave radiation patterns are largest for takeoff angles near the fault plane, these directions dominate the S-wave average over the focal sphere. We note that the  $\omega^{-1.5}$  falloff is not associated with the dynamic or stochastic aspects of the rupture model, but

is a consequence only of the fast rupture velocities of the models. Figure 8 demonstrates how strongly the intermediate trend dominates the rms S-wave acceleration spectra.

The rms P-wave spectra are more variable than the rms S-wave spectra. The spectra of the weak fault models are approximately flat above the corner frequency, although there is some variability. Because the rms P-wave spectrum of the uniform model has the strongest amplitude at the corner frequency, we interpret the variability as the result of the rupture complexity of the stochastic models. The rms spectra of the strong fault models have the same spectral characteristics as the weak fault models, but have more noise in the 6 to 20 Hz frequency band. The increased noise probably results from the slower rupture velocities; in modeling a continuous process using a discrete grid, the low frequency limit of the grid noise depends on the grid discretization and radiative rupture velocity as  $f_n \propto \langle v \rangle / dx$ .

The moments and long period levels of the strong fault models are slightly less than those of the weak fault models. This difference occurs because the computational duration of 0.64 s is insufficient for the

## 106 CONFINED RUPTURES

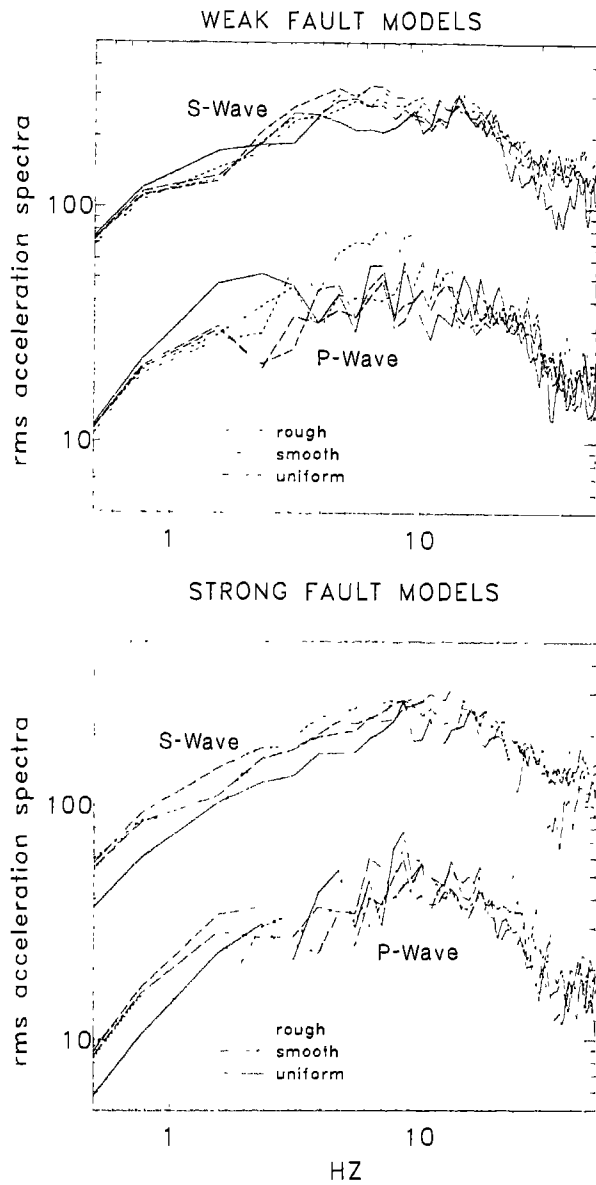


Fig. 8. Average P and S-wave spectra radiated by the 11 models, plotted as a function of frequency. The models are differentiated as weak and strong fault models. The line breaks correspond roughly with the complexity of the initial stress; the spectra of the uniform models are drawn with solid lines. Note the consistency of the S-wave spectra, all of which exhibit an extended intermediate slope. The relative scaling of the P and S-wave spectra is exact.

strong fault models to entirely rupture the area within the rupture perimeter. As a result of its long nucleation, during which time there is little energy radiated, the spectra of the uniform model with  $\langle S \rangle = 1.5$  has the highest corner frequency. The rupture finally accelerates at  $\approx 0.32$  s; at 0.64 s, the rupture area is only 70 % of the area enclosed by the rupture perimeter.

The major effect of "freezing" the rupture models at 0.64 s is to inhibit the stress overshoot (i.e., the ratio of the static stress drop to the dynamic stress drop). This effect can be estimated by comparing the static stress drops of the rupture models, calculated from the model moments and fault areas. Because the rms dynamic stress drops are fixed as  $\langle \Delta\sigma \rangle = 1.0$ , the static stress drops compiled in Table 1 equal the stress overshoots. The static stress drops of the models vary from  $1.09\langle \Delta\sigma \rangle$  to  $1.26\langle \Delta\sigma \rangle$ ; the models with slower rupture velocities have lower static stress drops.

*Radiated Energy*

To measure the total seismic energy radiated by these rupture models, the energy flux in the P and S waveforms is calculated by integrating the velocity power spectra over frequency at each of the 52 sample points. Before integrating, the velocity spectra are filtered similarly to the rms acceleration spectra plotted in Figure 8. The energy flux is then averaged over the focal sphere, and the average energy flux converted to radiated energy. In contrast to the moments of the rupture models, the radiated energies are approximately unaffected by the freezing of the fault slip at 0.64 s. The ruptures of the strong fault models appear to be confined within smaller, somewhat irregular, rupture perimeters. The instantaneous healing is coherent only for the takeoff angles normal to the fault plane ( $\theta = 0^\circ$ ), and these angles are not

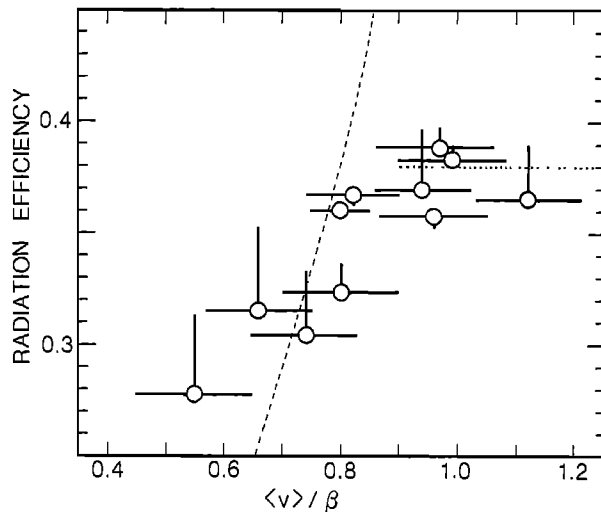


Fig. 9. Radiation efficiency plotted as a function of the radiative rupture velocity of the models. The vertical lines show the corrections of the radiation efficiencies for the variable stress overshoot of the models (see Table 1). The error bars for the radiative rupture velocity give the standard error of the estimate. The dashed line is the result derived by Sato and Hirasawa [1973] for the radiation efficiency of their circular kinematic models. The dotted line is the limit for the radiation efficiency of a dynamic model with a stress overshoot of 1.24, calculated following Madariaga [1976].

TABLE 1. Parameters of the Rupture Models

Model	Complexity	Overshoot	$\bar{v}/\beta$ $\langle v \rangle / \beta$	Partition of Energy	S-Wave	Radiation Efficiency	
						Total	Corrected
10	0.	1.24	$0.75 \pm 0.17$ $0.80 \pm 0.05$	12.3	.334 .027	.361	.361
11A	0.67	1.21	$0.88 \pm 0.38$ $0.94 \pm 0.08$	22.5	.381 .017	.398	.389
11B	0.56	1.26	$0.77 \pm 0.28$ $0.82 \pm 0.08$	21.2	.347 .016	.364	.368
12A	0.82	1.15	$0.85 \pm 0.61$ $1.12 \pm 0.09$	14.4	.364 .025	.390	.364
12B	0.83	1.26	$0.86 \pm 0.48$ $0.96 \pm 0.09$	17.9	.335 .019	.354	.358
12C	1.05	1.23	$0.88 \pm 0.40$ $0.97 \pm 0.09$	18.4	.367 .020	.387	.382
20B	0.	1.09	$0.47 \pm 0.18$ $0.55 \pm 0.10$	11.5	.287 .025	.314	.277
21A	0.51	1.14	$0.68 \pm 0.36$ $0.74 \pm 0.09$	16.3	.314 .019	.333	.305
21B	0.62	1.11	$0.64 \pm 0.31$ $0.66 \pm 0.09$	16.2	.334 .021	.354	.316
22A	1.24	1.18	$0.76 \pm 0.56$ $0.99 \pm 0.09$	22.4	.372 .017	.389	.370
22B	0.90	1.20	$0.62 \pm 0.42$ $0.80 \pm 0.10$	20.7	.321 .016	.336	.324

sampled in calculating the rms acceleration spectra and the radiated energy.

To compare the energies radiated by these rupture models, we calculate the radiation efficiencies, defined as

$$\varepsilon_C = \frac{\mu E_s^C}{\langle \Delta \sigma \rangle M_0} \quad (6)$$

where  $E_s^C$  is the energy radiated in wave-type  $C = P$  or  $S$ . The moments used to estimate the efficiencies in (6) have been corrected for the difference in overshoot among the models; the models are assumed to have the same stress overshoot as Model 10. The correction assumes that if the computational duration were longer, but the rupture area fixed at 0.64 s, the moments would increase without affecting the radiated energy. The vertical lines drawn from the hexagons in Figure 9 delineate the corrections.

The total radiated seismic energy and radiation efficiency are the sums of the seismic energy and radiation efficiency of each wave-type:

$$E_s = E_s^P + E_s^S \quad (7a)$$

$$\varepsilon = \varepsilon_P + \varepsilon_S \quad (7b)$$

In Figure 9, we have plotted the total radiation

efficiencies against the radiative rupture velocity, defined in (5) and plotted in Figure 5. As functions of rupture velocity, the rupture models fall into three groups: slow ( $\langle v \rangle < 0.70\beta$ ), mostly subsonic ( $0.70\beta < \langle v \rangle < 0.85\beta$ ), and partially transonic ( $0.85\beta < \langle v \rangle$ ). The dashed line drawn in the plot gives the radiation efficiency determined by Sato and Hirasawa [1973] for their kinematic rupture model. The results from the stochastic models increase more gradually than the kinematic curve. The radiation efficiency for the 3-D dynamic models does not increase for rupture velocities higher than the Rayleigh wave velocity; at these rupture velocities, the ruptures are already radiating all of the available seismic energy. In fact, the radiation efficiencies of the partially transonic models ( $0.85\beta < \langle v \rangle$ ) are at the theoretical limit for dynamic models. Using equation (36) of Madariaga (1976) to calculate an upper bound for the radiation efficiency gives  $\varepsilon \leq 0.38$  for dynamic models with a stress overshoot of 1.24; this bound is plotted as a dotted line. The efficiencies of the models with slow rupture velocities ( $\langle v \rangle < 0.70\beta$ ) are somewhat larger than predicted from the kinematic models, perhaps because of the increased high-frequency noise in the slower models.

By dividing the S-wave efficiency by the P-wave efficiency, we can directly calculate the partition of energy

## 108 CONFINED RUPTURES

for each of the models. The results are compiled in Table 1; the partition of energy does not appear to depend on the strength of fault; the uniform models have the smallest estimates. Taking the logarithmic average over the model estimates gives  $E_s^S/E_s^P = 17.2 \pm 4.3$ . We note that this estimate is conditioned by the low-pass filtering used in the analysis: without the low-pass filters, the estimate for the partition of energy is  $20.7 \pm 3.9$ . In an analysis of the Monticello earthquakes, Boatwright and Fletcher [1984], determined a range for the partition of energy from 14.4 to 27.3; recently, Boatwright [1985] obtained  $E_s^S/E_s^P = 14.7 \pm 2.2$  in an analysis of 26 aftershocks of the 1983 Borah Peak, Idaho, earthquake.

## Conclusions

The dynamic ruptures obtained using the 3-D boundary integral technique of Das [1981] and Quin [1986] and stochastic initial conditions exhibit complex rupture growth. The rupture fronts are irregularly shaped, the rupture growth is unsteady and asymmetric, and for the rough models, the rupture area may become slightly disconnected. The average rupture velocity depends on the normalized strength; for  $\langle S \rangle = 1.0$  and 1.5,  $\bar{v} = 0.85\beta$  and  $0.70\beta$ , respectively. The weak fault models exhibit a significant component of transonic rupture growth. The stochastic models have more transonic rupture growth than the uniform models.

To first order, the rms acceleration spectra and radiation efficiencies of these dynamic models do not depend on the complexity of the initial conditions. In particular, the rms S-wave acceleration spectra are nearly identical for all the models. The rms P-wave acceleration spectra are essentially that above the corner frequency, indicating that the assumed spectral fall off of the initial stress and strength (i.e.,  $|\tau(k)| \propto k^{1/2}$ ) produces sufficient rupture complexity to match most observations of body-wave spectral shape [Brune, 1970; Hanks and McGuire, 1981]. The average partition of energy is  $E_s^S/E_s^P = 17.2 \pm 4.3$ ; the partition of energy is lowest for the uniform models. The radiation efficiencies of the stochastic models with partially transonic rupture velocities are the largest:  $\epsilon = 0.37 \pm 0.02$ ; the radiation efficiencies of the models with mostly subsonic rupture velocities decrease with decreasing rupture velocity.

The ruptures analyzed in this paper are confined within an unbreakable perimeter, or rupture barrier. The rupture perimeter strongly conditions the seismic radiation from the uniform models; the stopping phases radiated when the rupture front stops at the perimeter are the strongest phases in the acceleration waveforms. For the stochastic models, the effect of the rupture perimeter is less marked, partly because the rupture fronts reach the perimeter as salients and embayments. Although its relative smoothness and "infinite" strength are unrealistic, the rupture perimeter allows the rupture models to be compared with earlier kinematic and dynamic models. More realistic initial conditions would replace the perimeter with a region of gradually decreasing stress drop, or

a set of irregular rupture barriers. The longer rupture durations of such partially confined models require a significant improvement in the computational method.

**Acknowledgments.** We thank J. Andrews for the help, insight, and many discussions which the authors required of him, as well as his critical review of the article. We are also indebted to K. Jacob and P. Spudich for their critical, but supportive, reviews. B. Gessner reformatted the manuscript for the camera-ready copy. H.Q. was partially supported by NSF grant EAR84-20318 and the U.S. Geological Survey.

## References

- Aki, K., and P.G. Richards, *Quantitative Seismology: Theory and Methods*, 577 pages, W. H. Freeman and Company, San Francisco, Calif., 1980.
- Andrews, D.J., A stochastic fault model 1. Static case, *J. Geophys. Res.*, **85**, 3867-3877, 1980.
- Andrews, D.J., A stochastic fault model 2. Time-Dependent case, *J. Geophys. Res.*, **86**, 10821-10834, 1981.
- Archuleta, R.J., Experimental and numerical three-dimensional simulation of strike-slip earthquakes, Ph.D. Dissertation, 128 pages, Univ. of Calif., San Diego, 1976.
- Boatwright, J., A spectral theory for circular seismic sources; simple estimates of source dimension, dynamic stress drop, and radiated energy, *Bull. Seismol. Soc. Am.*, **70**, 1-27, 1980.
- Boatwright, J., A dynamic model for far-field acceleration, *Bull. Seismol. Soc. Am.*, **72**, 1049-1068, 1982.
- Boatwright, J., Characteristics of the aftershock sequence of the Borah Peak, Idaho, earthquake determined from digital recordings of the events, *Bull. Seismol. Soc. Am.*, **75**, 1265-1284, 1985.
- Boatwright, J., and J.B. Fletcher, The partition of energy between P and S waves, *Bull. Seismol. Soc. Am.*, **74**, 361-376, 1984.
- Boore, D.M., and W.B. Joyner, The influence of rupture incoherence on seismic directivity, *Bull. Seismol. Soc. Am.*, **68**, 283-300, 1978.
- Brune, J.N., Tectonic stress and the spectra of seismic shear waves from earthquakes *J. Geophys. Res.*, **75**, 4997-5009, 1970.
- Das, S., A numerical method for determination of source time functions for general three-dimensional rupture propagation, *Geophys. J. R. Astron. Soc.*, **62**, 591-604, 1980.
- Das, S., Three-dimensional spontaneous rupture propagation and implications for the earthquake source mechanism, *Geophys. J. R. Astron. Soc.*, **67**, 375-393, 1981.
- Das, S., and K. Aki, A numerical study of two-dimensional spontaneous rupture propagation, *Geophys. J. R. Astron. Soc.*, **50**, 643-668, 1977a.
- Das, S., and K. Aki, Fault plane with barriers: A versatile

- earthquake model, *J. Geophys. Res.*, **82**, 5658–5670, 1977b.
- Hanks, T.C., and D.M. Boore, Moment-magnitude relations in theory and practice, *J. Geophys. Res.*, **89**, 6227–6235, 1984.
- Hanks, T.C., and R.K. McGuire, The character of high-frequency strong ground motion, *Bull. Seismol. Soc. Am.*, **71**, 2071–2095, 1981.
- Madariaga, R., Dynamics of an expanding circular fault, *Bull. Seismol. Soc. Am.*, **66**, 639–666, 1976.
- Mikumo, T., and T. Miyatake, Dynamical rupture process on a three-dimensional fault with non-uniform frictions and near-field seismic waves, *Geophys. J. R. Astron. Soc.*, **54**, 417–438, 1978.
- Mikumo, T., and T. Miyatake, Earthquake sequences on a frictional fault model with non-uniform strengths and relaxation time, *Geophys. J. R. Astron. Soc.*, **59**, 499–522, 1979.
- Quin, H., A hybrid solution of the boundary integral for dynamic rupture on a planar fault, *Bull. Seismol. Soc. Am.*, **76**, in press, 1986.
- Sato, T., and T. Hirasawa, Body wave spectra from propagating shear cracks, *J. Phys. Earth*, **21**, 415–431, 1973.
- Savage, J.C., Relation between P and S-wave corner frequency in the seismic spectrum, *Bull. Seismol. Soc. Am.*, **64**, 1621–1627, 1974.
- Tse, S.T., and J.R. Rice, Crustal earthquake instability in relation to the depth variation of frictional slip properties, *J. Geophys. Res.*, **91**, in press, 1986.
- Zuercher, H., and S.W. Smith, Spontaneous rupture simulation: variable fracture energy absorption, random fractal strength, *Eos Trans. Amer. Geophys. Un.*, **65**, 1113, 1984.

EFFECT OF TRANSVERSE ISOTROPY ON STRONG GROUND  
MOTION DUE TO STRIKE SLIP FAULTING

J. D. Achenbach and M.-K. Kuo<sup>1</sup>

Department of Civil Engineering, Northwestern University, Evanston, Illinois 60201

**Abstract.** The effect of transverse isotropy on intense ground motions generated by starting and stopping phases of a strike-slip faulting event has been investigated, for the case that the axis of symmetry of the transverse isotropy is normal to the earth's surface but the orientation of the fault plane is arbitrary. It is shown that motion in antiplane shear can be deduced from the corresponding motion in an isotropic solid by a transformation of relevant coordinates and parameters. Based on this result the paper describes wave-front fields along rays emitted by the rupture front due to starting and stopping events. For a selection of fault-plane angles, rupture-front speeds and durations of the faulting event, the particle velocities at the earth surface have been computed for different values of the ratio of the shear moduli  $\mu_2/\mu_1$ , where  $\mu_2/\mu_1 = 1$  corresponds to an isotropic earth. For the cases considered here the broad characteristics of the ground motion are not significantly affected by transverse isotropy, but the magnitudes of the signals may be significantly different.

#### Introduction

Anisotropy in the mechanical behavior of solids is a rather common phenomenon. In the earth it may occur for a variety of reasons including lithological alignments, stress induced effects, periodic sequences of fine layers, aligned cracks, and other multi-phase configurations. Generally, the effective anisotropy of the earth is on a scale smaller than wavelengths of seismic waves. In recent years a number of new developments for wave motion in anisotropic media have been published. For a recent review we refer to Crampin [1981].

In this paper we are interested in intense ground motions that are generated by starting and stopping phases of a faulting event. For

isotropic solids Madariaga [1977] and Achenbach and Harris [1978] have shown that the fields radiated from starting and stopping events can be approximated by using results of dynamic crack propagation in combination with elements of ray theory, see also Yamashita [1983]. Harris and Achenbach [1981] have further analyzed the reflection of these emitted waves from a free surface to estimate the ground motion in the near field. A related approach has been pursued by Spudich and Frazier [1984].

A transversely isotropic solid displays the simplest kind of anisotropy. It has an axis of symmetry, and its stress-strain relations contain five elastic constants. Stresses due to antiplane shear deformations normal to a plane containing the axis of symmetry are, however, described by two constants (two shear moduli rather than one as for an isotropic solid). Hence, wave fronts of transverse waves polarized normal to such a plane are ellipses rather than circles. The question of elliptical anisotropy has been discussed in some detail by Helbig [1983].

In this paper we consider the case that the edge of the rupture front is normal to the axis of symmetry of the transversely isotropic solid. The fault plane makes an arbitrary angle with the earth's surface. The results of the paper are based on the observation that anti-plane shear signals generated by crack propagation in a transversely isotropic solid can be deduced from corresponding solutions for an isotropic solid by a transformation of relevant coordinates and parameters. Based on this observation the paper describes the fields along rays emitted by the rupture front of a semi-infinite crack in an unbounded solid as the front propagates in Mode III. For a propagating rupture front in a half-space the near field ground motion can be computed by analyzing the direct reflections of the ray fields. The influence of the reflected wave field on the rupturing process has been neglected in this paper.

For a selection of fault-plane angles, rupture-front speeds and durations of the faulting event, the particle velocities at the free surface have been computed for different values of the ratio

<sup>1</sup>Now at Institute of Applied Mechanics,  
National Taiwan University, Taipei, Taiwan 107,  
ROC

## 112 TRANSVERSE ISOTROPY EFFECT

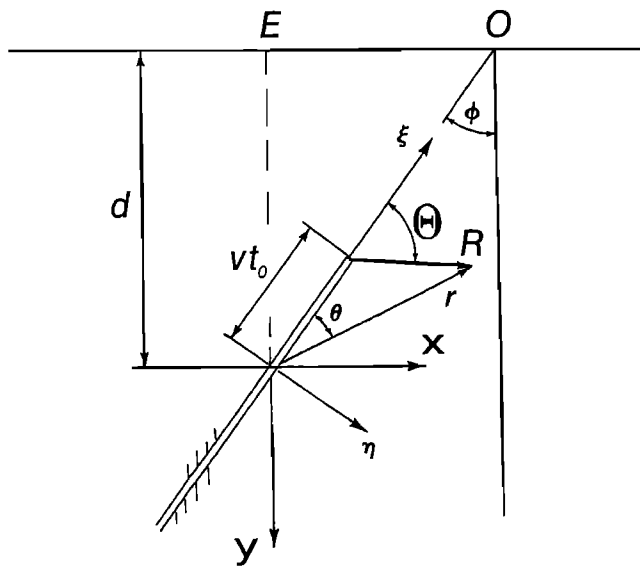


Fig. 1. Crack in a transversely isotropic half-plane, where the y-axis is the axis of symmetry. The configuration and the coordinate systems after the transformations of section 3 follow by replacing all quantities by their barred equivalents, i.e., replace  $x$  by  $\bar{x}$ , etc.

of the shear moduli  $\mu_2/\mu_1$ , where  $\mu_2/\mu_1 = 1$  corresponds to an isotropic earth. In a 2-D setting these results are exact at the wave-fronts, and they should be close approximations for short pulses due to faulting events of short duration. Slight curvature of the rupture front can be accounted for by a correction term. For the cases considered here the broad characteristics of the ground motion are not significantly affected by transverse isotropy, but the magnitudes of the signals may be significantly different.

## Problem Statement

In a stationary system of Cartesian coordinates  $(x, y)$ , where the y-axis is the axis of symmetry of the transversely isotropic solid, anti-plane wave motions are governed by

$$\mu_1 \frac{\partial^2 w}{\partial x^2} + \mu_2 \frac{\partial^2 w}{\partial y^2} = \rho \ddot{w}. \quad (1)$$

Here  $w(x, y, t)$  is the out-of-plane displacement,  $(\cdot) = \partial/\partial t$ ,  $\rho$  is the mass density, and  $\mu_i$  ( $i=1, 2$ ) are elastic shear moduli. The relevant shear stresses are

$$\tau_{xz} = \mu_1 \frac{\partial w}{\partial x}, \quad \tau_{yz} = \mu_2 \frac{\partial w}{\partial y} \quad (2)$$

It can easily be shown that the stress  $\tau_{nz}$  on a

plane making an angle  $\phi$  with the y-axis may be written as

$$\tau_{nz} = C_{45} \frac{\partial w}{\partial \xi} + C_{44} \frac{\partial w}{\partial \eta}, \quad (3)$$

where  $\xi, \eta$  are the rotated coordinates shown in Figure 1. The elastic moduli  $C_{ij}$  ( $i, j = 4, 5$ ) are related to  $\mu_1, \mu_2$ , and the angle  $\phi$  by

$$C_{44} = \mu_1 \cos^2 \phi + \mu_2 \sin^2 \phi, \quad (4a)$$

$$C_{45} = (\mu_1 - \mu_2) \sin \phi \cos \phi. \quad (4b)$$

At time  $t = 0$  the semi-infinite crack shown in Figure 1 starts to propagate at a subsonic crack-tip speed  $v$ . Crack propagation stops at time  $t = t_0$ . Just prior to crack propagation,  $t < 0$ , the anti-plane shear stress near the crack tip in the plane  $n = 0$  is

$$n = 0, \quad \xi < 0: \quad \tau_{nz} = \tau_f^s \quad (5a)$$

$$n = 0, \quad \xi > 0:$$

$$\tau_{nz} = (2\pi\xi)^{-\frac{1}{2}} K_{III}^c + \tau_f^s + O(\xi^{\frac{1}{2}}), \quad (5b)$$

where  $\tau_f^s$ , which is assumed constant, is the maximum static friction between the crack faces, and  $K_{III}^c$  is the critical value of the Mode-III stress intensity factor (the static fracture toughness) along the fault plane. When the crack tip propagates, and the crack faces slip the stresses drop to the kinetic friction  $\tau_f^k$ , along the slip region,  $-ct < \xi < vt$ , where  $c$  is the signal velocity of horizontally polarized transverse waves along the crack plane. Near the crack tip, the shear stresses in the plane  $n = 0$  then are

$$n = 0, \quad -ct < \xi < vt: \quad \tau_{nz} = \tau_f^k \quad (6a)$$

$$n = 0, \quad \xi > vt:$$

$$\tau_{nz} = (2\pi)^{-\frac{1}{2}} (\xi - vt)^{-\frac{1}{2}} K_{III}^d + \tau_f^k + O((\xi - vt)^{\frac{1}{2}}) \quad (6b)$$

The term  $\tau_f^k$  appears in (6b), because the non-singular part of the shear stress is continuous at the crack tip. When the crack tip stops at time  $t = t_0$ , the following stresses arise immediately along  $n = 0$  near the stopped crack tip,  $\xi = vt_0$ :

$$-ct < \xi < vt_0: \quad \tau_{nz} = \tau_f^k \quad (7a)$$

$$\xi > vt_0:$$

$$\tau_{nz} = (2\pi)^{-\frac{1}{2}} (\xi - vt_0)^{-\frac{1}{2}} K_{III}^{*} + \tau_f^k + O[(\xi - vt_0)^{\frac{1}{2}}] \quad (7b)$$

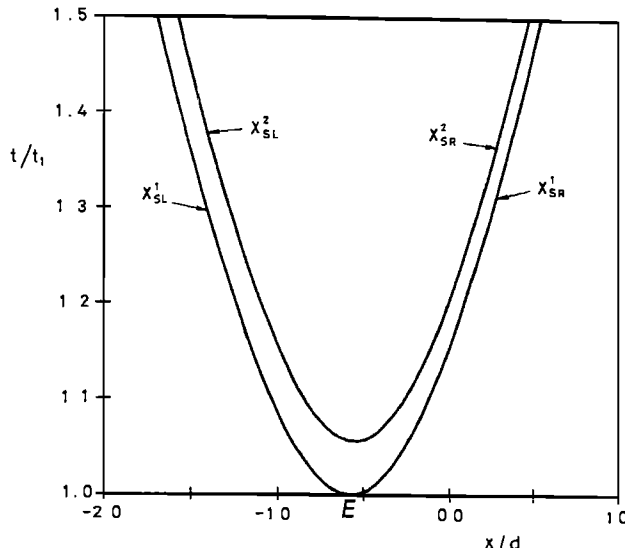


Fig. 2. Wave-front traces along the earth's surface for  $\phi = 30^\circ$ ,  $v/c = 0.5$ , and  $\mu_2/\mu_1 = 1$ .

In (6b) and (7b),  $K_{III}^d$  and  $K_{III}^*$  are Mode-III elastodynamic stress intensity factors for a propagating and a stationary crack, respectively, which have to be obtained analytically. Equation (7a) implies the assumption that the crack faces near the arrested rupture front keep moving in the same direction as before. The condition of zero tractions on the surface  $y = -d$  is

$$y = -d, -\infty < x < \infty : \tau_{yz} = 0 \quad (8)$$

The radiated fields due to the starting and stopping events can be analyzed by considering two separate superposition problems. The superposition problem for the starting event concerns a traction-free semi-infinite crack in an initially quiescent transversely isotropic half plane. At time  $t = 0$  the crack faces are subjected to appropriate crack-face tractions, and at the same time the crack starts to propagate. For the superposition problem the appropriate conditions on the crack faces and near the crack tip are:

$$\eta = 0, -ct < \xi < 0 : \tau_{\eta z} = -\sigma_o \quad (9a)$$

$$\eta = 0, 0 < \xi < vt :$$

$$\tau_{\eta z} = -(2\pi\xi)^{-\frac{1}{2}} K_{III}^c - \sigma_o + O(\xi^{\frac{1}{2}}), \quad (9b)$$

where

$$\sigma_o = \tau_f^s - \tau_f^k \quad (10)$$

is the difference between the maximum static

friction and the kinetic friction. The superposition problem for the stopping event concerns a stress-free transversely isotropic half plane containing a crack moving with constant crack-tip speed  $v$ . At time  $t = t_0$ , the crack tip passes through  $\xi = vt_0$ , and at the same time the crack faces defined by  $vt_0 < \xi < vt$  are subjected to crack-faces tractions. For the superposition problem the conditions on the crack faces are,

$$\eta = 0, \xi < vt_0 : \tau_{\eta z} = 0 \quad (11a)$$

$$\eta = 0, \xi > vt_0 :$$

$$\tau_{\eta z} = (2\pi)^{-\frac{1}{2}} (\xi - vt_0)^{-\frac{1}{2}} K_{III}^* + O[(\xi - vt_0)^{\frac{1}{2}}], \quad (11b)$$

where  $K_{III}^*$  can be related to  $K_{III}^d$ , and the latter has to be solved from the problem defined by (9a,9b).

Since the superposition problems only provide the correct adjustments for the fields right near the rupture front, they yield acceptable radiated fields only for short times after starting or stopping.

#### Coordinate Transformation

The transformation

$$\bar{x} = (\mu_2/C_{44})^{\frac{1}{2}} x, \bar{y} = (\mu_1/C_{44})^{\frac{1}{2}} y \quad (12)$$

reduces (7a,7b) to the standard wave equation:

$$\frac{\partial^2 w}{\partial \bar{x}^2} + \frac{\partial^2 w}{\partial \bar{y}^2} = \frac{1}{c_T^2} \ddot{w}, \quad \bar{c}_T^2 = \frac{\bar{\mu}}{\rho}, \quad (13)$$

where

$$\bar{\mu} = \mu_1 \mu_2 / C_{44} \quad (14)$$

Equation (13) suggests that it is possible to deduce anti-plane shear solutions for a transversely isotropic solid from a corresponding solution for an isotropic solid by a transformation of relevant parameters.

Under the transformation (12), straight lines in the  $xy$ -plane which make an angle  $\psi$  with the  $y$ -axis, remain straight lines in the  $xy$ -plane, but under an angle  $\bar{\psi}$  with the  $y$ -axis, where

$$\bar{\psi} = \tan^{-1}[(\mu_2/\mu_1)^{\frac{1}{2}} \tan \psi] \quad (15)$$

the crack geometry in the barred coordinate system is equivalent to Figure 1. Equation (15) implies that two orthogonal lines in the  $xy$ -plane will in general not remain orthogonal in the  $xy$ -plane. It should be noted that the  $\bar{\eta}$ -axis in Figure 1 is defined to be normal to the crack line in the  $xy$ -plane, and hence it is not the

## 114 TRANSVERSE ISOTROPY EFFECT

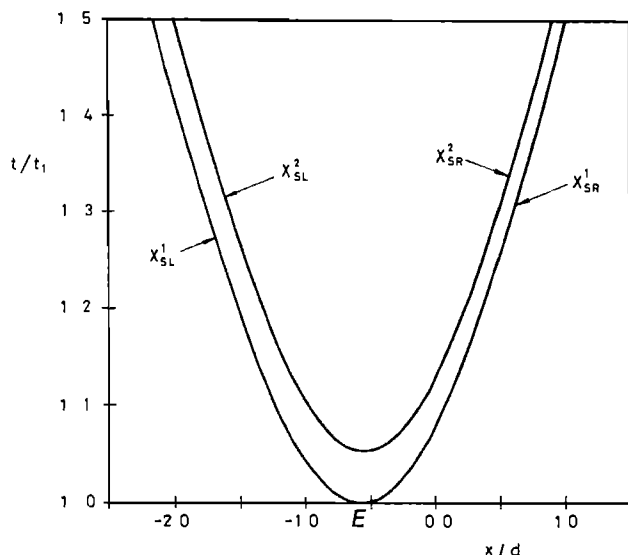


Fig. 3. Wave-front traces along the earth's free surface for  $\phi = 30^\circ$ ,  $v/c = 0.5$ , and  $\mu_2/\mu_1 = 0.5$ .

mapping of the  $\eta$ -axis from the  $xy$ -plane. The relation between  $(\bar{\xi}, \bar{\eta})$  coordinates and  $(\xi, \eta)$  coordinates follows from the geometry and (12) as

$$\bar{\xi} = \xi + \beta\eta, \quad \bar{\eta} = \gamma\eta, \quad (16)$$

where

$$\beta = -C_{45}/C_{44}, \quad \gamma = (\mu_1\mu_2)^{1/2}/C_{44} \quad (17)$$

Equation (16) and the chain rule of differentia-

tion imply:

$$\frac{\partial}{\partial \xi} = \frac{\partial}{\partial \bar{\xi}}, \quad \frac{\partial}{\partial \eta} = \beta \frac{\partial}{\partial \bar{\xi}} + \gamma \frac{\partial}{\partial \bar{\eta}} \quad (18)$$

It is then easily verified from (3), (12) and (17)-(18) that the relevant shear tractions in the physical coordinates are related to displacement derivatives in the transformed coordinates by

$$\tau_{yz} = \left(\frac{C_{44}}{\mu_1}\right)^{1/2} \bar{\mu} \frac{\partial w}{\partial \bar{y}}, \quad \tau_{\eta z} = \frac{1}{\gamma} \bar{\mu} \frac{\partial w}{\partial \bar{\eta}} \quad (19)$$

The corresponding transformed boundary condition at the surface of the half-space is

$$\bar{y} = -(\mu_1/C_{44})^{1/2}d, \quad -\infty < \bar{x} < \infty: \quad \bar{\mu} \frac{\partial w}{\partial \bar{y}} = 0 \quad (20)$$

For the starting event we have near the crack tip

$$\bar{\eta} = 0, \quad -ct < \bar{\xi} < 0: \quad \bar{\mu} \frac{\partial w}{\partial \bar{\eta}} = -\gamma\sigma_o \quad (21)$$

$$\bar{\eta} = 0, \quad 0 < \bar{\xi} < vt:$$

$$\bar{\mu} \frac{\partial w}{\partial \bar{\eta}} = -\gamma(2\pi\bar{\xi})^{-1/2} K_{III}^c - \gamma\sigma_o \quad (22)$$

The analogous equations for the stopping event are

$$\bar{\eta} = 0, \quad \bar{\xi} < vt_o: \quad \bar{\mu} \frac{\partial w}{\partial \bar{\eta}} = 0 \quad (23)$$

$$\bar{\eta} = 0, \quad \bar{\xi} > vt_o:$$

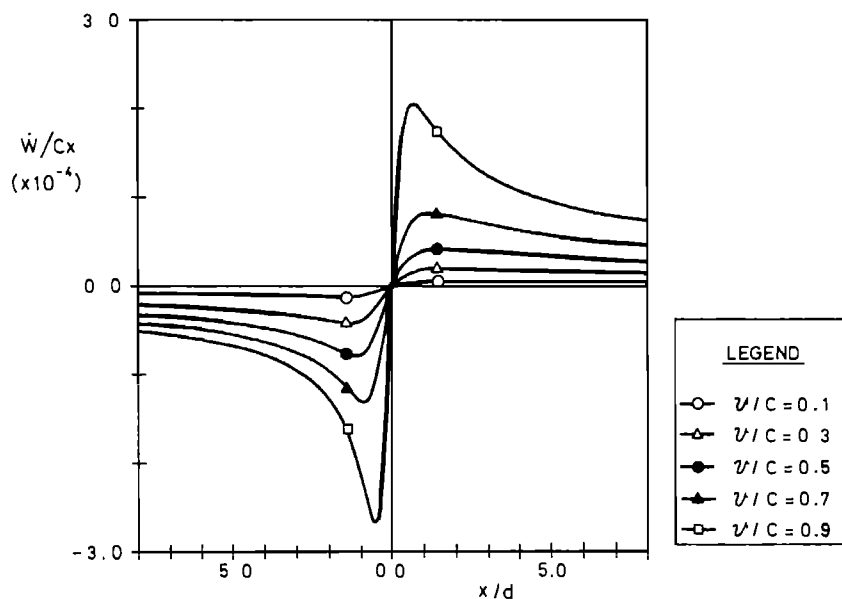


Fig. 4. Jump of the particle velocity at the wave-front on the free surface due to the starting event;  $\phi = 30^\circ$ ,  $\mu_2 = \mu_1$ , and various values of  $v/c$ .

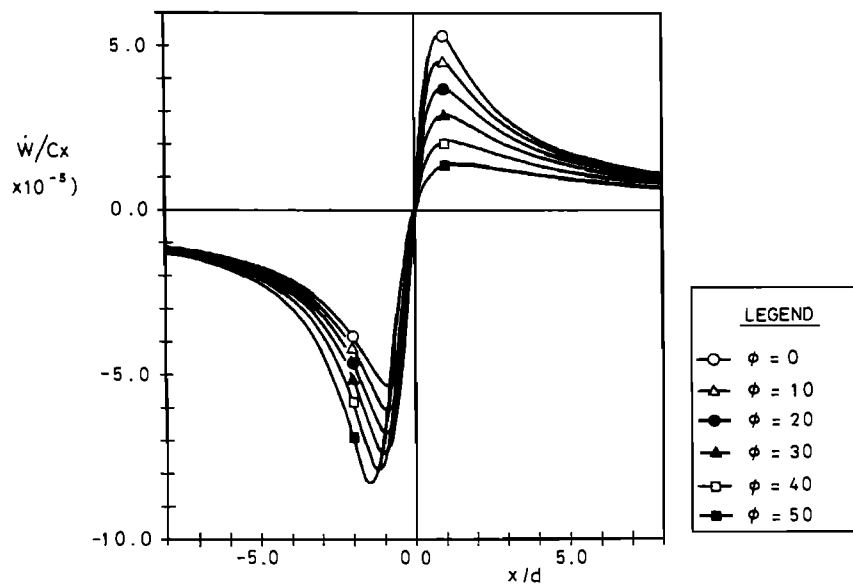


Fig. 5. Jump of the particle velocity at the wave-front on the free surface due to the starting event;  $\mu_2 = \mu_1$ ,  $v/c = 0.5$ , and various values of  $\phi$ .

$$\mu \frac{\partial w}{\partial \eta} = \gamma (2\pi)^{-\frac{1}{2}} (\bar{\xi} - vt_o)^{-\frac{1}{2}} K_{III}^* \quad (24)$$

The formulation given by (13) and (20)-(24) is formally identical to the one for an isotropic material. Hence, if we can solve for the isotropic solid, the solution for the transversely isotropic material can be obtained by appropriate substitutions for the coordinates  $\xi$  and  $\eta$ .

#### Radiated Fields

For an unbounded solid, the problem defined by (13) and (21)-(22) can be solved rigorously. One convenient way is to first consider two kinds of  $\delta$ -function crack-face loading. The first of these is of the form

$$\bar{n} = 0, \quad -\infty < \bar{\xi} < vt:$$

$$\mu \frac{\partial w}{\partial \eta} = \delta(\bar{\xi}/t + u) H(t) H(-\bar{\xi}) \quad (25)$$

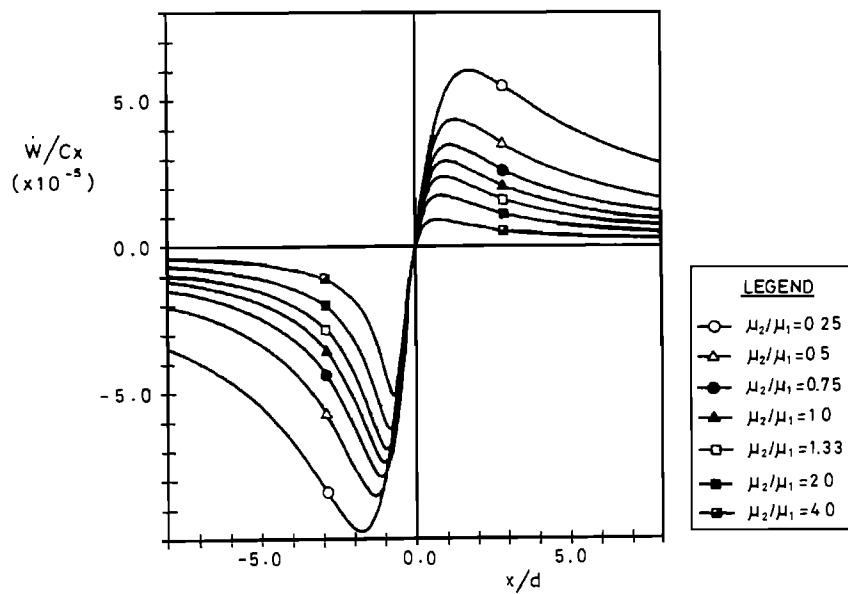


Fig. 6. Jump of the particle velocity at the wave-front on the free surface due to the starting event;  $\phi = 30^\circ$ ,  $v/c = 0.5$ , and various values of  $\mu_2/\mu_1$ .

## 116 TRANSVERSE ISOTROPY EFFECT

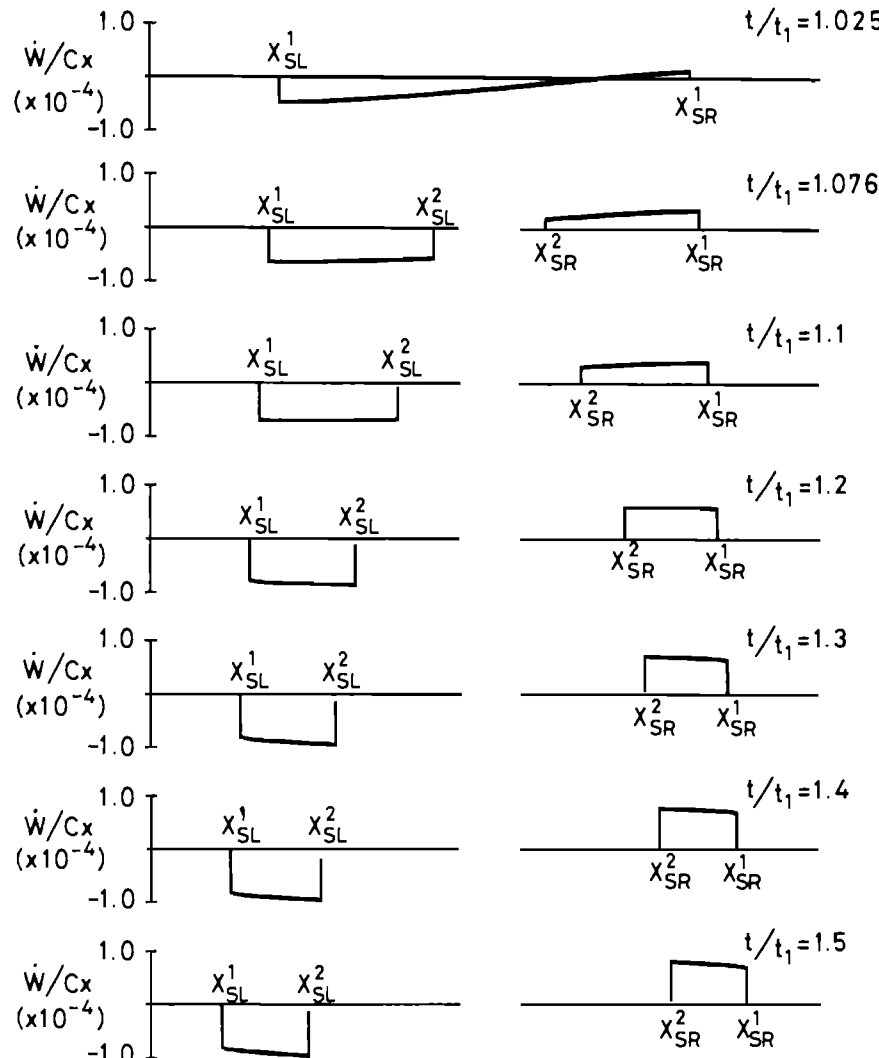


Fig. 7. Pulses on free surface due to a starting and stopping event,  $v/c = 0.5$ ,  $\phi = 10^\circ$ , and  $\mu_2/\mu_1 = 0.5$ .

The particle velocity for this problem is denoted by  $\dot{w}_a^G(\xi, n, t; u)$  or  $\dot{w}_a^G(r, \theta, t; u)$ . This solution applies to the problem of a solid containing a semi-infinite crack. The crack starts to propagate at time  $t = 0$ . At the same time the crack faces are subjected to delta-function loading, which propagates with constant velocity  $u$  in the negative  $\xi$ -direction, where  $u \leq c_T$ . In the second problem we consider crack-face loading of the form

$$\bar{n} = 0, -\infty < \bar{\xi} < vt:$$

$$\bar{u} \frac{\partial w}{\partial \bar{n}} = \delta(\bar{\xi} - \bar{\xi}_d) H(t - \bar{\xi}_d/v) H(vt - \bar{\xi}) \quad (26)$$

The solution for the particle velocity to this problem is denoted by  $\dot{w}_b^G(\xi, n, t; \bar{\xi}_d)$  or  $\dot{w}_b^G(r, \theta, t; \bar{\xi}_d)$ . This solution applies to the same

configuration as for  $\dot{w}_a^G$ , except that the crack faces are subjected to a time-independent delta-function loading which appears at time  $t = \bar{\xi}_d/v$  at position  $\xi = \bar{\xi}_d$ . Now, if the crack faces are subjected to

$$\bar{n} = 0, -\infty < \bar{\xi} < vt: \bar{u} \frac{\partial w}{\partial \bar{n}} = g(\bar{\xi}/t) H(\bar{\xi}/t + \bar{c}_T) H(-\bar{\xi}) + f(\bar{\xi}) H(\bar{\xi}) H(vt - \bar{\xi}), \quad (27)$$

where  $g(\bar{\xi}/t)$  depends on  $\bar{\xi}/t$  rather than  $\bar{\xi}$  and  $t$  separately, and  $f(\bar{\xi})$  depends on  $\bar{\xi}$  only, superposition can be used to write

$$\begin{aligned} \dot{w}(\bar{r}, \bar{\theta}, t) = & \int_0^{c_T} g(-u) \dot{w}_a^G(\bar{r}, \bar{\theta}, t; u) du \\ & + \int_0^{vt} f(\bar{\xi}_d) \dot{w}_b^G(\bar{r}, \bar{\theta}, t; \bar{\xi}_d) d\bar{\xi}_d \end{aligned} \quad (28)$$

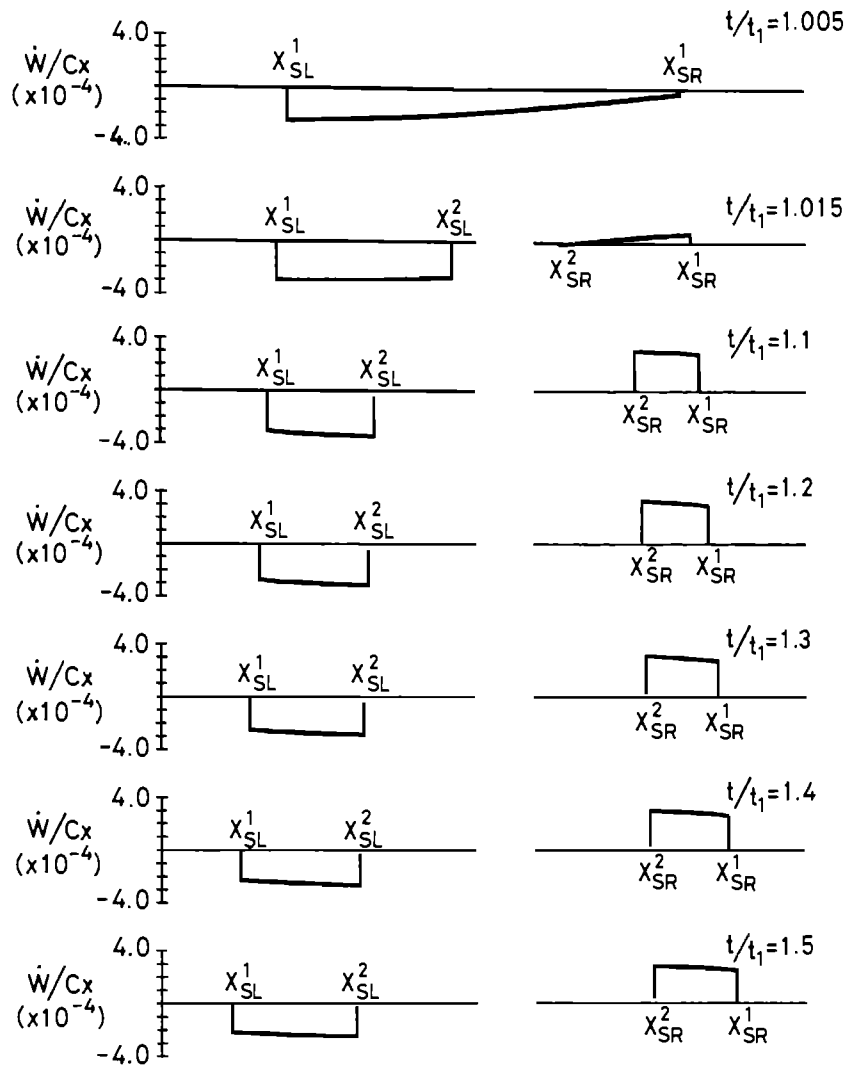


Fig. 8. Pulses on free surface due to a starting and stopping event,  $v/c = 0.9$ ,  $\phi = 30^\circ$  and  $\mu_2/\mu_1 = 0.5$ .

The first integral defines the particle velocity due to a moving crack-face loading on the old crack faces which is achieved by superimposing loads originating at the old crack tip and moving in the negative  $\xi$ -direction with velocities which decrease from  $c_T$  to zero. The second integral corresponds to a superposition of stationary loads which are applied at subsequent times  $t = \xi_d/v$  at points  $\xi_d = vt$ .

In this paper we are interested in wave front approximations, i.e. approximation for  $|t-s_T|/v \ll 1$ . We use the notation  $\bar{W}(\bar{r}, \bar{\theta}, t)$  and  $\bar{w}_a(\bar{r}, \bar{\theta}, t; u)$  to denote the wave front approximation to  $\dot{W}(\bar{r}, \bar{\theta}, t)$  and  $w_a(\bar{r}, \bar{\theta}, t; u)$ , respectively. After some manipulation the wave front approximation to (28) is obtained as

$$\dot{W}(\bar{r}, \bar{\theta}, t) = \int_0^{c_T} g(-u) \bar{w}_a^G(\bar{r}, \bar{\theta}, t; u) du$$

$$- \frac{v^{3/2}}{\pi \bar{s}_T} \frac{\sin \frac{1}{2}\bar{\theta} H(t-\bar{s}_T \bar{r})}{\bar{r}^2 (1-\bar{s}_T v \cos \bar{\theta})^{3/2}} \int_{\bar{s}_T \bar{r}}^t (t-\zeta)^{1/2} f \left[ \frac{v(\zeta-\bar{s}_T \bar{r})}{1-\bar{s}_T v \cos \bar{\theta}} \right] d\zeta \quad (29)$$

where  $\bar{s}_T = 1/c_T$ , and

$$\begin{aligned} \bar{w}_a^G(\bar{r}, \bar{\theta}, t; u) = & - \frac{1}{\pi \bar{s}_T} \frac{\sin \frac{1}{2}\bar{\theta} (t-\bar{s}_T \bar{r})^{1/2}}{\bar{r}^2 (1-\bar{s}_T v \cos \bar{\theta})^{3/2}} \\ & \times \frac{(v+u)^{1/2} [2(1+\bar{s}_T u)(1-\bar{s}_T v \cos \bar{\theta}) + (1-\bar{s}_T v) \times (1+\bar{s}_T u \cos \bar{\theta})]}{(1+\bar{s}_T u)^{3/2} (1+\bar{s}_T u \cos \bar{\theta})^2} \times H(t-\bar{s}_T \bar{r}). \end{aligned} \quad (30)$$

## 118 TRANSVERSE ISOTROPY EFFECT

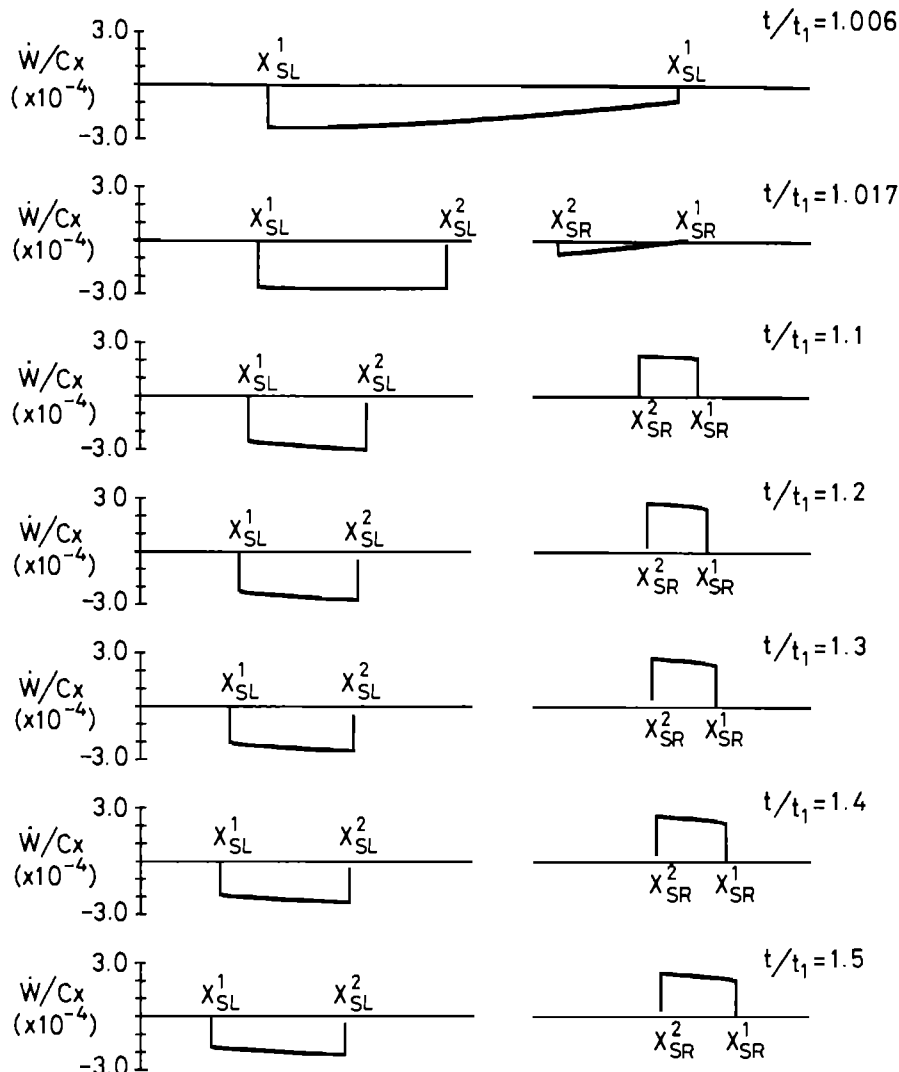


Fig. 9. Pulses on free surface due to a starting and stopping event,  $v/c = 0.9$ ,  $\phi = 10^\circ$ ,  $\mu_2/\mu_1 = 1$ .

It is of interest to point out that (29) shows that the angular dependence of the radiated particle velocity, even near the wave front, depends on the type of traction acting on the crack faces. It follows from (9a, 9b), (21)-(22) and (29)-(30) that for  $|t-s_T \bar{r}|/t \ll 1$ , and in an unbounded medium, the radiated fields corresponding to the starting event are

$$\dot{W}(\bar{r}, \bar{\theta}, t) = (\dot{w}_1 + \dot{w}_2 + \dot{w}_3) H(t - s_T \bar{r}), \quad (31)$$

where  $\dot{w}_i$  ( $i = 1, 2, 3$ ), which corresponds to the expanding loading  $-\gamma\sigma_0$  on the "old" crack faces, the square-root singular tractions  $-\gamma(2\pi\xi)^{1/2} K_C^{III}$  and the constant tractions  $-\gamma\sigma_0$  on the "new" crack faces, respectively,

are defined as

$$\begin{aligned} \dot{w}_1 &= -\dot{w}_3 \\ &+ \frac{\sqrt{2}}{\pi} \frac{\gamma\sigma_0}{\bar{\mu}} \frac{\sin \frac{\bar{\theta}}{2}}{(\bar{r})^{1/2}} \frac{(1+s_T v)^{3/2} (t-s_T \bar{r})^{1/2}}{s_T^{3/2} (1-s_T v \cos \bar{\theta})^{3/2} (1+\cos \bar{\theta})} \end{aligned} \quad (32a)$$

$$\dot{w}_2 = \frac{\gamma K_C^{III}}{\bar{\mu}\sqrt{2\pi}} \frac{\sin \frac{\bar{\theta}}{2}}{(\bar{r})^{1/2}} \frac{v}{(1-s_T v \cos \bar{\theta})} \quad (32b)$$

$$\dot{w}_3 = \frac{2\gamma\sigma_0}{\pi\bar{\mu}} \frac{\sin \frac{\bar{\theta}}{2}}{(\bar{r})^{1/2}} \frac{v^{3/2} (t-s_T \bar{r})^{1/2}}{(1-s_T v \cos \bar{\theta})^{3/2}} \quad (32c)$$

To analyze the stopping event, we must first solve for the stress intensity factor  $\bar{K}_{III}^*$  at the stopped crack tip. Solutions to the SIF of the Mode-III crack problem in isotropic solids have been reviewed by [Achenbach, 1974]. For the crack-face tractions defined by (9a, 9b) and (21)-(22) we have

$$\bar{K}_{III}^* = \gamma K_{III}^* = \gamma [K_{III}^c + \frac{2}{\sqrt{\pi}} \sigma_0 (ct + vt_0)^{\frac{1}{2}}] \quad (33)$$

It follows from (10), (23)-(24), (29)-(30) that for  $(t-s_T\bar{R})/\tau \ll 1$ , the radiated particle velocity for the stopping event is

$$\dot{w}_4 = - \frac{\gamma K_{III}^* |_{t=t_0}}{\mu \sqrt{2\pi}} \frac{\sin \bar{\theta}}{\bar{R}^{\frac{1}{2}}} \frac{v}{(1-\bar{s}_T v \cos \bar{\theta})} H(t-s_T\bar{R}) \quad (34)$$

where  $(\bar{R}, \bar{\theta})$  are the polar coordinates centered at  $(\xi = vt_0, \eta = 0)$  rather than  $(\xi = 0, \eta = 0)$ .

#### Particle Velocity at the Free Surface

Multiple reflections of wave motions between the free surface and the fault are neglected in this paper. We will, however, take into account the free surface reflection of the wave motion emitted by the starting and stopping rupture front. The wave-front approximations presented in the previous section simply double at the free surface. We have

$$\dot{w}(x, y=0, t) = 2(\dot{w}_1 + \dot{w}_2 + \dot{w}_3 + \dot{w}_4), \quad (35)$$

where  $w_i$  are defined by (32a, 32b) and (34).

For a point on the free surface the following relations can be deduced from Figure 1:

$$\bar{r} = [(\bar{x} + d \tan \bar{\phi})^2 + \bar{d}^2]^{\frac{1}{2}} \quad (36)$$

$$\bar{\theta} = \tan^{-1} \frac{\bar{x} + d \tan \bar{\phi}}{\bar{d}} - \bar{\phi} \quad (37)$$

where it follows from (12) that

$$\bar{x} = (\mu_2/c_{44})^{\frac{1}{2}} x, \quad \bar{d} = (\mu_1/c_{44})^{\frac{1}{2}} d, \quad (38)$$

while (15) gives

$$\bar{\phi} = \tan^{-1} [(\mu_2/\mu_1)^{\frac{1}{2}} \tan \phi]. \quad (39)$$

In the same manner we obtain

$$\bar{R} = [(\bar{x} + d \tan \bar{\phi} - vt_0 \sin \bar{\phi})^2 + (\bar{d} - vt_0 \cos \bar{\phi})^2]^{\frac{1}{2}} \quad (40)$$

$$\bar{\theta} = \tan^{-1} \left( \frac{\bar{x} + d \tan \bar{\phi} - vt_0 \sin \bar{\phi}}{\bar{d} - vt_0 \cos \bar{\phi}} \right) - \bar{\phi} \quad (41)$$

The particle velocities for the starting and the stopping events are expressed in terms of  $r, \theta, t$  and  $R, \theta, t$ , respectively. At the free surface the relations between  $r, \theta, R$  and  $d$  and the physical coordinate  $x$  and the depth  $d$  follow from (36)-(41).

There are numerous parameters in the present analysis. They may be subdivided into material parameters, geometrical parameters, and propagation parameters. The material parameters are the shear moduli  $\mu_1$  and  $\mu_2$ , the mass density  $\rho$ , the difference between static and kinetic friction,  $\sigma_0 = \tau_s - \tau_f$ , and the static fracture toughness  $K_{III}^c$ . The geometrical parameters are the depth  $d$  and the angle of fault-plane inclination  $\phi$ . The propagation parameters are the speed of the rupture front,  $v$ , and the length of time of the propagation event,  $t$ .

Numerical calculations have been carried out for various values of the parameters  $\mu_2/\mu_1$ ,  $\phi$  and  $v/c$ . Here  $c$  is the signal speed in the direction of the crack plane. This speed  $c$  depends on  $\mu_1, \mu_2$ , and  $\phi$ . As fixed parameters we have chosen

$$\frac{\sigma_0}{\mu_1} = 10^{-4}, \quad \frac{K_{III}^c}{\mu_1 (c t_0)^{\frac{1}{2}}} = 10^{-3}, \quad \frac{t_0}{t_1} = 10^{-1}, \quad (42)$$

where  $c_x = (\mu_1/\rho)^{\frac{1}{2}}$  is the signal speed in the  $x$ -direction. The time  $t_1 = d/c_x$ , where  $c_y = (\mu_2/\rho)^{\frac{1}{2}}$ , is the arrival time of the first signal at the epicenter, E. The choice of  $K_{III}^c$  was suggested by numerical values listed by Rudnicki [1980].

The wave front corresponding to the starting event is defined by  $r = c_T t$ . At the free surface the corresponding relation between  $\bar{x}$  and  $t$  then follows from (36), while (38) subsequently yields

$$x_{SL}^1 = x_{SL}^1(t) \text{ and } x_{SR}^1 = x_{SR}^1(t), \quad (43)$$

for the positions of the two wave fronts which spread from the point E to the left and the right, respectively. Similarly we have for the stopping event

$$x_{SL}^2 = x_{SL}^2(t) \text{ and } x_{SR}^2 = x_{SR}^2(t) \quad (44)$$

Figures 2 and 3 show  $x_{SL}^i = x_{SR}^i/d, i = 1, 2$ , and  $\beta = L, R$ , as functions of  $t/t_1$ , for  $\phi = 30^\circ$ ,  $v/c = 0.5$ , and the isotropic case,  $\mu_2/\mu_1 = 1$ , as well as the anisotropic case  $\mu_2/\mu_1 = 0.5$ . For  $\phi = 30^\circ$  the surface disturbances due to starting and stopping events spread out in an asymmetric manner. The lengths along the surface covered by the signals generally narrow as the pulses propagate further away

## 120 TRANSVERSE ISOTROPY EFFECT

from the epicenter E. The influence of anisotropy can be seen from Figures 2 and 3.

The particle velocity is discontinuous at the wave fronts generated by the starting and stopping events. The exact values of the discontinuities follow from  $\dot{W}_2$ , (32b) and  $\dot{W}_4$ , (34). Their magnitudes depend on position through  $r, \theta$  and  $R, \theta$ , respectively. These spatial variables can be expressed in terms of  $x$  and  $t$ , as discussed before. There is no particle velocity at 0 due to antisymmetry. For the starting event the magnitudes of the wave front particle velocities have been plotted in Figures 4-6. Figure 4 is for  $\phi = 30^\circ$ ,  $\mu_2 = \mu_1$  and for various values of the rupture-front speed. It is noted that the magnitude of the particle velocity increases as  $v/c$  increases. The distribution is asymmetric with respect to 0, and the largest particle velocities appear at the side of the slip zone. The effect of angle of fault-plane inclination is shown in Figure 5, for  $\mu_2/\mu_1 = 1$  and  $v/c = 0.5$ . On the side of the slip zone (to the left of 0 in Figure 1) the larger angle yields the larger particle velocity, while the opposite is true to the right of 0. The effect of anisotropy is illustrated in Figure 6 for  $\phi = 30^\circ$  and  $v/c = 0.5$ . The smaller  $\mu_2/\mu_1$ , the larger the wave front particle velocity at the free surface.

For  $v/c = 0.5$ ,  $\mu_2/\mu_1 = 0.5$  and  $\phi = 10^\circ$ . Figure 7 shows the actual pulses produced by a starting and stopping event. The differences in the ground motion pulses propagating to the left and the right, due to fault-plane inclination are noted. Similar results for  $v/c = 0.9$  are shown in Figure 8. For  $v/c = 0.9$  the pulse length is longer than for  $v/c = 0.5$ . The differences between the cases  $\mu_2/\mu_1 = 0.5$  and  $\mu_2/\mu_1 = 1$  can be seen by comparing the results of Figures 8 and 9.

Finally, the small gaps at the tail ends of the pulses show that the stopping event does not completely eliminate the signal generated by the starting event. The missing trailing ends of

the signals are not described by the present approximation.

Acknowledgment. This paper was written in the course of research sponsored by the National Science Foundation, Grant EAR-8207090.

## References

- Achenbach, J. D., Dynamic effects in brittle fracture, in Mechanics Today 1, 1-56, Pergamon, New York, 1974.
- Achenbach, J. D., and J. G. Harris, Ray method for elastodynamic radiation from a slip zone of arbitrary shape, J. Geophys. Res., 83, 2283-2291, 1978.
- Crampin, S., A review of wave motion in anisotropic and cracked elastic media, Wave Motion 3, 343-392, 1981.
- Harris, J. G., and J. D. Achenbach, Near-field surface motions excited by radiation from a slip zone of arbitrary shape, J. Geophys. Res. 86, 9352-9356, 1981.
- Helbig, K., Elliptical anisotropy - its significance and meaning, Geophysics 48, 825-832, 1983.
- Madariaga, R., High frequency radiation from crack (stress drop) models of earthquake faulting, Geophys. J.R. Astron. Soc. 51, 625-651, 1977.
- Rudnicki, J. W., Fracture mechanics applied to the earth's crust, Ann. Rev. Earth Planet Sci. 8, 489-525, 1980.
- Spudich, P., and L. N. Frazier, Use of ray theory to calculate high-frequency radiation from earthquake sources having spatially variable rupture velocity and stress drop, Bull. Seismol. Soc. Am. 74, 2061, 1984.
- Yamashita, T., High-frequency acceleration radiated by unsteadily propagating cracks and its near-source geometrical attenuation, J. Phys. Earth 31, 1-32, 1983.

## FAST NEAR SOURCE EVALUATION OF STRONG GROUND MOTION FOR COMPLEX SOURCE MODELS

V. Farra, P. Bernard, and R. Madariaga

Laboratoire de Sismologie, Institut de Physique du Globe de Paris,  
and UER Sciences Physiques de la Terre, Université Paris 7, France

**Abstract.** We propose that high-frequency synthetic accelerograms may be computed using ray theory. The method consists in neglecting the near-field terms in the Green's function for a point double couple source. The far-field terms may then be computed using ray theory, so that the technique is applicable to laterally heterogeneous structures. We discuss this approximation in the simple case of a finite line source buried in a homogeneous half-space. A complex rupture history was considered that included a segment in which velocity was super shear. Results show that the far-field term is a good approximation of the total field for wavelengths shorter than the closest distance to the fault. This result is independent of the overall size of the fault. We then extended the asymptotic technique based on isochrone integration in order to include all sorts of rays with real or complex amplitudes, such as critical reflections, reversed branches, etc... We propose a simple numerical method to calculate synthetics that does not require calculating the isochrones explicitly. The principal advantage of this method is that it is quite fast and it may be applied to calculate synthetics in laterally heterogeneous earth models. We applied this technique to the model of the source of the Imperial Valley earthquake of 1979, proposed by Archuleta.

## Introduction

Most methods of calculating synthetic acceleration or velocity in the vicinity of a seismic source are based on the numerical integration over the fault plane of the complete Green's function. Among the methods currently used, we may mention discrete wave number summation [Bouchon, 1979] and discrete wave number finite element summation [Olson et al., 1984]. A number of successful examples of modeling of filtered or integrated accelerograms have appeared in the literature (Bouchon [1982]; Archuleta [1984]; Hartzell and Heaton [1983]; among others). The main limitation of the methods using complete Green's function is that they only apply to vertically stratified media. There seems to be no

obvious way in which they could be extended to take into account realistic laterally varying structures. Another limitation appears at high frequency since the computational costs become rapidly prohibitive beyond a few Hz.

Several studies of radiation from dynamic source models have shown that it is possible to develop very efficient methods by using the asymptotic approximation of the Green's function at high frequencies (Bernard and Madariaga [1984]; Spudich and Frazer [1984]). This approximation leads to a number of simplifications in the calculation and to simple physical models for the generation of high-frequency waves.

In this paper, we continue the investigation of asymptotic methods using only the far-field term of the Green's function in an attempt to justify their use in a frequency range of engineering and seismological interest.

## Near-field and far-field

Radiation from a seismic source is a classical problem in elastodynamics. It may be easily calculated from a representation theorem. Let  $M(\underline{r}, t)$  be the seismic moment tensor distribution corresponding to a seismic fault  $\Sigma$ . The displacement is given by:

$$u_i(\underline{r}, t) = \iint G_{ij,k}(\underline{r}, t | \underline{r}_0) * M_{jk}(\underline{r}_0, t) d\Sigma(\underline{r}_0) \quad (1)$$

(see e.g. Aki and Richards [1980]), where the moment tensor distribution  $M_{jk}$  is:

$$\begin{aligned} M_{jk}(\underline{r}_0, t) = & \mu(\underline{r}_0) \Delta u(\underline{r}_0, t) [n_j(\underline{r}_0) v_k(\underline{r}_0) + \\ & + n_k(\underline{r}_0) v_j(\underline{r}_0)] \end{aligned}$$

$\mu$  and  $\Delta u$  are the rigidity and slip function at the point  $\underline{r}_0$ ,  $n$  a unit vector in the direction of slip,  $v$  the unit normal to the fault at  $\underline{r}_0$ , and  $G_{ij}$  is the elastodynamic Green's tensor.

We can write (1) in another way

## 122 FAST NEAR SOURCE STRONG MOTION EVALUATION

$$u_i(\underline{r}, t) = \iint_{\Sigma} H_i(\underline{r}, t | \underline{r}_0) * \Delta u(\underline{r}_0, t) d\Sigma(\underline{r}_0) \quad (2)$$

where  $H$  is the Green's function for a point dislocation source:

$$H_i(\underline{r}, t | \underline{r}_0) = \mu(\underline{r}_0) n_j(\underline{r}_0) v_k(\underline{r}_0) [G_{ij,k}(\underline{r}, t | \underline{r}_0) + G_{ik,j}(\underline{r}, t | \underline{r}_0)] \quad (3)$$

The exact calculation of  $H_i$  is a formidable problem that leads to very complicated numerical methods. Bernard and Madariaga [1984] and Spudich and Frazier [1984] independently proposed that, under certain circumstances, it is possible to use in (2) only the "far-field" Green's function.

The far-field Green's function may be written in the ray approximation as:

$$H_i(\underline{r}, t | \underline{r}_0) = \frac{\mu_0}{4\pi\rho_0 c_0} \left( \frac{\rho_0 c_0}{\rho c J} \right)^{1/2} \frac{c}{F} \delta(t-T) \quad (4)$$

where  $c$  is either the P or S wave velocity according to the type of wave under consideration.  $F$  is a vector radiation pattern which depends on the takeoff angle of the ray at the source and on the geometrical properties of the dislocation source,  $\delta$  is the derivative of Dirac's delta function,  $T$  is travel time, and  $J$  is the geometrical spreading.

In most studies of earthquake source mechanism, it is assumed that in the vicinity of the fault it is necessary to include near-field terms. A simple way to compare these two terms is by turning to the frequency domain. It is easily seen that their relative magnitude depends on the non dimensional ratio  $\omega T$ , i.e., the number of wavelengths between the dislocation source and the observer. Thus, the far-field Green's function will be applicable when the wavelengths under consideration are much shorter than the smallest distance to the fault. The range of validity of this approximation does not depend on the dimensions of the fault. There is some confusion in the literature between this asymptotic approximation and the Fraunhofer approximation which applies when the observer is at a distance far greater than the dimensions of the source. As we are going to show in the following, the use of the far-field Green's function yields good results even at distances of the order of the wavelength.

#### A Homogeneous Half Space Model

In order to test the relative importance of the near- and far-field terms, we study the velocity field in an infinite homogeneous medium. We used a very simple dislocation model

for the source (Figure 1). The rupture initiates at the focus 0 and expands along a straight line L with a variable rupture velocity. The line dislocation source, physically a plane fault with a very small width, is assumed to be a vertical strike-slip fault, 35 km long, located at a depth of 9 km. We used Archuleta's [1984] model of the Imperial Valley Earthquake, taking the rupture times of the points situated at a depth of 8 km and slip amplitudes averaged across the fault (Figure 2). The slip velocity has a boxcar shape:

$$\dot{\Delta u}(\lambda_0, t) = D(\lambda_0) \{ H[t-T_R(\lambda_0)] - H[t-T_D(\lambda_0)] \}$$

where  $T_D$  is the rise time at the point  $\lambda_0$ ,  $T_R$  is the rupture time, and  $D$  is the slip amplitude. The rise time will be assumed to be constant on the line source and equal to 1.4 s.

The medium was homogeneous with P velocity of 5.5 km/s and S velocity of 3.0 km/s. The synthetics were convolved by a boxcar function of width  $T_L$  equal to 1.5 s and amplitude  $\beta T_L$  ( $\beta$  being the S velocity) in order to simulate a fault with a 4.5 km width.

We computed synthetic velocity records at several points regularly spaced on a horizontal line perpendicular to the fault at 20 kilometers from the epicenter (Figure 1). The horizontal velocity components parallel and transverse to the fault are shown on Figures 3 and 4 respectively. We present the exact field, the far-field and the near-field calculated at each station and low passed with a two-pole causal Butterworth filter with a corner frequency of 1.0 Hz. All amplitudes are shown to the same scale for each component. At these points, the theoretical limit of validity for using the far field Green's function is  $f > 0.3$  Hz. The principal difference between the exact and the asymptotic fields is a low frequency wave of a period of about 6 s. Figure 3 shows, for horizontal distances greater than 10 km, that the near-field is surprisingly the leading term of the transverse component. This result is due to the fact that the far-field term, mainly SH waves, becomes parallel to the fault as the observation point is moved away from the fault trace on the horizontal line.

In Figures 5 and 6 we show the complete, and the far- and near-fields calculated in the previous figures but high passed with an additional two-pole Butterworth filter with corner frequency at 0.3 Hz. Therefore, these new synthetics are band-passed between 0.3 and 1 Hz. We could have calculated beyond 1 Hz without difficulty, but we wanted to demonstrate how sharp is the frequency limit from which the asymptotic theory becomes valid. The total and the far field synthetics are now nearly identical except for a slightly larger amplitude of the total field at  $y = 2.5$  km. The cut-off frequency of 0.3 Hz corresponds to an S wavelength of 10 km, while

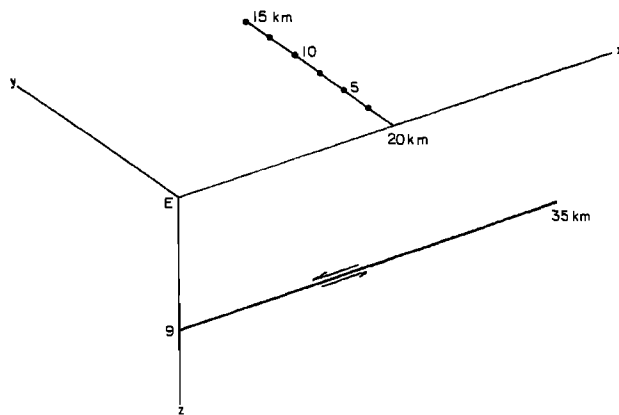


Fig. 1. Geometry of the dislocation model: the source model is a vertical strike slip fault elongated along the  $x$ -direction [thick line]. The fault is a 35 km long line located at a depth of 9 km. Synthetic velocities were computed at regularly distributed intervals along a horizontal line perpendicular to the fault 20 km away from the epicenter E. The distance between two observation points is 2.5 km.

the shortest distance to the fault from the station at  $y = 5.0$  km is 9.5 km. We conclude that the asymptotic method yields good results for wavelengths of the order of the distance to the fault and deteriorates relatively fast once the wavelengths become longer.

#### Asymptotic Seismograms In General Heterogeneous Media

We have justified numerically the use of the asymptotic Green's function at high frequencies for wavelengths shorter than the distance to the fault. By using it, the cost of calculating (1) is reduced by at least one order of magnitude. But this is not the only advantage of using far-field Green's functions. Since this function can be interpreted in terms of rays, it provides some important insight into the way high frequency waves are generated by very general source models.

In order to calculate the radiation in the high frequency approximation, we insert (4) in the representation theorem for a seismic fault (2). We obtain:

$$\underline{u}^c(\underline{r}, t) = \iint \frac{\mu_0}{\Sigma 4\pi\rho_0 c_0^3} \left( \frac{\rho_0 c_0}{\rho c J} \right)^{1/2} \frac{F}{c} \Delta u(\underline{r}_0, t-T) d\Sigma(\underline{r}_0) \quad (5)$$

We will use a simple dislocation model for the source. The slip function is expressed as:

$$\Delta u(\underline{r}_0, t) = D_0(\underline{r}_0) f[t - T_R(\underline{r}_0)] \quad (6)$$

where  $D_0$  is the total slip amplitude,  $f$  is the time shape of the displacement at the point  $\underline{r}_0$ , and  $T_R$  is the rupture time.

Let us introduce the slip velocity into (5) to obtain:

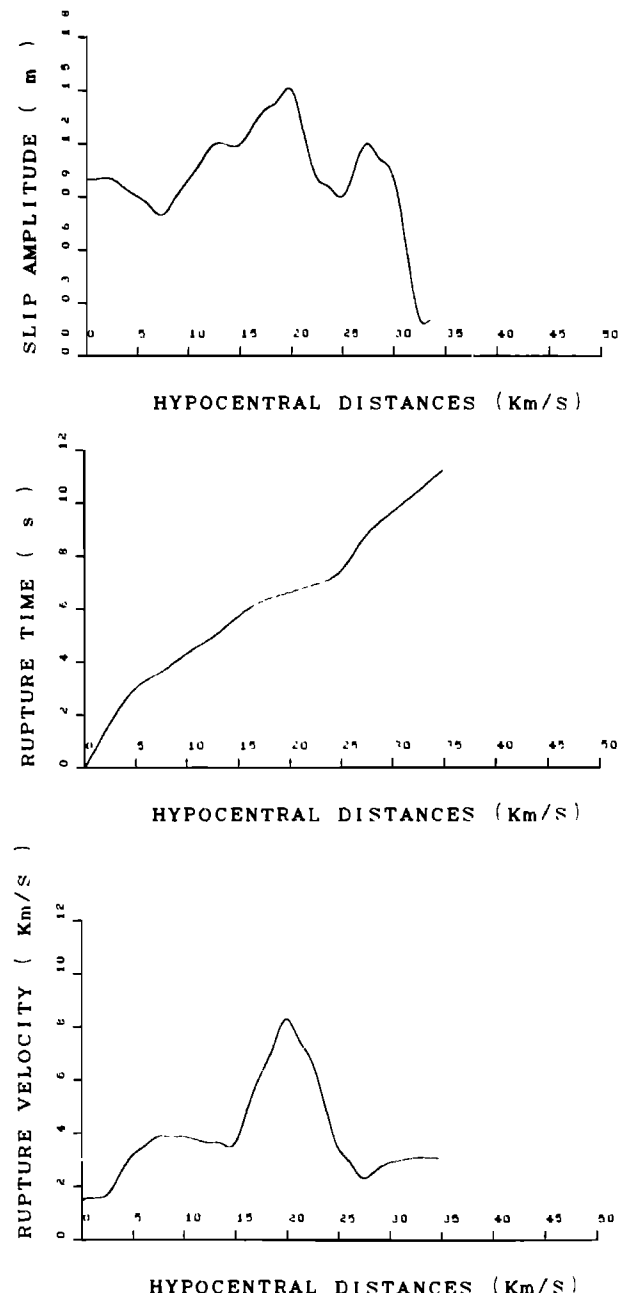


Fig. 2. Slip amplitude, rupture time, and rupture velocity as a function of distance along the fault used to calculate synthetics in the half-space model of Figure 1.

## 124 FAST NEAR SOURCE STRONG MOTION EVALUATION

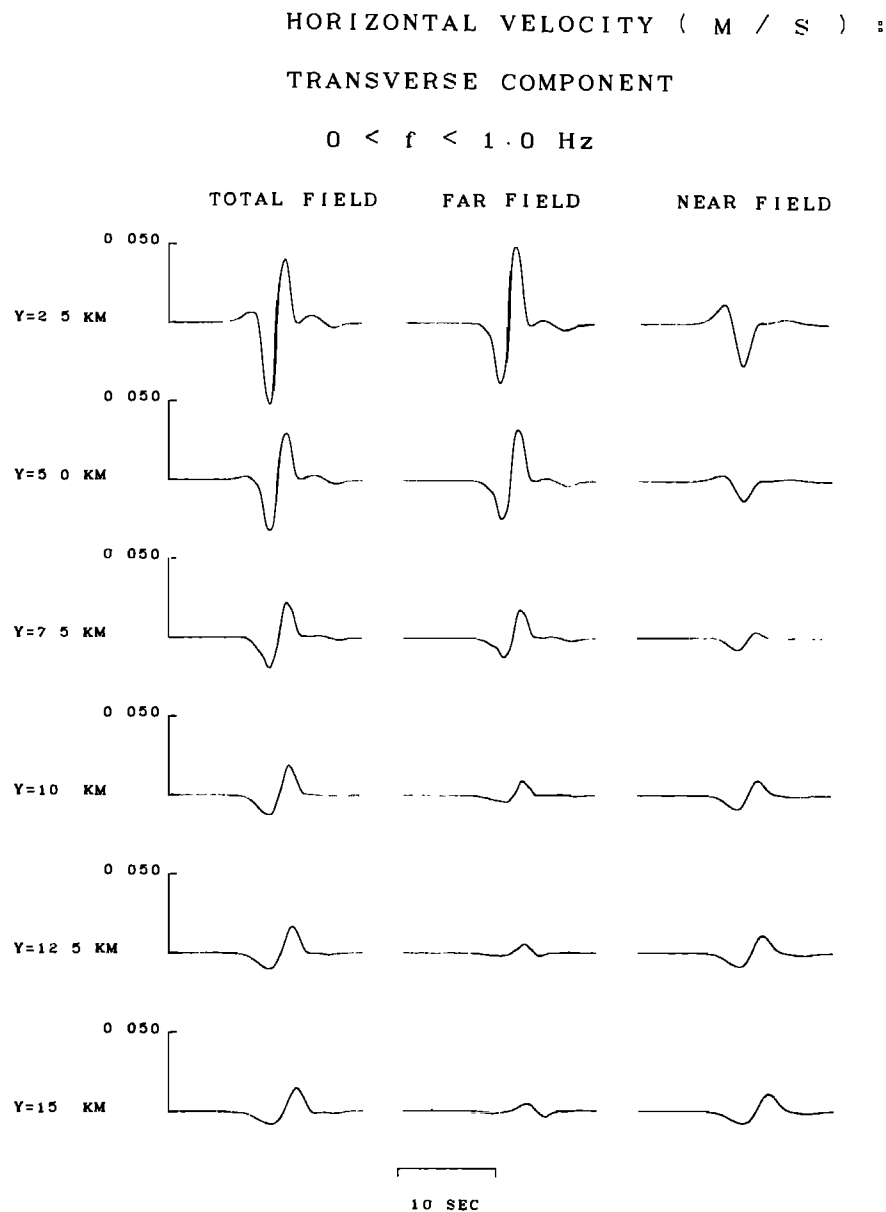


Fig. 3. Transverse component of synthetic velocities. The exact field, and the far- and near-field are plotted from left to and right. These synthetics were low passed with a two-pole Butterworth filter with a corner frequency of 1.0 Hz. Points of observation are given in Figure 1.

$$\underline{u}^c(\underline{x}, t) = \int f(t) * \iint \frac{\mu_0 D_0}{4\pi\rho_0 c_0} \left( \frac{\rho_0 c_0}{\rho c J} \right)^{1/2} F_c \delta(t-\tau) d\Sigma \quad (7)$$

$$\text{where } \tau(\underline{x}_0, \underline{x}) = T(\underline{x}_0) + T(\underline{x}_0, \underline{x}) \quad (8)$$

Using the sifting property of the delta function, the surface integral (7) may be reduced

to an integral along a line defined by  $t=\tau$ . Given the time  $t$ , (8) defines a curve on the fault plane that Bernard and Madariaga [1984] and Spudich and Frazer [1984] called the isochrone. This curve defines the set of points on the fault plane from which radiation arrives at the observation point, at time  $t$ . The different points on the isochrone do not radiate simultaneously, but at the time  $T_R$  when the rupture front arrives to them.

FARRA ET AL. 125

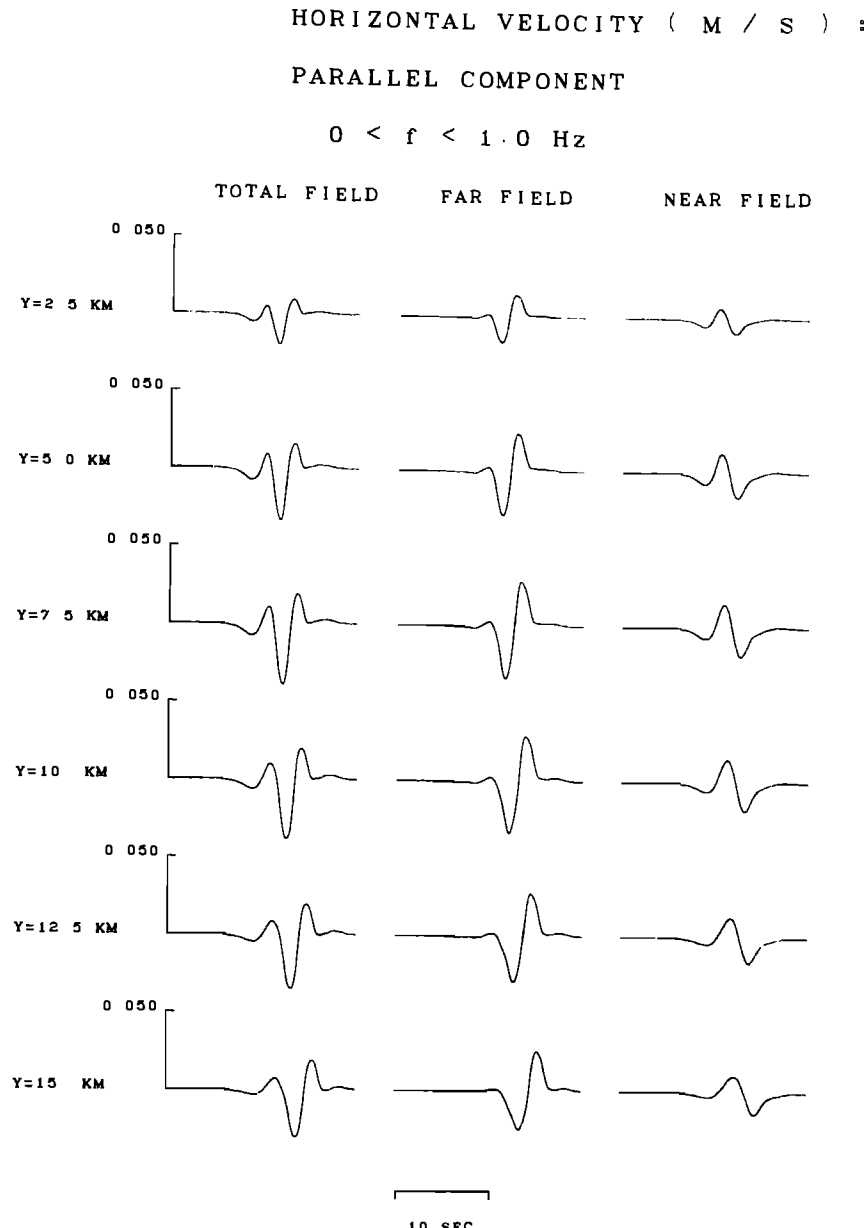


Fig. 4. Parallel component of synthetic velocities. The exact, far- and near-field were low passed with a two-pole Butterworth filter with a corner frequency of 1.0 Hz.

For every time  $t$ , the equation (8) for the isochrone can be solved numerically. Let  $L_0(\underline{r}, t)$  be this isochrone; then, the surface integral (5) reduces to the line integral:

$$\underline{u}^c(\underline{r}, t) = f(t) * \int \frac{\mu_0 D_0}{L_0} \left( \frac{\rho_0 c_0}{\rho c J} \right)^{1/2} \frac{F}{c} \frac{dl}{|\nabla_s \tau|} \quad (9)$$

where  $\nabla_s \tau$  is the surface gradient of the total

time delay  $\tau$ . Equation (9) is a very general formula for the calculation of near field asymptotic synthetics. As shown by Spudich and Frazer [1984], who derived it, it is closely related to the Kirchhoff approximation used in applied geophysics.

Equation (4) for the ray theoretical approximation to the Green's function is valid only for direct rays. We may however easily extend it to include multiple rays and maximum time phases. Following the methods described by Cerveny et

## 126 FAST NEAR SOURCE STRONG MOTION EVALUATION

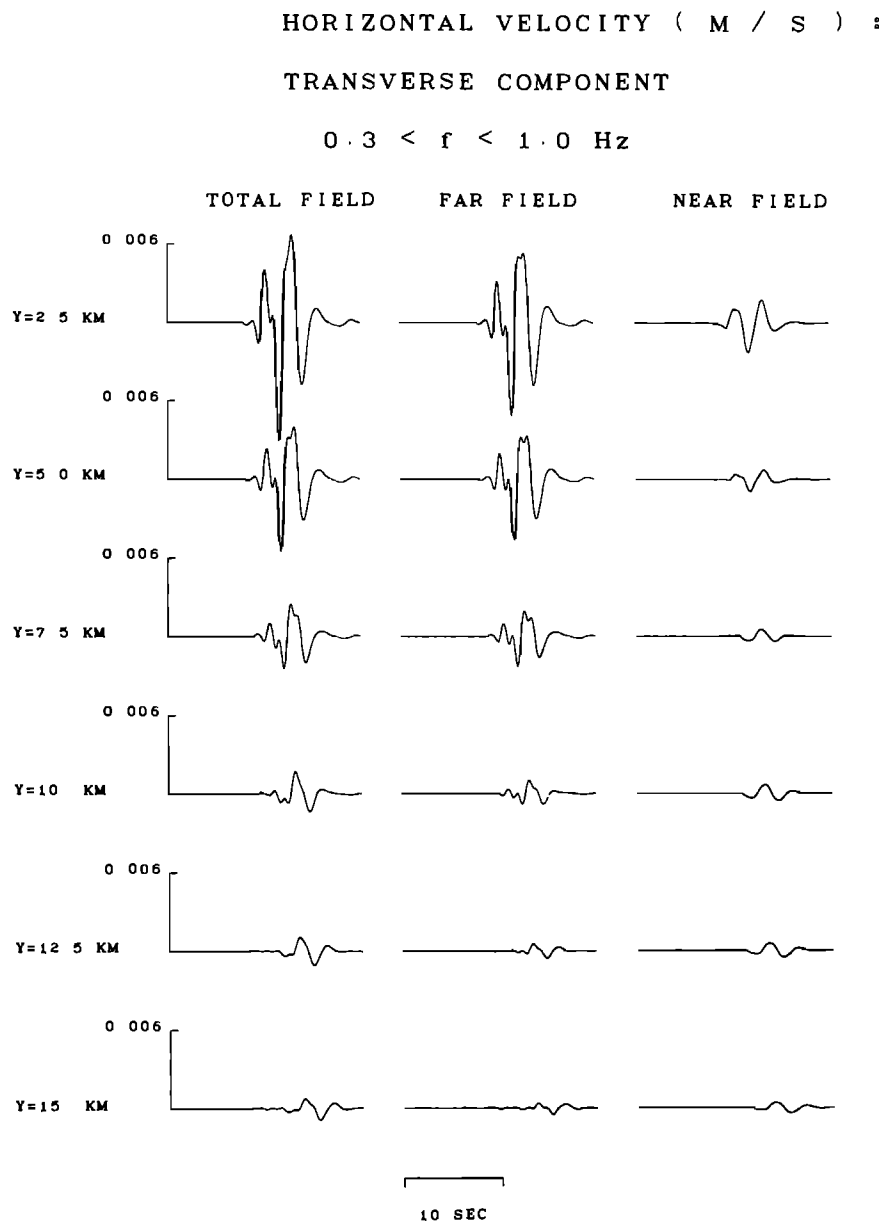


Fig. 5. Transverse component of the synthetic velocities of Figure 3, band passed with a Butterworth filter with corner frequencies of 0.3 and 1.0 Hz.

al. [1977] we write a general ray in the form:

$$H^L(\underline{r}, t | 0) = \frac{\mu_0}{4\pi\rho_0 c_0^3} \operatorname{Re} \left\{ \left( \frac{\rho_0 c_0}{\rho c J} \right)^{1/2} \frac{F}{c} \Pi \dot{\Delta}[t - T(\underline{r}_0)] \right\} \quad (10)$$

where  $\Delta(t) = \delta(t) - i \pi^{-1} t^{-1}$  is the analytic function that corresponds to Dirac's delta function.  $\Pi$  contains the product of all complex reflection and transmission coefficients at the

different interfaces encountered by the ray on its trajectory. For positive  $J$  and real  $\Pi$  it reduces to (4) with the additional factor  $\Pi$ . For complex  $\Pi$  and positive  $J$  it gives two terms:

$$\frac{d}{dt} [\operatorname{Re}\{\Pi\} \delta(t-T) + \operatorname{Im}\{\Pi\} \pi^{-1}(t-T)^{-1}]$$

instead of the derivative of the delta function in (4). Complex  $\Pi$  occurs when a ray is reflected at a supercritical angle. Finally, (10) also includes rays that have touched a caustic. For

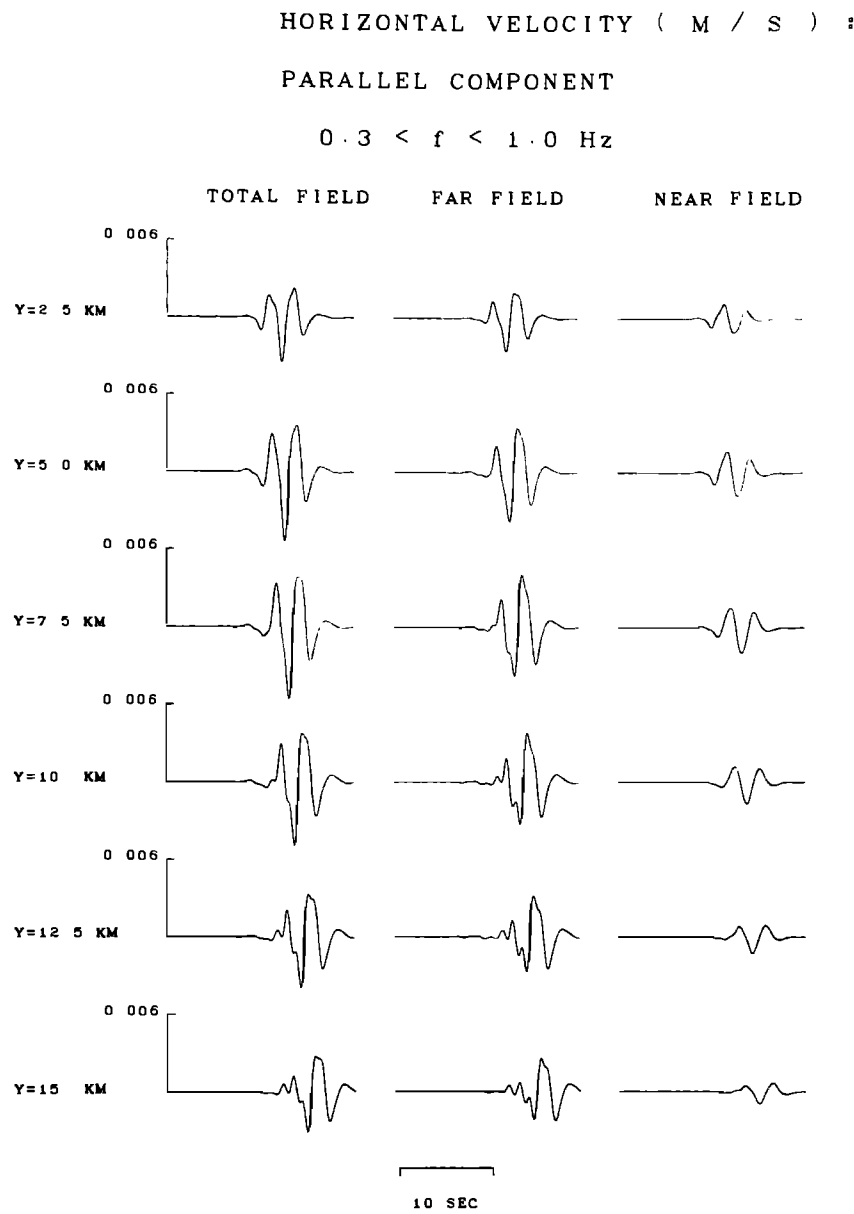


Fig. 6. Parallel component of the synthetic velocities calculated in Figure 4 band passed with a Butterworth filter with of 0.3 and 1.0 Hz.

these rays  $J \leq 0$ , and the square root in (10) should be chosen as:

$$\sqrt{J} = \sqrt{|J|} \exp(-i\pi/2)$$

Thus, (10) is very general and permits to calculate all geometrical rays. Inserting (10) into the representation theorem we obtain:

$$u(\underline{r}, t) = \operatorname{Re}\left\{ F(t) * \int_{L_0}^{\infty} \frac{\mu_0 D_0}{4\pi\rho_0 c_0^3} \left( \frac{\rho_0 c_0}{\rho c J} \right)^{1/2} \frac{dl}{|\nabla_s \tau|} \right\}$$

$$\frac{F}{c} \Pi \frac{dl}{|\nabla_s \tau|} \quad (11)$$

where  $F(t) = f(t) + i H[f(t)]$  is the analytic function corresponding to  $f(t)$ .  $H[\cdot]$  denotes the Hilbert transform.

#### Numerical Method

Although (11) has a very simple form it is difficult to evaluate numerically when the ray

## 128 FAST NEAR SOURCE STRONG MOTION EVALUATION

TABLE 1. Elastic Parameters for the Imperial Valley Model

Depth km	$V_p$ $\text{km s}^{-1}$	$V_s$ $\text{km s}^{-1}$	$\rho$ $\text{g cm}^{-3}$
0.	1.70	0.40	1.8
0.4	1.80	0.70	1.8
5.0	5.65	3.20	2.5
11.0	5.85	3.30	2.8
11.0	6.60	3.70	2.8
12.0	7.20	4.15	2.8

trajectories are complex. This difficulty comes from the calculation of isochrones which present corners, split into several disjoint curves, etc. While isochrones are very useful to understand where high frequency energy is coming from, they are not very practical for the evaluation of (11). For this reason instead of using (11) we return to a surface integral similar to (7) modified to take into account rays with complex amplitude. Using (10) into (2), we find the following generalization that is valid for any ray:

$$u(x,t) = f(t) * \operatorname{Re} \left\{ \int \frac{\mu_0 D_0}{L_0} \left( \frac{\rho_0 c_0}{\rho c J} \right)^{1/2} F_c \Pi S(t-\tau) d\Sigma \right\} \quad (12)$$

where  $\tau$  is defined in (8) and  $S(t-\tau)$  is an analytic function that is almost delta-like:

$$S(t) = -\frac{i}{\pi} \frac{1}{t - i\Delta t} \quad (13)$$

When  $\Delta t \rightarrow 0$ ,  $S(t)$  approaches the analytic delta function defined in (11), and equation (13) is exact. In practice, however, it is necessary to smooth the integrand before (12) may be evaluated in a computer. This is achieved with the use of a finite  $\Delta t$ . As shown by Madariaga and Papadimitriou [1985],  $S(t)$  is the convolution of the analytic delta function with the sampling function:

$$s(t) = \frac{1}{\pi} \frac{\Delta t}{t^2 + (\Delta t)^2}$$

The Fourier transform of  $s(t)$  is  $s(\omega) = \exp(-\omega \Delta t)$  so that the main effect of this sampling function is to reduce the spectral amplitudes for frequencies greater than  $1/\Delta t$ . The value of  $\Delta t$  is very important to insure numerical stability in the evaluation of (12). It must be chosen so that  $\Delta t >$  difference of arrival time between rays coming from two neighboring points on the fault. On the other hand,  $\Delta t$  should not be much longer than the sampling interval, otherwise the synthetic seismograms would be unnecessarily smoothed.

The use of  $s(t)$  is equivalent to summing the displacement due to discrete sources radiating a

time function proportional to  $s(t)$  at the time  $T_R$  when the rupture front passes through them. A physical interpretation of this is that isochrones are smeared, while still satisfying the uncertainty principle of the Fourier transform. One may also try to see  $s(t)$  as a new source function though it must be remarked that it is not a causal function. By means of this technique, we stabilize the evaluation of the sum, so that we can calculate the high frequency waves under very general conditions of rupture propagation even in case of rupture velocity jumps (barriers), slip discontinuities (asperities), supershear velocities, critically reflected waves, etc. Though it is necessary to evaluate a 2-D integral, the calculation of (12) is not more time consuming than (11) because it is not necessary to calculate isochrones. The numerical method proposed here is different from that of Spudich and Frazer [1984] who smoothed the integral along the isochrone using a boxcar function. Their method is equivalent to that proposed by Chapman [1978] for computing WKBJ seismograms.

## Example Of Synthetics For A Complex Medium

We have used the formalism described in the previous section to calculate synthetics in a complex medium. The models of the structure and source are nearly identical to those proposed by Archuleta [1984] who modeled the source rupture process of the Imperial Valley earthquake of 1979 by inversion of filtered velocity records. The elastic parameters are given in Table 1. Rupture times and slip at different points on the fault were smoothed from his final model. We only considered the strike-slip component of slip in our model. The slip velocity source time function is a boxcar of 1.4 s width and the fault dip angle is  $80^\circ$ . Our program interpolates on the array of input parameters and creates a grid with a 0.5 km spacing. The smoothing parameter in (12),  $\Delta t$ , was chosen equal to 0.2s.

In Figure 7 we show synthetic transverse velocity records and the corresponding observed velocity traces. The four stations considered belong to the El Centro array. Both the synthetic and observed velocity records were low-pass filtered at 0.5 Hz.

The agreement between observed and synthetics calculated by our asymptotic technique is quite good specially for stations 6 and 5 which are closer to the fault. The agreement between the synthetic and observed record at station 4 is not very good, but neither was this station well modeled in Archuleta's [1984] original work. The quality of fit deteriorates away from the fault for the same reasons mentioned in the discussion of Figures 3 to 5: the SH waves pass through a node in the vicinity of station 3. Thus the low-frequency field becomes dominant in this station. Synthetics were calculated for these stations by Archuleta [1984] using the discrete wave number finite-element method of Olson et al.,

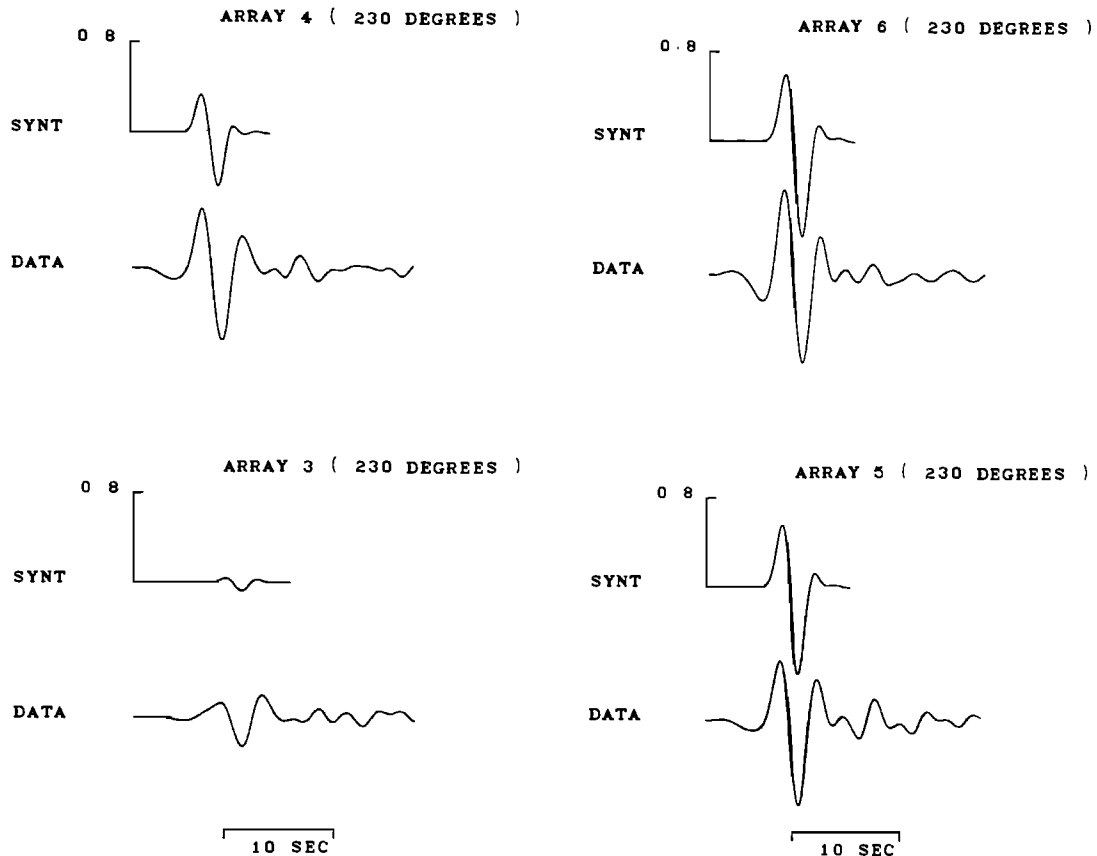


Fig. 7. Comparison of synthetic and observed transverse velocity recorded during the Imperial Valley earthquake of stations of the El Centro array. Both traces were low-pass filtered at 0.5 Hz.

[1984]. His synthetics also included slip on the Brawley fault which we did not incorporate in our model. The results of Figure 7 show that with the asymptotic method we obtain good fits to the amplitude and phase with a very modest expense of computer time.

Our synthetics included all the direct waves and simple reflections at the internal discontinuities. Figure 8 shows the individual contribution of direct and reflected waves to the complete synthetic seismogram calculated at station 4.

#### Conclusion

We calculated numerically the radiation from a simple line source buried in a homogeneous half space. The results obtained with the asymptotic method proposed by Bernard and Madariaga [1984] and Spudich and Frazer [1984] were compared with exact solutions. We demonstrated that the asymptotic methods were valid for wavelengths shorter than the distance from the observation point to the fault. At wavelengths shorter than this distance, the near-field terms become dominant and the approximation deteriorates

rapidly. In particular, for a fault buried at 9 km, the exact and asymptotic solutions at frequencies higher than 0.3 Hz ( $\lambda > 10$  Km) are almost indistinguishable at a distance of 10.5 km.

The asymptotic technique has been extended to include all sort of rays including critical reflections, reversed branches, etc. A simple method to evaluate the integrals on the fault is proposed. In this new method it is not necessary to calculate isochrones. This eliminates some severe numerical problems that appear in the calculation of isochrones. Also, since the method is based on ray theory, complex laterally heterogeneous structures may be included.

The new technique is used to calculate synthetics for a realistic model of the source of the Imperial Valley earthquake of 1979. All the rays contributing to the seismograms were included in the synthetics. Thus, with a minimum effort critically reflected waves and caustics are included in the calculations.

Application of this formalism to strong motion modeling problem aids our understanding of how ground motions are related to fault rupture and

130 FAST NEAR SOURCE STRONG MOTION EVALUT

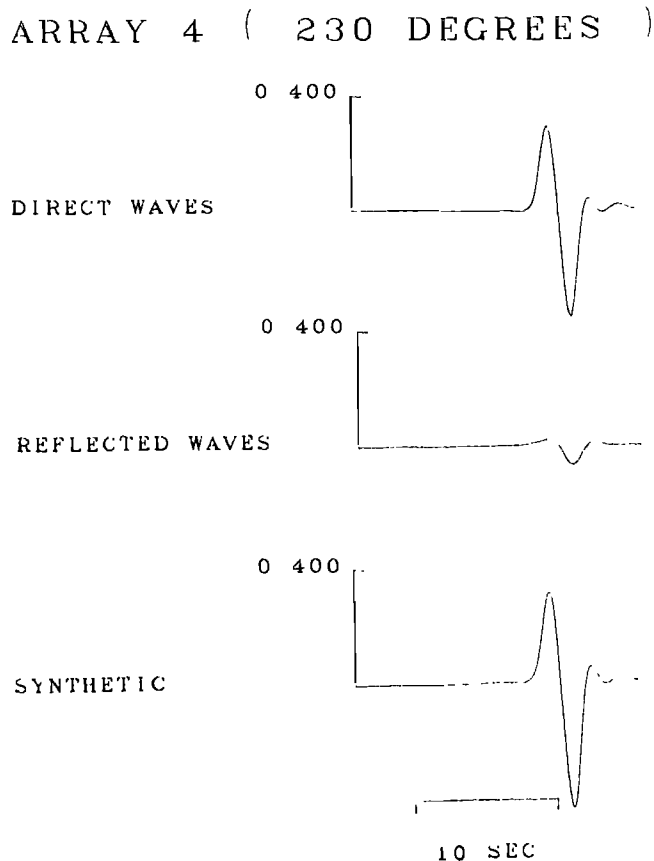


Fig. 8. Contribution of direct P and S waves and of single reflections to the asymptotic seismograms calculated at station 4 of the El Centro array. Seismograms were low-pass filtered at 0.5 H

leads to several simplifications in the synthesis of accelerograms, for example the concept of critical points [Bernard and Madariaga, 1984]. Moreover, it enhances our ability to calculate velocity synthetics in a frequency range of engineering and seismological interest. This can be used for seismic risk analysis and fast source inversion procedures.

Acknowledgments. This work was supported by Institut National des Sciences de l'Univers under a grant from ATP Sismogenèse. We thank D. P. Spudich for a very helpful and stimulating review.

Contribution IPG n° 844

#### References

- Aki, K., and P. Richards, Quantitative seismology, pp. 913, W.H. Freeman, San Francisco, Calif., 1980.
- Archuleta, R.J., A faulting model for the 1979 Imperial Valley Earthquake, J. Geophys. Res., 89, 4559-4585, 1984.
- Bernard, P. and R. Madariaga, A new asymptotic method for the modelling of near-field accelerograms, Bull. Seismol. Soc. Am., 74, 539-559, 1984.
- Bouchon, M., Discrete wave number representation of elastic wave fields in three space dimensions, J. Geophys. Res., 84, 3609-3614, 1979.
- Bouchon, M., The rupture mechanism of the Coyote Lake earthquake of August 6, 1979, inferred from near-field data, Bull. Seismol. Soc. Am., 72, 745-758, 1982.
- Cerveny, V., I. A. Molotkov, and I. Psensik, Ray Methods in Seismology, Karlova Univerzita, Prague, 1977.
- Chapman, C.H., A new method for computing synthetic seismograms, Geophys. J. R. Astron. Soc., 54, 481-518, 1978.
- Hartzell, S.H., and T. H. Heaton, Inversion of strong ground motion and teleseismic waveform for the fault rupture history of the 1979 Imperial Valley, California, Earthquake, Bull. Seismol. Soc. Am., 73, 1553-1583, 1983.
- Madariaga, R., and P. Papadimitriou, Gaussian beam modelling of upper mantle phases, Ann. Geophys., 3, 799-812, 1985.
- Olson, A.H., J. A. Orcutt, and G. A. Frazier, The discrete wavenumber/finite element method for synthetic seismograms, Geophys. J. R. Astron. Soc., 77, 421-460, 1984.
- Spudich, P., and L. N. Frazer, Use of ray theory to calculate high-frequency radiation from earthquake sources having spatially variable rupture velocity and stress drop, Bull. Seismol. Soc. Am., 74, 2061-2082, 1984.

## A DISCUSSION OF THE DEPTH EXTENT OF RUPTURE IN LARGE CONTINENTAL EARTHQUAKES

Jurgen Strehlau

Institut für Geophysik, Christian-Albrechts-Universität, 2300 Kiel  
Federal Republic of Germany

**Abstract.** How deep into the crust do seismic fault planes extend? Is downward rupture arrested at shallow levels, or may it propagate very deeply? Do depths of aftershock zones aid in evaluating the maximum depth of faulting? From a compilation of focal depth data for 36 well-studied continental earthquakes and their aftershocks, it is found that rupture of most main events initiates at depths between 7 and 13 km. The deepest aftershock locations are about 5±2 km below the main-event hypocentral depth. The observations are interpreted by combining static solutions of fault slip with a simple estimate of the relative shear strength distribution on a deep-reaching fault zone. This model complies with results from laboratory experiments and studies of rocks in deeply eroded fault zones and comprises three structural and rheological layers: an upper, frictional level of fault gouge; a middle, transitional level with complex semibrittle rock behavior; and a lower, ductile level of mylonitic shear belts. One arrives at the following conclusions. (1) Rupture in large earthquakes initiates in the transition layer where the shear strength of fault rocks may have a maximum. (2) If the lower edge of the aftershock zone delineates the bottom margin of the main-event fault plane, it follows that rupture is not driven more than about 5 km beneath the focus. Rupture comes to a stop in the transition layer because the high dynamic friction stress becomes larger with depth than the tectonic prestress. (3) Alternatively, if rupture extends deeply down beneath the zone of aftershocks, it should proceed at very low dynamic friction stress, perhaps due to shear melting of mylonites. This fairly smooth mode of fault slip does not cause deep aftershocks, since the molten fault plane may flow until it resolidifies. The results suggest that conclusions 2 and 3 do not exclude one another. Instead, they may together be regarded as potential concepts for source mechanisms in large continental earthquakes.

## Introduction

Depth distributions of continental earthquake foci provide insight into the seismogenic properties of deep-reaching fault zones. Except at sub-

duction zones, earthquake foci of all magnitudes are located in the upper continental crust and only rarely in the upper mantle; there seem to be none at all in the lower crust [Chen and Molnar, 1983; Meissner and Strehlau, 1982; Sibson, 1983]. Judging from the apparent lack of foci in the lower crust, the deep, aseismic level of faults appears sharply distinct from the shallow, seismic level. However, is it possible that these two levels do occasionally overlap? In other words, may rupture in a large earthquake penetrate downward into the lower level of crustal fault zones as was envisaged by Sibson [1980]? Do aftershock locations reveal anything in this case about the maximum depth extent of fault rupture? This paper addresses these questions. It attempts a conceptual synthesis of results obtained from seismological and geological studies and of models for the strength distribution on crustal faults. Literature pertinent to the depth of faulting in continental earthquakes is reviewed first.

## Evidence for Depth Extent of Seismic Rupture

The following is a simple description of the rupture process in earthquakes: rupture initiates at depth and spreads laterally over the fault plane; eventually, at least in the majority of larger events ( $M > 6$ ), it breaks through the earth's surface and finally stops progressively or abruptly on the perimeter of the fault plane. This concept of a propagating shear rupture has been used by many authors in numerically synthesizing the waveforms observed in teleseismic records. Studies of near-field records have shown that seismic slip is quite inhomogeneous: large earthquakes may consist of several subevents; there may be temporary arrests and reactivations of rupture on single fault segments; slip may occur on subsidiary faults [e.g., Heaton, 1982; Archuleta, 1984; Boatwright, 1984; Munguia and Brune, 1984; Spudich and Cranswick, 1984].

How deep does the rupture front progress from a hypocenter into the crust? Figure 1 illustrates two alternative concepts which will be discussed in this paper: one represents a shallow, the other a deep fault plane. It is fairly difficult to infer the depth of the lower margin of a fault plane from seismograms. If rupture propagates

## 132 DEPTH EXTENT OF RUPTURE

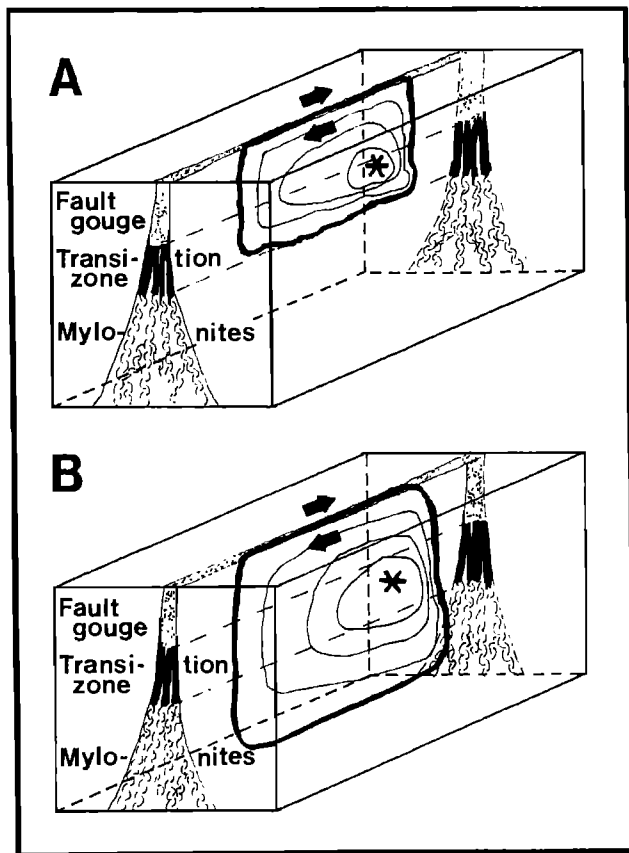


Fig. 1. Schematic diagrams of (a) shallow rupture and (b) deep rupture concepts for a planar crustal strike-slip fault zone. Asterisks indicate the hypocenter; light lines show idealized successive extents of the rupture front on fault planes. The structure of the fault, modified from Sibson [1983], corresponds to the three-layer model shown in Figure 4.

bilaterally away from the hypocenter, radiation arriving from the upward rupturing fault break interferes with radiation from the downward rupturing break. If radiation from the rupture going downward is quite intense, a fault model which attributes all energy to a rupture going upward will overestimate slip on the shallow fault section [Langston, 1978]. Furthermore, radiation from rupture extension below a hypocenter is concealed by the complexity of shallow fault planes and also by the complexity of energy transmission along wave paths. It is thus not surprising that just as a unilateral source model seems of little use for detecting rupture extension below the focus, so neither has bilateral rupture modeling been very fortunate up to now. Owing to this difficulty to possibly uncover deep rupture, the lower edge of fault planes is usually not a variable resolved by the modeling procedures, but

is often constrained to be only a few kilometers deeper than the hypocenter (shallow rupture, Figure 1a). Nevertheless, some indication of deep rupture has been found.

#### Indications of Deep Fault Slip

A number of earthquakes radiate short-period energy from small, isolated patches relative to the fault area which radiates long-period waves. This has been suggested as an explanation for discrepancies found between short-period and long-period seismic moments [Wallace et al., 1981; Ebel and Helmberger, 1982; Hartzell and Helmberger, 1982; Cohn et al., 1982]. In a few events, seismic moments computed from surface waves were much larger than those computed from the average lengths and displacements of the surface fault breaks. This has been interpreted [Dewey and Julian, 1976; Chen and Molnar, 1977; Hart et al., 1977; Ben-Menahem, 1978] as evidence for an extent of rupture to depths even comparable to local crustal thicknesses of up to about 40 km (deep rupture, Figure 1b). However, this inference is at present not conclusive due to uncertainties in estimating seismic moments and slip distributions on fault planes.

Static models of fault displacement represent a further technique for estimating the depth of the bottom edge of a seismogenic fault plane. Figure 2 presents schematic diagrams of elasto-static solutions for fault slip and corresponding stress drop as a function of depth (they will be utilized later). Such idealized models have been employed to calculate the geodetically observed decline of surface displacement with distance from a fault break. However, different models with maximum slip depths varying by a factor of 3 can be fitted equally well to the data [Chinnery and Petrak, 1968; Mavko, 1981]. Therefore, this method does not yield a satisfactory resolution of deep fault slip.

Certain indications exist for involvement of deep fault planes in slow seismogenic rupture. Bonafede et al. [1983] have suggested that episodic slip events occur as immediate precursors on deep shear zones below a short-period rupture zone and emit very long-period waves recorded on strainmeters. Recently, Eyidogan and Jackson [1985] have found evidence in long-period seismograms for relatively late and slow-rupturing, normal-slip earthquake subevents. These occurred on low-angle fault planes representing a downward continuation and flattening of steeper fault planes that broke through the surface. It thus seems probable that large earthquakes have several fault planes of different size and orientation, each of which may radiate a different range of seismic frequencies. Maximum depths of faulting might in this case be derivable from long-period records. It is, however, unresolved at present how deep the dominantly short- and long-period slip planes may extend into the crust.

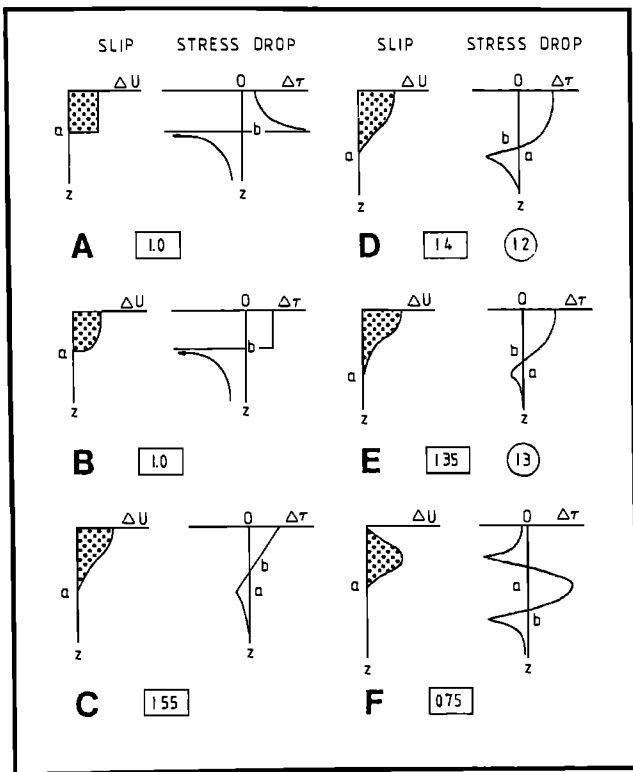


Fig. 2. Sketches of elastostatic fault slip ( $\Delta U$ ) and corresponding stress drop ( $\Delta \tau$ ) as functions of depth for strike-slip displacement. Slip is symmetrical about the fault axis, and only one half of it is shown. Stress drop is calculated relative to a constant prestress. Solutions are by the following authors: models A (dislocation) and B (crack): Chinnery [1969], Singh [1977]; model C (linear stress drop): Chinnery [1969], Yamashita [1978]; model D (quadratic stress drop): Barnett and Freund [1975], Mahrer and Nur [1979]; model E (cubic stress drop): Singh [1977]; model F (quadratic stress drop, solution for buried slip): Mahrer and Nur [1979]. Depth  $a$  indicates bottom edge of slip plane,  $b$  indicates equilibrium depth where stress drop changes sign (depths not to scale). Stress singularities in models A and B indicate that elastic theory does not apply and that plastic effects ought to be included. The numbers below each model are ratios  $r = a/b$  calculated from the solutions given in the above references, rounded to nearest 5%. Boxed values are for 1-D models of an infinitely long, narrow fault plane; circled values are for 2-D models of a circular fault plane. Solutions available for higher-order stress drop functions are not shown here but have similar shape as model E; in 1-D models [Yamashita, 1978],  $r = 1.3$  for fourth-order and  $r = 1.2$  for sixth-order stress drop; in 2-D models of fourth-order stress drop [Sato, 1972],  $r = 1.5$  for rectangular fault planes and  $r = 1.4$  for circular fault planes.

### Numerical Studies

While observational evidence for deep rupture extension is still rather indefinite, what has been learned from numerical rupture simulation? Burridge and Halliday [1971] solved the dynamical problem for a crack with constant tectonic stress and with dynamic stress drop varying quadratically with depth (static solution shown in model D, Figure 2). They found that the lower margin of the rupture plane is independent of the depth where rupture initiates. Dynamic slip extends to a depth 1.5 times the depth where stress drop becomes negative, thus overshooting the static slip depth by about 7%. Das [1982] and Day [1982] studied models with constant dynamic stress drop which showed that downward rupture may propagate far beyond the lower margin of high-stress drop regions, to depths where either zero or small stress drop was prescribed. Das and Scholz [1983] ran models with a linear increase of frictional strength and stress drop with depth and found a very small downward propagation for a crack nucleated at the deeper region with higher stress drop. A crack nucleating at shallow depth in the region with lower strength and stress drop did not propagate downward at all. Thus, the numerical results indicate that the relative depth distribution of frictional strength and stress drop controls the depth extent of seismic slip.

The relation between strength and slip is empirically explored in the remaining three chapters of this paper. In the following, I present a summary of focal depth data of continental earthquakes and their aftershock zones. Subsequently, the two fault concepts (shallow and deep extent of seismic rupture) will be tested using simple models for the relative distribution of shear and frictional strength on faults. In the final chapter, I will argue that it is perhaps premature at present to reject either of the two concepts.

### Main-Event Focal Depths and Depth Extent of Aftershock Zones

Most large earthquakes are followed by a series of aftershocks whose number decays exponentially with time. One can distinguish between three basic types of aftershocks: those distributed on a ruptured fault segment, those located at the margins of the rupture area, and those induced by the main event but located outside the fault break itself. The first type may be adjustments to inhomogeneities of rupture propagation left on the fault plane by the main event; the second type is thought to delineate unbroken barriers surrounding ruptured areas; the third type may spread over the volume in which strain energy was released by the main earthquake. The distribution of aftershocks among these three types depends on the physical and geometrical details of fault rupture and on time-dependent relaxation processes [Mikumo and Miyatake, 1979;

## 134 DEPTH EXTENT OF RUPTURE

TABLE I. List of Focal Depths of Continental Earthquakes

Year	Location	Main Event		Aftershocks	
		Focal Mechanism	Focal Depth (km)	90% Depth (km)	Deepest Event Depth (km)
1961	Robertson, Australia	T	19	18	19
1966	Parkfield, California	S	9	10	14
1966	Truckee, California	S	10	8	15
1968	Borrego Mountain, California	S	8	9	13
1971	San Fernando, California	T	13	11	15
1972	Bear Valley, California	S	7	8	11
1973	Point Mugu, California	T	12	16	18
1973	Picton, Australia	T	20	18	24
1973	Eastern Tennessee	(T)	9	8	15
1975	Haicheng, China	S	10*	12	17
1975	Pocatello, Idaho	N	9	10	16
1975	Pino Solo, Mexico	S	15	16	18
1975	Oroville, California	N	8*	9	12
1976	Guatemala, Central America	S	16	13	17
1976	Friuli, Italy	T	8*	11	15
1976	Songpan, China	T	10	14	19
1976	Mesa de Andrade, Mexico	S	9	12	13
1978	Puget Sound, Washington	S	24	25	28
1978	Thessaloniki, Greece	N	6	10	15
1978	Santa Barbara, California	T	13	14	15
1978	Swabian Jura, West Germany	S	7	10	13
1979	Coyote Lake, California	S	9*	10	11
1979	Imperial Valley, California	S	8	10	12
1980	Livermore Valley, California	S	11	12	15
1980	Pyrenees, France	(S)	4	6	8
1980	Mammoth Lakes, California	(S)	9	10	16
1980	Victoria, Mexico	S	12	13	14
1980	Sierentz, West Germany	S	12	13	14
1980	Sharpsburg, Kentucky	S	12*	14	15
1980	El Asnam, Algeria	T	12*	13	17
1980	Irpinea, Italy	N	16*	16	24
1981	Elk Lake, Washington	S	7	12	15
1982	New Brunswick, Canada	T	9	6	8
1983	Coalinga, California	T	9	11	14
1983	Guinea, Africa	S	13	12	15
1984	Morgan Hill, California	S	9	10	11

N. normal faulting; T. thrust faulting; S. strike slip. Parentheses indicate uncertain mechanisms.

\*Average of data from several authors.

Aki, 1979; Das and Scholz, 1981a,b; Reasenberg and Ellsworth, 1982; Stein and Lisowski, 1983; King and Yielding, 1984]. Here, in dealing with the depth distribution of seismicity, I compare the depth of rupture initiation in large earthquakes with the lower margin of their aftershock zones. From this comparison I intend to derive constraints on the two models of the depth extent of seismic rupture.

#### Focal Depth Data

Table I contains a list of 36 major continental earthquakes. The data given (location, focal

mechanism, hypocentral depth of the main events, and selected depths of aftershocks) were compiled from a literature survey. References for the data sources are omitted here for brevity but complete documentation will be given in another paper (J. Strehlau, manuscript in preparation, 1986). The list includes significant interplate and intra-plate events from 1966 to 1984 (plus one from 1961). Several other events were excluded from the data set, since depths (for either the main shock or the aftershocks) are not available.

The resolution of hypocentral location depends on station distribution, timing accuracy of arrivals, complexity of source time functions, and

quality of crustal velocity models. Hypocenters of about half of the main events were located with regional station networks, particularly those in California; the remainder were located by modeling teleseismic short- and/or long-period arrivals. Despite considerable progress with these techniques, the focal depths are not very accurate; uncertainties are usually around 3–5 km [Chen and Molnar, 1983; Christensen and Ruff, 1985]. An average value for the focal depth is used for those events for which conflicting results have been obtained by different authors (as indicated). The best-fitting point source depth derived from inversion of long-period waves (fault centroid) is perhaps shallower than the point of initial rupture located by short-period arrivals [Nakanishi and Kanamori, 1984]. There may thus be a systematic bias towards shallow depths for about half of the events in Table 1, but it is hoped that the size of the data set balances out these uncertainties.

Aftershocks were recorded by local station networks set up after the main events. Their depths are mostly precise to about 1–3 km. Two different aftershock depth values are given in Table 1: the 90% depth and the depth of the deepest aftershock. The 90% depth value indicates that particular depth above which 90% of those aftershocks given in the literature were located. Ten percent of the aftershocks were thus deeper than this depth. Introducing the 90% depth serves the purpose of providing an estimate for the depth range over which aftershock activity decays to zero. A comprehensive analysis of aftershock distributions revealed only occasionally abrupt terminations of seismic activity at depth (this was also noted by Sibson [1983]). Although aftershocks are usually concentrated towards the lower part of their depth distributions, the lowermost aftershocks often are just a few, isolated foci. Thus, the 90% depth assists in avoiding location errors which may in particular affect such isolated deep aftershocks; otherwise the conclusions drawn from an analysis of aftershock depths would inappropriately depend on the location of only single events. I will suggest in the discussion of shallow rupture that one may attach a physical significance to the 90% depth in the sense that it probably corresponds to the second of the three basic types of aftershocks mentioned above.

**Results.** Figure 3 shows a plot of 90% and deepest aftershock depths versus main-event depths of the earthquakes listed in Table 1. The figure reveals the following. (1) The hypocenters of 29 of the 36 main events are located between 7 and 13 km depth; two maxima are apparent, a major one at 9 km and a minor one at 12 km. (2) Of all located aftershocks, 90% are distributed between the earth's surface and a depth ranging 3–5 km above and below the hypocentral depth of the main event; the majority of the 90% depths lie up to 3 km below the main-event focus. (3) For two thirds of the main events, the deepest aftershocks are only up to 3–5 km deeper than the main-event

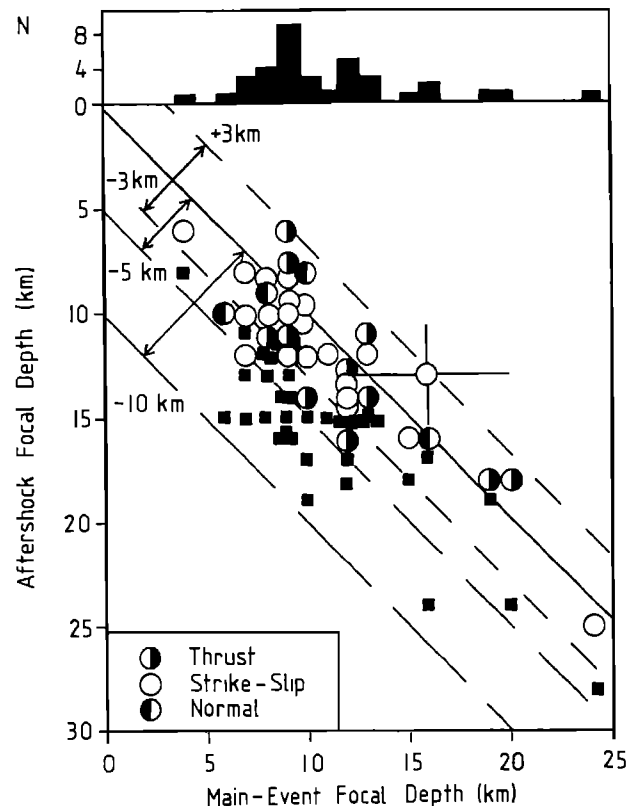


Fig. 3. Focal depths of main events versus selected focal depths of aftershocks (Table 1). Circles indicate 90% depth, squares show depths of deepest aftershock. Data plotted above (below) the solid line with slope 1 indicate depths above (below) the main-event hypocenter. Dashed lines indicate depths of 3 km above and 3, 5, and 10 km below the main-event hypocenters. The average location uncertainty affecting all depths is indicated for one data point. Histogram at top shows the frequency distribution of the main-event hypocenters.

hypocenters. For one third of them, the deepest aftershocks are significantly (more than 5 km) deeper than the main focus; however, there is no aftershock deeper than 9 km below it.

These observations appear to be independent of the focal depth and mechanism of the main events. Considering the uncertainties in the hypocentral locations, probably all one can safely conclude is that about 10% of the aftershocks are located below, but not more than about 5±2 km deeper than, the hypocenter of the main earthquakes. Thus, aftershock zones of continental earthquakes extend only marginally below the main hypocenter and do not reach deeply into the crust. Assuming that the sample of located earthquakes and aftershocks used here is a representative one, this result seems to be valid for all continents and for both interplate and intraplate regions.

## 136 DEPTH EXTENT OF RUPTURE

**Interpretation:**  
**Shallow and Deep Rupture Hypotheses**

What does the limited extent of deep aftershocks below main-event hypocenters imply for the depth of fault rupture? The size of aftershock zones is usually seen as direct indication for the downdip width (and length) of fault planes [Bonilla et al., 1984]. However, invoking the evidence for deep extent of rupture referred to earlier, I consider the two fault concepts (Figure 1) as alternative working hypotheses for interpreting the focal depth data. In the shallow rupture hypothesis, the lower boundary of an aftershock zone outlines the bottom margin of the main-event rupture area. This definition requires an explanation as to why rupture does not extend more than about 5±2 km beneath the hypocenter. In the deep rupture hypothesis, rupture does extend beyond the lower edge of the aftershock zone. Consequently, one needs to explain why aftershocks disappear at a depth of 5±2 km below the main-event hypocenter. In the first hypothesis, aftershocks are a constraint on inferring the depth extent of seismic rupture, whereas in the second hypothesis one would have to look for some other, independent evidence for the depth extent. The explanations needed will be derived from a fault strength model.

**Fault Strength Model**

It has been proposed that the dominantly temperature-dependent rheological properties of the crust determine the vertical extent of crustal microseismicity. This idea is compatible with geological observations at deeply eroded faults and textural studies of fault-related rocks (for a framework of terms for these rocks see Wise et al. [1984], Mawer et al. [1985], and Raymond et al. [1985]). Strehlau and Meissner [1983] have derived further support for this idea by showing that maximum focal depths in 40 seismically active areas on five continents correlate with conductive geotherms calculated from local heat flow data. Using friction and flow laws obtained from laboratory experiments, one can estimate shear strength profiles and explain the observed cut-off of seismicity by a change from frictional to ductile behavior of crustal rocks [e.g., Sibson, 1984]. A modified strength model for fault zones is suggested in this study. I will outline the rationale for constructing this model and present its relevant features; a detailed description and model calculations will be given elsewhere.

A relative distribution of fault strength corresponding to the fault structure depicted in Figure 1 is qualitatively shown in Figure 4. The model consists of three depth intervals (the depth values given below are averages for the San Andreas fault): (1) 0-9 km depth: a gouge zone with temperature-independent, frictional-sliding behavior, the strength (the maximum shear stress at failure) being negligible at the earth's sur-

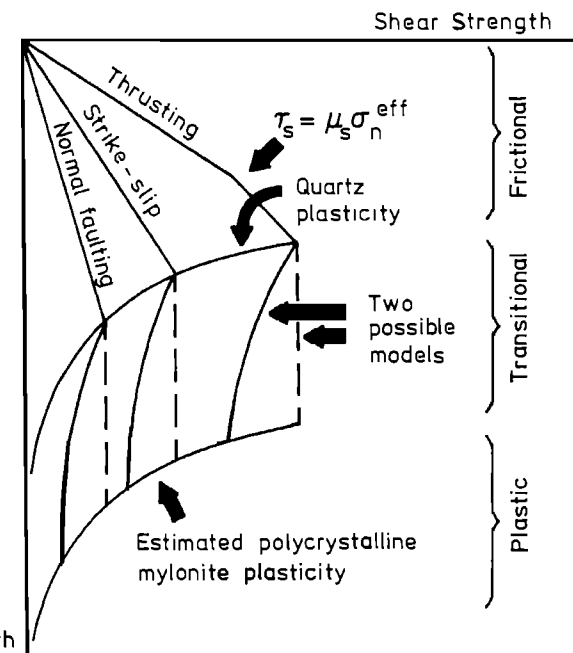


Fig. 4. The relative distribution of shear strength with depth for the three-layer fault model (Figure 1), as deduced from laboratory experiments and observations on fault rocks. Strength in the upper layer is assumed to follow Byerlee's [1978] results (static frictional shear stress  $\tau_s$  equals static coefficient of friction  $\mu_s$  times effective normal stress  $\sigma_n^{\text{eff}}$ ).  $\tau_s$  depends on the spatial orientation of principal stresses and, therefore, on the type of faulting according to the Anderson's criterion. Two hypothetical strength profiles are indicated in the transitional layer; the dashed profile is adopted here (see text). Strength in the lower layer is probably determined by steady state creep of mylonitic fault rocks. Scales are omitted to emphasize the current lack of reliable flow laws for fault rocks.

face and increasing linearly with depth according to Byerlee's [1978] results; (2) 9-15 km depth: a transition zone of combined brittle and ductile deformation, the strength resulting from an interaction between microcracking and crystal plastic flow; (3) below 15 km depth: a mylonite shear zone widening with depth and either ending in the lower crust or extending beneath the Moho into the upper mantle, the plastic (ductile) flow strength decreasing with depth due to increasing temperatures. Microseismic activity is thought to occur in the frictional and transition layers but to be absent in the fully plastic layer.

**Brittle-ductile transition.** To incorporate a transition zone in this model has primarily been motivated by results from studies of the brittle-ductile transition in rocks. A complex interaction between brittle (cataclasis) and ductile

(dislocation flow) micromechanisms, termed semi-brittle flow [e.g., Carter and Kirby, 1978; Carter et al., 1981; Bauer, 1984], has been found in experimentally deformed samples at intermediate confining pressures. Rock strength in the semibrittle regime has been reported to increase nonlinearly with increasing confining pressure. Although the deformation processes are rather complex and at present not fully understood, the semibrittle regime is taken into account because it has also been identified in specimens from naturally deformed shear zones [Hanmer, 1982; White and White, 1983].

A further argument supporting the concept of a transition zone is derived from the fact that steady state flow in crustal minerals [Kirby, 1983] covers a broad range in temperature at a given stress and strain rate. It is assumed here that the onset of brittle deformation in feldspar (a relatively strong mineral) determines the top edge of the plastic shear zone. The upper boundary of the transition layer is thought to be delineated by the onset of brittle behavior of quartz (a relatively weak mineral). In laboratory tests, the brittle-ductile transition occurs in quartz at temperatures about 200°C lower than in feldspar [Stesky, 1978; Tullis and Yund, 1980]. This divergence of the transition in the two dominant crustal minerals corresponds to a depth interval where brittle and ductile deformation processes overlap on fault zones. The depth and thickness of the transition zone may range from only a few kilometers to an extent involving middle and lower crustal levels, depending on geotherms and compositions of deep fault rocks.

Transition layer strength. A gradual shift in the orientation of fractures with increasing temperature has been found in semibrittle deformation: high-temperature faults are mainly oriented towards the direction of maximum resolved shear stress, i.e. close to an angle of 45° to the principal stress axes [Shelton et al., 1981; Ross et al., 1983; Bauer, 1984]. This suggests that the coefficient of internal friction in the Coulomb-Mohr failure criterion [Handin, 1969] approaches zero. Correspondingly, the coefficient of static friction may decrease with temperature (see also Stesky [1978]). This perhaps implies that the counteracting effects of pressure on frictional stress and of temperature on flow stress may roughly balance out, and it seems likely that the strengths for static friction and plastic flow coincide in the transition layer.

Two hypothetical strength profiles are shown in Figure 4. The solid line indicates a slightly depth-dependent strength decrease from a maximum at the depth where the frictional stress is equal to the quartz flow stress (an inverted curve with slightly increasing strength would similarly be possible). The dashed line indicates a constant strength which is adjusted in such a way that the flow stress of quartz at the transition layer's upper edge equals the flow stress of feldspar at its lower edge for identical strain rates, there-

by resulting in a depth-independent strength. This strength plateau in the transition zone is tentatively adopted in this paper.

This simplified, qualitative strength profile accounts for slip rate-independent, rock-on-rock frictional sliding and for low-strain, steady state deformation observed in the laboratory. Time-dependent fault behavior, however, is very important in the cyclic accumulation and release of crustal strain [Mavko, 1981; Thatcher, 1983]. Furthermore, fault rocks are intensely sheared; dynamic recrystallization and metamorphic reactions [White et al., 1980; Tullis et al., 1982] most likely alter the flow mechanisms compared to those operating in small-scale experiments of short duration. Therefore, the model provides a more or less tenable, though not necessarily realistic, approximation to true fault strengths. Disregarding these uncertainties, I utilize the model in the following to explain the implications of the two rupture hypotheses.

#### Influence of Fault Strength on Depth of Rupture

Semibrittle deformation in the transition zone gives rise to the formation of cracks at stress concentrations. The cracks may grow and coalesce gradually, their linkage involving stable frictional sliding on the crack surfaces. Eventually, when a crack has critical length, sliding becomes unstable and accelerates rapidly to seismogenic rupture [Das and Scholz, 1981a; S. T. Tse and J. R. Rice, unpublished manuscript, 1986]. Let us suppose that the strength contours sketched in Figure 4 represent the tectonic prestress on a fault immediately prior to a large earthquake. The critical-stress level rupture condition [Freund, 1979] permits the inference that rupture nucleates at the depth where the prestress equals the static frictional strength. In the context of the strength model, an earthquake focus would thus be located at the top of the transition zone. This is consistent with the focal depth data summarized above which showed that rupture initiates preferably at upper-crustal depths. The rupture front sweeps across the fault plane, with stress dropping to the dynamic friction stress. I consider in the following how the depth extent of rupture scales with the dynamic friction stress by parameterizing the stress drop relative to the constant prestress in the transition layer.

Stress drop models. Stress drop may fluctuate widely on a fault plane. A large number of complicated stress drop functions [Mavko, 1982] are available for inferring corresponding variations of friction stress. However, I approach this problem rather fundamentally by using the idealized elastostatic stress drop models from Figure 2. These solutions were calculated for constant prestress and are thus compatible with the strength plateau in the transition zone. Static fault slip corresponds to the low-frequency level in source spectra [Boatwright, 1984]. Therefore, I carefully make use of the term "slip" to dis-

## 138 DEPTH EXTENT OF RUPTURE

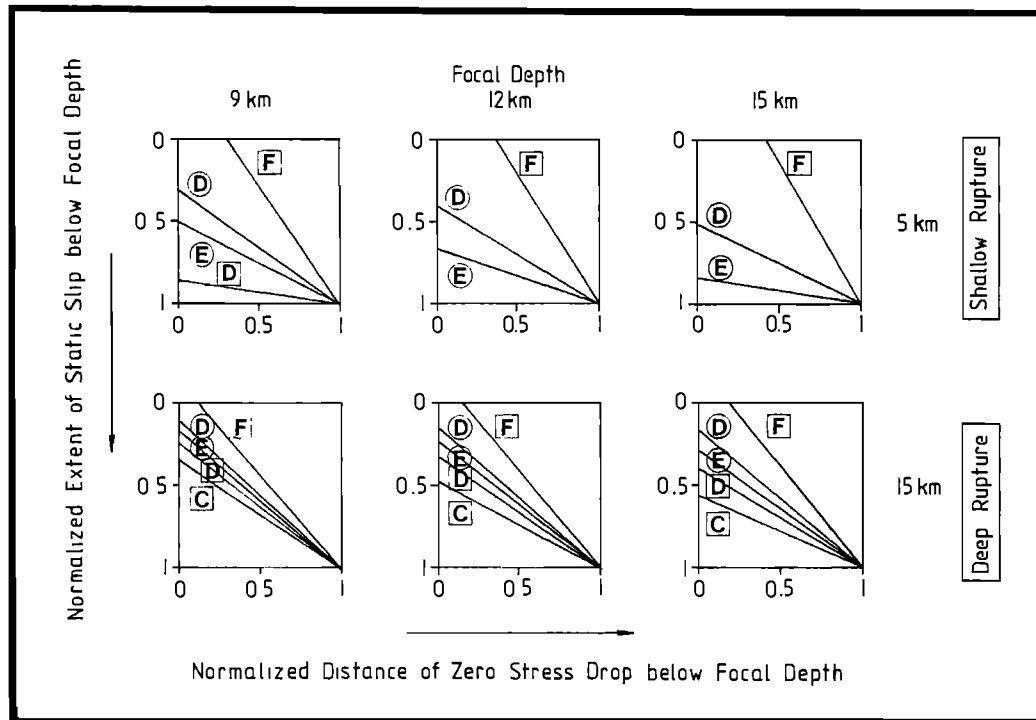


Fig. 5. Static slip extent below focus versus distance of zero (equilibrium) stress drop below focus, as predicted by solutions given in Figure 2 (capital letters). Boxed letters refer to rectangular slip planes, circled letters to circular slip planes. Plots are scaled according to the maximum slip extension below focus indicated at right (5 km, shallow rupture hypothesis; 15 km, deep rupture hypothesis). Focal depth values (9, 12, and 15 km) were chosen from the depth distribution shown in Figure 3. To obtain total depth extent of slip, add focal depth to appropriate fraction of 5 or 15 km, respectively. At each focal depth, the slopes of the curves correspond to the  $r$  values of the static slip solutions (Figure 2) and thus to the particular stress drop functions. Models that are compatible with the given maximum depth extents of slip are indicated. Curves for models A, B, as well as E (rectangular fault planes) are omitted.

tinguish static fault displacement from the truly dynamic rupture process in which abrupt changes in rupture velocity generate high-frequency acceleration pulses [Madariaga, 1983]. Note, however, that we are dealing with "dynamic" (i.e., kinetic, as opposed to static) friction stress.

We proceed as follows. The fault slip models shown in Figure 2 indicate that slip in an earthquake may actually increase stress on the lower section of the fault plane and even for some distance beyond its lower edge (negative static stress drop). The solutions result in an intrinsic coupling of maximum fault depth ( $a$ ) to the equilibrium depth ( $b$ ) where stress drop becomes negative. Ratios  $r = a/b$  are given in the figure;  $r$  varies from 0.75 (model F) to 1.55 (model C). The solutions predict the downward slip extension ( $d$ ) below the hypocenter depth ( $f$ ) to be governed by the distance ( $e$ ) by which the equilibrium depth is located below the hypocenter. One can thus write  $a = f + d$  and  $b = f + e$ . Substituting  $a = b r$ , one obtains  $d = r e + (r-1) f$ . Figure 5

displays plots of this expression normalized by two different maximum  $d$  values (5 and 15 km) and by corresponding maximum  $e$  values for three focal depths (9, 12, and 15 km). The figure indicates that the depth extent of slip below the focus for a given normalized equilibrium depth increases with increasing ratio  $r$ . This means that sliding is brought to a halt by the increasing difference between the prestress and the dynamic friction stress after passing the equilibrium depth. The distance over which slip can propagate into the negative stress drop region before being arrested depends on the stress drop solution and thus on the distribution of dynamic friction stress. For example, a maximum slip extension of 5 km below the focal depths chosen is incompatible with the dynamic stress drop given in model C. Let us see this in more detail. (Model F, where sliding stops in a region of positive stress drop, will briefly be discussed in the next chapter.)

Linear stress drop function. Model C is applied to demonstrate how dynamic friction stress

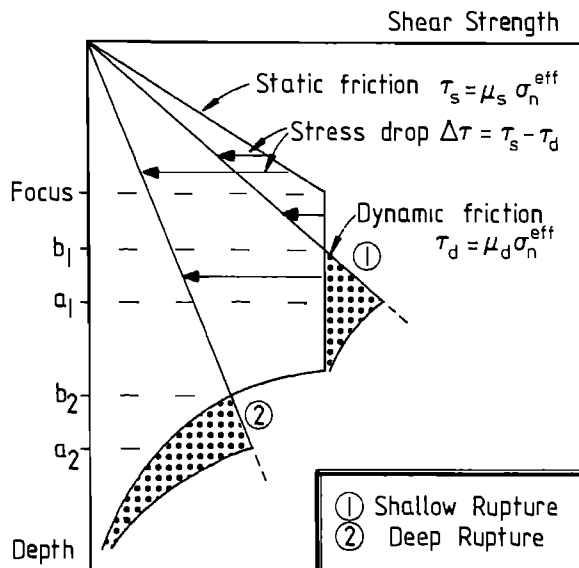


Fig. 6. Schematic diagram of fault strength distribution (from Figure 4) compared to two linear gradients of dynamic friction stress  $\tau_d$  (model C, Figure 2). The coefficient of dynamic friction  $\mu_d$  is high for shallow rupture extension and low for deep rupture extension. Depths  $a$  and  $b$  correspond to those used in Figure 2. Negative stress drop is indicated by dotted areas.

controls whether slip is stopped in the transition zone (shallow rupture hypothesis) or whether it penetrates deeply into the mylonite shear zone (deep rupture hypothesis). This is illustrated in Figure 6, showing the prestress model together with the corresponding dynamic friction stress. The diagram deviates from model C (Figure 2) in that stress drop in the uppermost layer is not constant but increases with depth. Accordingly, stress drop has a peak at the focus, though this is probably irrelevant for slip in the transition layer. Stress drop is negative below the equilibrium depth, where the dynamic friction stress becomes larger than the prestress. Abo-Zena [1981] has calculated that dynamic rupture for model C extends to a depth of about 1.7 times the equilibrium depth, overshooting the maximum depth of static slip by less than 10%. The static solution thus represents a reasonable approximation to the maximum depth of dynamic rupture.

The ratio of the coefficient of dynamic friction to the coefficient of static friction can be calculated from the equality of static friction stress at the focus to dynamic friction stress at the equilibrium depth, using the appropriate  $\tau$  value for model C. Results are plotted in Figure 7 against slip extent below the focus. For the shallow rupture hypothesis with focal depths of less than 12 km, the coefficient of dynamic friction is found to be 0.9–1.0 times the coefficient of static friction. This estimate agrees reason-

ably well with coefficients of dynamic friction measured in the laboratory (0.8–0.97, Dieterich [1974]). Thus, interpreting the observed cut-off depth of aftershocks as indicative of a shallow slip extension turns out to require a dynamic friction stress only slightly lower than the static friction stress. In the deep rupture hypothesis, slip propagating deeper into the crust than the maximum depth of aftershocks requires dynamic friction coefficients significantly lower than inferred above, namely as low as about 0.5 times the static friction coefficient (for slip extending up to 20 km beneath the focus).

The temperature influence on prestress in the plastic layer was ignored in this calculation. If it had been included, the ratio of dynamic to static coefficients of friction would decrease even more strongly with deep slip extent than is shown in Figure 7. Furthermore, model C implies constant friction coefficients and thus gives an upper bound for the estimated dynamic friction coefficient. If other models from Figure 2 had instead been used, the dynamic friction coefficients would vary with depth. Clearly, this would be more realistic than the simple assumption of a linear increase of friction stress with depth, since friction in dynamic rupture is probably a complex function of local tectonic prestress, slip velocity, and displacement on a fault plane.

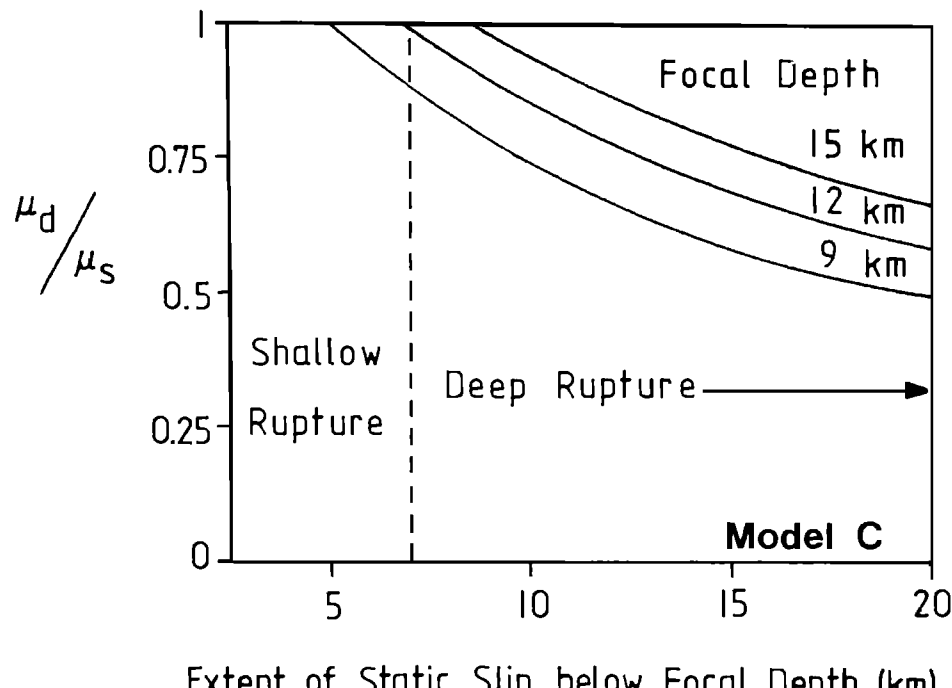
#### Discussion

Combining the fault strength model with the linear stress drop solution has indicated that a high coefficient of dynamic friction causes shallow rupture and a low coefficient causes deep rupture. Implications of this result for aftershock generation are now discussed separately for each faulting hypothesis.

#### Shallow Rupture Hypothesis

Seismic slip may be prevented from penetrating below the lower boundary of the transition zone by a dynamic friction stress increasing with depth and a tectonic prestress decreasing due to ductile flow in the mylonite layer. The negative stress drop below the focus is superimposed on the prestress in the transition zone. Although this stress concentration falls off beyond the lower edge of the fault plane, it may still be sufficiently high to reach the static friction strength which may perhaps be necessary for the initiation of deep aftershock activity. In this case, aftershocks may not only occur on the lower section of the ruptured fault plane but may also be induced underneath its lower edge. Thus, by considering the aftershock data summarized earlier on, it can be said that at least 90% of the aftershocks occur on the fault plane or are distributed within a volume around the fault at shallow depths. The deepest 5–10% of the aftershocks may be located beneath the ruptured fault plane assuming that slip extends only a very

## 140 DEPTH EXTENT OF RUPTURE



Extent of Static Slip below Focal Depth (km)

Fig. 7. Ratio of dynamic to static friction coefficients calculated from model C, Figure 2 (linear static stress drop) as a function of static slip extent below hypocenter. The shallow rupture hypothesis implies a slip extent of up to 5+2 km below the focus; the deep rupture hypothesis implies an extent of more than 7 km. Curves are shown for three focal depths (cf. Figure 5), assuming that the transition layer with constant prestress extends to depths of 29, 32, and 35 km, respectively.

short distance (less than 5 km) below the focus. Each aftershock redistributes the stress concentration of the main event by its own positive and negative stress drop. Aseismic stress relaxation may occur if the stress increase fails to reach the static friction strength.

This simple concept of aftershock generation may apply only if maximum fault displacement is at the surface, as in models A through E (Figure 2). The model for buried fault slip, model F, may be adequate for an earthquake with no, or only negligible, surface offset and with maximum slip around the hypocenter. The negative stress drop of this model may be too deep to surpass the static friction strength below the hypocenter. Therefore, a fault with buried displacement may not generate deep aftershocks, and the stress increase will perhaps be relaxed aseismically. In fact, deep aftershocks were not observed below the hypocenters of the following moderate strike-slip earthquakes in California with buried slip: 1966 Parkfield [Ak1, 1979; Bouchon, 1979], 1968 Borrego Mountain [Ebel and Helmberger, 1982], 1979 Coyote Lake [Reasenberg and Ellsworth, 1982; Liu and Helmberger, 1983], and 1979 Imperial Valley [Hartzell and Helmberger, 1982; Doser and Kanamori, 1986]. (The deep aftershocks of these events listed in Table 1 were located some distances away from the hypocenters.) However, the

relative scarcity of aftershocks also observed above the hypocenters of these events apparently indicates a positive stress drop on the shallow fault section which is not predicted by the static model for buried slip. This clearly points to the limited applicability of the simple elastostatic slip models in investigating the complex dynamic rupture process in large earthquakes.

#### Deep Rupture Hypothesis

In the alternative hypothesis, deep rupture propagation has been inferred to occur at low dynamic friction stress. While such inference seems inconsistent with results from friction experiments [Dieterich, 1974], several mechanisms for a reduction of dynamic friction during an earthquake have been proposed: fault melting [McKenzie and Brune, 1972; Sibson, 1975, 1979; Richards, 1976; Cardwell et al., 1978, 1979], dehydration of fault gouge [Raleigh, 1977], and thermal expansion of pore fluids [Sibson, 1973; Lachenbruch, 1980; Mase and Smith, 1985]. Each of these thermodynamic processes may cause fault lubrication and thus near-total stress release. Since these processes depend on the relative distribution of frictional heat that is generated and on ambient temperature, pore pressure, and permeability, they may occur at different depth

levels. Dehydration and pore fluid expansion are possibly effective on shallow fault sections where hydrated fault gouge is present. Fault melting could also be reasonably expected at shallow depths of less than about 5-10 km. Therefore, many of the pseudotachylite rocks that were probably generated by frictional melting on shallow sections of ancient faults seem to postdate the ductile deformation of uplifted and exposed mylonites in which they occur [Allen, 1979].

A key point is that fault melting might be a likely mechanism for deep rupture extension if temperatures at mid-crustal depths are above about one half of the melting temperature and if slip velocities around hypocenters are sufficiently high to induce melting [Richards, 1976]. Pseudotachylites can only be interpreted as field evidence for deep rupture extension if they originated at depths below 15-20 km by frictional melting of mylonites and subsequently deformed in a ductile manner. In fact, such traces of deeply propagating ruptures have occasionally been found in exposed mylonite shear zones [Sibson, 1980; Passchier, 1982, 1984; Obee and White, 1985]. However, these pseudotachylites may rarely be preserved, since they are probably easily obliterated by the extensive ductile shearing at these depths [Sibson, 1980]. To date, experience in the search for ductilely deformed pseudotachylites seems somewhat frustrating, because the deeper a fault rupture extends the less likely may geological evidence for it be obtainable. Deep fault rocks might be accessible only where they were carried rapidly toward the surface by sufficient uplift, erosion, and/or thrusting. Therefore, one should perhaps not anticipate surprising and unequivocal discoveries of very deeply generated pseudotachylites, and the maximum depth of seismic faulting might hence be expected to remain rather obscure. One is nonetheless tempted to speculate that a melt-lubricated fault plane may even extend down to the Moho, probably ending there because the melting temperature in the mantle is higher than in the lower crust.

Why then are aftershocks confined to the upper section of a deep fault plane? When deep rupture has stopped, the molten fault plane will presumably be very soft until it cools and solidifies. It may flow at low strength and will therefore not generate aftershocks. The cut-off depth of aftershocks may indicate the depth of onset of melting. An absence of shallow aftershocks may indicate that a reduction of friction stress and thus near-total stress release may also occur on the shallow section of fault planes. This seems compatible with the observed sparsity of shallow aftershocks in the earthquakes noted above.

#### Both Hypotheses as Potential Source Mechanisms

I am not aware at present of any physical argument which would rule out either one of the two fault plane hypotheses. Although this cannot provide absolute proof, there is some indication

that the deep rupture hypothesis can explain the seismological and geological observations in a reasonably consistent manner. Therefore, as long as it is still unknown to what depths seismogenic faulting does in fact extend, I suggest that both shallow and deep rupture be regarded as equally possible modes of source mechanisms in large earthquakes. To what extent the deep rupture model is an accurate description of seismic faulting is still to be fully determined.

For one thing, the influence of thermodynamic dissipation on dynamic rupture must be understood better before it can be decided with some certainty whether deep rupture extension due to fault plane melting indeed occurs. Perhaps one should also consider rapid plastic propagation of deep fault rupture, since the region ahead of the crack tip may not only fracture in a brittle mode but may also fail by plastic flow (slip line theory for nonlinear stress-strain relations). Either way, deep rupture propagation may proceed rather smoothly, with little radiation of high-frequency waves [Madariaga, 1983]. However, propagation of the deep rupture front may cease quite abruptly as soon as melt production stops for some reason. This sudden arrest would radiate a rather late but fairly energetic pulse (stopping phase) which may be observable on seismograms.

Information from aftershock data. Aftershock fault plane solutions may aid in detecting deep rupture extension. Rybicki [1973, p. 419] concluded, from 2-D dislocation models of the stress concentration induced by an earthquake with shallow fault plane, that "Aftershocks generated in the deeper part of the hypocentral zone should, in general, have the fault plane solution more different from that of the main shock than the aftershocks generated in the upper part of the hypocentral zone." Recently developed techniques to infer the regional best-fit stress tensor from multiple focal mechanisms of aftershock series [Vasseur et al., 1983; Gephart and Forsyth, 1984] may be applied to look for significant changes in the stress tensor with depth on a single fault section. One might infer that fault rupture is shallow in those earthquakes for which the deeper aftershocks show a strong deviation from the mean stress tensor fitting the shallower events. Conversely, a deep rupture extension could for those earthquakes be likely for which such stress deviations in the deeper aftershocks are not observed, because the stress field generated by the lower edge of the fault plane might be too deep to influence the aftershock stress tensor.

It is worth noting that lateral variations of maximum aftershock depths along fault planes are often observed [Reasenberg and Ellsworth, 1982]. Variations may occur in response to spatial heterogeneity of strength, temperature, pore pressure, rock type, fault dip, and pre-event history [Sibson, 1984]. The 1-D analysis carried out here is inadequate for inferring corresponding lateral variations in the depth extent of rupture. A large earthquake may well consist of a combina-

## 142 DEPTH EXTENT OF RUPTURE

tion of the shallow- and deep-slip rupture modes: the lower edge of the rupture plane may on some fault sections be indicated by the aftershock zone and may on other fault sections penetrate below the deepest aftershocks.

The maximum depth of aftershocks is perhaps determined by the depth in which the mechanism causing the time delay of aftershocks can operate. If stress corrosion [Anderson and Grew, 1977] is the delay mechanism, the depth to which water is present on a fault might be an important factor. In that case, aftershocks would have little to say about the maximum depth of seismic faulting. Temperature may also influence aftershock cut-off depths, since the data summarized above are from a variety of heat flow provinces.

## Conclusions

This paper has debated whether fault planes of continental earthquakes do extend deeply into the crust. Using idealized models of the distribution of tectonic prestress and static stress drop on a fault, it has been demonstrated that the dynamic friction stress may control the depth to which a fault break can advance. Two types of faulting (shallow and deep rupture) have accordingly been formulated as potential source mechanisms.

In the shallow rupture mechanism, fault slip extension to a depth of about 5±2 km below the main-event hypocenter (as inferred from maximum focal depths of aftershock locations) may occur if the dynamic friction stress at depth is high. Rupture apparently stops because the tectonic prestress becomes less than the stress that would be needed to further continue rupture. Using a linear stress drop function, the coefficient of dynamic friction has been estimated to be about 0.9 times the coefficient of static friction. In the deep rupture mechanism, the dynamic friction stress must be low enough to ensure rupture propagation down into the ductile layer of a fault. A mechanism which would likely reduce dynamic friction is frictional melting of deep fault rocks. In this case, aftershock activity would occur only on the upper part of a fault plane.

The results of this discussion emphasize that one may perhaps unintentionally arrive at erroneous estimates of the width of fault planes by inferring them directly from aftershock zones. While deep rupture has not been proven to indeed be an admissible source mechanism, it would seem advisable to search in seismograms, aftershock fault plane solutions, and deeply exposed shear zones for convincing indications of deep rupture extension in large earthquakes.

**Acknowledgments.** Several ideas presented here were inspired by discussions with K. Regenauer-Lieb. A conversation with R. Dmowska and J. Rice was beneficial at an early stage in my efforts to comprehend the source mechanics of deep rupture. Moreover, they were so kind as to inform me about results of their work ahead of publication. C.

Langston contributed a helpful comment. J. Savage and R. Sibson provided constructive reviews of the manuscript. P. Stegmann dedicated her time to help with drafting. My thanks go to each of these individuals and to the organizers of the Maurice Ewing Conference for making it possible for me to attend. Part of this work was supported by the Deutsche Forschungsgemeinschaft.

## References

- Abo-Zena, A., Strike-slip on a fault caused by an oblique wave, *Bull. Seismol. Soc. Am.*, 71, 405-422, 1981.
- Aki, K., Characterization of barriers on an earthquake fault, *J. Geophys. Res.*, 84, 6140-6148, 1979.
- Allen, A. R., Mechanism of frictional fusion in fault zones, *J. Struct. Geol.*, 1, 231-243, 1979.
- Anderson, O. L., and P. C. Grew, Stress corrosion theory of crack propagation with applications to geophysics, *Rev. Geophys.*, 15, 77-104, 1977.
- Archuleta, R. J., A faulting model for the 1979 Imperial Valley earthquake, *J. Geophys. Res.*, 89, 4559-4585, 1984.
- Barnett, D. M., and L. B. Freund, An estimate of strike-slip fault friction stress and fault depth from surface displacement data, *Bull. Seismol. Soc. Am.*, 65, 1259-1266, 1975.
- Bauer, S. J., Semibrittle deformation of granite at upper crustal conditions, Ph. D. thesis, 186 pp., Texas A&M Univ. College Station, 1984.
- Ben-Menahem, A., Source mechanism of the 1906 San Francisco earthquake, *Phys. Earth Planet. Inter.*, 17, 163-181, 1978.
- Boatwright, J., The effect of rupture complexity on estimates of source size, *J. Geophys. Res.*, 89, 1132-1146, 1984.
- Bonafede, M., E. Boschi, and M. Dragoni, Viscoelastic stress relaxation on deep fault sections as a possible source of very long period elastic waves, *J. Geophys. Res.*, 88, 2251-2260, 1983.
- Bonilla, M., R. K. Mark, and J. J. Lienkaemper, Statistical relations among earthquake magnitude, surface rupture length, and surface fault displacement, *Bull. Seismol. Soc. Am.*, 74, 2379-2411, 1984.
- Bouchon, M., Predictability of ground displacement and velocity near an earthquake fault: an example: the Parkfield earthquake of 1966, *J. Geophys. Res.*, 84, 6149-6156, 1979.
- Burridge, R., and G. S. Halliday, Dynamic shear cracks with friction as models for shallow focus earthquakes, *Geophys. J. R. Astron. Soc.*, 25, 261-283, 1971.
- Byerlee, J., Friction of rocks, *Pure Appl. Geophys.*, 116, 615-626, 1978.
- Cardwell, R. K., D. S. Chinn, G. F. Moore, and D. L. Turcotte, Frictional heating on a fault zone with finite thickness, *Geophys. J. R. Astron. Soc.*, 52, 525-530, 1978.
- Cardwell, R. K., D. S. Chinn, G. F. Moore, and D.

- L. Turcotte, Authors' reply to 'A comment on 'Frictional heating on a fault zone with finite thickness'', Geophys. J. R. Astron. Soc., 56, 239-240, 1979.
- Carter, N. L., and S. H. Kirby, Transient creep and semibrittle behavior of crystalline rocks, Pure Appl. Geophys., 116, 807-839, 1978.
- Carter, N. L., D. A. Anderson, F. D. Hansen, and R. L. Kranz, Creep and creep rupture of granitic rocks, in Mechanical Behavior of Crustal Rocks, edited by N. L. Carter, M. Friedman, J. M. Logan, and D. W. Stearns, pp. 61-82, Geophys. Monogr. Ser. 24, AGU, Washington, D.C., 1981.
- Chen, W.-P., and P. Molnar, Seismic moments of major earthquakes and the average rate of slip in Central Asia, J. Geophys. Res., 82, 2945-2969, 1977.
- Chen, W.-P., and P. Molnar, Focal depths of intracontinental and intraplate earthquakes and their implications for the thermal and mechanical properties of the lithosphere, J. Geophys. Res., 88, 4183-4214, 1983.
- Chinnery, M. A., Theoretical fault models, in A Symposium on Processes in the Focal Region, edited by K. Kasahara and A. E. Stevens, pp. 211-223, Publ. 37, Earth Phys. Branch, Ottawa, Ont., 1969.
- Chinnery, M. A., and J. A. Petrak, The dislocation fault model with a variable discontinuity, Tectonophysics, 5, 513-529, 1968.
- Christensen, D. H., and L. J. Ruff, Analysis of the trade-off between hypocentral depth and source time function, Bull. Seismol. Soc. Am., 75, 1637-1656, 1985.
- Cohn, S. N., T.-L. Hong, and D. V. Helmberger, The Oroville earthquakes: a study of source characteristics and site effects, J. Geophys. Res., 87, 4585-4594, 1982.
- Das, S., Appropriate boundary conditions for modeling very long earthquakes and physical consequences, Bull. Seismol. Soc. Am., 72, 1911-1926, 1982.
- Das, S., and C. H. Scholz, Theory of time-dependent rupture in the earth, J. Geophys. Res., 86, 6039-6051, 1981a.
- Das, S., and C. H. Scholz, Off-fault aftershock clusters caused by shear stress increase?, Bull. Seismol. Soc. Am., 71, 1669-1675, 1981b.
- Das, S., and C. H. Scholz, Why large earthquakes do not nucleate at shallow depths, Nature, 305, 621-623, 1983.
- Day, S. M., Three-dimensional simulation of spontaneous rupture: the effect of nonuniform prestress, Bull. Seismol. Soc. Am., 72, 1881-1902, 1982.
- Dewey, J. W., and B. R. Julian, Main event source parameters from teleseismic data, in The Guatemalan Earthquake of February 4, 1976, A Preliminary Report, pp. 19-23, U.S. Geol. Surv. Prof. Pap. 1002, 1976.
- Dieterich, J. H., Earthquake mechanisms and modeling, Annu. Rev. Earth Planet. Sci., 2, 275-301, 1974.
- Doser, D. I., and H. Kanamori, Depth of seismicity in the Imperial Valley region (1977-1983) and its relationship to heat flow, crustal structure, and the October 15, 1979, earthquake, J. Geophys. Res., 91, 675-688, 1986.
- Ebel, J., and D. V. Helmberger, P-wave complexity and fault asperities: the Borrego Mountain, California earthquake of 1968, Bull. Seismol. Soc. Am., 72, 413-437, 1982.
- Eyidogan, H., and J. Jackson, A seismological study of normal faulting in the Demirci, Alasehir and Gediz earthquakes of 1969-70 in western Turkey: implications for the nature and geometry of deformation in the continental crust, Geophys. J. R. Astron. Soc., 81, 569-607, 1985.
- Freund, L. B., The mechanics of dynamic shear crack propagation, J. Geophys. Res., 84, 2199-2209, 1979.
- Gephart, J. W., and D. W. Forsyth, An improved method for determining the regional stress tensor using earthquake focal mechanism data: application to the San Fernando earthquake sequence, J. Geophys. Res., 89, 9305-9320, 1984.
- Handin, J., On the Coulomb-Mohr failure criterion, J. Geophys. Res., 74, 5343-5348, 1969.
- Hanmer, S. K., Microstructure and geochemistry of plagioclase and microcline in naturally deformed granite, J. Struct. Geol., 4, 197-213, 1982.
- Hart, R. S., R. Butler, and H. Kanamori, Surface-wave constraints on the August 1, 1975, Oroville earthquake, Bull. Seismol. Soc. Am., 67, 1-7, 1977.
- Hartzell, S., and D. V. Helmberger, Strong-motion modeling of the Imperial Valley earthquake of 1979, Bull. Seismol. Soc. Am., 72, 571-596, 1982.
- Heaton, T. H., The 1971 San Fernando earthquake: a double event?, Bull. Seismol. Soc. Am., 72, 2037-2062, 1982.
- King, G., and G. Yielding, The evolution of a thrust fault system: processes of rupture initiation, propagation and termination in the 1980 El Asnam (Algeria) earthquake, Geophys. J. R. Astron. Soc., 77, 915-933, 1984.
- Kirby, S. H., Rheology of the lithosphere, Rev. Geophys., 21, 1458-1487, 1983.
- Lachenbruch, A. H., Frictional heating, fluid pressure, and the resistance to fault motion, J. Geophys. Res., 85, 6097-6112, 1980.
- Langston, C. A., The February 9, 1971 San Fernando earthquake: a study of source finiteness in teleseismic body waves, Bull. Seismol. Soc. Am., 68, 1-29, 1978.
- Liu, H.-L., and D. V. Helmberger, The near-source ground motion of the 6 August 1979 Coyote Lake, California, earthquake, Bull. Seismol. Soc. Am., 73, 201-218, 1983.
- Madariaga, R., High frequency radiation from dynamic earthquake fault models, Ann. Geophys., 1, 17-23, 1983.
- Mahrer, K. D., and A. Nur, Strike slip faulting in a downward varying crust, J. Geophys. Res., 84, 2296-2302, 1979.

## 144 DEPTH EXTENT OF RUPTURE

- Mase, C. W., and L. Smith, Pore-fluid pressures and frictional heating on a fault surface, *Pure Appl. Geophys.*, 122, 583-607, 1985.
- Mavko, G. M., Mechanics of motion on major faults, *Annu. Rev. Earth Planet Sci.*, 9, 81-111, 1981.
- Mavko, G. M., Easy computation of static stress drop, slip, and moment on two-dimensional heterogeneous faults, *Bull. Seismol. Soc. Am.*, 72, 1499-1508, 1982.
- Mawer, C. K., D. U. Wise, D. E. Dunn, J. T. Engelder, P. A. Geiser, R. D. Hatcher, S. A. Kish, A. L. Odom, and S. Schamel, Comment and reply on "Fault-related rocks: suggestions for terminology", *Geology*, 13, 378-379, 1985.
- McKenzie, D., and J. N. Brune, Melting on fault planes during large earthquakes, *Geophys. J. R. Astron. Soc.*, 29, 65-78, 1972.
- Meissner, R., and J. Strehlau, Limits of stresses in continental crusts and their relation to the depth-frequency distribution of shallow earthquakes, *Tectonics*, 1, 73-89, 1982.
- Mikumo, T., and T. Miyatake, Earthquake sequences on a frictional fault model with non-uniform strengths and relaxation times, *Geophys. J. R. Astron. Soc.*, 59, 497-522, 1979.
- Munguia, L., and J. N. Brune, Simulations of strong ground motion for earthquakes in the Mexicali-Imperial Valley region, *Geophys. J. R. Astron. Soc.*, 79, 747-771, 1984.
- Nakanishi, I., and H. Kanamori, Source mechanisms of twenty-six large, shallow earthquakes ( $M_s \geq 6.5$ ) during 1980 from P-wave first motion and long-period Rayleigh wave data, *Bull. Seismol. Soc. Am.*, 74, 805-818, 1984.
- Obee, H. K., and S. H. White, Faults and associated fault rocks of the Southern Arunta block, Alice Springs, Central Australia, *J. Struct. Geol.*, 7, 701-712, 1985.
- Passchier, C. W., Pseudotachylite and the development of ultramylonite bands in the Saint-Barthélemy Massif, French Pyrenees, *J. Struct. Geol.*, 4, 69-79, 1982.
- Passchier, C. W., The generation of ductile and brittle shear bands in a low-angle mylonite zone, *J. Struct. Geol.*, 6, 273-281, 1984.
- Raleigh, C. B., Frictional heating, dehydration, and earthquake stress drops, in *Proceedings of Conference II Experimental Studies of Rock Friction with Application to Earthquake Prediction*, pp. 291-304, U.S. Geological Survey, Menlo Park, Calif., 1977.
- Raymond, L. A., D. U. Wise, D. E. Dunn, T. Engelder, P. A. Geiser, R. D. Hatcher, S. A. Kish, A. L. Odom, S. Schamel, Comment and reply on "Fault-related rocks: suggestions for terminology", *Geology*, 13, 218-219, 1985.
- Reasenberg, P., and W. L. Ellsworth, Aftershocks of the Coyote Lake, California, earthquake of August 6, 1979: a detailed study, *J. Geophys. Res.*, 87, 10,637-10,655, 1982.
- Richards, P. G., Dynamic motions near an earthquake fault: a three-dimensional solution, *Bull. Seismol. Soc. Am.*, 66, 1-32, 1976.
- Ross, J. V., S. J. Bauer, and N. L. Carter, Effect of the  $\alpha$ - $\beta$  quartz transition on the creep properties of quartzite and granite, *Geophys. Res. Lett.*, 10, 1129-1132, 1983.
- Rybicki, K., Analysis of aftershocks on the basis of dislocation theory, *Phys. Earth Planet. Inter.*, 7, 409-422, 1973.
- Sato, R., Stress drop for a finite fault, *J. Phys. Earth*, 20, 397-407, 1972.
- Shelton, G. L., J. Tullis, and T. Tullis, Experimental high temperature and high pressure faults, *Geophys. Res. Lett.*, 8, 55-58, 1981.
- Sibson, R. H., Interactions between temperature and pore-fluid pressure during earthquake faulting and a mechanism for partial or total stress relief, *Nature Phys. Sci.*, 243, 66-68, 1973.
- Sibson, R. H., Generation of pseudotachylite by ancient seismic faulting, *Geophys. J. R. Astron. Soc.*, 43, 775-794, 1975.
- Sibson, R. H., A comment on 'Frictional heating on a fault zone with finite thickness', by R. K. Cardwell, D. S. Chinn, G. F. Moore and D. L. Turcotte, *Geophys. J. R. Astron. Soc.*, 56, 237-238, 1979.
- Sibson, R. H., Transient discontinuities in ductile shear zones, *J. Struct. Geol.*, 2, 165-171, 1980.
- Sibson, R. H., Continental fault structure and the shallow earthquake source, *J. geol. Soc. London*, 140, 741-767, 1983.
- Sibson, R. H., Roughness at the base of the seismogenic zone: contributing factors, *J. Geophys. Res.*, 89, 5791-5799, 1984.
- Singh, S. K., Slip and stress drop on a circular fault, *Bull. Seismol. Soc. Am.*, 67, 279-284, 1977.
- Spudich, P., and E. Cranswick, Direct observation of rupture propagation during the 1979 Imperial Valley earthquake using a short baseline accelerometer array, *Bull. Seismol. Soc. Am.*, 74, 2083-2114, 1984.
- Stein, R. S., and M. Lisowski, The 1979 Homestead Valley earthquake sequence, California: control of aftershocks and postseismic deformation, *J. Geophys. Res.*, 88, 6477-6490, 1983.
- Stesky, R. M., Mechanisms of high temperature frictional sliding in Westerly granite, *Can. J. Earth Sci.*, 15, 361-375, 1978.
- Strehlau, J., and R. Meissner, Earthquakes in continental crust: temperature dependence of maximum focal depth (abstract), *Terra Cognita*, 3, 89, 1983.
- Thatcher, W., Nonlinear strain buildup and the earthquake cycle on the San Andreas fault, *J. Geophys. Res.*, 88, 5893-5902, 1983.
- Tullis, J., and R. A. Yund, Hydrolytic weakening of experimentally deformed Westerly Granite and Hale Albite rock, *J. Struct. Geol.*, 2, 439-451, 1980.
- Tullis, J., A. W. Snee, and V. R. Todd, Significance and petrogenesis of mylonitic rocks, *Geology*, 10, 227-230, 1982.
- Vasseur, G., A. Etchecopar, and H. Philip, Stress

- state inferred from multiple focal mechanisms, Ann. Geophys., 1, 291-298, 1983.
- Wallace, T. C., D. V. Helmberger, and J. E. Ebel, A broadband study of the 13 August 1978 Santa Barbara earthquake, Bull. Seismol. Soc. Am., 71, 1701-1718, 1981.
- White, J. C., and S. H. White, Semi-brittle deformation within the Alpine fault zone, New Zealand, J. Struct. Geol., 5, 579-589, 1983.
- White, S. H., S. E. Burrows, J. Carreras, N. D. Shaw, and F. J. Humphreys, On mylonites in ductile shear zones, J. Struct. Geol., 2, 175-187, 1980.
- Wise, D. U., D. E. Dunn, J. T. Engelder, P. A. Geiser, R. D. Hatcher, S. A. Kish, A. L. Odom, and S. Schamel, Fault-related rocks: suggestions for terminology, Geology, 12, 391-394, 1984.
- Yamashita, T., Dislocation distribution and the mutual dependence of static source parameters in the presence of non-uniform initial stress, J. Phys. Earth, 26, 167-183, 1978.

## THE FRACTAL GEOMETRY OF FAULTS AND FAULTING

C.H. Scholz and C.A. Aviles

Lamont-Doherty Geological Observatory of Columbia University  
and Department of Geological Sciences, Palisades, New York 10964

**Abstract.** The topography of natural faults and fractures has been measured over nearly the entire band:  $10^5$  M to  $10^{-5}$  M. It is found that the surfaces are fractal or nearly fractal over this entire band but that the fractal dimension, D, is a function of spatial frequency. Both abrupt and gradual transitions in D are observed and over some scales, most notably at the high and low ends of the spectral band studied, the surfaces are smooth enough to be differentiable, i.e., they are Euclidean. From these results we can deduce that the asperity distribution on faults obeys an inverse power law and that fault roughness scales with spatial wavelength. The constants in these relationships, however, depend on D, and hence hold over only limited spatial bands.

On the scale of frictional sliding during an earthquake, rms roughness and asperity size scale up with slip, so that in slip-weakening models of the stick-slip instability the critical distance,  $d_c$ , will also be expected to scale with slip and hence earthquake size. As a result, the energy release rate G can also be expected to increase with rupture size and slip weakening models in which  $d_c$  is a fixed parameter may not be realistic. At longer wavelengths, the fractal nature of fault geometry provides a simple explanation for the randomness of strong ground motions and of the size distributions of earthquakes and faults. That large and small earthquakes belong to different hierarchies of size distributions is consistent with their different scaling relations.

## Introduction

In the recent seismological literature there has been extensive discussion of heterogeneity in the earthquake process, both in terms of the distribution, in time, space, and size of earthquakes, and with regard to the internal heterogeneity, on all scales, of the rupture process. There have been two general approaches, not unconnected, towards discussing this problem. The first has been the development of physical models based on the heterogeneity of strength, taken in

a general sense, of the fault surface, the most notable being the barrier model, introduced by Das and Aki [1977], and the asperity model, developed by Lay and Kanamori [1981]. The second approach is a strictly geometrical one and is based on the fractal model of Mandelbrot [1977], which is a powerful and general model of the geometry of irregular and chaotic systems. For example, Andrews [1980] developed a model in which he assumed that slip (or stress drop) was fractally distributed over the fault plane. He also showed, as did Aki [1981], that the size distribution of earthquakes is a result of the self-similarity implicit in any fractal set. More recently, Smalley et al. [1985] used a fractal approach to a cascade model of the stick-slip instability.

Okubo and Aki [1986] showed that at long wavelengths the trace of the San Andreas fault is a fractal and that its fractal dimension, D, varies along the trace of the fault. In this paper we examine, using a different but equivalent method, the fractal geometry of natural fractures and faults over the bandwidth  $10^5$  to  $10^{-5}$  M. There are two scales which are of interest and which are amenable for study: the scale of 1 M to  $10^{-5}$  M, which nearly encompasses the range of slip that can be expected to occur in an earthquake, and the scale of  $10^3$  M to  $10^5$  M, which covers the range of rupture dimensions of usual interest in earthquake studies. In terms of their physical relevance, the  $1-10^{-5}$  M band is important with regard to the frictional processes that occur during rupture, whereas the  $10^3-10^5$  M band is relevant to heterogeneity in the rupture propagation process. We do not have data in the mid-band,  $1-10^3$  M.

## Observations of the Topography of Fractures

The Weierstrass-Mandelbrot fractal function [Mandelbrot, 1977; Berry and Lewis, 1980], a continuous function that is nowhere differentiable, has been widely applied as a description of geometrically irregular surfaces ranging in scale from molecular surfaces [Avnir et al., 1984], fractures [Mandelbrot et al., 1984], to the topo-

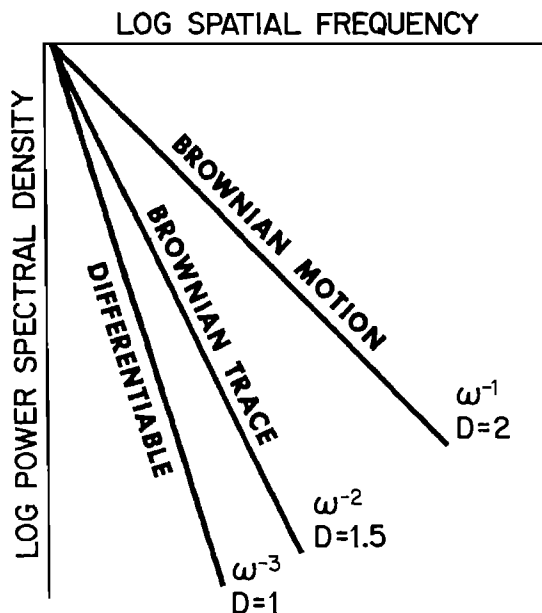


Fig. 1. Schematic diagram showing the spectral characteristics of the linear Weierstrass-Mandelbrot fractal function.

graphy of the seafloor [Fox and Hayes, 1985]. This function describes a family of nonstationary random processes which in the frequency domain can be regarded as red noise. A property of the linear function, which can be used to describe surface profiles, is that its power spectrum falls off with spatial frequency as  $\omega^{-(5-2D)}$ , where D is the fractal dimension: the parameter that describes the scaling of self-similarity that is implicit in the function. This property, which will be used in this paper to evaluate D, is illustrated in Figure 1 with several familiar examples. If the power spectrum of the surface falls off as  $\omega^{-1}$ , then  $D = 2$  and the function describes Brownian motion, which is space filling: spongelike materials have fractal dimensions that approach 2. If the spectrum falls off as  $\omega^{-2}$ ,  $D = 1.5$  and it is a Brownian trace (or trail) which is the most jagged surface that does not contain overhangs. All surfaces for which the power spectra fall off at  $\omega^{-3}$  or steeper are differentiable and hence Euclidean rather than fractal.

The fractal dimension of profiles of a wide variety of surfaces has been found to span nearly the entire permissible range  $1 \leq D \leq 2$ . As Mandelbrot [1977] pointed out, though, it is quite natural to expect that D is not a universal constant for a surface (although it has usually been presented so) but that it will depend upon the scale at which one is observing the surface. Prior to our work, surface measurements had been limited to only about two decades in spatial frequency so that it had not been possible to detect this expected scale dependence of D. Here we

report measurements of the fractal geometry of natural fractures and faults that span (though discontinuously) ten decades of spatial frequency. These results clearly show both gradual and abrupt transitions in D and also that Euclidean bands exist, typically at the high and low ends of the spectrum. In this section we will present these results and in the following we will couple them with some simple physical models with which we can interpret various seismological phenomena in terms of the fractal nature of faults.

#### The Micro-to Macro-Scale

The topography of a variety of natural rock surfaces has been studied over the band 1 M to  $10^{-5}$  M by Brown and Scholz [1985a]. A typical example is shown in Figure 2; that of a joint (Mode I fracture) in the Palisades diabase at Palisades, N.Y. The data were taken with two stylus profilometers: a laboratory instrument which records wavelengths from 1 cm to 10  $\mu\text{m}$  and height changes from 2 mm to 0.05  $\mu\text{m}$ , and a field instrument which records wavelengths of 1 M to 1 mm and heights from 5 cm to 10  $\mu\text{m}$ . The data in Figure 2 are ensemble averages in the frequency domain of five profiles measured with each instrument. The field instrument was held directly to the outcrop; cores of the surface were used for the lab measurements. Notice that data from the two instruments agree well within their region of overlap.

A careful study of Figure 2 shows that the slope of the power spectrum of this surface is not constant over this band; rather the spectrum is concave downwards, indicating that the fractal dimension is a function of  $\omega$ . A fairly abrupt slope change is observed at about 0.5 mm. At higher frequencies, in region C, the power spectrum,  $G(\omega)$ , falls off faster than  $\omega^{-3}$ , hence  $D = 1$  and the surface is smooth enough to be differentiable over most of its area. At longer wavelengths there is a gradual increase in D, from  $1.15 \pm 0.03$  in region B to  $1.26 \pm 0.04$  in region A.

This result is fairly simple to understand. The surface is, within this bandwidth, irregular and outward facing (i.e.,  $1 \leq D \leq 1.5$ ). On the outcrop scale (A) the surface has a higher D and hence is more jagged than on the hand specimen scale (B). On the scale of single crystals (C) the stylus primarily traverses weathered crystal cleavage surfaces and the surface, though not flat, is differentiable.

In a later section we will compare this data with that taken from the surface trace of a strike-slip fault (Mode II fracture). We recognize that the latter is also a wear surface so that the two are not strictly comparable. The one wear surface that we have so far studied is a glacially striated surface, which has a fractal characteristic quite similar to that shown in Figure 2 except that it is anisotropic [Brown and

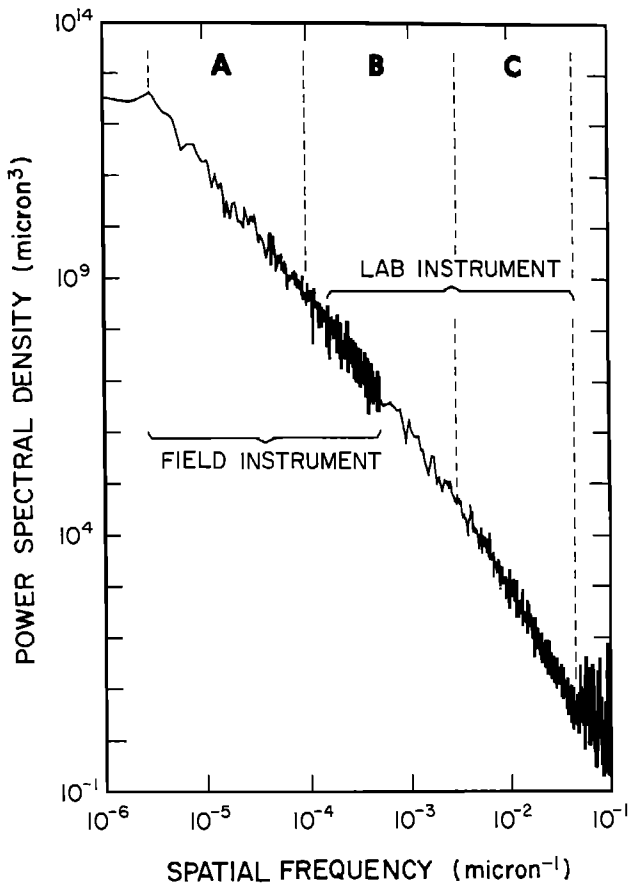


Fig. 2. Power spectrum of the topography of a joint in the Palisades Diabase, Palisades, N.Y.

Scholz, 1985a]. Thus although the comparison cannot be quantitatively made, we feel that it is apt since we have yet to measure any natural rock surface that is not fractal or nearly fractal over this entire band.

#### The Mega-Scale

This scale consists of the band ranging in wavelength from approximately  $10^3$  M to  $10^5$  M. Data was obtained by digitizing, at intervals of 0.1 km, the trace of the San Andreas fault from the Alquist-Priolo Act series of fault hazard maps, which are at a scale of 1:24,000. On this scale the fault is a discontinuous surface consisting of a series of offset strands, so in order to carry out this analysis a simple rule had to be adopted: adjacent strands were spliced together with the smoothest possible curves. This resulted in low-pass filtering of the data so that wavelengths less than 0.5 km cannot be interpreted.

In Figure 3 we show the spectrum of a typical seismogenic reach of the fault: that which ruptured in 1906. In comparison with Figure 2, more

noise is evident. This is largely because Figure 3 was obtained from a single profile whereas the data in Figure 2 were averaged from five, but it may also reflect inaccuracies in either the mapping or digitization procedures.

The spectrum of this section of the fault has a fractal character similar to that shown by fractures at the smaller scale (Figure 2) except that it is concave upwards rather than downwards. At wavelengths longer than 10 kms. the spectrum falls off close to  $\omega^{-3}$ , indicating that the fractal dimension is  $\approx 1$  and the trace is differentiable or nearly so.

There is a peak in the spectrum at about 10 km, beyond which it falls off as approximately  $\omega^{-2}$ . The fault is broken into offset strands in the length range 1-10 km [Wallace, 1973; Segal and Pollard, 1980]. Since the spectral technique is only appropriate for continuous functions we had to splice these strands together for the analysis. This results in the fault resembling a random boxcar function at this scale, which leads to the  $\omega^{-2}$  spectral falloff which therefore cannot be interpreted in terms of fractal dimension. In a more detailed study of the fractal geometry of the fault using the 'ruler' technique, which avoids this problem, we found that the fault is fractal with  $D$  just greater than 1, over the entire band  $10^5$  M -  $10^3$  M (Aviles, C. A., C.H. Scholz, J. Boatwright, in preparation, 1986). The dashed line sketched in Figure 3 accordingly indicates this result, i.e., it indicates the expected form of the fault spectrum if it were not contaminated by the  $\omega^{-2}$  overtones due to the fault offsets.

#### Scaling of Roughness and the Size Distribution of Asperities

Surface roughness, especially in the friction literature, is usually defined as the rms asperity height,  $\sigma$ . From the results described above, however, it is obvious that  $\sigma$  depends on the frequency band studied. Thus  $\sigma$  is related to  $G(\omega)$  by:

$$\sigma = \left| \frac{\omega_n}{\int G(\omega) d\omega} \right|^{1/2} \quad (1)$$

where  $\omega_n$  is the highest frequency studied and  $\omega_0$  is the lowest, which corresponds to the longest wavelength sampled,  $\lambda_0$ . For an earthquake,  $\lambda_0 \propto u$  and  $u \propto L$ , where  $u$  is the slip and  $L$  the rupture dimension. The latter proportionality is true only if stress drop is constant; the value of its proportionality constant is typically  $10^{-5}$  to  $10^{-4}$ , for interplate and intraplate earthquakes, respectively [Scholz, 1982]. Since all fractures and faults we have studied are outward facing fractals,  $1 \leq D \leq 1.5$ , the limiting cases are:  $D = 1.5$ ,  $\sigma = \kappa_1 \lambda^{1/2}$ ; and  $D = 1.0$ ,  $\sigma = \kappa_2 \lambda$ , where  $\kappa_1$  and  $\kappa_2$  are constants that depend on the surface studied.

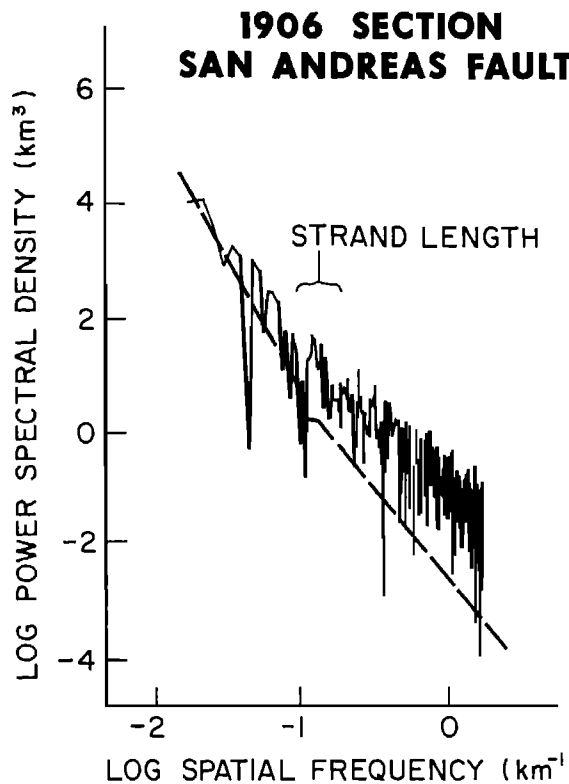


Fig. 3. Power spectrum of the trace of the San Andreas fault that ruptured in 1906. The peak in the spectrum at a wavelength of about 10 km, and the  $\omega^{-2}$  rolloff beyond that is attributed to the predominant strand length being at that band. The dashed curve indicates the expected fractal spectra estimated from another method, which does not include that periodicity.

The size distribution of asperities may be defined as the distribution of lengths between zero crossings of the topography (the zero-set). This is given [Mandelbrot, 1977] by

$$\Pr(X > x) = x^{-D} \quad (2)$$

thus asperities follow an inverse power law distribution with the exponent determined by  $D$ . Virtually all fractal sets have this size distribution, which follows strictly from self-similarity and is known historically as the Law of Pareto. Since we have found, however, that  $D$  depends on  $\omega$ , we should expect that, correspondingly, the size distribution of fractal sets will also vary with scale.

#### Consequences of the Fractal Nature of Faults on Earthquake Processes

To summarize the previous section, we show in Figure 4, plotted on the same scale, the data from Figure 2 and the spectrum of the San Andreas

fault from Pt. Arena to Parkfield, which includes both the 1906 rupture and the creeping section of the fault. Although we would not claim that one could directly interpolate between these two spectra, since different surfaces have been sampled, we would claim that a general interpolation is reasonable, in the sense that the intermediate band, which has not been sampled, is also fractal, although we would not claim to know the value of  $D$  in that band except that it is most likely to be in the range  $1 \leq D \leq 1.5$ . This argument is not based on these two spectra alone, but since the spectra of all natural rock surfaces studied in the high-frequency band by Brown and Scholz [1985a] and all faults studied in the low-frequency band (C. A. Aviles unpublished work, 1985) fall within 1-2 decades of power of those shown at the long period and short period limits, respectively, they would not look very different, at the scale of Figure 4, from those shown.

We would thus conclude that over this entire 10 decade band,  $10^5 - 10^{-5}$  M, that natural faults and fractures are outward facing heterogeneous fractals. These conclusions are strictly geometrical; in order to discuss the relevance of these observations to seismological phenomena we must introduce some physical models which link the geometry of the fault to the physics of the earthquake process. We do this with some very simple models which have found wide recent usage and acceptance.

#### Friction: Scaling in Slip-Weakening Models

The stick-slip instability in the frictional sliding of rock must generally result from some sort of slip-weakening or velocity weakening process. A simple slip-weakening model is illustrated in Figure 5. The frictional resistance to slip falls from an initial value  $\tau_f$ , to a final value,  $\tau_d$ , over some characteristic slip  $d_0$ . The area under the breakdown envelope (shaded) is equal to  $G$ , the energy release rate [Rice, 1980].

A constitutive model, based on laboratory friction measurements and which contains this type of instability, has been the focus of considerable recent work in modeling both laboratory friction measurements and the earthquake instability [Dieterich, 1979; Ruina, 1983; Dieterich, this volume]. It contains a basic scale length,  $d_c$ , which is analogous to the parameter  $d_0$  in the simple model illustrated. This parameter is interpreted as a critical slip displacement necessary to bring about a change in the population of contact areas (Dieterich, 1979). It can be measured in the laboratory where it is found to vary with asperity size, with values that thus increase with surface roughness [Dieterich, this volume; Okubo and Dieterich, 1984; Tullis et al., 1985]. The scaling of this process from the laboratory to earthquakes is thus intimately connected with the scaling of surface topography as discussed above.

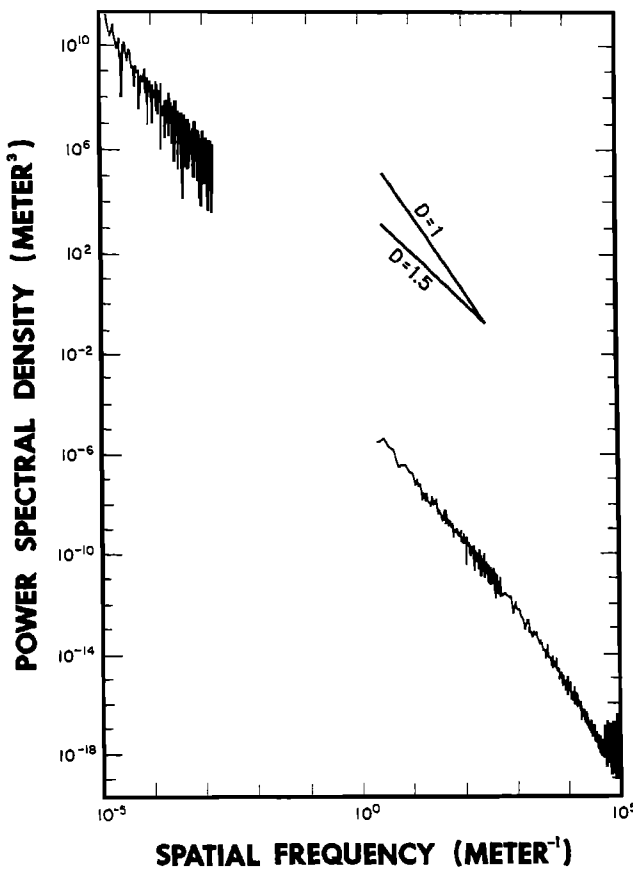


Fig. 4. The power spectrum of the San Andreas fault from Pt. Arena to Parkfield and of the joint in the Palisades Diabase plotted on the same scale.

In the laboratory studies cited above,  $d_c$  is found, for a given surface, to be a fixed parameter that corresponds to a maximum asperity size for that surface. The surfaces used in experimental studies are ground surfaces, which, unlike the natural fracture surfaces discussed herein, have topographic spectra which contain a corner frequency that corresponds to the grit size used in grinding [Brown and Scholz, 1985b]. For those surfaces the maximum asperity size, and hence  $d_c$ , are well-defined parameters. For natural surfaces, however, we have found that asperity height increases without limit as the surface sample length increases, so that we are faced not only with the problem of scaling  $d_c$  according to some fractal law, but we must conclude also that  $d_c$  cannot be a fixed parameter in the earthquake instability.

In Figure 6 we show the rms asperity height as a function of profile length, computed using (1) for the surface shown in Figure 2. The profile length scale relevant to an earthquake is the slip,  $u$ , which is itself a function of the physical dimensions of the rupture. If  $d_c$  is a function of asperity height, then, we can see

that it is impossible to define an a priori value to this parameter, since the heights of asperities encountered during slip will monotonically increase as rupture progresses. Models of the earthquake instability that incorporate this scaling of  $d_c$  are likely to behave quite differently than those that employ a fixed value of  $d_c$ , such as that of Dieterich [this volume].

If we return to the simple model shown in Figure 5, and consider  $d_o$  to be related to asperity size, we reach a similar conclusion. We can at least argue qualitatively, though, that  $d_o$ , and hence  $G$  must be much larger for earthquakes than for laboratory scale experiments. This may in part explain the difference between the very large values of  $G$  calculated from seismological parameters and the low values obtained in laboratory experiments [Wong, 1982].

#### Asperity and Barrier Models and the Generation of High Frequency Strong Ground Motions

Heterogeneity in the earthquake rupture process is usually ascribed to heterogeneity in fault strength, and models which incorporate such strength variations are called asperity and barrier models. In Figure 7 we schematically show a rupture propagating on the  $xy$  quarter-plane. At some point  $P$  outside the rupture we define a dimensionless strength [c.f., Das and Aki, 1977]

$$S = \frac{\tau_f - \tau_o}{\Delta \tau} \quad (3)$$

where  $\tau_f(x,y)$  and  $\tau_o(x,y)$  are the frictional strength and applied stress defined at  $P$  and

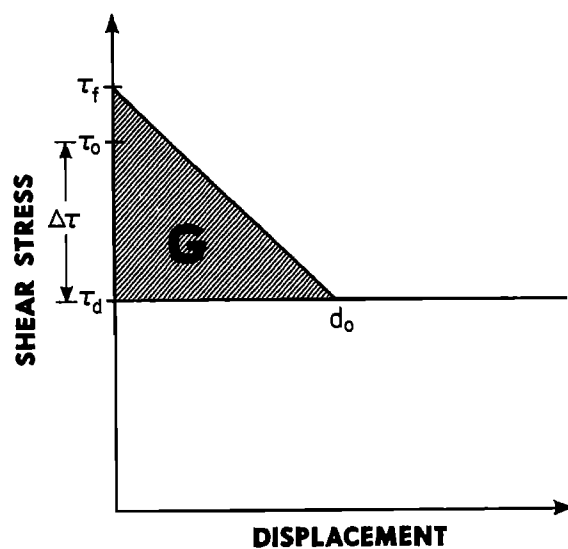


Fig. 5. Schematic diagram of a simple slip-weakening model.

## 152 FRACTAL GEOMETRY OF FAULTING

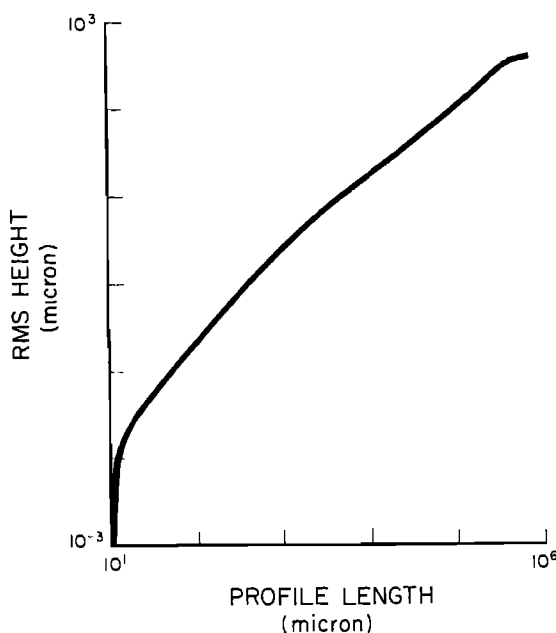


Fig. 6. rms asperity height vs profile length for the surface shown in Figure 2, computed with (2).

$\Delta\tau = (\tau_o - \tau_d)$  is the dynamic stress drop averaged over a portion  $A'$  of the rupture  $A$  adjacent to  $P$ . Here,  $\tau_d$  is the dynamic frictional strength, also a material property. The parameter  $S$  is therefore not a material property nor is it a property solely of point  $P$ . It is rather a combination of material properties at  $P$  and state variables that concisely contains a stress criterion for dynamic rupture.

The topography measurements described in the previous section refer to deviations in the  $z$  direction from the  $xy$  plane as observed for real faults. If we make the simple assumption that  $\tau_f = f_{nct}(x, y, z)$ , then since  $z$  is fractal,  $\tau_f$  must be as well. If everything else is uniform, then  $S$  will also be a fractal. In general, however, we can expect that  $\tau_o$ , which depends on the prior rupturing and loading history of the point  $P$ , and  $\Delta\tau$  will be fractal as well. It is variations in the parameter  $S$  that produce heterogeneity in the rupture process, and though one can imagine cases in which variations in either  $\tau_f$  or  $\tau_o$ , say, are primarily responsible for variations in  $S$ , these parameters cannot usually be determined independently by seismological means alone. In the barrier model [e.g., Das and Aki, 1977], a barrier is assumed to be a region of unusually high  $S$  where the rupture may be temporarily or permanently arrested. This may occur because  $\tau_f$  is unusually high, which may be called a geometrical barrier [Aki, 1979], or where  $\tau_o$  is unusually low, which may be called a relaxation barrier. The latter type is typified when a rupture impinges upon a zone previously

broken by a recent earthquake. In the asperity model a region of high dynamic moment-density release (high dynamic stress drop) is identified as a strong asperity [e.g., Lay et al., 1982].

In view of the mixed definition of the parameter  $S$ , it seems illadvised to use the terms "strong" and "weak" to refer to places in which such slip variations are observed in earthquakes. If the plate boundary interface is fractal, then the size distribution of asperities on it should follow a power law as given by (2). The explanation that different plate boundaries have different size earthquakes because they have different size asperities [Lay et al., 1982] seems rather superficial from this point of view. Indeed, for those cases where we have a long record of seismicity for a plate boundary [e.g., Ando, 1975], it does not appear that the earthquake size is stationary in time.

The generation of high-frequency strong ground motions is of particular interest in this discussion. It has long been known, and most recently re-emphasized by Hanks and McGuire [1981], that this kind of radiation is a type of random noise. Model studies have shown that strong ground motions are primarily produced by abrupt changes in rupture velocity due to variations in  $S$  on the fault [e.g., Madariaga, 1983; Day, 1982]. Numerous workers have suggested that this is due to randomness of fault friction [Nur, 1979; Segal and Pollard, 1980]. Since this radiation is largely in the band 3-30 Hz it must result from irregularities on the fault in the wavelength band 1 to 0.1 km. Since by interpo-

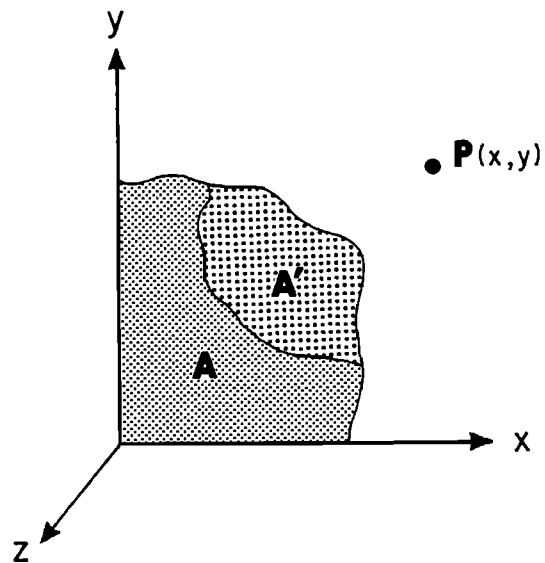


Fig. 7. Schematic diagram showing a rupture of area  $A$ , propagating outward on the  $xy$  plane towards a point  $P$ . At  $P$ , the strength of the fault is a function of  $xyz$ . The stress drop relevant to rupture at  $P$  is an average over the ruptured region adjacent to  $P$ ,  $A'$ .

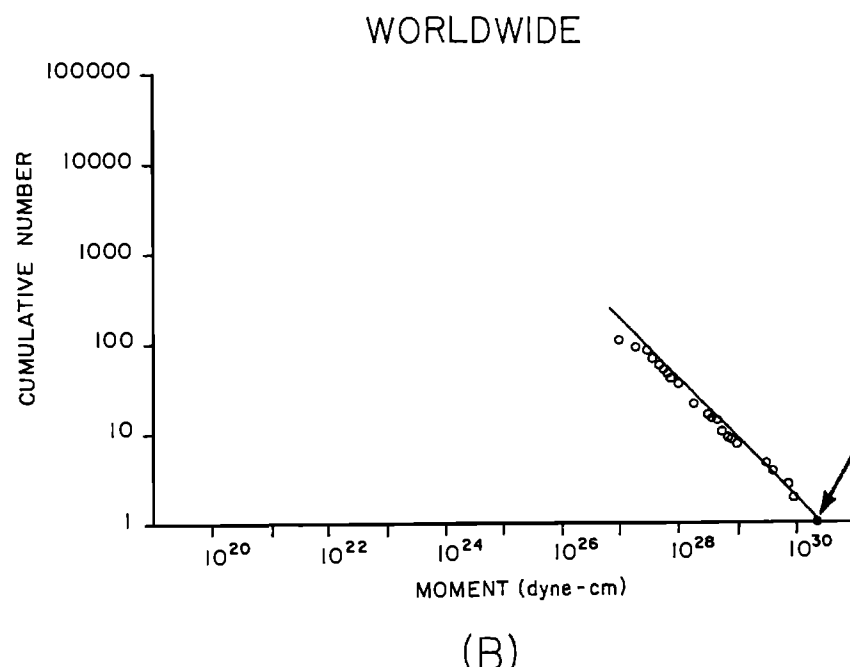
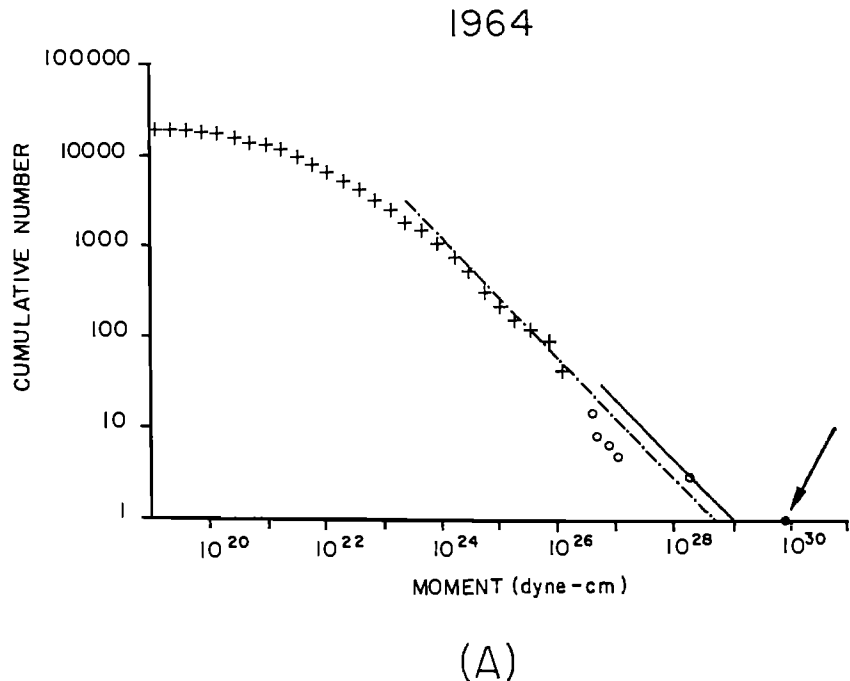


Fig. 8. An illustration of the characteristic earthquake model (after Davison and Scholz, 1985). Figure (a). Distribution of  $M>7$  earthquakes from the 80-year instrumental catalog (open circles) and  $M>5$  events from the WWSSN catalog, (+) that occurred in the rupture zone of the 1964 Alaskan earthquake, each normalized to the estimated repeat time of the earthquake. The 1964 event is indicated by the solid circle and arrow. (b) The worldwide distribution of all  $M_0 > 10^{27}$  dyne cm earthquakes from the 80 year instrumental catalog. The slope of the line is  $-2/3$ ; the 1960 Chile earthquake is indicated by the solid circle and arrow.

## 154 FRACTAL GEOMETRY OF FAULTING

lation of our results we would conclude that the topography of the fault is that of red noise in this band it is a simple conclusion that the generation of high-frequency strong ground motions is simply a consequence of this random irregularity of the fault on that scale.

Size Distributions

The power law distribution of asperity sizes given in (2) is a simple consequence of geometrical self-similarity [Mandelbrot, 1977]. We expect, and do see, the same power law size distribution for earthquakes, and for the same reason [Andrews, 1980, Aki, 1981]. Similarly, Wesnousky et al. [1983] showed, somewhat indirectly, that this can be traced to the size distribution of faults. On a smaller scale Segal and Pollard [1983] found the same size distribution for cracks and joints in granite.

It has recently been found, however, that this power law size distribution does not hold for a single fault or rupture zone of a plate boundary [Wesnousky et al., 1983; Singh et al., 1983; Davison and Scholz, 1985]. If one considers the population of earthquakes that occurs during one recurrence interval of a large plate-rupturing earthquake on the same rupture zone of that earthquake, one obtains a result such as illustrated in Figure 8a. One can see from the figure that all the small earthquakes that occur in the rupture zone obey a power law size distribution, but that the one large plate-rupturing earthquake does not belong to that population, being always 1-1 1/2 orders of magnitude larger than that which would be predicted by extrapolation of the power law. Thus the large earthquake is not self-similar with the small earthquakes; which is entirely consistent with the observation that large earthquakes do not scale the same way as small earthquakes [Scholz, 1982; Shimazaki, this volume]. Large earthquakes are self-similar among themselves, though, and obey a power law size distribution, as is illustrated in Figure 8b. We refer to the hierarchical jump between these two families of earthquakes as a fractal tear.

## Discussion

We have reported that the Weierstrass-Mandelbrot fractal function is an accurate representation of the topography of fractures and faults over the entire bandwidth relevant to the earthquake rupture process. The power of this result is that since it is entirely geometrical it must be imbedded in any physical model that seeks to explain seismological phenomena, and in particular, that any physical model must then contain the scaling and self-similarity properties inherent in the geometry. We have surveyed a number of areas in which we can incorporate these results with simple physical models to explain important seismological phenomena.

This approach is essentially a unifying one: a wide variety of phenomena can be seen to arise as simple manifestations of various properties that result from the fractal nature of faults. We have here attempted only a qualitative discussion of our results in terms of physical models and phenomena. These remarks should be simply taken as developing some guiding principles which can be incorporated into more quantitative modeling of these and related phenomena.

Acknowledgements. This work was supported by the U.S. Geological Survey under grant 14-08-0001-G1161 and by the National Aeronautics and Space Administration under NASA agreement number NAG 5-446. We thank S. Das, D. Simpson, and B. Kostrov for critical reviews. Lamont-Doherty Geological Observatory Contribution #3948.

## References

- Aki, K., Characterization of barriers on an earthquake fault, *J. Geophys. Res.*, **84**, 6140-6148, 1979.
- Aki, K., A probabilistic synthesis of precursory phenomena, in *Earthquake Prediction*, edited by D. Simpson and P. Richards, Maurice Ewing Series 4, pp. 566-574, AGU, Washington, D.C., 1981.
- Ando, M., Source mechanisms and tectonic significance of historical earthquakes along the Nankai trough, *Tectonophysics*, **27**, 119-140, 1975.
- Andrews, D.J., A stochastic fault model, static case, *J. Geophys. Res.*, **85**, 3867-3877, 1980.
- Avnir, D., D. Farin, and P. Pfeifer, Molecular fractal surfaces, *Nature*, **308**, 261-263, 1984.
- Berry, M.V., and S.V. Lewis, On the Weierstrass-Mandelbrot fractal function, *Proc. R. Soc. London, Ser. A*, **370**, 459-484, 1980.
- Brown, S.R., and C.H. Scholz, Broad band width study of the topography of natural rock surfaces, *J. Geophys. Res.*, **90**, 12,575-12,582, 1985a.
- Brown, S.R., and C.H. Scholz, Closure of random elastic surfaces in contact, *J. Geophys. Res.*, **90**, 5531-5545, 1985b.
- Das, S., and K. Aki, Fault planes with barriers: a versatile earthquake model, *J. Geophys. Res.*, **82**, 5658-5670, 1977.
- Davison, F.C., and C.H. Scholz, Frequency-moment distribution of earthquakes in the Aleutian arc: a test of the characteristic earthquake model, *Bull. Seismol. Soc. Am.*, **75**, 1349-1362, 1985.
- Day, S.M., Three-dimensional simulation of spontaneous rupture: the effect of nonuniform prestress, *Bull. Seismol. Soc. Am.*, **72**, 1881-1902, 1982.
- Dieterich, J.H., Modeling of rock friction, I, Experimental results and constitutive equations, *J. Geophys. Res.*, **84**, 2161-2168, 1979.

- Dieterich, J. H., A model for the nucleation of earthquake slip, this volume, 1986.
- Fox, C., and D. Hayes, Quantitative methods for analyzing the roughness of the seafloor, Rev. Geophys. Space Phys., 23, 1-48, 1985.
- Hanks, T.C., and R.K. McGuire, The character of high-frequency strong ground motion, Bull. Seismol. Soc. Am., 71, 2071-2095, 1981.
- Lay, T., and H. Kanamori, An asperity model of great earthquake sequences, in Earthquake Prediction: an International Review, edited by D. Simpson and P. Richards, pp. 579-592, AGU, Washington, D.C., 1981.
- Lay, T., L. Ruff, and H. Kanamori, The asperity model and the nature of large earthquake subduction zones, Earthquake Pred. Res., 1, 3-71, 1982.
- Madariaga, R., High frequency radiation from dynamic earthquake models, Ann. Geophys., 1, 17-23, 1983.
- Mandelbrot, B., Fractals: Form, Chance and Dimension, 365 pp, W.H. Freeman, San Francisco, Calif., 1977.
- Mandelbrot, B., D. Passoja, and A. Paullay, Fractal character of fracture surfaces of metals, Nature, 308, 721-722, 1984.
- Okubo, P., and K. Aki, Fractal geometry in the San Andreas fault system, J. Geophys. Res., in press, 1986.
- Okubo, P., and J. Dieterich, Effects of physical fault properties on frictional instabilities produced on simulated faults, J. Geophys. Res., 89, 5817-5827, 1984.
- Nur, A., Nonuniform friction as a physical basis for earthquake mechanics, Pure Appl. Geophys., 116, 964-991, 1979.
- Rice, J.R., The mechanics of earthquake rupture, in Proc. School of Physics of Earth's Interior, edited by A.M. Dziewonski and W. Boschi, pp. 555-649, North-Holland, Amsterdam, 1980.
- Ruina, A. L., Slip instability and static vari- able friction laws, J. Geophys. Res., 88, 10,359-10,370, 1983.
- Scholz, C.H., Scaling laws for large earthquakes: consequences for physical models, Bull. Seismol. Soc. Am., 72, 1-14, 1982.
- Segal, P., and D. Pollard, Mechanics of discontinuous faults, J. Geophys. Res., 85, 4337-4350, 1980.
- Segal, P., and D. Pollard, Joint formation in granitic rock of the Sierra Nevada, Geol. Soc. Am. Bull., 94, 563-575, 1983.
- Shimazaki, K., Small and large earthquakes: the effects of the thickness of the seismogenic layer and the free surface, this volume, 1986.
- Singh, S., M. Rodriguez, and L. Esteva, Statistics of small earthquakes and frequency of occurrence of large earthquakes along the Mexican subduction zone, Bull. Seismol. Soc. Am., 73, 1779-1796, 1983.
- Smalley, R., D. Turcotte, and S. Solla, A renormalization group approach to the stick-slip behavior of faults, J. Geophys. Res., 90, 1894-1900, 1985.
- Tullis, T. E., J. D. Weeks and M. L. Blanpied, Constitutive behavior and stability of frictional sliding of granite (Abstract), presented at Fifth Maurice Ewing on Earthquake Source Mechanics, Harrison, New York, 1985.
- Wallace, R., Surface fracture patterns along the San Andreas fault, in, Proc. Conf. Tecton. Problem of San Andreas Fault System, Publ. Geol. Sci. XIII, pp. 248-250, Stanford University Press, Palo Alto, Calif., 1973.
- Wesnousky, S., C. Scholz, K. Shimazaki, and T. Matsuda, Earthquake frequency distribution and the mechanics of faulting, J. Geophys. Res., 88, 9331-9340, 1983.
- Wong, T.-F., Shear fracture energy of Westerly Granite from post-failure behavior, J. Geophys. Res., 87, 990-1000, 1982.

## RUPTURE INTERACTION WITH FAULT JOGS

Richard H. Sibson

Department of Geological Sciences, University of California, Santa Barbara, California 93106

**Abstract.** Propagation of moderate to large earthquake ruptures within major transcurrent fault systems is affected by their large-scale brittle infrastructure, comprising echelon segmentation and curvature of principal slip surfaces (PSS) within typically  $\sim 1$  km wide main fault zones. These PSS irregularities are classified into dilational and antidilational fault jogs depending on the tendency for areal increase or reduction, respectively, across the jog structures. High precision microearthquake studies show that the jogs often extend throughout the seismogenic regime to depths of around 10 km. On geomorphic evidence, the larger jogs may persist for periods  $>10^5$  years. While antidilational jogs form obstacles to both short- and long-term displacements, dilational jogs appear to act as kinetic barriers capable of perturbing or arresting earthquake ruptures, but allowing time-dependent slip transfer. In the case of antidilational jogs slip transfer is accommodated by widespread subsidiary faulting, but for dilational jogs it additionally involves extensional fracture opening localized in the echelon step-over. In fluid-saturated crust, the rapid opening of linking extensional fracture systems to allow passage of earthquake ruptures is opposed by induced suctions which scale with the width of the jog. Rupture arrest at dilational jogs may then be followed by delayed slip transfer as fluid pressures reequilibrate by diffusion. Aftershock distributions associated with the different fault jogs reflect these contrasts in their internal structure and mechanical response.

## Introduction

In recent years an appreciation of the heterogeneous nature of shallow earthquake rupturing has come from: (1) detailed mapping of past and recent rupture traces [e.g. Vedder and Wallace, 1970; Tchalenko and Ambraseys, 1970]; (2) high precision microearthquake studies which demonstrate that irregularities in surface fault traces may extend throughout the seismogenic zone to depths of 10 km or more [e.g. Eaton et al., 1970; Bakun et al., 1980; Reasenberg and

Ellsworth, 1982], and; (3) the recognition from waveform analyses [e.g. Kanamori and Stewart, 1978] that large earthquakes are generally complex multiple events. Mathematical models of fault "barriers" [Das and Aki, 1977], "asperities" [Kanamori, 1981], "roughness" [Nur and Israel, 1980], and "ligaments" [Rudnicki and Kanamori, 1981], have been devised to account for rupture complexity, but the physical reality of such concepts often remains obscure. An important related matter has been the recognition from paleoseismic studies that certain segments of major faults rupture repeatedly, at fairly regular intervals, in similar sized "characteristic" earthquakes [Schwartz and Coppersmith, 1984; Bakun and McEvilly, 1984]. This implies that strong structural controls exist governing the nucleation and stopping of ruptures at particular localities along fault zones, and that these controls persist for extended time periods. From the viewpoint of hazard assessment, the controls are important not only because they govern the size of characteristic events, but also because rupture acceleration and deceleration induce high-frequency strong ground motion [Madariaga, 1983].

This paper considers possible causes for observed interactions between recent earthquake ruptures and the brittle infrastructure of major fault zones. Attention is focussed on strike-slip fault systems because of the high quality seismological data available for the San Andreas system in California, and because structural irregularities transverse to the fault slip vector and to the generally horizontal direction of rupture propagation are then revealed in map view by microearthquake epicentral distributions.

## Brittle Infrastructure of Fault Zones

Active continental transcurrent fault zones with displacements of tens or hundreds of kilometers typically occupy topographic furrows ranging in width from a few hundred meters to a kilometer or so [Kupfer, 1960; Ambraseys, 1970; Allen, 1981]. While permanent deformation related to the faulting such as echelon folding and subsidiary faulting may occur over a broad swathe

## 158 RUPTURE INTERACTION WITH FAULT JOGS

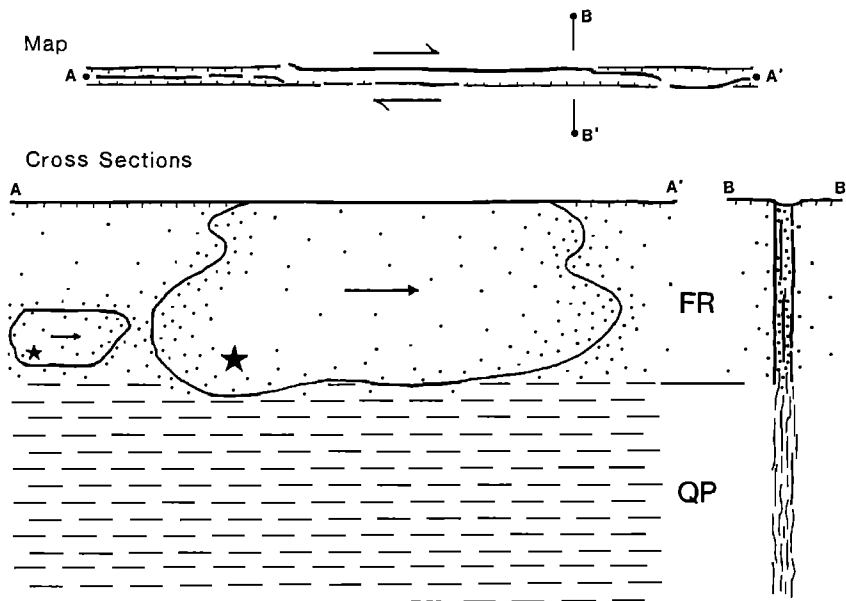


Fig. 1. Schematic diagram of strike-slip earthquake faulting, illustrating the concept of the seismogenic regime. Segmented trace of principal slip surface in a major fault zone shown in map view. Sections show foci (stars) and rupture bounds of larger earthquakes, with dots representing background microearthquakes and aftershocks. FR and QP refer to the frictional and quasi-plastic fault regimes.

[e.g. Aydin and Page, 1984], most of the intense deformation and displacement appears restricted to these dominant fault zones. Associated seismic activity is generally confined to the upper half of the continental crust, defining a seismogenic regime in which major displacements are accomplished largely by earthquake rupturing [Sibson, 1983]. Background microseismicity defines the vertical extent of the regime, while larger ( $M_L > 5.5$ ) earthquakes tend to nucleate at its base, rupturing mostly upwards and outwards so that their aftershocks are also restricted to the same zone (Figure 1). The base of the regime is interpreted as the transition from frictional (FR) faulting to aseismic quasi-plastic (QP) shearing localized in mylonite belts at depth.

#### Existence of Principal Slip Surfaces

Throughout the seismogenic regime, most of the displacement within these major fault zones appears to be accommodated on Principal Slip Surfaces (PSS), often segmented or curved, which persist for extended time periods and commonly occur at one or other boundary to the fault zones, occasionally switching between them. The existence of these PSS, often localized to within a few centimeters, is supported by maps of recent earthquake rupture traces [e.g. Vedder and Wallace, 1970], and by studies of deformation within ancient fault zones exhumed to the deep brittle level [e.g. Flinn, 1977]. An analogy can be made with laboratory shearing of artificial

gouge zones, where intermittent stick-slip behavior likewise tends to be restricted to discrete surfaces at the gouge-rock interface [Byerlee et al., 1978].

#### Discontinuous Nature of PSS

Studies of earthquake surface fault breaks reveal a complex and variable rupture infrastructure on different scales (see Figure 4). On a cross-strike scale of a few meters or so, a systematic fine-scale infrastructure comprising en echelon Riedel shears, pressure ridges and occasional extension fissures is often observed, and is generally interpreted in terms of near-surface failure kinematically induced by constrained planar slip at depth [Tchalenko and Ambrasays, 1970]. Sharp [1979] suggests this fine infrastructure often simplifies at depth to a single fault plane.

Broader scale complexity appears related to the overall width of major fault zones and is not so readily explicable in terms of simple shear kinematic control. Linear or gently curving PSS segments can rarely be followed for more than 10 km or so, suggesting that the largest strike-slip ruptures extending for tens or hundreds of kilometers are invariably multiple events [Wallace, 1973]. Slip then transfers across typical distances of  $10^2$ - $10^3$  m to an echelon rupture segment. The step-sense of the echelon rupture segments is much less consistent than in the fine infrastructure. A close correlation some-

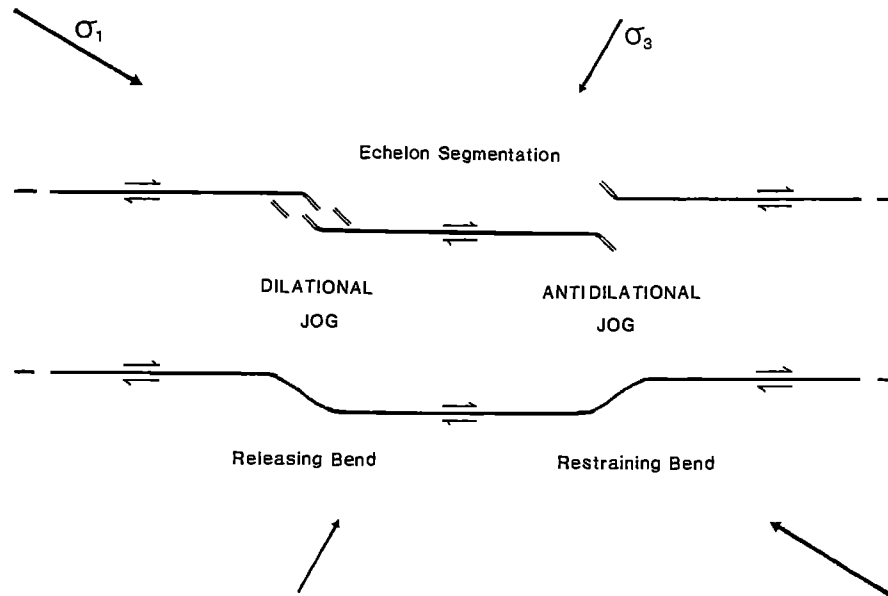


Fig. 2. Echelon segmentation and curvature of the principal slip surface classified into dilational and antidilational fault jogs. Far-field principal compressive stresses,  $\sigma_1 > \sigma_2$  (out of page)  $> \sigma_3$ . Short parallel lines denote likely extension fracture orientations.

times exists between these step-over widths and the geomorphic expression of the main fault zone, suggesting that in at least some instances the PSS is switching from one margin of the fault zone to the other. Subsidiary fracturing is often intense in the step-over regions, but it is comparatively rare for a principal rupture strand to curve continuously across such steps. High resolution microearthquake studies demonstrate that this broad infrastructure often extends throughout the seismogenic regime. Step-overs on this scale are also commonly associated with abrupt changes in the amount of slip accompanying individual earthquakes [Clark, 1972; Tchalenko and Berberian, 1975; Sieh, 1978].

#### Dilational and Antidilational Fault Jogs

Two main classes of irregularity, echelon segmentation and local bends, can be recognized within the broader PSS infrastructure of transcurrent fault zones. Each occurs in two alternative asymmetries with respect to the overall sense of shear (Figure 2). For ease of reference irrespective of faulting mode or sense of shear, the alternative forms for both classes of irregularity can be classed as dilational or antidilational jogs depending on the tendency for areal increase or reduction, respectively, in the plane defined by the slip vector and the pole to planar segments of the PSS. In a 2-D quasi-static elastic analysis, Segall and Pollard [1980] considered stress field perturbations arising from the alternate asymmetries of echelon segmentation, and their potential effects on fault

behavior. For a dilational jog, the elastic interaction between fault segments decreases the frictional resistance at the segment tips, facilitating slip, and also lowers the mean compressive stress throughout the inter-segment region, favoring the development of a linking fracture system involving extension and/or shear. In the case of an antidilational jog, however, both the frictional resistance at the segment tips and the mean compressive stress in the inter-segment region increase, inhibiting slip transfer across the step and causing deformation to spread out over a broad area. Similar situations arise when echelon PSS segments are linked by sigmoidally curving traces to form releasing and restraining bends [Crowell, 1974].

Thus, on this quasi-static analysis dilational jogs present no major impediment to the transfer of slip along a fault system, but antidilational jogs form potential locking points.

#### Longevity of Broad Infrastructure

A key question is for how long the broad infrastructure may remain in one configuration. Analyses of progressively displaced flights of river terraces and similar features [Lensen, 1968; Sieh and Jahns, 1984] have demonstrated that the PSS trace within a major transcurrent fault zone may remain fixed to  $<0.5$  m for periods  $>10^4$  years, over which time the cumulative displacement may exceed 100 m. An important consequence is that while incremental earthquake slip on echelon fault segments could conceivably be accommodated through step-over regions by

## 160 RUPTURE INTERACTION WITH FAULT JOGS

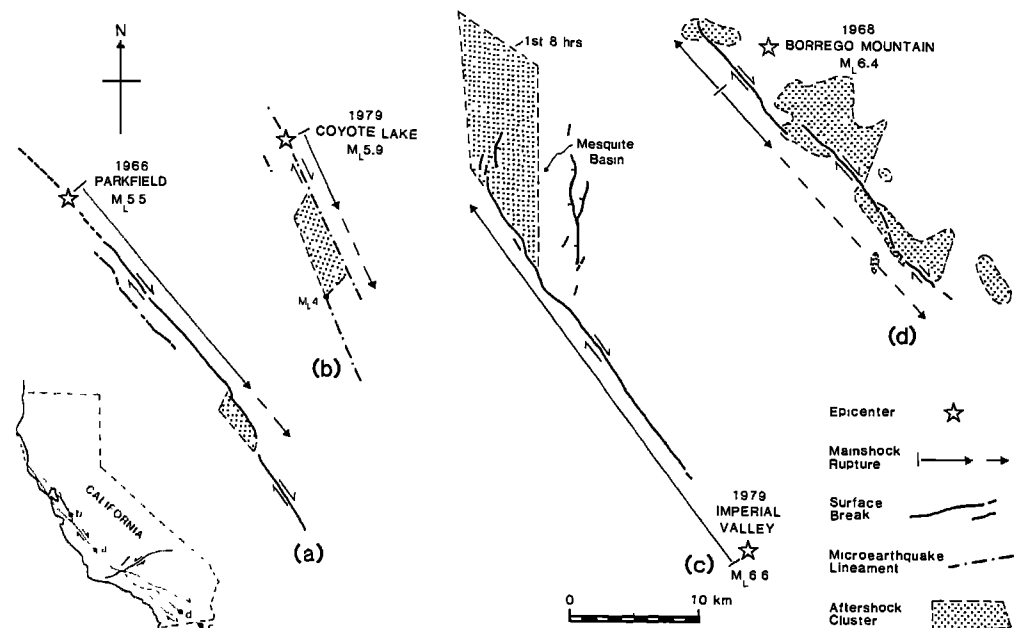


Fig. 3. Seismotectonic cartoons of recent right-lateral strike-slip ruptures within the San Andreas fault system.

localized elastic straining, long-term slip transfer inevitably requires substantial permanent deformation localized in the vicinity of the jogs. It is clear from their geomorphic expression and from ancillary structures that such deformation is indeed often associated with the broader fault infrastructure. Dilational jogs in the PSS trace are often delineated by small pull-apart basins [Mann et al., 1983], while upwarping as a result of localized folding and thrusting may occur in the vicinity of anti-dilational jogs [Sharp and Clark, 1972]. Thus it seems likely that the broad infrastructure may persist in a particular configuration for periods considerably greater than  $10^4$  years, perhaps exceeding  $10^5$  years in some instances.

#### Rupture Interactions With Jogs

Here, we consider some specific instances of earthquake rupture control within transcurrent fault zones. Information on the rupturing process of these moderate or greater ( $M_L > 5.5$ ) events is variably derived from surface rupture patterns, from both near-field and teleseismic waveform analyses, and from detailed studies of the distributions and focal mechanisms of aftershocks.

#### Dextral Ruptures within the San Andreas Fault System

1966  $M_L 5.5$  Parkfield earthquake. This event is the latest in a series of characteristic

$M_L \sim 5.5$  earthquakes that previously ruptured the same Parkfield-Cholame segment of the San Andreas fault in 1934, 1922, 1901, 1881, and also possibly in 1857 as an immediate foreshock to the  $M=8$  earthquake which ruptured through the "Big Bend" [Bakun and McEvilly, 1984; Sieh, 1978]. Waveform analyses of the last three events show they were virtually identical, with the implication of strong local controls on the nucleation and stopping of these characteristic ruptures. Final ground breakage associated with the 1966 event extended for  $\sim 35$  km [Brown et al., 1967] (Figure 3a). Structurally significant features along the trace include a slight restraining bend associated with the epicenter, and a pronounced  $\sim 1$  km dilational jog separating echelon segments across the Cholame Valley. While dextral strike-slip at the surface eventually reached  $\sim 0.2$  m near the center of the rupture, most, if not all of it developed by afterslip over a period of two months following the main shock [Smith and Wyss, 1968]. Aftershock epicenters occurred in a narrow band nearly coincident with the surface rupture trace. From this and the seismic strong motion data, it has been argued that the main coseismic rupture was vertical, extended from 3–8 km depth, and propagated unilaterally southeastward for  $\sim 25$  km from the epicentral bend with a mean slip of 0.6 m, to terminate in the vicinity of the dilational jog [Lindh and Boore, 1981]. The surface fault break was discontinuous across the jog, but aftershock activity was particularly intense beneath a  $3.5$  km  $\times$  1 km rhomboidal area immediately northwest of its inferred

position, indicating that the echelon segmentation persisted throughout the seismogenic regime to a depth of around 12 km. Focal mechanisms for the vast majority of aftershocks were consistent with dextral strike-slip on subvertical planes parallel to the main rupture, but a component of normal dip-slip was evident for a few solutions within the dilational jog [Eaton et al., 1970]. There are also indications of relative subsidence within this rhombic area over a period of weeks following the earthquake [Brown et al., 1967]. The 8 km fault break extending southeast of the jog was probably entirely the product of post-mainshock afterslip, decreasing logarithmically with time along with the aftershock activity [Smith and Wyss, 1968].

1979 M<sub>l</sub> 5.9 Coyote Lake earthquake. Interpretations of rupture development during this Calaveras fault event (Figure 3b) are based largely on high precision aftershock studies and waveform analyses, because no clear surface break developed. However, the seismological data indicate remarkable similarities to the Parkfield earthquake. Mainshock slip averaging ~0.2 m occurred on a subvertical rupture extending from 3–10 km depth, which propagated unilaterally southeastward from the focus for 6–14 km [Bouchon, 1982; Liu and Helmberger, 1983] to terminate adjacent to a dilational jog defined by diffuse aftershock activity. Some 5 hours after the main earthquake, beginning with an M<sub>l</sub> 4.0 event, aftershock activity extended ~2 km southwest to an echelon fault segment and then migrated southeastward over a period of days to define a subsidiary slip plane 8 km in length at depths between 3 and 7 km [Reasenberg and Ellsworth, 1982]. Aftershock mechanisms were almost uniformly consistent with dextral strike-slip on subvertical planes parallel to the main rupture, except that within the dilational jog a clockwise swing of ~14° in the strike of probable fault planes was noted.

1979 M<sub>l</sub> 6.6 Imperial Valley earthquake. Similar behavior occurred during this earthquake, with the rupture propagating unilaterally northwestward for ~35 km with an average coseismic slip of ~0.4 m to terminate at a much larger scale dilational jog defined by the downthrown Mesquite Basin (Figure 3c). Surface faulting occurred only on the northern three-quarters of the rupture along the Imperial fault, and also along the subsidiary Brawley fault. Detailed analysis of the main rupture [Archuleta, 1984] shows that the amount of strike-slip, the slip rate, and the rupture velocity all diminish abruptly north of the intersection with the Brawley fault, but that the rupture continued on past a small restraining bend to stop finally where the strike of the Imperial fault veers northwards. For the first 8 hours after the main shock, aftershocks were almost entirely concentrated beneath a 7 km × 11 km rhombic area extending north from the main rupture ter-

mination. Minor activity later spread to the southeast [Johnson and Hutton, 1982].

1968 M<sub>l</sub> 6.4 Borrego Mountain earthquake. The Borrego Mountain earthquake rupture on the Coyote Creek fault within the San Jacinto fault zone is more complex than the previous examples. Unfortunately only limited strong motion data are available to constrain the rupture process. The surface break was mapped over a period of days following the main shock [Clark, 1972]. It extended a total distance of 31 km, but consisted of three distinct segments separated by anti-dilational and dilational jogs with step-overs of ~1.5 km (Figure 3d). The northern segment may also be terminating in a dilational jog at its northwestern extremity. Quaternary sediments have been deformed into east-west trending folds in the immediate vicinity of the antidilational jog, suggesting it has been a long-term impediment to slip transfer along the fault [Sharp and Clark, 1972]. From focal mechanism and aftershock studies, the main rupture plane dipped steeply (>80°) northeast [Allen and Nordquist, 1972]. Measured dextral strike-slip along the surface break reached a maximum value of ~0.38 m along the northern segment with no significant afterslip apparent. Slip decreased to maximum values of ~0.27 m and ~0.11 m on the central and southern segments respectively, but in both cases this included extensive afterslip. On the central segment afterslip was observed shortly after the main shock, starting in the southeast close to the dilational jog but then extending over its entirety. On the southern segment its onset was delayed for perhaps a year [Clark, 1972]. The location of the focus for the main shock is consistent with rupture initiation at a depth of ~11 km in the center of the northern fault segment with possible bilateral rupture growth [Allen and Nordquist, 1972]. Subsequent detailed waveform analyses [Burdick and Mellman, 1976; Ebel and Helmberger, 1982] suggest that most of the radiated energy came from high stress drop faulting localized in this same northern segment.

Well-located aftershocks were distributed over a broad region at depths down to 12 km [Hamilton, 1972]. However, there appear to be some significant correlations with the surface rupture geometry. Epicenters for most of the aftershocks plot northeast of the rupture trace at distances greater than can be attributed to location error or to the probable dip of the fault surface. Comparatively few were located in the immediate vicinity of the mainshock epicenter. The greatest concentration occurred northeast of the central segment adjacent to the antidilational jog, a region of reduced mean stress according to the Segall and Pollard [1980] analysis. While aftershock mechanisms were generally consistent with strike-slip rupturing parallel to the main surface trace, a thrust component was locally evident in the area of this jog. In marked con-

## 162 RUPTURE INTERACTION WITH FAULT JOGS

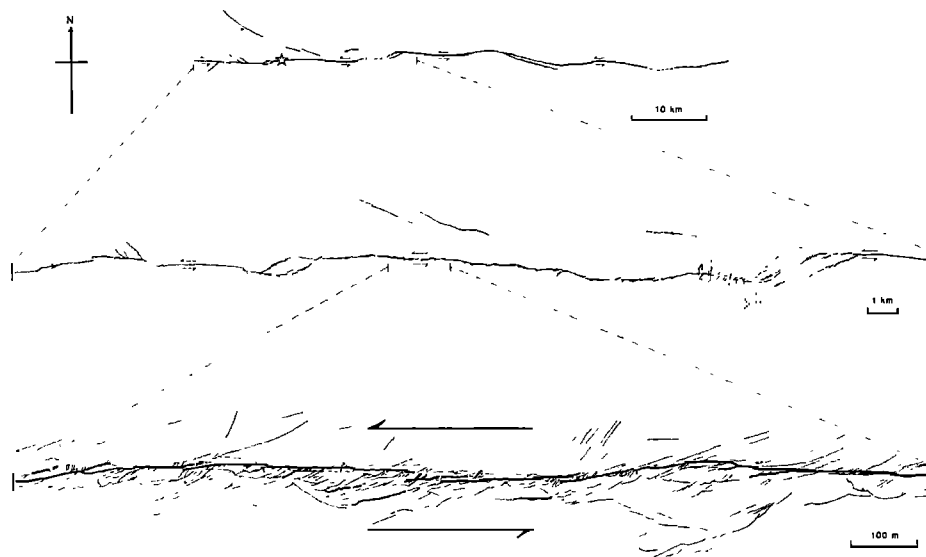


Fig. 4. Left-lateral rupture trace from the 1968  $M_s 7.2$  Dasht-e-Bayaz earthquake in northern Iran, showing broad and fine-scale infrastructure [after Tchalenko and Ambraseys, 1970; Tchalenko and Berberian, 1975]. Star indicates probable epicenter, stippling an area of intense sandblows.

trast, aftershocks in the vicinity of the southern dilational jog mostly lay between the rupture segments. Southeastward extension of activity along the southern rupture segment was noted a week after the main shock.

#### Dasht-e-Bayaz Rupture, N. E. Iran

Perturbation or control of strike-slip rupturing by fault jogs may also sometimes be inferred when no near-field seismological data are available, though the details of rupture interaction are then less certain. As an example we consider the left-lateral strike-slip rupture which resulted from the 1968  $M_s 7.2$  Dasht-e-Bayaz earthquake. About half of the ~80 km east-west rupture trace was mapped in detail [Tchalenko and Ambraseys, 1970; Tchalenko and Berberian, 1975], revealing both a fine and a broad scale infrastructure (Figure 4). Two dilational jogs with cross-strike dimensions of ~1 km are particularly prominent within the broad infrastructure. Abrupt changes in the measured slip occur in the vicinity of these features. An area of intense sandblows immediately adjacent to one of the jogs is also noteworthy. Although the instrumental epicenter is rather uncertain, the macroseismic epicenter lies close to one of the dilational jogs. Teleseismic waveform analysis suggests that the main rupture propagated from west to east in a highly erratic manner. "...at times decelerating to pause for several seconds" [Niazi, 1969], so that the overall average rupture velocity was only 0.5 km/s. It seems plausible that this irregular rupturing may be attributed to the major dilational jogs along the fault trace.

#### Summary of Rupture Behavior

A number of significant points emerge from the preceding discussion:

1. Broad infrastructure within major transcurrent fault zones can often be traced throughout the seismogenic zone by high precision microearthquake studies, reflecting irregularities in surface rupture patterns.
2. Structural control of rupture nucleation is only obvious in the case of the Parkfield earthquake where the epicenter coincides with a small restraining bend.
3. There is good evidence for rupture arrest at specific structural sites. Three of the four Californian ruptures considered in detail appear to have stopped at dilational fault jogs. During the Dasht-e-Bayaz earthquake, rupture growth was momentarily halted, probably at dilational jogs. However, southward expansion of the Borrego Mountain rupture was certainly impeded and possibly halted by an antidilational jog.
4. Where stopping occurs at a dilational jog, time-dependent slip transfer often leads to progressive extension of the aftershock zone onto an echelon fault segment. Such delayed slip transfer seems to occur over a wide range of time scales.
5. Contrasting aftershock patterns develop for ruptures arrested at dilational and antidilational jogs. At a dilational jog, aftershock epicenters tend to lie along the primary rupture or its extensions, with distinctive rhomboidal clusters, resembling swarm activity, associated with the jog. In the case of the Borrego Mountain earthquake where the initial rupture was at

least partly arrested by an antidilational jog, aftershocks were asymmetrically distributed over a broad area, mostly to one side of the rupture trace. For both varieties of jog, the greatest aftershock concentrations occur where mean stress may be inferred to have diminished as a consequence of the main rupture.

#### Internal Structure of Fault Jogs

From the foregoing it appears that dilational jogs may present a greater obstacle to the passage of earthquake ruptures than antidilational jogs, contrary to expectations from quasi-static analysis of echelon fault segmentation. This suggests that slip transfer across jogs may be additionally complicated by dynamic effects. Before exploring the mechanics of rupture interaction with fault jogs, we consider their probable internal structure with regard to incremental and long-term development.

#### Infrastructure of Dilational Jogs

The surface expression of dilational fault jogs is often characterized by elongate rhomboidal depressions contained within the main fault zone. In some cases, these depressions are sharply bounded by normal faults splaying off the strike-slip faults, in others the boundaries are obscured by marginal slumping [Freund, 1971; Mann et al., 1983]. However, given the dimensions and aspect ratios of these depressions, it seems implausible that the bounding normal faults are dominant structural components throughout the seismogenic regime. A further consideration is the strong tendency, demonstrable theoretically and experimentally, for echelon fault segments in this configuration to propagate into and become linked by extension cracks aligned perpendicular to the least principal compressive stress (Figure 2) [Brace and Bombolakis, 1963; Segall and Pollard, 1980]. This has also been widely observed in dilational jogs described on a range of scales from ancient fault zones [Spurr, 1925; Gamond, 1983]. Echelon fault segments tend to be linked through jogs by individual or multiple extension fractures, sometimes with subsidiary shears, or by the development of more extensive rhombic or lensoidal openings. Commonly, the linking fractures occur as hydrothermal extension veins or contain high-dilation, hydrothermally cemented breccias of angular wallrock fragments [Sibson, 1985]. Textures often record a history of incremental extensional opening, or of multi-episode brecciation and recementation.

The association of high b-value swarm seismicity with large-scale dilational jogs in the San Andreas fault system led Weaver and Hill [1979] to propose a fracture mesh model incorporating short conjugate strike-slip shears linked by vertical extension fractures. This accords with the preponderance of strike-slip focal mechanisms for aftershocks within dilational jogs, a normal slip component being evident in only a few instances.

Such a model, perhaps with some additional complexities from local normal faulting (Figure 5a), accounts satisfactorily for the observed characteristics of dilational fault jogs. An important geometrical consequence is that the total extensional opening across the linking fracture system in the direction of fault movement matches the slip transferred across the jog.

#### Infrastructure of Antidilational Jogs

Theory, experiments, and field observations demonstrate the tendency for the tips of echelon fault segments in antidilational jogs to diverge away from each other into extension fractures (Figure 2). However, the regions of possible tensile failure are small and development of subsidiary strike-slip faulting in a swathe linking and extending beyond the segment tips is more highly favored [Segall and Pollard, 1980]. In the case of the antidilational jog associated with the Borrego Mountain rupture this is borne out by aftershock focal mechanisms, which show that strike-slip faulting is dominant throughout the seismogenic regime with only minor thrusting. However, the problems of long-term slip transfer across the jog are manifested at the surface by extensive folding, thrusting and localized up-doming in the vicinity of such jogs (Figure 5a).

#### Mechanics of Rupture-Jog Interactions

An important mechanical distinction between dilational and antidilational jogs can therefore be made on the basis of their contrasting internal configurations (Figure 5a). Whereas slip transfer across an antidilational jog is accomplished largely by subsidiary faulting, across a dilational jog it additionally involves substantial opening of extension fractures. The field evidence for an association between hydrothermal fluid flow and dilational jog development suggests the further need to consider the mechanical effects of fluids during rupture-jog interactions.

#### Fluid Pressures, Fault Stability, and Aftershock Distributions

Background fluid pressures within mature fault zones are probably at hydrostatic levels or greater throughout the seismogenic regime, increasing downwards at >100 bars/km [Sibson, 1981]. It is now clear that seismic activity can be affected by changes in fluid pressure [Raleigh et al., 1972], and in turn, that large earthquakes may locally perturb fluid pressures [Nur and Booker, 1972]. In the upper few kilometers of the crust, at least, the frictional strength of faults appears to be adequately described by a simple failure criterion of Coulomb form,

$$\tau = C + \mu_s(\sigma_n - P) \quad (1)$$

where  $\tau$  and  $\sigma_n$  are respectively the shear and

## 164 RUPTURE INTERACTION WITH FAULT JOGS

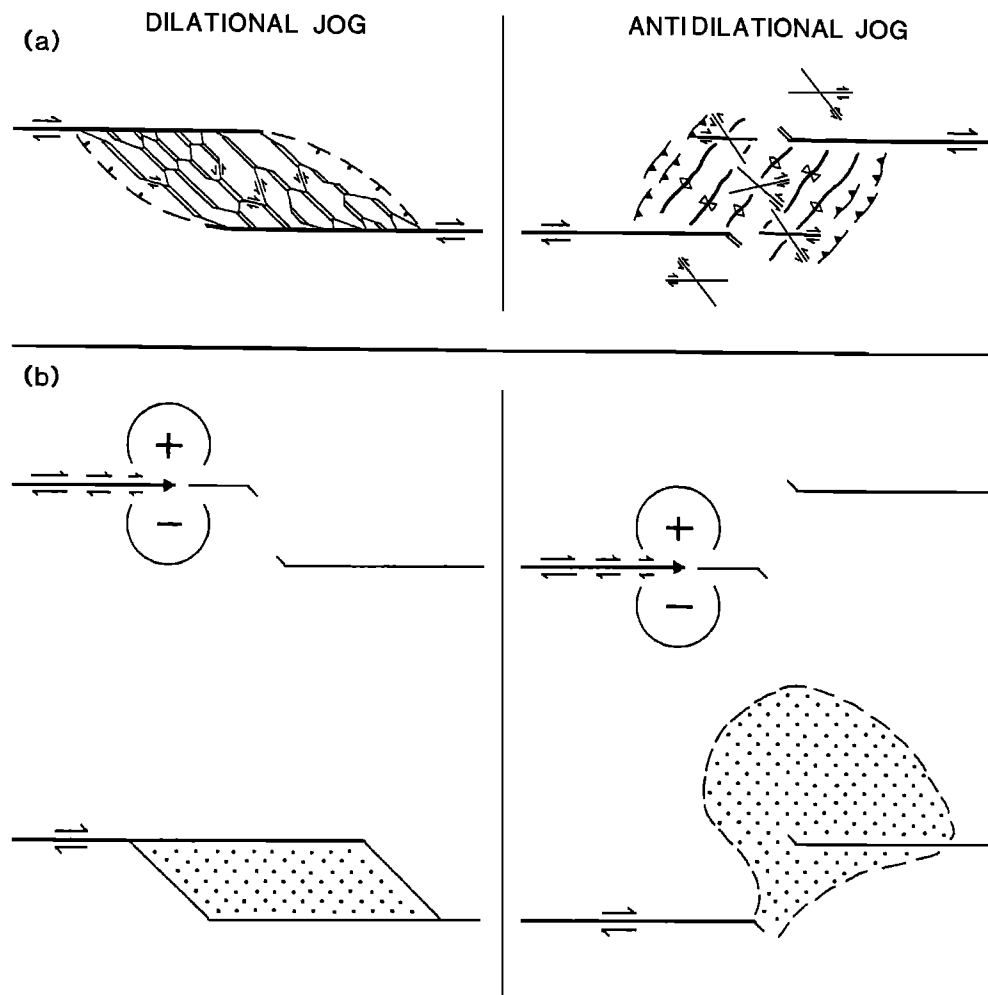


Fig. 5. (a) Synoptic maps of likely internal structure within dilational and antidilational fault jogs on a strike-slip fault. Extension fractures represented by parallel lines, subsidiary conjugate strike-slip faults by thin crisscross lines, normal faults by dashed lines with tick on downthrown side, thrusts by sawtooth lines and fold axial traces by thick wavy lines.

(b) Schematics of dextral ruptures terminating at dilational and antidilational fault jogs to produce contrasting aftershock distributions. Rupture tip fields of compression (+) and dilatation (-) are indicated.

normal stresses on the fault,  $P$  is the fluid pressure,  $C$  is the cohesive strength which may be rather low, and the coefficient of static friction,  $\mu_s$ , typically has a value of  $\sim 0.75$  [Sibson, 1983]. Seismic activity may therefore be triggered by increases in fluid pressure as well as by increased deviatoric stress. Conversely, faults are strengthened by a decrease in fluid pressure.

The contrasting patterns of aftershock activity developed following rupture arrest at dilational and antidilational jogs (Figure 5b) are consistent with Nur and Booker's [1972] hypothesis, and with subsequent elaborations [Booker,

1974; Rice and Cleary, 1976; Rudnicki - this volume], that the concentration and time-dependent decay of aftershock activity at rupture terminations are related to diffusion of aqueous fluids. In the Nur-Booker model, changes in fluid pressure immediately following the main shock reflect changes in mean stress, with fluids then migrating towards the zones of reduced stress. As fluid pressures within these zones return to their pre-mainshock values, shear failure occurs locally in accordance with equation (1), giving rise to aftershocks. At the specific structural sites under consideration, aftershock concentrations do indeed seem to be

occurring in regions where, from the Segall and Pollard [1980] analysis, mean stress should be lowered as a result of elastic interaction between echelon fault segments. For a dilational jog, mean stress is reduced between the echelon fault segments, but for an antidilational jog the areas of reduced stress lie adjacent to the step-over outside the main fault zone.

#### Rupture Interaction with Dilational Jogs

The observed perturbation or arrest of earthquake ruptures at dilational fault jogs, often followed by delayed slip transfer, suggests that these structures act as "kinetic barriers" which allow slow but oppose fast fault motion. One explanation for this behavior might be that easy slow slip transfer across such jogs leads to local destressing so that propagating ruptures are halted in regions of low strain energy concentration, the "seismic gap" method of rupture arrest [Husseini et al., 1975]. If this were the case, aseismic fault creep should be concentrated in the vicinity of dilational jogs prior to main-shock failure. To date, this has not been observed. At Parkfield, aseismic creep along the San Andreas fault dies out southeastward from the epicentral region toward the dilational jog [Burford and Harsh, 1980]. Moreover, the mechanism accounts for neither the time-dependent slip transfer following rupture arrest, nor the concentrations of aftershock activity within dilational jogs.

A preferred explanation for the time-dependent behavior of dilational jogs is based on the inference that seismic slip transfer across such structures requires concomitant opening of extension fractures. Even if deviatoric stresses are favorable, there are severe problems opening linking extensional fracture systems within fluid-saturated crust in periods comparable to earthquake slip durations of 1-10 seconds. Rapid extensional opening is strongly opposed by suctional forces from induced fluid pressure differentials which, for a wide range of possible rock permeabilities, can be expected to approach initial hydrostatic values at any depth through the seismogenic regime [Sibson, 1985]. The high-dilation breccias found in fossil dilational jogs are believed to form by hydraulic implosion of wallrock as a consequence of these transitory differences in fluid pressure. Drops in fluid pressure arising from incipient extensional opening within the jogs inhibit slip transfer further by strengthening subsidiary faults. The resistive forces scale with the width of the jogs. If the larger (~1 km wide) jogs are taken to extend through the seismogenic regime, the energy required for rapid slip transfer against induced suctions is comparable to the wave energy radiated by moderate or larger earthquakes. Once arrested at a dilational jog, strain energy concentrations at the rupture tip may be slowly dissipated by delayed slip transfer, leading to

aftershock migration as fluid pressures re-equilibrate by diffusion to allow extensional opening with the linking fracture system. The range of possible fluid diffusivities in the wallrock is sufficient to permit large variations in the rate of slip transfer, as is observed.

Large dilational jogs thus present formidable barriers to the rapid transfer of slip, though rupture arrest may sometimes only be momentary, as seems to have been the case with the Dasht-e-Bayaz earthquake. In connection with this event it is interesting to note the asymmetric localization of sandblow activity immediately to one side of a conspicuous dilational jog (Figure 4). For the west-to-east rupture propagation, this activity coincides with the expected compressional field associated with the tip of a rupture halted at the jog (cf. Figure 5b).

#### Rupture Interaction with Antidilational Jogs

In the case of antidilational jogs, it seems probable that the Segall and Pollard [1980] analysis holds good for both slow and fast slip transfer, so that the jogs persist as high strength barriers impeding all forms of fault motion.

#### Discussion

Dilational and antidilational fault jogs therefore present some interesting contrasts in behavior with regard to rapid and long-term slip transfer. Both types of jog may impede earthquake ruptures and lead to their partial or complete arrest. Observed aftershock distributions associated with ruptures terminating in both kinds of jog are consistent with Nur and Booker's [1972] hypothesis that they occur in regions of reduced mean stress as a consequence of induced fluid diffusion. For dilational jogs, the possibility of delayed slip transfer suggests they present no long-term impediment to fault motion in accordance with the quasi-static analysis of Segall and Pollard [1980]. Field evidence indicates they may often be long-lived features of fault zones [Mann et al., 1983]. In contrast, antidilational jogs form barriers to both incremental and long-term slip transfer. In view of this, one may speculate that they tend to be comparatively short-lived structures that have to be bypassed for large fault displacements to be accommodated.

Acknowledgments. Thanks to Ralph Archuleta and Peter Malin for helpful comments, and to Mrs. Ellie Dzuro for typing the manuscript. This work was supported by the National Science Foundation, grant number EAR83-05876.

#### References

Allen, C. R., The modern San Andreas fault, in The Geotectonic Development of California,

## 166 RUPTURE INTERACTION WITH FAULT JOGS

- edited by W. G. Ernst, pp. 511-534, Prentice-Hall, Inc., Englewood Cliffs, N. J., 1981.
- Allen, C. R., and J. M. Nordquist, Foreshock, mainshock and larger aftershocks of the Borrego Mountain earthquake, U.S. Geol. Surv. Prof. Pap. 787, 16-23, 1972.
- Ambraseys, N. N., Some characteristic features of the Anatolian fault zone, Tectonophysics 9, 143-165, 1970.
- Archuleta, R. J., A faulting model for the 1979 Imperial Valley earthquake, J. Geophys. Res. 89, 4559-4585, 1984.
- Aydin, A., and B. M. Page, Diverse Pliocene-Quaternary tectonics in a transform environment, San Francisco Bay region, California, Geol. Soc. Am. Bull. 95, 1303-1317, 1984.
- Bakun, W. H., and T. V. McEvilly, Recurrence models and Parkfield, California, earthquakes, J. Geophys. Res. 89, 3051-3058, 1984.
- Bakun, W. H., R. M. Stewart, C. G. Bufe, and S. M. Marks, Implication of seismicity for failure of a section of the San Andreas fault, Bull. Seismol. Soc. Am. 70, 185-201, 1980.
- Booker, J. R., Time-dependent strain following faulting of a porous medium, J. Geophys. Res. 79, 2037-2044, 1974.
- Bouchon, M., The rupture mechanism of the Coyote Lake earthquake of 6 August 1979 inferred from near-field data, Bull. Seismol. Soc. Am. 72, 745-757, 1982.
- Brace, W. F., and E. G. Bombolakis, A note on brittle crack growth in compression, J. Geophys. Res. 68, 3709-3713, 1963.
- Brown, R. D., J. G. Vedder, R. E. Wallace, E. F. Roth, R. F. Yerkes, R. O. Castle, A. O. Waanen, R. W. Page, and J. P. Eaton, The Parkfield-Cholame, California, earthquakes of June-August 1966, U.S. Geol. Surv. Prof. Pap. 579, 66 pp., 1967.
- Burdick, L. J., and G. R. Mellman, Inversion of body waves from Borrego Mountain earthquake to the source mechanism, Bull. Seismol. Soc. Am. 66, 1485-1499, 1976.
- Burford, R. O., and P. W. Harsh, Slip on the San Andreas fault in central California from alignment array surveys, Bull. Seismol. Soc. Am. 70, 1233-1261, 1980.
- Byerlee, J., V. Mjachkin, R. Summers, and O. Voevoda, Structures developed in fault gouge during stable sliding and stick-slip, Tectonophysics 44, 161-171, 1978.
- Clark, M. M., Surface rupture along the Coyote Creek fault, U.S. Geol. Surv. Prof. Pap. 787, 55-86, 1972.
- Crowell, J. C., Origin of Late Cenozoic basins in southern California, Soc. Econ. Paleo. Mineral. Spec. Publ. 22, 190-204, 1974.
- Das, S., and K. Aki, Fault plane with barriers: a versatile earthquake model, J. Geophys. Res. 82, 5658-5670, 1977.
- Eaton, J. P., M. E. O'Neill, and J. N. Murdock, Aftershocks of the 1966 Parkfield-Cholame, California, earthquake: a detailed study, Bull. Seismol. Soc. Am. 60, 1151-1197, 1970.
- Ebel, J. E., and D. V. Helmberger, P-wave com-
- plexity and fault asperities: the Borrego Mountain, California, earthquake of 1968, Bull. Seismol. Soc. Am. 72, 413-437, 1982.
- Flinn, D., Transcurrent faults and associated cataclasis in Shetland, J. Geol. Soc. London 133, 231-248, 1977.
- Freund, R., The Hope Fault: a strike-slip fault in New Zealand, N.Z. Geol. Surv. Bull. 86, 49 pp., 1971.
- Gamond, J. F., Displacement features associated with fault zones: a comparison between observed examples and experimental models, J. Struct. Geol. 5, 33-46, 1983.
- Hamilton, R. M., Aftershocks of the Borrego Mountain earthquake from April 12 to June 12, 1968, U.S. Geol. Surv. Prof. Pap. 787, 31-54, 1972.
- Husseini, M. I., D. B. Johanovich, M. J. Randall, and L. B. Freund, The fracture energy of earthquakes, Geophys. J. R. Astron. Soc. 43, 367-385, 1975.
- Johnson, C. E., and L. K. Hutton, Aftershocks and pre-earthquake seismicity, the Imperial Valley, California, earthquake, October 15, 1979, U.S. Geol. Surv. Prof. Pap. 1254, 59-76, 1982.
- Kanamori, H., The nature of seismicity patterns before large earthquakes, in Earthquake Prediction: an International Review, edited by D. W. Simpson and P. G. Richards, Maurice Ewing Ser. Vol. 4, pp. 1-19, AGU, Washington, D.C., 1981.
- Kanamori, H., and G. S. Stewart, Seismological aspects of the Guatemala earthquake of February 4, 1976, J. Geophys. Res. 83, 3427-3434, 1978.
- Kupfer, D. H., Width of the Alpine Fault Zone, New Zealand, N.Z. J. Geol. Geophys. 7, 685-701, 1960.
- Lensen, G. J., Analysis of progressive fault displacement during downcutting at the Branch River terraces, South Island, New Zealand, Geol. Soc. Am. Bull. 79, 545-555, 1968.
- Lindh, A. G., and D. M. Boore, Control of rupture by fault geometry during the 1966 Parkfield earthquake, Bull. Seismol. Soc. Am. 71, 95-116, 1981.
- Liu, H-L., and D. V. Helmberger, The near-source ground motion of the 6 August 1979 Coyote Lake, California, earthquake, Bull. Seismol. Soc. Am. 73, 201-218, 1983.
- Madariaga, R., High frequency radiation from dynamic fault models, Annales Geophysicae 1, 17-23, 1983.
- Mann, P., M. R. Hempton, D. C. Bradley, and K. Burke, Development of pull-apart basins, J. Geol. 91, 529-554, 1983.
- Niazi, M., Source dynamics of the Dasht-e-Bayaz earthquake of August 31, 1968, Bull. Seismol. Soc. Am. 59, 1843-1861, 1969.
- Nur, A., and J. R. Booker, Aftershocks caused by pore fluid flow? Science 175, 885-887, 1972.
- Nur, A., and M. Israel, The role of heterogeneities in faulting, Phys. Earth Planet. Inter. 21, 225-236, 1980.
- Raleigh, C. B., J. H. Healy, and J. D. Bredehoeft, Faulting and crustal stress at

- Rangely, Colorado, Geophys. Monogr. Ser. 16, 275-284, AGU, Washington, D.C., 1972.
- Reasenberg, P., and W. L. Ellsworth, Aftershocks of the Coyote Lake, California, earthquake of August 6, 1979: a detailed study, J. Geophys. Res. 87, 10,637-10,655, 1982.
- Rice, J. R., and M. P. Cleary, Some basic stress-diffusion solutions for fluid-saturated elastic porous media with compressible constituents, Rev. Geophys. Space Phys. 14, 227-241, 1976.
- Rudnicki, J. W., Coupled deformation-fluid diffusion effects accompanying slip on an impermeable fault, - this volume.
- Rudnicki, J. W., and H. Kanamori, Effects of fault interaction on moment, stress drop, and strain energy release, J. Geophys. Res. 86, 1785-1793, 1981.
- Schwartz, D. P., and K. J. Coppersmith, Fault behavior and characteristic earthquakes: examples from the Wasatch and San Andreas fault zones, J. Geophys. Res. 89, 5681-5698, 1984.
- Segall, P., and D. D. Pollard, Mechanics of discontinuous faults, J. Geophys. Res. 85, 4337-4350, 1980.
- Sharp, R. V., Implications of surficial strike-slip fault patterns for simplification and widening with depth, U.S. Geol. Surv. Open file Rep. 79-1239, 66-78, 1979.
- Sharp, R. V., and M. M. Clark, Geologic evidence of previous faulting near the 1968 rupture on the Coyote Creek fault, U.S. Geol. Surv. Prof. Pap. 787, 131-140, 1972.
- Sibson, R. H., Fluid flow accompanying faulting: field evidence and models, in Earthquake Prediction: an International Review, edited by D. W. Simpson and P. G. Richards, Maurice Ewing Ser. 4, pp. 593-603, AGU, Washington, D.C., 1981.
- Sibson, R. H., Continental fault structure and the shallow earthquake source, J. Geol. Soc. London 140, 741-767, 1983.
- Sibson, R. H., Stopping of earthquake ruptures at dilatational fault jogs, Nature 316, 248-251, 1985.
- Sieh, K. E., Slip along the San Andreas fault associated with the great 1857 earthquake, Bull. Seismol. Soc. Am. 68, 1421-1448, 1978.
- Sieh, K. E., and R. H. Jahns, Holocene activity of the San Andreas fault at Wallace Creek, California, Geol. Soc. Am. Bull. 95, 883-896, 1984.
- Smith, S. W., and M. Wyss, Displacement on the San Andreas fault subsequent to the 1966 Park-field earthquake, Bull. Seismol. Soc. Am. 58, 1955-1973, 1968.
- Spurr, J. E., The Camp Bird compound veindike, Econ. Geol. 20, 115-152, 1925.
- Tchalenko, J. S., and N. N. Ambraseys, Structural analysis of the Dasht-e-Bayaz (Iran) earthquake fractures, Geol. Soc. Am. Bull. 81, 41-60, 1970.
- Tchalenko, J. S., and M. Berberian, Dasht-e-Bayaz fault, Iran: earthquake and earlier related structures in bed rock, Geol. Soc. Am. Bull. 86, 703-709, 1975.
- Vedder, J. G., and R. E. Wallace, Map showing recently active fault breaks along the San Andreas and related faults between Cholame Valley and Tejon Pass, California, scale 1:24,000, Geol. Misc. Invest. Map 1-574, U.S. Geol. Surv., Reston, Va., 1970.
- Wallace, R. E., Surface fracture patterns along the San Andreas fault, in Proceedings of the Conference on Tectonic Problems of the San Andreas fault system, edited by R. L. Kovach and A. Nur, Spec. Publ. Geol. Sci. XIII, pp. 248-250, Stanford University Press, Palo Alto, Ca., 1973.
- Weaver, C. S., and D. P. Hill, Earthquake swarms and local crustal spreading along major strike-slip faults in California, Pure Appl. Geophys. 117, 51-64, 1979.

VARIATIONS IN THE GEOMETRY AND AMOUNT OF SLIP ON THE HAIYUAN  
(NANXIHAUSHAN) FAULT ZONE, CHINA AND THE SURFACE RUPTURE  
OF THE 1920 HAIYUAN EARTHQUAKE

Deng Qidong, Chen Shefa, Song Fangmin, Zhu Shilong, and Wang Yipeng

Institute of Geology, State Seismological Bureau, Beijing, China

Zhang Weiqi and Jiao Decheng

Seismological Bureau of Ningxia-Hui Autonomous Region, Yinchuan, China

B.C. Burchfiel, P. Molnar, L. Royden, and Zhang Peizhen

Department of Earth, Atmospheric, and Planetary Sciences  
Massachusetts Institute of Technology, Cambridge, Massachusetts 02139

**Abstract.** The Haiyuan earthquake ( $M = 8.7$ ) of December 16, 1920, in China caused strike-slip displacement along 220 km of the Haiyuan (or Nanxihaushan) Fault Zone, which lies on the northeastern margin of the Qinghai-Xizang (Tibetan) plateau. The Haiyuan fault zone, which strikes  $285^\circ$ - $295^\circ$ , apparently became an active sinistral strike-slip during Pleistocene time. The fault zone is composed of at least eight major subparallel shear fractures, most of which are arranged in a left-stepping pattern, and as many as six pull-apart basins have formed in the central segment of the fault zone. River systems of different ages have been sinistrally offset different amounts. Variations in the sense of vertical motion have occurred along segments of the fault, and pull-apart basins are commonly associated with the areas where normal components on subparallel segments prevail. Relatively young faults with oblique normal slip strike parallel to the overall trend of the fault zone and intersect the major subparallel shear faults with acute angles (10 to  $15^\circ$ ). The earthquake fault of 1920 caused slip along the major strike-slip fault segments and along oblique normal faults within pull-apart basins. Thus segments with pure strike-slip and with oblique normal slip, were activated in 1920, each with different surficial features and with different amounts of slip.

#### Introduction

A disastrous earthquake ( $M = 8.7$ ) occurred near the boundary between the southernmost part of the Ningxia-Hui Autonomous Region and Gansu in Central China: the Haiyuan earthquake of December

16, 1920. Its intensity in the epicentral area reached XII, and many of the cities and villages near the fault were destroyed by the shock. According to historic records [Lanzhou Institute of Seismology and Seismology Brigade of the Ningxia-Hui Autonomous Region, 1980], 234,117 people died because of the earthquake. This number of casualties is one of the largest associated with an earthquake in this century.

The Haiyuan earthquake occurred along the Haiyuan fault, often also called the Nanxihaushan fault, which is a major active fault in the northeastern marginal belt of Qinghai-Xizang (Tibetan) Plateau [e.g. Deng, 1982]. Surface faulting and macroseismic effects suggest a rupture length of 220 km. Since 1981, we have been investigating the geometry and sense of slip on the many strands of different dimensions associated with the latest phase of activity. This paper deals mainly with the geometric features of the 1920 surface rupture, the distribution of dislocations, and their relation to deformation along the Haiyuan fault zone during Pleistocene time.

#### Haiyuan Fault Zone

The Haiyuan fault zone is a major active fault on the northeastern margin of the tectonic belt of the Qinghai-Xizang (Tibetan) Plateau (Figure 1). It connects the northern marginal faults of the Qilianshan range on the west with the eastern piedmont faults of the Liupanshan on the east. To the north are the Tianjingshan fault and Niushoushan fault, which are shorter than the Haiyuan fault and along which there is a large reverse component of slip [Deng et al., 1984].

170 HAIYUAN FAULT ZONE

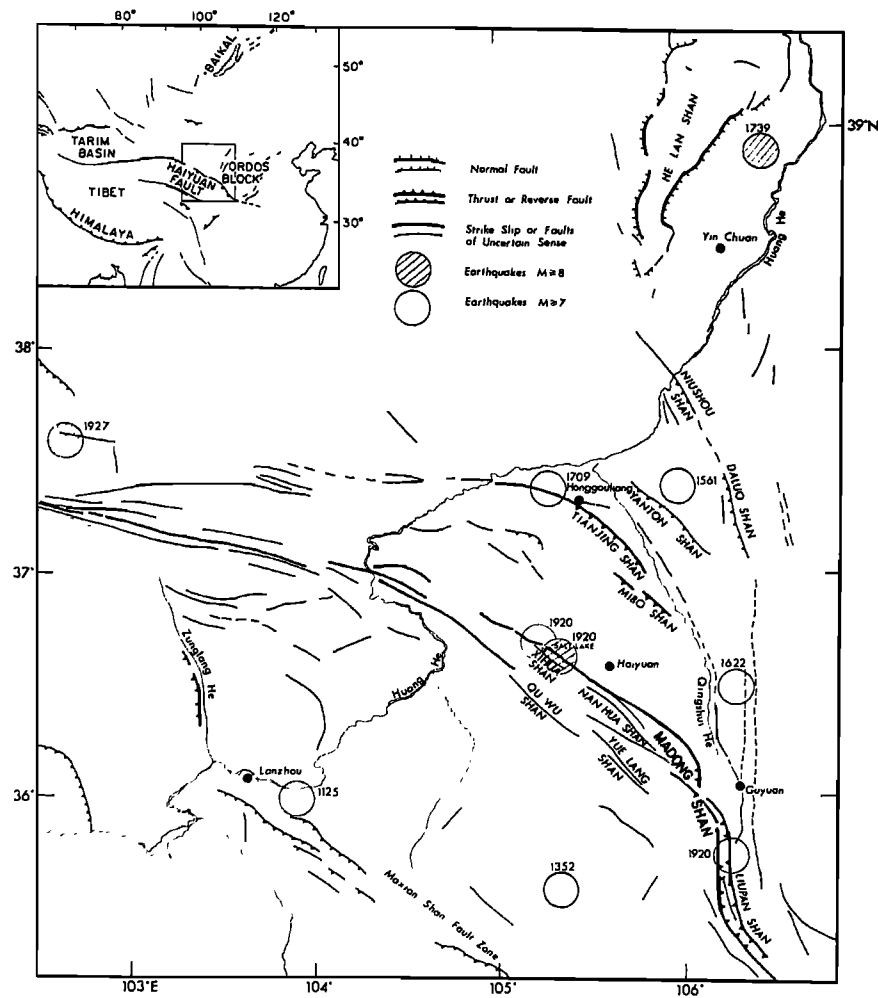


Fig. 1. The regional tectonic setting of the Haiyuan fault zone.

The Haiyuan fault zone is a left-lateral strike slip fault zone with an overall strike of  $285^{\circ}$ - $295^{\circ}$  but with a strike of  $320^{\circ}$  at its eastern end. Displacement appears to have begun in Quaternary time. The streams and gullies that cross the fault are of different ages and have been sinistrally offset different amounts (Figure 2). The fault cuts crests of ridges and all geologic formations [Deng et al., 1984; Song et al., 1983]. The intense shear deformation is concentrated in a narrow zone 1-4 km wide. Within the segment 170-180 km long where we have worked, the strike-slip fault zone is composed of eight distinct segments with quite different lengths. Except for the eastern segment SF<sub>1</sub>, all segments intersect the overall trend of the strike-slip fault zone with acute angles of about  $10^{\circ}$ - $15^{\circ}$ . Therefore, the surface trace of the overall fault zone is not one single, straight strand, but instead consists of a series of discontinuous subparallel shear fractures labeled SF in Figure 3. This arrangement of fractures

within a fault zone has been referred to as a pinnate arrangement [Chen and Deng, 1985; Deng et al., 1966; Deng and Zhang, 1984]. Table 1 and Figure 3 show basic characteristics of each of the subparallel fractures in the region studied. Portions of the subparallel fractures show reverse components of oblique left-lateral strike slip, while other portions show normal components of slip faulting. Therefore, they display pivotal movement (Table 1). The one notable exception is SF<sub>1</sub>, which trends more southeasterly than the others and across which there is a large component of crustal shortening.

Among these subparallel shear fractures, SF<sub>1</sub> and SF<sub>2</sub> show a right-stepping discontinuity, and the others show a left-stepping discontinuity (Figure 3). Therefore, crustal shortening occurs in the overlapping segment of SF<sub>1</sub> and SF<sub>2</sub>, and pull-apart basins of different sizes have formed between the other overlapping segments. The sizes of the pull-apart basins are quite different from one another, probably because of

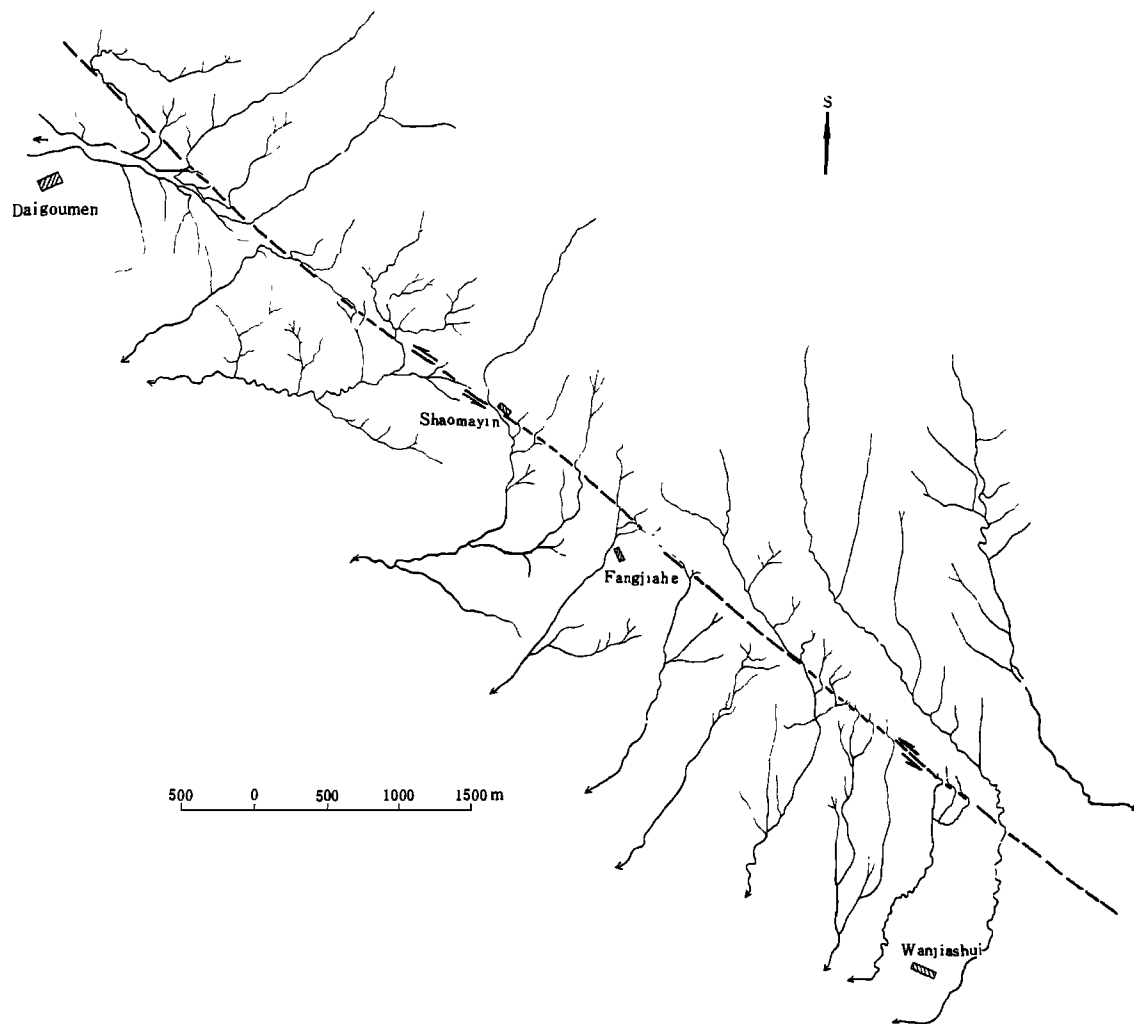


Fig. 2. Offset drainage systems along the northern piedmont fault of the Xihuashan range (middle segment of SF<sub>2</sub>).

different amounts of overlap and different distances between overlapping segments. Two sides of the pull-apart basins are bounded by subparallel shear faults generally with normal components of displacement. These pull-apart basins have formed mainly in the middle segment of the Haiyuan strike-slip fault zone. The Salt Lake Basin (PB<sub>1</sub>), the Dayingshui Basin (PB<sub>4</sub>), the Shaoshui Basin (PB<sub>5</sub>) and the Huangliangtan Basin (PB<sub>6</sub>) are typical of rhombic pull-apart basins within a shear zone (Figure 3). The Qingjiawan and Lijiagou Basins (PB<sub>2</sub> and PB<sub>3</sub>, Figure 3b) are smaller and younger than the other basins. The main characteristics of the pull-apart basins are described in Table 2.

At the ends of the pull-apart basins, usually there are a series of bounding normal fault systems (labeled NF on Figure 3) that intersect the subparallel shear faults with a large angle.

The western normal fault system of Shaoshui Basin (NF<sub>2</sub>) and northwestern normal fault system of the Salt Lake Basin (NF<sub>1</sub>) are typical. The northwestern bounding normal fault of the Shaoshui Basin (NF<sub>2</sub>) extends for 2.5 km and is composed of several normal faults, forming multi-stepped fault scarps. The heights of individual fault scarps are 1-5 m, but the cumulative height of multi-stepped fault scarps reaches 15-25 m. The fault scarps strike 058° and dip southeast, approximately perpendicular to subparallel shear faults of the basins. The normal fault system on the northwestern edge of the Salt Lake Basin strikes about 080°. Three main bounding normal faults are approximately parallel to each other, and displacement on them causes a gentle average slope of the mountain on the northwestern side of the basin. Along the fault system, 13 small normal fault scarps

## 172 HAIYUAN FAULT ZONE

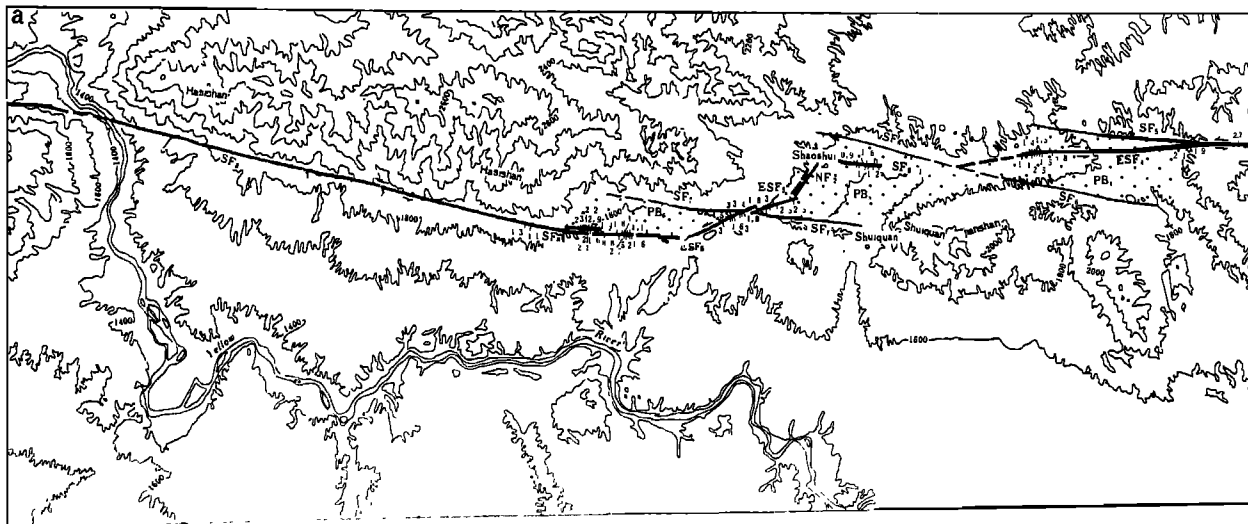


Fig. 3a.

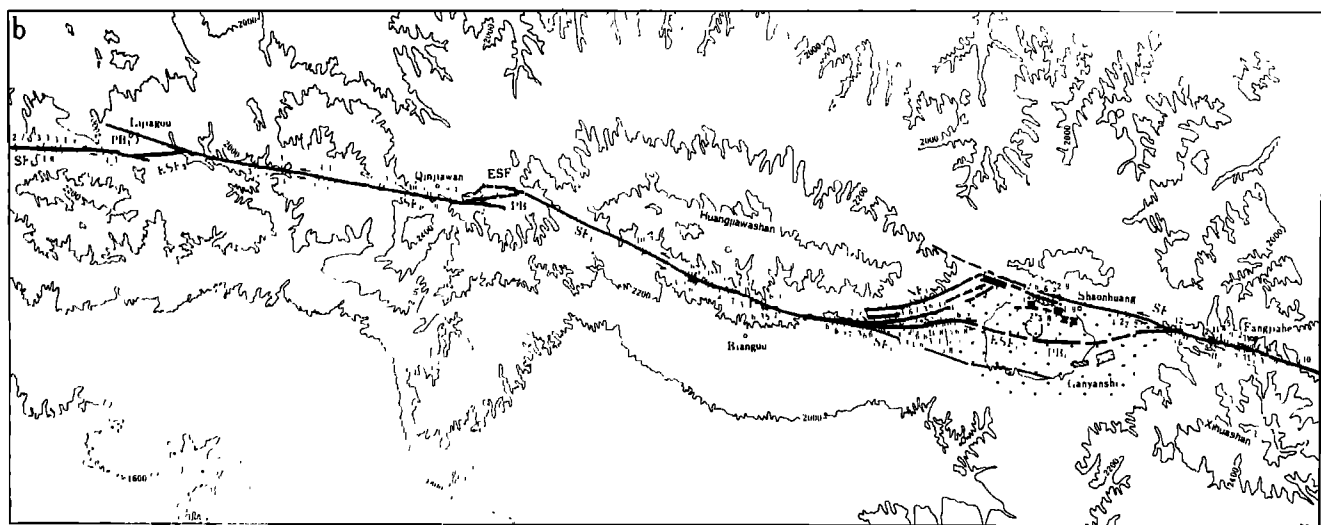


Fig. 3b.

Fig. 3. Distribution of surface faulting and measured offsets associated with the 1920 Haiyuan earthquake: (a) western part; (b) middle part; and (c) eastern part. Legend on 3c is as follows: 1. Surface rupture; 2. the active fault of late Quaternary age; 3. surface rupture with a strike-slip sense; 4. normal sense; 5. thrust sense; 6. offset ridge crests or farming walls; 7. offset gullies; 8. pull-apart basins of approximately middle Pleistocene to Holocene age; 9. the pull-apart basin of approximately late Pleistocene to Holocene age; 10. springs; 11. ruins caused by the 1920 earthquake; 12. SF<sub>1</sub>-SF<sub>8</sub> -- subparallel shear faults; 13. NF<sub>1</sub> and NF<sub>2</sub> -- marginal normal faults; 14. ESF<sub>1</sub>-ESF<sub>6</sub> -- inner-tensile shear faults; 15. PB<sub>1</sub>-PB<sub>6</sub> -- pull-apart basins.

striking 265°-270° with 7.8 m of combined total vertical displacement formed during the Haiyuan earthquake.

It should be noted that within the basins we have found groups of strike-slip faults with normal components, striking nearly parallel to

the general strike of the Haiyuan fault zone and intersecting the subparallel shear faults with acute angles 10°-15°. Their detailed features are listed in Table 3. Generally speaking, this type of faulting has been relatively intense during late Holocene time, and these faults often

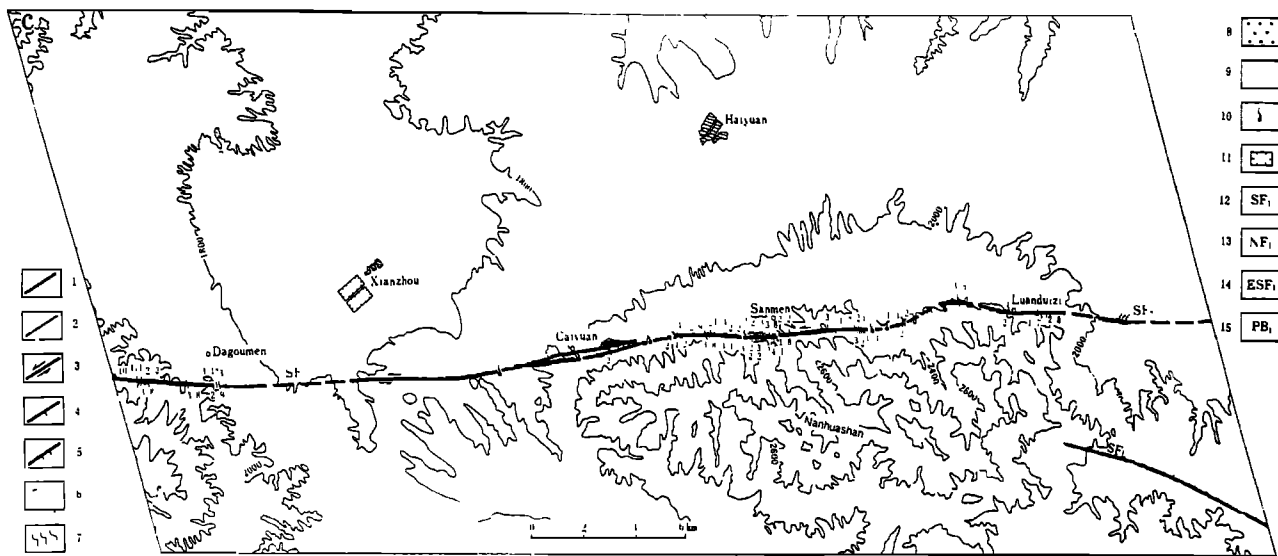


Fig. 3c.

bound the deepest parts of the basins and the areas with the thickest accumulations of sediments. They offset young gullies and show obvious sinistral strike-slip movement, but they form fault scarps with different heights. Faulting is generally oblique normal slip, and we call these faults inner tensile-shear faults. They seem to have developed after the pull-apart basins formed. The secondary shear faults bounding the two sides of the pull-apart basins are linked with each other by this group of faults. Based on our field work, the surface ruptures within pull-apart basins produced by the 1920 Haiyuan earthquake occurred mostly along this type of fault.

The pull-apart basins mentioned above began to develop during the middle part of Pleistocene time. On the south side of the Salt Lake Basin, conglomerates assigned an early Pleistocene age dip south away from the basin. Studies of pebble imbrication in these conglomerates indicate the source of the clasts was from the north. The conglomerates now form a ridge that is topographically higher than the basin to the north and that is bounded by faults forming the southern boundary of the basin. Thus the basin must have begun to form after deposition of these conglomerates. Loess deposits assigned a late Pleistocene age unconformably overlie the early Pleistocene conglomerates and dip into the basin from Salt Lake Basin, which formed between the times of deposition of these two formations, approximately during the middle part of Pleistocene time. Before middle Pleistocene time, a number of parallel thrust faults with northwest to west-northwest strikes ( $295^{\circ}$ - $315^{\circ}$ ), and some depressions associated with them, developed within the region. In the

Huang-liangtan Basin, the youngest formation cut by the thrust faults is a gravel layer assigned an early Pleistocene age (Figure 4).

North of the thrust faults and parallel to them, an active normal fault bounds the southern side of the basin. Similar relations between older thrust faults and active normal faults in other areas along the Haiyuan fault suggest that a change from thrust faulting to normal faulting took place since the early part of Pleistocene time. Furthermore, these relations suggest some segments of the Haiyuan left-lateral strike-slip fault may have formed along the base of a thrust fault system of pre-middle Pleistocene age. We imagine that within a narrow zone of shear strain a series of discontinuous subparallel shear faults may have formed along different segments of pre-existing thrust fault.

#### Surface Faulting Associated With the 1920 Haiyuan Earthquake

Many phenomena produced by the 1920 earthquake can be seen clearly after more than 60 years. The style of deformation associated with that earthquake appears to be quite similar to that produced during earlier displacements on the Haiyuan fault. The earthquake rupture, which has some features of brittle shear ruptures, was most clearly developed along segments SF<sub>2</sub>, SF<sub>4</sub>, SF<sub>8</sub>, the middle and western segments of SF<sub>3</sub>, and the eastern segment of SF<sub>5</sub>.

A number of en echelon tensile cracks striking nearly east-west and small grabens and mole tracks striking northwest-southeast formed during the earthquake. Ridge crests, old farming walls, and gullies were displaced sinistrally across the fault, and the maximum measured horizontal

TABLE 1. The Active Features of the Major Subparallel Shear Faults of the Haiyuan Fault Zone

Number	Length (km)	Strike	Dip Direction of Fault and Its Variation	Sense of Slip	Description of Amounts of Slip or Separation
SF <sub>1</sub>	60	300°-320°		normal and strike slip	The maximum displacement is in the middle segment. The unconformity between Tertiary and Precambrian rocks is sinistrally offset approximately 14 km; the offsets of gullies (A) and (B)* reach 500-600m and 50-90m, respectively, but decrease towards both the east and the west.
SF <sub>2</sub>	63	305°-310°	eastern segment: NNE middle segment: SSW western segment: SSW	reverse and strike slip normal and strike slip	Offsets of streams (A) and (B) reach 180-260m and 30-80m, respectively.
SF <sub>3</sub>	20	305°	NNE	normal and strike slip in the eastern part and reverse strike slip in the western part	Offsets of streams (A) and (B) reach 10km; offsets of streams (A) reach 120-170m.
SF <sub>4</sub>	15	300°	NNE	reverse and strike slip	A layer of Lower silurian rock is sinistrally separated 10km; offsets of streams (A) reach 120-170m.
SF <sub>5</sub>	15	295°	SSW	reverse and strike slip in the eastern part, normal and strike slip in the western part.	Offsets of streams (A) and (B) reach 190m and 20-35m, respectively.
SF <sub>6</sub>	15	300°	NNE in east segment SSW in west segment	normal and strike slip	A layer of Carboniferous rock is sinistrally separated 8km.
SF <sub>7</sub>	12	295°	NNE	normal and strike slip in the eastern part; reverse and strike slip in the western part	Triangular facets formed in Shaoshui Basin.
SF <sub>8</sub>	>25	300°	NNE	normal and strike-slip in the eastern part; reverse and strike slip in the western part.	Offsets of streams (A) and (B) reach 120-200m and 30-50m, respectively.

\*The streams (A) probably formed during latest Pleistocene time and streams (B) during middle or late Holocene time.

TABLE 2. The Basic Features of Pull-apart Basins Along the Middle Segment of the Hailuyan Fault Zone

Number	Basin Name	Size L W (km)			Quaternary Thickness (m)	Age for Basin	Age for Basement	Comment
PB1	Salt Lake	8	3	2.7	176.15	Q2-Q4	Precambrian	The center is located north of inner tensile-shear fault and the floor of the basin dips toward the north.
PB2	Qingjiawan	2	1	2	quite thin	Q3-Q4		Small size shown topographically as a depression, 160m below surrounding mountains, and covered with loess on the surface.
PB3	Lijigou	2	1	2	quite thin	Q3-Q4		Small size; a topographic depression 50m below surrounding mountains.
PB4	Dayingshui	8	2.5	3.2	>750.15	Q2-Q4	Devonian-Triassic	The Holocene center is bounded by an inner tensile-shear fault; the floor of the basin dips to the north.
PB5	Shaoshui	4	3	1.3	>335.15	Q2-Q4	Silurian-Devonian	The deepest part is bounded by a normal fault on its western margin; the floor of the basin dips to the west.
PB6	Huangliang-tan	5.5	1.5	3.7	>120.91	Q2-Q4		The deepest part is located near the southern fault; the floor of the basin dips to the south.

## 176 HAIYUAN FAULT ZONE

TABLE 3. The Basic Features of Inner Tensile-Shear Faults

Number	Locality	Orientation	Behavior	Length (km)	Comments
ESF1	Salt Lake Basin	280°-300° strike dips to the north in the eastern part; and to the south in the western part.	oblique normal strike slip fault	13	Fault at surface curves as a reverse "S" shape; the youngest gullies were offset sinistrally; in the west segment surface faulting from 1920 shows 6.5-7.5m of offset on a fault scarp dipping to the south with 2.3m of vertical slip, revealed by trenching; in the eastern segment, the fault scarp is 2m high and dips to the north.
ESF2	Qingjiawan Basin	290° strike	oblique normal strike slip	>2	The town wall of Sanjiao was offset sinistrally 2m by the 1920 earthquake.
ESF3	Lijiaogou Basin	284° strike	oblique normal strike slip	2	
ESF4	Dayingshui Basin	286° strike dips to the south	oblique normal strike slip	9	The youngest gullies were offset sinistrally; the maximum horizontal component of the slip in 1920 reached 5.8m; the fault scarp is 10m high; the deepest part of the basin is located on the south side of this fault.
ESF5	Shaoshui Basin		oblique normal strike slip	1.5	The horizontal component of slip during the 1920 earthquake fault reaches 2-3m; the youngest gullies have been offset 25-35m.
ESF6	Huangliangtan Basin		oblique normal strike slip	3	The youngest gullies have been offset sinistrally about 20-40m.

TABLE 4. The Distribution of Horizontal Dislocations Associated with the 1920 Haizhuan Earthquake

Fault type and Its Number	Maximum Horizontal Dislocation (m)	Average of the Measured Horizontal Dislocations (m)	Number of Measurements	Notes
SF2 middle segment	4-5	2.55	34	
	10-11	5.70	25	(approximate epicenter of M=8, Dec. 16, 1920)
west segment	4-6	3.49	11	
SF3	8.5-10.2	5.76	22	(approximate epicenter of M=7 aftershock, Dec. 25, 1920)
SF4	7.7-10.5	5.74	12	
SF5	4.3	3.43	6	
SF6-1	1.6	1.17	4	
SF8 east segment	4.5-5.2	2.97	17	
ESF1	6.5-7.5	4.89	17	
ESF2	2.0	2.0	1	
ESF4	5.8	2.64	8	
ESF5	3.0	2.45	4	
ESF6	4.5	2.90	7	
Tot 1	10-11	4.02	168	

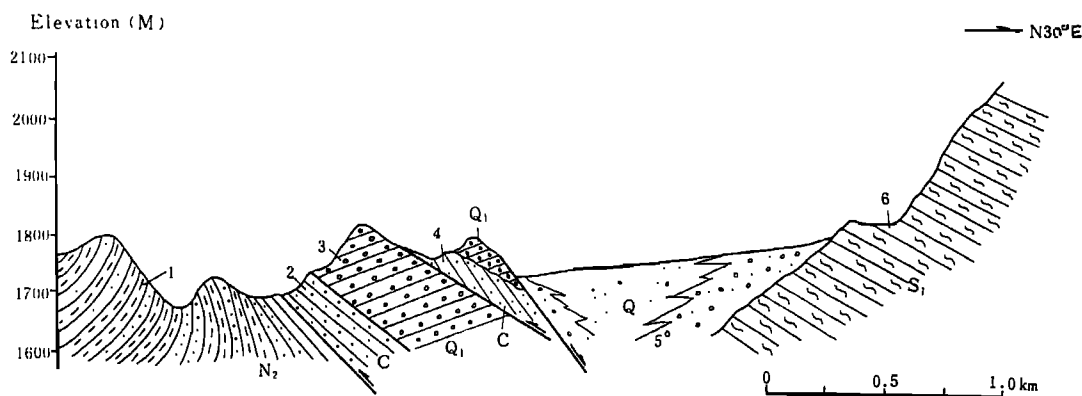


Fig. 4. Cross section in Huangliangtan area. 1. red sandstone and mudstone; 2. grey and green sandstone; 3. conglomerate; 4. yellow sandstone; 5. sand and gravel; and 6. slate. Location shown on Figure 3.

displacement reached 10–11 m. The surface rupture follows the major segments of the fault zone and also consists of several discontinuous, subparallel shear ruptures. Landslides and rock slides of varying sizes occurred where faults were covered by loess and where the topographic slope was steep. For instance, a large lake located at the eastern segment of SF<sub>1</sub> was dammed by a large landslide, and several small landslides occurred along SF<sub>4</sub>.

Surface faulting is rare along strike-slip faults at the margins of pull-apart basins, but is present in a few places. For instance, the shear faults of both the western segment of SF<sub>2</sub> and the eastern segment of SF<sub>8</sub> ruptured during the 1920 earthquake. No surface faulting was observed along the shear fault SF<sub>6</sub> north of the Shaoshui Basin, but south of SF<sub>6</sub> a surface rupture lies parallel to the overall strike of SF<sub>6</sub>. Generally, surface ruptures at the margins of the pull-apart basins are complicated and consist of a series of scarps and grabens. Such fractures are clearly observed striking west-northwest north of Salt Lake Basin. Except for these faults, there are no surface ruptures along the shear faults bounding the other pull-apart basins, such as along the southern margin of the Salt Lake Basin, the southern and northern margins of the Dayingshui Basin, the western segments of SF<sub>5</sub> and SF<sub>6</sub>, the southern margin of the Shaoshui Basin, and the northern margin of the Huangliangtan Basin, SF<sub>7</sub>.

Why did surface faulting not occur on shear faults bounding these pull-apart basins? Perhaps displacement was transferred from shear faults outside the basin to inner tensile-shear faults (labeled ESF<sub>1</sub>–ESF<sub>6</sub> in Figure 3) within the pull-apart basins. Indeed, there are obvious traces of dislocations and surface faulting along all of the inner-tensile shear faults. For example, surface ruptures on ESF in the Salt Lake Basin, associated with the 1920 Haiyuan earthquake, include several fault scarps over 2 m

high, en echelon tensile cracks, en echelon mole tracks, and small grabens. More than ten farming walls and gullies on the western edge of the Salt Lake Basin were dislocated sinistrally. Finally, following the earthquake, the salt lake in the basin shifted about 500 m towards the north. Presumably tilting was associated with strike-slip and normal slip on both inner tensile-shear faults and the shear fault on the northern margin of Salt Lake Basin [Lanzhou Institute of Seismology and the Seismology Brigade of the Ningxia Hui Autonomous Region, 1980]. In the Qingjiawan Basin, the town wall of Shangjiaocheng was displaced sinistrally 2 m. Faulting also occurred along ESF<sub>4</sub> in Dayingshui Basin, creating young fault scarps and offsetting small gullies sinistrally. Along ESF<sub>5</sub> surface faulting can be observed only at the western corner of Shaoshui Basin and where ESF<sub>5</sub> links up with ESF<sub>6</sub> in the east corner of Huangliangtan Basin.

During the 1920 earthquake, slip also occurred on some segments of normal faults bounding the pull-apart basins. For example, many traces of surface faulting are present on the normal faults (NF<sub>1</sub>, NF<sub>2</sub>), that bound the western sides of the Salt Lake and the Shaoshui Basins. A free face 0.2–2 m high with a dip of 45°–63.7° is clearly preserved on the lower parts of a normal fault scarp (NF<sub>2</sub> on the western margin) of Shaoshui Basin. The combined vertical displacement on this fault scarp and on adjacent normal fault scarps reaches 2.7–7.6 m. Because this amount of displacement occurred in 1920, it would appear that this earthquake produced large total vertical displacements on the normal faults bounding the pull-apart basins. Thirteen small fault scarps that strike 265°–270° on the west edge of the Salt Lake Basin might have formed during the earthquake of 1920; their cumulative vertical displacement reaches 7.8 m.

Surface ruptures associated with the Haiyuan earthquake of 1920 show mainly left-lateral

strike-slip displacement. Because the earthquake occurred more than 60 years ago, and because the region is covered with loess, fault scarps have been heavily eroded and it is difficult to find and measure many preserved examples of displacement, especially the vertical component of displacement. We measured only the horizontal component of displacement where we could observe clear offsets at different places along the fault. It is important to look carefully for reliable indicators for measurement. Traces of human activity from before the earthquake and small gullies along the fault are the only features that show clear offsets. We paid careful attention to multiple dislocations in places where slip occurred on subparallel strands, but in some cases we may have underestimated the amount of slip by overlooking such strands. Most measurements were made with a compass and tape measure, but on some segments we used a plane table to map the detailed topography. Altogether, we have 168 separate estimates of the horizontal displacements associated with the earthquake (Figures 3 and 5).

Some features are revealed by analyzing the horizontal displacements of the 1920 Haiyuan earthquake fault.

1. The maximum measured horizontal dislocations were found near the Xianshou-Salt Lake Basin where the earthquake-induced damage was also the heaviest. The horizontal dislocations that we measured were correspondingly large over a distance of 10 km along SF<sub>2</sub> from Dagoumen in the west of the Xianzhou Basin to Wanjiashui in the east of the Salt Lake Basin (Figure 5). Except for one uncertain measurement (12 m) just east of the Salt Lake Basin (Figure 3b), the maximum measured horizontal dislocation was 10-11 m. West of the Salt Lake Basin, SF<sub>3</sub> forms another segment of the rupture zone with large horizontal dislocations (8.5-10 m). The heaviest damage associated with the strongest aftershock of the 1920 Haiyuan earthquake, on December 25, 1920 with M = 7, occurred near this area.

2. The horizontal displacements measured for the various segments of the fault are quite different from one another. Maximum measured horizontal displacements along SF<sub>2</sub>, SF<sub>3</sub>, and SF<sub>4</sub> reach 10 m, but those for the other segments are less. This suggests that strain release during the 1920 earthquake was inhomogeneous on the fault.

3. Along the earthquake fault, the largest horizontal displacements occurred on the main subparallel shear fault, the next largest displacements occurred on the inner tensile shear faults and smallest displacements occurred on the normal faults bounding the pull-apart basins. (The latter exhibit only dip slip.) Therefore, the measured horizontal displacements along the entire surface rupture show several variations. The horizontal displacements in the segments where subparallel shear fractures overlap are

notably smaller than where only one strand can be recognized. These overlapping fractures are the areas where pull-apart basins are located. This phenomenon may indicate that in the areas of extensional deformation the horizontal component of displacement occurs by normal faulting rather than by strike-slip movement. Alternatively, these observations may imply that the rupture process of each segment of shear fault is relatively independent of that on other segments.

4. Along some of the individual fault strands, maximum horizontal displacements were measured in the middle of the segment, while on others it was measured nearer the ends of the fault segments (see Figures 3 and 5). This phenomenon occurs not only along the principal shear faults but also along secondary shear fractures within the large shear zones. Because our investigation was carried out 60 years after the earthquake occurred, we could not gather enough data to examine variations in slip on individual segments in detail. However, we have observed at Shikaguan Valley, in the middle part of SF<sub>2</sub>, that five small adjacent gullies along the surface rupture were displaced. Precise estimates for three of them are 8, 11, and 11.5 m, each with an uncertainty of about 2 m. Two other gullies also were offset measurable amounts, 5 and 2 m, respectively, but the uncertainties are much greater than those of the first three.

5. When the earthquake occurred in 1920, most of the shear faults bounding the pull-apart basins did not rupture. Surface faulting occurred almost entirely along inner tensile-shear faults within the basins. Where shear faults bounding the basins have obvious displacements, their magnitudes are generally smaller than those of inner tensile-shear faults. As shown in Figure 3, the horizontal displacement on ESF<sub>1</sub> is larger than that on the western segment of SF<sub>2</sub> north of Salt Lake Basin. The maximum measured displacement reaches 6.5-7 m. This may suggest that after the subparallel shear faults were connected by the inner tensile-shear faults, the shear deformation bypassed the end of subparallel shear faults and was restricted to a shorter period of the subparallel shear fault.

#### Summary

Before the middle part of the Pleistocene epoch, a thrust or reverse fault system, striking northwest to west-northwest, and associated compressional basins, had developed in this region. Since approximately middle Pleistocene time, the Haiyuan strike-slip fault zone developed. The fault zone is composed of eight en echelon subparallel shear fractures some of which probably formed along pre-existing thrust faults (Figure 6). A series of pull-apart basins, such as the Salt Lake, Dayingshui, Shaoshui, and Huangliangtan Basins, were formed

## 180 HAIYUAN FAULT ZONE

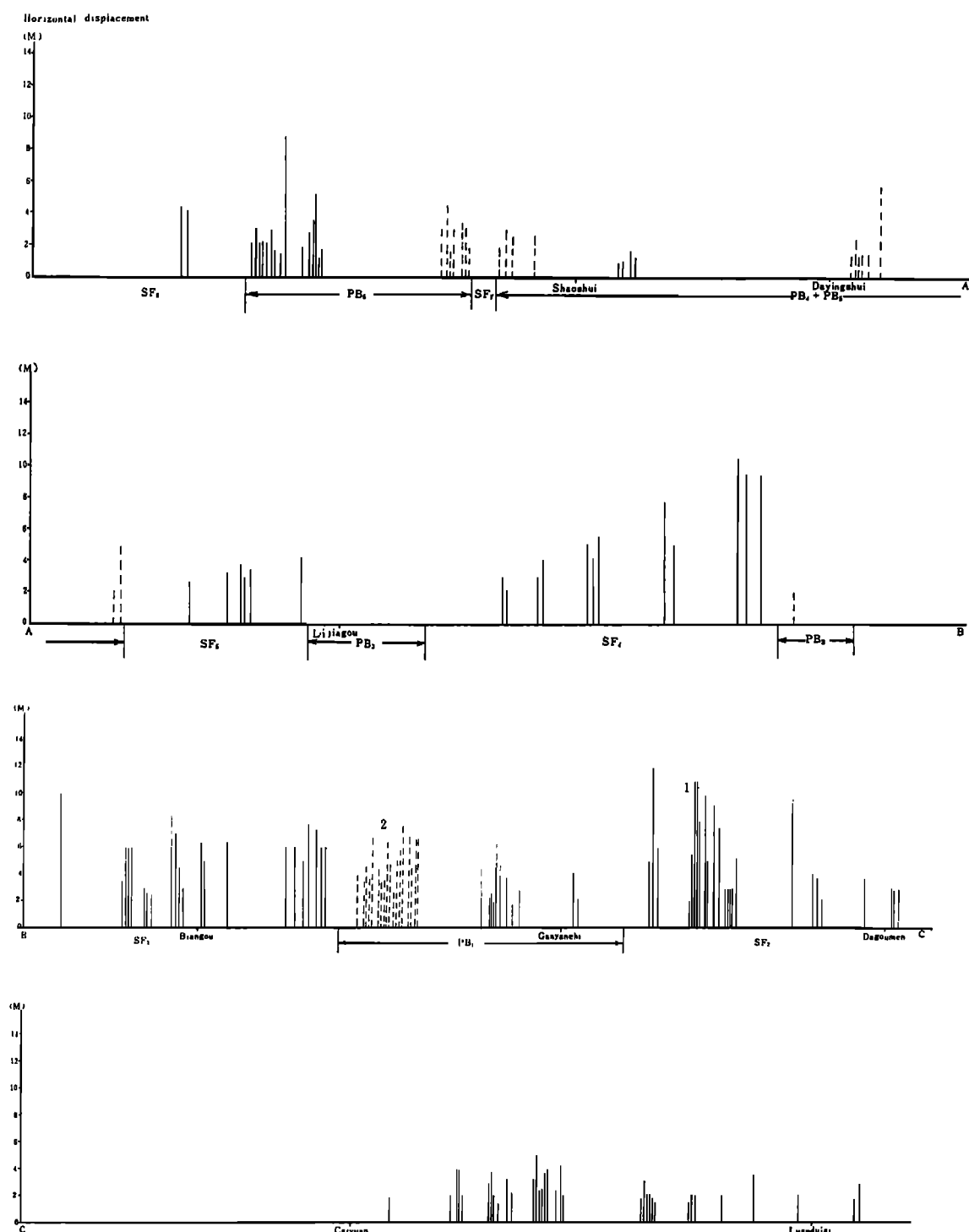


Fig. 5. The distribution of the measured horizontal offsets associated with the Haiyuan earthquake. Solid lines show offsets on the major subparallel shear fractures, and dashed lines show offsets on inner-tensile shear faults.

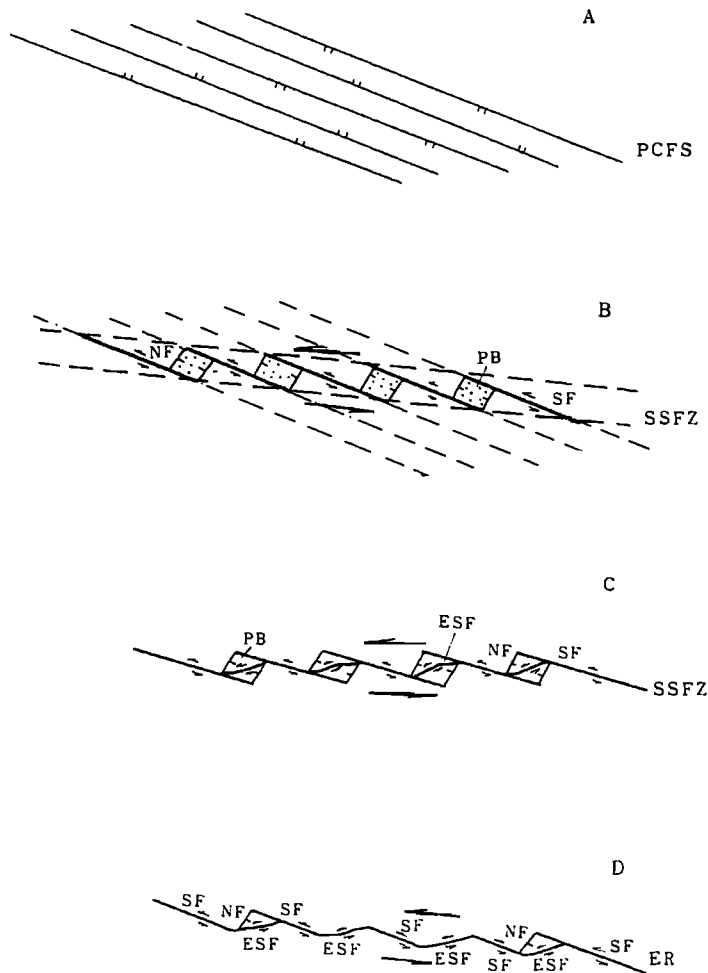


Fig. 6. Simple schematic evolution of the Haiyuan fault zone. A. Lines indicate the average trends of thrust faults active before some time in the Pleistocene epoch. B. Initiation of strike-slip faulting along a trend different from that of the thrust faults, some time in Pleistocene time. C. Evolution of subparallel strike-slip faults, or shear fractures, and the formation of pull-apart basins during late Quaternary time. D. Surface faulting during the Haiyuan earthquake.

in the areas where left-lateral, left-stepping subparallel shear fractures overlap. The Qingjiawan and Lijiagou pull-apart basins probably began to form at a later time than the other basins. Probably in late Pleistocene time, the inner tensile-shear faults were created within the pull-apart basins and linked the subparallel shear faults. Surface ruptures associated with the 1920 Haiyuan earthquake and prehistoric earthquakes (which will be discussed elsewhere) are present mainly along the subparallel shear faults and the inner tensile-shear faults in the pull-apart basins. Only in a few basins, such as the Shaoshui and Salt Lake Basins are the surface ruptures present along the normal faults bounding the basins. The

maximum measured horizontal displacements appear to be near the areas of maximum damage associated with the main shock and the largest aftershock. There are distinct differences in the displacement measured on a single subparallel shear fracture; the displacement measured is consistently smaller near the pull-apart basins than it is between them. There are also distinct differences in the displacements measured on different subparallel shear fractures. This may suggest that before the earthquake stress was concentrated at several, somewhat isolated portions of the fault, and that slip on the different segments may have occurred somewhat independently of one another, once the rupture began.

## 182 HAIYUAN FAULT ZONE

## References

- Chen S., and Deng Q., The pull-apart basins within Nanxihuashan fault zone, (in Chinese), R. Crust. Mov., 1, 1985.
- Deng Q., The active faults in China, in The Active Faults in China, pp. 19-27, 1982.
- Deng Q., and Zhang P., Research on the geometry of shear fracture zones, J. Geophys. Res., 89, 5699-5710, 1984.
- Deng Q., Zhong J., and Ma Z., Characteristics of the shearing fracture zone and conditions of its formation, (in Chinese), Sci. Geol. Sin., 13, 1966.
- Deng Q., Song F., Zhu S., Li M., Wang T., Zhang W., B.C. Burchfiel, P. Molnar, and Zhang P., Active faulting and tectonics of the Ningxia-Hui Autonomous Region, China, J. Geophys. Res., 89, 4427-4445, 1984.
- Lanzhou Institute of Seismology and Seismology Brigade of the Ningxia-Hui Autonomous Region, The 1920 Great Haiyuan Earthquake, Seismology Publishing House, Beijing, 1980.
- Song F., Zhu S., Wang Y., Deng Q. and Zhang W., The maximum horizontal displacement in the Haiyuan earthquake of 1920 and estimation of earthquake recurrence on northern marginal fault of the Xihuashan, (in Chinese), Seismology and Geology, 4, 1983.

STRAIN ACCUMULATION AND RUPTURE PROCESSES IN THE SUBDUCTION ZONE  
ALONG THE NANKAI-SURUGA TROUGH IN WESTERN JAPAN

Kiyoo Mogi

Earthquake Research Institute, University of Tokyo, Tokyo 113, Japan

**Abstract.** On the basis of the spatial distribution of focal regions of great shallow earthquakes and the configuration of the deep seismic plane, the seismic belt along the Nankai-Suruga trough is divided into the three blocks: Nankaido, Tonankai and Tokai. Ruptures of these blocks tend to occur more or less simultaneously. However, this past regularity has broken down in this century. This recent irregularity may be attributed to the Nobi earthquake of M 8 that occurred within the Eurasian plate and along the discontinuous boundary of the deep seismic plane. In this century, great earthquakes have already occurred in the Tonankai and the Nankaido blocks, but the strain in the Tokai block along the Suruga Trough has not yet been released through the occurrence of a large earthquake, and is steadily building up. Consequently a large earthquake is expected to occur in the Tokai block in the future. According to the examination of the submarine topography, the configuration of deep seismic plane, space-time distributions of shallow earthquakes and crustal movements, the Tokai block is by no means seismotectonically monotonous, but actually quite complex. One possibility is that only a part of the Tokai block ruptures. Next, the focal processes of large shallow earthquakes are discussed by focusing on the manner in which anomalous changes occur prior to large earthquakes. They are classified into three cases and the mechanism of each case is examined in conjunction with specific examples, such as the 1944 Tonankai earthquake and the 1983 Japan Sea earthquake. The difference in the focal process depends on mechanical features such as the heterogeneity of the distribution of strength in the fault plane associated with the earthquake. Based on these results, the focal process of the "Tokai earthquake" is discussed.

#### Introduction

Large interplate earthquakes occur due to strain gradually accumulating between the plates as the result of the steady plate movement, and

when this strain reaches a limit, rupture occurs. Since plates move at a more or less fixed rate, this process whereby strain accumulates and then is released suddenly over a wide area through a large earthquake is regularly repeated at plate boundaries.

Comparatively reliable data covering a long period are available on large earthquakes along the Nankai-Suruga Trough, which lies at the northern tip of the boundary between the Eurasian plate and the Philippine Sea plate, and the marked regularity of these earthquakes has been pointed out in the past. In spatial terms, low-angle thrust-type faulting tends to occur more or less simultaneously in this subduction zone. It seems, however, that this past regularity whereby ruptures occur almost simultaneously has broken down in this century, particularly in the Tokai region along the Suruga Trough. In both 1707 and 1854 the Tokai region ruptures at the same times as large earthquakes occurred along the Nankai Trough, but in this century it has not yet ruptured. This is one important ground for forecasting that a "Tokai earthquake" will occur in the Suruga Trough in the near future. What then has interrupted the steady regularity in the occurrence of large earthquakes along the plate boundaries? This subject is discussed in this paper.

Ishibashi [1976] has proposed a fault model of the "Tokai earthquake" that is expected to be the next large earthquake to occur along the Nankai-Suruga Trough. After examining the features of the Tokai region from a seismotectonic viewpoint, the author of the present paper has reached the conclusion that the area has a rather complex structure. This result forms the basis in a consideration of the characteristics of the large earthquake that is expected to occur in this region.

The focal process by which these large earthquakes occur is also a major issue. Here the author discusses this process by focusing on anomalous precursory changes observed in the focal region (or its vicinity) prior to the occurrence of the large earthquake. Based on these results, this paper will examine the process by which the forthcoming "Tokai earthquake" will occur.

## 184 STRAIN ACCUMULATION AND RUPTURE PROCESSES

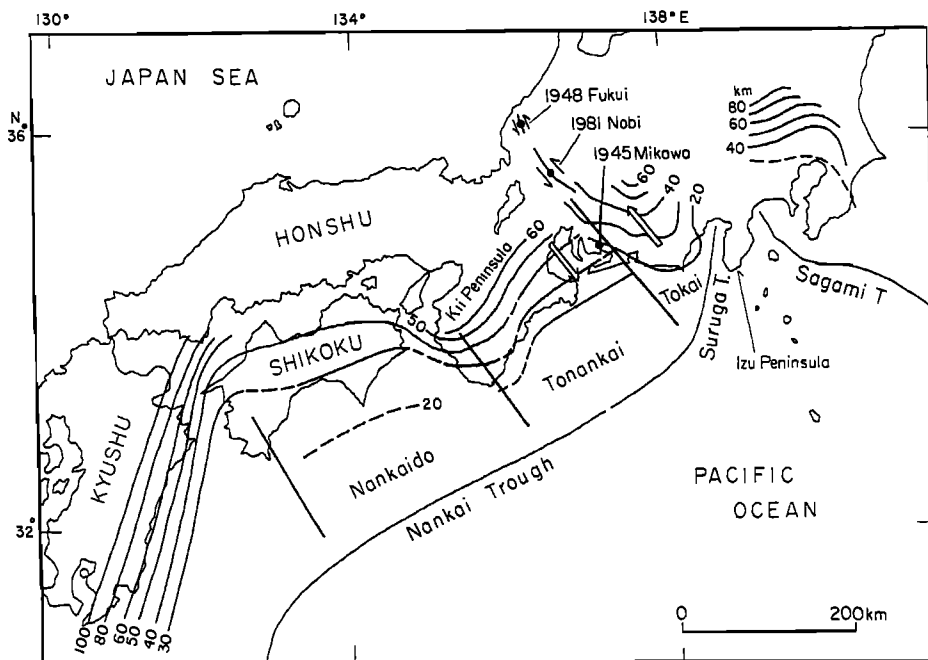


Fig 1. Configuration of the deep seismic plane accompanying the subduction of the northern tip of the Philippine Sea plate, compiled from Yamazaki and Ooida [1985] and Mizoue et al. [1983]. The boundaries between the Nankaido, the Tonankai, and the Tokai blocks along the Nankai-Suruga Trough and the conceivable effects of the left-lateral strike-slip movement by the 1891 Nobi earthquake are indicated.

#### The Regular Occurrence of Great Earthquakes along The Nankai-Suruga Trough, and Activity in Recent Years

Records are available for great earthquakes along the Nankai Trough in western Japan for the period since 684 A.D., and these records reveal that the earthquakes have occurred repeatedly. Ando [1975] and more recently Utsu [1977] divided the entire fault region along the Nankai-Suruga Trough into several fault planes and discussed the location and manner of repetition of past earthquakes. This result reveals that great earthquakes along the Nankai Trough recur at intervals of 100-250 years. Whereas the interval between earthquakes in olden times stood at 200-250 years, however, in the past 500 years or so earthquakes have occurred at intervals of 100-150 years. At this stage it is not clear whether the long intervals in the older period actually were this long or merely seem so owing to the lack of data. It must be noted that estimates of the magnitude and focal region of earthquakes in the old period are uncertain.

Focusing on the period since the great Meio earthquake in 1498, great earthquakes have occurred at roughly constant intervals of over 100 years (see Figure 2). However, the focal regions of the 1498 and 1605 earthquakes are not completely clear, and so problems lie in discussing the intervals of repetition in the same region. Abun-

dant data are available for great earthquakes since 1707, and it is possible to form a reliable estimate of the focal regions. As discussed in Shimazaki and Nakata [1980] and Mogi [1981a], Nankaido earthquakes occur when the stress level in the focal region reaches a certain limiting value.

The configuration of the deep seismic plane accompanying the subduction of the northern tip of the Philippine Sea plate, compiled from Yamazaki and Ooida [1985] and Mizoue et al. [1983], is shown in Figure 1. This is thought to show the upper surface of the subducting Philippine Sea plate. Noteworthy here is the fact that this surface is by no means a simple one, but that it has quite a complex configuration. A look at the part along the Nankai-Suruga Trough west of the Izu Peninsula shows a discontinuous belt running in a northwest-southeast direction between the Chubu District and the Kii Peninsula, and it is noteworthy that the part directly under the western Kii Peninsula is appreciably curved. A comparison of the shape of this deep seismic plane and the distribution of the focal regions of the great shallow earthquakes along this subduction zone reveals a close relationship between the two. The places where the shape of the deep seismic plane suddenly changes are located right on the boundaries of the focal regions of the great earthquakes, and great earthquakes occur repeatedly within each of these blocks. Consequently, the

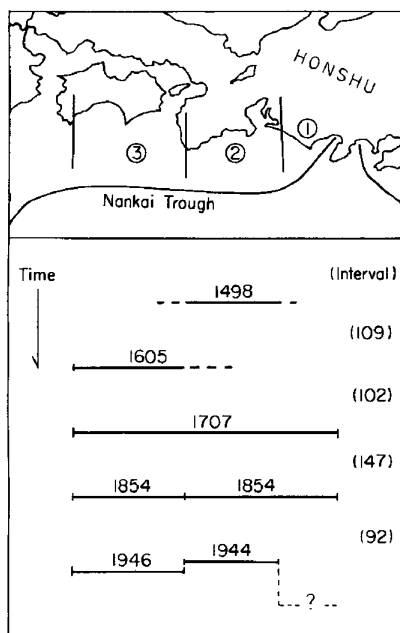


Fig. 2. Space-time distribution of great shallow earthquakes along the Nankai-Suruga Trough since 1498. 1, 2, and 3 are the Tokai, the Tonankai, and the Nankaido blocks, respectively. The numerals on the right side show intervals in the Nankaido block.

discussion in this section divides the seismic belt along the Nankai-Suruga Trough into three blocks - the Nankaido, Tonankai and Tokai blocks, as shown in Figure 1. It is noted that the deep seismic plane of the Nankaido and the Tonankai blocks are simple, but the Tokai block is complex. Figure 2 shows the space-time distribution of ruptures of these three blocks. In 1707 and 1854, ruptures occurred almost simultaneously in these three blocks. The focal region of the large earthquake in 1707 covers the whole area. In 1854 the rupture occurred in the eastern part (Tonankai and Tokai) at first, followed 32 hours later by a rupture in the western part (Nankaido). By contrast, in this century the Tonankai earthquake occurred in 1944, and then the Nankaido earthquake (1946) occurred about 2 years (744 days) later. However, no earthquake has occurred yet in the Tokai block. The unreliability of data on the old period must be taken into account, but ever since the Meio earthquake (1498) there has been a more or less simultaneous repetition of large-scale ruptures in the Nankai Trough. However, in this century the ruptures in each block have occurred at different times. (Records show that in even older times earthquakes in the western part occurred 1 to 3 years after earthquakes in the eastern part, but this will not be discussed here.)

Perhaps the irregularity of the great earthquakes in this century could be viewed as a mere coincidence, but the author believes that this may be attributed to the Nobi earthquake (1891, M 8)

that occurred within the Eurasian plate. The Nobi earthquake is one of the largest intraplate earthquakes in this region, and is said to occur at intervals of over 1,000 years [Matsuda, 1977]. The Nobi earthquake occurred through a left-lateral strike-slip fault movement with a northwest-southeast trend. Noteworthy here is the fact that the direction and location of this fault roughly correspond to the discontinuous belt of the deep seismic plane shown in Figure 1. Thus the Nobi earthquake can be considered as a large-scale inland earthquake that occurred in the active tectonic belt extending down to this deep part. If this is the case, it is highly possible that this will affect the occurrence of great interplate earthquakes along the Nankai Trough caused by subduction of the Philippine Sea plate. There are strong indications to this effect from the fact that the Mikawa earthquake (1945, M 7.1) and Fukui earthquake (1948, M 7.3), which are regarded as aftershocks of the Tonankai earthquake (1944) in a broad sense, occurred in the active tectonic belt running in a northwest-southeast direction to include the fault associated with the Nobi earthquake.

In Figure 1, the following are the conceivable effects of the left-lateral strike-slip movement caused by the Nobi earthquake.

1. Strain in the Tokai block was released to a certain extent, thus slightly delaying the occurrence of the next earthquake in the Tokai block.
2. Strain in the Tonankai block increased somewhat, thus slightly advancing the occurrence of the next earthquake in this region.

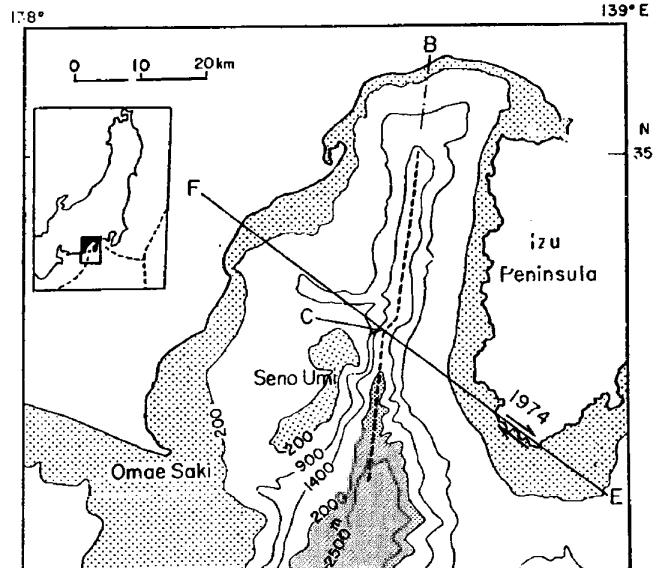


Fig. 3. Submarine topography of Suruga Bay and the proposed tectonic line (EF) which is the extension of the 1974 Izu-Hanto-Oki earthquake fault [Mogi, 1977a]. The right-lateral displacement of the 1974 earthquake fault and the similar dislocation of the trough axis at the center (c) in Suruga Bay are noticeable.

## 186 STRAIN ACCUMULATION AND RUPTURE PROCESSES

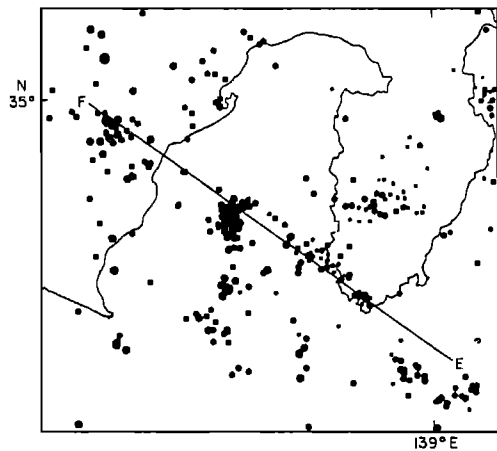


Fig. 4. Epicentral distribution of shallow microearthquakes in the Suruga Bay region (February 1, 1983~April 30, 1984) [Earthquake Research Institute, 1984]. The solid line (EF) is the same as in Figure 3.

3. The Nankaido block is separate from the fault associated with the Nobi earthquake, so is unaffected.

Consequently, the 1946 Nankaido earthquake occurred with a regularity conforming to the time-predictable model [Shimazaki and Nakata, 1980], but the Tonankai earthquake (1944) occurred somewhat ahead of time, about 2 years before the Nankaido earthquake, while the "Tokai earthquake" on the eastern side of the fault zone of the Nobi earthquake has not yet occurred.

Mogi [1981a] has suggested that the Nobi earthquake may have delayed the occurrence of the "Tokai earthquake". This paper takes the discussion a step further by indicating the possibility that the Nobi earthquake occurred in an important tectonic zone that is also related to the deep structure, and so it may be closely related to the manner in which great earthquakes along the Nankai Trough occur, and that the discrepancy in the times of occurrence of the Tonankai earthquake and the Nankaido earthquake may also be due to the effect of the Nobi earthquake. It is the author's belief that this is a plausible explanation of the irregularity of great earthquakes along the Nankai-Suruga Trough in this century.

#### The Complexity of the Assumed Focal Region of The "Tokai Earthquake"

What kind of earthquake is expected to occur in the Tokai block? Ishibashi [1976] has proposed a model of a westerly dipping thrust-type fault that runs along the Suruga Trough, and that is about 115 km long and 70 km wide. He assumes that this fault model is of the same type of other great earthquakes along the Nankai Trough. In this case the fault plane will reach as far as the back of Suruga Bay, and its magnitude (M) would be

about 8. It is anticipated therefore that the "Tokai earthquake" will inflict huge damage on the densely populated area centered on Shizuoka Prefecture, and the prediction system has been established as one means of reducing this damage.

However, in the eastern part of the Nankai-Suruga Trough, the trough trend suddenly changes from east-northeast to north-northeast, and in the northern part of the Suruga Trough the Izu Peninsula presses in on the eastern side and the northern tip reaches the land, and the size of the Tokai block is considerably smaller than those of other blocks, so that it is unique area. It seems questionable whether the large earthquakes occurring here can be assumed to be simple ones similar to those in typical subduction zones such as the Tonankai and Nankaido blocks.

Furthermore, Mogi [1977a] has advanced the hypothesis that the active tectonic line (belt) passing through the tip of the Izu Peninsula and running in the same northwest-southeast direction as the direction of movement of the Philippine Sea plate cuts across the Suruga Trough, and had focused on the different structures of the southern and northern sides of this tectonic belt. Since then there have been reports of data and research to further substantiate the existence of this active tectonic belt, and it has become evident that the part which is assumed to be the focal region of the "Tokai earthquake" must be regarded as being considerably complex in tectonic terms. Consequently, any examination of the manner in which the "Tokai earthquake" will occur must take into full account the peculiar features and complexity of this structure.

The following is an explanation of several points demonstrating that the Tokai block is by no means seismotectonically simple, but actually quite complex.

Submarine topography. In Figure 3, the tecto-

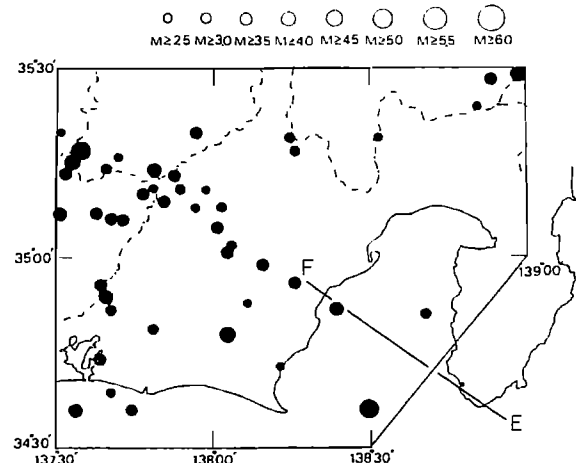


Fig. 5. Linear arrangement (northwest-southeast) of small earthquakes of focal depths (40~60 km) in the Tokai region [Yoshida, 1983]. The solid line (EF) is the same as in Figure 3.

## Northward migration of seismicity along the Suruga trough, Japan

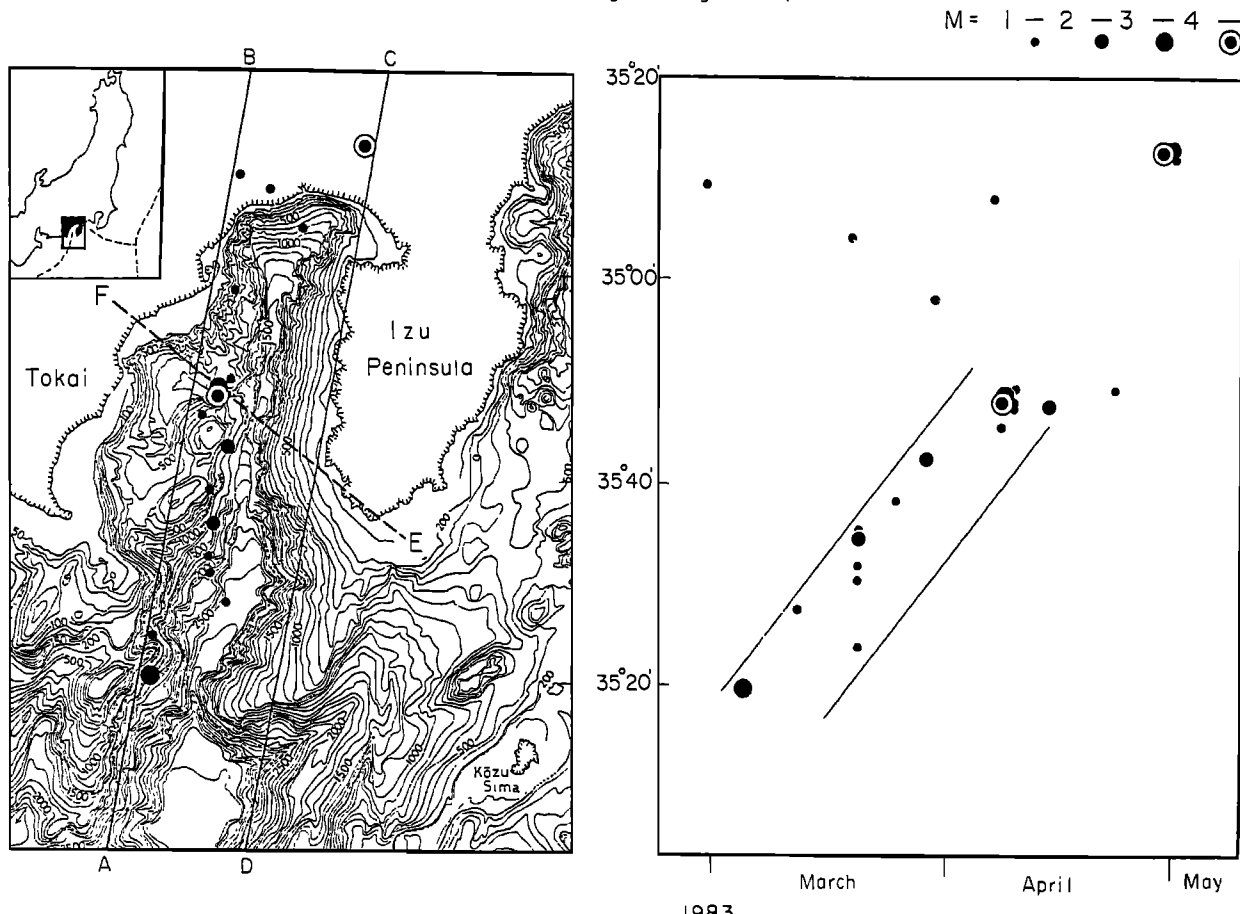


Fig. 6. Migration of small earthquakes along the western side of the Suruga Trough and its relation to the tectonic line (EF). Left: submarine topography and epicentral locations of earthquakes; right: space-time distribution of earthquakes. Seismic data from Nagoya University [1983].

nic line (EF) proposed by Mogi [1977a] has been added to a simplified figure of the submarine topography of Suruga Bay. At the place where this tectonic line intersects the Suruga Trough a right lateral dislocation of the trough axis can be seen. Moreover, on the northern side of this tectonic line the trough forms a V-shaped topography, but on the southern side the east and west regions have a topography peculiar to asymmetrical subduction in relation to the trough axis. In addition to these submarine topographical features, this tectonic line has been proposed on the basis of the fact that the 1974 Izu-Hanto-Oki earthquake (right-lateral strike-slip,  $M 6.9$ ) occurred on the line's extension to the east, and small and medium earthquakes are concentrated on its extension to the west.

Distribution of microearthquakes. Yamazaki and Ooida [1979] pointed out a linear arrangement of microearthquakes along a line (western part of

EF above) and the extreme quiescence in the northern part of Suruga Bay. Figure 4 shows the distribution (February 1, 1983 - April 30, 1984) of microearthquakes in and around Suruga Bay [Earthquake Research Institute, 1984]. This pattern of distribution of recent microearthquakes shows the existence of the tectonic system described above and the differences between activity on the northern and southern sides.

Linear arrangement of small earthquakes. There is a tendency for small and medium earthquakes to be arranged along the tectonic line mentioned in the submarine topography discussion. Figure 5 shows one of the epicentral distribution figures drawn up by Yoshida [1983] based on the Japan Meteorological Agency data classified by depth. At depths of 40-60 km, the linear arrangement is particularly marked on the western side of the trough. It is noteworthy that this reaches quite far inland. This linear arrange-

## 188 STRAIN ACCUMULATION AND RUPTURE PROCESSES

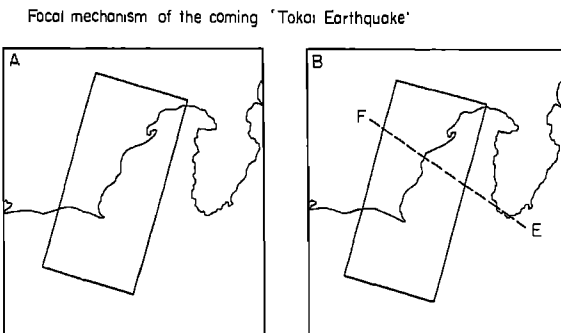


Fig. 7. Assumed focal region of the forthcoming "Tokai earthquake". A: simple rupture plane model proposed by Ishibashi [1976]; B: complex model suggested in this study.

ment is not so obvious in shallow earthquakes, so it is thought that this active line (belt) is located within the Philippine Sea plate that subducts to the west.

Migration of small earthquakes. As shown in Figure 6, from March to April 1983, observations [Nagoya University, 1983] were made of a phenomenon whereby the region of activity of small earthquakes migrated systematically to the north along the western side of the Suruga Trough. Noteworthy here is the fact that this migration stopped when it reached the tectonic system described in the submarine topography discussion, and there the largest earthquake - one of M 4.0 - occurred (April 8, 1983), followed by continued aftershocks. This indicates directly that this tectonic system is a mechanical discontinuous boundary line.

Deep seismic plane. The contour lines of the deep seismic plane assumed from the 3-D distribution of the earthquake does not run parallel to the trough axis, but is rather curved, differing from typical subduction, as shown in Figure 1 [Yamazaki and Ooida, 1985].

Crustal movements. According to leveling surveys, the western coast of Suruga Bay is continuing to subside steadily, and trilateration surveys reveal that east-west compression is proceeding on either side of the trough, thus indicating the accumulation of strain in the subduction zone. However, a look at the spatial distribution of vertical displacement reveals that by no means is this proceeding uniformly (e.g. Geographical Survey Institute, 1984]. The results of geological studies also have revealed that the structure of the western side of the Suruga Trough has continued complex movements that lack uniformity [Tsuchi, 1984].

For these reasons the focal region of the expected "Tokai earthquake" must be regarded as considerably complex. Further examinations are therefore necessary as to whether or not a large earthquake occurs in accordance with the simple model put forward at the outset by Ishibashi

[1976]. The existence to the active tectonic belt proposed by Mogi [1977a] is becoming increasingly conclusive, and if the noteworthy movement of the Philippine Sea plate and the existence of the Izu Peninsula block are taken into account, there is nothing unusual about the existence here of an active tectonic belt. The role played by this tectonic belt in the occurrence of large earthquakes, that is, in the occurrence and progression of ruptures, is a subject for future examination, but one possibility is that only the part on the southern side of this tectonic belt ruptures (Figure 7). In this case not only will the magnitude of the earthquake be small, but also the damage inflicted will be substantially reduced because the main part of the fault associated with the earthquake is far off from the land. Naturally, in forecasting an earthquake disaster and devising countermeasures, it is vital to base these measurement on the assumption of an earthquake of the maximum magnitude, but it is also necessary to examine what kind of earthquake might occur and which is most likely to occur.

#### Focal Process

Let us now consider the focal process of great earthquakes along the Nankai Trough and of the forthcoming "Tokai earthquake". As stated earlier, large earthquakes occur when the strain that has accumulated over a wide area reaches the limit and large-scale rupture occurs. Accordingly, when strain approaches limiting value, the question arises of what changes take place in the focal region leading up to the large-scale rupture, and from where does this rupture commence. Throwing light on this process leading up to the occurrence of large earthquakes is one of the most fundamental subjects in focal mechanics [e.g. Rundle et al., 1984]. In the belief that an analysis of the anomalous changes preceding large earthquakes is bound to provide a clue to this problem, this paper has focused on the manner in which anomalous changes occur prior to large earthquakes. (The anomalous changes discussed here are those in the focal region and its vicinity, and do not include those that are far distant from the focal region and which are probably also the result of the singular features of that location.) Though the manner in which these anomalous changes appear varies greatly, here the author has classified them into the following four cases and examined the mechanism behind each case in conjunction with specific examples.

#### Case 1

Case 1 is the case in which no conspicuous precursory phenomena are seen in the vicinity of the main shock, but marked changes are observed in other parts of the focal region.

Tonankai earthquake (1944, M 7.9). As shown in Figure 8a, the epicenter was located offshore southeast from the Kii Peninsula, and the rupture

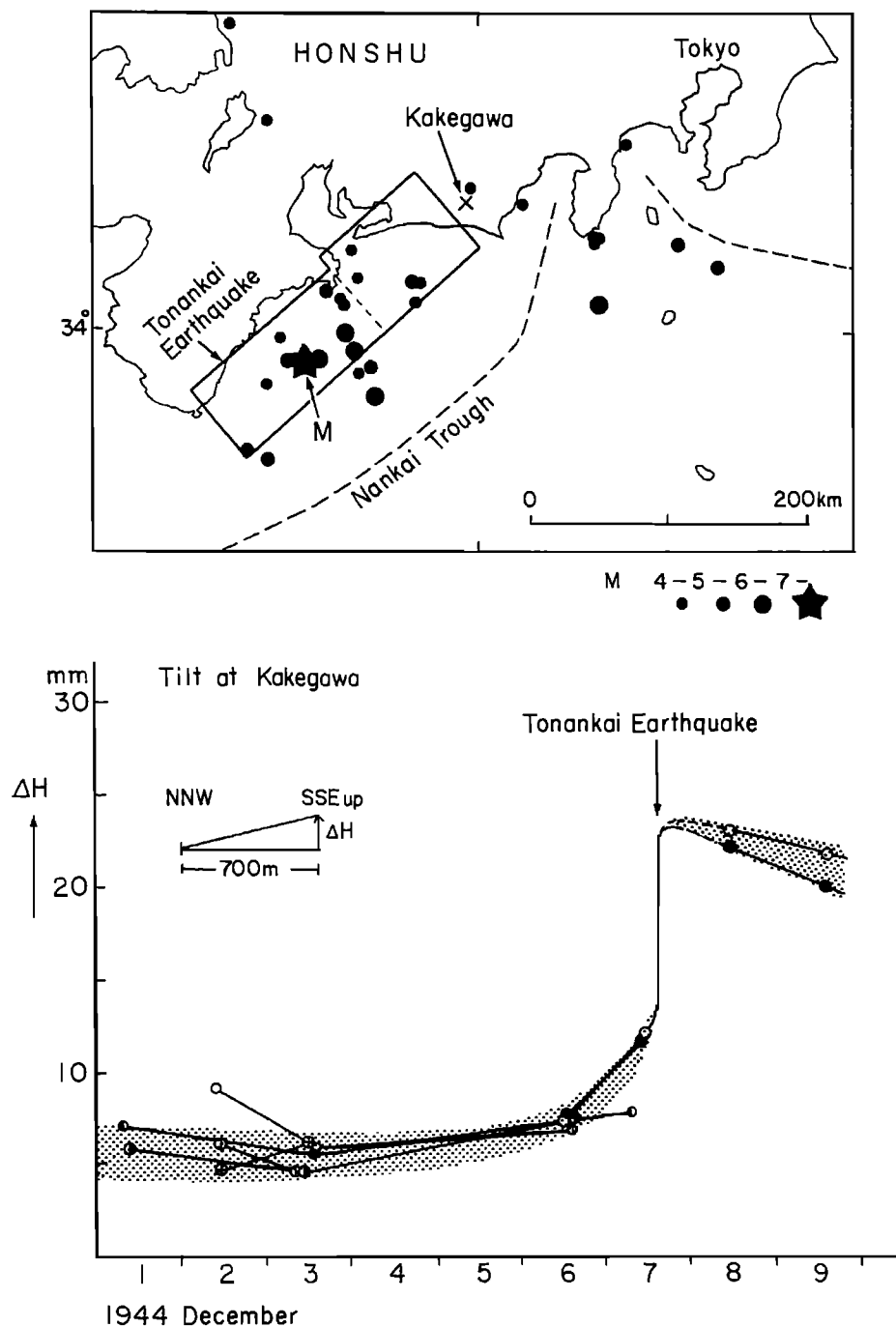


Fig. 8. (a) Focal region (rectangular) of the 1944 Tonankai earthquake of M 7.9 deduced from the crustal movement data [Inouchi and Sato, 1975]. Star shows the epicenter of the main shock and solid circles show earthquakes immediately after the main shock. (b) Precursory crustal movement (ground tilt) prior to the Tonankai earthquake at Kakegawa, which was obtained by leveling surveys [Mogi, 1984/1985].

## 190 STRAIN ACCUMULATION AND RUPTURE PROCESSES

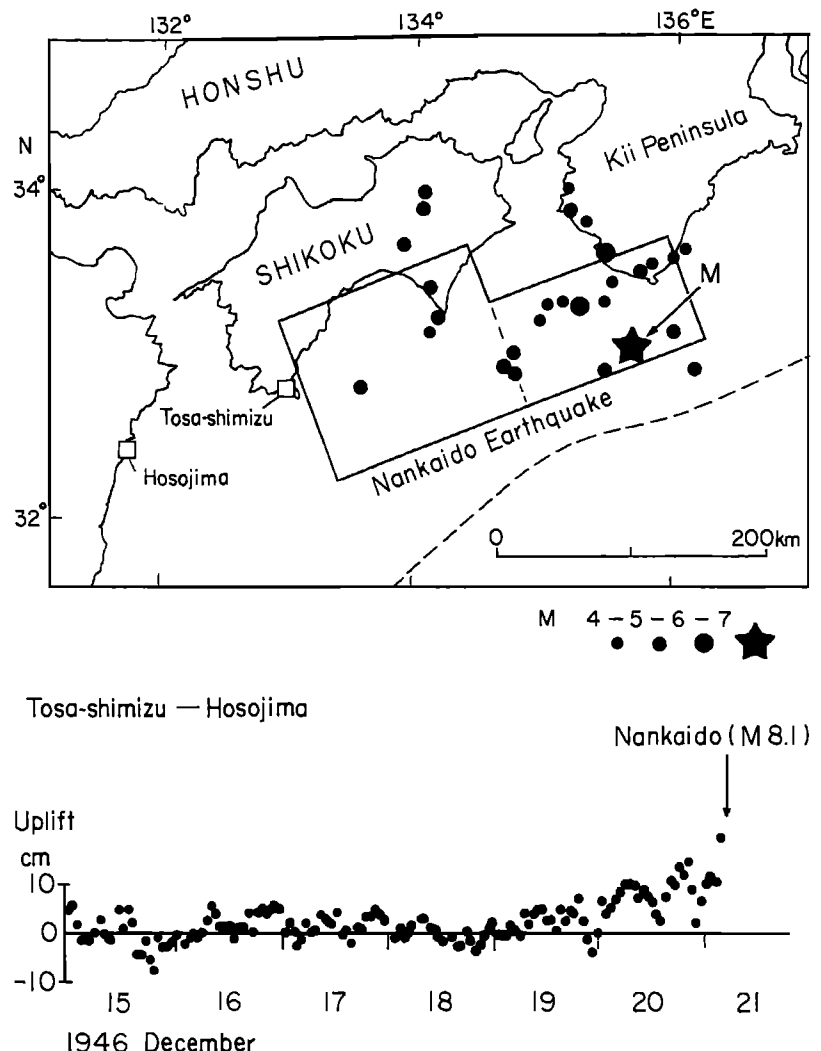


Fig. 9. (a) Focal region (rectangular) of the 1946 Nankaido earthquake of M 8.1 deduced from the crustal movement data [Ando, 1975]. Star shows the epicenter of the main shock and solid circles show earthquakes immediately after the main shock. (b) Precursory crustal uplift at Tosashimizu observed by tide gages [Sato, 1977]. The vertical axis is the difference in tide levels between Tosashimizu and Hosojima (Kyushu island).

developed in a northwesterly direction, reaching as far as near Lake Hamana [Inouchi and Sato, 1975]. An analysis [Mogi, 1984/1985] of the result of leveling surveys carried out at the time reveals that the marked tilt of the ground accelerated about 2 days before the earthquake, as shown in Figure 8b. However, no noticeable foreshocks immediately prior to the earthquake were observed near the epicenter, and the tide station nearby was unable to confirm any phenomenon that could be regarded as a conspicuous precursory disturbance. In sum, it is thought that aseismic crustal movement proceeded gradually at locations distant from the epicenter, leading up to the occurrence of the large earthquake.

Nankaido earthquake (1946, M 8.1). As shown in

Figure 9a, the epicenter of the Nankaido earthquake lay offshore from the southern tip of the Kii Peninsula, and the rupture developed as far as 300 km to the west [Fitch and Scholz, 1971; Ando, 1975]. In this earthquake also no noticeable foreshocks were observed near the epicenter immediately prior to the earthquake, nor were any changes in the tide level observed at the tide station nearby (Stat. Kushimoto in the Kii Peninsula). However, records of the tide level at Tosashimizu (on the southwestern tip of Shikoku island), which is the western tip of the rupture zone, reveal that this site had been gradually uplifting for the day or two before the earthquake (Figure 9b) [Sato, 1977]. Noticeable ground water changes were also observed, such as wells in a wide

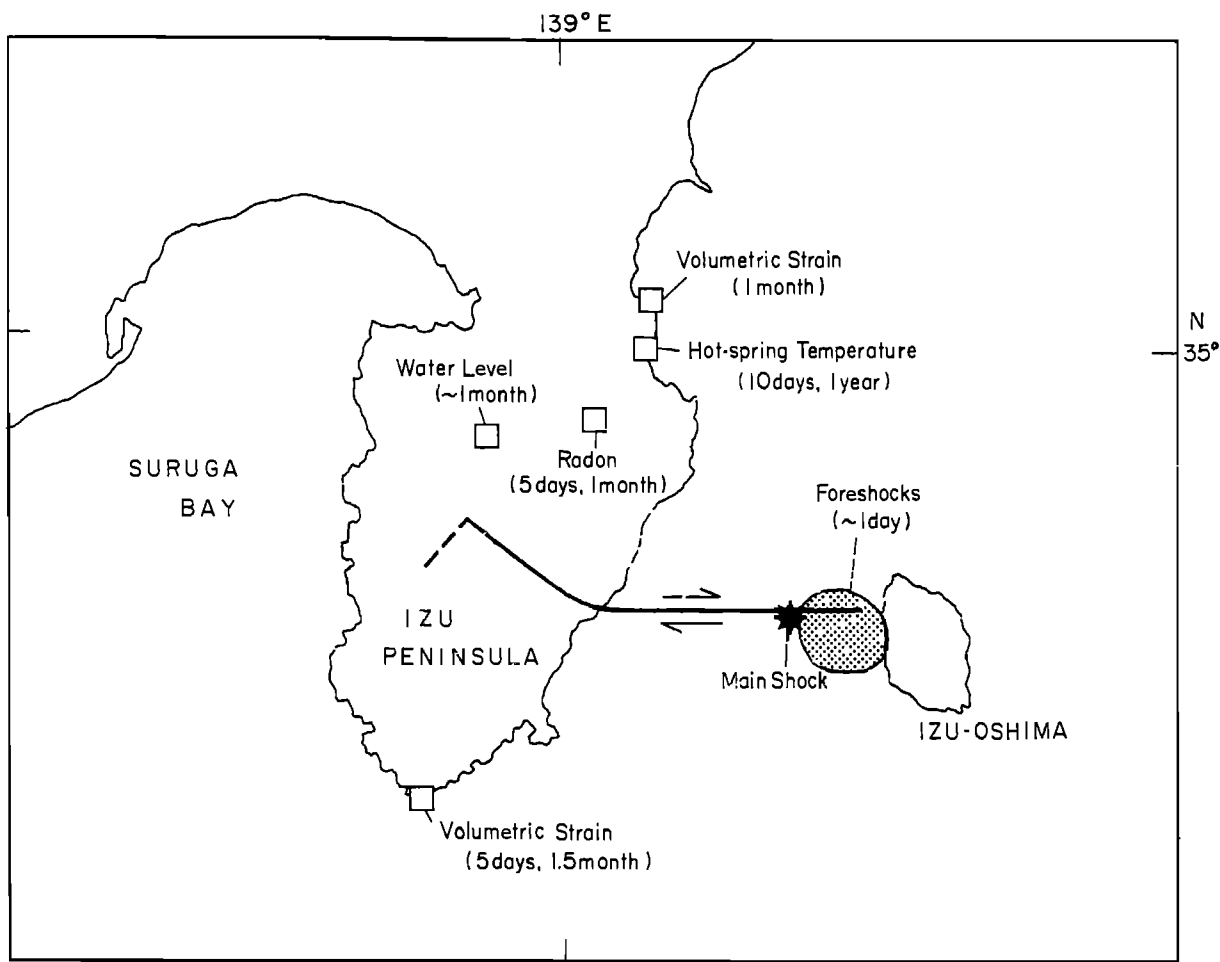


Fig. 10. Locations of the right-lateral strike-slip fault of the 1978 Izu-Oshima-Kinkai earthquake of M 7.0 and sites at which various precursory phenomena were observed. Numbers show the duration of precursory change.

area within the rupture zone drying up before the earthquake, or the well water becoming dirty, so it is thought that crustal movements took place over an extensive area before the earthquake occurred.

This can be explained if it is supposed that these two earthquakes along the Nankai Trough occurred in line with the following process. First, aseismic deformation (inelastic shear deformation or aseismic slip along the fault plane) proceeded in parts other than the epicentral part, and gradually accelerated. Second, the deformation rate increased, stress concentrated in the non-deformed part (known as an asperity) near the epicenter, and when this reached the limit, rupture commenced and developed throughout the whole focal region. (This corresponds more or less to what is known as the asperity model.)

#### Case 2

Case 2 is the case in which there are precursory changes immediately before the earthquake in

the vicinity of the main shock, as well as conspicuous changes in other parts of the focal region.

Izu-Oshima-Kinkai earthquake (1978, M 7.0). As shown in Figure 10, the epicenter was located out to sea from the western coast of Izu-Oshima island, and the earthquake occurred as the result of the movement of a right-lateral strike-slip fault. Its western tip reached as far as the center of the Izu Peninsula. In this case very noticeable foreshocks occurred near the epicenter for about 15 hours before the main shock, reaching a peak 2 to 3 hours beforehand, and then their activity abated temporarily before the occurrence of the main shock. However, on the Izu Peninsula, which is at a considerable distance from the site of the main shock, various precursory changes had begun to occur between several days and 1 or 2 months before the earthquake [e.g. Mogi, 1981b]. The sites at which these changes were observed are shown in Figure 10. These changes are understandable if it is supposed that precursory deformation proceeded gradually not only in a restricted part

## 192 STRAIN ACCUMULATION AND RUPTURE PROCESSES

## 1983 Japan Sea Earthquake

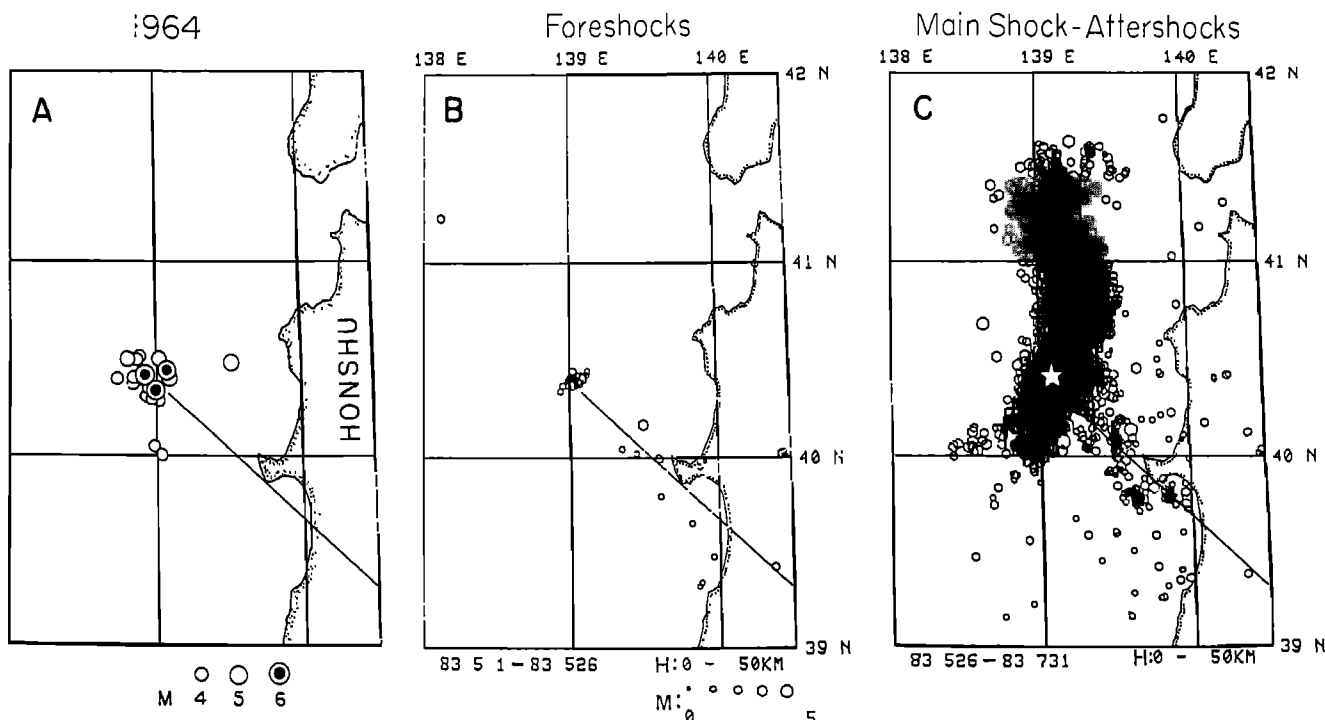


Fig. 11. Epicentral locations of the Oga-Hanto-Oki earthquakes (A, data from JMA Catalogue), and the foreshocks (B) and the main shock-aftershocks (C) of the 1983 Japan Sea earthquake [Hasegawa et al., 1983]. The northwest-southeast solid line is the active tectonic line proposed by Mogi [1985]. Microearthquake activities along the northwest-southeast line before and after the 1983 Japan Sea earthquake are noticeable.

of the epicenter, but also throughout a wide area of the fault plane. It is difficult to explain this by supposing that a precursory rupture occurred and progresses only in the confined epicentral part.

In this case aseismic deformation progressed and accelerated in the wide area of the rupture zone. This may be explained by assuming that deformation in the epicentral part was small, but that stress gradually concentrated here and reached a limiting value immediately before the earthquake, when small ruptures (foreshocks) began to occur, and the rupture started from here.

### Case 3

Case 3 is the case in which precursory changes immediately before the earthquake occur only near the epicenter, and no noticeable changes are observed in parts other than the epicentral region.

Japan Sea earthquake (1983, M 7.7). In this case, the epicenter was located offshore from the northern part of Honshu, so it was difficult to observe precursory changes immediately before the earthquake. Nevertheless, 14 days before the earthquake, foreshocks had continued to occur

right at the site of the epicenter of the main shock [Hasegawa et al., 1983]. The analyses of long-term seismicity and tectonics suggest that the epicentral region of the main shock is a singular site in structure and the large-scale rupture started from this site [Mogi, 1985].

Figure 11 shows the epicentral locations of the 1964 earthquake sequence including M 6.9 and 6.5 earthquakes, and the foreshocks and the main shock of the 1983 Japan Sea earthquake. It is noteworthy that these epicenters were located at the same site where the northwest-southeast tectonic line shown by a solid line [Mogi, 1985] intersects the plate boundary [e.g. Nakamura, 1983] along the eastern margin of the Japan Sea. The zone covering this region is comparatively inactive in seismic terms, and the fact that these earthquake sequences selectively occurred here alone indicates that this site is weak and that it is a place where stress concentrates easily due to its tectonic singularity. The large rupture extending over 120 km commenced at this site, but precursory changes immediately prior to the earthquake were not observed in other regions of the rupture zone.

As this example illustrates, the mechanism

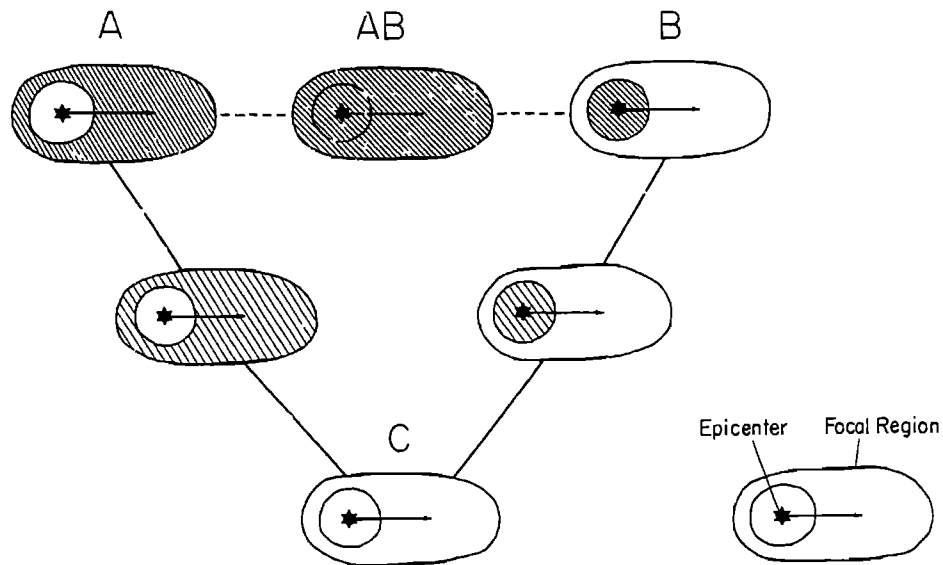


Fig. 12. Simplified three focal processes (A, B, C) classified by focusing on precursory deformation in the focal region. Star and large oval indicate the epicenter of the main shock and the final rupture zone, respectively. The white areas indicate places that are strong and where no anomalous deformation occurs until the start of the main rupture, and the striped sections indicate places which are weak and where precursory slip and rupture occur.

whereby the rupture commences at a weak place or a place where stress is concentrated and then develops into a large rupture, i.e., the rupture starts from a small fracture and develops into a full-scale rupture, is the most common process by which rupture proceed.

#### Case 4

Case 4 is the case in which no outstanding precursory changes are observed before the earthquake either in the epicentral region or other parts of the focal region.

Without doubt there are many cases in which insufficient observations make it impossible to observe precursory changes that are actually occurring. There are also numerous instances in which absolutely no outstanding precursory phenomena were observed immediately before the earthquake despite the fact that accurate observations were being carried out. In this case rupture occurs suddenly. The fact that the rupture occurs unexpectedly with virtually no warning is not unusual as a rupture phenomena. Such unexpected ruptures occur in brittle materials with a homogeneous structure. Consequently, it is conceivable that ruptures occur unexpectedly if the fault plane is quite homogeneous in mechanical terms.

For the sake of convenience, here the author has divided the manner in which anomalous changes appear into four cases. Figure 12 shows the relationship between these. Basically it is appropriate to suppose the three cases of A (case 1), B

(case 3), and C (case 4). Case 2 lies between A and B and could be referred to as AB. In this figure the large oval indicates the final rupture zone, the \* within the oval indicates the epicenter of the main shock, the small circles surrounding this indicate the region in the vicinity of the epicenter, the striped sections indicate places which are weak and where precursory slip and rupture occur, and the white places indicate areas that are strong and where no anomalous deformation occurs until the start of the rupture. For instance, A shows that the vicinity of the epicenter is strong, and that deformation proceeds in other parts of the focal region, which finally becomes unstable, and the rupture starts from the epicenter. These models have been discussed by a number of investigators [e.g. Das and Aki, 1977; Kanamori, 1981; Lay et al., 1982; Mogi, 1977b; Rundle et al., 1984; Stuart and Mavko, 1979].

In the author's opinion, it is not a question of whether A or B is appropriate as the focal process of large earthquakes, A, B, or C is possible. The author believes that the question of whether it is A, B, or C depends on mechanical features such as the heterogeneity or homogeneity of the distribution of strength in the fault plane associated with the earthquake. Thus in-between cases are also possible.

Earlier it was stated that large earthquakes along the Nankai Trough are of the A-type. It is highly likely that this is a feature of the faults associated with earthquakes that occur as the result of subduction along the Nankai Trough. This

## 194 STRAIN ACCUMULATION AND RUPTURE PROCESSES

signifies that it is highly likely that the "Tokai earthquake" that is expected to occur along the Suruga Trough, which is the eastwards extension of the Nankai Trough, will also be of the A-type. Thus the possibility exists of observing precursory disturbances that are not confined to the epicentral region.

## References

- Ando, M., Source mechanisms and tectonic significance of historical earthquakes along the Nankai Trough, Japan, Tectonophysics, 27, 119-140, 1975.
- Das, S., and K. Aki, Fault planes with barriers: A versatile earthquake model, J. Geophys. Res., 82, 5658-5670, 1977.
- Earthquake Research Institute, Seismic activity in the Izu Peninsula and its vicinity (November, 1983 - April, 1984), (in Japanese) Rep. Coord. Comm. Earthquake Predict., 32, 179-183, 1984.
- Fitch, T. J., and C. H. Scholz, Mechanism of underthrusting in southwest Japan: A model of convergent plate interactions, J. Geophys. Res., 76, 7260-7279, 1971.
- Geographical Survey Institute, Vertical movement in the Tokai region, (in Japanese) Rep. Coord. Comm. Earthquake Predict., 31, 303-315, 1984.
- Hasegawa, A., et al., 1983 Japan Sea earthquake (1). Seismic activity, (in Japanese) (abstract), Seismol. Soc. Jpn., 1983 No. 2, p. 3, 1983.
- Inouchi, N., and H. Sato, Vertical crustal deformation accompanied with the Tonankai earthquake of 1944, Bull. Geogr. Surv. Inst. Jpn., 21, 10-18, 1975.
- Ishibashi, K., Re-examination of a great earthquake expected in the Tokai district: possibility of the "Suruga Bay earthquake", (in Japanese) (abstract), Seismol. Soc. Jpn., 1976 No. 2, pp. 30-34, 1976.
- Kanamori, H., The nature of seismicity pattern before major earthquakes, in Earthquake Prediction, An International Review, edited by D. W. Simpson and P. G. Richards, Maurice Ewing Ser., vol. 4, pp. 1-19, AGU, Washington, D.C., 1981.
- Lay, T., H. Kanamori, and L. Ruff, The asperity model and the nature of large subduction zone earthquakes, Earthquake Predict. Res., 1, 3-71, 1982.
- Matsuda, T., Estimation of future destructive earthquakes from active faults on land in Japan, J. Phys. Earth, 25, Suppl., S251-S260, 1977.
- Mizoue, M., M. Nakamura, N. Seto, Y. Ishiketa, and T. Yokota, Three-layered distribution of micro-earthquakes in relation to focal mechanism variation in the Kii Peninsula, southwestern Honshu, Japan, Bull. Earthquake Res. Inst., 58, 287-310, 1983.
- Mogi, K., An interpretation of the recent tectonic activity in the Izu-Tokai district, (in Japanese) Bull. Earthquake Res. Inst., 52, 315-331, 1977a.
- Mogi, K., Seismic activity and earthquake prediction, (in Japanese) Proc. Symp. Earthquake Predict. Res., pp. 203-214, 1977b.
- Mogi, K., Seismicity in western Japan and long-term earthquake forecasting, in Earthquake Prediction, An International Review, edited by D. W. Simpson and P. G. Richards, Maurice Ewing Ser., vol. 4, pp. 43-51, AGU, Washington, D.C., 1981a.
- Mogi, K., Earthquake prediction program in Japan, in Earthquake Prediction, An International Review, edited by D. W. Simpson and P. G. Richards, Maurice Ewing Ser., vol. 4, pp. 635-666, AGU, Washington, D.C., 1981b.
- Mogi, K., Temporal variation of crustal deformation during the days preceding a thrust-type great earthquake - the 1944 Tonankai earthquake of magnitude 8.1, Japan, Pageoph, 122, 765-780, 1984/1985.
- Mogi, K., 1983 Japan Sea earthquake (M 7.7) and seismotectonics in northeastern Japan (in Japanese) Bull. Earthquake Res. Inst., 60, 401-428, 1985.
- Nagoya University, Distribution of microearthquakes in Tokai district (November 1, 1982 - April 30, 1983), (in Japanese) Rep. Coord. Comm. Earthquake Predict., 30, 178-181, 1983.
- Nakamura, K., Possible nascent trench along the eastern Japan Sea as the convergent boundary between Eurasian and North American plates, (in Japanese) Bull. Earthquake Res. Inst., 58, 711-722, 1983.
- Rundle, J. B., H. Kanamori, and K. C. McNally, An inhomogeneous fault model for gaps, asperities, barriers, and seismicity migration, J. Geophys. Res., 89, 10219-10231, 1984.
- Sato, H., Some precursors prior to recent great earthquakes along the Nankai trough, J. Phys. Earth, 25, Suppl., S115-S121, 1977.
- Shimazaki, K., and T. Nakata, Time-predictable recurrence model for large earthquakes, Geophys. Res. Lett., 7, 279-282, 1980.
- Stuart, W. D., and G. Mavko, Earthquake instability on a strike-slip fault, J. Geophys. Res., 84, 2153-2160, 1979.
- Tsuchi, R., Neogene and quaternary structures of the area around Suruga trough and their neotectonics, (in Japanese) Quat. Res., 23, 155-164, 1984.
- Utsu, T., Seismology, Kyoritsu-Shuppansha, Tokyo, (in Japanese) 286 pp., 1977.
- Yamazaki, F., and T. Ooida, Seismicity in and near Suruga Bay, (in Japanese) J. Seismol. Soc. Jpn., (2), 32, 451-462, 1979.
- Yamazaki, F., and T. Ooida, Configuration of subducted Philippine Sea Plate beneath the Chubu District, central Japan, (in Japanese) J. Seismol. Soc. Jpn., (2), 38, 193-201, 1985.
- Yoshida, A., Seismicity on the west side of Suruga Trough, (in Japanese) J. Seismol. Soc. Jpn., (2), 36, 111-113, 1983.

## SEISMIC SLIP, ASEISMIC SLIP, AND THE MECHANICS OF REPEATING EARTHQUAKES ON THE CALAVERAS FAULT, CALIFORNIA

William H. Bakun<sup>1</sup>, Geoffrey C. P. King<sup>2</sup>, and Robert S. Cockerham<sup>1</sup>

<sup>1</sup>U.S. Geological Survey, Menlo Park, California 94025

<sup>2</sup>Department of Earth Sciences, Cambridge CB2 3EQ, England

**Abstract.** The 1969–1984 history of seismic slip on the Calaveras fault in central California can be used to examine how slip is distributed in time and is partitioned between different deformation processes. Nowhere is there evidence that brittle deformation is the predominant failure mode over the entire depth range for which small earthquakes can be located (between about 2 and 15 km). The closest approach to completely brittle strain release occurs only for a more limited range of depths in a part of the region that ruptured during the 1984 Morgan Hill earthquake. Elsewhere aseismic deformation appears to contribute substantially to the total deformation. Except for the Hollister Valley, it is not known whether creep occurs on the fault, or in the surrounding media. In the Hollister Valley, creepmeter data suggest that fault creep can entirely accommodate the slip. Previous work indicates that rupture on the Calaveras fault, in both the Coyote Lake and Morgan Hill earthquakes, initiated and terminated at bends or offsets. Mechanisms invoking purely brittle and elastic behavior have been offered to explain observations of this type. The results that we present suggest that creep, as well as elastic-brittle processes, must play an important role in the micro-mechanics of these regions.

### Introduction

Over the last few years it has been recognized that moderate earthquakes recur along the same segments of some faults. The clearest example of this repeating behavior is provided by Parkfield earthquakes [Bakun and Lindh, 1985] but the concept of characteristic earthquakes also provides an appealing explanation for geomorphic features observed in association with active faulting elsewhere [e.g., Schwarz and Coppersmith, 1984; Vita-Finzi and King, 1985]. The repeating or characteristic behavior has been ascribed to rupture being constrained by long-lived geometric features of the fault, such as bends [e.g., King and Nabelek, 1985; Sibson, 1985]. An alternative mechanism is that rupture is contained between creeping or ‘stress relaxed’ zones [Husseini et al., 1975; King, 1986].

Taken as a whole, the observations suggest that complete earthquake cycles exist but, as yet, we have little detailed knowledge of their nature. We do not know how stresses

are stored or relaxed between earthquakes and hence determine whether geometric processes or stress relaxation constrains the extent of rupture of individual events. This arises mainly as a result of a lack of detailed seismic data collected over long periods of time. In no part of the world has a dense seismic array been operated long enough to provide good data that covers a complete seismic cycle.

We have therefore chosen to examine a part of California that not only has high quality data over a considerable part of the seismic cycle, but also includes two well-studied magnitude 6 events. We believe that, for the Calaveras fault, in the regions of the Coyote Lake and Morgan Hill earthquakes, we have detailed information for about 20% of a cycle and partial information for an additional 20%. Despite the limitation of this data set, interesting features emerge that we believe can be extrapolated to the complete cycle. To place our study in context we also examine parts of the fault to the north and south of the segments that slipped in these events: the Hollister Valley segment to the south, which is known to be creeping, and the Calaveras-Sunol fault and Concord fault to the north for which less is known but which may be the locations of future destructive earthquakes.

Studying seismicity in central California has certain advantages over similar studies in other parts of the world. Over a number of years a reliable moment-magnitude relation [Bakun, 1984] has been established that permits us to look at slip rather than simply hypocentral location. Location accuracies are good and having converted from magnitude to moment and distributed slip spatially, according to the size of the event, we plot the result as a function of depth and horizontal position along the fault. This slip distribution can be compared with geodetically-determined slip rates to permit us to examine the way in which slip is apportioned between brittle, ductile, and elastic deformation as a function of position on the fault. There are limitations in our ability to do this. Lack of data for the complete seismic cycle is the most serious. We also only have a limited understanding of the roles of adjacent active faults. The Busch and Hayward faults play a role that we only estimate. A further source of error is our assumption that we can sum all moments as if they only contribute

TABLE 1. Source Parameters.

$M_L$	$M_0$ (dyne - cm) <sup>†</sup>	$u_1$ (cm) <sup>‡</sup>	$W = L/2$ (km)	$N_L^{\$}$	$N_W^{\$}$
1	$1.70 \times 10^{18}$	$5.66 \times 10^{-4}$	0.17	1	1
2	$2.75 \times 10^{19}$	$9.18 \times 10^{-3}$	0.42	1	1
3	$4.47 \times 10^{20}$	0.149	1.06	1	1
4	$1.00 \times 10^{22}$	3.33	2.99	7	3
5	$3.16 \times 10^{23}$	105.41	9.45	19	9
6	$1.00 \times 10^{25}$	3333.	29.9	*	*

<sup>†</sup>  $\log M_0 = \begin{cases} 1.2 M_L + 17 & \text{for } M_L \text{ or coda duration magnitude } M_D < 3.5 \\ 1.5 M_L + 16 & \text{for } M_L \leq 3.5 \end{cases}$

<sup>‡</sup>  $u_1$  for faulting area  $A = 1 \times 1 \text{ km}^2$  and  $\mu = 3 \times 10^{11} \text{ dyne/cm}^2$ .

<sup>§</sup>  $N_L$  and  $N_W$  are the number of 1-km-long cells in length and width necessary to distribute  $u_1$  over source length  $L$  and source width  $W$  respectively.  $N_L$ ,  $N_W$ , and the position of the center cell are easily changed when additional source parameter constraints are available (see \*).

\* Fault width exceeds the 20-km depth of the seismogenic zone assumed in these calculations so that  $N_L$  and  $N_W$  must be adjusted.

right-lateral, strike-slip motion. It is known, from aftershock studies, that not all events are of this character [e.g., Reasenberg and Ellsworth, 1982; Cockerham and Eaton, 1984]. Nonetheless, the relative number of 'anomalous' mechanisms is small, and, notwithstanding the foregoing limitations, we believe that we gain insights into the mechanics of faulting. In particular, we confirm the results of Bakun [1980] that larger events tend to occur in gaps in the seismic moment release of smaller events. We also find that complete brittle release is limited to a narrow depth range and that slip deficits in bend regions, where major events start and stop, appear to be accommodated, not only by many smaller events during the 'interseismic' period, but also by aseismic creep.

#### Data

The major earthquakes that concern this study are the  $M_L = 5.8$  Coyote Lake earthquake of August 6, 1979 and the  $M_L = 6.2$  Morgan Hill earthquake of April 24, 1984. These apparently repeated events in 1897 and 1911, respectively, suggest a recurrence time of 75–80 years [Reasenberg and Ellsworth, 1982; Bakun et al., 1984]. Other events relevant to this study are the  $M_L = 5.4$  earthquake on the Concord fault on October 24, 1955, the  $M_L = 5.5$  shock on September 5, 1955 near the north end of Halls Valley, the  $M_L = 5.2$  event on March 9, 1949 at the northeast end of the Hollister Valley (all from Bolt and Miller [1975]) and the  $M_L = 5.1$  Thanksgiving Day shock of November 28, 1974 on the Busch fault.

The rest of the seismicity is taken from the U.S. Geological Survey's (USGS) catalogs of central California earthquakes for the years 1969–1978 [Lee et al., 1972a,b,c; Wesson et al., 1972a,b, 1973, 1974a,b; Bufe et al., 1975; Lester et al., 1976a,b; Lester and Meagher, 1978; McHugh and Lester, 1978, 1979; Marks and Lester, 1980a,b; Marks and

Fluty, 1981; Fluty and Marks, 1981] and unpublished catalogs for 1978–1984. The catalogs are generally complete down to a magnitude of 1.5 [Reasenberg, 1985] and a comparison of the catalogs for 1978–1984 with those of the University of California, Berkeley, Seismograph Station (UCB) indicates that they are complete for shocks with magnitudes greater than 2.5, the reporting threshold of UCB. Because we weight by seismic moment, the omission of a few  $M \lesssim 3$  shocks has little effect on the distributions of slip considered in this analysis (see Table 1).

Magnitude estimates for  $M \lesssim 3.5$  shocks are based on coda durations [Lee et al., 1972d]. Magnitude  $\gtrsim 3.5$  estimates are  $M_L$  determined using amplitudes recorded on Wood-Anderson seismographs operated in central California by UCB. The coda-duration magnitudes  $M_D$  (or the seismic moment to  $M_D$  relations described below) are not adjusted for developorder magnification changes early in 1977. Preliminary comparisons of  $M_D$  with UCB's  $M_L$  [Bakun, unpublished USGS internal report, 1979] show that  $M_D$  after the developorder change in 1977 are, on average,  $0.26 \pm 0.06$  and  $0.23 \pm 0.06$  less than comparable pre-1977  $M_D$  for the north and south halves respectively of the polygon in Figure 1. (Additive  $M_D$  corrections of 0.2 and 0.1 were used by Bakun [1980] and Reasenberg and Ellsworth [1982] respectively in their analyses of seismicity within the south half of the polygon.) Because the  $\log M_0$  to  $M_D$  relation [Bakun, 1984] is based on post-1977 seismicity, systematic errors in the seismic slip distributions caused by uncompensated developorder changes probably are limited to the 1969–1976 data. We believe these errors do not seriously affect our results because the errors are spatially nearly uniform, the weighting by seismic moment substantially decreases the contribution of small shocks for which  $M_D$  are used, and most of the seismic slip occurred in the more active post-1977 period for which the  $\log M_0$  to  $M_D$  relations are known to be reliable.

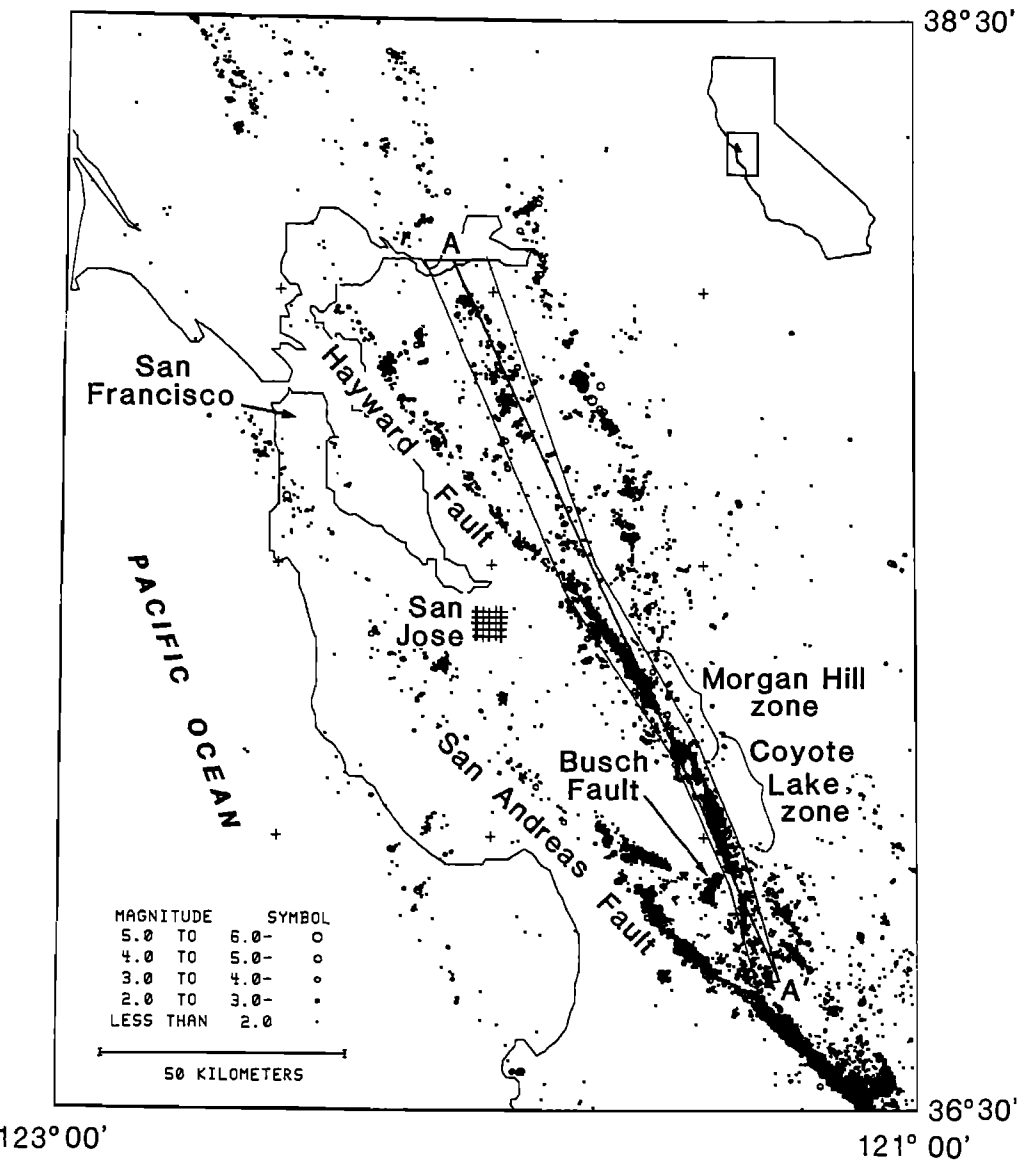


Fig. 1. Seismicity (magnitude > 1.3) in the San Francisco Bay area for 1976-1984. The polygon encloses epicenters of shocks associated with the Calaveras fault, Calaveras-Sunol fault, and Concord fault (see Figure 2).

All of the earthquakes in the USGS catalogs located in the polygon are used in this study. Those in the 1969-1971 catalogs have a hypocentral precision no better than a few kilometers while those in the 1977-1984 catalogs are generally located to within 1 km. To test for the effect of poorly located events, we used a subset of better solutions; where each event was recorded on at least one close station. The epicentral and depth distributions for the complete and reduced data sets are shown in Figure 2 and the criteria for selection are described in the caption. Except for shallow depths, and for part of the aftershock sequence of the Morgan Hill earthquake where some larger aftershocks

are deleted, the two distributions are similar and produce nearly identical slip distributions. We use the complete, rather than the reduced set, for later discussions.

Bearing in mind the location accuracies, we adopt a fault area cell size of 1 km by 1 km within which to estimate slip. The lateral cell boundaries are set by the arbitrary northwest end of the cross section AA' in Figure 1 and the depth cell boundaries by using zero focal depth as the upper edge of the first layer of cells. Each hypocenter is relocated at the center of the cell within which its true hypocenter lies. Thus, we convert the hypocenters from a continuous distribution along the fault to a discrete distribution of 1 km

## 198 MECHANICS OF REPEATING EARTHQUAKES

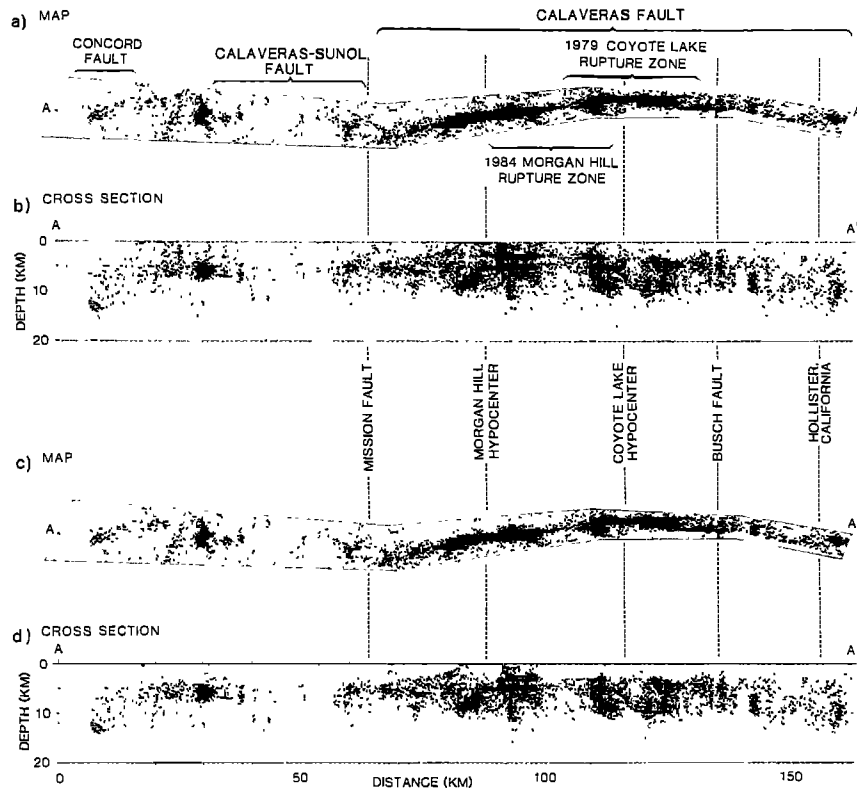


Fig. 2. Seismicity within the polygon (Figure 1) for 1969–1984. (a) map and (b) vertical cross sections of hypocenters of all earthquakes in the USGS CALNET earthquake catalogs. (c) and (d) Map and cross sections of hypocenters subject to accuracy criteria. We use shocks with  $DMIN$ , the epicentral distance to the closest seismograph that recorded the shock, less than 5 km, the standard error of the epicenter less than 2.5 km, and the standard error of the hypocenter  $< 2.5$  km. Also included are shocks with  $DMIN < 2$  focal depths.

grid spacing located on a vertical plane beneath the section AA'. In subsequent sections, 'kilometer positions' refer to this grid.

#### Conversion from Magnitude to Slip

Seismic moment  $M_0$  defined in terms of a shear-dislocation earthquake source model [Aki, 1966] is given by

$$M_0 = \mu U A ,$$

where  $\mu$  = modulus of rigidity,  $A$  = fault area, and  $U$  = average slip amplitude over  $A$ .

The logarithm of seismic moment,  $\log M_0$ , can be estimated to a precision of 0.2 from USGS coda duration magnitudes  $M_D$  for  $1 \leq M_D \leq 3.5$  earthquakes in central California using  $\log M_0 = 1.2 M_D + 17$  [Bakun, 1984]. For shocks with  $3 \leq M_L \leq 6$ , the  $\log M_0 = 1.5 M_L + 16$  relation obtained by Thatcher and Hanks [1973] for southern California earthquakes is consistent with central California  $\log M_0$  and  $M_L$  data [Bakun, 1984]. Seismic moment has been estimated independently for the  $M_L \gtrsim 5.5$  shocks considered:  $M_0 = 1.9 - 2.1 \times 10^{25}$  dyne-cm for the 1984

Morgan Hill earthquake [Prescott et al., 1984; Ekström, 1984] and  $M_0 = 5.5 - 5.6 \times 10^{24}$  dyne-cm for the 1979 Coyote Lake earthquake [Bouchon, 1982; Uhrhammer, 1980; Nábelék and Toksöz, 1981].

To convert from seismic moment to slip it is necessary to make assumptions. If we use the same value for rigidity ( $3 \times 10^{11}$  dyne cm $^{-2}$ ) used to determine the moments originally, then the modulus cancels. Distributing slip on the fault plane is less straightforward. We assume a rectangular rupture area  $A$  with length  $L$  and width  $W$  (depth). For the largest events direct information is available to constrain the values of  $L$  and  $W$ . For other events we use:

$$L = 2W = 4 \left( \frac{u_1}{K} \right)^{1/3} ,$$

where  $u_1$  is the slip for  $A = 1$  km $^2$  and  $K = 10^{-5}$ . Values of the foregoing parameters for earthquakes with integral magnitudes between 1 and 6 are listed in Table 1. These source parameters correspond to stress drops of a few bars [e.g., Scholz, 1982], clearly at the lower end of the 10–100 bars usually obtained for shocks on the San Andreas fault

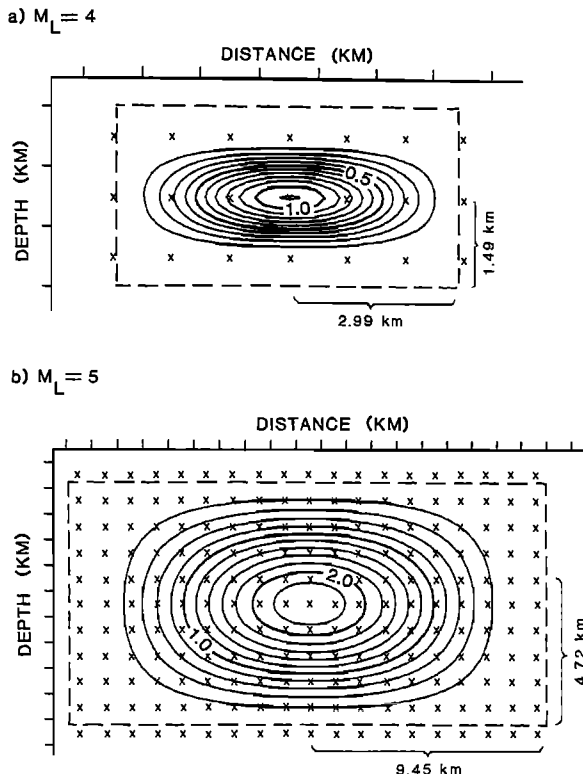


Fig. 3. Distribution of slip (cm) contoured on the fault plane for (a)  $M_L = 4$  and (b)  $M_L = 5$  earthquakes. The rectangular source dimensions shown by dashed lines are calculated from the moment-magnitude relations as described in the text. The cells used are only those whose centers (marked by crosses) fall within the source area. The central cross and outermost crosses have a weight of  $lw/LW$  and 0 respectively.

system. We use these small stress drops (large  $W$  and  $L$ ) in part because they produce a spatial smoothing of the slip distribution that allows for some of the uncertainties of location and extent of rupture of individual earthquakes.

Rather than distribute slip at a constant amplitude over the regions determined by the above method, we use a 'cosine-squared' weighting so that slip is larger near the center of the slip area than at the edges [e.g., Madariaga, 1976]. No special significance should be attached to the cosine-squared form other than that it is reasonable and numerically easy to handle. A suitable distribution, such that  $M_0$  summed over all the cells equals the earthquake  $M_0$  is provided by:

$$u_{n,m} = u_1 \left\{ \frac{l}{L} \cos^2 \frac{\pi}{2} \left( \frac{l}{L} n \right) \right\} \left\{ \frac{w}{W} \cos^2 \frac{\pi}{2} \left( \frac{w}{W} m \right) \right\}$$

where  $u_{n,m}$  = slip in cell  $n, m$  and  $n, m$  are cell numbers (numbered along the length and width respectively) relative to the hypocenter cell ( $n = m = 0$ ),  $l$  = length increment

of each cell (1 km is used here),  $w$  = width increment of each cell (1 km is used here), and  $-L/l \leq n \leq L/l$  and  $-W/w \leq m \leq W/w$ . The slip distributions that result from this scheme for magnitude 4 and 5 shocks are shown in Figure 3.

It is necessary to satisfy different constraints on the slip distribution for large shocks where  $L$  and  $W$  are comparable to the thickness of the seismogenic zone and the hypocenter cannot be assumed to be at the center of the slip distribution. For example, the  $M_L = 6.2$  Morgan Hill earthquake ruptured unilaterally to the southeast along the fault with a second energetic source of seismic radiation located near the end of its rupture zone [Bakun et al., 1984]. These two sources can be represented by an  $M_L = 5.8$  shock near the hypocenter and an  $M_L = 6.1$  source near the hypocenter of the second source. A two-source slip distribution with appropriate values for  $L$  and  $W$  has been chosen such that the 10-cm slip contour approximates the slip boundary of the Morgan Hill main shock that was inferred by Cockerham and Eaton [1984] from the spatial distribution of aftershock hypocenters (see Figure 4). Similarly, a slip distribution was devised for the 1979 Coyote Lake main shock (Figure 5) using the spatial pattern of aftershock hypocenters in the area designated zone I by Reasenberg and Ellsworth [1982]. The slip distributions found in this way are consistent with results obtained from modeling near-source, strong-ground motions [Hartzell and Heaton, 1986; Liu and Helmberger, 1983].

#### Seismic Slip on the Calaveras Fault

The foregoing techniques allow us to look at seismic slip on the Calaveras fault as a function of time and compare it to geodetic rates. Since slip is estimated in 1 km by 1 km cells we are able to view it in considerable detail as a function of position. To represent slip as a function of position we have adopted two methods. First we contour the slip over the fault plane and look at time variations with a series of selected time windows as separate plots (Figures 6 to 8). We also plot graphs of summed slip amplitude as a function of position for different depth ranges (Figures 7c, 8b, and 8d).

Figures 6 and 7 show the slip development in the Coyote Lake and Morgan Hill earthquakes region (kilometers position 70 to 135). Figure 6a shows the slip in the 10.5-year period before the Coyote Lake earthquake. During that time most of the slip occurred at shallow depths to the northwest of the rupture zone of the Coyote Lake main shock (indicated as a dotted line on the figure). It is important to appreciate that seismic activity on the Busch fault which joins near the southern end of the rupture zone (kilometer position 135) is not included in the scheme adopted in this paper. An equivalent event on the Calaveras would represent as much slip to the southeast before the main shock as we see in shallow events to the northwest. Most of the seismic slip in the Coyote Lake aftershock sequence, however, does occur at the southeast end of the rupture and northwest of the intersection with the Busch fault (kilometer position 125 to 135).

## 200 MECHANICS OF REPEATING EARTHQUAKES

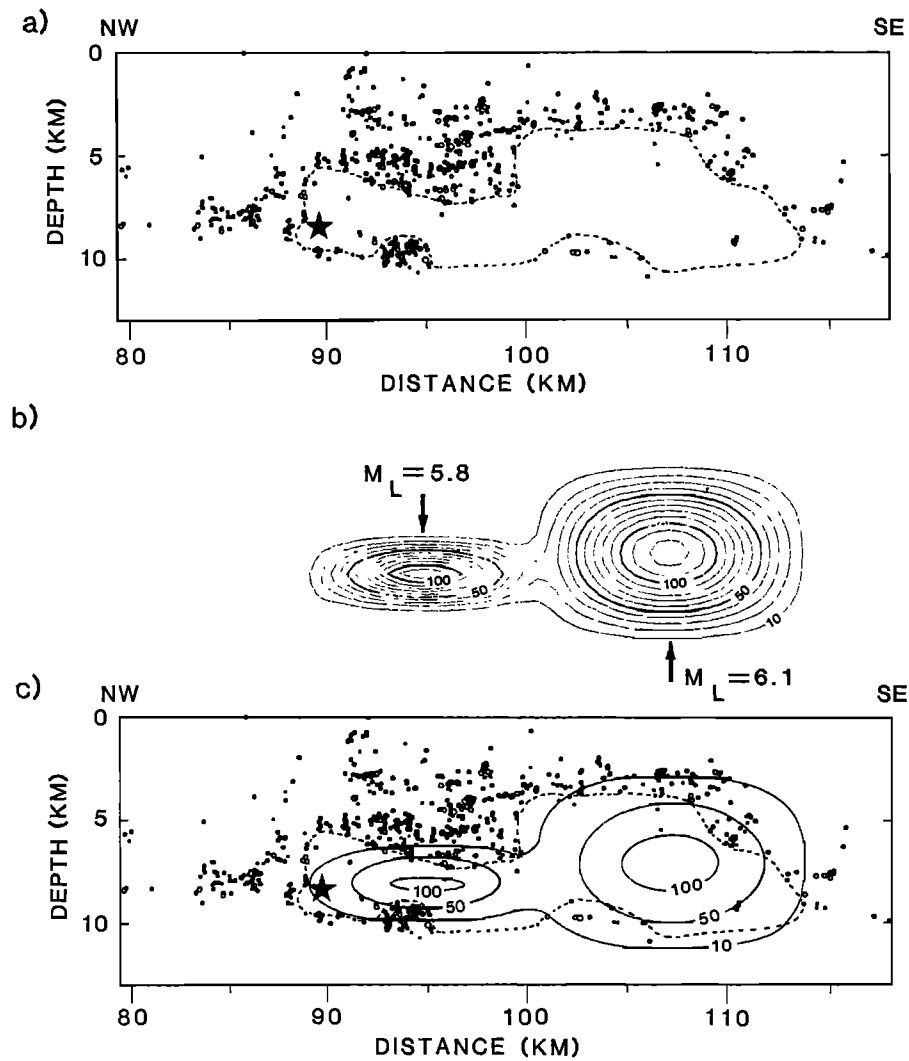


Fig. 4. (a) Cross section showing aftershocks of the 1984 Morgan Hill earthquake with epicenters located within a 2.1-km-wide band along the Calaveras fault (taken from Cockerham and Eaton [1984]). A dashed line outlines a central quiet area interpreted by Cockerham and Eaton to be the section that slipped during the main shock. The hypocenter of the main shock is shown as a star. (b) Contours of constant seismic slip (cm) obtained using two sources: an  $M_L$  5.8 source to the northwest and an  $M_L$  6.1 source to the southeast. The location, length, and width of the sources were adjusted so that the boundary of significant slip mimics the dashed line in (a). (c) The 10-, 50-, and 100-cm-slip contours from (b) superimposed on (a).

Following the Coyote Lake aftershock sequence, which produced minimal slip after 3 months, seismic slip occurred mainly at the northwest end of the rupture zone of the 1984 Morgan Hill earthquake (Figure 6c). If this is summed with the slip, before, during, and after the Coyote Lake event, we find the slip distribution shown in Figure 6d. The most striking feature of this distribution is a slip deficit that extends for 20 km in the lower part of the seismogenic zone (depths greater than 6 km). The hypocenter of the Morgan Hill event was located at the northwest end of this

zone of 'lagged slip' and rupture during the main shock was unilateral to the south-southeast so that slip in the main shock occurred mainly over the lagged section (Figure 7a).

The spatial variation of slip, for various time and depth range windows, is plotted in Figure 7c. Slip before the Morgan Hill event is shown for depth ranges of 6–15 and 0–15 km for a 15.3-year period. For the 0–15 km-depth range the September 1955 magnitude 5.5 shock [Bolt and Miller, 1975] is also included to approximate the slip for a 30-year period. We also include an event, from the same

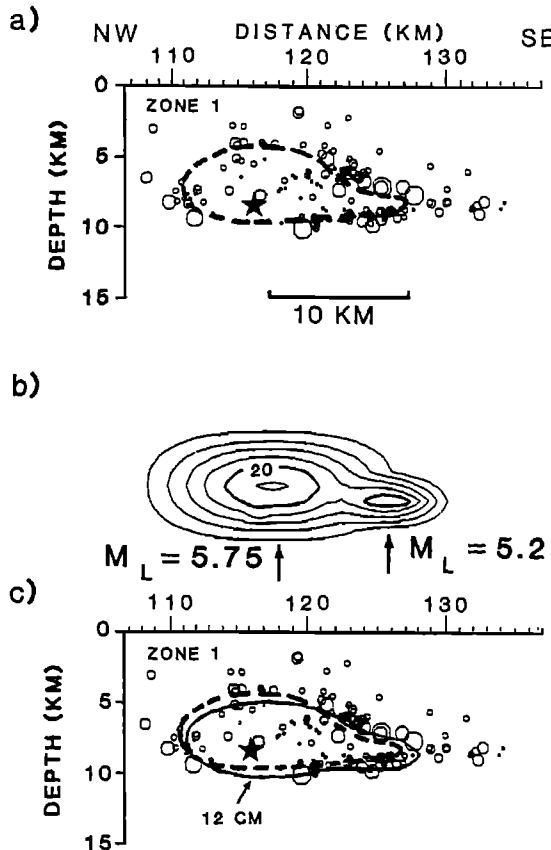


Fig. 5. (a) Cross section along the Calaveras fault showing the 1979 Coyote Lake main shock and magnitude 0.5 and larger aftershocks located on Zone 1, the easternmost section (taken from Reasenberg and Ellsworth [1982]). Symbol size is proportional to magnitude. The hypocenter of the main shock is shown as a star. A dashed line encloses a central area around which larger aftershocks are located. Although aftershocks on Zones II and III are located farther southeast, there is no evidence that rupture during the main shock extended to these segments. (b) Contours of constant seismic slip (cm) obtained using two sources: an  $M_L = 5.75$  event near the main shock hypocenter and an  $M_L = 5.2$  source located 9 km to the southeast. The two sources were arbitrarily adjusted so that the slip contours mimic the spatial pattern of larger aftershocks on Zone 1. The 12-cm-slip contour from (b) (solid line) superimposed on (a).

catalog, of magnitude 5.2 that occurred on March 9, 1949 at the southeast end of the Coyote Lake rupture zone. The resulting slip distribution before the Morgan Hill earthquake confirms the suggestion [Bakun, 1980] that deficits in cumulative seismic slip can mark sections of the fault where subsequent larger shocks will occur. The presentation adopted here, however, allows us to see in more detail what is happening. The relative slip deficit, over the short interval of 15 years, is not pronounced at the northwest

end; there was not much total slip in the kilometer positions 80–85 region. The relative deficit is more pronounced if only a 6–15 km-depth range is averaged. If, however, the earlier seismicity described by Bolt and Miller [1975] is included, then the deficit becomes clear.

#### Comparison of Seismic and Geodetic Slip

Having determined the seismic slip on the Calaveras fault it is now possible to compare it with that determined geodetically. We interpret the geodetic slip rates to be the motion that would occur on all parts of the fault if no elastic or ductile deformation takes place between the fault and the points where geodetic slip is determined. The 'geodetic slip' so defined, can be thought of as approximating an idealized rigid block boundary condition at a distance from the fault. Geodetic data has a limited ability to distinguish changes of rate as a consequence of the infrequent sampling imposed by a limited number of surveys. However, it seems that if the motion is measured between points at a substantial distance on each side of a fault then motion appears to be nearly constant over long periods [Matsu'ura et al., 1986]. We therefore believe that we can extrapolate rates over a period of time long compared to the total measurement interval. The rate we take for the Calaveras fault southwest of the region of intersection with the Hayward fault is taken to be 1.5 cm/yr [Savage et al., 1979] and we use 0.7 cm/yr to the northeast [Prescott et al., 1981]. The difference between these rates may be presumed to result from motion transferred to the Hayward fault but, of course, other structures may be active.

The geodetic and seismic slip over the entire length of the fault studied here (kilometer positions 0 to 165) are shown in composite Figure 8. The complete seismicity from the USGS catalog is shown in Figure 8e and Figure 8a is the same data converted to slip with the contributions from the Morgan Hill and Coyote Lake earthquakes added. The historical earthquakes referred to earlier are added to the slip distribution to produce Figure 8c. Figures 8b and d are plots of slip for sections through the distributions in Figures 8a and c respectively. Slip for various depth intervals are shown and the expected geodetic slip, for 15- and 80-year intervals, is indicated by wavy lines.

It is immediately apparent from Figures 8b and d that the Morgan Hill earthquake (kilometer positions 100 to 110) was associated with more fault slip in the seismogenic zone (5–8 or 4–9 km ranges) than had accumulated in a period of 15 years. On the other hand, the peak slip is comparable to that predicted for an 80-year return period. It is therefore possible to conclude that this part of the fault can be failing by brittle, seismogenic processes alone. Above and below this depth range, however, it is apparent that creep must provide a large contribution to the motion. This deficit need not occur as fault creep. The geodetic results allow it to be accommodated as volume creep in a zone that extends for several kilometers on each side of the fault.

In the Hollister Valley (kilometers positions 140–162 in the figures), fault creep does occur and the seismicity for

202 MECHANICS OF REPEATING EARTHQUAKES

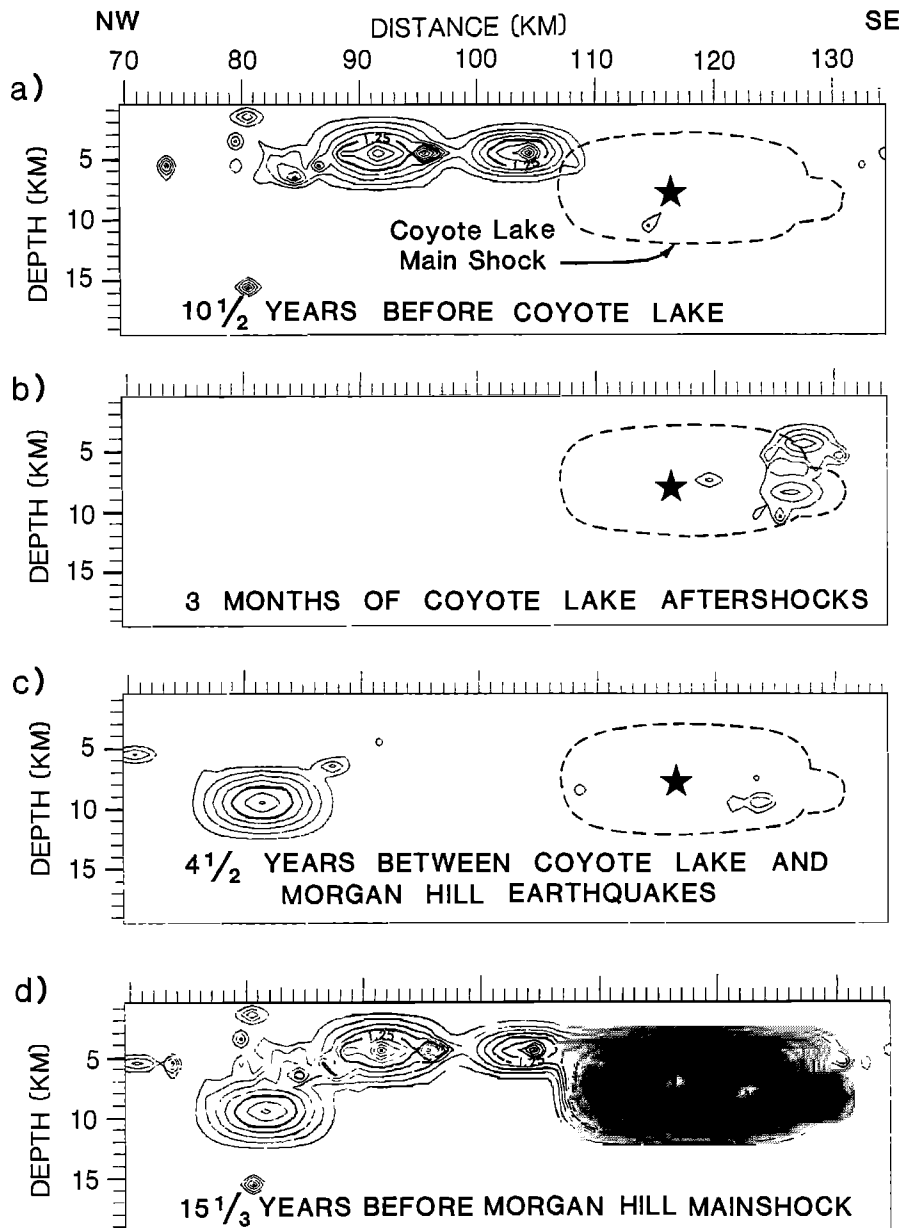


Fig. 6. Contours of constant seismic slip before the Morgan Hill earthquake on the section of AA' (Figure 1) from kilometer positions 70 to 135 for (a) January 1, 1969 to August 5, 1979, (b) August 6, 1979 to November 6, 1979, (c) November 7, 1979 to April 23, 1984, and (d) January 1, 1969 to April 23, 1984. Contour interval = 0.25 cm. Hypocenter (star) and 1-cm seismic slip contour (dashed line) of the Coyote Lake main shock (Figure 5) are superposed on (a), (b), and (c).

the 15-year period indicates a trivial contribution from brittle deformation. Since there are no known historical earthquakes large enough ( $M_L > 5$ ) to alter the seismic slip pattern and since the fault creep rate approximates the geodetic rate [Rogers and Nason, 1971; Schulz, 1984], we conclude that deformation in the Hollister region is restricted to the fault as fault creep.

What is happening over other parts of the fault is less clear. For our slip distribution, the peak displacement of the Coyote Lake earthquake (around kilometer position 118) accounts for no more than 15 years of accumulated slip. We must therefore conclude, either that some events are missing from the historical catalog, or that in the seismogenic depth range, no more than 20% of the slip is ac-

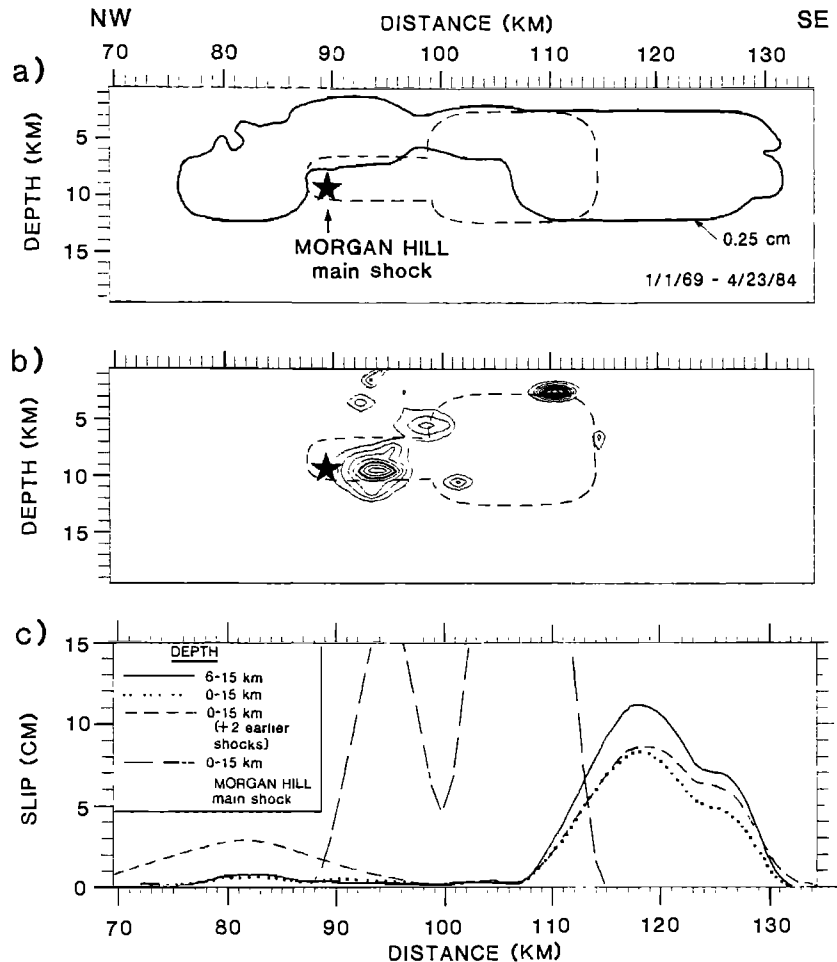


Fig. 7. Seismic slip on the section AA' (Figure 1) for kilometer positions 70 to 135. (a) Boundary contour (0.25 cm) of seismic slip from Figure 6d. (b) Slip contours for April 24, 1984 to July 23, 1984. Contour interval = 0.25 cm. Hypocenter (star) and 1-cm contour of seismic slip (dashed line) of the Morgan Hill main shock (Figure 4b) are superposed on (a) and (b). (c) Seismic slip (per  $\text{km}^2$  of fault area) for the Morgan Hill main shock (Figure 4b) averaged over the depth interval of 0 to 15 km is shown as a bold dashed line. The time from January 1, 1969 to April 23, 1984 (Figure 6d) averaged over depths of 0 to 15 km and 6 to 15 km are shown as dotted and thin solid lines respectively. The time from January 1, 1969 to April 23, 1984 plus the March 9, 1949 ( $M_L = 5.2$ ) and the September 5, 1955 ( $M_L = 5.5$ ) shocks averaged over depths of 0 to 15 km is shown as a thin dashed line.

commodated by brittle motion with the rest being accommodated by fault creep or volume creep. Alternatively we could follow Reasenberg and Ellsworth [1982] and localize the slip of the event such that a very small region releases all of the geodetic motion. This does not alter the conclusion that creep is an important mechanism over the fault plane as a whole.

Similar arguments apply to the northern part of the Morgan Hill rupture and the Halls Valley region (kilometer positions 75–85). The peak slip in the earthquake is only 30% of the 80-year slip and the slip to the north of that, even including the September 5, 1955 earthquake (see Figure

8d), is only 5% of the 80-year slip. It should, however, be noted that the low stress drop assumed for the 1955 event smooths its slip over a wide region. If we were to reduce the fault area by four the event could account for 20% of the 80-year slip but over a restricted area. Whatever the adjustments, we are forced to conclude, either that many events in the magnitude 5 range are absent from the catalog, or that the largest proportion of the deformation occurs as volume or fault creep.

The seismic slip along the northern section of the Calaveras fault, the Calaveras–Sunol fault and the Concord fault (kilometer positions 0 to 80) is significantly less than the

## 204 MECHANICS OF REPEATING EARTHQUAKES

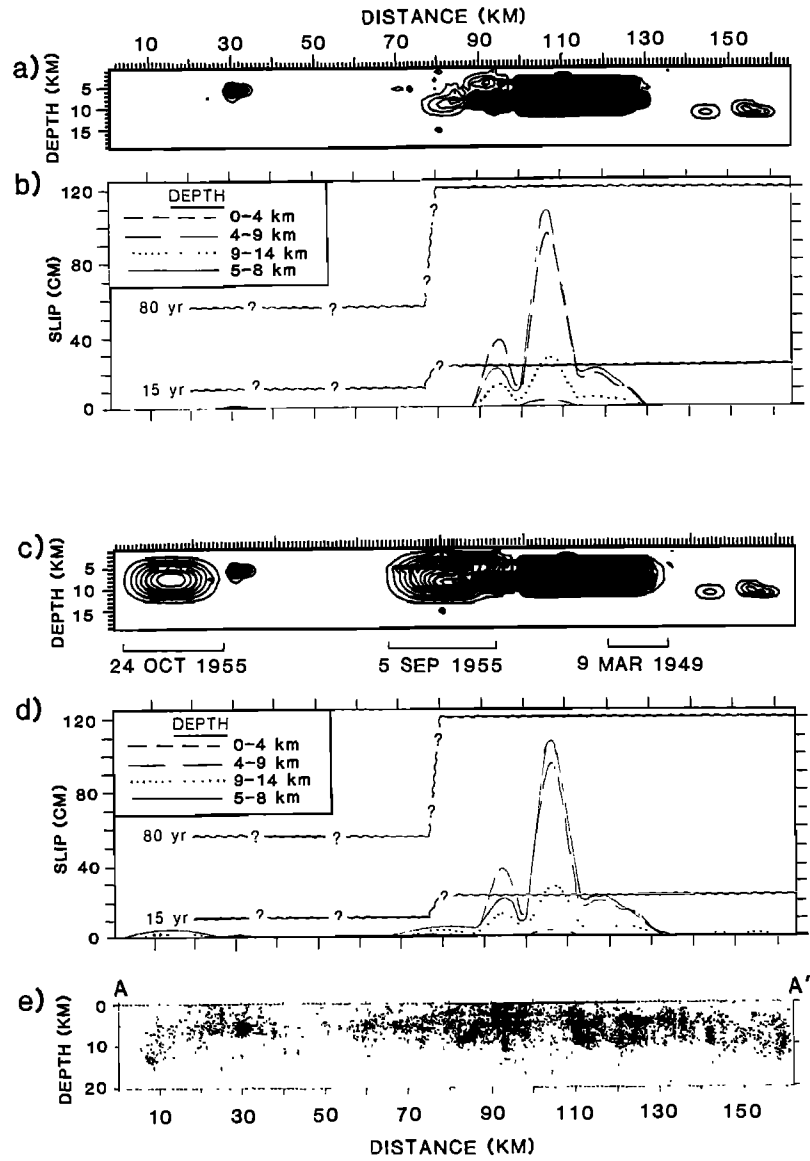


Fig. 8. Seismic slip on the section AA'. (a) Cross section for January 1, 1969 to January 1, 1985 with contour interval = 0.50 cm. (b) Slip on (a) averaged over depth intervals of 0-4, 4-9, 9-14, and 5-8 km compared with slip potential (wavy lines) for 15 and 80 years inferred from geodetic observations. The geodetic slip potential uses 1.5 cm/yr [Savage et al., 1979] for 80-162 km and 0.7 cm/yr [Prescott et al., 1981] for 30-75 km. The transition at kilometer positions 75 to 80 is arbitrarily drawn midway between the intersections of the Mission and Hayward faults with the Calaveras fault. (c) and (d) show (a) and (b) with seismic slip for the March 9, 1949 ( $M_L = 5.2$ ), the September 5, 1955 ( $M_L = 5.5$ ), and the October 24, 1955 ( $M_L = 5.4$ ) shocks added. The length, and especially the width, of spatial slip shown for these pre-1969 shocks is arbitrary. (e) Figure 2b repeated for comparison.

seismic slip along the sections to the southeast and substantially less than the potential slip inferred from geodetic observations (Figure 8d). In view of the foregoing however, it is not clear that we can conclude that a large earthquake is to be expected in the region; equally, we cannot exclude the possibility. The difference between the seismic slip and

the potential slip may represent fault creep, off-fault creep, or earthquakes missing from the seismicity catalogs.

The northern 20 km of the section AA', however, is associated with the clear morphological expression of the Concord fault which is offset by a right lateral step from the north end of the Calaveras-Sunol fault. Thus, on purely

geological grounds, we can speculate that the  $M_L$  5.4 Concord earthquake of October 24, 1955 (shown in Figures 8c and d) might be a characteristic Concord fault earthquake.

### Discussion

Reid [1910] postulated, in his elastic rebound theory, that distant motion is stored as strain energy near to faults and is released by fault slip during earthquakes. Seismic hazard evaluations [e.g., Lindh, 1983; Sykes and Nishenko, 1984] and long-term earthquake prediction models [e.g., Shimizaki and Nakata, 1980; Bakun and Lindh, 1985] implicitly assume an earthquake process incorporating a nearly constant rate of strain accumulation in some elastic-brittle zone that is loaded by relative plate motion and releases stress abruptly by seismic slip in infrequent large shocks. Comparisons of potential slip inferred from geodetic observations with seismic slip on different parts of the Calaveras fault provide a detailed display of this earthquake generating process.

It is evident that, unless our information and assumptions about historical seismicity are seriously in error, the elastic-brittle zone is very limited in depth and in spatial extent. Only for a part of the rupture zone of the Morgan Hill earthquake can we argue that all of the slip is accommodated by seismogenic processes, elsewhere volume creep or fault creep is demanded. In the Hollister Valley we can distinguish between the two. Fault creep, measured at the surface, is certainly sufficient to accommodate all of the deformation measured geodetically. Elsewhere the situation is ambiguous because of a lack of creepmeter data. The presence of drag folds associated with faults in the San Andreas system [Moody and Hill, 1956] certainly suggests that volume deformation can occur over geological time but does not, of course, demonstrate that it is occurring now in the Calaveras fault region.

Rupture initiation and termination during the 1979 Coyote Lake and 1984 Morgan Hill earthquakes was apparently related to bends and/or offsets in the fault [Bakun, 1980; Bakun et al., 1984]. It follows naturally from geometric considerations that off-fault deformation must occur in these regions and it has been suggested, also from geometric considerations that this must occur by motion on faults with a hierarchy of sizes that form a fractal system [King, 1983, 1986; King and Nábelék, 1985]. While all of these faults may exist, it is evident that not all of the deformation is seismogenic (or more events would occur). On the other hand, since events do occur at all magnitudes, we can speculate that, either some proportion of faults at all scales creep, or that in the long interseismic periods creep occurs uniformly over a volume in such a way that it does not selectively reduce the proportion of events in any particular magnitude range. We do not, at present, see how to distinguish between these two possibilities.

Numerous studies have been made of the effective elastic thickness of continental crust using either loading models or spectral comparisons between topography and gravity [e.g., Forsyth, 1985]. These result in surprisingly small estimates of elastic thickness of between 1 and 5 km. We

can recouch our results in these terms by determining the thickness of an entirely elastic-brittle layer that would release all of the observed seismic radiation. The total moment release in the kilometer position range of 80 to 160 is  $2.60 \times 10^{25}$  dyne-cm for the 15-year period. This is less than would be released in an 80-year period. Taking this as the total release gives a brittle-elastic layer only 0.90 km thick. Alternatively if we consider the slip for only a 15-year period, then the effective thickness would be 4.8 km. In either case the effective elastic thickness is much less than the 15 km depth to which seismicity extends and agrees in thickness with the estimates using completely different techniques.

### Conclusions

The distribution of seismic slip on the Calaveras fault for 1969–1984 suggests that:

1. Seismic gap theory, used to predict major earthquakes at plate boundaries, may also be applied to smaller events. The methods that we outline, therefore, offer a potential tool for earthquake prediction. Larger shocks tend to occur within regions of slip deficit left by earlier earthquakes. This is most clearly seen for the 1984 Morgan Hill earthquake even though only 15 years of detailed seismic history exist and the recurrence interval of larger shocks on the southern part of the Calaveras fault is 75 to 80 years. Consideration of earlier shocks on the Calaveras fault enhances the pre-Morgan Hill slip deficit, indicating that it would be more apparent if a larger period of detailed seismicity were available. It is also apparent that, in the Morgan Hill case, shallow seismicity above the 5–9 km depth range partly obscures the slip deficit, emphasizing the importance of looking at slip as a function of depth.

2. Comparison of the seismic slip distribution with potential slip inferred from geodetic observations illustrates details of the earthquake generation process. Only for a limited region associated with the Morgan Hill earthquake is seismic slip comparable to the geodetic motion and then only for a limited depth range. The deficit elsewhere may be explained by a combination of processes. These include incomplete seismicity catalogs, fault creep, off-fault aseismic deformation and a not yet realized potential for seismic slip in future shocks. However we apportion these influences, it seems that creep must play an important role.

3. If the seismicity is considered to act entirely in a narrow, perfectly brittle-elastic zone, the zone would be between 1 and 4 km thick. This is in broad agreement with estimates of the effective elastic thickness of the crust derived by other methods [e.g., Forsyth, 1985].

4. Bends and offsets are thought to control the initiation and termination of earthquake rupture. It has been proposed that geometric processes distribute faulting over a process zone in these regions and it is this region of fragmentation that controls the onset and cessation of rupture [King, 1986]. This model is entirely brittle in character and it is evident that the bend zones we examine do not have this property. Although the clustering of seismicity

## 206 MECHANICS OF REPEATING EARTHQUAKES

is expected from the model, there are too few events. Motion must be accommodated by creep in some form. We cannot tell from this study whether this occurs by creep on many faults of different scale sizes or by volume processes. Whatever the mechanism may turn out to be, understanding the role of creep in the 'micromechanics' of bends will be important for understanding the physics of earthquakes.

**Acknowledgments.** We would like to thank D. Oppenheimer and P. Reasenberg for reading earlier versions of this paper and providing helpful suggestions. Support for G.K. came from the Nuffield Foundation and The Natural Environment Research Council GR3/3904. This is Cambridge Earth Sciences contribution number 725.

## References

- Aki, K., Generation and propagation of  $G$  waves from the Niigata earthquake of June 16, 1964. Part 2. Estimation of earthquake movement, released energy, and stress-strain drop from  $G$  wave spectrum, *Bull. Earthquake Res. Inst. Tokyo Univ.*, **44**, 73–88, 1966.
- Bakun, W. H., Seismic activity on the southern Calaveras fault in central California, *Bull. Seismol. Soc. Am.*, **70**, 1181–1197, 1980.
- Bakun, W. H., Seismic moments, local magnitudes, and coda-duration magnitudes for earthquakes in central California, *Bull. Seismol. Soc. Am.*, **74**, 439–458, 1984.
- Bakun, W. H., and A. G. Lindh, The Parkfield, California, earthquake prediction experiment, *Science*, **229**, 619–624, 1985.
- Bakun, W. H., M. M. Clark, R. S. Cockerham, W. L. Ellsworth, A. G. Lindh, W. H. Prescott, A. F. Shakal, and P. Spudich, The 1984 Morgan Hill, California, earthquake, *Science*, **225**, 288–291, 1984.
- Bolt, B. A., and R. D. Miller, Catalogue of earthquakes in northern California and adjoining areas 1 January 1910–31 December 1972, *Seismographic Stations, Univ. of California, Berkeley*, 567 pp., 1975.
- Bouchon, M., The rupture mechanism of the Coyote Lake earthquake of August 6, 1979, inferred from near-field data, *Bull. Seismol. Soc. Am.*, **72**, 745–758, 1982.
- Bufe, C. G., F. W. Lester, K. L. Meagher, and R. L. Wesson, Catalog of earthquakes along the San Andreas fault system in central California, April–June 1973, *U.S. Geol. Surv. Open File Rep.* **75-125**, 44 pp., 1975.
- Cockerham, R. S., and J. P. Eaton, The April 24, 1984 Morgan Hill earthquake and its aftershocks: April 24 through September 30, 1984, in *The 1984 Morgan Hill, California, Earthquake*, edited by J. H. Bennett and R. W. Sherburne, Calif. Div. Mines and Geol., Sacramento, CA, Spec. Publ. **68**, pp. 215–236, 1984.
- Ekström, G., Central-moment tensor solution for the April 24, 1984 Morgan Hill, California, earthquake, in *The 1984 Morgan Hill, California, Earthquake*, edited by J. H. Bennett and R. W. Sherburne, Calif. Div. Mines and Geol., Sacramento, CA, Spec. Publ. **68**, pp. 209–213, 1984.
- Fluty, L., and S. M. Marks, Catalog of earthquakes along the San Andreas fault system in central California October–December 1977, *U.S. Geol. Surv. Open File Rep. 81-1925*, 48 pp., 1981.
- Forsyth, D. W., Subsurface loading and estimates of the flexural rigidity of continental lithosphere, *J. Geophys. Res.*, **90**, 12623–12632, 1985.
- Hartzell, S. H., and T. H. Heaton, Rupture history of the 1984 Morgan Hill, California, earthquake from the inversion of strong motion records, *Bull. Seismol. Soc. Am.*, *in press*, 1986.
- Husseini, M. I., D. B. Jovanovich, M. J. Randall, and L. B. Freund, The fracture energy of earthquakes, *Geophys. J.*, **49**, 367–385, 1975.
- King, G. C. P., The accommodation of large strains in the upper lithosphere of the Earth and other solids by self-similar fault systems: The geometrical origin of  $b$ -value, *Pageoph.*, **121**, 761–815, 1983.
- King, G. C. P., The geometry of the initiation and termination of earthquake rupture and the evolution of morphology and geological structures, *Pageoph.*, *in press*, 1986.
- King, G. C. P., and J. Nábělek, The role of bends in faults in the initiation of termination of earthquake rupture, *Science*, **228**, 984–987, 1985.
- Lee, W. H. K., J. C. Roller, P. G. Bauer, and J. D. Johnson, Catalog of earthquakes along the San Andreas fault system in central California for the year 1969, *U.S. Geol. Surv. Open File Rep.*, 48 pp., 1972a.
- Lee, W. H. K., J. C. Roller, K. L. Meagher, and R. E. Bennett, Catalog of earthquakes along the San Andreas fault system in central California for the year 1970, *U.S. Geol. Surv. Open File Rep.*, 73 pp., 1972b.
- Lee, W. H. K., K. L. Meagher, R. E. Bennett, and E. E. Matamoros, Catalog of earthquakes along the San Andreas fault system in central California for the year 1971, *U.S. Geol. Surv. Open File Rep.*, 73 pp., 1972c.
- Lee, W. H. K., R. E. Bennett, and K. L. Meagher, A method of estimating magnitude of local earthquakes from signal duration, *U.S. Geol. Surv. Open File Rep.*, 28 pp., 1972d.
- Lester, F. W., and K. L. Meagher, Catalog of earthquakes along the San Andreas fault system in central California for the year 1974, *U.S. Geol. Surv. Open File Rep.* **78-1010**, 89 pp., 1978.
- Lester, F. W., K. L. Meagher, and R. L. Wesson, Catalog of earthquakes along the San Andreas fault system in central California, July–September 1973, *U.S. Geol. Surv. Open File Rep. 76-169*, 38 pp., 1976a.
- Lester, F. W., S. L. Kirkman, and K. L. Meagher, Catalog of earthquakes along the San Andreas fault system in central California, October–December 1973, *U.S. Geol. Surv. Open File Rep. 76-792*, 37 pp., 1976b.
- Lindh, A. G., Preliminary assessment of long-term probabilities for large earthquakes along selected fault segments of the San Andreas fault system in California, *U.S. Geol. Surv. Open File Rep. 89-86*, 15 pp., 1983.

- Liu, H.-P., and D. V. Helmberger, The near-source ground motion of the 6 August 1979 Coyote Lake, California, earthquake, *Bull. Seismol. Soc. Am.*, **73**, 201–218, 1983.
- Madariaga, R., Dynamics of an expanding circular fault, *Bull. Seismol. Soc. Am.*, **66**, 639–666, 1976.
- Marks, S. M., and L. Fluty, Catalog of earthquakes along the San Andreas fault system in central California, July–September 1977, *U.S. Geol. Surv. Open File Rep. 81-462*, 43 pp., 1981.
- Marks, S. M., and F. W. Lester, Catalog of earthquakes along the San Andreas fault system in central California, January–March 1977, *U.S. Geol. Surv. Open File Rep. 80-1233*, 47 pp., 1980a.
- Marks, S. M., and F. W. Lester, Catalog of earthquakes along the San Andreas fault system in central California, April–June 1977, *U.S. Geol. Surv. Open File Rep. 80-1264*, 47 pp., 1980b.
- Matsu'ura, M., D. D. Jackson, and A. Cheng, Dislocation model for aseismic crustal deformation at Hollister, California, *J. Geophys. Res.*, *in press*, 1986.
- McHugh, C. A., and F. W. Lester, Catalog of earthquakes along the San Andreas fault system in central California, for the year 1975, *U.S. Geol. Surv. Open File Rep. 78-1051*, 91 pp., 1978.
- McHugh, C. A., and F. W. Lester, Catalog of earthquakes along the San Andreas fault system in central California for the year 1975, *U.S. Geol. Surv. Open File Rep. 79-1138*, 91 pp., 1979.
- Moody, J. D., and M. J. Hill, Wrench-fault tectonics, *Geol. Soc. Am. Bull.*, **67**, 1207–1266, 1956.
- Nábelék, J., and M. N. Toksöz, Applications of WWSSN seismograms to the study of the Coyote Lake earthquake of August 6, 1979 (abstract), *IASPEI Meeting, Int. Assoc. Seismol. and Phys. of the Earth's Inter., London, Ontario*,
- Prescott, W. H., M. Lisowski, and J. C. Savage, Geodetic measurements of crustal deformation on the San Andreas, Hayward, and Calaveras faults near San Francisco, California, *J. Geophys. Res.*, **86**, 10853–10869, 1981.
- Prescott, W. H., N. E. King, and G. H. Gu, Preseismic, coseismic, and postseismic deformation associated with the 1984 Morgan Hill, California, earthquake, in *The 1984 Morgan Hill, California, earthquake*, edited by J. H. Bennett and R. W. Sherburne, *Calif. Div. Mines and Geol., Sacramento, CA, Spec. Publ. 68*, pp. 137–148, 1984.
- Reasenberg, P., Second-order moment of central California seismicity, 1969–1982, *J. Geophys. Res.*, **90**, 5479–5495, 1985.
- Reasenberg, P., and W. L. Ellsworth, Aftershocks of the Coyote Lake, California, earthquake of August 6, 1979; A detailed study, *J. Geophys. Res.*, **87**, 10637–10655, 1982.
- Reid, H. F., *The California earthquake of April 18, 1906, 2, Mechanics of the Earthquake*, 192 pp., Carnegie Institute of Washington, Washington, D.C.
- Rogers, T. H., and R. D. Nason, Active displacement on the Calaveras fault zone at Hollister, California, *Bull. Seismol. Soc. Am.*, **61**, 399–416, 1971.
- Savage, J. C., W. H. Prescott, M. Lisowski, and N. King, Geodolite measurements of deformation near Hollister, California, 1971–1978, *J. Geophys. Res.*, **84**, 7599–7615, 1979.
- Scholz, C. H., Scaling laws for large earthquakes: Consequences for physical models, *Bull. Seismol. Soc. Am.*, **72**, 1–14, 1982.
- Schulz, S. S., Triggered creep near Hollister after the April 24, 1984, Morgan Hill, California, earthquake, in *The 1984 Morgan Hill, California, earthquake*, edited by J. H. Bennett and R. W. Sherburne, *Calif. Div. Mines and Geol., Sacramento, CA, Spec. Publ. 68*, pp. 175–182, 1984.
- Schwarz, D. P., and K. J. Coppersmith, Fault behavior and characteristic earthquakes: Examples from the Wasatch and San Andreas fault zones, *J. Geophys. Res.*, **89**, 5681–5698, 1984.
- Shimazaki, K., and T. Nakata, Time-predictable recurrence model for large earthquakes, *Geophys. Res. Lett.*, **7**, 279–282, 1980.
- Sibson, R. H., Stopping of earthquake ruptures at dilational fault jogs, *Nature*, **316**, 248–251, 1985.
- Sykes, L. R., and S. P. Nishenko, Probabilities of occurrence of large plate rupturing earthquakes for the San Andreas, San Jacinto, and Imperial faults, California, *J. Geophys. Res.*, **89**, 5905–5927, 1984.
- Thatcher, W., and T. C. Hanks, Source parameters of southern California earthquakes, *J. Geophys. Res.*, **78**, 8547–8576, 1973.
- Uhrhammer, R. A., Observations of the Coyote Lake, California, earthquake sequence of August 6, 1979, *Bull. Seismol. Soc. Am.*, **70**, 559–570, 1980.
- Vita-Finzi, C., and G. C. P. King, The seismicity, geomorphology, and structural evolution of the Corinth area of Greece, *Philos. Trans. R. Soc. London Ser. A*, **314**, 379–407, 1985.
- Wesson, R. L., R. E. Bennett, and K. L. Meagher, Catalog of earthquakes along the San Andreas fault system in central California January–March 1972, *U.S. Geol. Surv. Open File Rep.*, 60 pp., 1972a.
- Wesson, R. L., R. E. Bennett, and F. W. Lester, Catalog of earthquakes along the San Andreas fault system in central California April–June 1972, *U.S. Geol. Surv. Open File Rep.*, 42 pp., 1972b.
- Wesson, R. L., K. L. Meagher, and F. W. Lester, Catalog of earthquakes along the San Andreas fault system in central California July–September 1972, *U.S. Geol. Surv. Open File Rep.*, 49 pp., 1973.
- Wesson, R. L., F. W. Lester, and K. L. Meagher, Catalog of earthquakes along the San Andreas fault system in central California October–December 1972, *U.S. Geol. Surv. Open File Rep.*, 46 pp., 1974a.
- Wesson, R. L., F. W. Lester, and K. L. Meagher, Catalog of earthquakes along the San Andreas fault system in central California January–March 1973, *U.S. Geol. Surv. Open File Rep.*, 74-186, 47 pp., 1974b.

SMALL AND LARGE EARTHQUAKES:  
THE EFFECTS OF THE THICKNESS OF SEISMOGENIC LAYER AND THE FREE SURFACE

Kunihiro Shimazaki

Earthquake Research Institute, University of Tokyo, Bunkyo-ku, Tokyo, Japan 113

**Abstract.** An examination of a set of well-determined source parameters for Japanese intraplate earthquakes shows that small earthquakes obey a scaling law different from large earthquakes:  $Mo \propto L^3$  for small events but  $Mo \propto L^2$  for large events where  $Mo$  is seismic moment and  $L$  is rupture length. Also an offset of a factor of 1.5–2.2 in the seismic moment is found at the transition between small and large earthquakes. Since a linear dimension of earthquakes at the transition is comparable to the thickness of the seismogenic layer, the difference in scaling strongly suggests that the fault width for small earthquakes is unbounded while that for large earthquakes is bounded by the thickness of the seismogenic layer. Namely, it implies that  $u \propto L \propto W$  for small earthquakes and that  $u \propto L$  but  $W = \text{constant}$  for large earthquakes where  $u$  is slip and  $W$  is fault width. Thus we can classify earthquakes into large and small earthquakes according to whether or not an earthquake fault cuts across the entire thickness of the seismogenic layer. The offset in the seismic moment appears to be due to the difference in boundary conditions between buried and surface faults; in a certain idealized case, the amount of dislocation for surface fault is theoretically expected to be twice that of a buried fault if the stress drop is the same for both faults. The effect of the free surface has been overlooked probably because it tends to be masked by the difference in the slopes of the linear relationship between small and large earthquakes. A naive least-square fitting results in  $Mo \propto L^3$  relationship for the whole data set. The maximum likelihood estimate of the parameters and the selection of a statistical model based on the Akaike Information Criterion show that the whole data set is not satisfactorily modeled by one regression line. But it is best modeled by two regression lines, one for large event and another for small event, with the threshold moment of  $7.5 \times 10^{25}$  dyne-cm.

### Introduction

Most empirical relationships indicate that the seismic moment is proportional to a cube of the fault length [e.g., Kanamori and Anderson, 1975;

Geller, 1976]. Because the seismic moment  $Mo$  is expressed as a product of the rigidity  $\mu$ , the fault area  $S$ , and the average dislocation  $u$  [Aki, 1966]  $Mo = \mu u S$ , the empirical scaling relation suggests that both the fault width and slip are proportional to the fault length  $L$  for a rectangular fault. However, Wesnousky et al. [1983] obtained a least-square solution  $\log Mo = 1.94 \log L + 23.5$  for 18 well-studied intraplate earthquakes with seismic moment larger than  $10^{25}$  dyne-cm in Japan. This relationship suggests that the seismic moment is proportional to a square of the fault length, which is consistent with Scholz's [1982] L-model in which the slip is proportional to the fault length but the fault width is not. A simple explanation is that the width of an intraplate fault has an upper limit as the faulting is bounded within the seismogenic layer [Scholz, 1982]. In fact, most of the Japanese intraplate events take place within the upper 15 km of the crust [e.g., Oike, 1975; Takagi et al., 1977; Watanabe et al., 1978]. Only in a limited part of the Japanese islands, is found microearthquake activity as deep as 20 km. Thus we can classify Japanese intraplate earthquakes into small and large events according to whether or not an earthquake fault cuts across the entire thickness of the seismogenic layer.

If the interpretation on the scaling relation  $Mo \propto L^2$  for large earthquakes is correct, we can expect that the ordinary scaling rule  $Mo \propto L^3$  holds for smaller earthquakes. In this paper, we will examine this prediction. We will also see some complication at the transition between small and large earthquakes, which suggests an effect of the earth's free surface on seismic dislocation. We use a data set of Japanese intraplate earthquakes because the fault length of moderate-sized earthquakes have been accurately estimated on the basis of the distribution of well-located aftershocks determined by recently installed microearthquake observation networks.

### Data Set

Source parameters for several recent earthquakes are added to a data set in Table 2 of Wesnousky et al. [1982] and will be used in this

## 210 SEISMOGENIC LAYER AND THE FREE SURFACE EFFECTS

TABLE 1. Source Parameters of Japanese Intraplate Earthquakes

Name	Date	Fault Type	L, km	Mo, $10^{26}$ dyne-cm	Ref
Japan Sea	May 26, 1983	thrust	120	75	1
Niigata	Jun 16, 1964	thrust	80	32	2
Shakotan	Aug 1, 1940	thrust	100	24	3
Nobi	Oct 28, 1981	strike-slip	80	15	2
Riku-u	Aug 31, 1896	thrust	50	14	2
Tango	Mar 27, 1927	strike-slip	33	4.6	2
Oga	May 7, 1964	thrust	50	4.3	2
Tottori	Sep 10, 1943	strike-slip	33	3.6	2
Fukui	Jun 28, 1948	strike-slip	30	3.3	2
N. Izu	Nov 25, 1930	strike-slip	22	2.7	2
Izu-Oshima	Jan 14, 1978	strike-slip	17	1.1	2
Kita-Mino	Aug 19, 1961	mixed	12	0.9	2
Mikawa	Jan 13, 1945	mixed	12	0.87	2
Saitama	Sep 21, 1931	strike-slip	20	0.68	2
Izu-Oki	May 8, 1974	strike-slip	18	0.59	2
Gifu	Sep 9, 1969	strike-slip	18	0.35	2
Wakasa-Bay	Mar 26, 1963	strike-slip	20	0.33	2
W. Nagano	Sep 13, 1984	strike-slip	12	0.3	4,5
Akita	Oct 16, 1970	mixed	14	0.22	2
Shizuoka	Jul 11, 1935	strike-slip	11	0.22	2
C. Tottori	Oct 30, 1983	strike-slip	7	0.035	6,7
Kawazu	Aug 17, 1976	strike-slip	9	0.0021	2
S. Izu	Mar 21, 1934	strike-slip	7	0.0095	2
Amagi	Jul 9, 1974	strike-slip	3.5	0.0032	2
Yamasaki	May 30, 1984	strike-slip	4.5	0.0032	8

References for data: (1) Shimazaki and Mori (unpublished manuscript, 1986), (2) Wesnousky et al. [1982], (3) Satake [1986], (4) Takeo and Mikami (unpublished manuscript, 1986), (5) Mikumo et al. [1985], (6) Dziewonski et al. [1984], (7) Tsukuda et al. [1984], and (8) Tsukuda [1984].

study. Also revised parameters will be used when they are available. All the parameters used in this study are listed in Table 1. A few typographical errors in Table 2 of Wesnousky et al. [1982] are corrected.

Five among twenty-five events used in this study took place in the eastern margin of the Japan Sea and may represent interplate events between the North American and Eurasian plates as a new plate boundary is proposed in this region [e.g., Nakamura, 1983]. Thus it might be necessary to treat these events separately. However, the faults of these events appear to be mostly confined in the uppermost 15–20 km of the earth, thus no distinction is made. Well-relocated aftershocks of the Japan Sea earthquake of 1983 are bounded in a region between the earth's surface and a depth of 15–20 km [Sato et al., 1984].

All events can be classified into three groups according to their focal mechanisms, thrust, strike-slip, and mixed events. However, no significant difference is found for the following discussions, unless otherwise stated.

## Scaling Relations

The seismic moment is usually determined directly from the amplitude of seismic waves and is

the least ambiguously determined source parameter. On the other hand, the fault length is determined from the length of fault lines on the earth's surface or more often from the distribution of aftershocks and is intrinsically much less well-defined than the seismic moment. Thus we use the logarithm of the seismic moment,  $x = \log Mo$  as the independent variable and that of fault length,  $y = \log L$  as the dependent variable; we apply an ordinary linear regression analysis in which it is assumed that only the variable  $y$  contains errors. Also the variance of  $y$  is implicitly assumed to be independent of  $x$ . Because the accuracy of the fault length of small events depends mostly on the accuracy of the location of aftershocks, we only use fault parameters of events whose aftershocks are well located.

As was already mentioned, the seismic moment of the large Japanese intraplate events are roughly proportional to a square of the fault length. However, smaller events do not appear to fit to this relation. Thus the whole data set is divided into two, one with seismic moment larger than a certain threshold value and another with moment less than that. We will examine in a later section whether this segmented fit is statistically better than a single line fit.

The division of the data set into small and

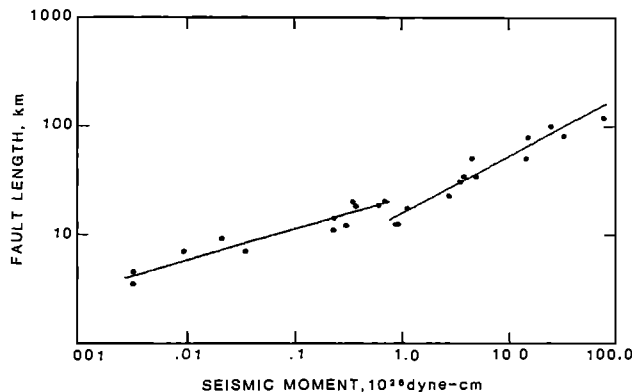


Fig. 1. A plot of logarithm of fault length against that of seismic moment. The whole dataset for Japanese intraplate earthquakes are divided into two at the seismic moment of  $7.5 \times 10^{25}$  dyne-cm and the linear regression analysis is applied to each dataset. This segmented fit is shown to be statistically better than models shown in Figure 2.

large events is arbitrarily set at  $M_o = 5, 7.5,$  and  $10.0 \times 10^{25}$  dyne-cm. The obtained least-square solutions for the first case are:

$$\log L = 0.473 \log M_o - 11.06 \quad \text{for } M_o \geq 5 \times 10^{25} \text{ dyne-cm} \quad (1)$$

and

$$\log L = 0.279 \log M_o - 5.93 \quad \text{for } M_o < 5 \times 10^{25} \text{ dyne-cm}, \quad (2)$$

where the seismic moment is in unit of dyne-cm and the fault length in km. In the second case the obtained solutions are:

$$\log L = 0.524 \log M_o - 12.44 \quad \text{for } M_o \geq 7.5 \times 10^{25} \text{ dyne-cm} \quad (3)$$

and

$$\log L = 0.281 \log M_o - 5.98 \quad \text{for } M_o < 7.5 \times 10^{25} \text{ dyne-cm}. \quad (4)$$

And in the third case, we obtain

$$\log L = 0.477 \log M_o - 11.16 \quad \text{for } M_o \geq 1.0 \times 10^{26} \text{ dyne-cm} \quad (5)$$

and

$$\log L = 0.239 \log M_o - 4.97 \quad \text{for } M_o < 1.0 \times 10^{26} \text{ dyne-cm}. \quad (6)$$

It now becomes necessary to judge which model fits to the observation better than other models. This could be easily performed by estimating the variance of the error or by calculating the sum of squared errors. However, in the next section, we

need to compare models with different numbers of parameters. Thus we introduce the Akaike Information Criterion (AIC) [Akaike, 1974] as a measure for selecting the best among the competing models under a fixed data set. This is a measure to see which model most frequently reproduces similar features to the given observations and is defined by

$$\text{AIC} = (-2)\text{Max}(\ln L) + 2(\text{number of used parameters}) \quad (7)$$

where  $L$  and  $\ln$  denote the likelihood and the natural logarithm, respectively. The model with the smaller AIC shows the better fit to the data. It should also be noted that the maximum likelihood solution is the ordinary least-square solution in the present problem. The likelihood function is shown in the appendix. The obtained AIC are as follows

$$\text{AIC} = -39.5 \quad \text{for threshold moment of } 5.0 \times 10^{25} \text{ dyne-cm},$$

$$\text{AIC} = -45.2 \quad \text{for threshold moment of } 7.5 \times 10^{25} \text{ dyne-cm},$$

and

$$\text{AIC} = -37.5 \quad \text{for threshold moment of } 1.0 \times 10^{26} \text{ dyne-cm}.$$

Thus the best-fit model is that with the threshold moment of  $7.5 \times 10^{25}$  dyne-cm and is shown in Figure 1. The 95% confidence intervals for the slopes are  $0.281 \pm 0.069$  for small events and  $0.524 \pm 0.088$  for large events. These correspond to that  $M_o \propto L^{2.9 \sim 4.7}$  for small events and that  $M_o \propto L^{1.6 \sim 2.3}$  for large events. The result indicates that the difference in scaling relations between small and large earthquakes is statistically significant and suggests that the seismic moment is proportional to a cube of the fault length for small events while for large events the moment is proportional to a square of the fault length. This is consistent with our simple prediction.

By substituting  $M_o = 7.5 \times 10^{25}$  dyne-cm, we obtain  $L = 13$  and  $20$  km, from (3) and (4), respectively. For faults with dip angles  $90^\circ$  (vertical),  $45^\circ$ , and  $30^\circ$ , the maximum widths constrained by the seismogenic layer thickness are 15, 21, and 30 km, respectively. Thus the fault length at the transition between small and large earthquakes is comparable to the maximum thickness of the fault bounded within the seismogenic layer. This suggests that the aspect ratio of the fault  $L/W$  is roughly one for small earthquakes.

Perhaps more important is that the two regression lines, one for small and another for large events, do not meet at the threshold moment. Actually, we will have a poorer fit to the data, if we constrain two lines to meet at the threshold moment. This point will be discussed in the next

## 212 SEISMOGENIC LAYER AND THE FREE SURFACE EFFECTS

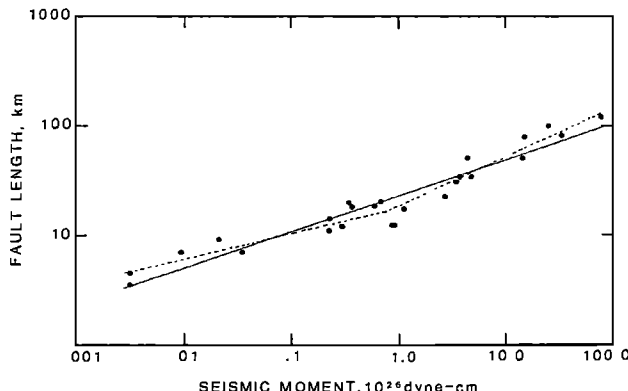


Figure 2. Two statistical models for a relation between logarithm of fault length and that of seismic moment. These models are shown to be statistically inferior to the segmented fit shown in Figure 1.

section. Thus we expect that the complication shown at the transition between small and large events should have some physical significance. We will interpret it in the following as caused by the difference of boundary conditions between buried and surface faults.

In an ideal case of infinitely long strike-slip fault, the solution to the crack problem indicates that average displacement for a surface fault is twice that of a deeply buried fault, if the two faults have the same stress drop and the same width [Knopoff, 1958]. Thus the factor of two difference in seismic moment can be expected between the surface and buried faults with the same fault size and the same stress drop. Figure 1 shows that two different moment values may be observed for earthquakes with the same fault length. If we substitute  $L = 20\text{-}25 \text{ km}$  in (3) and (4), a factor of 1.5-2.2 offset in seismic moment can be obtained between large and small events.

The ratio of seismic moment of surface to buried faults with the same stress drop and the same fault size, varies with source mechanism, the aspect ratio of the fault  $L/W$ , and the depth of the upper edge of the buried fault. It is also a function of the stress drop distribution on the fault. Boore and Dunbar [1977] carried out calculations for a case of constant stress drop over the vertical strike-slip fault. Figure 1 of their paper shows that the ratios are 1.2 and 1.7 for the aspect ratio of one and two, respectively. For a case of constant displacement over a dip slip fault with a dip angle of  $30^\circ$ , the ratios of the shallow to deep faults are shown to be 1.3 and 1.6 for the aspect ratio of 0.67 and 1.5, respectively [Sykes and Quittmeyer, 1981]. In this case, the depth of the upper edge of the shallow fault is 6.7% of the fault width and the stress drops determined at the center of dislocation are the same for the shallow and deep faults.

An effect of a low rigidity surface layer is considered by Kasahara [1964] for a case of infi-

nitely long strike-slip fault. He noted that the maximum fault displacement becomes almost doubled when the rigidity of the surface layer decreases one-ninth that of the underlying semi-infinite layer. These theoretical results suggest that the observed offset in seismic moment is mostly explained by the effect of the earth's free surface on seismic dislocation.

Thus the stress drop seems to be independent of whether a fault is buried or not, although the observed offset in seismic moment at the transition may appear to indicate a systematic difference in moment. The relationship that the seismic moment is proportional to a cube of fault length for small earthquakes also suggests that the stress drop does not vary systematically with the seismic moment. Scholz [1982] suggests that the stress drop becomes proportional to  $u/L$  instead of  $u/W$ , if the fault cuts across the entire thickness of the seismogenic layer. This is called an L-model. If this is the case, then the obtained scaling law for large earthquakes also indicates that the stress drop is constant.

However, Scholz's [1982] L-model implies some special physical boundary condition at the bottom of the seismogenic layer. Das [1982] examined an appropriate boundary condition by numerically modeling spontaneous rupture propagation [Das, 1981], but failed to produce the scaling  $u \propto L$  by realistic models of earthquake source with constant stress drop. The realistic boundary condition at the bottom of the seismogenic zone which satisfies Scholz's L-model is not yet found. According to the ordinary model in which the stress drop is proportional to  $u/W$ , the stress drop of the largest event is calculated to be about 100 times that of the smallest surface faulting.

#### Discussions

In the previous section, the segmented fit to the whole data set was shown and we gave its geophysical interpretations. However, a question arises whether or not the data set can be fitted statistically better to a single line than the double line segment. Thus a single line is fitted to all the data and is shown in Figure 2. The obtained result is  $\log L = 0.325 \log M_0 - 7.10$  and  $AIC = -28.3$ . The AIC shows that any segmented fit shown in the previous section is statistically better than this single fit. The result corresponds to a scaling rule that the seismic moment is proportional to a cube of fault length. A comparison with Figure 1 indicates that the effect of the free surface tends to be masked by the difference in the slopes of the linear relationship between  $\log L$  and  $\log M_0$ . This probably explains why the effect of the free surface has been overlooked so far.

One might further argue whether or not the offset in seismic moment suggested in the previous section is statistically significant. An alternative would be that which constrains two lines to meet at the threshold moment. The details of this

statistical model are given in the appendix. The obtained result for the threshold moment of  $7.5 \times 10^{25}$  dyne-cm is:

$$\log L = 0.444 (\log M_0 - \log (7.5 \times 10^{25})) + 1.22 \quad \text{for } M_0 \geq 7.5 \times 10^{25} \text{ dyne-cm},$$

$$\log L = 0.234 (\log M_0 - \log (7.5 \times 10^{25})) + 1.22 \quad \text{for } M_0 < 7.5 \times 10^{25} \text{ dyne-cm},$$

and

$$AIC = -34.2.$$

Again any model with an offset shown in the previous section is statistically better than this model.

According to the interpretations of the offset in seismic moment, all large earthquakes should be surface faults and all small earthquakes should be buried faults. The reason why we do not observe small surface faults is given by King [1986]. He suggests that stress relaxation occurs by chemical processes in joints and fissures near the earth's surface. Thus the stress relaxation time is long enough for the surface layer to act as a relaxation barrier preventing slip for small earthquakes from reaching the surface.

Surface breaks were observed for all large earthquakes presented in this study, except for those occurring under the ocean and the 1948 Fukui earthquake and the 1961 Kita-Mino earthquake. The Fukui earthquake is of strike-slip fault type and Kasahara [1964] explained co-seismic horizontal crustal movements by assuming a low-rigidity surface layer overlying the seismic fault. As discussed in the previous section, he showed that the low-rigidity surface layer has only a minor effect on seismic dislocation compared with the effect of the free surface. This explains why this earthquake belongs to a group of surface faults in our analysis. Also the following discussion shows the reason why the Kita-Mino earthquake belongs to a group of surface faults in our analysis. This earthquake is a thrust event with considerable amount of strike slip. Sykes and Quittmeyer [1981] showed the dip-slip component of dislocation for a shallow fault is significantly affected by the free surface as was discussed in the previous section. According to the analysis made by Kawasaki [1975], the upper edge of this earthquake fault is only 2 km deep.

No surface breakage was observed for all small earthquakes but one. The exception is the 1974 Izu-Oki earthquake. Abe [1978] estimated the amount of fault slip to be 1.2 m from the leveling data. But the maximum fault slip observed on the surface was only 50 cm [Matsuda and Yamashina, 1974]. It is most likely that the fault slip is concentrated in the deeper part of the fault. If this is the case, it contradicts the assumption of a crack model for the source for which the fault slip is a maximum at the surface and goes to zero at the lower edge of the fault.

### Conclusions

An examination of a set of well-determined source parameters for the Japanese intraplate earthquakes shows (1) the seismic moment for large earthquakes is proportional to a square of the fault length while the moment for small earthquakes is proportional to a cube of the length; (2) the fault length of earthquakes at the transition between small and large earthquakes is comparable to the thickness of the seismogenic layer; and (3) There is an offset of factor of 1.5-2.2 in the seismic moment at the transition.

Since a linear dimension of earthquakes at the transition is comparable to the thickness of the seismogenic layer, the difference in scaling strongly suggests that the fault width for small earthquakes is unbounded while that for large earthquakes is bounded by the thickness of the seismogenic layer. Namely, it implies that  $u \ll W$  for small earthquakes and that  $u \ll L$  but  $W = \text{constant}$  for large earthquakes where  $u$  is slip and  $W$  is fault width. Thus we can classify earthquakes into large and small earthquakes according to whether or not an earthquake fault cuts across the entire thickness of the seismogenic layer. The offset in the seismic moment appears to be due to the difference in boundary conditions between buried and surface faults; in a certain idealized case, the amount of dislocation for surface fault is theoretically expected to be twice that of a buried fault with the same linear dimension if the stress drop is the same for both faults. If a special boundary condition at the bottom of the seismogenic layer exists as was suggested by Scholz [1982], these observations suggest that a stress drop is independent of seismic moment for the Japanese intraplate earthquakes with seismic moment ranging from  $5 \times 10^{23}$  to  $10^{28}$  dyne-cm.

The effect of the free surface has been overlooked probably because it tends to be masked by the difference in the slopes of the linear relationship between small and large earthquakes. A naive least-square fitting results in  $M_0 \propto L^3$  relationship for the whole data set. The maximum likelihood estimate of the parameters and the selection of a statistical model based on the Akaike Information Criterion show that the whole data set is not satisfactorily modeled by one regression line. But it is best modeled by two regression lines, one for large event and another for small event, with the threshold moment of  $7.5 \times 10^{25}$  dyne-cm.

### Appendix

#### A Single Line Fit

In an ordinary regression analysis, we assume that

$$y_i = a + b x_i + r_i \quad (i = 1, 2, \dots, n)$$

where  $y_i$  and  $x_i$  are observed data for the depend-

## 214 SEISMOGENIC LAYER AND THE FREE SURFACE EFFECTS

ent and independent variables, respectively,  $a$  a constant,  $b$  the regression coefficient which gives the slope,  $r_i$  normally distributed random errors with its mean 0 and variance  $v$ , and  $n$  the number of data points. The likelihood function is given by

$$\begin{aligned} L(y_1, \dots, y_n | a, b, v) \\ = \frac{1}{n! \sqrt{2\pi v}} \exp[-\frac{1}{2v} (y_i - a - bx_i)^2] \\ = (2\pi v)^{-n/2} \exp[-\frac{1}{2v} \sum_{i=1}^n e_i^2] \end{aligned}$$

where

$$e_i = y_i - a - b x_i.$$

Then we get

$$l = \ln L = -\frac{n}{2} \ln(2\pi v) - \frac{1}{2v} \sum_{i=1}^n e_i^2$$

The maximum likelihood solutions for  $a$ ,  $b$ , and  $v$  are given by

$$\begin{aligned} a &= \frac{\sum_{i=1}^n x_i^2 \sum_{i=1}^n y_i - \sum_{i=1}^n x_i \sum_{i=1}^n x_i y_i}{\sum_{i=1}^n x_i^2 - (\sum_{i=1}^n x_i)^2} \\ b &= \frac{\sum_{i=1}^n x_i y_i - \sum_{i=1}^n x_i \sum_{i=1}^n y_i}{\sum_{i=1}^n x_i^2 - (\sum_{i=1}^n x_i)^2} \\ v &= (\sum_{i=1}^n y_i^2 - a \sum_{i=1}^n y_i - b \sum_{i=1}^n x_i y_i) / n \end{aligned}$$

Since  $\max(l)$  is given by  $-n \ln(2\pi v) / 2 - n / 2$ , we get

$$AIC = n \ln(2\pi v) + n + 6.$$

Double-Line-Segment Fit

We divide the whole data set at  $x_0$  and assume that

$$y_i = a_1 + b_1 x_i + r_i \quad \text{for } x_i \geq x_0 \quad (i = 1, \dots, m)$$

and

$$y_i = a_2 + b_2 x_i + r_i \quad \text{for } x_i < x_0 \quad (i = m+1, \dots, n)$$

where  $a_1$  and  $a_2$  are constants and  $b_1$  and  $b_2$  the regression coefficients which give the slopes. The likelihood function is given by

$$\begin{aligned} L(y_1, \dots, y_n | a_1, b_1, a_2, b_2, v) \\ = (2\pi v)^{-n/2} \exp[-\frac{1}{2v} \sum_{i=1}^m e_{1i}^2] \exp[-\frac{1}{2v} \sum_{i=m+1}^n e_{2i}^2] \end{aligned}$$

where

$$e_{1i} = y_i - a_1 - b_1 x_i \quad \text{for } x_i \geq x_0$$

$$e_{2i} = y_i - a_2 - b_2 x_i \quad \text{for } x_i < x_0.$$

Then we get

$$\begin{aligned} \ln L \\ = -n \ln(2\pi v) / 2 - \frac{\sum_{i=1}^m e_{1i}^2}{2v} - \frac{\sum_{i=m+1}^n e_{2i}^2}{2v} \end{aligned}$$

The maximum likelihood solutions for  $a_1$ ,  $b_1$ ,  $a_2$ ,  $b_2$ , and  $v$  are given by

$$a_1 = \frac{\sum_{i=1}^m x_i^2 \sum_{i=1}^m y_i - \sum_{i=1}^m x_i \sum_{i=1}^m x_i y_i}{\sum_{i=1}^m x_i^2 - (\sum_{i=1}^m x_i)^2}$$

$$b_1 = \frac{\sum_{i=1}^m x_i y_i - \sum_{i=1}^m x_i \sum_{i=1}^m y_i}{\sum_{i=1}^m x_i^2 - (\sum_{i=1}^m x_i)^2}$$

$$a_2 = \frac{\sum_{i=m+1}^n x_i^2 \sum_{i=m+1}^n y_i - \sum_{i=m+1}^n x_i \sum_{i=m+1}^n x_i y_i}{\sum_{i=m+1}^n x_i^2 - (\sum_{i=m+1}^n x_i)^2}$$

$$b_2 = \frac{\sum_{i=m+1}^n x_i y_i - \sum_{i=m+1}^n x_i \sum_{i=m+1}^n y_i}{\sum_{i=m+1}^n x_i^2 - (\sum_{i=m+1}^n x_i)^2}$$

$$v = (\sum_{i=1}^n y_i^2 - a_1 \sum_{i=1}^m y_i - b_1 \sum_{i=1}^m x_i y_i - a_2 \sum_{i=m+1}^n y_i - b_2 \sum_{i=m+1}^n x_i y_i) / n.$$

Since  $\max(l)$  is given by  $-n \ln(2\pi v) / 2 - n / 2$ , we get

$$AIC = n \ln(2\pi v) + n + 10.$$

Fit to Two Lines Meeting at  $x = x_0$ 

We divide the whole data set at  $x_0$  and assume that

$$y_i = y_0 + b_1 (x_i - x_0) + r_i \quad \text{for } x_i \geq x_0 \quad (i = 1, \dots, m)$$

and

$$y_i = y_0 + b_2 (x_i - x_0) + r_i \quad \text{for } x_i < x_0 \quad (i = m+1, \dots, n)$$

where  $y_0$  is a constant. The likelihood function is given by

$$\begin{aligned} L(y_1, \dots, y_n | y_0, b_1, b_2, v) \\ = (2\pi v)^{-n/2} \exp \left[ -\frac{1}{2v} \sum_{i=1}^m e_{1i}^2 \right] \exp \left[ -\frac{1}{2v} \sum_{i=m+1}^n e_{2i}^2 \right] \end{aligned}$$

where

$$e_{1i} = y_i - y_0 - b_1 (x_i - x_0) \quad \text{for } x_i \geq x_0$$

$$e_{2i} = y_i - y_0 - b_2 (x_i - x_0) \quad \text{for } x_i < x_0.$$

Then we get

$$\ln L$$

$$= -n \ln(2\pi v) / 2 - \sum_{i=1}^m e_{1i}^2 / 2v - \sum_{i=m+1}^n e_{2i}^2 / 2v$$

The maximum likelihood solutions for  $y_0$ ,  $b_1$ ,  $b_2$ , and  $v$  are given by

$$y_0 = \frac{c \sum_{i=1}^m u_i y_i + d \sum_{i=m+1}^n u_i y_i}{c \sum_{i=1}^m u_i^2 + d \sum_{i=m+1}^n u_i^2} - \frac{\sum_{i=1}^m y_i}{\sum_{i=1}^m u_i}$$

$$b_1 = c \left( \sum_{i=1}^m u_i y_i - y_0 \sum_{i=1}^m u_i \right)$$

$$b_2 = d \left( \sum_{i=m+1}^n u_i y_i - y_0 \sum_{i=m+1}^n u_i \right)$$

$$v = \left( \sum_{i=1}^m y_i^2 - y_0^2 \sum_{i=1}^m u_i^2 - b_1^2 \sum_{i=1}^m u_i y_i \right)$$

$$- b_2^2 \sum_{i=m+1}^n u_i y_i \right) / n$$

where

$$u_i = x_i - x_0$$

$$c = 1 / \sum_{i=1}^m u_i^2, \quad d = 1 / \sum_{i=m+1}^n u_i^2.$$

## References

- Abe, K., Dislocations, source dimensions and stresses associated with earthquakes in the Izu peninsula, Japan, *J. Phys. Earth*, **26**, 253-274, 1978.
- Akaike, H., A new look at the statistical model identification, *IEEE Trans. Autom. Control*, **AC-19**, 716-723, 1974.
- Aki, K., Generation and propagation of G waves from the Niigata earthquake of June 16, 1964, Part 2, *Bull. Earthquake Res. Inst. Univ. Tokyo*, **44**, 73-88, 1966.
- Boore, D. M., and W. S. Dunbar, Effect of the free surface on calculated stress drops, *Bull. Seismol. Soc. Am.*, **67**, 1661-1664, 1977.
- Das, S., Three-dimensional spontaneous rupture propagation and implications for the earthquake source mechanism, *Geophys. J.*, **67**, 375-393, 1981.
- Das, S., Appropriate boundary conditions for modeling very long earthquakes and physical consequences, *Bull. Seismol. Soc. Am.*, **72**, 1911-1926, 1982.
- Dziewonski, A. M., J. E. Franzen, and J. H. Woodhouse, Centroid-moment tensor solutions for July-September, 1983, *Phys. Earth Planet. Inter.*, **34**, 1-8, 1984.
- Geller, R. J., Scaling relations for earthquake source parameters and magnitudes, *Bull. Seismol. Soc. Am.*, **66**, 1501-1523, 1976.
- Kanamori, H., and D. L. Anderson, Theoretical basis of some empirical relations in seismology, *Bull. Seismol. Soc. Am.*, **65**, 1073-1095, 1975.
- Kasahara, K., A strike-slip fault buried in a layered medium, *Bull. Earthquake Res. Inst. Univ. Tokyo*, **42**, 609-619, 1964.
- Kawasaki, I., The focal process of the Kita-Mino earthquake of August 19, 1961, and its relationship to a Quaternary fault, the Hatogayu-Koike fault, *J. Phys. Earth*, **23**, 227-250, 1975.
- King, G. C. P., The geometry of the initiation and termination of earthquake rupture and the evolution of morphology and geological structures, *Geophys. Monograph*, this volume, 1986.
- Knopoff, L., Energy release in earthquakes, *Geophys. J.*, **1**, 44-52, 1958.
- Matsuda, T., and K. Yamashina, Surface faults associated with the Izu-Hanto-Oki earthquake of 1974, Japan (in Japanese), *Spec. Bull. Earthquake Res. Inst. Univ. Tokyo*, **14**, 135-158, 1974.
- Mikumo, T., H. Wada, S. Kaneshima, K. Imagawa, and M. Koizumi, Seismic activity in the northern Hida region before and after the 1984 Western Nagano Prefecture earthquake, and the faulting mechanism of the main shock event (in Japanese), in *Report on the 1984 Western Nagano Prefecture Earthquake and Its Damage*, Edited by K. Iida, pp.21-33, Aichi Institute of Technology, Toyoda, Japan, 1985.

## 216 SEISMOGENIC LAYER AND THE FREE SURFACE EFFECTS

- Nakamura, K., Possible nascent trench along the eastern Japan Sea as the convergent boundary between Eurasian and North American plates (in Japanese with English abstract), *Bull. Earthquake Res. Inst. Univ. Tokyo*, 58, 711-722, 1983.
- Oike, K., On a list of hypocenters compiled by the Tottori Microearthquake Observatory (in Japanese with English abstract), *J. Seismol. Soc. Jpn., Ser. 2*, 28, 331-346, 1975.
- Satake, K., Re-examination of the 1940 Shakotan-Oki earthquake and the fault parameters for the earthquakes along the eastern margin of the Japan Sea, *Phys. Earth Planet. Inter.*, in press, 1986.
- Sato, T., M. Kosuge, T. Tanaka, and H. Sato, Aftershock distribution of the Nihonkai-Chubu earthquake -- Relocation with a dipping layer model (in Japanese), *Res. Rept. Natural Disasters in the Tohoku district*, 20, 1-6, 1984.
- Scholz, C. H., Scaling laws for large earthquakes: consequences for physical models, *Bull. Seismol. Soc. Am.*, 72, 1-14, 1982.
- Sykes, L. R., and R. C. Quittmeyer, Repeat times of great earthquakes along simple plate boundaries, in *Earthquake Prediction: International Review*, Maurice Ewing Ser., 4, 217-247, AGU, Washington, D.C., 1981.
- Takagi, A., A. Hasegawa, and N. Umino, Seismic activity in the northeastern Japan arc, *J. Phys. Earth*, 25, S95-S104, 1977.
- Tsukuda, T., The Yamasaki earthquake (M5.6) of May 30, 1984: Change in seismic activity, aftershock distribution, and focal process (in Japanese), *Programme and Abstracts, Seismol. Soc. Jpn.*, 1984, No. 2, 5, 1984.
- Tsukuda, T., S. Nakao, and R. Nishida, Spatial distribution of aftershocks associated with the Tottori earthquake (M6.2) of October 31, 1983 (in Japanese), *Programme and Abstracts, Seismol. Soc. Jpn.*, 1984, No. 1, 107, 1984.
- Watanabe, K., N. Hirano, and Y. Kishimoto, Seismicity in the Hokuriku district (in Japanese with English abstract), *J. Seismol. Soc. Jpn.*, 31, 35-47, 1978.
- Wesnousky, S. G., C. H. Scholz, and K. Shimazaki, Deformation of an island arc: rate of moment-release and crustal shortening in intraplate Japan determined from seismicity and Quaternary fault data, *J. Geophys. Res.*, 87, 6829-6852, 1982.
- Wesnousky, S. G., C. H. Scholz, K. Shimazaki, and T. Matsuda, Earthquake frequency distribution and the mechanics of faulting, *J. Geophys. Res.*, 88, 9331-9340, 1983.

## SOME OBSERVATIONS INDICATING COMPLICATIONS IN THE NATURE OF EARTHQUAKE SCALING

A. McGarr

U. S. Geological Survey, Menlo Park, California 94025

**Abstract.** From basic scaling principles, in conjunction with the general observation that earthquake stress drops do not show any systematic dependence on seismic moment  $M_o$ , it is straightforward to determine the moment-dependence of the various ground motion parameters. For peak acceleration,  $a$ , the parameter  $\rho R a$ , where  $\rho$  is density and  $R$  is hypocentral distance, should be independent of  $M_o$  and the peak velocity parameter  $Rv$  is expected to scale according to  $M_o^{1/3}$  assuming that the effects of attenuation and band limitation are negligible. In a recently published study in which the near-source ground motion from earthquakes recorded in many diverse tectonic situations was analyzed, it was found that the larger events in a particular sequence showed the expected scaling and, more interestingly, the ground motion parameters were found to be functions of both focal depth and the state of stress. In contrast, however, analyses of earthquakes within individual sequences, for which a broad range of  $M_o$  is represented, have revealed a marked transition in scaling from the smaller to the larger events. The ground motion scaling for a particular sequence can be characterized by  $Rv = A M_o^\gamma$ , where  $A$  is a constant and for  $M_o < M_o$  (transition)  $\gamma$  is within the range 0.6 to 0.8. For  $M_o \geq M_o$  (transition)  $\gamma \approx 1/3$ , as expected from the scaling considerations mentioned above. The change in scaling is observed to be very abrupt at  $M_o$  (transition), which varies from sequence to sequence. Of the six earthquake sequences investigated to date, 1971 San Fernando, 1982 Miramichi, New Brunswick, South African mine tremors, 1980 Mammoth Lakes, 1975 Oroville and 1983 Coalinga, the last two provided the most definitive data regarding the nature of the scaling. At Oroville, events in the  $M_o$  range from  $10^{10}$  to  $3 \times 10^{14}$  N-m scale according to  $Rv \propto M_o^{0.77}$  whereas for  $M_o > 3 \times 10^{14}$  N-m,  $Rv \propto M_o^{1/3}$ . For the Coalinga events  $Rv \propto M_o^{0.73}$  for  $M_o < 10^{17}$  N-m, above which  $M_o^{1/3}$  scaling applies; thus, at Coalinga the transition moment is substantially greater than at Oroville. The Coalinga earthquakes also exhibit unusual scaling for the peak acceleration parameter  $\rho R a$ , the stress drop  $\Delta\tau$  and the source radius  $r_s$  for  $M_o < 10^{17}$  N-m; specifically,

$\rho R a \propto M_o^{0.67}$ ,  $\Delta\tau \propto M_o^{0.60}$  and  $r_s \propto M_o^{0.13}$ . For several reasons it seems more likely that source processes rather than either anelastic attenuation or band-limited recording play the major role in the scaling transitions described here. First, the source parameters  $\Delta\tau$  and  $r_s$  show scaling that is entirely consistent with that of the ground motion parameters. Second, ground motion parameters for  $P$ -waves scale identically to their  $S$ -wave counterparts.

## Introduction

From basic scaling principles a solution to the elastodynamic problem with small displacements can be transformed into another solution using four independent scaling factors for length, displacement amplitude, elastic modulus and density [e.g., Dieterich, 1973; Andrews, 1975]. Within a seismogenic zone neither the elastic modulus nor the density varies substantially and so for purposes of relating earthquakes of different sizes there are only two scaling factors to consider.

The observation, first noted by Hanks [1977] and later extended by McGarr et al. [1981], that the seismic stress drop  $\Delta\tau$  does not depend systematically on seismic moment  $M_o$  serves to eliminate one of the remaining two scaling factors because stress drop is proportional to the ratio of displacement amplitude to source dimension. In each of these studies the stress drop data were for earthquakes representing a great many earthquake sequences that occurred in a variety of tectonic circumstances. Essentially, the vast majority of stress drops were found to be within the range of 0.1 to 10 MPa over a range of seismic moment extending from about  $10^9$  to  $10^{19}$  N-m. Thus, the idea that stress drops for earthquakes in general do not depend on moment seems persuasive and, if so, then a single parameter, such as seismic moment or source dimension, can be used to scale results from earthquakes of one size to those of another at least to the extent that effects of attenuation and band limitation can be neglected.

In a similar spirit McGarr [1984] analyzed ground motion parameters for 66 earthquakes that occurred in a multitude of tectonic environments and found that the single-

## 218 COMPLICATIONS IN EARTHQUAKE SCALING

parameter scaling was reasonably viable. Moreover, it was found that the ground motion parameters were strongly dependent on both focal depth and the state of stress. The most essential observations presented by McGarr [1984] are represented by the regression fits for peak acceleration  $\underline{a}$

$$\rho R \underline{a} (\text{ext.}) = -1.08 \text{ MPa} + 3.06 \text{ (MPa/km)}z \quad (1a)$$

$$\rho R \underline{a} (\text{comp.}) = 5.65 \text{ MPa} + 8.76 \text{ (MPa/km)}z \quad (1b)$$

and for peak velocity  $\underline{v}$

$$\begin{aligned} R \underline{v} / M_o^{1/3} (\text{ext.}) &= 10^{-4} \text{ (m}^2/\text{s)(N}\cdot\text{m)}^{-1/3} \cdot \\ &\quad [3.00 + 0.69 \text{ (km}^{-1}\text{)}z] \end{aligned} \quad (2a)$$

$$\begin{aligned} R \underline{v} / M_o^{1/3} (\text{comp.}) &= 10^{-4} \text{ (m}^2/\text{s)(N}\cdot\text{m)}^{-1/3} \cdot \\ &\quad [4.63 + 1.82 \text{ (km}^{-1}\text{)}z] \end{aligned} \quad (2b)$$

where  $R$  is the hypocentral distance,  $\rho$  is density, and  $z$  is focal depth. The peak ground motion values used here are the total vector motion as would be recorded in a whole space. "Compressional" and "extensional" refer to states of stress giving rise to thrust and normal faulting, respectively. In the work leading to equations (1) and (2) as well as in the analysis discussed here care has been taken to measure the peak motion of corresponding pulses from component to component and from site to site so as to maximize the ground motion parameter  $R \underline{v}$ . Thus, on a particular component, the measurement used here may not be the actual peak value of that trace. Moreover, only pulses associated with far-field body waves, usually  $S$ , as measured at epicentral distances comparable to, or less than, the focal depth have been analyzed.

Equations (1) and (2), which are consistent with constant-stress-drop, or single parameter, scaling serve as the point of departure for the present study, which, in contrast to the previous work, investigates the nature of scaling within a particular earthquake sequence rather than for earthquakes in general.

The analysis reported here is an outgrowth of an investigation of ground motion and source parameters of the 1983 Coalinga, California earthquakes [McGarr et al., 1985; Andrews et al., 1984]. Because the scaling determined for those events was both well-defined and unanticipated it was necessary to perform similar analyses for other earthquake sequences to find out what, if anything, was unique to the Coalinga data. Accordingly, this paper reports the scaling results for six earthquake sequences including the Coalinga shocks. It turns out that earthquakes within individual sequences display scaling complexities that were not apparent in the previous studies involving many earthquake sequences considered together. Moreover, it seems that the scaling found for the Coalinga sequence is typical of that found for other sequences, even for those occurring in completely different tectonic circumstances.

Although many studies have emphasized seismic stress drop in attempting to characterize the nature of earthquake scaling [e.g., Archuleta et al., 1982; Fletcher et al., 1984; Haar et al., 1984; Chouet et al., 1978] the vehicle for describing scaling here is the peak velocity parameter  $R \underline{v}$  for a number of reasons. The peak velocity is a very straightforward, largely uncontested measurement in contrast to the stress drop [Brune, 1970] which normally entails the analyses of spectral shapes or pulse widths with the attendant possibilities of subjectivity influencing the results [e.g., Brune et al., 1979]; in addition, the physical significance of the stress drop is dubious inasmuch as estimates of  $r_o$ , from which stress drop is estimated using  $\Delta\tau = 7/16 M_o/r_o^3$  [Brune, 1970] are quite model-dependent [e.g., Savage, 1972]. Furthermore, whereas peak velocity data have a direct relevance to earthquake hazards assessment, the connection between stress drop and seismic hazard is controversial at best [e.g., McGarr, 1981, 1984]; thus, any insight gained with regard to the scaling of peak velocity has immediate practical applicability.

For the constant-stress-drop scaling implicit in equations (1) and (2) the peak acceleration parameter is expected to be independent of earthquake size and the peak velocity parameter scales as  $M_o^{1/3}$ . Departures from such scaling have generally been attributed to the effects of bandwidth limitations [e.g., Boore, 1983] and anelastic attenuation, characterized as  $f_{\max}$ , for example, by Hanks [1982]. For the Coalinga events, however, McGarr et al. [1985] were able to discount effects exterior to the source region that might have caused the observed departures from the expected scaling.

There are a number of issues of current interest associated with the topic of ground motion scaling addressed here. For instance, it has been suggested by Nuttli [1983] that earthquakes in eastern North America scale differently from those in the west. Such an effect is important to the assessment of earthquake hazards in the east but this interpretation of the data is not universally accepted [e.g., Kanamori and Anderson, 1975; Atkinson, 1984]. A more fundamental question involves the viability of the notion of self-similarity of crustal earthquakes whose rupture dimensions do not exceed the thickness of the seismogenic zone, approximately 10 to 20 km. If the source processes of small earthquakes scale differently from those of larger events, contained within the seismogenic zone, then clearly theoretical analyses that assume similarity principles [e.g., Boore, 1983; Joyner, 1984] would have to be reassessed.

### Scaling Analysis

The six earthquake sequences analyzed here are evenly distributed between compressional and extensional tectonic environments and represent a broad spectrum of regional strain rates. Thus, whatever scaling features are found to

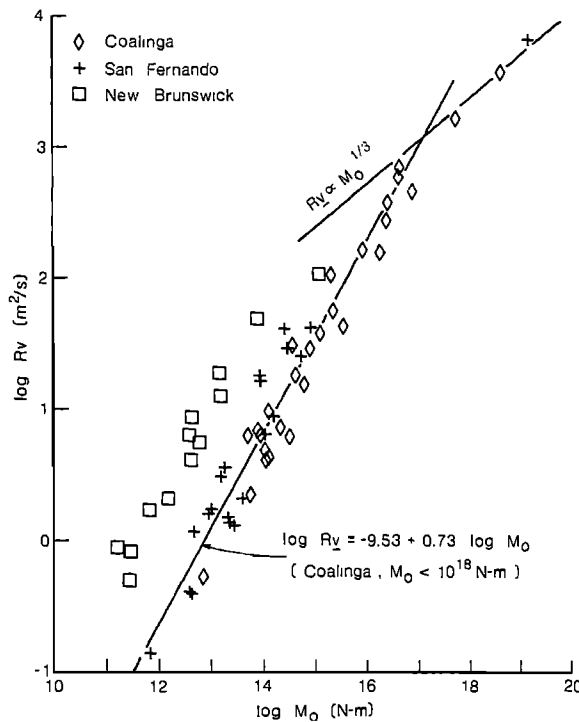


Fig. 1. Peak-velocity parameter as a function of seismic moment for three sequences in compressional tectonic settings.

be common to all of these sequences are unlikely to have any geographical specificity.

The scaling of the ground motion parameter  $R_v$  with the seismic source parameters is straightforward because most, if not all, seismic source models yield

$$R_v \propto \Delta\tau \tau_o \quad (3)$$

where  $\tau_o$  is the source radius. For example, McGarr et al. [1981] showed that the peak velocity implied by the Brune [1970] source model is  $R_v = 0.57 \beta \Delta\tau \tau_o / \mu$ , where  $\beta$  is the shear wave velocity and  $\mu$  is the modulus of rigidity. Because  $\Delta\tau$  and  $\tau_o$  are related according to [Brune, 1970]

$$\Delta\tau = (7/16) M_o / \tau_o^3 \quad (4)$$

the scaling of  $R_v$  is related uniquely to that of  $\Delta\tau$ . Specifically, if

$$R_v \propto M_o^\gamma \quad (5a)$$

then from (3) and (4)

$$\Delta\tau \propto M_o^{(3\gamma-1)/2} \quad (5b)$$

Constant stress-drop scaling, of course, corresponds to  $\gamma = 1/3$ .

As seen in Figures 1 and 2, which present the essential observations analyzed here,  $R_v$  for all six sequences departs markedly from the  $M_o^{1/3}$  scaling. Although the largest events within a particular sequence seem to scale according to  $R_v \propto M_o^{1/3}$  the vast majority of peak velocity data appear to be much more consistent with  $R_v \propto M_o^{0.70}$ ; that is, the moment-dependence is more than twice as strong as expected. In the case of the 1975 Oroville, California, sequence (Figure 2), for example, for  $M_o > 10^{15}$  N-m,  $R_v \propto M_o^{1/3}$  [McGarr, 1984] but the smaller events generated peak velocities consistent with  $R_v \propto M_o^{0.77}$ . The regression line was fit to digitally recorded data presented in Fletcher [1980] for which  $M_o < 10^{13}$  N-m but this same line is quite compatible with the smallest events with  $10^{14} < M_o < 3 \times 10^{14}$  N-m, recorded using SMA-1 accelerographs [Fletcher et al., 1984; A. G. Brady, unpublished data, 1984]. Thus, for the Oroville events a transition in scaling seems to occur at approximately  $M_o \approx 3 \times 10^{14}$  N-m; this transition, moreover, appears to be abrupt.

Generally, the  $R_v$  scaling seen in Figures 1 and 2 looks much the same for all six sequences except that the tran-

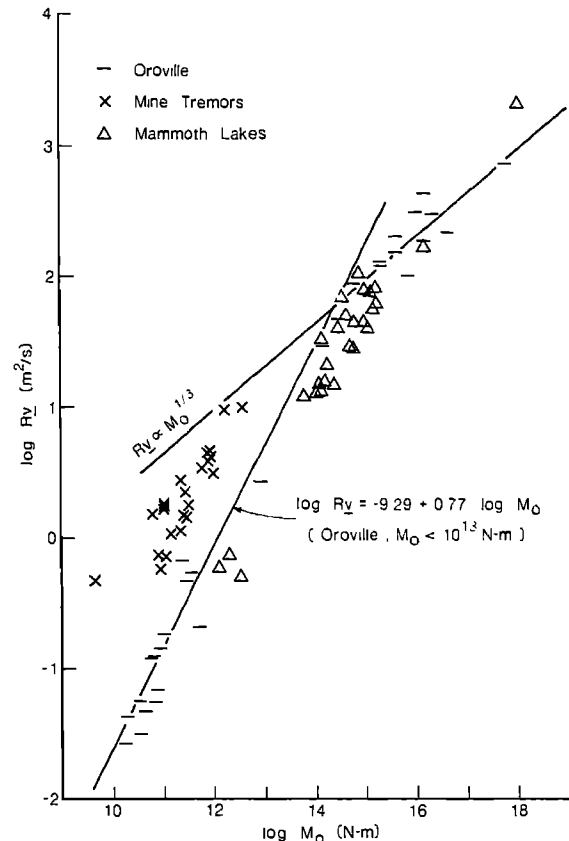


Fig. 2. Peak-velocity parameter as a function of seismic moment for three sequences in extensional tectonic settings.

## 220 COMPLICATIONS IN EARTHQUAKE SCALING

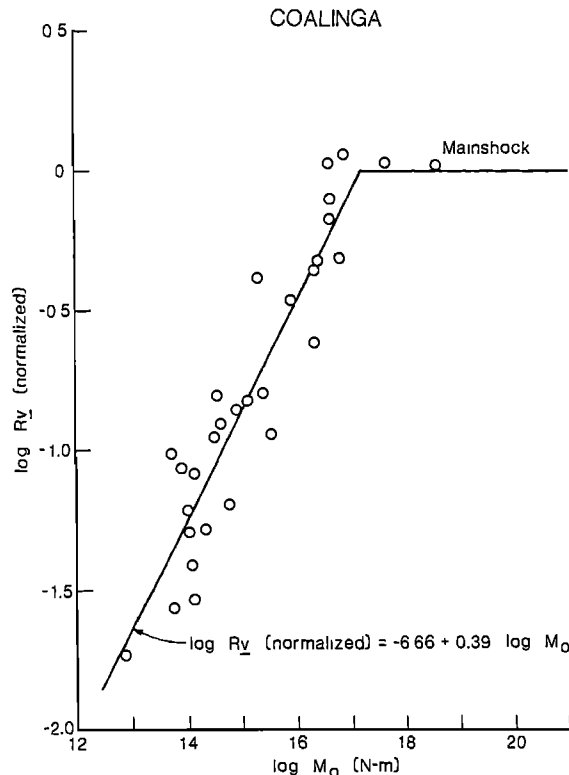


Fig. 3. Peak-velocity parameter, normalized using equation (3), as a function of seismic moment for Coalinga sequence.

sition point varies considerably as well as absolute levels. The Miramichi, New Brunswick data, for example, show much higher values of  $R_v$  at fixed  $M_o$  than for Coalinga. For Coalinga the transition in scaling seems to be near  $M_o = 10^{17}$  N-m [McGarr et al., 1985] whereas, as noted before, the corresponding transition in the Oroville sequence is close to  $3 \times 10^{14}$  N-m.

This overview of the data plotted in Figures 1 and 2 thus suggests that constant-stress-drop scaling may not be appropriate for describing the scaling within individual sequences. The possibility exists, however, that these departures from the expected scaling are simply consequences of other effects not taken into account as yet [e.g., Boore, 1985]. Such effects include anelastic attenuation [e.g., Hanks, 1982], band-limited data [e.g., Boore, 1983] and focal depth [McGarr, 1984]. These possibilities are dealt with, at least to some extent, in the following discussion which deals more specifically with each sequence.

**Coalinga.** For the Coalinga data, as well as those for the other five sequences considered here, equations (2) have been used in an attempt, not necessarily appropriate, to account for the effects of focal depth and the expected cube root scaling with seismic moment in the analysis of peak velocity. Because the Coalinga events were in a compres-

sional tectonic environment peak velocity values have been normalized using equation (2b). Specifically,

$$R_v \text{ (normalized)} = \frac{10^4 (N\cdot m)^{-1/3} R_v}{M_o^{1/3} [4.63 + 1.82 (km^{-1}) s]} \quad (6)$$

The Coalinga data, normalized from information presented in Table 1 of McGarr et al. [1985], are shown in Figure 3, where we see that this normalization procedure is, at least, effective for purposes of highlighting the transition in scaling. The intersection of the regression line, fit to all of the data except for the mainshock, intersects the horizontal line corresponding to the previously expected value of  $R_v$  [McGarr, 1984; equation (2b)] at  $M_o = 1.2 \times 10^{17}$  N-m, confirming more precisely the scaling transition inferred from the Coalinga data in Figure 1. Thus, after taking focal depth into account the peak velocity parameter shows a total moment dependence of  $R_v \propto M_o^{0.72}$ , in good agreement with the previously inferred moment dependence seen in Figure 1. Note also the sharpness of the transition; the data do not suggest any diminution in slope as the transition point is approached from below.

As was discussed in McGarr et al. [1985], the peak accelerations of the Coalinga events also showed a well-defined and unexpected moment dependence; specifically

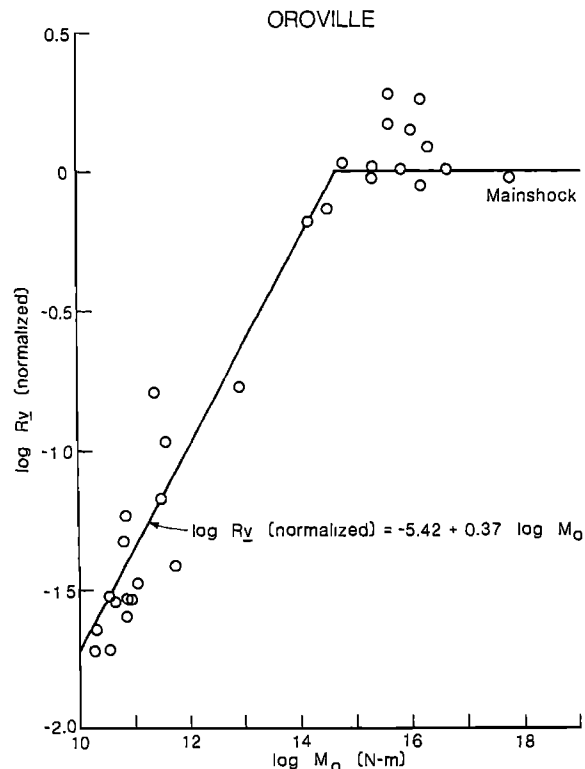


Fig. 4. Peak-velocity parameter, normalized using equation (4), as a function of seismic moment for Oroville sequence.

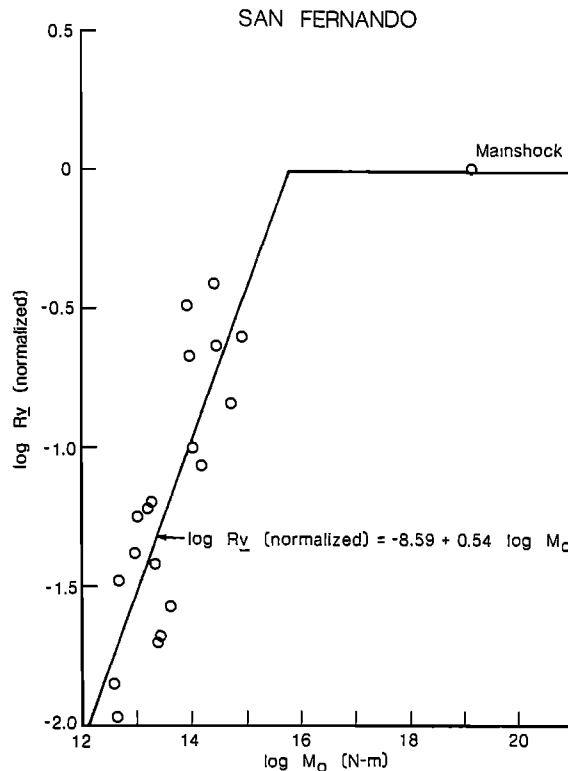


Fig. 5. Peak-velocity parameter, normalized using equation (3), as a function of seismic moment, for San Fernando sequence.

$\rho R_d \propto M_o^{0.67}$  with a similarly located transition to no moment dependence as seen for  $R_d$  in Figure 3. Perhaps most interestingly, the stress drops, estimated using the Brune [1970] methodology, fit tightly about a regression line corresponding to  $\Delta\tau \propto M_o^{0.60}$ , exactly as predicted from equations (5).

With regard to the possibility that anelastic attenuation or band-limited recording might be responsible for the unexpected scaling, exemplified in Figure 3, the two most direct arguments, proffered by McGarr et al. [1985], discounting such effects are: (1) The stress drop shows scaling that is consistent with that of the ground motion parameters and yet the corner frequencies were observed to be well-separated from estimates of  $f_{max}$  in the spectra of ground displacement. (2) Ground motion parameters for  $P$  waves  $\rho R_d(P)$  and  $R_d(P)$  showed scaling identical to their  $S$  wave counterparts, an unexpected result if anelastic attenuation is a controlling factor.

Oroville. Of the sequences investigated here, the data for the Oroville events are the most comprehensive from the viewpoint of representation both above and below the transition in scaling (Figure 4). Because these earthquakes occurred in an extensional tectonic environment, equation (2a) was used to normalize the peak velocities yielding

$$R_d (\text{normalized}) = \frac{10^4 (N\cdot m)^{-1/3} R_d}{M_o^{1/3} [s.00+0.69(km^{-1})_z]} \quad (7)$$

The regression line (Figure 4), which was fit to the events for which  $M_o < 10^{13}$  [Fletcher, 1980], has nearly the same slope as that of the Coalinga sequence (Figure 3) but the transition moment of  $4.5 \times 10^{14}$  N-m is more than two orders of magnitude less than that of the Coalinga data.

The question of whether or not anelastic attenuation played a substantial role in suppressing peak values of ground velocity for the smaller events has already been addressed by Fletcher [1980], who chose recording sites on outcropping bedrock at small epicentral distances. For these data  $f_{max}$  is in excess of 40 Hz for  $S$  waves.

San Fernando. In contrast to the events at Coalinga and Oroville, the 1971 San Fernando mainshock did not generate an aftershock sequence that was rich in large earthquakes. Accordingly the mainshock [McGarr, 1984] provided the only data (Figure 5) above the transition point at  $M_o = 8.1 \times 10^{15}$  N-m. The tectonic setting is similar to that at Coalinga in having a compressional stress state and being situated in the environs of the San Andreas fault. Hence equation (6) was used to normalize the peak velocities. The resulting transition moment is about an order of magnitude less than inferred for Coalinga largely because the small  $M_o$  data, from Tucker [1975], define a stronger moment dependence of 0.54, as compared to 0.39 for Coalinga (Figure 3). Because the seismometers for the

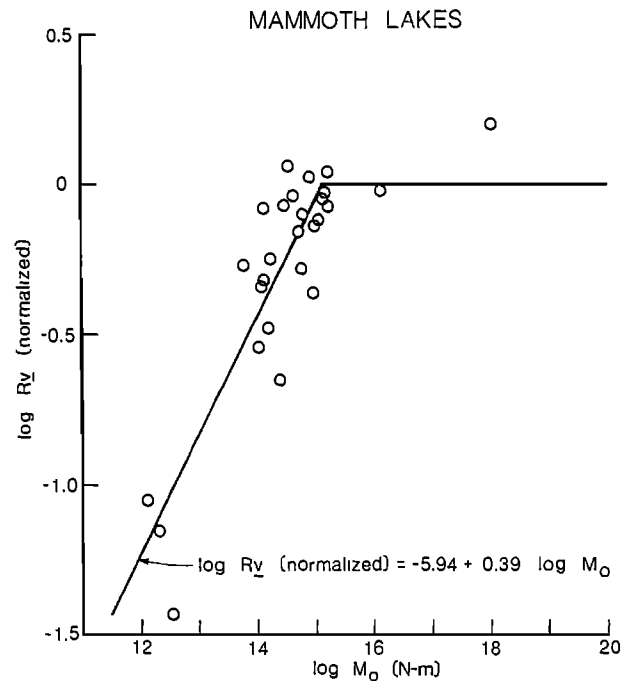


Fig. 6. Peak-velocity parameter, normalized using equation (4), as a function of seismic moment for Mammoth Lakes events.

## 222 COMPLICATIONS IN EARTHQUAKE SCALING

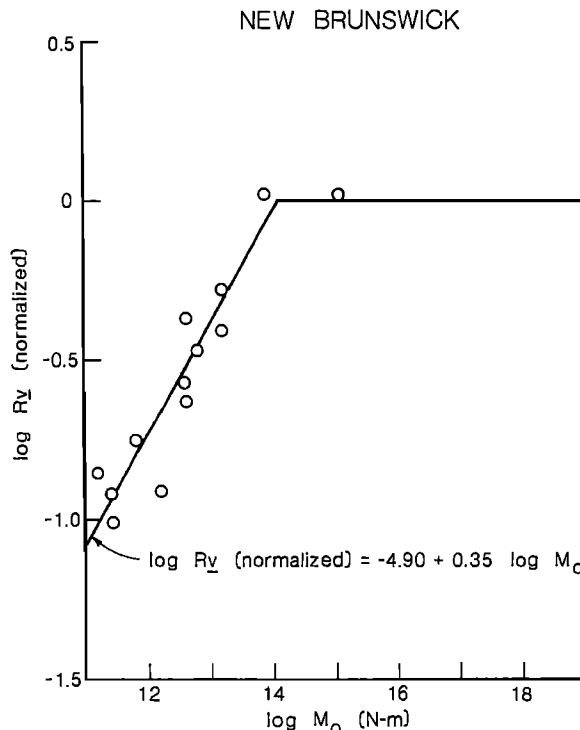


Fig. 7. Peak-velocity parameter, normalized using equation (3), as a function of seismic moment for New Brunswick aftershocks.

digitally recorded data were on granite outcrops and the recording bandwidth extended to 75 Hz, it seems unlikely that the moment dependence seen in Figure 5 is due to either anelastic attenuation or limited bandwidth recording. The *S* wave displacement spectra presented by Tucker [1975] serve to buttress this argument in that their high-frequency asymptotes, showing a constant dependence on frequency, are well defined over a broad bandwidth.

**Mammoth Lakes.** The Mammoth Lakes sequence generated peak velocity parameters (Figures 2 and 6) with a moment dependence quite similar to those of Oroville [Archuleta et al., 1982; McGarr, 1984; R. Archuleta, written communication, 1983]. Values of  $R_y$  for  $M_o < 10^{16}$  N-m were used to define the regression line (Figure 6) whose slope of 0.39 agrees closely with those for Coalinga and Oroville, 0.39 and 0.37, respectively. Because the tectonic environment at Mammoth Lakes is extensional, equation (7) was used in the normalization. The resulting transition in scaling at  $M_o = 1.7 \times 10^{15}$  N-m is somewhat greater than that for Oroville but nearly two orders of magnitude less than the corresponding point inferred for Coalinga. The largest event analyzed here, with  $M_o = 10^{18}$  N-m, occurred on 27 May 1980 at 14:50 UT, and is one of the events considered to have a non-double-couple focal mechanism [e.g., Julian and Sipkin, 1985]. The ground motion data for this

event were extracted from Moslem et al. [1983] and the hypocentral location was provided by C. Cramer [written communication, 1985]. In spite of the unusual focal mechanism the peak ground motion of the large earthquake of 27 May seems to be in reasonably good agreement with that predicted on the basis of equation (2a) as seen in Figure 6.

**Miramichi, New Brunswick.** The 1982 Miramichi earthquake, which generated an extensive and well-recorded aftershock sequence [Cranswick et al., 1982; Boatwright and Astrue, 1983] occurred at shallow depths in a compressional tectonic setting and, thus, equation (6) has been used to normalize the peak velocities plotted in Figure 7. The normalized velocity data for which  $M_o < 10^{14}$  N-m defined a regression line with a slope of 0.35, slightly lower than corresponding slopes for Coalinga and Oroville, but probably not significantly so. The transition in scaling, although somewhat equivocal, appears to occur at a point slightly in excess of  $M_o = 10^{14}$  N-m, which is even lower than the same point for the Oroville sequence. As seen in Figure 1, at a given moment  $R_y$  for the Miramichi sequence is substantially higher than for Coalinga or San Fernando.

**Mine Tremors.** The peak velocities plotted in Figure 8 [McGarr, 1981; Spottiswoode, 1984] were measured at three gold mines in South Africa. Because the state of stress there is extensional, equation (7) was used for normalization. All of the events for which  $M_o < 10^{13}$  N-m are listed in Table 1 of McGarr [1984], occurred at depths of 2 to 3 km, and were recorded using transducers installed in the same depth range. Because of the broadband underground recording, typical hypocentral distances of several hundred meters, and the high-*Q* nature of the quartzitic

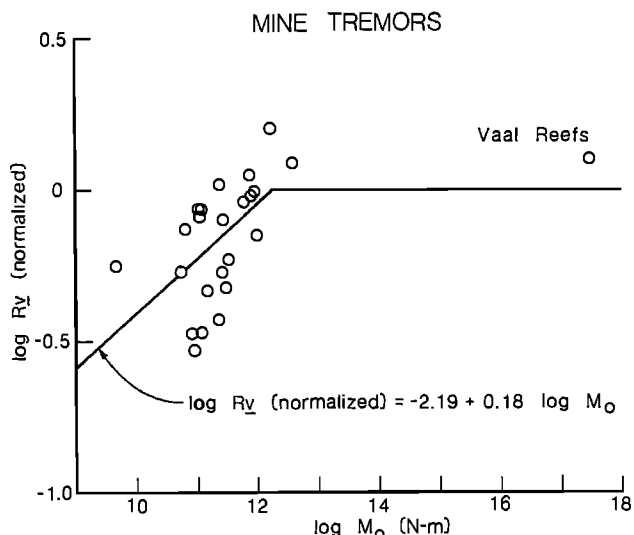


Fig. 8. Peak-velocity parameter, normalized using equation (4), as a function of seismic moment for South African mine tremors.

TABLE 1. Scaling Characteristics of Sequences

Sequence	Stress State	Transition Moment	Small $M_o$ Scaling*
Coalinga 1983	Compressional	$1.2 \times 10^{17}$ N-m	$Rv \propto M_o^{0.72}$
Oroville 1975	Extensional	$4.5 \times 10^{14}$	$M_o^{0.70}$
San Fernando 1971	Compressional	$8.1 \times 10^{15}$	$M_o^{0.87}$
Mammoth 1980	Extensional	$1.7 \times 10^{15}$	$M_o^{0.72}$
Miramichi 1982	Compressional	$1 \times 10^{14}$	$M_o^{0.68}$
Mine Tremors	Extensional	$1.5 \times 10^{12}$	$M_o^{0.51}$

\* The scaling listed here was obtained by adding the expected scaling exponent of 0.33 to the slopes of the regression fits in Figures 3 to 8.

strata through which the waves propagated, it seems unlikely that any of the observed moment dependence can be attributed to factors outside the source region although this viewpoint is not beyond dispute [Boore, 1983]. The large-moment event (Vaal Reefs) occurred in the Klerksdorp mining district as reported by Fernandez and van der Heever [1984], who presented the ground motion data used to analyze this exceptionally large mine tremor.

Although the regression line in Figure 8 is somewhat poorly determined because the mine tremor data do not appear to be well-defined functions of  $M_o$ , the transition in scaling at about  $M_o = 1.5 \times 10^{12}$  N-m is reasonably well constrained by the data. The slope of the regression line of 0.18 is by far the lowest of the six sequences considered here but, as seen in Figure 8, its uncertainty is considerable. The ill-defined moment dependence may be the result of the substantial perturbation of the state of stress in the environs of the mine excavations [e.g., McGarr et al., 1975]. McGarr [1984] circumvented this problem by only plotting averages of many mine data, which presumably sampled a variety of stress states distributed about the ambient state.

In Figure 2 we see that at a given moment the peak velocity parameters of the mine tremors are considerably in excess of those for Oroville and Mammoth Lakes. Thus, for extensional stress states, the mine tremor data are related to those of the California sequences similarly to the way that the Miramichi data (Figure 1) are situated relative to those of the California sequences in compressional tectonic environments.

#### Discussion

The question that originally motivated this study regarding the uniqueness of the unexpected scaling of the Coalinga sequence [McGarr et al., 1985] seems to have been resolved unequivocally. That is, the essential features found for Coalinga (e.g., Figures 1 and 3) are clearly not unique but instead were discovered in each of the other

five sequences included in this study. These features, abstracted from Figures 3 to 8, are listed in Table 1 for convenience. For all of the sequences it was found that the peak ground velocity parameter  $Rv$ , normalized for stress state and focal depth, showed a typical moment dependence of  $M_o^{0.70}$ , which exceeds the expected scaling by more than a factor of two. Observed variations from sequence to sequence of the small-moment scaling exponent are probably not significant in view of the experimental uncertainties.

The transition moments, however, at which the scaling exponent changes by more than a factor of two, show considerable variation from sequence to sequence. A perusal of the transition points listed in Table 1 leads one to suspect that these values may be related somehow to the geologic setting. The two sequences showing the highest values, Coalinga and San Fernando, are each in a compressional environment adjacent to the San Andreas fault covering a range in hypocentral depth of about 4 to 14 km. The two intermediate values are for Oroville and Mammoth, both regions of extensional tectonics within California but not close to the San Andreas fault system. In view, however, of the vastly different rates of crustal deformation at Oroville and Mammoth it appears that strain rate does not play an essential role in the ground motion scaling. The two lowest transition moments were inferred for the Miramichi sequence and the South African mine tremors. In both sequences the events are quite shallow, within the topmost 5 km of the crust, but perhaps more importantly, the geologic settings of both are Precambrian shields. Note also (Figures 1 and 2) that at a given moment both the Miramichi and mine velocities are substantially higher than their California counterparts. This feature may be associated with the strength of the rock formations, granite and quartzite, within which these two sequences occurred.

The nature of the scaling complexities within individual sequences, reviewed here, has some immediate implications regarding the suggestion by Nuttli [1983], mentioned ear-

## 224 COMPLICATIONS IN EARTHQUAKE SCALING

lier, that midplate earthquakes scale differently from those near plate margins. Specifically, he concluded that  $M_o \propto r_o^4$  for midplate events in presumed contrast to  $M_o \propto r_o^3$  near the margins. To relate Nuttli's result to the scaling of peak velocity emphasized here equations (3) and (4) can be used to yield  $Rv \propto M_o^{0.5}$  for midplate shocks, and, of course,  $Rv \propto M_o^{0.33}$  for plate margin events. In Figures 3 to 8 individual sequences both near and far from plate margins have shown corresponding scaling exponents ranging from 0.33 to more than 0.70. Thus, the geographical distinction drawn by Nuttli may be a consequence of the size range of midplate earthquakes used in his analysis.

Needless to say, the notion that principles of earthquake similarity do not appear to apply to individual sequences is not original to this study. What is novel here is the application of the ground motion parameter  $Rv$  for purposes of defining the scaling complexities. Equations (5) can be employed to compare the results presented here with those of other studies for which stress drop was used to express the scaling [e.g., Chouet et al., 1978; Archuleta et al., 1982; Fletcher et al., 1984]. Typically, below the transition point  $Rv \propto M_o^{0.70}$  which corresponds to  $\Delta\tau \propto M_o^{0.55}$ . This general result is in reasonable agreement with those of a number of studies for which stress drops were estimated for events within a single sequence. As noted before, the scaling of  $Rv$  is quite compatible with that for  $\Delta\tau$  for the Coalinga sequence. The same can be said for the Oroville, Mammoth Lakes, San Fernando and Miramichi sequences, although for these other sequences  $\Delta\tau$  was not found to be such a well-defined function of  $M_o$  as for the Coalinga events. Stress drops measured for events in the 1982 Enola Arkansas swarm, however, do show an unambiguous moment dependence of  $\Delta\tau \propto M_o^{0.6}$  with an apparent transition in scaling at  $M_o \approx 10^{13}$  N-m [Haar et al., 1984]. Numerous similar examples could be cited.

The conclusions of McGarr [1984] regarding the constant-stress-drop scaling of ground motion parameters and their relationship to the crustal environment near the hypocenter still seem appropriate for events above the scaling transition point but are clearly inappropriate for smaller events. The smaller shocks do not display the clearcut link to the hypocentral environment that was found for the largest events in a particular sequence, which were used to develop equations (1) and (2).

**Acknowledgments.** I thank M.C. Andrews and D.M. Boore for careful reviews of this manuscript that led to considerable improvement. Discussions with R. W. E. Green during the initial stages of this analysis helped to clarify some of the ideas involved here. C. Sullivan provided capable editorial assistance.

## References

- Andrews, D. J., From antimoment to moment: Plane strain models of earthquakes that stop, *Bull. Seismol. Soc. Am.*, **65**, 163–182, 1975.
- Archuleta, R. J., C. S. Mueller, and P. Spudich, Source parameters of the 1980 Mammoth Lakes, California, earthquake sequence, *J. Geophys. Res.*, **87**, 4595–4607, 1982.
- Atkinson, G. M., Attenuation of strong ground motion in Canada from a random vibrations approach, *Bull. Seismol. Soc. Am.*, **74**, 2629–2653, 1984.
- Boatwright, J., and M. Astrue, Report on source parameters of New Brunswick earthquakes, *Earthquake Notes*, **54**, 6, 1983.
- Boore, D. M., Stochastic simulation of high-frequency ground motions based on seismological models of the radiated spectra, *Bull. Seismol. Soc. Am.*, **73**, 1865–1894, 1983.
- Boore, D. M., The effect of finite bandwidth on seismic scaling relationships, *This volume*, 1985.
- Brune, J. N., Tectonic stress and the spectra of seismic shear waves, *J. Geophys. Res.*, **75**, 4997–5009, 1970. (Correction, *J. Geophys. Res.*, **76**, 5002, 1971.)
- Brune, J. N., R. J. Archuleta, and S. Hartzell, Far-field S-wave spectra, corner frequencies, and pulse shapes, *J. Geophys. Res.*, **84**, 2262–2272, 1979.
- Chouet, B., K. Aki, and M. Tsujiura, Regional variation of the scaling law of earthquake source spectra, *Bull. Seismol. Soc. Am.*, **68**, 49–79, 1978.
- Cranswick, E., C. Mueller, R. Wetmiller, and E. Sembera, Local multi-station digital recordings of aftershocks of the January 9, 1982 New Brunswick earthquake, *U. S. Geol. Surv. Open File Rep.*, **82-777**, 1982.
- Dieterich, J. H., A deterministic near-field source model, *Paper presented at the 5th World Conference on Earthquake Engineering*, Rome, 1973.
- Fernandez, L. M., and P. K. van der Heever, Ground movement and damage accompanying a large seismic event in the Klerksdorp district, in *Rockbursts and Seismicity in Mines*, edited by N. C. Gay and E. H. Wainwright, pp. 193–198, South African Institute of Mining and Metallurgy, 1984.
- Fletcher, J. B., Spectra from high-dynamic range digital recordings of Oroville, California aftershocks and their source parameters, *Bull. Seismol. Soc. Am.*, **70**, 735–755, 1980.
- Fletcher, J. B., J. Boatwright, L. Haar, T. Hanks, and A. McGarr, Source parameters for aftershocks of the Oroville, California, earthquake, *Bull. Seismol. Soc. Am.*, **74**, 1101–1123, 1984.
- Haar, L. C., J. B. Fletcher, and C. S. Mueller, The 1982 Enola, Arkansas, swarm and scaling of ground motion in the eastern United States, *Bull. Seismol. Soc. Am.*, **74**, 2463–2483, 1984.
- Hanks, T. C., Earthquake stress drops, ambient tectonic

- stresses and stresses that drive plate motions, Pure Appl. Geophys., 115, 441–458, 1977.
- Hanks, T. C.,  $f_{\max}$ , Bull. Seismol. Soc. Am., 72, 1867–1879, 1982.
- Joyner, W. B., A scaling law for the spectra of large earthquakes, Bull. Seismol. Soc. Am., 74, 1167–1188, 1984.
- Julian, B. R., and S. A. Sipkin, Earthquake processes in the Long Valley caldera area, California, J. Geophys. Res., 90, 11,155–11,169, 1985.
- Kanamori, H., and D. L. Anderson, Theoretical basis of some empirical relations in seismology, Bull. Seismol. Soc. Am., 65, 1073–1096, 1975.
- McGarr, A., Analysis of peak ground motion in terms of a model of inhomogeneous faulting, J. Geophys. Res., 86, 3901–3912, 1981.
- McGarr, A., Scaling of ground motion parameters, state of stress, and focal depth, J. Geophys. Res., 89, 6969–6979, 1984.
- McGarr, A., S. M. Spottiswoode, and N. C. Gay, Relationship of mine tremors to induced stresses and to rock properties in the focal region, Bull. Seismol. Soc. Am., 65, 981–993, 1975.
- McGarr, A., R. W. E. Green, and S. M. Spottiswoode, Strong ground motion of mine tremors: Some implications for near source ground motion parameters, Bull. Seismol. Soc. Am., 71, 295–319, 1981.
- McGarr, A., C. Mueller, J. B. Fletcher, and M. Andrews, Ground motion and source parameters of the 1983 Coalinga, California earthquake sequence, U.S. Geol. Surv. Prof. Pap., in press, 1985.
- Moslem, K., A. Amini, B. Kontic, J. G. Anderson, and T. H. Heaton, Accelerograms from the Mammoth Lakes, California earthquake sequence of May–July, 1980 recorded on a temporary array, Report No. C. E. 83-01, Univ. of S. California, Dept. of Civil Engineering, 1983.
- Nuttli, O., Average seismic source-parameter relations for mid-plate earthquakes, Bull. Seismol. Soc. Am., 73, 519–535, 1983.
- Savage, J. C., Relation of corner frequency to fault dimensions, J. Geophys. Res., 77, 3788–3795, 1972.
- Spottiswoode, S. M., Source mechanisms of mine tremors at Blyvooruitzicht Gold Mine, Proc. 1st Int. Cong. Rockbursts and Seismicity in Mines, edited by N. C. Gay and E. H. Wainwright, South African Institute of Mining and Metallurgy, Johannesburg, 29–37, 1984.
- Tucker, B. E., Source Mechanisms of Aftershocks of the 1971 San Fernando, California Earthquake, Ph.D. thesis, 230 pp., University of California at San Diego, 1975.

## EARTHQUAKE REPEAT TIME AND AVERAGE STRESS DROP

Hiroo Kanamori and Clarence R. Allen

Seismological Laboratory, California Institute of Technology, Pasadena, California 91125

**Abstract.** Existing data on source parameters of large crustal earthquakes (subduction events are not considered here) over a wide range of repeat times indicate that, for a given magnitude ( $M_s$  or  $M_w$ ), earthquakes with long repeat times have shorter fault lengths than those with short repeat times. A shorter fault length for a given magnitude indicates a larger average stress drop which reflects the average strength of the fault zone. Our result therefore suggests that faults with longer repeat times are stronger than those with shorter repeat times. In terms of an asperity model in which the average strength of a fault zone is determined by the ratio,  $r_a$ , of the total area of the asperities (strong spots on a fault plane) to the total area of the fault zone, the above result suggests that  $r_a$  is proportional to the repeat time. Our result provides a method to estimate seismic source spectra from the fault length and the repeat time of a potential causative fault.

## 1. Introduction

The repeat time of earthquakes on a given fault segment is controlled by the rate of tectonic loading (long-term slip rate) and the stress accumulation and release mechanism on the fault. Most large earthquakes at active plate margins have relatively short (30 to 200 years) repeat times, while some intraplate events have repeat times as long as several thousand years, even if they are relatively close to a plate boundary.

In this paper, we examine published source parameters of large crustal earthquakes for which repeat times have been estimated, in an attempt to see whether events with grossly different repeat times have different source characteristics. In particular, we examine average stress drops associated with faulting. Although stress drops may be controlled by many parameters other than the repeat time, the large range of the repeat times (i.e., 20 to several thousand years) among different earthquakes would help isolate the factor that determines the earthquake stress drop.

Earthquakes on subduction thrust boundaries are not considered here, because they involve fault geometries and depths very different from the crustal earthquakes considered here.

## 2. Data

The data on the source parameters and the repeat times are summarized in Table 1. Among the various source parameters, we use the surface-wave magnitude  $M_s$ , the seismic moment  $M_0$  (or the corresponding moment magnitude  $M_w = (\log M_0 - 16.1)/1.5$ ), the fault length  $L$ , and the fault width  $W$ .

The surface-wave magnitude,  $M_s$ , is the most widely used parameter and is available for very old events as well as recent events. Although the seismic moment,  $M_0$ , is not available for

some of the old events, it directly represents the overall size of the source ( $M_0 = \mu DS$ , where  $\mu$  = rigidity,  $D$  = fault offset,  $S$  = fault area), and allows more quantitative interpretations of the data than does the magnitude.

The fault length,  $L$ , can be determined from various data such as the extent of the surface break, geodetic data, aftershock area, macro-seismic data, and the spectrum of radiated seismic waves. However, surface breaks do not always represent the entire extent of the fault, particularly for small events. The size of the aftershock area is often used to estimate the fault length. Since the aftershock area is not always defined rigorously, and because it varies as a function of time, some ambiguity exists in this method, too. However, several studies have demonstrated that the size of the aftershock area at a relatively early stage of the aftershock activity is indeed a good approximation of the fault length [Benioff, 1962; Ben-Menahem and Toksöz, 1963; Mogi, 1968; Wyss, 1979; Kanamori and Given, 1981]. The fault length estimated from the size of the aftershock area can be checked against macro-seismic data, such as the intensity distribution, the tsunami source area, and the surface rupture. Geodetic data can also be used to crosscheck the result.

Since the aftershock data are available for most events of Table 1, we primarily use this method in this paper. In several cases, some subjective judgment is necessary, as discussed in the Appendix. Despite these inevitable ambiguities, we believe that the fault length estimated from the initial aftershock area is a reasonably good approximation of the length of the seismic rupture zone, at least for the events examined here.

Many recent studies suggest that the slip is not uniform on the fault plane defined by the aftershock area, but is concentrated in a much smaller area [e.g., 1968 Borrego Mountain earthquake, Burdick and Mellman, [1976]; 1979 Imperial Valley earthquake, Hartzell and Helmberger [1982]; 1979 Coyote Lake earthquake, Liu and Helmberger [1983]]. Although we consider this nonuniformity to be an important feature of seismic faulting, we first use the fault length defined by the extent of the aftershock area to establish the scaling relations.

The width of the fault,  $W$ , is even more difficult to determine than the fault length,  $L$ . The vertical extent of the aftershock area can be used, but the lack of aftershocks at a large depth does not necessarily mean that no seismic slip occurs there. Because of the increased temperature at large depths, the fault zone there may not be capable of generating aftershocks, even if it can slip coseismically.

In principle, the vertical extent of the fault can be estimated from geodetic data, but the available data are seldom complete enough to resolve it. Furthermore, geodetic observations usually include afterslip as well as the coseismic slip. In this paper, the

## 228 EARTHQUAKE REPEAT TIME AND STRESS DROP

TABLE 1. Earthquake Source Parameters (for details, see the Appendix)

Event	$M_s$	$M_w$	$M_0$ ( $10^{27}$ dyne-cm)	L (km)	W (km)	S (km $^2$ )	t (years)
Alaska, 1958	7.9	7.8	7.0	300	16	4800	60-110
Borah Peak, 1983	7.3	7.0	0.34	30	18	540	5600
Borrego Mt., 1968	6.7	6.6	0.1	40	13	520	100
Coyote Lake, 1979	5.7	5.6	0.0035	25	8	200	75
Daofu, 1981	6.8	6.7	0.13	46	10	460	100
Guatemala, 1976	7.5	7.5	2.6	250	15	3750	180-755
Haiyuan, 1920	8.6			220			700-1000
Hebgen Lake, 1959	7.5	7.3	1.0	30	15	450	$2800 \pm 1100$
Imperial Valley, 1979	6.5	6.5	0.06	42	10	420	40
Izu, 1930	7.2	6.9	0.25	22	12	264	700-1000
Izu-Oki, 1974	6.5	6.4	0.059	20	11	220	1000
Kern County, 1952	7.7	7.3	1.0	70	20	1400	170-450
Luhuo, 1973	7.4	7.4	1.8	110	15	1650	100
Mikawa, 1945	6.8	6.6	0.087	12	11	132	$2000-4 \times 10^4$
Morgan Hill, 1984	6.1	6.1	0.02	30	10	300	75
N. Anatolian, 1939	7.8			350	15	5250	150-200
N. Anatolian, 1943	7.6			265	15	3975	150-200
N. Anatolian, 1944	7.4			190	15	2850	150-200
Niigata, 1964	7.5	7.6	3.0	60	25	1500	560
Parkfield, 1966	6.0	6.0	0.014	30	13	390	22
Pleasant Valley, 1915	7.7			62			5000
San Fernando, 1971	6.6	6.7	0.12	17	17	289	100-300
Tabas, 1978	7.4	7.4	1.5	65	20	1300	>1300
Tango, 1927	7.6	7.0	0.46	35	13	455	$2000-6 \times 10^4$
Tangshan, 1976	7.8	7.4	1.8	80	15	1200	>2000
Tottori, 1943	7.4	7.0	0.36	33	13	429	6000

width estimated from the aftershocks is used for most events.

We present two diagrams: (1)  $M_s$  versus L, (2)  $M_w$  versus L. The  $M_s$  versus L diagram (Figure 1) involves the parameters which are directly determined from the data without much interpretation. The  $M_w$  versus L diagram (Figure 2) is similar to the  $M_s$  versus L diagram, but it involves the seismic moment,  $M_0$ . Since the method and the type of the data used for the determination of  $M_0$  vary among the investigators and the events, some ambiguity exists concerning the value of  $M_0$ . However,  $M_0$  represents the physical size of the source more directly than  $M_s$  and is easier to interpret. In this paper, the values of  $M_0$  determined from the amplitude of seismic waves and the geodetic data are used, and the values obtained by different methods for each event are crosschecked for consistency (for details, see the Appendix).

The repeat time,  $\tau$ , of earthquakes has been estimated by various methods. For many Japanese events, the slip rate, V, along a fault estimated from geomorphological data supplemented by  $C^{14}$  dates, and the amount of slip, D, in a large earthquake judged to be characteristic of the fault are used to estimate  $\tau$  ( $= D/V$ ) [Matsuda, 1975a].

When historical data are available for a very long period of time, repeat times can be estimated from such data (e.g., earthquakes along the North Anatolian fault: Allen [1975]; Ambraseys [1970]). More recently, the offset patterns in fault zones exposed by trenching are used to determine the time history of the activity of the fault [e.g., Clark et al., 1972; Sieh, 1978].

In this study, we use the values of  $\tau$  determined by various methods, and the references are given in the Appendix. A number of the published recurrence intervals, such as those for the 1952 Kern County and 1971 San Fernando earthquakes, are admittedly

based on very scanty and debatable evidence; nevertheless, we have felt obligated to use such numbers when no other data are available.

### 3. Results

**3.1  $M_s$  Versus L and  $M_w$  Versus L Diagram.** Figure 1 shows the relation between the surface-wave magnitude,  $M_s$ , and the fault length, L, for earthquakes having different repeat times.

In general, for a given  $M_s$ , earthquakes having a longer repeat time have a shorter fault length (see the events with  $7 < M_s < 8$ ). On the other hand, for a given L, earthquakes with a longer repeat time tend to have a larger  $M_s$  (see the events with  $30 < L < 50$  km), although the total number of events is relatively small. This situation is best illustrated by comparing three representative earthquakes: 1927 Tango, 1966 Parkfield, and the 1976 Guatemala earthquakes. Both the Guatemala and Tango earthquakes have about the same  $M_s$ , yet  $L = 250$  and 35 km for the Guatemala and Tango earthquakes, respectively. The repeat time is about 180 to 755 years for the Guatemala event [Schwartz et al., 1979] and several thousand years for the Tango earthquake [Matsuda, 1975a]. Both the Parkfield and Tango earthquakes have about the same L, but they have a very different  $M_s$ :  $M_s = 7.6$  for Tango and  $M_s = 6.0$  for Parkfield. The Parkfield earthquake has a very short repeat time (about 22 years; Bakun and McEvilly [1984]) compared with that for the Tango earthquake (at least 2000 years).

Since  $M_s$  is a purely empirical parameter, and since only one spatial dimension, L, is given, we cannot directly interpret the  $M_s$  versus log L diagram in terms of the stress drop. Here we define the average stress drop by

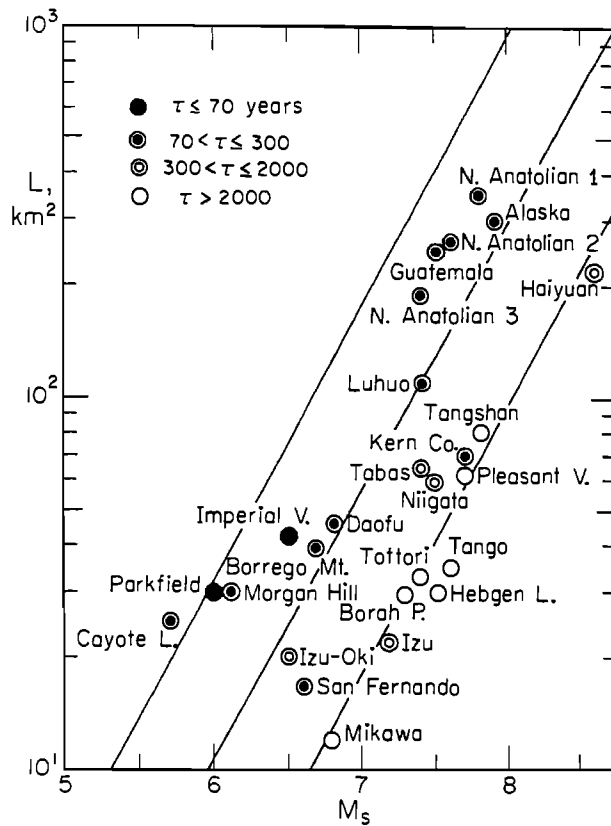


Fig. 1. The relation between the surface-wave magnitude,  $M_s$ , and the fault length,  $L$ . The solid lines indicate the trend for a constant stress drop.

$$\overline{\Delta\sigma} = \int_s \Delta\sigma D dS / \int_s D dS$$

where  $\Delta\sigma$  and  $D$  are the stress drop and the dislocation on the fault plane,  $S$ , respectively. Following Kanamori [1977], the numerator can be written as  $2E_S$  where  $E_S$  is the energy radiated in seismic waves. Although direct determinations of  $E_S$  are seldom available, Gutenberg and Richter's [1956] magnitude-energy relation,  $\log E_S = 1.5 M_s + 11.8$ , is generally considered a good approximation for earthquakes with  $M_s < 8$ . Using this relation, the above relation can be written as

$$\overline{\Delta\sigma} = 2\mu E_S / M_0 = 2 \times 10^{1.5M_s + 11.8} / L W \bar{D}$$

where  $W$  is the width of the fault and  $\bar{D}$  is the average dislocation. If both  $W$  and  $\bar{D}$  are proportional to  $L$ ,  $\log L \propto (1.5/3)M_s - (1/3)\log\Delta\sigma$ . However, for large crustal earthquakes,  $W$  is more or less bounded by the thickness of the seismogenic zone, and would not increase as fast as  $L$ . If  $W$  and  $\bar{D}$  are fixed, then  $\log L \propto (1.5M_s - \log\Delta\sigma)$ . However, it is unlikely that both  $W$  and  $D$  stay completely constant as  $L$  increases. In fact, Scholz [1982] found that  $L \propto \bar{D}$  for most crustal earthquakes. In this case, if the variation of  $W$  is small,  $\log L \propto (1.5/2)M_s - (1/2)\log\Delta\sigma$ , which is intermediate of the above two extreme cases. The solid lines in Figure 1 indicate the lines of constant stress drop for this intermediate case. The trend in Figure 1 indicates that the earthquakes having a longer repeat time have a higher average stress drop. Since the details of the scaling relations are unknown, these lines should not be given too much significance; they should be con-

sidered as the reference to which the earthquake data are compared. A use of the other relations (e.g.,  $\log L \propto 0.5 M_s$ ,  $\log L \propto 1.5 M_s$ ) does not affect the conclusion of this paper qualitatively.

Figure 2 shows the relation between  $M_w$  and  $L$ , which is essentially similar to Figure 1.

#### 4. Interpretation

Experimental studies on rocks and other materials demonstrate that the static friction between two surfaces generally increases as the time of stationary contact increases [e.g., Scholtz and Engelder, 1976; Shimamoto and Logan, 1984; Richardson and Nolle, 1976]. Our results are consistent with these laboratory results, although the time scales involved are very different between laboratory and in-situ conditions.

Many recent studies indicate that the displacement and the stress change on a fault plane are very nonuniform in space. One of the best documented cases is the 1979 Imperial Valley, California, earthquake for which a large number of near-field strong-motion records are available for detailed modeling. Hartzell and Helmberger [1982], Olson and Apsel [1982], Hartzell and Heaton [1983] and Archuleta [1984] made extensive analyses of this data set to determine the distribution of slip on the fault. Although the results obtained in these studies differ in detail, an important conclusion is that a major proportion of the slip is concentrated in an area which is much smaller than the total aftershock area. Hartzell

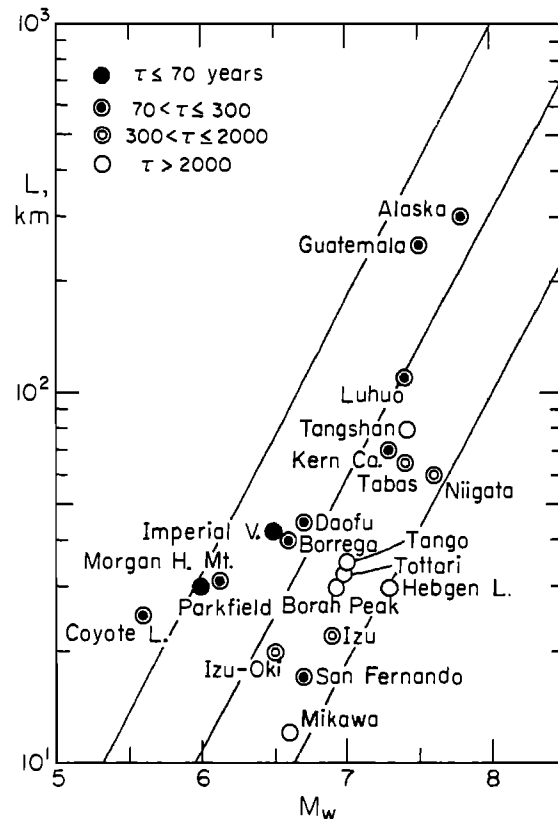


Fig. 2. The relations between the moment magnitude,  $M_w$ , and the fault length,  $L$ . The solid lines indicate the trend for a constant stress drop.

## 230 EARTHQUAKE REPEAT TIME AND STRESS DROP

and Helmberger [1982] estimate that the average stress drop,  $\bar{\Delta\sigma}$ , is 5 to 10 bars, but the local stress drop,  $\Delta\sigma_a$ , is about 200 bars.

We assume that the area where a large amount of slip occurred is a strong spot on the fault plane, and will call it the (fault) asperity. Then the average strength of the fault and the average stress drop  $\bar{\Delta\sigma}$  are proportional to the ratio,  $r_a$ , of the total area of the asperity (or asperities, if more than one asperity exists) to the total area of the fault plane. In terms of this asperity model, our results can be interpreted that  $r_a$  increases as the repeat time increases.

## 5. Discussion

Kanamori and Anderson [1975] demonstrate that the average stress drop is higher for intraplate than interplate earthquakes. Since intraplate events have generally longer repeat times than interplate events, our result is essentially the same as that of Kanamori and Anderson [1975]. However, the distinction between "intraplate" and "interplate" is often ambiguous. The use of repeat time, or slip rate, as a parameter in the scaling relation provides a clearer physical basis.

The present result suggests a scheme to estimate strong ground motions of intraplate events with very long repeat times such as those in the eastern United States. Boore [1983] used an  $\omega$ -square source model and successfully explained most essential features of strong ground motions of earthquakes in the western United States by scaling the spectrum with an appropriate stress scaling parameter,  $\Delta\sigma_s$ . To apply this method to regions such as the eastern United States is difficult because no seismological data to estimate the stress parameter are available. In such a case, geological estimates of the length of a potential causative fault and the repeat time are the key parameters. Given the fault length and the repeat time, we can estimate, from Figure 1, the magnitude and the average stress drop of the expected event. Although the average stress drop and the stress scaling parameter are not necessarily the same, we may assume that they are proportional to each other, since both of them are related to the strength of the fault zone. Once the scaling parameter is estimated, Boore's [1983] method can be applied. For the  $\omega$ -square model, the corner frequency is proportional to  $\Delta\sigma_s^{1/3}$ , and the high-frequency acceleration spectral amplitude is proportional to  $\Delta\sigma_s^{2/3}$ . Hence, for a given seismic moment, a factor of 5 difference in the stress drop suggests a factor of 3 difference in the acceleration spectral amplitude. A factor of 5 difference in the average stress drop is commonly seen between intraplate and interplate earthquakes. [Kanamori and Anderson, 1975; Scholz, 1982].

However, the details of the source spectrum at high frequencies are still unknown. It is possible that the spectral shape is better represented by a model other than the  $\omega$ -square model. In that case the above scaling is not appropriate.

In general, faults with short repeat times have large slip rates and vice versa. Our results therefore can be restated that faster moving faults have smaller ratios of asperity area to the total fault area. Although we do not have a direct evidence for this, it is instructive to consider the limiting cases where  $V \rightarrow 0$  or  $V \rightarrow \infty$ . When  $V$  becomes very large, the repeat time decreases. However, at the same time,  $\Delta\sigma$  decreases, and the earthquake would have creeplike character and the seismicity may be characterized by frequent small events without any large events. This situation may be compared to that along the transform faults in the East Pacific Rise which represent the fastest moving plate boundary ( $\approx 20$  cm/year). The seismicity there is characterized by the absence of large earthquakes, although this may be partly due to their proximity to the spreading center and to the relatively high-temperature lithosphere there. Along the transform faults in the Mid-Atlantic ridge where the slip rate is very low ( $\approx 2$  cm/year), relatively large

( $M_s > 6$ ) earthquakes occur occasionally. When  $V$  becomes very small, the repeat time increases indefinitely and, at a certain point, the fault zone would cease to be seismogenic.

The data set used in this study includes events with strike-slip, thrust and normal-fault mechanisms. It is possible that the average stress drop varies depending upon the fault type; most probably it is greatest for thrust events, least for normal-fault events, and intermediate for strike-slip events [e.g., Sibson, 1974]. No obvious trend is found, however, in the data set used here.

Ruff and Kanamori [1980] show that the strength of plate coupling at subduction zones generally increases with the convergence rate. This conclusion may appear to contradict the conclusion of the present paper. However, the conclusion of Ruff and Kanamori [1980] was for subduction-zone events for which the repeat time is within a very small range, 30 to 200 years, while the present model intends to explain the variation of the stress drop over a much wider range of the repeat time, 30 to several thousand years. The variation of stress drops within a narrow range of repeat time may be controlled by other factors, such as the fault geometry.

## 6. Conclusion

Existing data on source parameters of crustal earthquakes over a wide range of repeat times indicate that the earthquakes with long repeat times have higher average stress drops than those with short repeat times. The repeat time is therefore a useful parameter to scale seismic spectra.

Recent studies [e.g., Hanks and McGuire, 1981; Boore, 1983] have shown that high-frequency strong motions in the western United States can be explained by an  $\omega$ -square source model if the spectrum is scaled by an appropriate stress scaling parameter. To apply this method to regions where no seismological data are available, an estimate of the stress parameter is required. Our results (Figures 1 and 2) may be used to estimate it, if the fault length and the repeat time of a potential causative fault are estimated by geological methods.

## Appendix

## Source parameters of the events used in this paper

Alaska, July 10, 1958, 06:15:56, 59.3, -136.5

$M_s=7.9$ ,  $m_b=7.4$  [Abe, 1981].

Moment: Kanamori [1977] gives  $2.9 \times 10^{28}$  dyne-cm, but this value is estimated from the rupture area, and is not reliable. Ando [1977] gives  $4 \times 10^{27}$  dyne-cm, and Ben-Menahem [1977] gives  $7 \times 10^{27}$  dyne-cm.

L and W: From Kelleher and Savino [1975], L is estimated to be about 300 km. W is assumed to be 16 km.

t: Plafker et al. [1978] give two recurrence intervals: 110 years or less, and 60 years.

Borah Peak, October 28, 1983, 14:06:22.5, 44.03, -113.91

$M_s=7.3$  ( NEIS )

Moment: Doser and Smith [1985] give  $2.1 \times 10^{26}$  dyne-cm from body waves. Tanimoto and Kanamori [1985] give  $3.4 \times 10^{26}$  dyne-cm from long-period surface waves.

L and W: Doser and Smith [1985] give L=21 km for the unilateral rupture length. L=30 km is inferred from the aftershock area.

- W is estimated to be 18 km from the depth of the main shock. Stein and Barrientos [1985] used L=21 to 35 km, and W=18 km, and obtained a geodetic moment of  $3.3 \times 10^{26}$  dyne-cm.
- $\tau$ : Scott et al. [1985] state that the last displacement occurred between  $4320 \pm 130$  and 6800 years ago. This estimate is based on radiometric dating. Salyard [1985] estimates it to be 5600 years on the basis of scarp geomorphology.
- Borrego Mountain, April 9, 1968, 02:28;59.1, 33.19, -116.13  
Ms=6.7 [Kanamori and Jennings, 1978].
- Moment:  $1.1 \times 10^{26}$  dyne-cm from body waves [Burdick and Mellman, 1976] and surface waves [Butler, 1983].
- L and W: L=38 km from the aftershocks during the first 22 hours [Allen and Nordquist, 1972]. L=40 km from the aftershocks during the period from April 12 to April 18 [Hamilton, 1972]. W is estimated to be 13 km from Hamilton [1972].
- $\tau$ : Sharp [1981] gives a range 30 to 860 years, but states that, if the magnitude and displacement of the 1968 event are typical, approximately one such event per century at a given point is predicted.
- Coyote Lake, August 6, 1979, 17:05;22.3, 37.11, -121.53  
Ms=5.7 (NEIS)
- Moment:  $M_0 = 6 \times 10^{24}$  dyne-cm [Uhrhammer, 1980].  $M_0 = 3.5 \times 10^{24}$  dyne-cm [Liu and Helmberger, 1983].
- L and W: L=25 km [Lee et al., 1979]. L=23 km [Uhrhammer, 1980]. W=8 km is considered appropriate.
- $\tau$ : Bakun et al., [1984] estimate the recurrence interval to be about 75 years.
- Daofu, January 23, 1981, 21:13;51.7, 30.927, 101.098  
Ms=6.8 (NEIS)
- Moment:  $M_0 = 1.3 \times 10^{26}$  dyne-cm [Zhou et al., 1983a].
- L and W: From the aftershock data, L=46 km, W=10 km [Zhou et al., 1983a].
- $\tau$ : There is no paleoseismological work on the Xianshuihe fault. The estimate of slip rate (5 to 10 mm/year, Tang et al. [1984] and historical seismicity indicate a recurrence interval of about 100 years.
- Guatemala, February 4, 1976, 09:01;42.2, 15.27, -89.25  
Ms=7.5, mb=5.8
- Moment: Kanamori and Stewart [1978] obtained  $2.6 \times 10^{27}$  dyne-cm from long-period surface waves. This value is consistent with the geodetic data [Lisowski and Thatcher, 1981].
- L and W: L=250 km from the aftershock area [Langer et al., 1976]. The extent of the surface break is about 190 km [Plafker,
- 1976]. W is estimated to be 15 km from the aftershock distribution given by Langer et al. [1976].
- $\tau$ : 180 to 755 years [Schwartz et al., 1979]
- Schwartz (1985) suggests an interval of 425 to 725 years between the 1976 earthquake and the previous event along the Motagua fault.
- Haiyuan, December 16, 1920, 12:05:48, 36., 105.  
Ms=8.6, mb=7.9 [Abe, 1981].
- L and W: L=220 km is given by Deng et al. [1985]. W is not given.
- $\tau$ : 700 to 1000 years (personal communication, Qidong Deng, 1985).
- Hebgen Lake, August 18, 1959, 06:37:15, 44.7, -110.8  
Ms=7.5, mb=7.3 [Abe, 1981].
- Moment: Doser [1985] gives  $1 \times 10^{27}$  dyne-cm from body waves. Geodetic data indicate  $1.35 \times 10^{27}$  dyne-cm [Savage and Hastie, 1966].
- L and W: Doser [1985] gives L=28 km for the unilateral rupture length. Savage and Hastie [1966] used 30 km. From the focal depth and the geodetic data, W=15 km is considered appropriate.
- $\tau$ :  $3250 \pm 850$  years [Nash, 1981],  $2800 \pm 1100$  years [Nash, 1984].
- Imperial Valley, October 15, 1979, 23:16:53.4, 32.61, -115.32  
Ms=6.9 is given by NEIS, but this value is strongly influenced by European data. If a proper azimuthal average is taken Ms=6.5, which is considered to be more appropriate.
- Moment:  $M_0 = 6 \times 10^{25}$  dyne-cm from surface waves [Kanamori and Regan, 1982], and  $M_0 = 5 \times 10^{25}$  dyne-cm from strong-motion data [Hartzell and Helmberger, 1982].
- L and W: L=42 km determined by the distance between the epicenter and the cluster near Brawley [Johnson and Hutton, 1982]. W is assumed to be 10 km.
- $\tau$ : 39 years assumed.
- Izu, November 25, 1930, 19:02:47, 35.0, 139.0  
Ms=7.2, mb=6.8 [Abe, 1981].
- Moment:  $M_0 = 2.7 \times 10^{26}$  dyne-cm [Abe, 1978]. Kanamori and Anderson [1975] give  $2.4 \times 10^{26}$  dyne-cm as the average of Kasahara [1957] and Chinnery [1964].
- L and W: L=22 km and W=12 km [Abe, 1978]. Kanamori and Anderson [1975] give L x W=240 km<sup>2</sup> as the average of Kasahara [1957], Chinnery [1964], and Iida [1959].
- $\tau$ : 700 to 1000 years [Tanna Fault Trenching Research Group, 1983].
- Izu-Oki, May 08, 1974, 23:33;25.2, 34.6, 138.8

## 232 EARTHQUAKE REPEAT TIME AND STRESS DROP

- M<sub>s</sub>=6.5 ( NEIS )**
- Moment:  $M_0=5.9 \times 10^{25}$  dyne-cm [Abe, 1978].
- L and W: L=20 km, W=11 km [Research Group for Aftershocks, 1975, quoted in [Abe, 1978]].
- $\tau$ : 1000 years [Matsuda, 1975, Matsuda, 1977].
- Kern County, July 21, 1952, 11:52:14, 35.0, -119.02
- M<sub>s</sub>=7.7 [Kanamori and Jennings, 1978]. Abe [1981] gives 7.8.
- Moment: Kanamori and Anderson [1975] give 2 x  $10^{27}$  dyne-cm from Kanamori's unpublished result. Ben-Menahem [1977] gives  $0.84 \times 10^{27}$  dyne-cm. Stein and Thatcher [1981] give  $0.84 \times 10^{27}$  dyne-cm from geodetic data.  $M_0=1 \times 10^{27}$  dyne-cm seems appropriate.
- L and W: From Benioff [1955] and Stein and Thatcher [1981], L=70 km, and W=20 km are considered appropriate.
- $\tau$ : 170 to 450 years [Stein and Thatcher, 1981].
- Luhuo, February 6, 1973, 10:37:10.1, 31.4, 100.6
- M<sub>s</sub>=7.4 ( NEIS )
- Moment:  $M_0=1.8 \times 10^{27}$  dyne-cm [Zhou et al., 1983b].
- L and W: From the aftershocks L=110 km, and W=15 km [Zhou et al., 1983b].
- $\tau$ : See the description for the Daofu earthquake.
- Mikawa, January 12, 1945, 18:38:26, 34.75, 136.75
- M<sub>s</sub>=6.8, m<sub>B</sub>=7.2 [Abe, 1981].
- Moment: Ando [1974] gives  $M_0=8.7 \times 10^{25}$  dyne-cm from geodetic data.
- L and W: L=12 km and W=11 km [Ando, 1974].
- $\tau$ : Matsuda [1977] gives 2 to  $4 \times 10^4$  years; however, Matsuda [1982, written communication] states that this value is subject to large uncertainty. According to Matsuda,  $\tau > 2000$  years.
- Morgan Hill, April 24, 1984, 21:15:19.0, 37.32, -121.70
- M<sub>s</sub>=6.1, m<sub>B</sub>=5.7
- Moment:  $2.0 \times 10^{25}$  dyne-cm [Ekstrom, 1985]. This value agrees well with that determined from long-period Rayleigh waves recorded by the IDA network,  $2.3 \times 10^{25}$  dyne-cm.
- L and W: The aftershock area determined by Cockerham and Eaton [1985] indicate L=30 km, and W=10 km.
- $\tau$ : Bakun et al. [1984] estimate the recurrence time to be approximately 75 years.
- N. Anatolian 1, December 26, 1939, 23:57:21, 39.5, 38.5
- M<sub>s</sub>=7.8, m<sub>B</sub>=7.7 [Abe, 1981].
- L and W: L=350 km Slemmons [1977]. W=15 km assumed.
- $\tau$ : 200 years [Allen, 1975]. 150 years [Ambraseys, 1970].
- N. Anatolian 2, November 26, 1943, 22:20:36
- M<sub>s</sub>=7.6, m<sub>B</sub>=7.3 [Abe, 1981].
- L: L=265 km [Slemmons, 1977], W=15 km is assumed.
- $\tau$ : 200 years [Allen, 1975].  $\tau = 150$  years [Ambraseys, 1970].
- N. Anatolian 3, February 1, 1944, 03:22:36, 41.5, 32.5
- M<sub>s</sub>=7.4, m<sub>B</sub>=7.5
- L: L=190 km [Slemmons, 1977], W=15 km is assumed.
- $\tau$ : 200 years [Allen, 1975]. 150 years [Ambraseys, 1970].
- Niigata, June 16, 1964, 04:01:40, 38.4, 139.3
- M<sub>s</sub>=7.5 [Abe, 1981].
- Moment:  $M_0=3 \times 10^{27}$  dyne-cm [Aki, 1966],  $M_0=3.2 \times 10^{27}$  dyne-cm [Abe, 1975].
- L and W: L=60 km [Kayano, 1968], W=25 km (estimated from the vertical extent of the aftershock area, Kayano [1968]. Abe [1975] estimated LxW to be  $80 \times 30 \text{ km}^2$  from geodetic data).
- $\tau$ : 560 years [Nakamura et al., 1964].
- Parkfield, June 28, 1966, 04:26:14, 35.92, -120.53
- M<sub>s</sub>=6.0 [Kanamori and Jennings, 1978].
- Moment: Purcaru and Berckhemer [1982] give  $1.4 \times 10^{25}$  dyne-cm as the average of 6 determinations.
- L and W: L=30 km, W=13 km [Eaton et al., 1970].
- $\tau$ : 22 years [Bakun and McEvilly, 1984].
- Pleasant Valley, October 3, 1915
- M<sub>s</sub>=7.7, m<sub>B</sub>=7.3
- L and W: L=62 km [Slemmons, 1977].
- $\tau$ : 5000 years [Wallace [1984]; and private communication, 1985].
- San Fernando, February 9, 1971, 14:00:41.8, 34.41, -118.4
- M<sub>s</sub>=6.6 [Kanamori and Jennings, 1978].
- Moment: Kanamori and Anderson [1975] give  $1.2 \times 10^{27}$  dyne-cm as the average of 8 determinations. Heaton and Helmberger [1979] give  $1.4 \times 10^{26}$  dyne-cm.
- L and W: L=20 km, and W=20 km [Allen et al., 1971]. Kanamori and Anderson [1975] give  $17 \times 17 \text{ km}^2$  as an average.
- $\tau$ : 100-300 years [Bonilla, 1973].
- Tabas, September 16, 1978, 15:36:56, 33.39, 57.43
- M<sub>s</sub>=7.4 ( NEIS, 12 observations )
- Moment:  $M_0=1.5 \times 10^{27}$  dyne-cm [Niazi and Kanamori, 1981].
- L and W: L=65 km from the aftershock area [Berberian, 1979]. W=20 km is used from figure 2 of Berberian [1979].
- $\tau > 1100$  years [Berberian, 1979].

Tango, March 7, 1927, 09:27:36, 35.75, 134.75

$M_s=7.6$ ,  $m_B=7.6$  [Abe, 1981].

Moment: Kanamori and Anderson [1975] give  $M_0=4.6 \times 10^{26}$  dyne-cm on the basis of Kasahara [1957] and Kanamori [1973].

L and W: L=35 km is from the aftershock area determined by Nasu [1935]. W=13 to 15 km is used by Kasahara [1957] and Kanamori [1973] to interpret the geodetic data.

t: Matsuda [1977] gives 3 to  $6 \times 10^4$  years. However, Matsuda (written communication, 1982) states that this value is very uncertain. Matsuda believes that it is longer than 2000 years.

Tangshan, July 27, 1976, 19:42:54, 39.6, 117.9

$M_s=7.8$  [Abe, 1981], NEIS gives 7.9

Moment:  $M_0=1.8 \times 10^{27}$  dyne-cm [Butler et al., 1979].

L and W: Butler et al. [1979] give L=140 km on the basis of the extent of the aftershock area determined from teleseismic data. However, this is probably an overestimate because of the errors involved in teleseismic data. Chinese local data indicate L=80 km, if the aftershocks of the largest aftershock are removed. W=15 km is assumed.

t: Since there seems to have been no historical earthquake on the same fault, the recurrence interval is probably more than 2000 years.

Tottori, September 10, 1943, 08:36:53, 35.25, 134.00

$M_s=7.4$ ,  $m_B=7.1$  [Abe, 1981].

Moment:  $M_0=3.6 \times 10^{26}$  dyne-cm [Kanamori, 1972].

L and W: L=33 km is estimated from the aftershocks located by Omote [1955]. Kanamori [1972] used L=33 km and W=13 km to interpret the geodetic data.

t: Matsuda [1977] gives 2 to  $6 \times 10^4$  years. However, Matsuda (written communication, 1982) states that this value is very uncertain. Matsuda believes that  $\tau > 2000$  years. Okada et al. [1981] give 4000 to 8000 years. Tsukuda [1984] gives 6000 years.

**Acknowledgements.** We thank T. Heaton, S. Honda, T. Matsuda, J. Pechmann, David Schwartz, K. Sieh, and S. Wesnousky for discussion and comments on the manuscript. This research was partially supported by U. S. Geological Survey contracts 14-08-0001-G-979 and 14-08-0001-21981. Contribution number 4245, Division of Geological and Planetary Sciences, California Institute of Technology, Pasadena, California 91125.

#### References

Abe, K., A fault model for the Niigata earthquake of 1964, *J. Phys. Earth*, 23, 349-366, 1975.

Abe, K., Dislocations, source dimensions and stresses associated with earthquakes in the Izu peninsula, Japan, *J. Phys. Earth*, 26, 253-274, 1978.

Abe, K., Magnitude of large shallow earthquakes from 1904 to 1980, *Phys. Earth Planet. Inter.*, 27, 72-92, 1981.

Aki, K., Generation and propagation of G waves from the Niigata earthquake of June 16, 1964. Part 2. Estimation of earthquake moment, from the G wave spectrum, *Bull. Earthquake Res. Inst. Tokyo Univ.*, 44, 73-88, 1966.

Allen, C. R., Geological criteria for evaluating seismicity, *Geol. Soc. Am. Bull.*, 86, 1041-1057, 1975.

Allen, C. R., and J. M. Nordquist, Foreshock, main shock, and larger aftershocks of the Borrego Mountain earthquake, The Borrego Mountain Earthquake of April 9, 1968, *U.S. Geol. Sur. Prof. Pap.*, 787, 16-23, 1972.

Allen, C. R., G. R. Engen, T. C. Hanks, J. M. Nordquist, and W. R. Thatcher, Main shock and larger aftershocks of the San Fernando earthquake, February 9 through March 1, 1971, *U.S. Geol. Sur. Prof. Pap.*, 733, 17-20, 1971.

Ambraseys, N. N., Some characteristic features of the Anatolian fault zone, *Tectonophysics*, 9, 143-165, 1970.

Ando, M., Faulting of the Mikawa earthquake of 1945, *Tectonophysics*, 22, 173-186, 1974.

Ando, M., Slip rates and recurrence times from analysis of major earthquakes on Pacific-North American plate boundary in western North America, *EOS. Trans. AGU*, 58, 438, 1977.

Archuleta, R. J., A faulting model for the 1979 Imperial Valley earthquake, *J. Geophys. Res.*, 89, 4559-4585, 1984.

Bakun, W. H., and T. V. McEvilly, Recurrence models and Parkfield, California, earthquakes, *J. Geophys. Res.*, 89, 3051-3058, 1984.

Bakun, W. H., Clark, M. M., Cockerham, R. S., Ellsworth, W. L., Lindh, A. G., Prescott, W. H., Shakal, A. F., and Spudich, P., The 1984 Morgan Hill, California, earthquake, *Science*, 225, 288-291, 1984.

Ben-Menahem, A., Renormalization of the magnitude scale, *Phys. Earth Planet. Inter.*, 15, 315-340, 1977.

Ben-Menahem, A., and M. N. Toksoz, Source mechanism from spectrum of long-period surface waves. 2. The Kamchatka earthquake of November 4, 1952, *J. Geophys. Res.*, 68, 5207-5222, 1963.

Benioff, H., Mechanism and strain characteristics of the White Wolf fault as indicated by the aftershock sequence, in *Earthquakes in Kern County, California, During 1952*, edited by G. B. Oakesshott pp. 199-202, Division of Mines, State of California, 1955.

Benioff, H., Movements on major transcurrent faults, in *Continental Drift*, edited by S.K. Runcorn, pp. 103-134, Academic Press, London, 1962.

Berberian, M., Earthquake faulting and bedding thrust associated with the Tabas-e Golshan (Iran) earthquake of September 16, 1978, *Bull. Seismol. Soc. Am.*, 69, 1861-1887, 1979.

Berberian, M., I. Asudeh, R. G. Bilham, C. H. Scholz, and C. Soufleris, Mechanism of the main shock and the aftershock study of the Tabas-Golshan (Iran) earthquake of September 16, 1978: A preliminary report, *Bull. Seismol. Soc. Am.*, 69, 1851-1859, 1979.

Bonilla, M. G., Trench exposures across surface fault ruptures associated with the San Fernando earthquake, in *San Fernando earthquake of February 9, 1971*, edited by L. M. Murphy, pp. 173-182, NOAA, Washington, D. C., Vol. 3, 1973.

## 234 EARTHQUAKE REPEAT TIME AND STRESS DROP

- Boore, D. M., Stochastic simulation of high-frequency ground motions based on seismological models of the radiated spectra, *Bull. Seismol. Soc. Am.*, 54, 1865-1894, 1983.
- Burdick, L. J., and G. R. Mellman, Inversion of the body waves from the Borrego mountain earthquake to the source mechanism, *Bull. Seismol. Soc. Am.*, 66, 1485-1499, 1976.
- Butler, R., Surface wave analysis of the 9 April 1968 Borrego Mountain earthquake, *Bull. Seismol. Soc. Am.*, 73, 879-883, 1983.
- Butler, R., G. S. Stewart, and H. Kanamori, The July 27, 1976 Tangshan, China earthquake - A complex sequence of intraplate events, *Bull. Seismol. Soc. Am.*, 69, 207-220, 1979.
- Chinnery, M. A., The strength of the earth's crust under horizontal shear stress, *J. Geophys. Res.*, 69, 2085-2089, 1964.
- Clark, M. M., A. Grantz, and M. Rubin, Holocene activity of the Coyote Creek fault as recorded in sediments of Lake Cahuilla, *U.S. Geol. Surv. Prof. Pap.*, 787, 190-207, 1972.
- Cockerham, R. S., and J. P. Eaton, The April 24, 1984 Morgan Hill earthquake and its aftershocks: April 24 through September 30, 1984, in *The 1984 Morgan Hill, California Earthquake*, edited by J. H. Bennett and R. W. Sherburne, pp. 215-236, California Department of Conservation, Sacramento, Calif., 1985.
- Deng Q., Chen S., Song F., Zhu S., Wang Y., Zhang W., Jiao D., P. Molnar, B. C. Burchfiel, I. Ryoden, and Zhang P., The behavior and formation mechanism of Nanxihuashan fault zone and Haiyuan earthquake fault of 1920 in China, paper presented at the 5th Ewing Symposium on Earthquake Source Mechanics, May 20-24, 1985, Harriman, N. Y., 1985.
- Doser, D., Source parameters and faulting processes of the 1959 Hebgen Lake, Montana earthquake sequence, *J. Geophys. Res.*, 90, 4537-4556, 1985.
- Doser, D., and R. B. Smith, Source parameters of the October 28, 1983, Borah Peak, Idaho, earthquake from body wave analysis, *Bull. Seismol. Soc. Am.*, 75, in press, 1985.
- Eaton, J. P., M. E. O'Neil, and J. N. Murdock, Aftershocks of the 1966 Parkfield-Cholame, California, earthquake: A detailed study, *Bull. Seismol. Soc. Am.*, 60, 1151-1197, 1970.
- Ekstrom, G., Centroid-moment tensor solution for the April 24, 1984 Morgan Hill, California, earthquake, in *The 1984 Morgan Hill, California Earthquake*, edited by J. H. Bennett and R. W. Sherburne, pp. 209-213, California Department of Conservation, Sacramento, Calif., 1985.
- Gutenberg, B., and C. F. Richter, Earthquake magnitude, intensity, energy and acceleration, *Bull. Seismol. Soc. Am.*, 46, 105-145, 1956.
- Hamilton, R. M., Aftershocks of the Borrego Mountain earthquake from April 12, 1968, The Borrego Mountain Earthquake of April 9, 1968, *U. S. Geol. Surv. Prof. Pap.*, 787, 31- 54, 1972.
- Hanks, T. C., and R. K. McGuire, The character of high frequency strong ground motion, *Bull. Seismol. Soc. Am.*, 71, 2071-2095, 1981.
- Hartzell, S. H., and T. H. Heaton, Inversion of strong ground motion and teleseismic waveform data for the fault rupture history of the 1979 Imperial Valley, California, earthquakes, *Bull. Seismol. Soc. Am.*, 73, 1553-1583, 1983.
- Hartzell, S., and D. V. Helmberger, Strong-motion modeling of the Imperial Valley earthquake of 1979, *Bull. Seismol. Soc. Am.*, 72, 571-596, 1982.
- Heaton, T. H., and D. V. Helmberger, Generalized ray models of the San Fernando earthquake, *Bull. Seismol. Soc. Am.*, 69, 1311-1341, 1979.
- Iida, K., Earthquake energy and earthquake fault, *J. Earth. Sci., Nagoya Univ.*, 7, 98-107, 1959.
- Johnson, C. E., and L. K. Hutton, Aftershocks and preearthquake seismicity, The Imperial Valley, California, Earthquake of October 15, 1979, *U. S. Geol. Surv. Prof. Pap.*, 1254, 59-76, pp. 451, 1982.
- Kanamori, H., Determination of effective tectonic stress associated with earthquake faulting. The Tottori earthquake of 1943, *Phys. Earth Planet. Inter.*, 5, 426-434, 1972.
- Kanamori, H., Mode of strain release associated with major earthquakes in Japan, *Ann. Rev. Earth Planet. Sci.*, 1, 213-239, 1973.
- Kanamori, H., The energy release in great earthquakes, *J. Geophys. Res.*, 82, 2981-2876, 1977.
- Kanamori, H., and D. L. Anderson, Theoretical basis of some empirical relations in seismology, *Bull. Seismol. Soc. Am.*, 65, 1073-1095, 1975.
- Kanamori, H., and J. W. Given, Use of long-period surface waves for rapid determination of earthquake-source parameters, *Phys. Earth Planet. Inter.*, 27, 8-31, 1981.
- Kanamori, H., and P. C. Jennings, Determination of local magnitude  $M_L$ , from strong motion accelerograms, *Bull. Seismol. Soc. Am.*, 68, 471-485, 1978.
- Kanamori, H., and J. Regan, Long-period surface waves generated by the Imperial Valley earthquake of 1979, in *The Imperial Valley California earthquake of October 15, 1979*, pp. 55-58, *U. S. Geol. Surv. Prof. Pap.*, 1254, 1982.
- Kanamori, H., and G. S. Stewart, Seismological aspects of the Guatemala earthquake of February 4, 1976, *J. Geophys. Res.*, 83, 3427-3434, 1978.
- Kasahara, K., The nature of seismic origins as inferred from seismological and geodetic observations, 1, *Bull. Earthquake Res. Inst. Tokyo Univ.*, 35, 473-532, 1957.
- Kayano, I., Determination of origin times, epicenters and focal depths of aftershocks of the Niigata earthquake of June 16, 1964, *Bull. Earthquake Res. Inst. Tokyo Univ.*, 46, 223-269, 1968.
- Kelleher, J., and J. Savino, Distribution of seismicity before large strike slip and thrust-type earthquakes, *J. Geophys. Res.*, 80, 260-271, 1975.
- Langer, C. J., J. P. Whitcomb, and A. Aburto Q., Aftershocks from local data, The Guatemalan earthquake of February 4, 1976, A Preliminary Report, *U. S. Geol. Surv. Prof. Pap.*, 1002, 30-37, 1976.
- Lee, W. H. K., D. G. Herd, V. Cagnetti, W. H. Bakun, and A. Rapport, A preliminary study of the Coyote Lake earthquake of August 6, 1979 and its major aftershocks, *U.S. Geol. Surv., Open File Rep.*, 79-1621, 1979.
- Lisowski, M., and W. Thatcher, Geodetic determination of horizontal deformation associated with the Guatemala earthquake of 4 February 1976, *Bull. Seismol. Soc. Am.*, 71, 845-856, 1981.
- Liu, H-L., and D. V. Helmberger, The near-source ground motion of the 6 August 1979 Coyote Lake, California, earthquake, *Bull. Seismol. Soc. Am.*, 73, 201-218, 1983.
- Matsuda, T., Magnitude and recurrence interval of earthquakes from a fault, *J. Seismol. Soc. Jpn.*, 28, 269-282, 1975a.
- Matsuda, T., Active fault assessment for Irozaki fault system, Izu Peninsula (in Japanese), in *Research Report on Investigation of the Damage Caused by the 1974 Izu-Hanto-Oki Earthquake*, pp. 121-125, Earthquake Res. Inst. Tokyo Univ., Tokyo, 1975b.

- Matsuda, T., Estimation of future destructive earthquakes from active faults on land in Japan, *J. Phys. Earth.*, 25, S251-S260, 1977.
- Mogi, K., Development of aftershock areas of great earthquakes, *Bull. Earthquake Res. Inst. Tokyo Univ.*, 46, 175-203, 1968.
- Nakamura, K., K. Kasahara, and T. Matsuda, Tilting and uplift of an Island, Awashima, near the epicenter of the Niigata earthquake in 1964, *J. Geodetic Soc. Jpn.*, 10, 172-179, 1964.
- Nash, D. B., Fault scarp morphology: Indicator of paleoseismic chronology, *U.S. Geol. Surv. Final Technical Report, Contract No. 14-08-0001-19109*, 132p., 1981.
- Nash, D. B., Morphological dating of fluvial terrace scarps and fault scarps near West Yellowstone, Montana, *Geol. Soc. Am. Bull.*, 95, 1413-1424, 1984.
- Nasu, N., Supplementary study on the stereometrical distribution of the aftershocks of the great Tango earthquake of 1927, *Bull. Earthquake Res. Inst. Tokyo Univ.*, 13, 325-399, 1935.
- Niazi, M., and H. Kanamori, Source parameters of 1978 Tabas and 1979 Qainat, Iran, earthquakes from long-period surface waves, *Bull. Seismol. Soc. Am.*, 71, 1201-1213, 1981.
- Okada, A., M. Ando, and T. Tsukuda, Trenches, late Holocene displacement and seismicity of the Shikano fault associated with the 1943 Tottori earthquake, in Japanese, *Ann. Rep. Disaster Prevention Inst., Kyoto Univ.*, 24, 1-22, 1981.
- Olsen, A. H., and R. J. Apsel, Finite faults and inverse theory with applications to the 1979 Imperial Valley earthquake, *Bull. Seismol. Soc. Am.*, 72, 1969-2001, 1982.
- Omote, S., Aftershocks that accompanied the Tottori earthquake of Sept. 10, 1943, *Bull. Earthquake Res. Inst. Tokyo Univ.*, 641-661, 1955.
- Plafker, G., Tectonic aspects of the Guatemala earthquake of 4 February 1976, *Science*, 93, 1201-1208, 1976.
- Plafker, G., Hudson, T., Bruns, T., and Rubin, M., Late Quaternary offsets along the Fairweather fault and crustal plate interactions in southern Alaska, *Can. J. Earth Sci.*, 15, 805-816, 1978.
- Purcaru, G., and H. Berckhemer, Quantitative relations of seismic source parameters and a classification of earthquakes, *Tectonophysics*, 84, 57-128, 1982.
- Richardson, R. S. H., and H. Nolle, Surface friction under time-dependent loads, *Wear*, 37, 87-101, 1976.
- Ruff, L., and H. Kanamori, Seismicity and the subduction process, *Phys. Earth Planet. Inter.*, 23, 240-252, 1980.
- Salyard, S. L., Pattern of offset associated with the 1983 Borah Peak, Idaho, earthquake and previous events, in *Proc. Workshop 28 on the Borah Peak, Idaho, earthquake*, edited by R. S. Stein and R. C. Bucknam, pp. 59-75, U.S. Geol. Surv. Open File Rep., 85-290, 1985.
- Savage, J. C., and L. M. Hastie, Surface deformation associated with dip-slip faulting, *J. Geophys. Res.*, 71, 4897-4904, 1966.
- Scholz, C. H., Scaling relations for strong ground motion in large earthquakes, *Bull. Seismol. Soc. Am.*, 72, 1903-1909, 1982.
- Scholz, C. H., and J. T. Engelder, The role of asperity indentation and ploughing in rock friction-1. Asperity creep and stick-slip, *Int. J. Rock Mech. Min. Sci. Geomech. (abstract)*, 13, 149-154, 1976.
- Schwartz, D. P., The Caribbean-North American plate boundary in Central America: New data on Quaternary tectonics, (abstract), *Earthquake Notes*, 55, 28, 1985.
- Schwartz, D. P., L. S. Cluff, and T. W. Donnelly, Quaternary faulting along the Caribbean-North American plate boundary in central America, *Tectonophysics*, 52, 431-445, 1979.
- Scott, W. E., K. L. Pierce, and M. H. Hait, Jr., Quaternary tectonic setting of the 1983 Borah Peak, Idaho, earthquake, central Idaho, *U.S. Geol. Surv. Open File Rep.*, 85-290, 1-16, 1985.
- Sharp, R. V., Variable rates of strike slip on the San Jacinto fault zone, *J. Geophys. Res.*, 86, 1754-1762, 1981.
- Shimamoto, T., and J. M. Logan, Laboratory friction experiments and natural earthquakes: An argument for long-term tests, *Tectonophysics*, 109, 165-175, 1984.
- Sibson, R. H., Frictional constraints on thrust, wrench, and normal faults, *Nature*, 249, 542-544, 1974.
- Sieh, K. E., Prehistoric large earthquakes produced by slip on the San Andreas fault at Pallett Creek, California, *J. Geophys. Res.*, 83, 3907-3939, 1978.
- Slemmons, D. B., Faults and earthquake magnitude, U.S. Army Engineer Waterways Experiment Station, Vicksburg, Miss., *Misc. Pap. 73-1, Rep. 6*, 129 pp., 1977.
- Stein, R. S., and S. E. Barrientos, The 1983 Borah Peak, Idaho, earthquake: Geodetic evidence for deep rupture on a planar fault, *U.S. Geol. Surv. Open File Rep.*, in press, 1985.
- Stein, R. S., and W. Thatcher, Seismic and aseismic deformation associated with the 1952 Kern County, California, earthquake and relationship to the Quaternary history of the White Wolf fault, *J. Geophys. Res.*, 86, 4913-4928, 1981.
- Tang, R., Huang, Z., Qian, H., Deng, T., Jiang, L., Ge, P., Liu, S., Cao, Y., and Zhang, C., On the recent tectonic activity and earthquake of the Xianshuihe fault zone, A Collection of Papers of International Symposium on Continental Seismicity and Earthquake Prediction, pp. 347-363, *Seismological Press*, Beijin, 1984.
- Tanimoto, T., and H. Kanamori, Linear programming approach to moment tensor inversion of earthquake sources and some tests on the three dimensional structure of upper mantle, *Geophys. J. R. Astron. Soc.*, in press, 1985.
- Tanna Fault Trenching Research Group, Trenching study for Tanna fault, Izu, at Myoga, Shizuoka prefecture, Japan, *Bull. Earthquake Res. Inst. Tokyo Univ.*, 58, 797-830, 1983.
- Tsukuda, T., Trenching of active faults in southwest Japan, (*abstract*), *Japan-China Symposium on Earthquake Prediction*, pp. 47-48, Tokyo University, Tokyo, 1984.
- Uhrhammer, R. A., Observations of the Coyote Lake, California earthquake sequence of August 6, 1979, *Bull. Seismol. Soc. Am.*, 70, 559-570, 1980.
- Wallace, R. E., Fault scarps formed during the earthquakes of October 2, 1915, in Pleasant Valley, Nevada, and some tectonic implications, *U.S. Geol. Surv. Prof. Pap.*, 1274A, 33, 1984.
- Wyss, M., Estimating maximum expectable magnitude of earthquakes from fault dimensions, *Geology*, 7, 336-340, 1979.
- Zhou, H., H-L. Liu, and H. Kanamori, Source processes of large earthquakes along the Xianshuihe fault in Southwestern China, *Bull. Seismol. Soc. Am.*, 73, 537-551, 1983a.
- Zhou, H-L., C. R. Allen, and Kanamori, H., Rupture complexity of the 1970 Tonghai and the 1973 Luhuo earthquakes, China, from P-wave inversion and relationship to surface faulting, *Bull. Seismol. Soc. Am.*, 73, 1585-1597, 1983b.

## LOW STRESS-DROP EARTHQUAKES IN THE LIGHT OF NEW DATA FROM THE ANZA, CALIFORNIA TELEMETERED DIGITAL ARRAY

James N. Brune,<sup>1</sup> Joe Fletcher,<sup>2</sup> Frank Vernon,<sup>1</sup> Linda Haar,<sup>2</sup>  
Tom Hanks,<sup>2</sup> and Jon Berger<sup>1</sup>

**Abstract.** Recent data from the Anza, California array (10 station 3-component 16 bit 250 samples per second, digitally telemetered array) offer the opportunity to test explanations of one of the earliest observations of high resolution spectral analysis of small earthquakes, namely the existence of small low stress drop events intermixed with events with stress drops comparable to expected effective stresses. Preliminary analysis of the Anza data suggests that the partial stress drop model of Brune (1970) may be an explanation for these events, but the results are somewhat confused by unknown attenuation effects, site effects, and possible contamination of spectra (for smaller events). It is suggested that very high stress drop events ( $> 300$  bars) may represent a third type of event where high stresses are caused by rapid quasi-static strain build-up.

### Introduction

Since the earliest days of high resolution spectral analysis of small earthquakes, a recurrent puzzle has appeared. Along with events with stress drops of the order of a hundred bars, there have occurred many events with very low stress drops, extending as low as 1/10 bar [Douglas and Ryall, 1972; Tucker and Brune, 1973; Tsujiura, 1981]. There is usually an apparent correlation of inferred stress drop with size. The mechanism by which such low stress-drop events can occur in the same environment as high stress-drop events has not been established. In this study we hope to use new high resolution data from the Anza telemetered digital array to better understand these events.

### Theoretical Models

There are two basic types of explanations for low stress drop events - partial stress drop models [Brune, 1970] and low effective stress models. Partial stress drop events might occur when the fault locks (heals) itself soon after the rupture passes so that the average slip over the fault cannot reach a value corresponding to the average dynamic stress drop over the whole fault, or when the stress release is not uniform and coherent over the whole fault plane, but rather is more like a series of multiple events with parts of the fault remaining locked. These complexities could occur as a result of asperities or barriers on the fault, or complex fault

plane geometry. This class of models could include some of the barrier models of Papageorgiou and Aki [1983a,b], breaking asperity models such as that of Hartzell and Brune [1977] and McGarr [1981], and more recent barrier models of McGarr (personal communication, 1985), Joyner and Boore [1981], and Stevens and Day [1985].

A common feature of all these partial stress drop models is the existence of an  $\omega^{-1}$  fall-off in the source spectrum for frequencies just above the corner frequency (corresponding to the overall fault dimension). This feature is caused by the fact that the fault, or parts of the fault, initially move toward a relatively large stress drop, i.e. have initial velocities which are large, but the fault motion is prevented from going to the corresponding equilibrium stress drop over the whole fault by the premature locking or the presence of asperities or barriers on the fault. This is illustrated by Figure 1 (after Figure 6.9, Brune [1976]) which is a schematic diagram of the average equivalent source time function for slip on the fault. The fault initially moves with a high velocity toward the equilibrium displacement indicated by the dashed line ( $\epsilon = 1$ ) but is prevented from reaching this position (for  $\epsilon = 0.1$  reaches only 10% of it). Diffraction around the fault causes the far-field displacement pulse to return to zero at a time approximately given by the dimension of the fault divided by the shear wave velocity, so that the far-field pulse has the shape indicated by the dotted line in Figure 1. The corresponding spectra are indicated in Figure 2 (taken from Figure 6.10 of Brune [1976]). Any far-field displacement pulse having approximately this shape will have an  $\omega^{-1}$  section in its spectrum. It is seen that for a very small partial stress drop event ( $\epsilon = .01$ ) there is a broad frequency band over which the spectrum falls off as  $\omega^{-1}$ , and has relatively much more high frequency energy than a complete stress drop event of the same moment (crosshatched area of equivalent spectrum).

Tucker and Brune [1973] noticed that there was a correlation between estimated stress drop and high-frequency spectral fall off and suggested that this might be a result of the smaller stress drop events corresponding to partial stress drops while the larger events,  $\Delta\sigma \sim 100$  bars, might correspond to total stress drop events. If we average the slopes in their data for events with  $\Delta\sigma > 100$  bars, we obtain an average slope of  $\gamma = 2.9$ , whereas if we average the slopes for events with  $\Delta\sigma < 2$  bars, we obtain an average slope of  $\gamma = 2$ , in agreement with the 1 unit difference in slope expected for the partial stress drop model. However, the absolute values of the fall-off are higher than predicted by simple theory and require a further explanation. In the Tucker and Brune [1973] study, only two stations at most were available for each event, and thus the statistical confidence in the results was low. For that reason it is important to check the results with an array having more stations, such as the Anza array. For some of

<sup>1</sup>Institute of Geophysics and Planetary Physics, Scripps Institution of Oceanography (A-025), University of California, San Diego, La Jolla, CA 92093

<sup>2</sup>U. S. Dept. of the Interior Geological Survey, 345 Middlefield Road, Menlo Park, CA 94025

## 238 LOW STRESS-DROP EARTHQUAKES

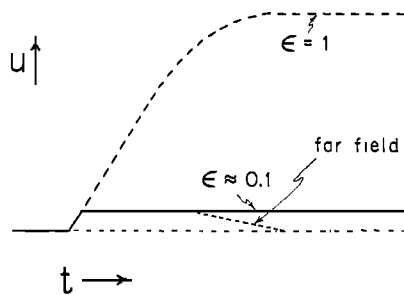


Fig. 1. Schematic diagram of the average equivalent source time function for slip on the fault (from Brune, 1976).

the larger San Fernando events, Tucker and Brune [1973] also pointed out evidence for an  $\omega^{-1}$  slope to the spectra extending to lower frequencies ( $\sim 1$  Hz), leading to high excitation of surface waves.

Savage [1965] proposed another explanation for an  $\omega^{-1}$  fall-off in the spectra for earthquakes with a large aspect ratio (long, thin faults) based on a kinematic Haskell model of fault slip. Although it is very likely that the effect of high aspect ratio occurs for large earthquakes which rupture the upper crust for long distances along the fault [Scholz, 1982], it is not likely to be appropriate for most small earthquakes where there is no clear mechanism for producing a high aspect ratio.

The other main type of dynamic models for explaining low stress drops can be classified as low effective stress models, i.e. the effective stress available for accelerating the fault is at all times low (not initially high, or high over parts of the fault as in the partial stress drop model). These types of models have spec-

trial shapes and far-field pulse shapes similar to that for large stress drop events, only the amplitudes are smaller (i.e. there is no  $\omega^{-1}$  fall-off in the spectrum just beyond the corner frequency — lower-most dashed line below crosshatching, Figure 2). In this model for small stress drop events, since the effective stress is very low, the particle velocities are very small, and the events approach what we might call "creep" events or "slow earthquakes" initiated by a rapid rupture propagation (so that the overall time duration is approximately the same as for large stress drop events). Although it would in one sense be appealing to accept this explanation, because we would not have to deal with "partial" stress drops, it raises a lot of questions. How can the effective stress for some events be more than 100 times smaller than for others in essentially the same region? Can the effective stress change so rapidly with time and/or position? Does it make sense to talk about earthquakes with total stress drops of 0.1 bars?

Lastly, we should consider the possibility that the observed low stress drop events are a result of experimental error and not real. The apparent corner frequencies for the smaller events might be caused by attenuation or filtering of high frequencies by propagation effects ( $Q$ , scattering) or site effects. Probably many investigators have dismissed the results for very low stress drop events for this reason. In order to confirm the results and to possibly test the different models, it is important to have a state-of-the-art data system, and this was one of the many motivations for setting up the Anza digital array.

#### The Anza Telemetry Digital Array

The Anza array is described in detail by Berger et al. [1984]. Only those features of the array important for the present study will be presented here. The overall objective was to install and operate a state-of-the-art digital array in a region of high seismi-

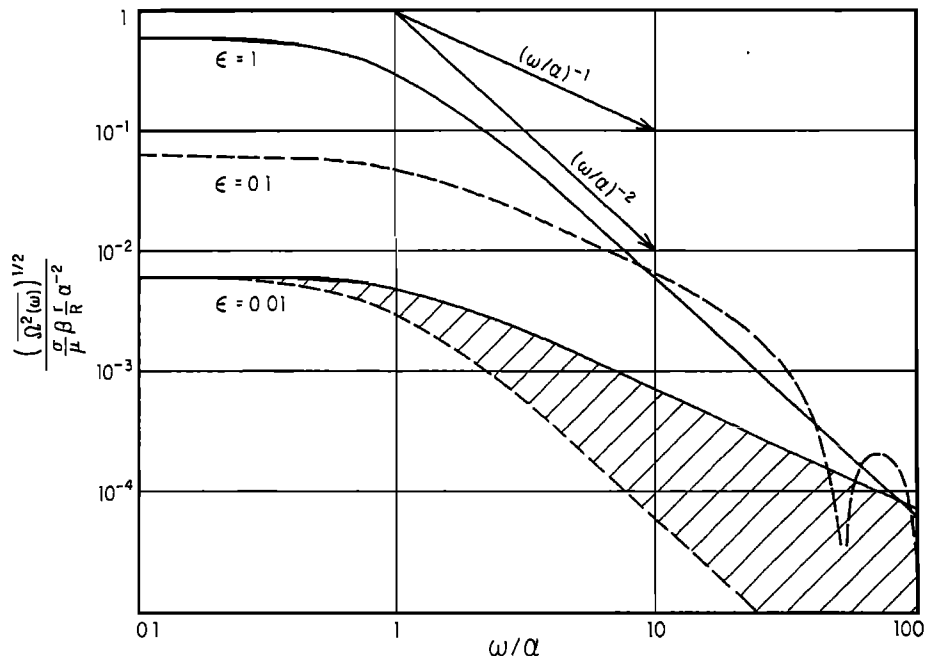


Fig. 2. Far-field spectra for various values of  $\epsilon$ . The crosshatched area represents the part of the spectra which is important in distinguishing between the partial stress drop model (e.g.,  $\epsilon = 0.01$ ) and Orowan's model ( $\epsilon = 1$ ) (from Brune, 1976).

Table 1.

	$\bar{\gamma}$ (average slope)	$\Delta\gamma$ (standard deviation)	$\epsilon$ (no. of readings)	(standard error of mean)
High stress drop events	3.67	.57	43	.09
Low stress drop events	2.52	.63	304	.04
Difference	1.15			

city, low attenuation, and structural simplicity so that wave forms from earthquakes would be as little distorted as possible. The region of the array includes the San Jacinto fault zone with several branches to the southeast. The structure is simple in the sense that the basic structure throughout the array consists of granitic rocks of the Peninsular Range batholith, which we would expect to be relatively uniform and to have low attenuation. The state-of-the-art features of the array include: 10 3-component stations, 16 bit, 250 samples per second. Our basic gain level is set so as to record on-scale events of  $M_L \sim 3-4$  and to record an average of a few events per week. However, for one week we recorded at 128 times higher sensitivity to record much smaller events, which included many apparently very low stress drop events, with computed stress drops of the order of 0.1 bars. These data, when compared with data for higher stress drop events ( $\sim 100$  bars) recorded during normal operation of the array, constitute the data of interest for this study.

#### Routine Processing of Anza Data and Preliminary Results for Stress Drops

The processing of data for the Anza array and initial interpretation of source parameters are given by Fletcher et al. [1985]. One of the parameters routinely calculated is stress drop, based on the Brune [1970, 1971] models with corner frequency in the spectrum,  $f_0$ , and a long period level,  $\Omega_0$ , proportional to seismic moment. Fletcher et al. [1985] state that for a suite of 11 events the average relative uncertainty in estimating the corner frequency and source dimension was 0.16 for  $P$  waves and 0.12 for  $S$  waves, remarkably small compared to some other studies. The inferred source radii vary by only about a factor of 2 to 3 over the suite of events studied (moments from about  $10^{17}$  to  $10^{21}$  dyne-cm). The average uncertainty for estimating stress drop is about 53% of the mean.

Estimated stress drop versus depth is indicated in Figure 11a of Fletcher et al. [1985]. Results from different clusters of events are indicated by different symbols. It will be noticed that at depths of about 8½ km, 11 km, and 13 to 14½ km, there are events with estimated stress drop of about 100 bars. On the other hand, over the same depth range, and in some of the same clusters, there are some events with estimated stress drops of less than 1 bar. The explanation for the great range in stress drop is

the focus of this study. Fletcher et al. [1985] show that for the Anza data, there is a strong dependence of stress drop on moment and at the same time a clear increase of source radius with moment for larger events, but with a cut-off radius of about  $7 \times 10^3$  cm (70 meters) similar to that found in previous studies [Archuleta et al., 1982; Tucker and Brune, 1973]. This cut-off in source radius corresponds to a cut off in corner frequency of about 30 Hz and could be attributed to attenuation or site effects, or some source phenomenon. It is probably related to the  $f_{max}$  phenomenon reported by Hanks (1982) who attributed it to a site effect. The  $f_{max}$  phenomenon has also been explained as a source effect [Papageorgiou and Aki, 1983a,b]. Fletcher et al. [1985] consider  $f_{max}$  as a station effect and estimate it for stations PFO, KNW, and RDM as 32 Hz, 38 Hz, and 50 Hz, respectively. Thus, any results inferring stress drop for events with corner frequencies much higher than 20 Hz will be in question. Nevertheless, there are enough data to make some preliminary estimates of the differences between high and low stress drop events.

#### Preliminary Results for $\gamma$ from Anza Data

Initially two sets of data were selected for analysis, one set consisting of five events with stress drops of about 100 bars and a second set with 27 events with stress drops between 0.1 and 2 bars. The high frequency asymptote on a log-log plot were fit by eye with a straight line for all spectra which appeared to be reasonably approximated in this manner. Each horizontal component was considered an independent measurement (the vertical component was considered separately). The results for the horizontal components were (where  $\gamma$  is equal to power of high-frequency fall-off, i.e., slope on log-log plot) (Table 1). The difference is consistent with the low stress drop events having a lower fall-off than high stress drop events by the difference expected between partial stress drop and total stress drop events, but the fall-off for both is about a power of about 1.5 greater than predicted, and remains to be explained. This selection of a bimodal sample of stress drops is purely for convenience to emphasize the differences. We checked intermediate stress drop events also, but we do not report the results here. There is a range of stress drops bridging the gap.

A careful analysis of the data revealed that certain stations seemed to reflect site effect distortions in their signals. Stations

Table 2.

	$\bar{\gamma}$ (average slope)	$\Delta\gamma$ (standard deviation)	$\epsilon$ (no. of readings)	(standard error of mean)
High stress drop events	3.59	.44	29	.08
Low stress drop events	2.32	.61	151	.05
Difference	1.27			

## 240 LOW STRESS-DROP EARTHQUAKES

WMC, LVA, CRY, and SND consistently showed lower average corner frequencies and/or higher-frequency fall-offs than others, and their signals appeared less pulselike and more distorted. In order to test the stability of the above result we decided to look at the results with data from these stations removed.

Considering only stations RDM, KNW, PFO, BZN, and FRD gave the results shown in Table 2.

Thus, eliminating the questionable stations has slightly changed the average high-frequency fall-offs, but the difference between the high stress drop and low stress drop events remains.

## Interpretations

The basic observation of importance here is that for a suite of about 30 events, interpreted by Fletcher et al. [1985] as having low stress drops ( $\sim 0.1$  bar to  $1.0$  bar), the average high-frequency spectral fall-off,  $\gamma$ , is approximately 1 unit less than for a suite of five events interpreted as having high stress drops ( $\sim 100$  bars). Although we need more high stress drop events before we can be sure of the statistical validity of this result, we feel that the data are reliable enough to warrant a preliminary interpretation.

The difference in  $\gamma$  between the high stress drop and low stress drop events can be explained if the high stress drop events represent total effective stress drop and the lower stress drop events represent partial stress drop events; however, this leaves unexplained why the fall-off parameter  $\gamma$  is so high for both groups of events. Simple theory without attenuation would have predicted that the high stress drop events would have had  $\gamma = 2$  and the low stress drop events  $\gamma = 1$ , whereas the actual average values are approximately 3.5 and 2.5 respectively, about 1.5 units in  $\gamma$  too high. Until this effect is understood there will remain some doubt about the interpretation.

## Effect of Attenuation

One explanation for the higher  $\gamma$  values could be the effect of attenuation of higher frequencies, especially since no  $Q$  corrections were made for these spectra. If the attenuation is represented by a constant  $Q$  model ( $Q$  independent of frequency), and if the exponential corner (on a log-log plot) is in the neighborhood of the corner frequencies (10–20 Hz), then the added experimental fall-off in the spectra could cause the inferred values for  $\gamma$  to be too high. At the suggestion of John Anderson (personal communication, 1985), this explanation was tested by estimating slopes on synthetic spectra with an exponential decay factor of 0.01 s ( $A \sim \exp(-0.01\omega)/2$ ). The inferred slopes were increased about 1 unit in  $\gamma$  for the  $\omega^{-2}$  model and about 2 units in  $\gamma$  for the  $\omega^{-1}$  model. Thus the effect of a  $t^*$  of about 0.01 s works in the right direction. It is clear that the effect of some high-frequency attenuation mechanism could increase the estimated high-frequency slopes. This likely explains the lower average fall-offs in the Tucker and Brune [1973] data, since they corrected for  $Q$  before measuring slopes.

## Other Explanations for the Anomalous One-Unit in the Power of the Spectral Fall-off

Above we have suggested that the explanation for the average observed spectral fall-off being 1.5 units higher than predicted may be due to attenuation or site effects. It is also possible that it is a source effect. If we view the fault rupture from a kinematic rather than a dynamic point of view, then there are several effects which lead to a higher spectral fall-off. If we make the slip on the

fault build up gradually, and the rupture front begins at a point and spreads out, then a plausible kinematic representation will have the far-field radiation build up as a quadratic in the time domain and fall off as  $\omega^{-3}$  at high frequencies in the spectral domain [Savage, 1972, 1974]. Unfortunately, we have no way of telling the frequency at which the fall-off will occur because we do not know the detailed form of the slip function nor the rupture progression. In the true dynamic rupture, the slip function is likely to vary with position and the rupture front is likely to accelerate and decelerate. Nevertheless, the kinematic perspective allows us to see how real ruptures might have  $\omega^{-3}$  fall-offs in the far field. Such fall-offs could also be a result of the slip weakening and energy absorption as suggested by Papageorgiou and Aki (1983a,b). If the higher spectral fall-off is a source effect rather than an attenuation effect, the partial stress drop concept could still remain as the explanation for the difference in fall-off between the low stress drop and high stress drop events.

## Preliminary Estimates of the Effect of Attenuation at Anza

As mentioned earlier, one of the reasons for choosing the Anza site was the expectation that attenuation at Anza would be low as a consequence of the relatively homogeneous crystalline rocks on both sides of the fault. An indication of a small  $Q^{-1}$  (high  $Q$ ) is supported by the fact that we measure appreciable seismic energy up to 100 Hz at epicentral ranges out to 30 or 40 km. Very simple shear wave pulses are also observed with relatively little scattered energy. With this in mind we estimated  $Q^{-1}$  using a spectral ratio technique similar to the one used for data in the Imperial Valley by Singh et al. [1982]. However, we did not compute theoretical seismograms to check the geometrical spreading as they did, and thus we assumed that geometrical spreading introduced an  $R^{-1}$  distance dependence. We compare our results to other published values of  $Q^{-1}$  at different frequencies in Figure 3. We give results for all observed paths and for selected paths which pass only through crystalline rock, not crossing the main faults. The estimates of  $Q^{-1}$  in the Anza area appears to be higher (lower  $Q$ ) than other estimates shown in the figure throughout the frequencies of interest. There are several things to note however. The estimates of  $Q^{-1}$  taken from the literature are determined by three different methods. One method uses  $L_g$  phases, another is the Aki single station  $Q$  method, and the other is the spectral ratio method. To our knowledge there is no study which adequately compares these methods to each other. We plan to make estimates of  $Q$  using the single-station  $Q$  method as well as improving our spectral ratio results.

However, we believe that present results are adequate for preliminary interpretation of the results from Anza. The results indicate that  $Q$  increases with frequency approximately linearly, with an approximate formula  $Q = 12.9 + .11.8f$  as independently determined by Fletcher et al. (preprint, 5th Maurice Ewing Symposium, May, 1985, AGU [this volume]). Such a linear dependence of  $Q$  on frequency will not affect the spectral shape, but will only shift its level. Thus these preliminary results indicate that attenuation by propagation in the crust will not significantly distort the spectral shapes and thus will not effect the conclusions concerning high-frequency spectral fall-off.

The spectral ratio method, however, cannot determine attenuation effects common to all recording sites since these effects will cancel out in the ratio. For example, a site-effect attenuation common to both sites for any given ratio might result from a near surface weathered layer at both sites, and thus not be determined by this method.

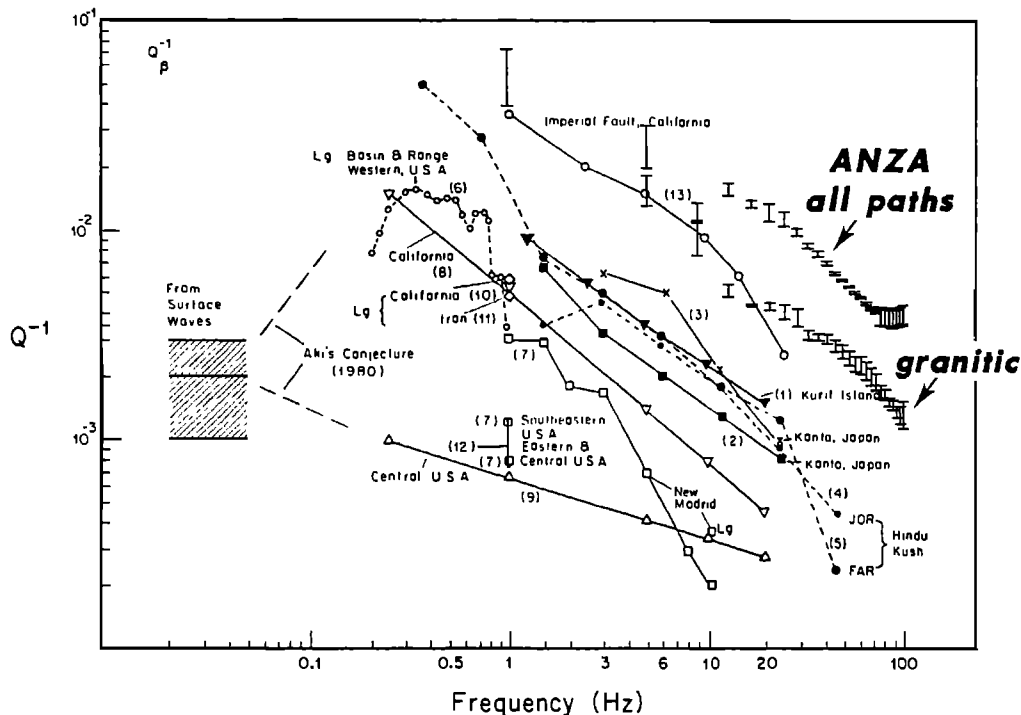


Fig. 3. A collection of  $Q^{-1}$  versus frequency measurements. The results from the Anza area are indicated with those for purely granitic path shown separately.

#### Possible Site-Effect Attenuation

One would expect that site-effect attenuation would be small for recording sites in granitic rocks such as those at Anza. However, an attenuating surface layer due to weathering and fracturing of the granite might be present and would be difficult to establish for certain without drilling. A recent method for estimating this effect based on an assumed  $\omega^{-2}$  model for larger earthquakes has been presented by Anderson and Hough [1984] and Anderson [this volume]. They have applied their technique to data for earthquakes outside the Anza array and have obtained results indicating that site attenuation effects are lower at Anza than at any of the other sites they studied, and, using their data, are not significantly different from zero ( $\kappa_0$  in their model not significantly different from zero). Their method does not yield any estimate of the  $Q$  component which is a linear function of frequency, and thus does not "see" the kind of  $Q^{-1}$  dependence shown in Figure 3. The projected value of  $Q$  for very high frequencies (near 50 Hz) in Figure 3 is of the order of 1000, and thus may represent the approximate "constant  $Q$ " portion of the attenuation at Anza. This high value is consistent with the low estimates of  $\kappa_0$  by Anderson and Hough [1984] (not significantly different from zero).

Thus we conclude that the preliminary evidence at Anza suggests that attenuation will not effect the conclusions presented here. The final interpretation will have to await better determination of attenuation and site effects for the Anza region, perhaps using drill holes to penetrate the surface layer. Based on these preliminary results from the Anza array we conclude that the spectra are consistent with inferred low stress drop events being

partial stress drop events, while the few higher stress drop events ( $\Delta\sigma \sim 100$  bars) have spectra consistent with a complete effective stress drop, provided an additional high-frequency fall-off of about 1 to 1.5 in  $\gamma$  is attributed at present to unknown path attenuation or site effects, or unknown source mechanism effects.

#### P-Wave Spectra

For the set of data analyzed here, the average corner frequency for  $P$  waves was higher than that for  $S$  waves and the high frequency fall-off was steeper, both for the high stress drop and low stress drop events. The results were:

For high stress drop events

$$\bar{f}_0 = 18.5; 1\sigma = 9; \bar{\gamma} = 3.8$$

For low stress drop events

$$\bar{f}_0 = 19.5; 1\sigma = 9; \bar{\gamma} = 3.2 \pm 1.1$$

Thus there is no significant difference in the average  $P$ -wave corner frequency for the high stress drop and low stress drop events, but there does seem to be a somewhat higher average fall-off of  $P$ -wave spectra for high stress drop events versus low stress drop events, similar to the result for  $S$  waves. The average  $P$ -wave corner frequencies are significantly higher than for  $S$  waves as observed in many studies [Molnar et al., 1973; Hanks, 1981].

The average high-frequency fall-off for  $P$  waves is higher than

## 242 LOW STRESS-DROP EARTHQUAKES

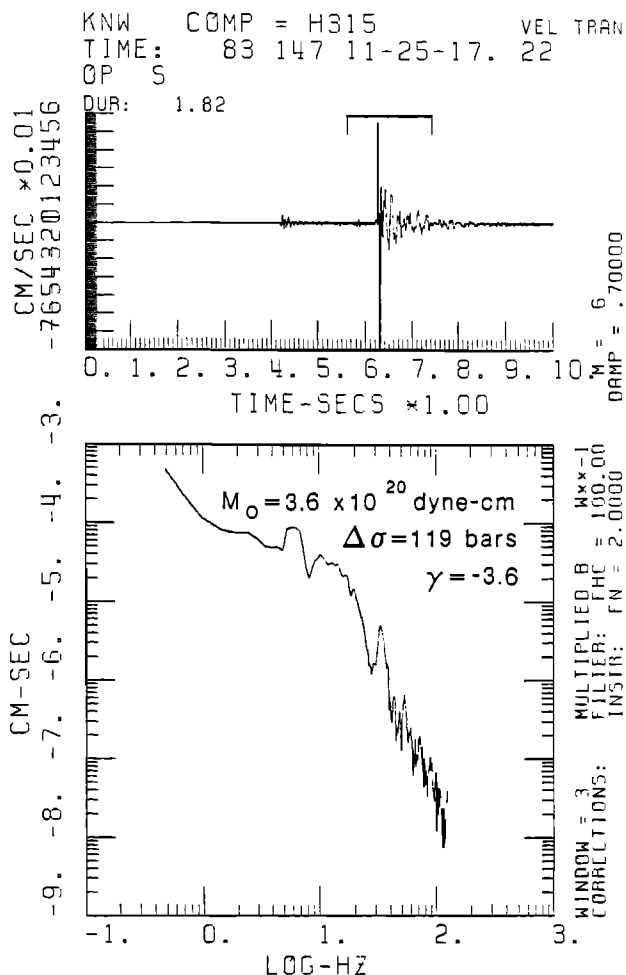


Fig. 4a. The pulse shape and amplitude spectrum for high stress drop event at KNW ( $\Delta\sigma \sim 100$  bars).

for S waves, for both the high stress drop (3.8 versus 3.6) and low stress drop (3.2 versus 2.5) events. This could be an effect caused by the average rupture velocity being closer to the shear wave velocity than the compressional velocity (Savage [1972, 1974]; Evernden et al., preprint 1985), or a result of different attenuation for P waves and S waves.

#### Plots of Data from KNW

Examples of a high stress drop and low stress drop event are shown in Figures 4-d from station KNW, which consistently records relatively simple pulses from earthquakes in the Hot Springs cluster (defined by Fletcher et al. [1985]). Comparison of events with different stress drops, but from the same cluster and recorded at the same station, should to first order eliminate path effects as an explanation for the differences. Figure 4a shows the pulse shape and amplitude spectrum for a high stress drop event ( $\Delta\sigma \sim 100$  bars) at KNW and Figures 4b-d show seismograms and spectra for low stress drop events at KNW. Figure 5 shows a comparison of 4a and 4d on the same plot. These figures illustrate

features often seen in these comparisons: the high stress drop event is a simple pulse with a well-defined corner frequency and relatively steep high-frequency fall-off, whereas many of the low stress drop events are more complex, both in the time and frequency domains, and obviously contain higher frequencies. However, these features are not universally common. In some cases there are relatively simple pulse shapes and spectra for low stress drop events, and sometimes complicated pulse shapes and spectra for high stress drop events. Some of the same features of spectra were reported by Tsujiura [1981] for families of small earthquakes off the coast of Japan. Unfortunately, the number of high stress drop events is not yet sufficient to guarantee statistical reliability, and we must await further data before finally accepting these results.

#### Speculations on Very High Stress Drop Events

If the partial stress drop mechanism is accepted as the explanation of the events with low stress drop, then the events with stress drops near 100 bars represent "full" stress drop events, i.e., the stress has dropped the full amount available above friction, the

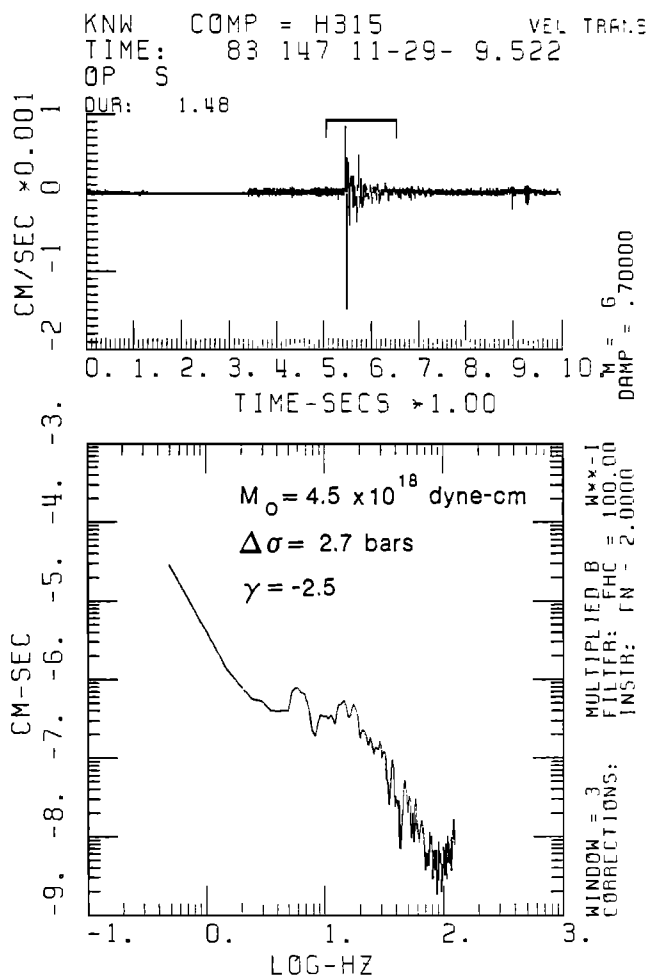


Fig. 4b. Seismogram and spectra for low stress drop event at KNW.

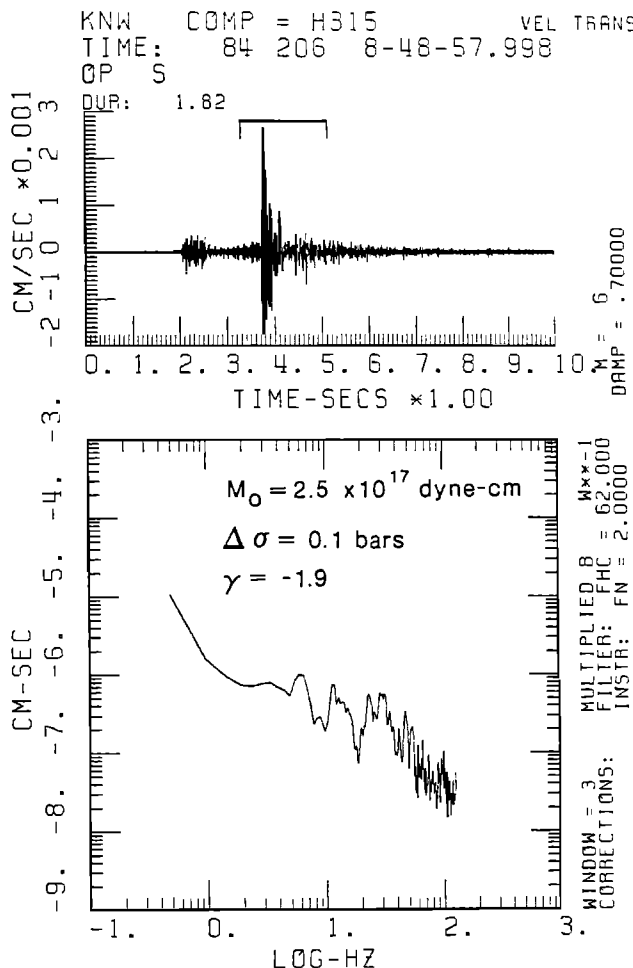


Fig. 4c. Seismogram and spectra for low stress drop event at KNW.

100 bars "effective" stress. This result would be consistent with rms stress drops determined by Hanks and McGuire [1981].

In a recent study, Munguia and Brune [1984a] found several events with stress drops of about 1 kilobar in the Victoria, Mexico earthquake swarm of March 1978, and in aftershocks of the Victoria, Mexico 1980 earthquake. In a later study, Munguia and Brune [1984b] found that the near-source strong motion records for the 1980 Victoria earthquake ( $M \sim 6.1$ ) could be simulated by summation of high stress drop subevents. The minimum number of events necessary to explain near-source strong motion records appears to be of the order of 1 for  $M < 5$  and of the order of 5–10 for magnitudes around 6 to 7, and perhaps of the order of 10–100 for  $M=8$ . It seems clear that the probability of very high stress drop subevents is higher the larger the main shock. Mori and Shimizaki [1984] interpreted strong motion records of the 1968 Tokachi-Oki ( $M_s = 7.9$ ) earthquake to indicate at least two very high stress drop subevents (~4 kilobars).

One interpretation of the occurrence of such very high stress drop events is, of course, that the slow process of tectonic stress build up produces large static stress concentrations on the fault,

possibly due to strength inhomogeneities (barriers or asperities), and that these high stress concentrations are relieved during the earthquake. Without more conclusive data we cannot rule out this explanation (i.e. strength variations). However, there is another possibility, i.e. that during the process of failure fault slip causes rapid quasi-static stress build up to levels much higher than could be maintained by the rocks on the time scale of long-term tectonic processes (implying frequency-dependent strength). If such a mechanism is applicable, then the very high stress drop events are indicative of rapid quasi-static fault slip and not necessarily indicative of regions which were under high stress long before the earthquake. Thus, in the Victoria 1978 earthquake swarm we can imagine quasi-static fault slip occurring over a time period of the order of hours to a day which repeatedly stresses parts of the fault system to the level of kilobars, resulting in high stress drop events, but after a few days the quasi-static slip has slowed to the point where stresses are no longer built up to the kilobar level. This mechanism is suggested in the Victoria swarm because it occurred in a region in which we would not have expected high stress drops, i.e., a region of high heat flow (high temperature),

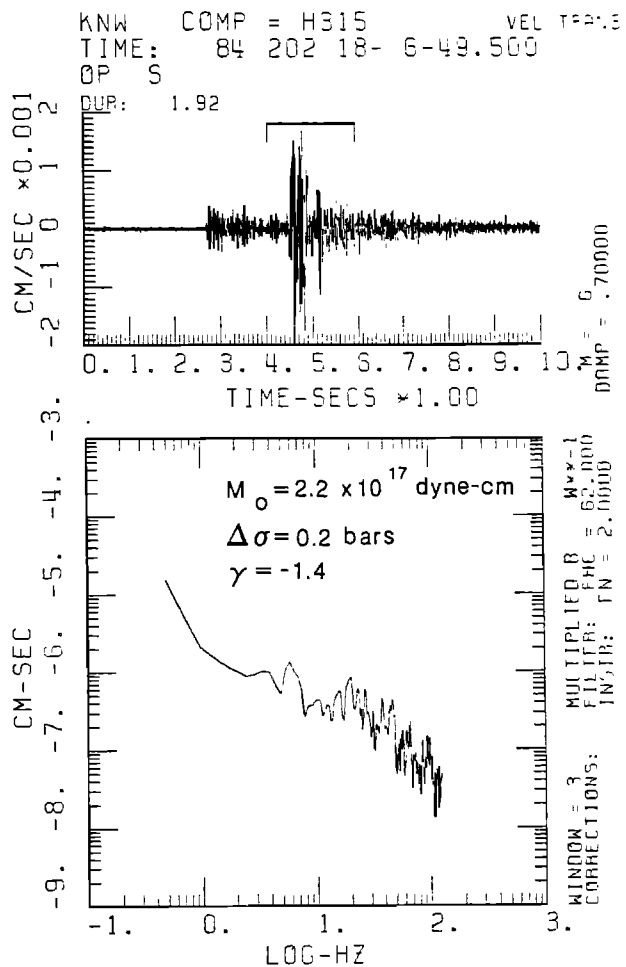


Fig. 4d. Seismogram and spectra for low stress drop event at KNW.

## 244 LOW STRESS-DROP EARTHQUAKES

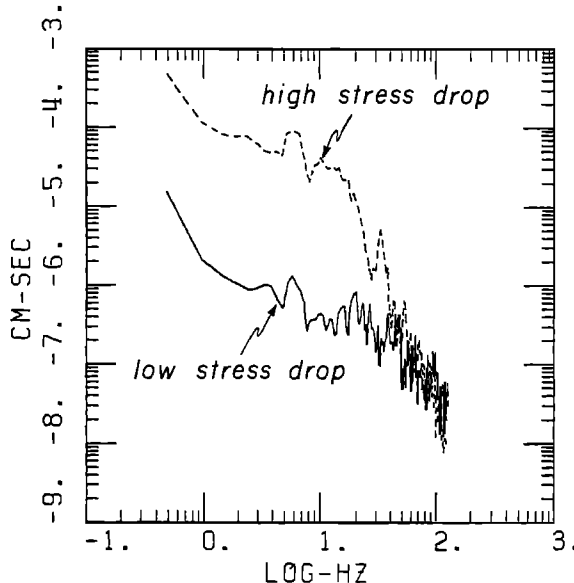


Fig. 5. Spectra of Figures 4a and 4d superimposed.

water saturation, intense faulting, basic rocks, and tectonic crustal spreading.

If the mechanism is common in earthquakes, it has important implications for source mechanism, strong motion, and earthquake prediction. It in effect suggests that the high stress drop subevents in large earthquakes may not imply corresponding high static stress fields prior to the earthquake. On the other hand the occurrence of very isolated high stress drop events or high stress drop foreshocks may be indicative of rapid quasi-static slip which could be precursory to a larger event.

### Three Classes of Earthquakes

If the above interpretations are correct, they suggest that stress drop events can be divided into at least three classes: partial stress drop events ( $\Delta\sigma < 100$  bars), full stress drop events ( $\Delta\sigma \sim 100$  bars), and "overstress" stress drop events with stress drops greater than the absolute effective stress which can be maintained over years of time ( $\Delta\sigma > 300$  bars).

### Conclusions

The interpretations suggested above must remain speculative until more data are obtained and possible sources of distortion and contamination of the spectra are better understood. Alternate obvious interpretations of the results cannot be rejected. Thus the main purpose of this paper is to stimulate future efforts by pointing to the range of possible alternatives still allowed by the data, to illustrate some of the differences which will need to be overcome, and to point out the potential of a state of the art digital seismic array.

To reach definitive conclusions we will probably have to:

1. Increase the observation to include a wider range of moments and source dimensions. This will require a number of larger events recorded on strong motion instruments.
2. Determine the effects of attenuation and scattering.

*Acknowledgment.* This research was supported by U.S. Geological Survey contract 14-08-001-21893.

### References

- Anderson, J. G., Implication of attenuation for studies of the earthquake source, this volume.
- Anderson, J. G., and S. E. Hough, A model for the shape of the Fourier amplitude spectrum of acceleration at high frequencies, *Bull. Seismol. Soc. Am.*, 74, 1969–1994, 1984.
- Archuleta, R. J., E. Cranswick, C. Mueller, and P. Spudich, Source parameters of the 1980 Mammoth Lakes, California earthquake sequence, *J. Geophys. Res.*, 87, 4559–4585, 1982.
- Berger, J., L. N. Baker, J. N. Brune, J. B. Fletcher, T. C. Hanks, and F. L. Vernon, The Anza array: a high dynamic-range, broad-band, digitally radio-telemetered seismic array, *Bull. Seismol. Soc. Am.*, 74, 1469–1682, 1984.
- Brune, J. N., Tectonic stress and the spectra of seismic shear waves from earthquakes, *J. Geophys. Res.*, 75, 4997–5009, 1970.
- Brune, J. N., Seismic sources, fault plane studies and tectonics, *EOS Trans. AGU*, 52, 178–187, 1971.
- Brune, J. N., The physics of earthquake strong motion, in *Seismic Risk and Engineering Decisions*, edited by C. Lomnitz and E. Rosenblueth, pp. 141–177, Elsevier, New York, 1976.
- Douglas, B. M., and A. Ryall, Spectral characteristics and stress drop for microearthquakes near Fairview Peak, Nevada, *J. Geophys. Res.*, 77, 351–359, 1972.
- Fletcher, J., L. Haar, T. Hanks, F. L. Vernon III, J. N. Brune, and J. Berger, The digital array at Anza, California: Processing and initial interpretation of source parameters, *J. Geophys. Res.*, in press.
- Fletcher, J., L. C. Haar, F. W. Vernon, J. N. Brune, T. C. Hanks, and J. Berger, The effects of attenuation on the scaling of source parameters for earthquakes at Anza, California, this volume.
- Hanks, T. C., The corner frequency shift, earthquake source models, and  $Q$ , *Bull. Seismol. Soc. Am.*, 71, 597–612, 1981.
- Hanks, T. C.,  $f_{\max}$ , *Bull. Seismol. Soc. Am.*, 72, 18677–1880, 1982.
- Hanks, T. C., and R. K. McGuire, The character of high-frequency strong ground motion, *Bull. Seismol. Soc. Am.*, 71, 2071–2096, 1981.
- Hartzell, S. H., and J. N. Brune, Source parameters for the January, 1975 Brawley-Imperial Valley earthquake swarm, *Pageoph.*, 115, 333–355, 1977.
- Joyner, W. B., and D. M. Boore, Peak horizontal acceleration and velocity from strong-motion records including records from the 1979 Imperial Valley, California earthquake, *Bull. Seismol. Soc. Am.*, 71, 2011–2038, 1981.
- McGarr, A., Analysis of peak ground motion in terms of a model of inhomogeneous faulting, *J. Geophys. Res.*, 86, 3901–3912, 1981.
- Molnar, P., B. E. Tucker, and J. N. Brune, Corner frequencies of  $P$  and  $S$  waves and models of earthquake sources, *Bull. Seismol. Soc. Am.*, 63, 2091–2104, 1973.
- Mori, J., and K. Shimizaki, High stress drops of short period subevents from the 1968 Tokachi-Oki earthquake as observed on strong motion records, *Bull. Seismol. Soc. Am.*, 74, 1529–1544, 1984.
- Munguia, L., and J. N. Brune, High stress drop events in the Victoria, Baja California, Mexico, earthquake swarm of 1978 March, *Geophys. J. R. Astron. Soc.*, 76, 725–752, 1984a.
- Munguia, L., and J. N. Brune, Simulations of strong ground motion for earthquakes in the Mexicali-Imperial Valley, *Geophys. J. R. Astron. Soc.*, 79, 747–771, 1984b.

- Papageorgiou, A. S., and K. Aki, A specific barrier model for the quantitative description of inhomogeneous faulting and the prediction of strong ground motion. Part I. Description of the model, *Bull. Seismol. Soc. Am.*, 73, 693–722, 1983a.
- Papageorgiou, A. S., and K. Aki, A specific barrier model for the quantitative description of inhomogenous faulting and the prediction of strong ground motion. Part II. Description of the model, *Bull. Seismol. Soc. Am.*, 73, 953–978, 1983b.
- Savage, J. C., The effect of rupture velocity upon seismic first motions, *Bull. Seismol. Soc. Am.*, 55, 263–275, 1965.
- Savage, J. C., Relation of corner frequency to fault dimensions, *J. Geophys. Res.*, 77, 3788–3795, 1972.
- Savage, J. C., Relation between P- and S-wave corner frequencies in the seismic spectrum *Bull. Seismol. Soc. Am.*, 64, 1621–1627, 1974.
- Scholz, D. H., Scaling laws for large earthquakes, consequences for physical models, *Bull. Seismol. Soc. Am.*, 72, 1–14, 1982.
- Singh, S. K., R. J. Apsel, J. Fried, and J. N. Brune, Spectral attenuation of SH-waves along the Imperial fault, *Bull. Seismol. Soc. Am.*, 72, 2003–2016, 1982.
- Stevens, J. L., and S. M. Day, The physical basis of  $m_b$ :  $M_S$  and variable frequency magnitude methods for earthquake/explosion discrimination, *J. Geophys. Res.*, 90, 3009–3020, 1985.
- Tsujiura, M., Activity mode of the 1980 earthquake swarm off the east coast of the Izu Peninsula, *Bull. Earthquake Res. Inst.*, 56, 1–24, 1981.
- Tucker, B. E., and J. N. Brune, Seismograms, S-wave spectra and source parameters for aftershocks of the San Fernando earthquake, pp. 69–121, in *San Fernando, California earthquake of February 9, 1971*, NOAA Special Report, 1973.

## RUPTURE OF THE VALPARAISO (CHILE) GAP FROM 1971 TO 1985

I. Korrat and R. Madariaga

Laboratoire de Sismologie, Institut de Physique du Globe de Paris and  
UER Sciences Physiques de la Terre, Université Paris VII, France.

**Abstract.** We discuss the seismicity near Valparaiso (Chile) from 1965 to 1985. This area was the site of a large  $M = 8.2$  earthquake on August 16, 1906, and had been identified as a gap by Kelleher. We performed a detailed study of all the body waves and some surface waves for all the shocks of  $M \geq 5.8$  which occurred in the gap since 1965. This analysis was necessary to separate the different populations of earthquakes that included several large (up to  $M = 7.5$ ) events of intraplate origin and a few events on the outer rise of the Nazca plate. From these studies a plausible scenario for the rupture of the Valparaiso gap is proposed. Rupture started with a large earthquake ( $M_0 = 5.6 \cdot 10^{20}$  Nm) on July 9, 1971 and continued with several large aftershocks and a medium sized ( $M_0 = 2.8 \cdot 10^{19}$  Nm) earthquake in October 5, 1973. The latter earthquake occurred at the southern end of the aftershock zone of the 1971 event. A large barrier appears to have impeded the propagation of rupture to the south of Valparaiso. We propose that the failure of this barrier initiated the March 1985 earthquake which was a relatively simple large event with a small foreshock of about 10% of the total moment release. The main event started 10 s after the foreshock with a very sharp onset and then propagated rapidly toward the south. From the aftershock area it appears that the earthquake propagated also toward the less stressed region to the north, rupturing almost halfway into the source area of the July 9, 1971 earthquake.

## Introduction

On March 3, 1985 a large earthquake of  $M_s = 7.8$  (P.D.E.) occurred under the coast of Central Chile producing severe damage. The area of the earthquake had been identified as a seismic gap by Kelleher [1972] based on the data collected by Lomnitz [1970] on the historical seismicity of Chile. McCann et al. [1979] had identified this zone as a gap of their category 2, i.e., a zone that had been the site of a great earthquake less than 100 but more than 30 years ago. Even more recently Nishenko [1985] estimated that this area

had the highest probability of recurrence for a large earthquake. The Valparaiso area of Central Chile ( $32^\circ\text{S}$  to  $35^\circ\text{S}$ ) had been the site of four major earthquakes in historic times: 1647, 1730, 1822, and 1906, giving a return period for major earthquakes of  $86 \pm 10$  years. The event of March 3, 1985 occurred within this time interval demonstrating that major gap-filling earthquakes in the Valparaiso area have an almost periodic temporal behavior. This is therefore an ideal site for the test of many ideas about earthquake cycles, gaps, and the study of rupture development before and after the major event of March 3, 1985.

The Central Chile area was the site of increased activity since 1971, specially in the northern part of the rupture zone of the Valparaiso earthquake of 1906. Several large earthquakes with magnitude from 6 to 7.5 occurred prior to the March 1985 event. The purpose of this study is to analyze these events in order to establish the main characteristics of the rupture process that started in July 9, 1971 with the La Ligua earthquake of  $M = 7.5$  and ended with the recent event of March 1985. The fault appears to have been prepared by the large shocks which occurred to the north in 1971 and 1973. The main event of 1985 was nucleated at the southern end of the 1973 source area and subsequently ruptured about 65% of the area of the 1906 event [Comte et al., 1986].

## Earthquakes in the Valparaiso Area 1965-1985

A map of the seismicity of the area between  $31^\circ\text{S}$  and  $36^\circ\text{S}$  is shown in Figure 1 for the period from January 1965 to March 3, 1985, just before the main shock. The seismicity before 1965 is very incomplete for this zone and the catalog is definitely nonhomogeneous since the number of regional stations in Chile and Western Argentina used for locations has steadily increased since 1965. All the events plotted are shallow to intermediate with reported depths between 4 and 114 km. Within this period of time six important earthquakes occurred in the area: March 28, 1965; July 9, 1971; October 5, 1973; March 23, 1981;

## 248 RUPTURE OF THE VALPARAISO (CHILE) GAP FROM 1971 TO 1985

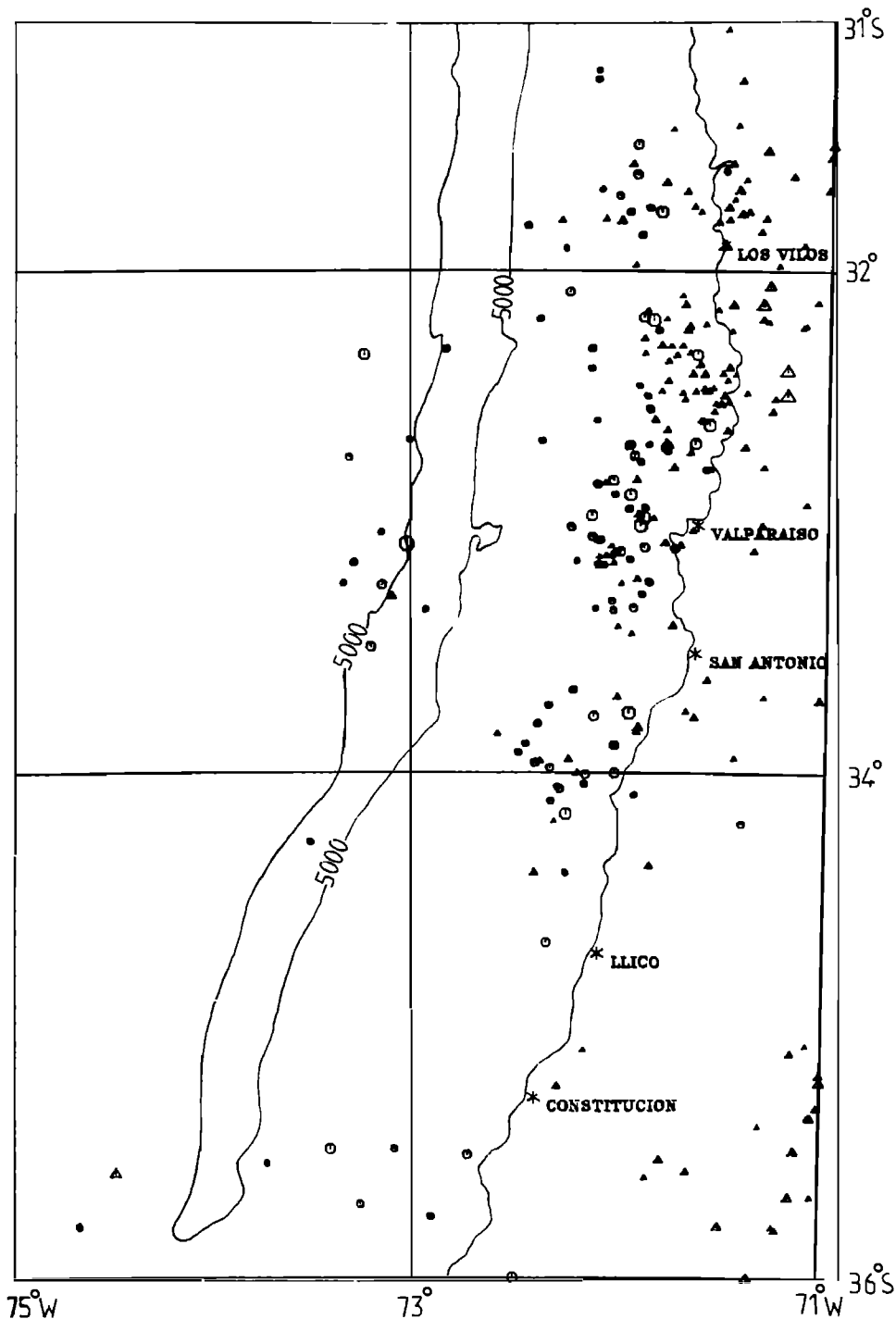


Fig. 1. Seismicity of Central Chile ( $M > 4.5$ ) from 1965 to March 3, 1985, just before the Valparaíso earthquake.

October 16, 1981; and November 7, 1981. The first two events were studied in detail by Malgrange et al. [1981] who showed that the first earthquake was an extensional event inside the subducted

plate and that the second one was a large shallow thrust earthquake. The event of October 5, 1973 is also a shallow thrust earthquake with an aftershock zone that extended to the south of

TABLE 1. Locations of the Studied Earthquakes

Nº	Date	Time	Lat. (S°)	Long. (W°)	Depth (km)		Ms	mb	Mechanism
					ISC	Modeling			
M1	March 28, 1965	16:33	32.40	71.20	68	72	7.5	6.4	T
1	Sept. 14, 1970	15:36	34.02	72.22	31	-	5.5	5.5	C
2	Sept. 19, 1970	6:37	33.56	71.95	22	24	5.6	5.4	C
M2	July 9, 1971	3:03	32.54	71.15	40	40	7.5	6.6	C
3	July 11, 1971	9:51	32.19	71.72	36	22	6.3	5.8	C
4	July 31, 1971	22:08	32.43	71.68	46	32	-	5.5	C
5	Sept. 25, 1971	13:05	32.40	73.06	4	-	5.8	5.5	T?
6	May 13, 1972	15:19	32.66	71.62	46	30	5.3	5.5	C
7	Oct. 5, 1973	5:45	32.92	71.88	8	23	6.5	5.7	C
8	Oct. 5, 1973	7:07	32.90	71.93	33	-	5.6	5.5	C
9	July 6, 1979	2:01	32.15	71.32	51	52	5.6	5.7	C
10	June 11, 1980	14:21	32.72	71.65	41	30	5.5	5.5	C
11	March 23, 1981	19:28	33.66	71.89	28	25	6.2	5.8	C
12	Oct. 16, 1981	3:25	33.13	73.07	18	30	7.2	6.2	C
13	Nov. 7, 1981	3:29	32.20	71.34	57	63.5	6.5	6.2	C
14	Dec. 15, 1981	20:02	31.62	71.92	42	-	-	5.1	T?
15	Feb. 25, 1982	21:59	33.30	73.09	27	-	-	5.2	C

Valparaiso. The earthquake of March 23, 1981 is a thrust interplate event but is much smaller than that of 1973. The event of October 16, 1981 occurred on the outer rise of the Nazca plate and was studied by Christensen and Ruff [1982]. The last event, of November 7, 1981, is a compressional event that occurred inside the subducted plate. This event is similar to that of March 28, 1965 [Malgrange and Madariaga, 1983]. Hypocenter information for all the important earthquakes that we studied is listed in Table 1. Several of these events are in fact aftershocks of the larger earthquakes of 1971, 1973, and 1981.

No evidence for long-term quiescence in the period from 1965 to 1985 is observed in Figure 1, except in the area from 34.5°S to 35°S which had a very low level of seismicity. This zone has remained quiet after the event of March 3, 1985. It corresponds to the northern part of the inferred rupture zone of the  $M = 7.9$  Talca earthquake of December 1, 1928 [Lomnitz, 1970]. The lack of quiescence is clearer on the time section from January 1965 to June 1985, shown in Figure 2. In this section we reported all events of magnitude larger than 4.5. The source extent of the 1906 earthquake is also indicated at the top of the figure. Although it is possible that some events have relatively large location errors, the main features are probably stable. Seismicity is higher toward the north, decreasing to the south. Several clusters are apparent; they correspond to the aftershock zones of the main events of 1971, 1973, 1981, 1985, and a swarm that occurred in 1970 near 34°S. Activity was continuous in the region north of 33.5°S and intermittent in some places south of it, but there is no evidence for large-scale quiescence as reported before some other large earthquakes

(see e.g., Kanamori [1981] for a review). On the contrary, a rather important activity started with the large La Ligua earthquake of July 9, 1971 ( $M = 7.5$ ) and continued until March 1985. The only area that may be identified as a possible zone of quiescence extends south of 33.5°S from 1981 to 1985, but it is difficult to estimate its statistical significance at this time.

#### Mechanisms of Large Events ( $M > 5.5$ ) in the Period 1965-1985

For earthquakes in South America, focal mechanism solutions are poorly constrained due to the scarcity of stations to the west of the epicenters. This problem affects both the determination of fault planes and the depth of the hypocenters. Body wave modeling is necessary to improve the determination of these two parameters. We conducted an exhaustive study of the body waves for most events reported on Table 1. Details of the technique used to model body waves are described by Kanamori and Stewart [1976] and, in the particular version used here, by Deschamps et al. [1980]. For lack of information about local structure, the surface reflected phases were calculated using a mean P-wave velocity above the source of  $7.5 \text{ km s}^{-1}$  and an S-velocity of  $4.5 \text{ km s}^{-1}$ . Attenuation was incorporated using Futterman's operator with  $T/Q = 1$  for P-waves. Vertical components of the P-waves recorded by the World-Wide Standard Seismograph Network (WWSSN) stations digitized at 0.5 s interval were used in the modeling. Only data from distances  $30^\circ$  to  $90^\circ$  were modeled in order to avoid problems with triplications in the upper mantle or diffraction by the core.

Because of the limited azimuthal coverage

## 250 RUPTURE OF THE VALPARAISO (CHILE) GAP FROM 1971 TO 1985

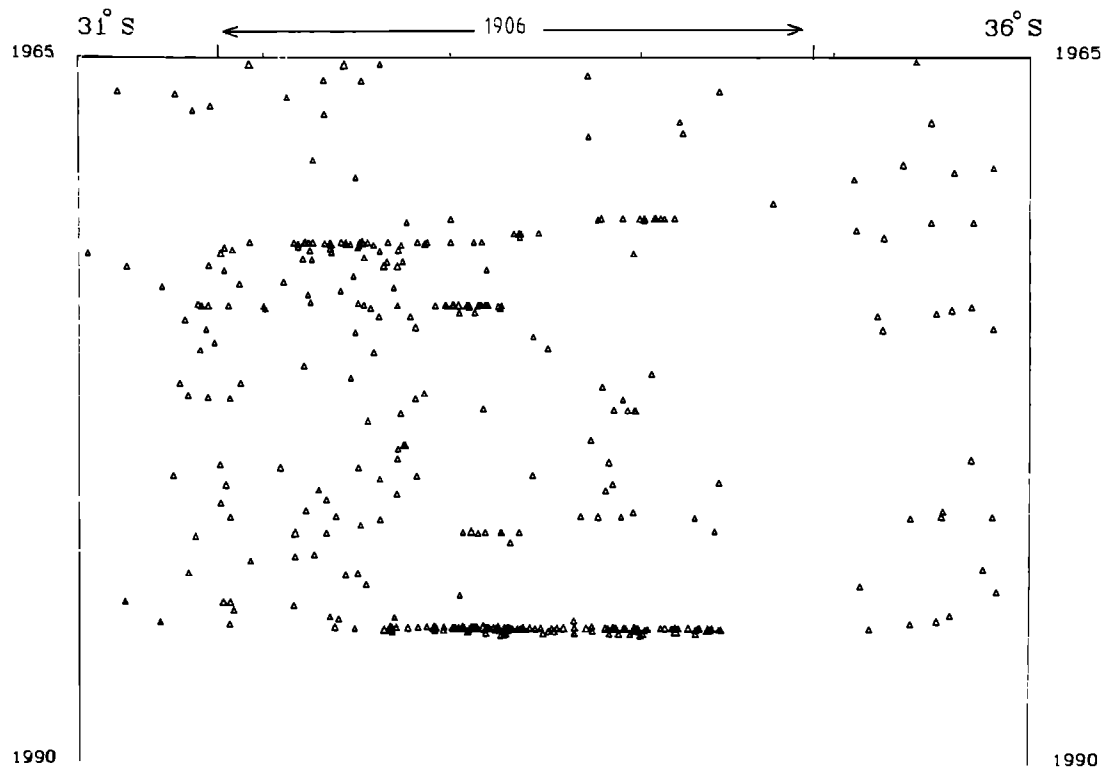


Fig. 2. Time section of the seismicity of Central Chile ( $M > 4.5$ ) from  $31^{\circ}$ S to  $36^{\circ}$ S in the period January 1965 to June 1985. The aftershocks of the March 3, 1985 earthquake are clustered at bottom of the figure. On the top we indicate the latitudinal extent of the 1906 the earthquake.

available we assumed planar dislocations at the source and did not attempt to do a moment tensor inversion. The main source of error in this procedure comes from the lack of data on the structure under the Chilean coast. Thus depths may have to be reconsidered if data on the structure becomes available.

Once the depth and mechanism of the events were determined, we relocated them at fixed depths using a master event technique [Spence, 1980] in which we considered the event of October 5, 1973 as fixed. Results do not differ significantly from the locations reported by the U.S. Geological Survey.

Figure 3 shows the results of this study; a detailed report on the modeling will be published elsewhere (Korrat and Madariaga, in preparation). The figure shows that most of the events have the typical thrust mechanism of interplate earthquakes in a subduction zone, this represents a further confirmation that the interplate contact zone was very active during this period. Two of the events (M1 and 14 in Table 1) are of the normal fault type, these events are deeper and are probably due to extension inside the subducted Nazca plate. Three other events occurred outside the outer bulge in the Nazca plate before it plunges under the South American

plate. Of these, event n° 5 was a very shallow normal fault but its mechanism is very poorly constrained. Earthquakes n° 12 and 15 are thrust earthquakes of the type already studied by Christensen and Ruff [1982].

In Figure 4 we show the aftershock zones determined for the three main interplate events before 1985: 1971, 1973, and 1981. The data used for these plots comes from the U.S. Geological Survey file. No attempt was made to relocate the small shocks because there is seldom enough intersection of the stations used to locate them. The aftershock zones are therefore very likely to overestimate the actual rupture zones of these earthquakes. Let us note a difference with the rupture zone proposed by Malgrange et al. [1981] for the 1971 earthquake. This is due to a different definition of time period used to define the aftershock zone. We followed Nishenko [1985] in using the seismicity for 3 months after the main shock of July 9, 1971.

#### Historical Seismicity

The historical seismicity of the Valparaiso area is relatively well known since this is the main center of population in Chile since 1541. The basic references for historical earthquakes

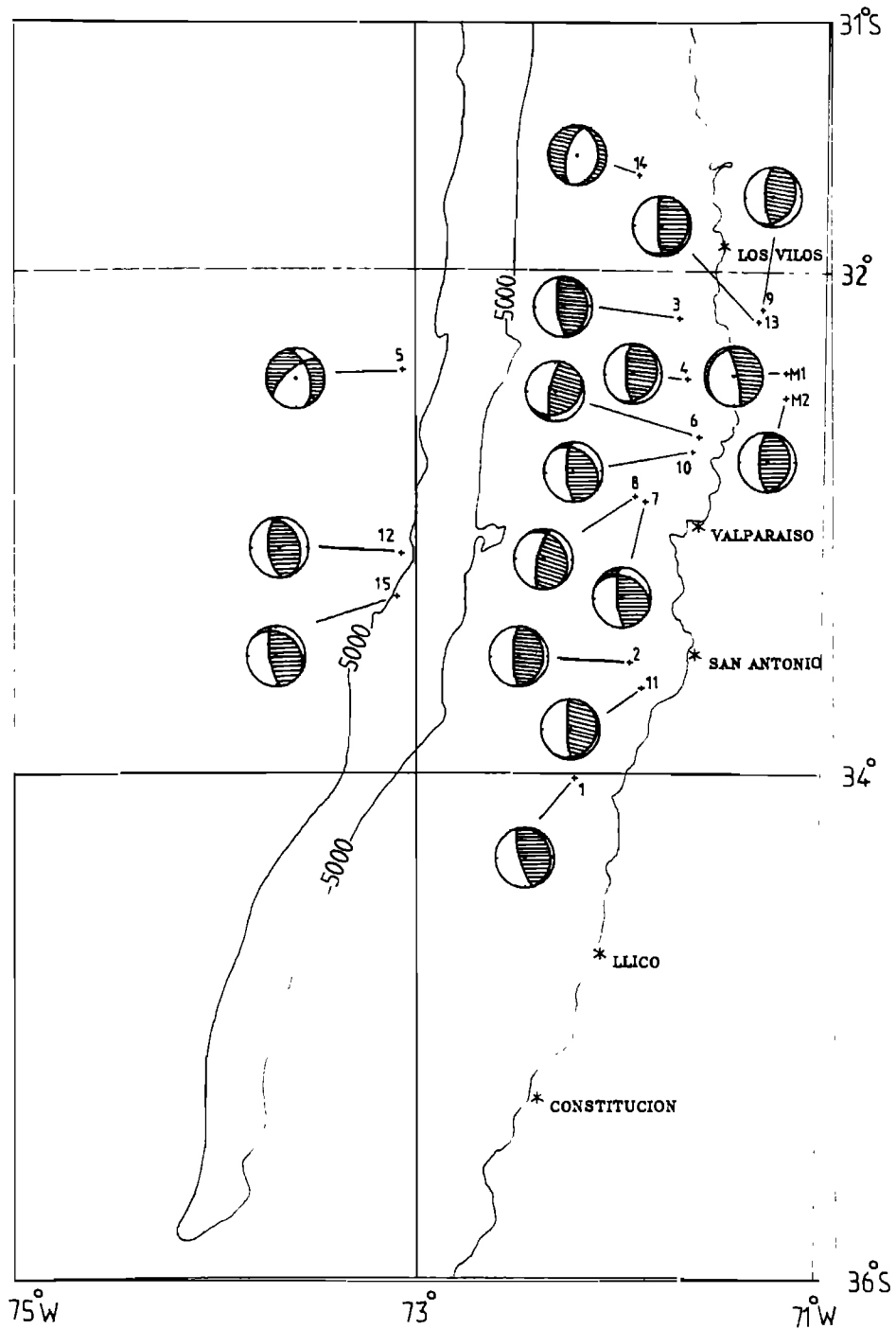


Fig. 3. Fault plane solution of the earthquakes with  $M > 5.5$  that occurred in the Valparaiso gap before the main event of March 3, 1985.

are Montessus de Ballore [1916] and Lomnitz [1970]. Nishenko [1985] has recently discussed available data and his analysis will not be repeated here. Four major earthquakes occurred in

the Valparaiso gap in 1647, 1730, 1822, and 1906. The latter event was studied in detail by Montessus de Ballore [1916] who visited the rupture zone and traced a detailed isoseismal

## 252 RUPTURE OF THE VALPARAISO (CHILE) GAP FROM 1971 TO 1985

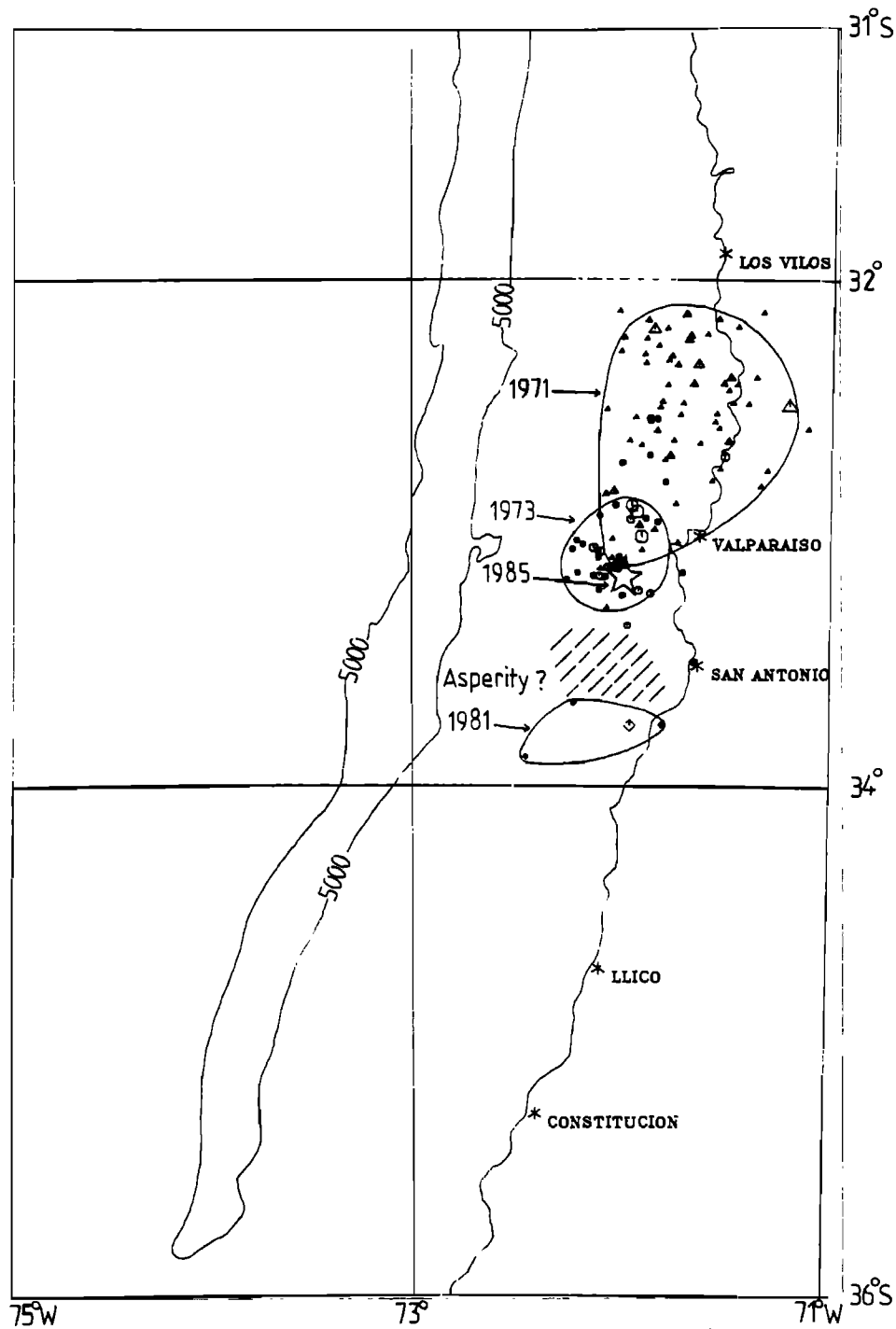


Fig. 4. Aftershock zones of the three larger earthquakes preceding that of March 3, 1985. Each zone includes aftershocks of  $M > 3.7$  determined by the U. S. Geological Survey for a period of 3 months after the main shock.

map. He also made a number of observations that permitted him to define clearly the rupture zone of 1906 between the towns of Llico and Los Vilos. These villages are indicated on the

different maps and serve as reference in order to locate the gap. Nishenko [1985] discusses the determination of the seismic moment for the 1906 earthquake, the value of  $2.8 \times 10^{21}$  Nm ( $10^{28}$  dyn.-

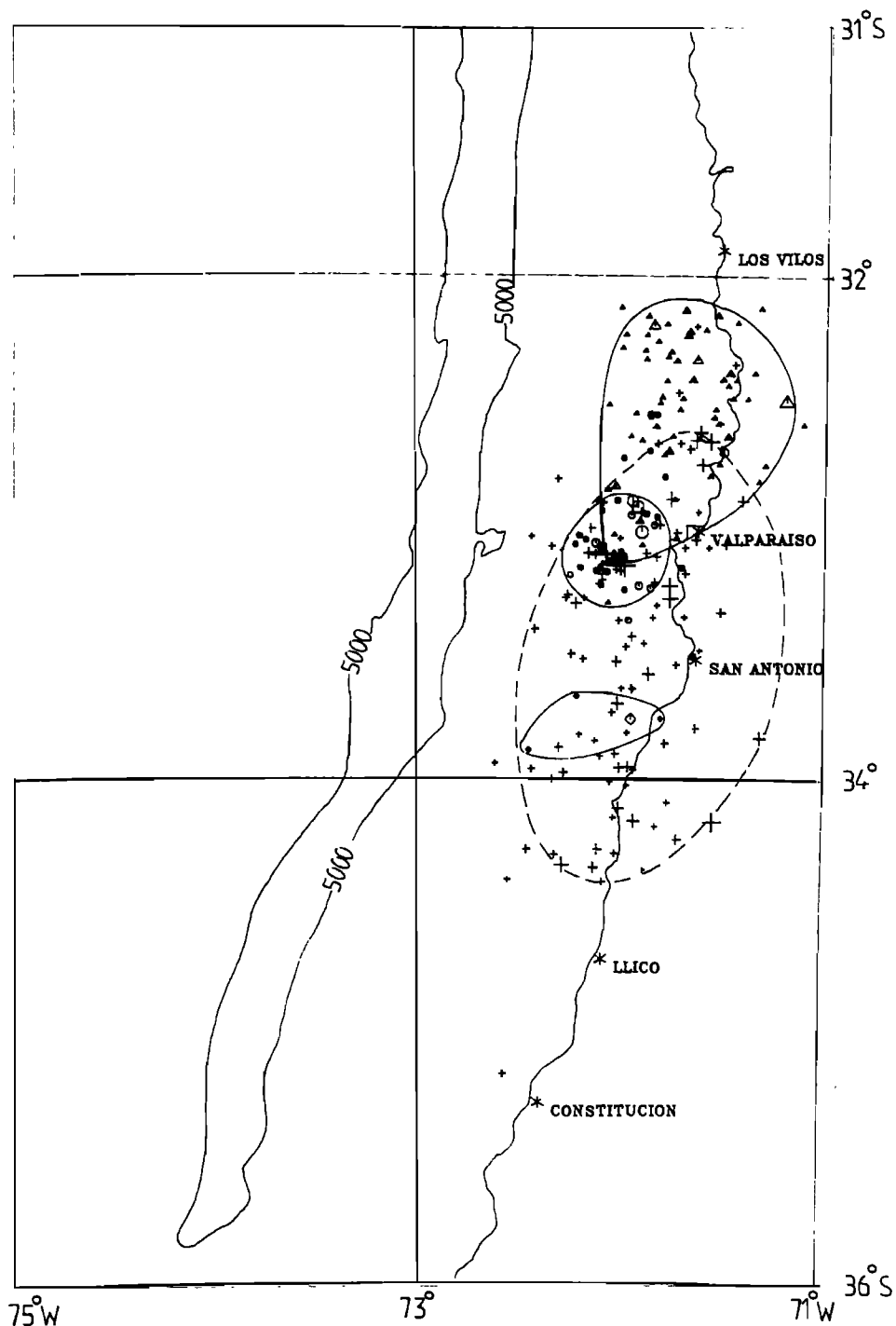


Fig. 5. First 3-month aftershocks of the March 3, 1985 earthquake. The aftershock zone is superimposed on the aftershock zones of the 1971, 1973, and 1981 events.

cm) estimated by Kanamori [1977] may be too low and the value deduced from Tsunami amplitude  $5 \times 10^{21}$  Nm may be more appropriate. This corresponds to a moment magnitude of 8.2 to 8.4.

The Valparaíso gap is clearly defined by two

great earthquakes during this century. To the south the Talca earthquake of December 1, 1928 ( $M = 7.9$ ) ruptured the area from  $34.5^\circ\text{S}$  to at least  $36^\circ\text{S}$ . This corresponds to the very quiet zone that may be clearly identified in Figures 1 and

## 254 RUPTURE OF THE VALPARAISO (CHILE) GAP FROM 1971 TO 1985

2. To the north, the Illapel earthquake of April 6, 1943 ruptured the zone from  $30^{\circ}\text{S}$  to  $32^{\circ}\text{S}$  as is clearly observed in the isoseismals reported by Greve [1964].

## Preliminary Study of the March 3, 1985 Earthquake

The presently available data is only fragmentary and a detailed study will require all the records from WWSSN stations for this earthquake. The results obtained so far, however, permit us to describe the main features of the earthquake and its aftershock series. The main event was preceded by a series of foreshocks in the vicinity of the epicenter of the March 3, 1985 earthquake. Seven events of  $M > 4.3$  are listed by the U.S. Geological Survey from February 22 to March 2, 1985. The epicenter of the main event was located south of Valparaiso in the area of the aftershock zone of the 1973 earthquake (see Figure 4). An intense aftershock activity with several events of magnitude higher than 6 followed the earthquake. The aftershocks located by U.S. Geological Survey during 3 months following the main event are shown in Figure 5. For reference we also show in this figure the aftershock zones of the 1971, 1973, and 1981 events. The aftershock zone covers the region from  $32.5^{\circ}\text{S}$  to  $34.5^{\circ}\text{S}$  as is also clearly seen in the time section of Figure 2. A more detailed study of aftershocks made with a portable network is reported by Comte et al. [1985]. Their results do not differ substantially from those in Figure 5. The 1985 aftershock zone is clearly smaller than the area from Los Vilos to Llico that appears to have been the most likely rupture zone of the 1906 earthquake, as determined from the damage data collected by Montessus de Ballore [1916]. Thus, the rupture zone of the 1985 earthquake is 35% smaller than that of the 1906 event. The clearest difference is in the northern part from  $31.8^{\circ}\text{S}$  to  $32.6^{\circ}\text{S}$  where no aftershocks occurred. This is precisely the area where the 1971 event took place.

On Figure 6 we plot the seismicity from  $31^{\circ}\text{S}$  to  $36^{\circ}\text{S}$  for the period from January 1, 1985 to June 10, 1985. This plot shows that the aftershock activity of 1985 did not cover the northernmost segment of the gap. The foreshock activity immediately north of the hypocenter of the March 3 earthquake is also observed in this figure. Although further work on the locations, and particularly on the analysis of local recordings made with a portable network (Ponce, personal communication, 1985) is necessary; it is clear that the March 3, 1985 earthquake was smaller than that of 1906.

The seismic moment for the 1985 earthquake has been determined using data from the GEOSCOPE network (Romanowicz and Monfret, personal communication, 1985). A value of  $1.5 \cdot 10^{21} \text{ Nm}$  ( $10^{28} \text{ dyne cm}$ ) was obtained from multiple passages of surface waves recorded at stations in Europe and Africa. The mechanism determined with

this data is entirely compatible with the fault plane solution for the July 9, 1971 earthquake reported by Malgrange et al. [1981]. It is a shallow thrust event with a subhorizontal (dip =  $23^{\circ}$ ) fault plane. The almost vertical auxiliary plane typical of shallow interplate earthquakes in the Peru Chile trench (see Figure 3) is well controlled but not the shallower one. The moment for the 1985 earthquake may be compared in Table 2 with that of the other major events in the area from 1971 to 1985. The moment  $M_0 = 5.6 \cdot 10^{20} \text{ Nm}$  for the July 9, 1971 earthquake, determined from surface wave analysis by Malgrange et al. [1981] is about half that of the March 3, 1985 earthquake. This is consistent with the difference in magnitude of the two events (7.5 for 1971 and 7.8 for 1985) and with the hypothesis that stresses in the northernmost part of the gap were relieved by the 1971 earthquake.

We collected several body wave recordings for the earthquake of 1985, unfortunately most of them are of diffracted P waves. For this reason we will only model the record from station FDF in Martinique. This station has the same response as a WWSSN station. It recorded several of the large aftershocks. We selected two of them, March 19, 1985 and April 9, 1985, for comparison with the main shock. They may be considered as "Green's functions" for the main event since their source processes had durations of about 7 s and their recordings at FDF are relatively simple. On Figure 7 we show observed (above) and synthetic (below) P-waves at FDF for the two aftershocks. The signals are quite typical of medium-sized earthquakes in this area as may be verified by comparing these records to those obtained for the October 5, 1973 earthquake at SJG and for March 23, 1981 at TRN. The stations SJG, TRN, and FDF are sufficiently close that they may be compared directly, without equalization.

In Figure 8 we show the deconvolved source time functions and the modeling of the two large earthquakes in the Valparaiso gap in 1971 and 1985. The difference between the two is striking. The waveforms of the 1985 event are much more complex than those of the 1971 event, although their moments differ only by a factor of 2. Standard scaling relations indicate that the duration of the two events should differ by a factor of  $2^{1/3}$ . The duration of the 1971 P-waves are about 24 s at the base of the source time function, about 16 s if a mean source time is calculated at midheight as done by Malgrange et al. [1981]. The source time function for 1971 shown in Figure 8 is different from that of Malgrange et al. [1981] because they used a mean source time function to fit all stations while here we modeled the single record at BHP. Our new source function fits the observed signal much better. As noticed by Malgrange et al. [1981] in order to fit the small minimum at about 7 s into the signal, different source time functions would have had to be used for every station. This appears to be a directivity effect favoring the

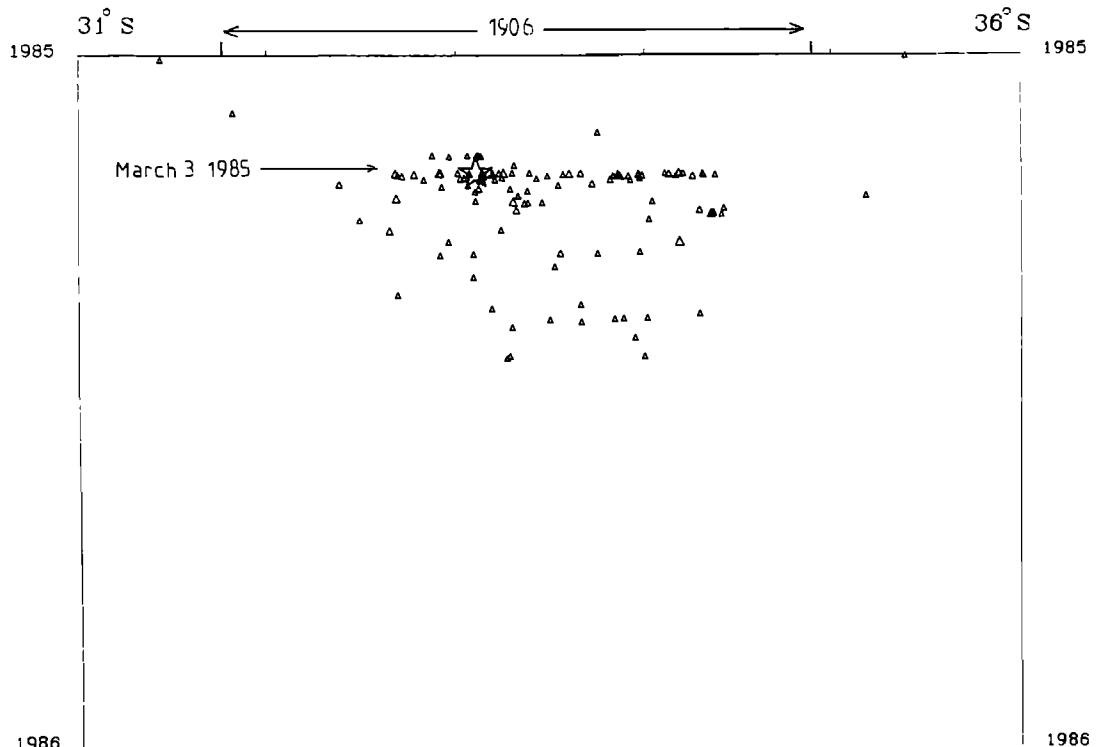


Fig. 6. Time section of the seismicity of Central Chile ( $M > 4.5$ ) from January 1985 through June 1985. The event of March 3, 1985 is indicated.

interpretation of the inflection as being due to a double shock nature for the earthquake. Although a structural origin may not be entirely ruled out, the simple recordings obtained for the smaller shocks of Figure 7 tend to favor the former hypothesis. Apart for the notch on the source time function this is quite similar to that reported by Malgrange et al. [1981].

Let us consider now the March 3, 1985 earthquake. Duration of the source time function is close to 53 s at the base and it clearly shows the presence of a double shock. The first impulse with about one tenth of the total moment precedes by about 10 s the main part of moment release.

The main shock has a duration of 40 s itself. The source time functions in Figure 8 are not to scale. From the record at FDF a seismic moment of  $3.3 \cdot 10^{20}$  Nm was determined, the difference between this value and that determined from surface waves is very large. Although it may be partially due to local amplification problems at FDF, it may be also due to a slow component in the source process that is unobservable with a WWSSN instrument.

#### Discussion

Recent studies of complex earthquake processes in several Island arcs by Ruff [1983] and Beck

TABLE 2. Source Parameters

Date	Source Duration (s)	$M_0$ (dyne cm $\times 10^{25}$ )	$M_w$
July 9, 1971	24	560	7.8
July 11, 1971	5.5	6	6.4
July 31, 1971	4	0.46	5.7
Oct. 5, 1973	11	28	6.9
March 23, 1981	9	6.6	6.5
March 3, 1985	40	1500	8.0
March 19, 1985	7	5	6.4
April 9, 1985	7	40	7.0

## 256 RUPTURE OF THE VALPARAISO (CHILE) GAP FROM 1971 TO 1985

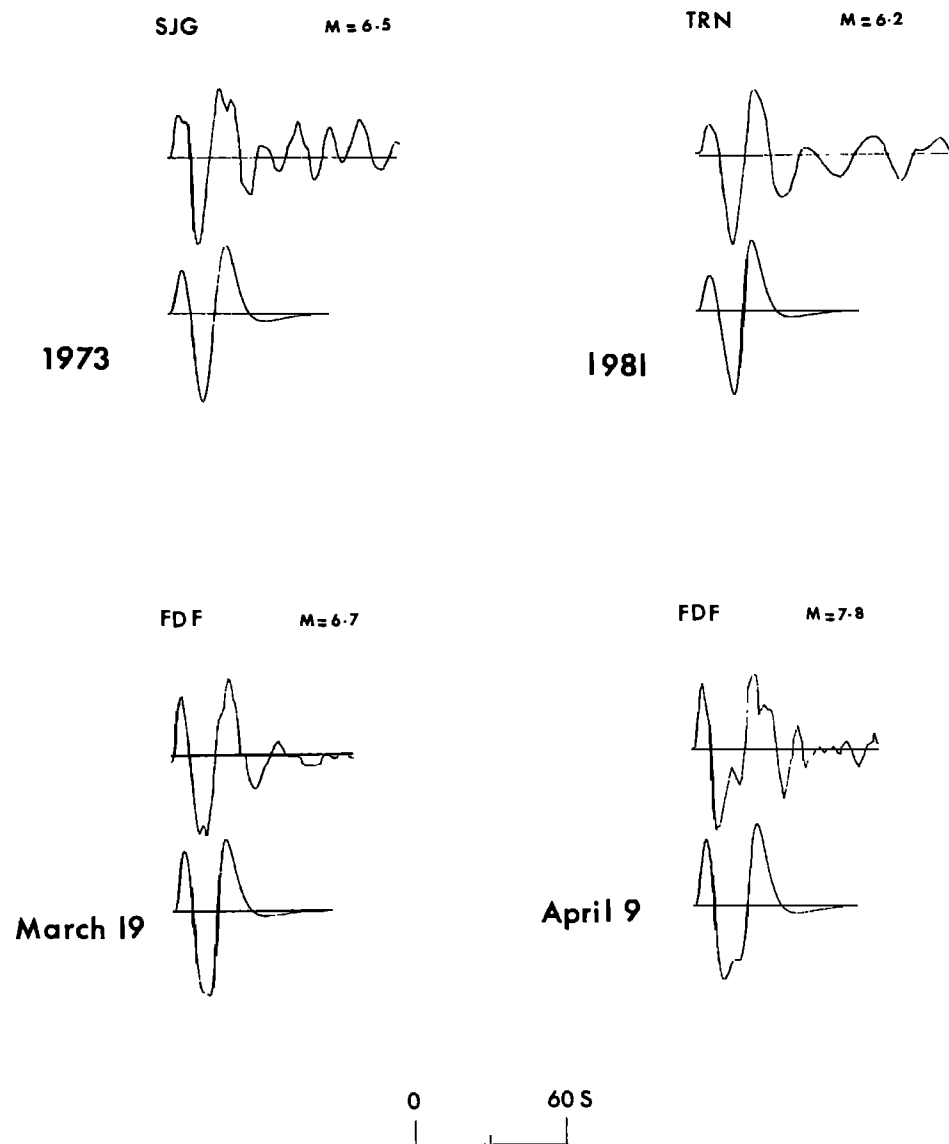


Fig. 7. Modeling of P-waves recorded at Caribbean stations for four smaller events in the Valparaiso gap. SJG for October 5, 1973; TRN for March 23, 1981; and FDF (Martinique) for the two aftershocks of March 19 and April 9, 1985.

and Ruff [1984] have shown that a wide variety of situations may develop depending on the time evolution of rupture on the gap. Many of these features may be explained in terms of source complexity within the asperity [Lay et al., 1982] or barrier models [Das and Aki, 1977] of source dynamics. These models are end members of the possible behaviors that may be observed in actual faults. The evolution of rupture in the Valparaiso gap may help in further refining these models.

Although the data for the recent March 3, 1985 earthquake is not complete we may hypothesize the following rupture process: rupture started from

the northern end of the fault zone in the area north of Valparaiso which was probably under higher tectonic stress than the southern part of the gap. The 1971 earthquake occurred there but was arrested by a barrier as it propagated to the south in the vicinity of Valparaiso. The source process was relatively rapid and completed in about 24 s. No perceptible difference was found between the body and surface wave moments. To the north the 1971 earthquake was stopped when running into the rupture area of the 1943 Illapel earthquake. Lack of driving stress produced the arrest of rupture in this area. The medium-size event of 1973 ( $M_0 = 2.8 \cdot 10^{19}$  Nm) occurred at the

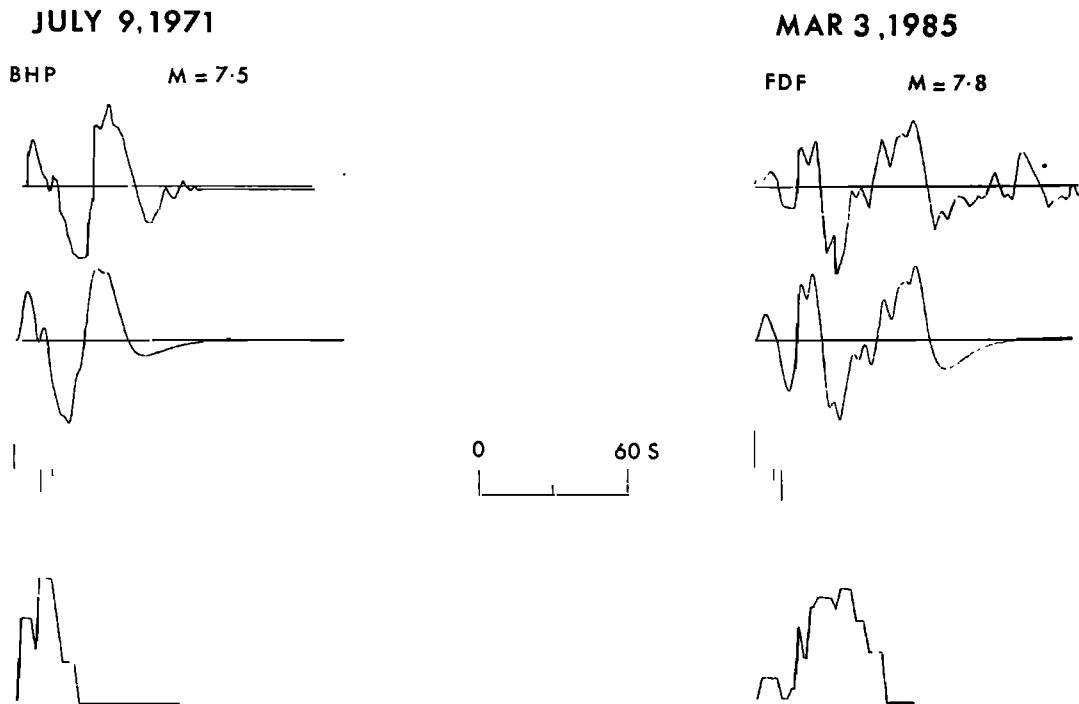


Fig. 8. Modeling of the two largest earthquakes, July 9, 1971 and March 3, 1985. The former was recorded at BHP and the second at FDF (Martinique). The source time functions are not on scale.

southern edge of the rupture zone for the 1971 earthquake, where we propose the presence of an unbroken barrier. The rupture in 1973 was brief and eventually stopped again at an even stronger patch which became strongly loaded by the stress release to the north. This is the site where the March 1985 earthquake started. Before this major event, a small ( $M_0 = 6.6 \cdot 10^{18}$  Nm) earthquake occurred on March 1981 near  $33.7^\circ$ S. The initial shock of 1985 ruptured the area between the 1973 and the small shock of 1981. It then suddenly accelerated and went on to rupture most of the highly stressed areas of the Valparaiso gap. To the north, it propagated into the rupture zone of the 1971 earthquake; to the south it was arrested as it ran into the quiet zone near  $34.5^\circ$ S, the source area for the Talca earthquake of December 1, 1928.

The rupture process proposed above is compatible with the asperity model in which successive earthquakes transfer stress to the adjoining unbroken areas of the fault. For these patches to behave as asperities they must be stronger and act as barriers for previous earthquakes. Thus the spatial-time variation of strength along the fault is a crucial parameter to describe these complicated suites of earthquakes.

Finally, let us remark that the total seismic moment released from 1971 to 1985 is about  $2 \cdot 10^{21}$  Nm, which is definitely smaller than any of the

estimates of the moment of the 1906 earthquake ( $2.8$  to  $5.0 \cdot 10^{21}$  Nm). The significance of this difference is difficult to evaluate since, as remarked by Nishenko [1985] an aseismic component of slip in this area is not to be excluded.

#### Conclusions

We have reported on a continuing study of the seismicity of the Valparaiso gap in Central Chile from 1965 up to 1985. This work complements that of Malgrange et al. [1981]. Our main conclusions are:

Two large earthquakes occurred in the gap on July 9, 1971 and March 3, 1985, the moments of these events differ by a factor of 2 ( $5.6$  and  $15 \cdot 10^{20}$  Nm, respectively). Total seismic moment released in the area is on the order of  $2 \cdot 10^{21}$  Nm which is smaller by a factor of 1.5 to 3 from that of the previous great earthquake of August 1906.

No evidence for large scale quiescence was observed during the 20 years that preceded the earthquake, except for a short time (1981-1985) in the southern edge of the gap ( $33.5^\circ$ S to  $35^\circ$ S). In fact, not only the large earthquake of July 1971 occurred in the northern end of the gap, but several events of magnitude between 6 and 7 prepared the area for the larger shock of March 3, 1985.

A plausible scenario for the evolution of rupture within the gap could be established on

## 258 RUPTURE OF THE VALPARAISO (CHILE) GAP FROM 1971 TO 1985

the basis of the activity from 1971 to 1985. Further improvements on this model require a complete analysis of all available data for the 1985 shock. The complex interplay of strong patches on the fault which act as barriers for the early events and then as asperities for the later one is clearly substantiated. The rupture of the March 1985 earthquake started near a barrier that had apparently successfully arrested both the 1971 and 1973 earthquakes from propagating to the south. Once the asperity was broken rupture propagated more slowly than that of 1971 filling about 65% of the rupture zone of the 1906 earthquake.

Acknowledgments. This work was supported by a number of grants by ATP Sismogénese of The Institut National des Sciences de l'Univers from 1979 to 1983. We thank S. Nishenko for several interesting discussions during the summer of 1983. I. Korrat was supported by a fellowship from the Egyptian government. I.P.G. Publication n° 843.

## References

- Beck, S., and L. Ruff, The rupture process of the great 1979 Colombia Earthquake: Evidence for the asperity model., J. Geophys. Res., 89, 9281-9291, 1984.
- Christensen, D., and L. Ruff, Implications of the shallow thrust earthquake of Oct. 16, 1981 on the outer rise off Central Chile, (abstract), EOS Trans., AGU, 63, 1041, 1982.
- Comte, D., A. Eisenberg, E. Lorca, M. Pardo, L. Ponce, R. Saragoni, S.K. Singh, and G. Suarez, The Central Chile Earthquake of 3 March 1985: A repeat of previous great earthquake in the region?, Science, in press, 1986.
- Das, S., and K. Aki, Fault plane with barriers: a versatile earthquake model, J. Geophys. Res., 82, 5658-5670, 1977.
- Deschamps, A., H. Lyon-Caen, and R. Madariaga, Mise au point des méthodes de calcul de sismogrammes synthétiques de longue période, Ann. Geophys., 36, 167-178, 1980.
- Greve, F., Historia de la Sismología en Chile, Instituto de Geofísica y Sismología, Universidad de Chile, Santiago, 1964.
- Kanamori, H., The energy release in great earthquakes, J. Geophys. Res., 82, 2981-2987, 1977.
- Kanamori, H., The nature of seismicity patterns before large earthquakes, in Earthquake Prediction: an International Review, Maurice Ewing Ser., V. 4, edited by D.W. Simpson and P.G. Richards, pp. 1-19, AGU, Washington, D.C., 1981.
- Kanamori, H., and G. Stewart, Mode of strain release along the Gibbs fracture zone, mid-Atlantic ridge, Phys. Earth Planet. Inter., 11, 312-332, 1976.
- Kelleher, Rupture zones of large South American Earthquakes and some predictions, J. Geophys. Res., 77, 2087-2103, 1972.
- Lay, T., H. Kanamori, and L. Ruff, The asperity model and the nature of large subduction zone earthquakes, Earthquake Pred. Res., 1, 3-71, 1982.
- Lomnitz, C., Major earthquakes and Tsunamis in Chile during the period 1535 to 1955, Geol. Rundschau, 59, 938-960, 1970.
- Malgrange, M., and R. Madariaga, Complex distribution of large thrust and normal fault earthquakes in the Chilean subduction zone, Geophys. J. R. astron. Soc., 73, 489-505, 1983.
- Malgrange, M., A. Deschamps, and R. Madariaga, Thrust and extensional faulting under the Chilean coast: 1965, 1971 Aconcagua earthquakes Geophys. J. R. astron. Soc., 66, 313-332, 1981.
- McCann, W., S. Nishenko, L. Sykes, and J. Krause, Seismic gaps and plate tectonics : seismic potential for major boundaries, Pageoph, 117, 1082-1147, 1979.
- Montessus de Ballore, F., Historia sísmica de los Andes meridionales, Cervantes, Santiago de Chile, 1916.
- Nishenko, S., Seismic potential for large and great interplate earthquakes along the Chilean and Southern Peruvian margins of South America: a quantitative reappraisal, J. Geophys. Res., 90, 3589-3615, 1985.
- Ruff, L., Fault asperities inferred from seismic body waves, in Earthquakes: Observation, Theory and Interpretation, edited by H. Kanamori and E. Boschi, pp. 251-276, Soc. Italiana di Fisica, Bologna, Italy, 1983.
- Spence, W., Relative epicenter determination using P-wave arrival-time differences, Bull. Seismol. Soc. Am., 70, 171-183, 1980.

## OBJECTIVE DETERMINATION OF SOURCE PARAMETERS AND SIMILARITY OF EARTHQUAKES OF DIFFERENT SIZE

D. J. Andrews

U.S. Geological Survey, Menlo Park, California 94025

**Abstract.** The omega-squared spectral model with two independent parameters (stress drop, moment) provides a simple parameterization of ground motion spectra for statistical analysis. Accurate determination of source parameters of small earthquakes requires accounting for distortion of the source spectrum by each site response spectrum. Record spectra are inverted here to find separate station and event spectra. Source parameters are found by an automated objective method using integrals of each event spectrum. Quantitative estimates of error are carried through the entire analysis. These methods are applied to digital records of aftershocks of the 1980 Mammoth Lakes California earthquake sequence. Stress drop is found to be independent of source radius for the 90 events with best-determined source parameters. The ratio of Hanks to Brune stress drop is remarkably constant and independent of source radius, showing that the spectra, on average, have a constant shape that is scaled by two parameters, corner frequency and low-frequency level. Stress drops have a log-normal distribution with the standard deviation being about a factor of 2.

### Introduction

Aki [1967] and Brune [1970] have characterized the average spectrum radiated by an earthquake by a spectral model with two independent parameters, the low-frequency spectral level and the corner frequency. Above the corner frequency the spectrum is assumed to fall off as a power of frequency; the exponent for the displacement transform is implicitly assumed to be  $-2$  in this work, and some evidence supporting this choice will be shown. From the two spectral parameters various source parameters (moment, stress drop, source radius, etc.) can be found, any two of which are independent. While this kind of data analysis does not provide a detailed picture of an earthquake source, it is better than using a single parameter, magnitude. Characterization of earthquake sources by two parameters is simple enough that scaling of the parameters and their statistical distribution over a set of earthquakes can be examined. These scaling relations and probability distribution functions provide predictions of strong ground motion. Near-source ground motion depends more strongly on stress drop than on moment, so the scaling re-

lation and probability distribution function of stress drop have great practical importance. Source parameter studies of small earthquakes can provide the scaling relation and distribution function of stress drop, but the uncertainty in the stress drop determination needs to be reduced from a factor of 10 down to less than a factor of 2 to be useful for engineering applications. In addition, source-parameter studies can provide data for statistical source theories, such as fractal modeling.

This paper is concerned first with finding an accurate, objective, and stable methodology of determining source parameters of the two-parameter spectral model. The data consist of digital recordings of ground motion obtained by the U. S. Geological Survey on a local array of event recorders of aftershocks of the 1980 Mammoth Lakes California earthquake sequence [Spudich et al., 1981; Mueller et al., 1981; Archuleta et al., 1982]. The hypocentral distance from each event to the nearest station is generally less than 10 km, and often less than 5 km. The events have corner frequencies in the range 1 to 10 Hz. At these frequencies the recorded spectrum is sensitive to near-surface structure at each station site. A naively determined corner frequency may be related more to a near-surface layer thickness or near-surface attenuation than to the earthquake source size [Granswick et al., 1985; Malin and Waller, 1985; Peppin, 1985; Frankel, 1982]. In this work, spectra of S-wave records are inverted to find both station-response spectra and event spectra. Then source parameters are found from various integrals of each event spectrum.

After source parameters and quantitative estimates of their uncertainty are determined, the second phase of this study examines the distribution of source parameters over an ensemble of events. Events are excluded from the ensemble if the relative uncertainty of a source parameter is greater than a cutoff value. The distribution of source parameters can be affected by a detection threshold, although this effect is not explicitly considered in this paper.

### Data Selection

I examined all the U.S.G.S. digital seismograms of 1980 Mammoth Lakes aftershocks and selected those three-component records that triggered on the P-wave arrival and

## 260 DETERMINATION OF SOURCE PARAMETERS

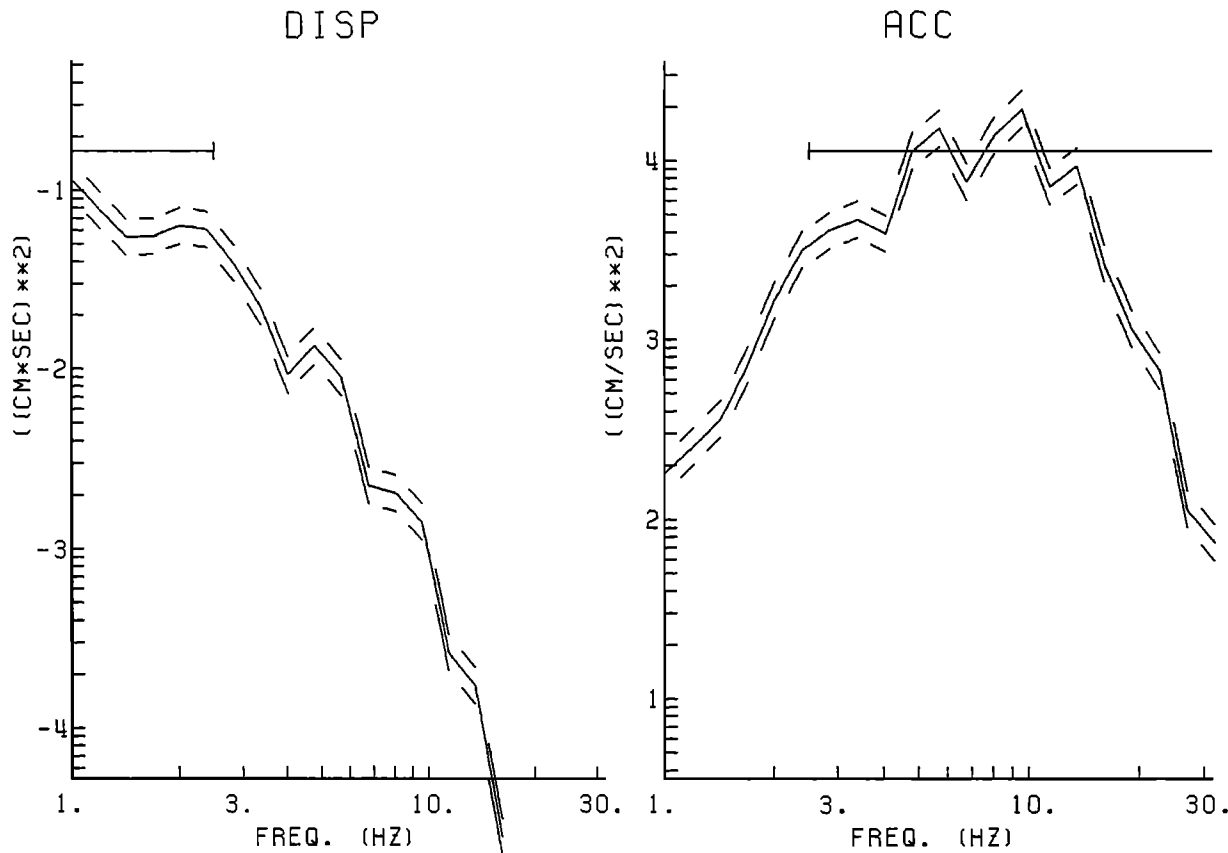


Fig. 1. Spectrum of event 149 05 16, normalized to 1 km hypocentral distance. Left panel shows displacement spectrum and low-frequency level pick; right panel shows acceleration spectrum and acceleration spectral level pick. Dashed lines are drawn at plus and minus one standard error.

had clear P and S onset times. This selection criterion eliminated those records that triggered on the S-wave arrival (more than half of the total). This loss of data was counterbalanced by three advantages: (1) a pre-event noise sample was available; (2) a voltage step in the DR100 instrument at the trigger time did not contaminate the S-wave signal; and (3) the hypocentral distance of each record could be estimated from the S- minus P-arrival times. The S waves so selected are not entirely free of instrument problems, however, for there is a voltage transient with amplitude of 1 or 2 digital bits 2 s after the trigger time (E. Cranswick, personal communication, 1982). Records without a clear S onset were rejected, so the data set is biased against "slow" and complex events.

The horizontal components were each multiplied by a bell-shaped window function containing the S arrival and were Fourier transformed and corrected for instrument response. Then the squared magnitudes of the transforms of the two horizontal components were added together. The motivation for this summing of power spectra was that epicentral distances were small enough that there was little point in separating radial and transverse components, and that as much data as possible should be used at high

frequencies where signals are random. The same window length, 1.28 s, was used for all S waves, and this length is sufficient to resolve corner frequencies above 1.6 Hz. Only two or three events in this data set had smaller corner frequencies, and they are excluded from the results to be shown below.

In order to save storage space and computational time in the following analysis, each spectrum was averaged over 24 frequency bands, each band spanning a factor of  $2^{1/4} = 1.19$  (a quarter of an octave) in frequency. The averaging method conserved the integral of the power spectrum.

A noise spectrum was found similarly from a time window before the P arrival. This spectrum of ground noise was augmented with an instrumental noise spectrum, taken to be the spectrum of a white-noise signal with amplitude of 2 digital bits.

### Data Analysis

#### Method to Find Event Spectra

Source parameters (corner frequency, moment, stress drop) have conventionally been found from the spectrum

of each record of an event and then averaged. A better method is to multiply the power spectrum of each record by hypocentral distance squared to correct for geometrical spreading, average the power spectra, and then determine source parameters. The latter method will tend to average out site effects, source directivity, and random fluctuations of the high-frequency spectrum. Weighting factors, dependent on signal-to-noise ratio, can be applied in the averaging.

An even better method is to invert the record spectra to find separate station and event spectra. Assume that each record spectrum is the product of a station-response spectrum and an event spectrum,

$$S_{i(k)}(f) E_{j(k)}(f) = R_k(f). \quad (1)$$

Here  $R_k(f)$  is the velocity power spectrum, corrected for geometrical spreading, of the  $k$ th record as a function of frequency,  $S_i(f)$  is the impulse-response spectrum of station  $i$ ,  $E_j(f)$  is the source spectrum of event  $j$ ,  $i(k)$  is the station number of record  $k$ , and  $j(k)$  is the event number of record  $k$ . I formerly applied (1) to the coda spectra of a group of seven events at nearly the same hypocentral location [Andrews, 1982]. In that case (1) should be an excellent model of the data, because the coda averages the directivity of the source, and the propagation path to each station is nearly the same for each event. For the present case of S-wave spectra from events throughout the area of the instrument array, (1) is not such a good approximation, because it does not account for directional effects of the source nor for attenuation of the signal at depth. Propagation effects near the surface in the vicinity of each station, however, where all ray paths are nearly vertical, are correctly accounted for in (1). Mueller [1985] has used the record of a small event as an impulse response to deconvolve the record of a larger event by finding a quotient

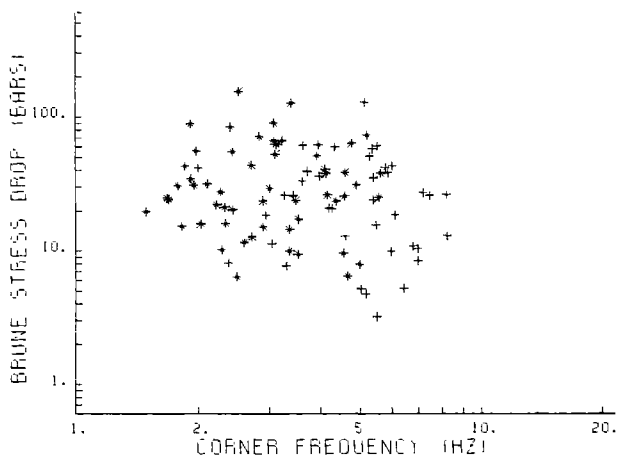


Fig. 2. Brune stress drop plotted against corner frequency for events with less than 20% uncertainty in  $f_0$ . Asterisks: events recorded at more than one station. Plus signs: singly recorded events. Lines of constant moment are labeled by  $\log_{10} M_0$ .

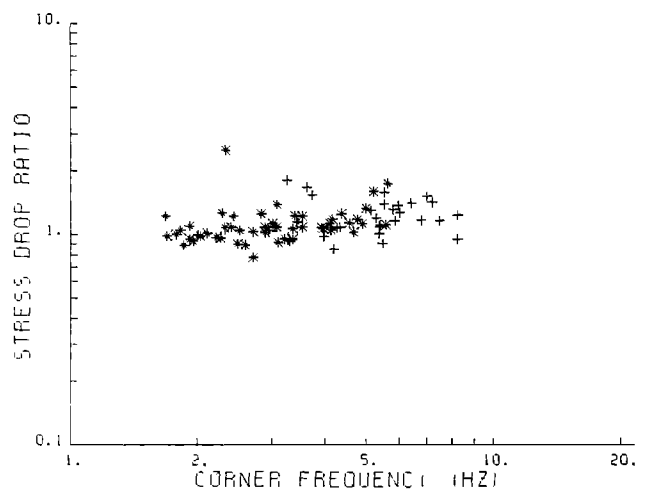


Fig. 3. Ratio of Hanks to Brune stress drop plotted against corner frequency for events with uncertainty in this ratio less than 40%. Asterisks: multiply recorded events; plus signs: singly recorded events.

in the transform domain. Equation (1) is essentially an extension of Mueller's method to all records in a set of data.

For  $K$  records,  $I$  stations, and  $J$  events, (1) is a system of  $K$  equations to determine  $I + J$  unknowns for each frequency band. There is one undetermined degree of freedom: if all station spectra are multiplied by one arbitrary function of frequency, and all event spectra divided by the same function, the fit is not changed. This undetermined degree of freedom can be fixed by prescribing any one of the station spectra or, as is done in this work, by setting the average of the station spectra at the better sites equal to one.

The system of equations is linearized by taking logarithms,

$$\log S_{i(k)} + \log E_{j(k)} = \log R_k. \quad (2)$$

Here the frequency argument is suppressed, it being understood that (2) is to be applied separately in each frequency band. Note that  $i$  and  $j$  are not the matrix indices; the matrix has  $K$  rows and  $I + J$  columns. Each row is unique, with only two nonzero elements. I have solved the matrix equation by singular value decomposition. One singular value is zero (since there is an undetermined degree of freedom), but the other singular values do not span a very large range, so there is no loss of accuracy in the solution.

The system of equations I actually solve is a weighted version of (2)

$$w_k \log S_{i(k)} + w_k \log E_{j(k)} = w_k \log R_k, \quad (3)$$

where each element of the data vector and the corresponding row of the matrix is multiplied by a weighting factor  $w_k$ . The weighting factors are chosen such that each data element has unit variance, and the solution variance

## 262 DETERMINATION OF SOURCE PARAMETERS

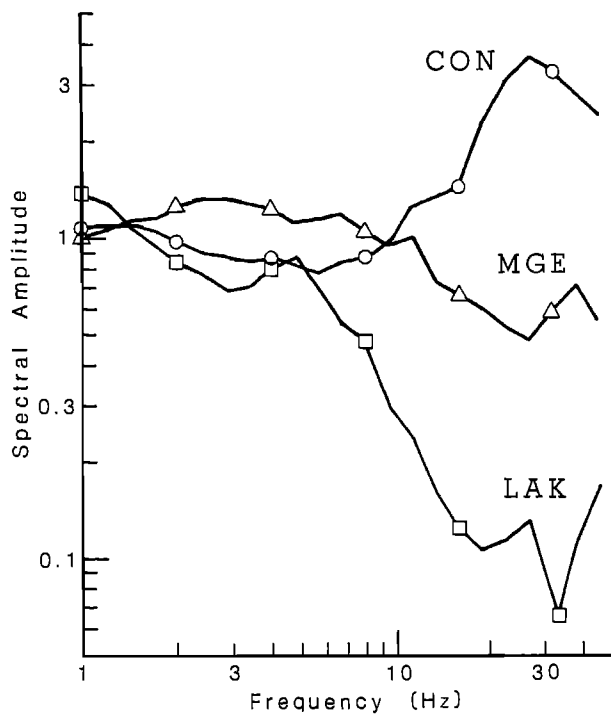


Fig. 4. Station response amplitude at three of the twelve stations.

is found from standard formulas [Menke, 1984, p. 122]. If a signal  $R$  has standard deviation (noise)  $N$ , then  $\log_e R$  has standard deviation  $N/R$  for small noise-to-signal ratio. Then an appropriate weighting factor would be the signal-to-noise ratio of the record spectrum in each frequency band,

$$w_k = R_k/N_k, \quad (4)$$

if (1) were a good model of the data. Since (1) is not a good model of the data, it is desirable to eliminate directional effects of the source by averaging as many good records as possible with equal weights. I decided arbitrarily to give equal weight to all data with signal-to-noise ratio greater than 4.0,

$$w_k = \min(4.0, R_k/N_k). \quad (5)$$

This is equivalent to saying that all data have a minimum standard deviation of 25%. Station and event spectra found in the solution may have smaller standard errors, depending on how many records contribute to determining each solution element. Weighting factors were reduced to half of that given by (5) for records that did not have impulsive S onsets, and records were weighted inversely with hypocentral distance at distances greater than 10 km.

I selected record spectra of the 35 best-recorded events of the data set. Solution of (3) with 12 stations, 35 events, and 150 records required 7 min of CPU time on a VAX 780 VMS computer. Solution for the entire data set of 350 events and 550 records did not run to completion, but

would have required 40 hours. Station spectra were rather well determined by the 35 event analysis, however, so the remaining record spectra were divided by station spectra and averaged to find event spectra in only 1 min of CPU time.

#### Method to Determine Source Parameters

The inversion described in the preceding subsection provides a signal and a noise spectrum for each event. This subsection describes an objective quantitative procedure for determining source parameters from integrals of each spectrum. The desirability of using integrals of spectra has been emphasized before by Linde et al. [1980], Snoke et al. [1983], and Silver [1983].

The velocity power spectrum of each event  $E_j(f)$ , as found in the previous subsection, is divided by 4 to account for the free surface. Then this corrected velocity power spectrum  $V^2(f)$  and the displacement power spectrum  $D^2(f) = V^2(f)/(2\pi f)^2$  are used to calculate the following integrals

$$S_{D2} = 2 \int_0^\infty D^2(f) df, \quad (6)$$

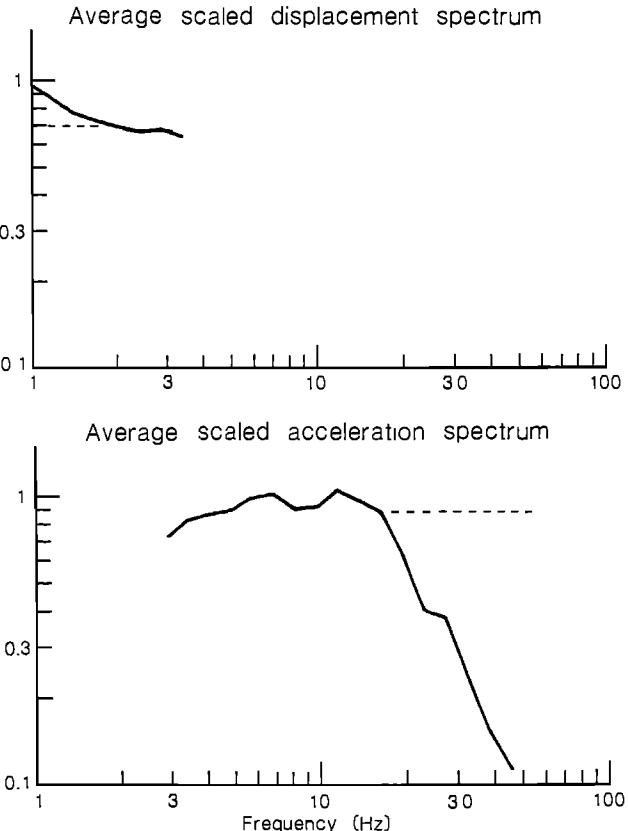


Fig. 5. Top: Average scaled displacement spectrum of events with  $f_0 > 4.0$  Hz. Bottom: Average scaled acceleration spectrum of events with  $f_0 < 2.5$  Hz.

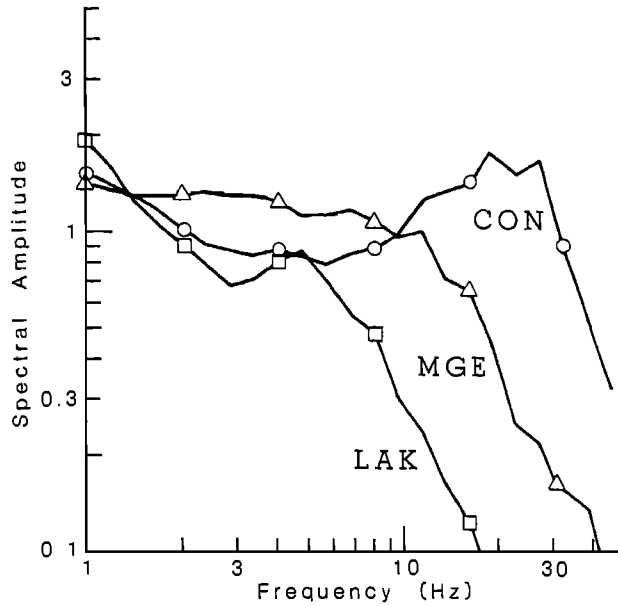


Fig. 6. Adjusted station response amplitudes.

$$S_{V2} = 2 \int_0^\infty V^2(f) df. \quad (7)$$

Numerical values of these integrals are affected by resolution near zero frequency being limited by reciprocal of window length and by truncation at the Nyquist frequency. These effects are not significant for the spectra in this study.

One source parameter, radiated energy, is found immediately as

$$E_{\text{rad}} = 4\pi\rho\beta S_{V2}. \quad (8)$$

Corner frequency  $f_0$  is found from the integrals (6) and (7) using a formula that holds for a model shape, the Brune spectrum,

$$D_{\text{Brune}}(f) = \frac{\Omega}{1 + (f/f_0)^2}. \quad (9)$$

The integrals (6) and (7) of this spectrum are  $S_{D2} = \frac{1}{4}\Omega^2(2\pi f_0)$  and  $S_{V2} = \frac{1}{4}\Omega^2(2\pi f_0)^3$ . Then corner frequency in terms of the integrals is

$$f_0 = \frac{1}{2\pi} \sqrt{S_{V2}/S_{D2}}. \quad (10)$$

This expression can be calculated for any spectrum, and it is adopted here as the definition of corner frequency. In random vibration theory (10) is the definition of predominant frequency [Boore, 1983; Cartwright and Longuet-Higgins, 1956].

For the Brune spectrum the low-frequency spectral level is related to the integrals as

$$\Omega^2 = 4 S_{D2}^{3/2} S_{V2}^{-1/2}. \quad (11)$$

In this work the low-frequency spectral level is defined by (11). The instruments are not reliable enough at low fre-

quency to use the spectral value at zero frequency for  $\Omega$ . The moment of the event is

$$M_0 = 4\pi\rho\beta^3\Omega/R, \quad (12)$$

where  $R = \sqrt{2/5}$  is the root-mean-square radiation pattern. Note that hypocentral distance was accounted for at an earlier stage.

Apparent stress is defined to be

$$\sigma_a = \rho\beta^2 E_{\text{rad}}/M_0. \quad (13)$$

The Brune stress drop [Brune, 1970] is

$$\sigma_B = \frac{\rho(2\pi f_0)^3\Omega}{2.34R}. \quad (14)$$

Substituting (10) and (11), these two stress parameters are expressed in terms of the integrals (6) and (7) as

$$\begin{aligned} \sigma_B &= \frac{2\rho}{2.34R} \frac{S_{V2}^{5/4}}{S_{D2}^{3/4}} \\ \sigma_a &= \frac{\rho R}{2} \frac{S_{V2}^{5/4}}{S_{D2}^{3/4}} \end{aligned} \quad (15)$$

Therefore, using (10) and (11) as definitions of corner frequency and low-frequency spectral level, the Brune stress drop and apparent stress are not independent parameters; for a spectrum of any shape,

$$\sigma_B \equiv \frac{4}{2.34R^2} \sigma_a \equiv 4.3 \sigma_a. \quad (16)$$

A two-parameter spectral model is determined by the integrals (6) and (7). A third independent spectral measure will be found here, in order to examine variability of spectral shape and to find an independent stress parameter. This final source parameter is the Hanks or dynamic stress drop,  $\sigma_H$ , which is related to root-mean-square acceleration [Hanks and McGuire, 1981] by a formula proposed as a stress drop measure by Boatwright [1982]. Here the Hanks stress drop is found in the spectral domain, and an acceleration spectral level is needed. The acceleration power spectrum  $A^2(f) = (2\pi f)^2 V^2(f)$  is used to calculate the following integrals

$$S_{A2} = \int_0^{f_m} A^2(f) df \quad (17)$$

$$S_{A4} = \int_0^{f_m} A^4(f) df \quad (18)$$

The upper limit on the integrals  $f_m$  can be any finite frequency that is somewhat greater than  $f_0$ . The acceleration power spectral level is taken to be

$$\langle A^2 \rangle = S_{A4}/S_{A2}. \quad (19)$$

This formula is not sensitive to choice of the upper limit  $f_m$ , and it gives the acceleration spectral level exactly if

## 264 DETERMINATION OF SOURCE PARAMETERS

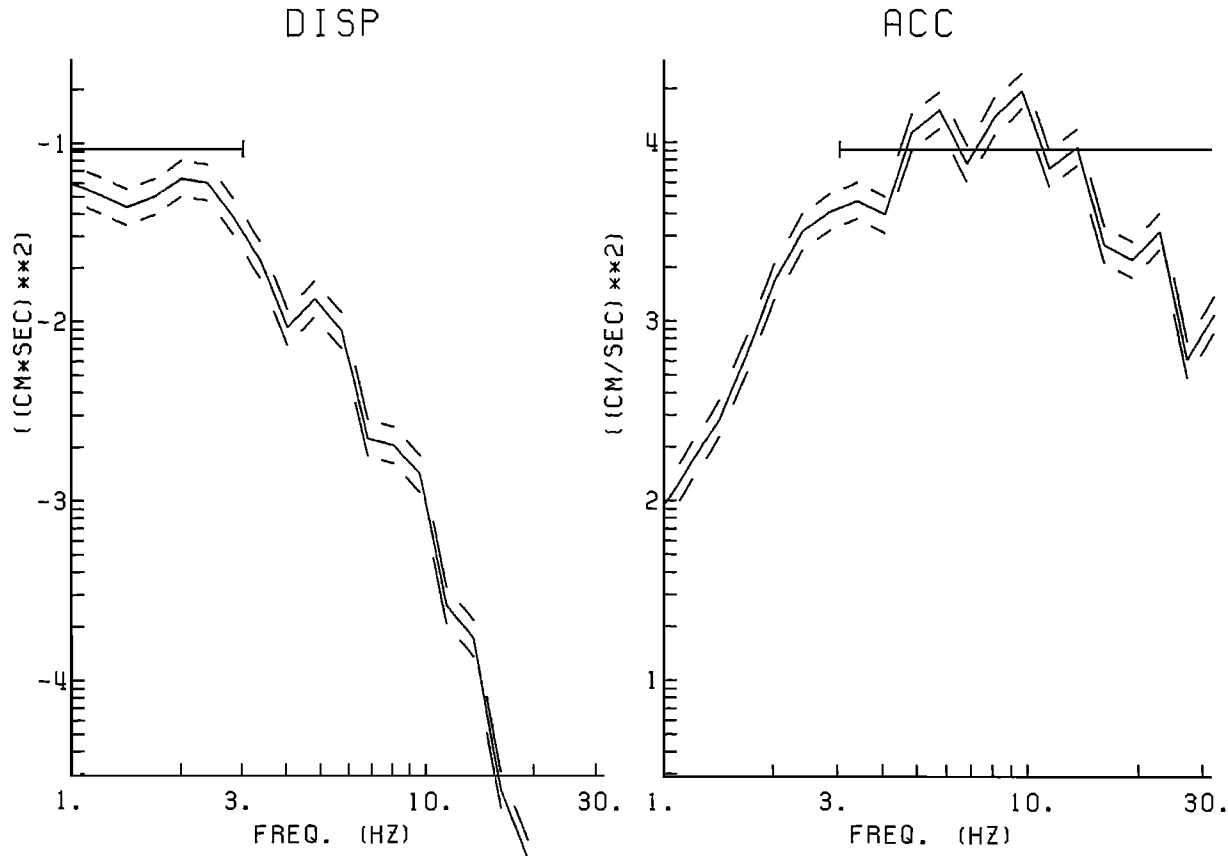


Fig. 7. Adjusted spectrum of event 149 05 16. Same format as Figure 1.

$A^2(f)$  has a boxcar shape. The Hanks stress drop is

$$\sigma_H = \frac{2\pi f_0 \rho}{2.34 R} \sqrt{\langle A^2 \rangle} \quad (20)$$

The numerical factor in this definition is chosen such that  $\sigma_H = \sigma_B$  for a spectrum with the Brune shape (9). The ratio  $\sigma_H/\sigma_B$  will differ from unity for spectra with other shapes.

This quantitative determination of source parameters allows a quantitative estimate of error, if the correlation of spectral noise in different frequency bands is known or assumed. The resultant error is larger for correlated than for uncorrelated noise. I have arbitrarily assumed that spectral noise is correlated below 5 Hz and uncorrelated above 5 Hz in spectral bands a quarter of an octave wide.

### Results

One of the better-determined event spectra, normalized to 1 km hypocentral distance, is shown in Figure 1. The left panel is the displacement spectrum. The horizontal line is the low-frequency spectral level from (11), and it extends to the corner frequency found from (10). The acceleration spectrum is shown in the right panel, where the horizontal

line starting at the corner frequency is the acceleration spectral level from (19). The dashed lines are spaced one standard error above and below the spectrum.

About 90 events had corner frequencies with uncertainties less than 20%. Brune stress drops of these events are plotted against corner frequency in Figure 2. Lines of constant moment are labeled by the value of  $\log_{10} M_0$ . There is a large scatter in the stress drops, but there is no clear correlation with corner frequency, implying no correlation with source radius.

The ratio of Hanks stress drop to Brune stress drop is plotted against corner frequency in Figure 3 for those events for which the uncertainty of this ratio is less than 40%. Recall that this ratio will be constant for a constant spectral shape that is scaled by two parameters, corner frequency and low-frequency level. The ratios found from the data cluster rather tightly around a constant value, and are remarkably independent of corner frequency. Three conclusions may be drawn: (1) the analysis method is stable, (2) the average spectral shape as measured by this ratio varies little between events, and (3) the spectral shape is independent of source radius. I said in the introduction that spectra would be analyzed in terms of a two-parameter model. I am calculating three spectral parameters,  $f_0$ ,  $\Omega$ , and  $\langle A^2 \rangle$  from independent formulas, so the stress param-

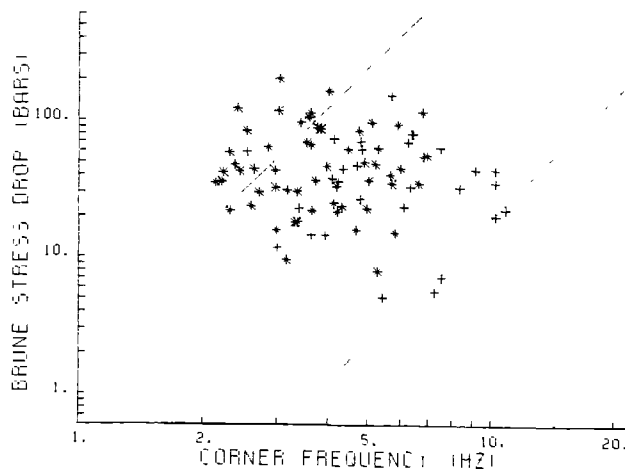


Fig. 8. Brune stress drop plotted against corner frequency, found from adjusted event spectra. Same format as Figure 2.

eters  $\sigma_B$  and  $\sigma_H$  are determined independently. Figure 3 shows that  $\sigma_B$  and  $\sigma_H$ , as actually found in the data, are not independent, so that a two-parameter spectral model fits the data, on average, very well.

Station response spectra for three of the twelve stations are plotted in Figure 4. Ratios of these spectra are well-determined, but all station spectra may be multiplied by an arbitrary common function of frequency. The geometric mean of station spectra at CON, MGE, and five other sites was constrained to be unity. Spectra at LAK and other sites with poor reception of high frequencies were not considered in the constraint. There are large differences between station spectra at high frequency.

The shape of the average event displacement spectrum at low frequencies is shown by the solid curve at the top of Figure 5. To find this curve, the displacement spectrum of each event is divided by its low-frequency spectral level, and a weighted average is found for events with corner frequencies greater than 4.0 Hz. Below a frequency somewhat less than 4.0 Hz the solid curve shows the trend of an average displacement spectrum. The rising trend toward smaller frequency may be partly due to near-field terms (hypocentral distances as small as 5 km are common in the data set), but could be largely due to instrumental problems. It would be reasonable to take advantage of the undetermined degree of freedom in the inversion, dividing all event spectra by a common function to make this average flat below 2 Hz (the dashed line in the figure), and multiplying all station spectra by the same common function.

The solid curve at the bottom of Figure 5 is found by dividing each acceleration spectrum by its acceleration spectral level and finding a weighted average for events with corner frequencies less than 2.5 Hz. The curve above 3 or 4 Hz represents an average acceleration spectrum of more than 20 events. The curve is remarkably flat from 4 to 16 Hz, supporting a  $f^{-2}$  trend of displacement transform above the corner frequency. The falloff above 16 Hz may be

due to attenuation, and it might be reasonable to extend the spectrum along the dashed line.

The source parameter analysis was repeated with adjusted spectra. All event spectra were divided by a common function to make the average scaled displacement spectrum flat below 2 Hz and the average scaled acceleration spectrum flat above 16 Hz. The common function was equal to unity from 2 to 16 Hz, so spectra were not altered in that range. Station spectra were multiplied by the same common function. Note that the most important conclusions of this paper, that stress drop and spectral shape are independent of source radius, have been established with unadjusted data.

Figure 6 shows three of the adjusted station spectra. With this adjustment all station spectra show a falling trend at high frequency. The frequency  $f_{max}$  at which the falloff begins varies with station site and correlates inversely with the thickness of soft sediment at each site.

Figure 7 shows the adjusted spectrum of the same event shown in Figure 1. This spectrum is closer to the model Brune shape, so the corner frequency and level picks are better visual fits.

Figure 8 is a repeat of Figure 2 with parameters found from adjusted spectra. The Brune stress drop is plotted against corner frequency for those events with uncertainty in corner frequency less than 20%. Points here are generally shifted upward and to the right relative to Figure 2. Again there is no correlation between stress drop and corner frequency. The probability distribution function of these stress drop values is log normal with the standard deviation being somewhat greater than a factor of 2.

The ratio of Hanks stress drop to Brune stress drop is plotted against corner frequency for the adjusted data in Figure 9. These points cluster tightly around a constant value, as do the points in Figure 3, and are independent of corner frequency. This ratio of stress drops is plotted against Brune stress drop in Figure 10. There may be a

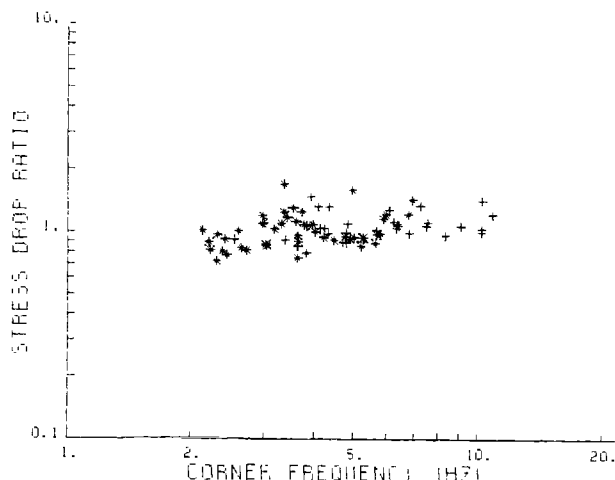


Fig. 9. Ratio of Hanks to Brune stress drop plotted against corner frequency, found from adjusted spectra.

## 266 DETERMINATION OF SOURCE PARAMETERS

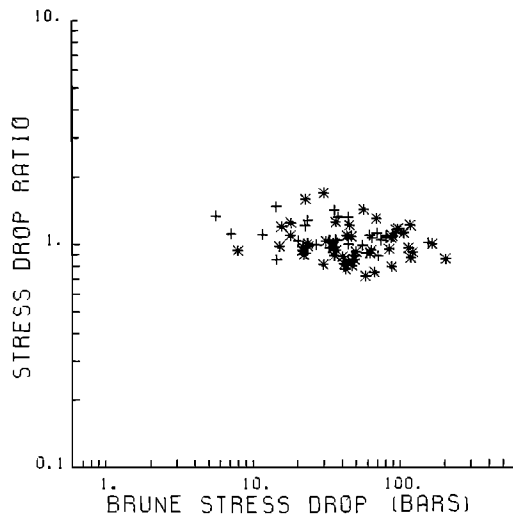


Fig. 10. Ratio of Hanks to Brune stress drop plotted against Brune stress drop, found from adjusted spectra.

small decreasing trend of these points with increasing stress drop. Brune et al. [1986] suggest that events with small stress drop are complex and have spectra with a significant  $f^{-1}$  segment. Such a spectral shape would be seen as a larger  $\sigma_H/\sigma_B$  ratio here. These data marginally support Brune's idea.

#### Conclusions

S-wave spectra recorded at small hypocentral distances have been analyzed to find source parameters by a new objective method. Recorded spectra are inverted to find separate event and station response spectra. Corner frequency and other spectral parameters are found stably and robustly from integrals of each event spectrum. The stability of the method is demonstrated by the fact that the ratio of Hanks to Brune stress drop is remarkably constant for all well-recorded events. The fact that this ratio is independent of corner frequency shows that spectral shape (and, by inference, physical mechanisms) are scale independent.

Dynamic stress drop and Brune stress drop individually have a large scatter, which I interpret to be real, but neither has any correlation with corner frequency. Archuleta et al. [1982] determined stress drops of 67 events of the 1980 Mammoth Lakes sequence and found a trend of decreasing stress drop with decreasing moment for moments less than  $10^{20}$  dyne-cm. They deliberately sought some small events to include in their data set. I have plotted 94 events selected objectively on the basis of source parameter accuracy, and there are no events in my data set with moments much below  $10^{20}$  dyne-cm. Neither data set has events with corner frequencies much greater than 10 Hz. This may be due to the detection threshold, because amplitudes will be more attenuated for events with higher corner frequencies.

I find that the probability distribution function of stress drop is log normal with the standard deviation being somewhat greater than a factor of 2. A more careful statistical analysis of the distribution of these stress drops would require consideration of the detection threshold; events with smaller signal level have decreased probability of being included in the data set. I have shown [Andrews, 1985] that the lower and right limits of the cloud of points in Figure 8 may be a detection effect. It is possible that stress drops with values extending down to zero are common. The stress drop distribution function could be an inverse power law, as might be expected in a fractal model, with a gradual transition to a cutoff at the total shear stress. At 5 km depth in a normal faulting environment with hydrostatic fluid pressure shear stress is 330 bars [McGarr, 1984]. Stress drops found here range up to two-thirds of that value.

It is a reasonable supposition that the stress drop distribution scales with total shear stress. Shear stress, and therefore the stress drop distribution, might increase linearly with depth. Depth resolution of the 1980 Mammoth Lakes aftershocks might be improved by relocating with improved velocity models (C. Mueller, personal communication, 1983). I have not attempted to do this and have not examined the correlation of stress drop with depth. Shear stress will also depend on whether the tectonic regime is extensional or compressional. Stress drops, and hence ground motion intensity, could be significantly higher in compressional regions. This data analysis method needs to be applied to other data sets with good depth resolution in compressional as well as extensional environments.

**Acknowledgment.** Edward Cranswick helped me use the digital records and understand their quirks. I am grateful for comments by Charles Mueller, John Boatwright, David Boore, and J. A. Snee.

#### References

- Aki, K., Scaling law of seismic spectrum, *J. Geophys. Res.*, 72, 1217-1231, 1967.
- Andrews, D. J., Separation of source and propagation spectra of seven Mammoth Lakes aftershocks, in Proceedings of Workshop XVI, Dynamic Characteristics of Faulting, 1981, U.S. Geol. Sur. Open File Rep. 82-591, p. 437, 1982.
- Andrews, D. J., The effect of detection threshold and high-frequency attenuation on distribution of observed earthquake source parameters (abstract), *EOS Trans. AGU*, 66, 972, 1985.
- Archuleta, R. J., E. Cranswick, C. Mueller, and P. Spudich, Source parameters of the 1980 Mammoth Lakes California earthquake sequence, *J. Geophys. Res.*, 87, 4595-4607, 1982.
- Boatwright, J., A dynamic model for far-field acceleration, *Bull. Seismol. Soc. Am.*, 72, 1049-1068, 1982.
- Boore, D. M., Stochastic simulation of high-frequency ground motions, *Bull. Seismol. Soc. Am.*, 73, 1865-1894, 1983.

- Brune, J. N., Tectonic stress and the spectra of seismic shear waves from earthquakes, *J. Geophys. Res.*, 75, 4997–5009, 1970, Correction, *J. Geophys. Res.*, 76, 5002, 1971.
- Brune, J. N., J. B. Fletcher, F. L. Vernon, L. C. Haar, T. C. Hanks, and J. Berger, Low stress drop earthquakes in the light of new data from the Anza, California telemetered digital array, this volume, 1986.
- Cartwright, D. E., and M. S. Longuet-Higgins, The statistical distribution of the maxima of a random function, *Proc. R. Soc. London, Ser. A* 237, 212–223, 1956.
- Cranswick, E., R. Wetmiller, and J. Boatwright, High-frequency observations and source parameters of micro-earthquakes recorded at hard-rock sites, *Bull. Seismol. Soc. Am.*, 75, 1535–1567, 1985.
- Frankel, A., The effects of attenuation and site response on the spectra of microearthquakes in the northeastern Caribbean, *Bull. Seismol. Soc. Am.*, 72, 1379–1402, 1982.
- Hanks, T. C., and R. K. McGuire, The character of high-frequency strong ground motion, *Bull. Seismol. Soc. Am.*, 71, 2071–2095, 1981.
- Linde, A. T., R. Stefansson, and I. S. Sacks, A technique for high relative accuracy in the determination of earthquake stress drops, *EOS Trans. AGU*, 61, 294, 1980.
- Malin, P. E., and J. A. Waller, Preliminary results from vertical seismic profiling of Oroville microearthquake S waves, *Geophys. Res. Lett.*, 12, 137–140, 1985.
- McGarr, A., Scaling of ground motion parameters, state of stress, and focal depth, *J. Geophys. Res.*, 89, 6969–6979, 1984.
- Menke, W., *Geophysical Data Analysis: Discrete Inverse Theory*, Academic, New York, 260 pp., 1984.
- Mueller, C. S., Source pulse enhancement by deconvolution of an empirical Green's function, *Geophys. Res. Lett.*, 12, 33–36, 1985.
- Mueller, C. S., P. Spudich, E. Cranswick, and R. J. Archuleta, Preliminary analysis of digital seismograms from the Mammoth Lakes California earthquake sequence of May–June, 1980, U. S. Geol. Sur. Open File Rep. 81–155, 1981.
- Peppin, W. A., What do spectral corner frequencies mean anyway? (abstract), *Earthquake Notes*, 55, 14, 1985.
- Silver, P. G., Retrieval of source-extent parameters and the interpretation of corner frequency, *Bull. Seismol. Soc. Am.*, 73, 1499–1511, 1983.
- Snoke, J. A., A. T. Linde, and I. S. Sacks, Apparent stress: an estimate of the stress drop, *Bull. Seismol. Soc. Am.*, 73, 339–348, 1983.
- Spudich, P., E. Cranswick, J. Fletcher, E. Harp, C. Mueller, R. Navarro, J. Sarmiento, J. Vinton, and R. Warrick, Acquisition of digital seismograms during the Mammoth Lakes California earthquake sequence of May–June 1980, U. S. Geol. Sur. Open File Rep. 81–38, 1981.

ON SIMULATING LARGE EARTHQUAKES BY GREEN'S-FUNCTION  
ADDITION OF SMALLER EARTHQUAKES

William B. Joyner  
David M. Boore

U.S. Geological Survey, Menlo Park, California 94025

**Abstract.** Simulation of ground motion from large earthquakes has been attempted by a number of authors using small earthquakes (subevents) as Green's functions and summing them, generally in a random way. We present a simple model for the random summation of subevents to illustrate how seismic scaling relations can be used to constrain methods of summation. In the model  $\eta$  identical subevents are added together with their start times randomly distributed over the source duration  $T$  and their waveforms scaled by a factor  $\kappa$ . The subevents can be considered to be distributed on a fault with later start times at progressively greater distances from the focus, simulating the irregular propagation of a coherent rupture front. For simplicity the distance between source and observer is assumed large compared to the source dimensions of the simulated event. By proper choice of  $\eta$  and  $\kappa$  the spectrum of the simulated event deduced from these assumptions can be made to conform at both low- and high-frequency limits to any arbitrary seismic scaling law. For the  $\omega$ -squared model with similarity (that is, with constant  $M_0 f_0^3$  scaling, where  $f_0$  is the corner frequency), the required values are  $\eta = (M_0/M_{0e})^{4/3}$  and  $\kappa = (M_0/M_{0e})^{-1/3}$ , where  $M_0$  is moment of the simulated event and  $M_{0e}$  is the moment of the subevent. The spectra resulting from other choices of  $\eta$  and  $\kappa$  will not conform at both high and low frequency. If  $\eta$  is determined by the ratio of the rupture area of the simulated event to that of the subevent and  $\kappa = 1$ , the simulated spectrum will conform at high frequency to the  $\omega$ -squared model with similarity, but not at low frequency. Because the high-frequency part of the spectrum is generally the important part for engineering applications, however, this choice of values for  $\eta$  and  $\kappa$  may be satisfactory in many cases. If  $\eta$  is determined by the ratio of the moment of the simulated event to that of the subevent and  $\kappa = 1$ , the simulated spectrum will conform at low frequency to the  $\omega$ -squared model with similarity, but not at high frequency. Interestingly, the high-frequency scaling implied by this latter choice of  $\eta$  and  $\kappa$  corresponds to an  $\omega$ -squared model with constant  $M_0 f_0^4$ —a scaling law proposed by Nuttli, although questioned recently by Haar and others.

Simple scaling with  $\kappa$  equal to unity and  $\eta$  equal to the moment ratio would work if the high-frequency spectral

decay were  $\omega^{-1.5}$  instead of  $\omega^{-2}$ . Just the required decay is exhibited by the stochastic source model recently proposed by Joyner, if the dislocation-time function is deconvolved out of the spectrum. Simulated motions derived from such source models could be used as subevents rather than recorded motions as is usually done. This strategy is a promising approach to simulation of ground motion from an extended rupture.

### Introduction

The lack of near-source recordings of ground motion in large earthquakes has generated interest in methods of simulating such motion for purposes of engineering design. Simulation of ground motion from large earthquakes requires consideration of source, path, and local site effects. Numerous authors have attempted to remove the uncertainty in the path and site effects by using small earthquakes as Green's functions in the simulation of ground motion from larger events [Hartzell, 1978, 1982; Wu, 1978; Kanamori, 1979; Hadley and Helmberger, 1980; Mikumo et al., 1981; Irikura and Muramatu, 1982; Irikura, 1983; Coats et al., 1984; Houston and Kanamori, 1984; Imagawa et al., 1984; Munguiá and Brune, 1984; Hutchings, 1985]. The small earthquakes (henceforth called subevents) ideally are located near the hypothetical source and recorded at the site, but these ideal conditions are commonly relaxed. The method of Green's-function addition not only has the advantage of incorporating wave-propagation effects and local site effects, it also is capable of incorporating the effects of rupture propagation and source-station geometry. In particular the method should model, at least in part, the effect of directivity. Users of the method generally postulate some distribution of subevents over a fault plane and sum them in accordance with an assumed geometry of rupture propagation. Some authors associate with each element of the fault plane a series of subevents spread out in time. Imagawa et al. [1984] filtered subevent records by a filter designed to correct for the difference in rise time between subevent and simulated event.

In this paper we are not advocating the method of Green's-function addition or demonstrating it. Our sole purpose is to show how, in the practical situation, seismic

## 270 LARGE EARTHQUAKE SIMULATIONS

scaling considerations can be used to derive constraints useful in applying the method.

The heterogeneity of earthquake source processes is a crucial issue in the application of the method. Irikura [1983] used the method to simulate ground motion from a shallow magnitude 6.7 earthquake on the assumption of a rupture uniform in both rupture velocity and total dislocation. The resulting motion was deficient at high frequency relative to the observed ground motion, leading to the conclusion that the real rupture was not uniform and forcing a modification of the summing method to enhance the high frequency. Imagawa et al. [1984] attempted to model a different earthquake as a uniform rupture and also came to the conclusion that the rupture was not uniform. Authors other than Irikura have generally included randomness of some sort in their methods for summing subevents. This randomness may be thought to represent a degree of random heterogeneity characteristic of large earthquakes. It also performs an important function in preventing spurious periodicities in the simulated motion resulting from summing over uniform grids in space or over points equally spaced in time. Irikura [1983], who did not use any randomness in his summation, relied on a special smoothing technique to eliminate spurious periodicities.

In the spirit of the original concept of the subevent as a Green's function, the corner frequency of the subevent should be higher than any frequency of interest in the simulated motion. In that case the subevent record will be a true impulse response, and the spectrum of the simulated event will depend on how the subevents are distributed over the fault and in time. The quality of the simulation will depend, accordingly, upon how well the distribution of slip is represented over the fault and in time, in particular, how well the degree and kind of heterogeneity of faulting is represented. In the general case, however, because of limited dynamic range in the subevent records, it may not be possible to use subevents so small that their corner frequencies are higher than any frequency of engineering interest and still maintain the desired bandwidth in the simulated motion. If we wanted to keep the subevent corner frequencies above 3 Hz, we could use subevents no larger than a moment magnitude of about 4; if we wanted to keep the subevent corner frequencies above 10 Hz, we could use subevents no larger than a moment magnitude of about 3. Those who have done simulations by the method of Green's-function addition have generally used much larger subevents, a practice which suggests that it is generally necessary to consider frequencies above the subevent corner.

It is important to note that the effect of directivity will not be correctly modeled at frequencies above the subevent corner frequency unless the angle between the rupture direction and the source-to-station vector is the same for the simulated event as the subevent.

The necessity to consider frequencies above the subevent corner introduces a strong constraint on methods for random summation of subevents, a constraint that, as far as we are aware, has not been explicitly discussed in the lit-

erature. At very low frequency the subevent spectra will add coherently and the spectral values of the simulated event will be equal to the sum of the subevent values. At sufficiently high frequency the subevent spectra will add incoherently and the spectral values of the simulated event will be equal to the square root of the sum of squares of the subevent values. These rules in combination with seismic scaling relations form the constraint on methods of random summation. We present here a very simple method of random summation, and use it to illustrate the constraint.

#### Spectrum of the Simulated Event

In the method  $\eta$  subevents are added together with their start times distributed randomly with uniform probability over the source duration  $T$  and their waveforms scaled by a factor  $\kappa$ . Although randomly distributed in time the subevents can be considered to be distributed on a fault with later start times at progressively greater distances from the focus, simulating the irregular propagation of a coherent rupture front. For most of the discussion the waveforms of the subevents are assumed identical. This not only simplifies the discussion, it also corresponds to the practical situation in which generally many times as many subevents are needed as there are small earthquake records available. The case in which the subevents are not identical is considered in the Appendix. For simplicity the distance between source and observer is assumed large compared to the source dimensions of the simulated event. With these assumptions the source spectrum of the simulated event averaged over the ensemble is shown to be

$$S(\omega) = \left\{ \eta \left[ 1 + (\eta - 1) \frac{\sin^2(\omega T/2)}{(\omega T/2)^2} \right] \right\}^{1/2} \kappa S_e(\omega), \quad (1)$$

where  $S_e(\omega)$  is the subevent source spectrum. The derivation is given in the Appendix.

At sufficiently high frequencies the shape of the spectrum described by (1) is controlled by the subevent spectrum. Below the corner frequency of the subevent, the subevent spectrum is flat, and the shape of the simulated event spectrum depends upon the quantity in braces in (1). At low frequencies the simulated event spectrum is flat, and at intermediate frequencies it has a trend proportional to  $\omega^{-1}$ , a consequence of the uniform probability distribution assumed for the random summation, which was a choice made for the sake of simplicity. Other rates of falloff at intermediate frequencies could be obtained by appropriate choice of distribution function. The intersection of the low- and intermediate-frequency trends is at a frequency  $f = f_0/\pi$ , where  $f_0 = 1/T$ . We will use the low- and high-frequency limits to constrain methods of summation.

At low frequency (1) simplifies to

$$S(\omega) = \eta \kappa S_e(\omega), \quad \omega \rightarrow 0, \quad (2)$$

and at sufficiently high frequency the second term in square brackets is negligible, and

$$S(\omega) = \sqrt{\eta} \kappa S_e(\omega), \quad \omega \rightarrow \infty. \quad (3)$$

This is just what one should expect; the spectra add coherently at low frequency and incoherently at high frequency. The "sufficiently high" frequency  $f (= \omega/2\pi)$  needed for (3) to be applicable is given approximately by

$$fT > \sqrt{\eta}/\pi. \quad (4)$$

Thus we have

$$LF \propto \eta \kappa$$

$$HF \propto \sqrt{\eta} \kappa.$$

where  $LF$  and  $HF$  are shorthand for the ratios between the spectrum of the simulated event and the subevent at low and high frequency, respectively.

#### The Constraint

We are now in a position to use the scaling laws of earthquake spectra to determine  $\eta$  and  $\kappa$ . We emphasize the  $\omega$ -squared model [Aki, 1967; Brune, 1970]. The stochastic version of the  $\omega$ -squared model proposed by Hanks and McGuire [1981] has been successful in predicting measures of ground motion over a broad range in moment magnitude [Hanks and McGuire, 1981; Boore, 1983; Hanks and Boore, 1984]. For the sake of generality, however, we derive the equations determining  $\eta$  and  $\kappa$  for arbitrary scaling laws. If the displacement spectrum falls off at high frequency as  $f^{-\gamma}$ , then the high-frequency trend can be written as  $M_0(f_0/f)^\beta$ , where  $M_0$  is the seismic moment and  $f_0$  is the corner frequency defined as the frequency at which the low-frequency and high-frequency trends intersect. If the scaling conforms to constant  $M_0 f_0^\beta$ , then spectral values at high frequency are proportional to  $M_0^{1-\gamma/\beta}$ , and  $HF = (M_0/M_{0e})^{1-\gamma/\beta}$ , where  $M_{0e}$  is the subevent moment. Noting that  $LF = M_0/M_{0e}$  and applying a little algebra gives

$$\begin{aligned} \eta &= \left( \frac{M_0}{M_{0e}} \right)^{2\gamma/\beta} \\ \kappa &= \left( \frac{M_0}{M_{0e}} \right)^{1-2\gamma/\beta}. \end{aligned} \quad (5)$$

For the  $\omega$ -squared model  $\gamma = 2$ . If similarity holds,  $M_0 f_0^3$  is constant for all earthquakes, and  $\beta = 3$ . So, for the  $\omega$ -squared model with similarity

$$\begin{aligned} \eta &= \left( \frac{M_0}{M_{0e}} \right)^{4/3} \\ \kappa &= \left( \frac{M_0}{M_{0e}} \right)^{-1/3}. \end{aligned} \quad (6)$$

Notice that the exponent in the equation for  $\kappa$  is negative. The subevent records must be reduced in amplitude, and correspondingly larger numbers of them added together in order to satisfy the high-frequency and low-frequency requirements simultaneously.

The high-frequency approximation given by (3) is valid above a frequency  $f_h$  determined by the inequality (4). Since  $f_0 = 1/T$ ,

$$f_h/f_0 = \sqrt{\eta}/\pi.$$

For the  $\omega$ -squared model with similarity (6) can be used to obtain

$$\frac{f_h}{f_0} = \frac{1}{\pi} \left( \frac{M_0}{M_{0e}} \right)^{2/3}. \quad (7)$$

With similarity  $M_0 f_0^3$  is constant and

$$\frac{f_e}{f_0} = \left( \frac{M_0}{M_{0e}} \right)^{1/3}, \quad (8)$$

where  $f_e$  is the subevent corner frequency. Equations (7) and (8) imply that  $f_h = f_e$  for a moment magnitude difference of approximately one unit between simulated event and subevent. For larger differences  $f_h$  is greater than  $f_e$ , and for smaller differences it is less.

Figure 1 shows the spectrum (light line) of a simulated event, using the values of  $\eta$  and  $\kappa$  given above, for the case in which the difference in moment magnitude between the simulated event and the subevent is one unit. The subevent spectrum is assumed to be

$$S_e(\omega) = \frac{1}{1 + (f/f_e)^2}$$

[Brune, 1970]. The heavy line on Figure 1 shows, for comparison, the spectrum that would result from scaling the subevent spectrum up to the moment of the simulated event in accordance with similarity, that is, with  $M_0 f_0^3$  held constant. The value of  $f_e$  in Figure 1 is  $\sqrt{10} f_0$ , and the value of  $f_h$  is about  $3 f_0$ , approximately the same, as predicted above. Figure 2 shows the same comparison for the case in which the difference in moment magnitude between the simulated event and the subevent is

## 272 LARGE EARTHQUAKE SIMULATIONS

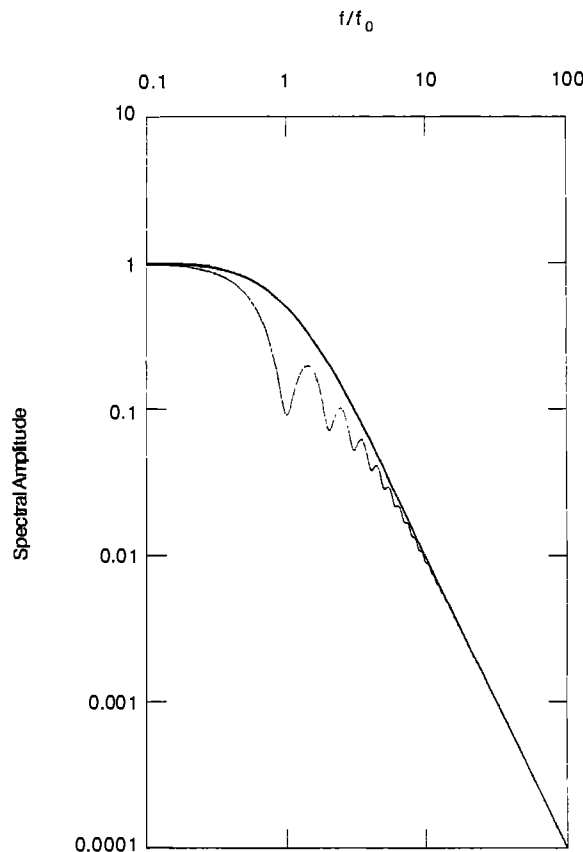


Fig. 1. Spectrum (light line) of the simulated event for a difference of one unit in moment magnitude between simulated event and subevent, compared to the  $\omega$ -squared spectrum (heavy line) obtained as described in the text. Spectra are normalized to the low-frequency level.

two units. For the case shown in Figure 2,  $f_c = 10f_0$ , and (4) is satisfied at frequencies above about  $30f_0$ . The simulated spectra in Figures 1 and 2 are constrained only at the low-frequency and high-frequency limits but are within a factor of two of the target spectra over most of the intermediate-frequency range, indicating that even this oversimplified method of summation gives reasonably satisfactory simulations at intermediate frequencies, at least as long as the magnitude difference between simulated event and subevent does not exceed the two units illustrated in Figure 2. One might hope that more realistic methods of summation would give even better results.

Similarity breaks down for earthquakes larger than that value of moment which corresponds to rupture of the entire width of the seismogenic zone. Joyner [1984] has proposed a scaling law applicable to such events. Consistency with that law can be attained by choosing  $\eta$  and  $\kappa$  such that  $LF$  is equal to  $M_0/M_{0e}$  and  $HF$  is equal to the square root of the ratio of rupture areas.

## Applications

The approach used to develop (6) can be applied to show the consequences of other methods of summation. Suppose that  $\eta$  is determined by the ratio of the rupture area of the simulated event to that of the subevent and  $\kappa = 1$ . In an  $\omega$ -squared model with similarity, rupture area  $A \propto M_0^{2/3}$ , so

$$LF = (M_0/M_{0e})^{2/3}$$

$$HF = (M_0/M_{0e})^{1/3}.$$

These relations satisfy the high-frequency but not the low-frequency constraint. The high-frequency part of the spectrum is generally the important part for engineering applications, however, and this method will give satisfactory results in many cases.

Suppose that  $\eta$  is determined by the ratio of the moment of the simulated event to that of the subevent and  $\kappa = 1$ . Then  $\eta = M_0/M_{0e}$ , and

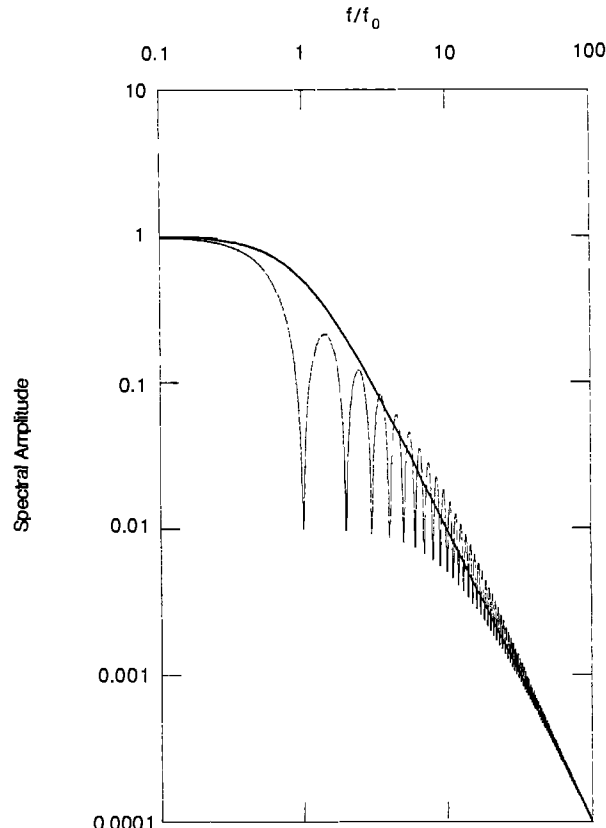


Fig. 2. Spectrum (light line) of the simulated event for a difference of two units in moment magnitude between simulated event and subevent, compared to the  $\omega$ -squared spectrum (heavy line) obtained as described in the text. Spectra are normalized to the low-frequency level.

$$LF = M_0/M_{0e}$$

$$HF = (M_0/M_{0e})^{1/2}.$$

This satisfies the low-frequency constraint but not the high-frequency constraint demanded by the  $\omega$ -squared model with similarity. Interestingly, the  $HF$  scaling, combined with the high-frequency dependence of  $M_0 f_0^2$  for an  $\omega$ -squared model implies that

$$M_0 f_0^4 = \text{constant},$$

a scaling law proposed by Nuttli [1983], although questioned recently by Haar et al. [1984] and by Atkinson and Boore [1985].

The method of summation proposed by Hadley and Helmberger [1980] is not consistent with the condition expressed by (6). They divide the fault rupture into  $n$  elements with  $n$  chosen to approximate the ratio of rupture areas between simulated event and subevent. For every element they sum randomly  $N$  subevents, each multiplied by  $\xi/N$ , where  $\xi$  ( $A_0$  in their terminology) is chosen so as to give the correct moment for the simulated event and  $N$  is the ratio of the rise time of the simulated event to the rise time of the subevent. If similarity holds, then

$$N = \left( \frac{M_0}{M_{0e}} \right)^{1/3}.$$

If the subevents are equal in moment, then

$$n\xi = \frac{M_0}{M_{0e}}. \quad (9)$$

Since the total number of events  $\eta = nN$ ,

$$\eta = \frac{1}{\xi} \left( \frac{M_0}{M_{0e}} \right)^{4/3},$$

and since the factor  $\kappa$  by which the subevents are multiplied is  $\xi/N$ ,

$$\kappa = \xi \left( \frac{M_0}{M_{0e}} \right)^{-1/3}.$$

These expressions are equivalent to (6) if and only if  $\xi = 1$ , but by (9)  $\xi = 1$  only if  $n$  is equal to the moment ratio between simulated event and subevent. Thus, the method of summation proposed by Hadley and Helmberger [1980] would agree with (6) if  $n$  were equal to the moment ratio. They proposed, however, that  $n$  be chosen as the ratio of rupture areas.

### Simulated Motions as Subevents

The discussion in this paper has been framed in terms of using recorded motions for the subevents, but stochastic simulations could be used just as well. With methods such as those described by Boore [1983] and Joyner [1984], stochastic simulations could be generated representing point sources, and motions from a number of point sources could be added together to represent motion from a fault rupture too large to be treated as a point source. Such an approach may be a particularly efficient way of simulating an extended rupture. One possible source model to be used in the generation of the time series for each subevent is that of Joyner [1984], who proposed a kinematic source model in which the spectrum, with the dislocation-time function deconvolved out, has a high-frequency decay of  $f^{-1.5}$ . If similarity is assumed, (5) leads to  $\kappa$  equal to unity and  $\eta$  equal to the moment ratio. The dislocation-time function could be included by convolution, as the last step in the simulation process, after the subevent time series had been summed. The concept of using subevents with the dislocation-time function deconvolved out is physically appealing, and the simple addition of subevents using a scale factor of unity has an attractive simplicity.

### Appendix

To form the simulated event we take  $\eta$  subevents with spectra  $S_{ej}(\omega)$ . The subevents all have the same moment, but the spectra are not necessarily identical. We multiply the subevents by  $\kappa$  and add them together with delay times  $t_j$  distributed with uniform probability between 0 and  $T$ . The expected value of the squared modulus spectrum is

$$S^2(\omega) = E \left\{ \left( \sum_{j=1}^{\eta} \kappa S_{ej}(\omega) e^{-i\omega t_j} \right) \cdot \left( \sum_{k=1}^{\eta} \kappa S_{ek}^*(\omega) e^{i\omega t_k} \right) \right\},$$

where  $E$  is the expected value operator and  $*$  denotes the complex conjugate.  $S_{ej}$  and  $S_{ek}$  are independent of  $t_j$  and  $t_k$ , and, for  $j \neq k$ ,  $t_j$  is independent of  $t_k$ . The probability that  $t_j$  takes on a given value is

$$\frac{dt_j}{T} \quad 0 \leq t_j \leq T$$

$$0 \quad \text{otherwise.}$$

$$S^2(\omega) = \sum_{j=1}^{\eta} \int_0^T \frac{dt_j}{T} \kappa^2 E \{ S_{ej}(\omega) S_{ej}^*(\omega) \}$$

$$+ \sum_{j=1}^{\eta} \sum_{k=1, k \neq j}^{\eta} \int_0^T e^{-i\omega t_j} \frac{dt_j}{T} \int_0^T e^{i\omega t_k} \frac{dt_k}{T} \kappa^2 E \{ S_{ej}(\omega) S_{ek}^*(\omega) \}.$$

Performing the integrations gives

## 274 LARGE EARTHQUAKE SIMULATIONS

$$S^2(\omega) = \eta \kappa^2 S_e^2(\omega) + \eta(\eta - 1) \frac{\sin^2(\omega T/2)}{(\omega T/2)^2} \kappa^2 E\{S_{ej}(\omega) S_{ek}^*(\omega)\}, \quad (\text{A1})$$

where  $S^2(\omega)$  is the expected value of the squared modulus of the subevent spectrum. If the subevents are identical, then

$$S^2(\omega) = \eta \left[ 1 + (\eta - 1) \frac{\sin^2(\omega T/2)}{(\omega T/2)^2} \right] \kappa^2 S_e^2(\omega). \quad (\text{A2})$$

Taking the square root of (A2) gives (1) of the text. If the subevents are not identical then the spectrum of the simulated event depends upon the statistical properties of the random process represented by the subevent spectra. In the low-frequency limit the subevents must be identical because they have the same moment, and so the low-frequency limit of (A1) is the same as that of (A2). At sufficiently high frequency the second term in (A1) can be neglected, and the high-frequency limit of (A1) is the same as that of (A2).

**Acknowledgments.** We are grateful to P. Spudich, S. Hartzell, and K. Irikura for careful reviews and valuable suggestions for improving the manuscript. This research was partially supported by a grant from the Nuclear Regulatory Commission.

## References

- Aki, K., Scaling law of seismic spectrum, *J. Geophys. Res.*, **72**, 1217–1231, 1967.
- Atkinson, G. M., and D. M. Boore, Implications of digital seismograph data for ground motion scaling in eastern North America (abstract), *Earthquake Notes* **56**, 4, 1985.
- Boore, D. M., Stochastic simulation of high-frequency ground motions based on seismological models of the radiated spectra, *Bull. Seismol. Soc. Am.*, **73**, 1865–1894, 1983.
- Brune, J. N., Tectonic stress and the spectra of seismic shear waves from earthquakes, *J. Geophys. Res.*, **75**, 4997–5009, 1970.
- Coats, D. A., H. Kanamori, and H. Houston, Simulation of strong motion from the 1984 Alaskan earthquake (abstract), *Earthquake Notes*, **55**, 18, 1984.
- Haar, L. C., J. B. Fletcher, and C. S. Mueller, The 1982 Enola, Arkansas, swarm and scaling of ground motion in the eastern United States, *Bull. Seismol. Soc. Am.*, **74**, 2463–2482, 1984.
- Hadley, D. M., and D. V. Helmberger, Simulation of strong ground motions, *Bull. Seismol. Soc. Am.*, **70**, 617–630, 1980.
- Hanks, T. C., and D. M. Boore, Moment-magnitude relations in theory and practice, *J. Geophys. Res.*, **89**, 6229–6235, 1984.
- Hanks, T. C., and R. K. McGuire, The character of high-frequency strong ground motion, *Bull. Seismol. Soc. Am.*, **71**, 2071–2095, 1981.
- Hartzell, S. H., Earthquake aftershocks as Green's functions, *Geophys. Res. Lett.*, **5**, 1–4, 1978.
- Hartzell, S. H., Simulation of ground accelerations for the May 1980 Mammoth Lakes, California, earthquakes, *Bull. Seismol. Soc. Am.*, **72**, 2381–2387, 1982.
- Houston, H., and H. Kanamori, The effect of asperities on short-period seismic radiation with application to the 1984 Alaskan earthquake (abstract), *Earthquake Notes*, **55**, 18, 1984.
- Hutchings, L., Modeling earthquakes with empirical Green's functions (abstract), *Earthquake Notes*, **56**, 14, 1985.
- Imagawa, K., N. Mikami, and T. Mikumo, Analytical and semi-empirical synthesis of near-field seismic waveforms for investigating the rupture mechanism of major earthquakes, *J. Phys. Earth*, **32**, 317–338, 1984.
- Irikura, K., Semi-empirical estimation of strong ground motions during large earthquakes, *Bull. Disaster Prevention Res. Inst. (Kyoto Univ.)*, **33**, 63–104, 1983.
- Irikura, K., and I. Muramatu, Synthesis of strong ground motions from large earthquakes using observed seismograms of small events, *Proceedings of the 3rd International Microzonation Conference*, vol. 1, 447–458, Seattle, 1982.
- Joyner, W. B., A scaling law for the spectra of large earthquakes, *Bull. Seismol. Soc. Am.*, **74**, 1167–1188, 1984.
- Kanamori, H., A semi-empirical approach to prediction of long-period ground motions from great earthquakes, *Bull. Seismol. Soc. Am.*, **69**, 1645–1670, 1979.
- Mikumo, T., K. Irikura, and K. Imagawa, Near-field strong-motion synthesis from foreshock and aftershock records and the rupture process of the main shock fault (abstract), *IASPEI 21st General Assembly*, London, Canada, July 20–30, 1981.
- Munguia, L., and J. N. Brune, Simulations of strong ground motion for earthquakes in the Mexicali-Imperial valley, *Earthquake Engineering Research Institute, Workshop on Strong Ground Motion Simulation and Earthquake Engineering Applications*, Los Altos, California, 1984.
- Nuttli, O. W., Average seismic source-parameter relations for mid-plate earthquakes, *Bull. Seismol. Soc. Am.*, **73**, 519–535, 1983.
- Wu, F. T., Prediction of strong ground motion using small earthquakes, *Proceedings of the 2nd International Microzonation Conference*, vol. 2, 701–704, San Francisco, 1978.

## THE EFFECT OF FINITE BANDWIDTH ON SEISMIC SCALING RELATIONSHIPS

D. M. Boore

U. S. Geological Survey, Menlo Park, California 94025

**Abstract.** A breakdown of similarity is generally observed in earthquake sequences below a magnitude of about 5. Although usually manifested as an upper limit on observed corner frequencies (and therefore a decrease of calculated stress drop with decreasing moment), the apparent breakdown can also be seen as changes in the slope of various peak motions plotted against moment. This effect can be explained by a moment-independent high-frequency limit on the band of the recorded signal without specifying whether the limit is imposed by the source, the propagation path, the local site, or the recording instrument. With such a limit, the logarithm of peak acceleration, peak velocity, peak displacement, response spectra, apparent stress, and stress drop will scale for small earthquakes as  $1.0 \log M_0$ , in contrast to the lesser dependence on moment exhibited for larger earthquakes. The particular filter used in this paper to produce the high-frequency band limitation had the form  $\exp(-\pi\kappa f)$ , where  $\kappa$  is a parameter controlling the effective corner frequency of the filter. Using an  $\omega$ -squared, constant-stress-parameter spectral model and a previously published simulation method, I have simulated seismograms for two cases, one for a generic model, with the upper limit to the spectral band spanning a wide range of frequencies, and the other for the aftershock sequence of the 1983 Coalinga, California, earthquake, with  $\kappa$  based on measurements of the spectra. In the first case, the simulations reproduced the general observations with respect to the moment dependence of corner frequencies, stress parameters, and the various measures of peak ground motion. In the second case, the simulations are consistent with the observed seismic-moment scaling of the peak accelerations and peak velocities, for both  $P$  and  $S$  waves.

### Introduction

A pervasive finding of studies of recordings from suites of earthquakes is a breakdown in similarity for earthquakes with magnitudes less than about 5. This breakdown is usually seen as an upper limit to the observed corner frequency and consequently a derived stress drop that decreases with earthquake size. Besides those studies referenced in McGarr [this volume], an apparent breakdown in similarity is also found by Bakun et al. [1976], Rautian et al. [1978],

Fletcher [1982], Nuttli [1983], Scherbaum and Stoll [1983], Haar et al. [1984], Scherbaum and Kisslinger [1984], I. Apopei [personal communication, 1985], and A. Rovelli [personal communication, 1985], among others. The earthquakes studied in the referenced papers occurred in California, Alaska, South Carolina, Arkansas, Missouri, Tadzhikistan (USSR), Italy, Romania, and Germany. Another manifestation of this apparent breakdown in similarity is the divergence of the scaling of peak acceleration and velocity from that expected from theoretical arguments based on source spectra obeying the similarity conditions [McGarr et al., 1986; McGarr, this volume].

This nonsimilar behavior has been interpreted widely as a source effect (involving either an upper limit to the frequency radiated or a dependence of stress on moment). The purpose of this paper is to explore the possibility that the effect could be explained by any process that limits high frequencies, whether it be due to the instrument, source, or site. Others have remarked on the influence of the bandwidth on observed ground motions and derived source parameters [e.g., Hanks, 1982; Hanks and McGuire, 1981; Hanks and Boore, 1984]. This paper presents a more comprehensive and quantitative investigation of the effects than has been previously published.

### Method

Although the apparent divergence from similarity has most often been seen in plots of seismic moment versus corner frequency or stress drop, the emphasis in this paper will be on the scaling of peak velocity ( $v_p$ ) and acceleration ( $a_p$ ) on seismic moment, as the effect of a finite bandwidth is less obvious for these measures than it is for stress drop. Hanks [1982] has discussed the implications of a moment-independent bandwidth on stress drop.

The approach is to derive theoretical estimates of  $v_p$  and  $a_p$  corresponding to a spectral model of the radiated energy that includes a moment-independent low-pass filter. The method for deriving theoretical estimates of  $v_p$  and  $a_p$  has been presented before [Boore, 1983]; it basically consists of filtering a time series made up of windowed, white Gaussian noise. It might seem that the method, being based on a stochastic series, might be inapplicable for the simula-

## 276 EFFECT OF BANDWIDTH ON SEISMIC SCALING

TABLE 1. Amplification Factors for *P* and *S* Waves

Frequency (Hz)	$\delta$ ( <i>P</i> waves)*	$\delta$ ( <i>S</i> waves)*
0.10	0.01	0.01
0.32	0.04	0.04
1.	0.13	0.13
3.2	0.17	0.34
10.	0.19	0.37

From Boore [1986].

\*Amplification =  $10^6$ .

tion of the simple pulselike waveforms often characterizing records from small events. This, however, is not the case. The simulated ground motion can be simple or complex in appearance, depending on the filter parameters [Boore, 1983, Figure 5]. The spectrum of the motion used in the filtering of the random time series was taken to be:

$$R(f) = C(2\pi f)^n S(f) A(f) D(f) \quad (1)$$

where the power  $n$  determines whether the velocity ( $n = 1$ ) or acceleration ( $n = 2$ ) is being considered. The factors  $C$ ,  $S(f)$ ,  $A(f)$ , and  $D(f)$  stand for a scaling factor, the source spectrum, an amplification factor, and diminution factor, respectively. Only  $S(f)$  depends on the seismic moment.  $C$  was given by

$$C = \frac{\langle R_{\Theta\Phi} \rangle FV}{4\pi\rho_s c_s^3} \left( \frac{1}{r} \right) \quad (2)$$

where  $\langle R_{\Theta\Phi} \rangle$  is an average of the radiation pattern,  $F$  is included to account for free-surface effects,  $V$  represents the partition of a vector into horizontal components (in some cases this is absorbed into  $\langle R_{\Theta\Phi} \rangle$ ),  $\rho_s$  and  $c_s$  are the density and seismic velocity in the vicinity of the source, and  $r$  is the distance from the source to the point of estimation. A standard  $\omega$ -square model was used:

$$S(f) = M_0 / [1 + (f/f_0)^2] \quad (3)$$

$M_0$ , the static seismic moment, and  $f_0$ , the corner frequency, were related through a parameter,  $\Delta\sigma$ , having dimensions of stress, according to the following formula adapted from Boore [1983]:

$$f_0 = 4.9 \times 10^4 \beta \lambda (\Delta\sigma/M_0)^{1/3} \quad (4)$$

where  $\beta$  is the shear velocity in km/s and, for *P*-waves,  $\lambda$  is the ratio of the *P* and *S* corner frequencies. The units of  $\Delta\sigma$  and  $M_0$  are MPa and N m, respectively. It is important to distinguish the stress quantity  $\Delta\sigma$ , used as a parameter in the theoretical calculations, from the stress drop derived from measurements of long period spectral level and corner

frequency; as will be shown (and Hanks [1982] has pointed out), high-frequency filtering effects can obscure the source corner frequency  $f_0$ .

The amplification filter  $A(f)$  can take various forms. It is included in an attempt to account for the relatively broadband amplification expected for any propagation upward through the progressively slower velocity materials usually found in the upper few kilometers of the crust. The details are contained in Boore [1986], and the amplification factors are given in Table 1. Briefly, the amplification is given by the square root of the ratio of the seismic velocity near the source and the near-surface velocity. An effective velocity over a quarter wavelength is used for the latter, thus making the amplification dependent on frequency. This amplification is in addition to the resonant amplification that would be produced by strong impedance contrasts; resonant amplification is not included in this study.

The final term in (1) represents the bandwidth limitation, whose influence is the subject of this paper. A useful form of this filter is

$$D(f) = \exp(-\pi fr/Q(f)c) \exp(-\pi\kappa f) \quad (5)$$

The first term represents the attenuation in propagating a distance  $r$  and the second term is a distance-independent low-pass filter. The latter term is of the form proposed by Anderson and Hough [1984], although they allow the coefficient in front of the frequency to be a function of distance; at the risk of some confusion in terminology, I have taken  $\kappa$  to be independent of distance. A possible physical mechanism for the second term would be near-site attenuation in the last few kilometers of the ray path. For small distances or large  $Q$ , the second term contributes most of the attenuation and the effect of the filter  $D(f)$  on peak velocity and acceleration is then roughly equivalent to a step high-cut filter with cutoff frequency ( $f_{\max}$ ) equal to  $1/\pi\kappa$  (a relation pointed out to me by J. Boatwright and subsequently confirmed by my simulations).

## Results

A suite of spectra derived from (1) are shown in Figure 1. The parameters have been chosen so as to make these spectra similar to those of Anderson [this volume]. With the reasonable assumption that peak motions are proportional to the maximum spectral amplitudes, the following qualitative conclusions about the scaling of the peak motions can be drawn without complex calculations, simply from the spectral shapes and the spacing between the spectral maxima: for large earthquakes, the peak velocity will be a stronger function of seismic moment (or, equivalently, moment magnitude) than will peak acceleration. In contrast, the moment dependence of both peak acceleration and peak velocity will be identical for small earthquakes and will have a stronger dependence on moment than do either  $a_p$  and  $v_p$  for large earthquakes.

Quantitative analysis of the expected scaling gives

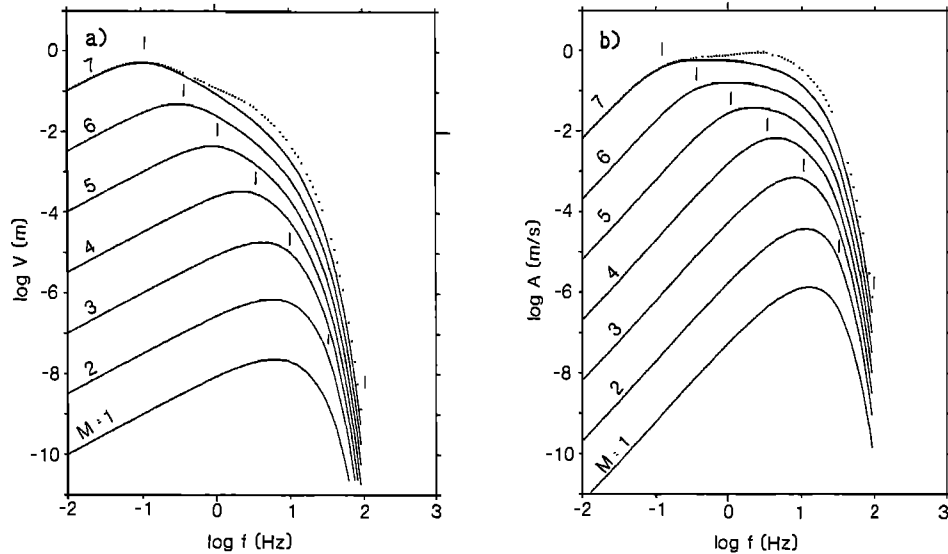


Fig. 1. Velocity and acceleration spectra for a range of moment magnitudes, computed for  $r = 10$  km,  $\rho_s = 2.7$  gm/cc,  $c_s = 3.2$  km/s,  $\langle R_{\text{eff}} \rangle = 0.5$ ,  $F = 1.0$ ,  $V = 1.0$ ,  $\kappa = 0.05$ , and a stress parameter of 10 MPa (see equations (1) through (4) for meaning of terms). The vertical bars indicate corner frequencies, computed from equation (5) in Boore [1983]. Dots show modification of  $M = 7$  spectra for amplification factors given in Table 1.

$$\log v_p \propto 0.37 \log M_0 \quad (6a)$$

and

$$\log a_p \propto 0.20 \log M_0 \quad (6b)$$

for large  $M_0$  (Boore [1983]; for a different model, McGarr [1984] gives  $\log v_p \propto 0.33 \log M_0$  and  $\log a_p \propto 0.0 \log M_0$ ). For small events, the scaling is

$$\log v_p \propto 1.0 \log M_0 \quad (7a)$$

and

$$\log a_p \propto 1.0 \log M_0 \quad (7b)$$

The scaling for small  $M_0$  is a direct consequence of the upper limit on the bandwidth. If frequencies are not present above a cutoff which is small compared to the reciprocal source duration, then the seismic record will be a simple impulse response with amplitude proportional to  $M_0$ . The time series for any particular type of ground motion or instrument type will have the same shape independent of  $M_0$  and the amplitude will be proportional to  $M_0$ . In particular, the logarithms of the peak response of a Wood-Anderson instrument (and thus  $M_L$ ), the peak ground displacement and the peak response spectra will scale the same way as do  $v_p$  and  $a_p$  in (7); radiated energy will scale as  $M_0^{2.0}$ . Therefore, the presence of a bandwidth limiting effect, due to instrument response or source- or site-processes, can produce significant differences in the expected scaling of peak motions for large and small earth-

quakes. It is also clear from comparing the specified corner frequencies (vertical bars in Figure 1) with the spectra that observed corner frequencies for small earthquakes will be constant, in apparent violation of the constant stress drop model used in deriving the results. Because derived stress drop is proportional to the product of moment and the cube of corner frequency, the derived stress drop will scale as  $M_0^{1.0}$ , just as do  $v_p$  and  $a_p$ .

The scaling results given above only apply for very large and very small earthquakes. I have made a more complete analysis by simulating the acceleration and velocity time series using the method of Boore [1983]. Peak acceleration, velocity, and apparent stress have been derived from the geometrical mean of the corresponding quantities, for ensembles of 100 simulations. Two models have been considered. The first uses the same stress and  $\kappa$  parameters used by Anderson [this volume] in investigating the moment dependence of the frequency characterizing the upper end of the spectral bandwidth. (This frequency was named  $f_{95}$  by Anderson and is similar in effect and meaning to Hanks'  $f_{\max}$  [Hanks, 1982]). My results thus complement his by considering the influence of finite bandwidth on observational quantities other than  $f_{95}$ . A second model is specific to the data set from the 1983 Coalinga, California, earthquake sequence. This sequence was well recorded on portable, high-dynamic-range, digital-recording portable instruments [Mueller et al., 1984] and provides an excellent data set for studying the scaling of ground motion for small to moderate events.

For the first model, the scaling of  $v_p$  and  $a_p$  from  $S$  waves confirms the earlier predictions based on examina-

## 278 EFFECT OF BANDWIDTH ON SEISMIC SCALING

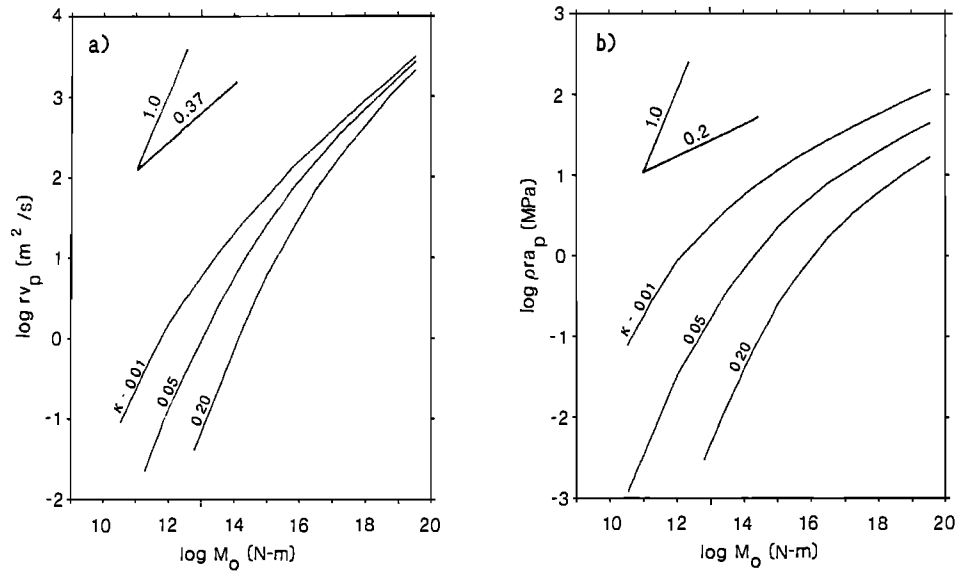


Fig. 2. Peak velocity and acceleration, corrected for geometrical spreading, as a function of moment for values of  $\kappa$  used by Anderson [this volume]. Other parameters given in caption to Figure 1. Short lines show expected scaling for earthquakes with large and small seismic moments (equations (6) and (7)).

tion of the spectra (Figure 2). The transition between the different slopes is a function of the parameter  $\kappa$ . If thought of as representing anelastic attenuation (i.e.,  $\kappa = r/Qc$ ),  $\kappa = 0.01$ , and  $\kappa = 0.20$  correspond to small and large attenuation, respectively [Anderson, this volume].  $\kappa = 0.05$  is an average value for weathered rock. Recordings of aftershock sequences using portable digital instruments are usually dominated by earthquakes in the  $10^{11}$  to  $10^{16}$  N-m ( $10^{18}$  to  $10^{23}$  dyne-cm) range of seismic moment, and thus Figure 2 indicates that the source systematics derived from such recordings can be strongly influenced by finite bandwidth effects.

Another quantity computed from seismic observation is the apparent stress, defined as:

$$\sigma_a = \mu E_s / M_0 \quad (8)$$

where  $\mu$  is the rigidity and  $E_s$  is the radiated seismic energy. This quantity has been computed for the first model. Time domain velocities were integrated to derive energy, and a correction was applied to account for whole-path attenuation at the frequency of the peaks in the velocity spectra. The results show a pronounced dependence of apparent stress on moment, with an abrupt transition to an approximately constant level (Figure 3). The slope of  $\log \sigma_a$  vs  $\log M_0$  is unity for small earthquakes, in perfect agreement with the expectation from (1) and (3), when Parseval's theorem is used to relate the time domain and frequency domain estimates of energy. Observational studies of the 1976 Friuli earthquake in Italy (A. Rovelli, personal communication, 1985) and the 1983 Coalinga, California, earthquake (M. Andrews, personal communication,

1985) are in agreement with the expected slope, although the  $\sigma_a$  values for the latter earthquake show considerable scatter.

The results in Figures 2 and 3 are for a generic model,

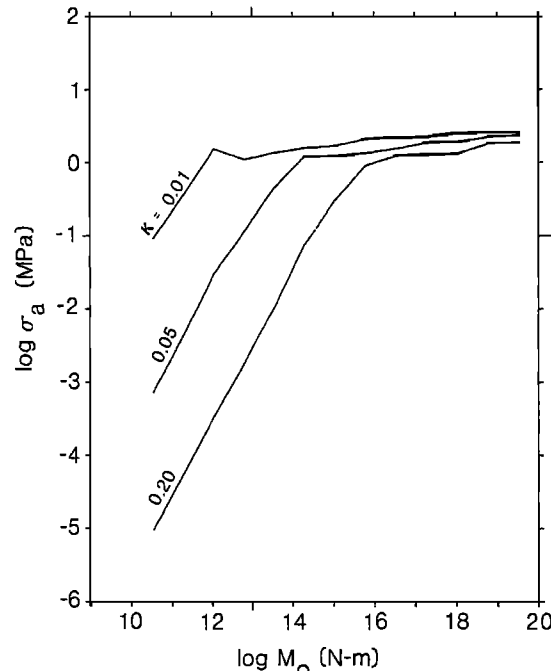


Fig. 3. Moment dependence of apparent stress for model used in Figures 1 and 2.

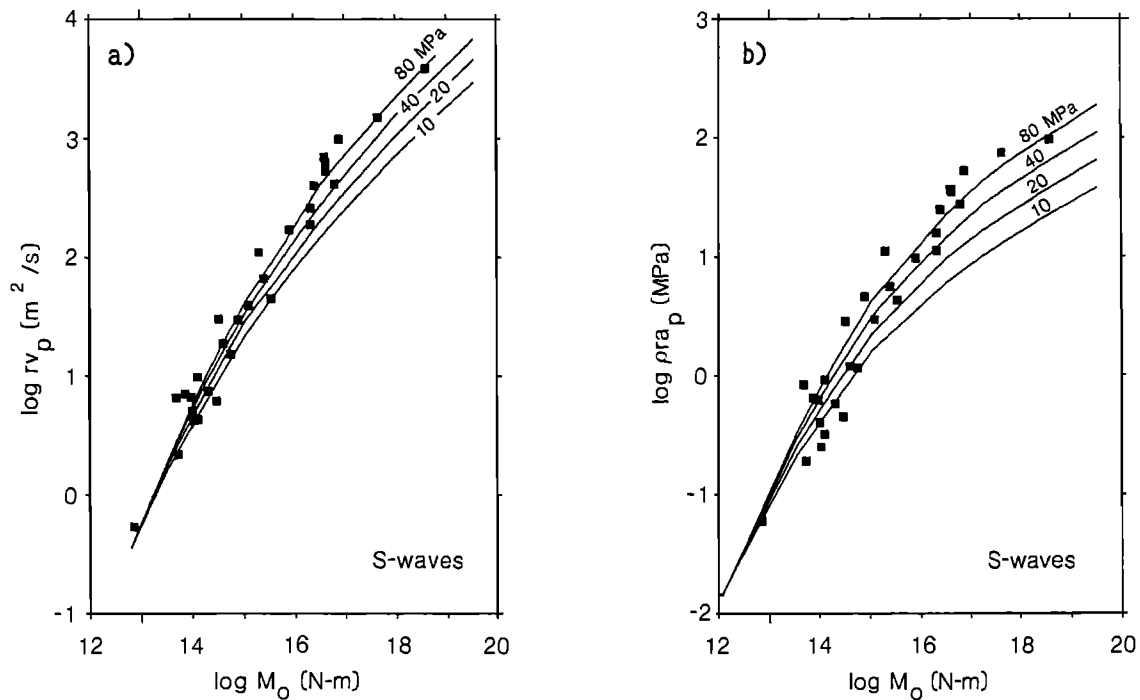


Fig. 4. Observed (squares) and predicted (lines) velocities and accelerations for *S* waves from 1983 Coalinga, California, earthquake sequence. Data from McGarr et al. [1986]. Theoretical calculations used  $Q(f)$  given by equation (6) in Boore [1984],  $\kappa = 0.07$ ,  $(R_{\Theta\Phi}) = 0.6$ ,  $F = 1.0$ ,  $V = 1.0$ ,  $\rho_s = 2.7$  gm/cm<sup>3</sup>,  $c_s = 3.2$  km/s, and  $\Delta\sigma$  ranging from 10 to 80 MPa. No amplification was included.

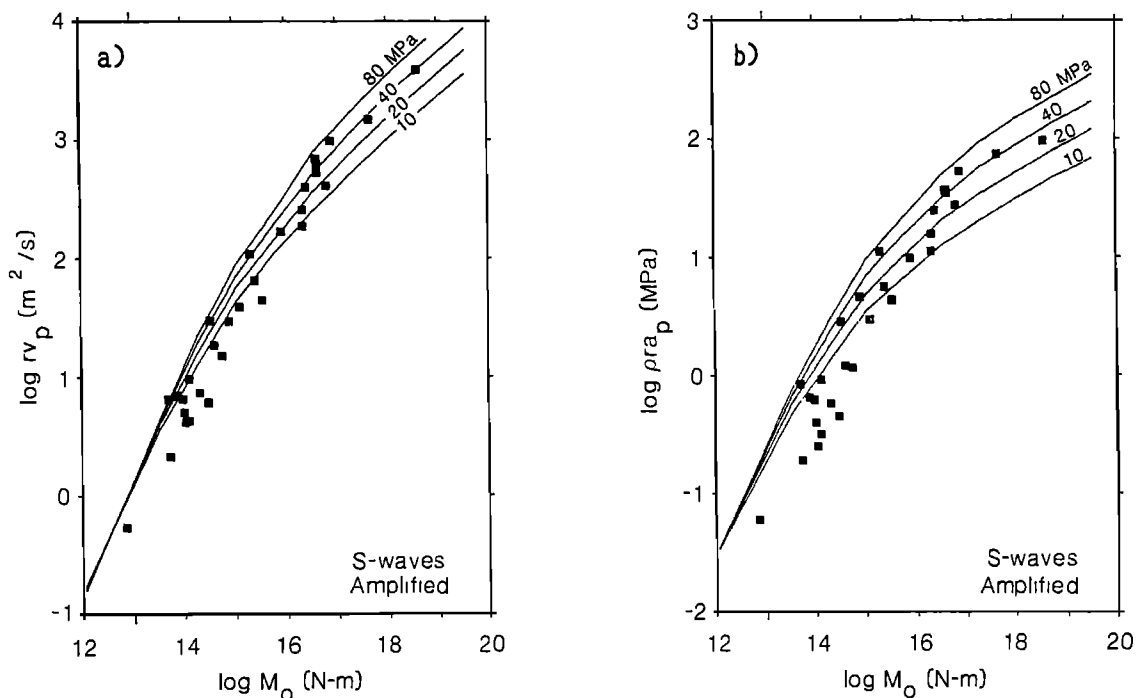


Fig. 5. *S* wave observations and predictions (using amplifications in Table 1). See Figure 4 for other parameters.

## 280 EFFECT OF BANDWIDTH ON SEISMIC SCALING

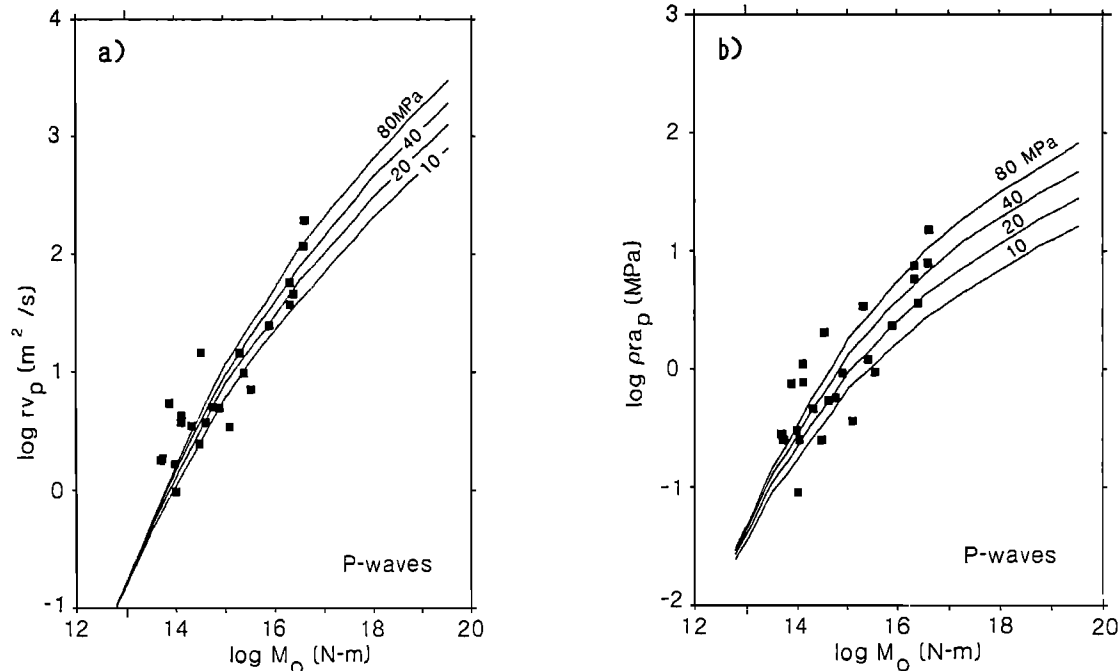


Fig. 6. The same as Figure 4, but for  $P$  rather than  $S$  waves and  $\kappa = 0.047$ ,  $c_s = 5.5$  km/s,  $\langle R_{\Theta\Phi} \rangle = 0.36$ , and the  $P$  corner frequency equal to 1.5 times the  $S$  corner frequency. Amplification has not been included.

chosen to be consistent with that considered by Anderson [this volume] and intended to illustrate the general effects expected from bandwidth limitations. The second application is specific to the data collected from the 1983 Coalinga, California, earthquake sequence. McGarr et al. [1986] have measured  $a_p$  and  $v_p$  using records from portable digital seismographs and analog accelerographs. Most of the earthquakes were recorded at a number of sites, with the digital instruments providing the bulk of the data. Accelerograph recordings at one station were used for the mainshock. McGarr et al. [1986] removed the free-surface effect and combined the components vectorially to yield the peak motion. They reduced the measurements to unit distance by multiplying  $v_p$  and  $a_p$  by  $r$  and  $\rho_s r$ , respectively. An attempt was made to maximize the values of  $rv_p$  averaged over the suite of recordings of any one earthquake, using a similar part of the waveform at all stations; consequently, the  $v_p$  used may not correspond to the actual peak motions on any one seismogram. This should be kept in mind when comparing the observations with the theoretical calculations, which represent the peak value of motions from a point source.

To permit comparison with the results of McGarr et al. [1986] and McGarr [this volume], the free-surface effect was ignored ( $F = 1$ ). Furthermore, McGarr and colleagues consider vector motion, so  $V$  was set to unity. Following Boore and Boatwright [1984], the value of  $\langle R_{\Theta\Phi} \rangle$  was derived from an average of the logarithm of the radiation

pattern of the total  $S$ - and  $P$ -wave motion at close distances from a buried dip-slip source ( $\langle R_{\Theta\Phi} \rangle = 0.6$  and  $\langle R_{\Theta\Phi} \rangle = 0.36$  for  $S$  and  $P$  waves, respectively). The value of  $\kappa$  used in the calculations of the  $S$ -wave motions was a rough average of values measured by M. Andrews (personal communication, 1985) from acceleration spectra for a set of Coalinga data that overlaps, but is not identical to, the earthquake/station pairs providing McGarr et al.'s [1986]  $a_p$  and  $v_p$  data. Using the method of Anderson and Hough [1984], Andrews' estimates were based on fitting a straight line, in the range of frequencies from about 5 to 20 Hz, to log-linear plots of the spectra. The limited distance range and the large scatter precluded finding a dependence of  $\kappa$  on distance.

A comparison of observations and theory, without amplification, is given in Figure 4. A range of stress parameters,  $\Delta\sigma$ , from 10 to 80 MPa was used. As expected,  $\Delta\sigma$  has little effect on the motions of small earthquakes, whose spectral amplitudes are a function of  $M_0$  only (e.g., Figure 1). As seen in Figure 2, the effect of  $\kappa$  is complementary to that of  $\Delta\sigma$ , for it has more influence on small earthquakes than large events.

A comparison of the normalized  $a_p$  and  $v_p$  data shows that although they both have a similar trend for small earthquakes (with a slope close to unity), the dependence on seismic moment is different for large earthquakes, with  $v_p$  being a stronger function of  $M_0$  than is  $a_p$ . This corresponds directly to the theoretical expectations expressed

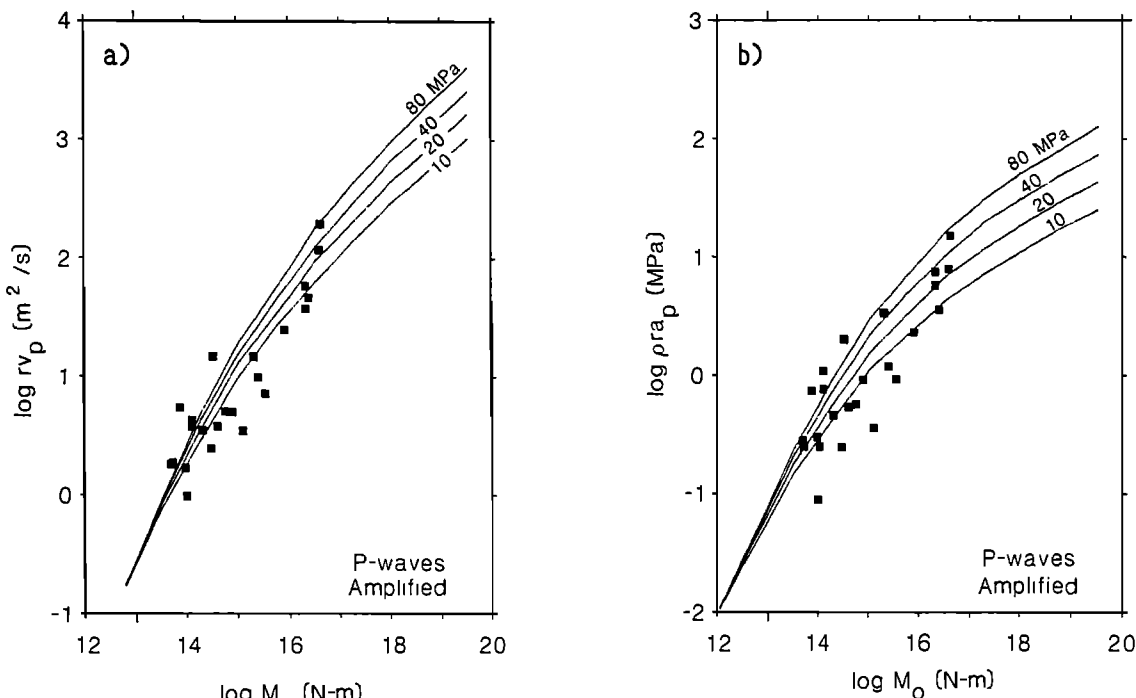


Fig. 7.  $P$  wave observations and predictions, using amplifications in Table 1. See Figure 6 for other parameters.

in (6) and (7). The fits to the absolute values are not bad for the smaller earthquakes, but for the large earthquakes the theory requires  $\Delta\sigma$  close to 80 MPa. Including amplification makes it possible to fit the data with  $\Delta\sigma \approx 30$  MPa, a high but not unreasonable value (Figure 5). The amplification factors used in the calculations are for motions on the highly fractured rock typical of much of California; for soil sites the amplification could be as much as a factor of two larger. Since a number of the Coalinga recordings were obtained on sites underlain by soil, it is possible that the amplification factors could be larger than in Table 1, thus leading to a stress parameter less than 30 MPa. With amplification, the data for smaller earthquakes do not fit the theory as well as they did without amplification, but there is a consistent explanation for this: the moments used for the data were measured without correcting for amplification. If amplification exists, the moments derived for the data should be decreased, and if the amplification is due to propagation through a near-surface velocity gradient, the correction should be larger for small earthquakes than for large earthquakes (see, e.g., the solid and dashed curves in Figure 1). According to Table 1, this correction could amount to over 0.3 log units for the smaller earthquakes.

The measurements of  $P$  wave amplitudes from the Coalinga earthquake recordings provide another opportunity to compare the predicted effect of finite bandwidth with observations. Comparisons of predicted and observed peak motions, without and with amplification, are given in Fig-

ures 6 and 7, respectively. As with the  $S$  waves, the comparison is good, both in trend and absolute amplitude. In making the predictions, the ratio of  $P$  and  $S$  corner frequencies was taken to be 1.5, following the observations of McGarr et al. [1986]. The ratio of  $\kappa$  was also assumed to be 1.5, with  $\kappa$  smaller for  $P$  waves. The amplification factors given in Table 1 were used in the calculations.

### Conclusions

A moment-independent filter that attenuates high frequencies produces marked changes in the scaling expected from the usual analysis of self-similar models. For small earthquakes many quantities derived from the ground motion will scale directly with the seismic moment, even though for large earthquakes the quantities might depend weakly, if at all, on seismic moment. Examples of quantities scaling linearly with moment include stress drop, apparent stress, peak displacement, peak acceleration, peak velocity, and peak response of a Wood-Anderson instrument. These conclusions are important because earthquakes in the moment range expected to be affected by bandwidth limitations are numerous (particularly in aftershock sequences) and are often recorded. Most studies of such events have found the type of effects predicted here, but have usually attributed them to a breakdown in the self-similarity of the earthquake source. Of course, I have not shown that the source is not the ultimate cause of

## 282 EFFECT OF BANDWIDTH ON SEISMIC SCALING

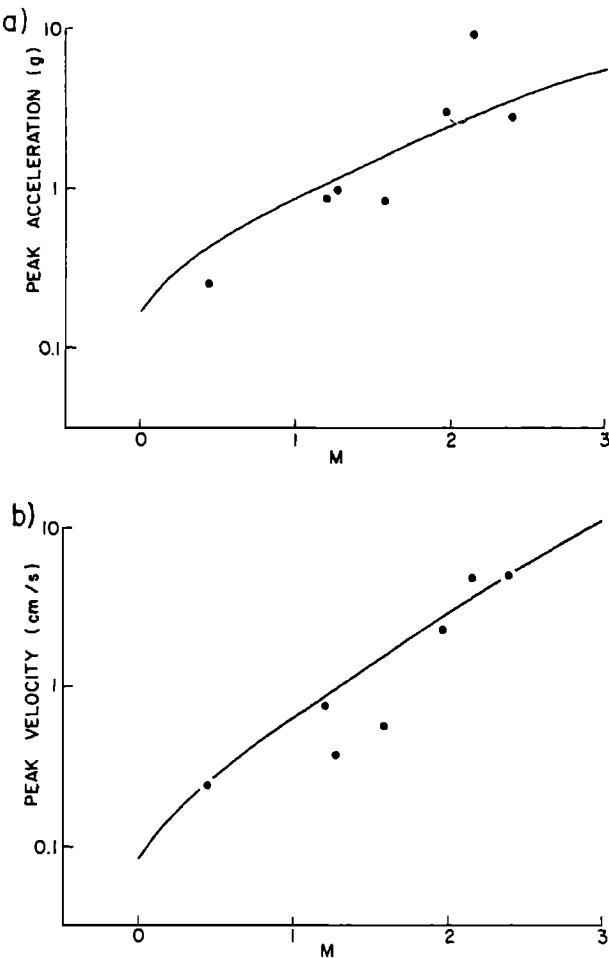


Fig. 8. Comparison of peak accelerations and velocities from South African accelerograms (figure from Boore [1983]). Data: dots, theory: lines. Calculations at 200 m, using  $c_s = 3.8$  km/s,  $Q(f) = 600$ ,  $\Delta\sigma = 5$  MPa, and a high-frequency cutoff of 400 Hz.

the band limitation. I have simply investigated the consequences of such a high-frequency filter, regardless of its origin. The origin cannot be neglected, however, for whether or not high-frequency waves are radiated from the source can have important consequences for the design of structures. If high-frequency waves are radiated from the source and are attenuated in the vicinity of the recording site, then a study of the attenuation characteristics of proposed sites would be an important aspect of planning short-period structures. If high-frequency waves are not radiated from the source, then such a study is not necessary. Although it is reasonable to expect attenuation during wave propagation through the material near the earth's surface (even on rock sites), a definitive study of the causes of the removal of high frequencies from the radiated field will require recordings at varying depths in the earth and at a variety of surface sites for a suite of earthquakes.

The results of peak-velocity scaling for a number of earthquake sequences, summarized by McGarr [this volume], are roughly consistent with the prediction from Figure 2 that the more competent the rock near the recording site, the lower the moment at which the transition in scaling takes place. The extremes in McGarr's data correspond to the Coalinga and the mine-tremor data, recorded on soils and incompetent rock in the first case and very sound rock in the second. The Mirimichi, New Brunswick, data are from sites that fall between these extremes. I have considered the Coalinga data in this paper and in an earlier paper [Boore, 1983] showed that a standard  $\omega$ -square, constant-stress-parameter model could simultaneously explain both the peak accelerations and the peak velocities from the deep-mine tremors, using a high-frequency filter appropriate for the recording site. This is shown in Figure 8 (fewer data were available for that study than are presented in McGarr). These quantitative comparisons, as well as the general trends of the transition moments in McGarr [this volume], suggest that near-site attenuation plays an important role in the observed scaling.

**Acknowledgments.** I thank Mary Andrews, William Joyner, and Art McGarr of the U.S. Geological Survey for stimulating discussions and Ezio Faccioli, Charles Mueller, Antonio Rovelli, and Frank Scherbaum for thoughtful reviews. This research was partially supported by a grant from the U.S. Nuclear Regulatory Commission.

## References

- Anderson, J. G., Implication of attenuation for studies of the earthquake source, this volume, 1986.
- Anderson, J. G., and S. E. Hough, A model for the shape of the Fourier amplitude spectrum of acceleration at high frequencies, *Bull. Seismol. Soc. Am.*, **74**, 1969–1993, 1984.
- Bakun, W. H., C. G. Bufe, and R. M. Stewart, Body-wave spectra of central California earthquakes, *Bull. Seismol. Soc. Am.*, **66**, 363–384, 1976.
- Boore, D. M., Stochastic simulation of high-frequency ground motions based on seismological models of the radiated spectra, *Bull. Seismol. Soc. Am.*, **73**, 1865–1894, 1983.
- Boore, D. M., Use of seismoscope records to determine  $M_L$  and peak velocities, *Bull. Seismol. Soc. Am.*, **74**, 315–324, 1984.
- Boore, D. M., Short-period P- and S-wave radiation from large earthquakes: implications for spectral scaling relations, *Bull. Seismol. Soc. Am.*, **76**, 43–64, 1986.
- Boore, D. M., and J. Boatwright, Average body-wave radiation coefficients, *Bull. Seismol. Soc. Am.*, **74**, 1615–1621, 1984.
- Fletcher, J. B., A comparison between tectonic stress measured in situ and stress parameters from induced seismicity at Monticello Reservoir, South Carolina, *J. Geophys. Res.*, **87**, 6931–6944, 1982.
- Haar, L. C., J. B. Fletcher, and C. S. Mueller, The 1982 Enola, Arkansas, swarm and scaling of ground motion in

- the eastern United States, Bull. Seismol. Soc. Am., 74, 2463–2482, 1984.
- Hanks, T. C.,  $f_{\max}$ , Bull. Seismol. Soc. Am., 72, 1867–1879, 1982.
- Hanks, T. C., and D. M. Boore, Moment-magnitude relations in theory and practice, J. Geophys. Res., 89, 6229–6235, 1984.
- Hanks, T. C., and R. K. McGuire, The character of high-frequency strong ground motion, Bull. Seismol. Soc. Am., 71, 2071–2095, 1981.
- McGarr, A., Scaling of ground motion parameters, state of stress, and focal depth, J. Geophys. Res., 89, 6969–6979, 1984.
- McGarr, A., Some observations indicating complications in the nature of earthquake scaling, this volume, 1986.
- McGarr, A., C. Mueller, J. B. Fletcher, and M. Andrews, Ground motion and source parameters of the 1983 Coalinga, California earthquake sequence, in The Coalinga, California, earthquake sequence of May 2, 1983, U.S. Geol. Surv. Prof. Pap., in press, 1986.
- Mueller, C. S., E. Sembera, and L. Wennerberg, Digital recordings of aftershocks of the May 2, 1983 Coalinga, California earthquake, U.S. Geol. Surv. Open-File Rep., 84-697, 57 pp., 1984.
- Nuttli, O. W., Average seismic source-parameter relations for mid-plate earthquakes, Bull. Seismol. Soc. Am., 73, 519–535, 1983.
- Rautian, T. G., V. I. Khalturin, V. G. Martynov, and P. Molnar, Preliminary analysis of the spectral content of  $P$  and  $S$  waves from local earthquakes in the Garm, Tadzhikistan region, Bull. Seismol. Soc. Am., 68, 949–971, 1978.
- Scherbaum, F., and C. Kisslinger, Variations of apparent stresses and stress drops prior to the earthquake of 6 May 1984 ( $m_b = 5.8$ ) in the Adak seismic zone, Bull. Seismol. Soc. Am., 74, 2577–2592, 1984.
- Scherbaum, F., and D. Stoll, Source parameters and scaling laws of the 1978 Swabian Jura (southwest Germany) aftershocks, Bull. Seismol. Soc. Am., 73, 1321–1343, 1983.

## DENSE SEISMOGRAPH ARRAY OBSERVATIONS OF EARTHQUAKE RUPTURE DYNAMICS

Paul Spudich and David Oppenheimer

U.S. Geological Survey, Menlo Park, California 94025

**Abstract.** A dense seismograph array provides a means of understanding in detail the ground motion at a particular site. The earthquake energy impinging on the array site is composed of waves which travel directly from the source to the site and waves which are scattered by geological heterogeneities. For simplicity, consider a dense array which records only the direct waves radiated by a hypothetical earthquake having completely uniform slip and rupture velocity. Even though each part of the fault radiates the same amount of energy, the array will receive differing amounts of energy coming from different parts of the fault, due to the combined influence of radiation patterns, geometrical spreading, and directivity. The power distribution observed on the fault will be a convolution of the apparent power distribution (product of radiation patterns, directivity, etc.) with the array beam pattern. We show examples of these phenomena in a synthetic test case designed to match the geometry of a magnitude 6 event on the San Andreas fault at Parkfield, California. In this test we placed 26 array elements in a  $10 \text{ km}^2$  region located about 13 km off the fault. We calculated synthetic ground-velocity seismograms from an irregularly expanding rupture on the fault. We performed frequency-wavenumber ( $f - k$ ) analysis on sequential time windows of the array data. For each 1.6-s-long window, the power distribution in  $f - k$  space was converted into the frequency-slowness domain. Each point in the slowness plane corresponds to a seismic ray incident upon the array with known angle of incidence and azimuth of approach. By using ray-tracing, each ray was projected back onto its point of origin on the fault, yielding a snapshot of the power radiated from the rupturing fault for each time window. The expanding rupture can be seen in the sequence of snapshots.

If scattered energy is added, the image of the rupture may be degraded. However, with a dense array it is possible to selectively distinguish and reject energy coming from unwanted azimuths, which cannot be done with isolated stations. Moreover, dense arrays make it possible to analyze high-frequency ground motions (1–20 Hz) in terms of rupture behavior, which is currently difficult using waveform inversion methods due to the massive computations involved.

## Introduction

When the instrumentation has been available, seismologists have almost always deployed seismographs in groups.

In reconnaissance studies the desires to monitor seismic activity in as large an area as possible and to have good azimuthal coverage of seismic sources have caused seismologists to place seismographs as far away from each other as practicable. For some types of investigations, such as the enhancement of teleseismic signals necessary for discrimination of nuclear blasts from earthquakes, and the detailed mapping of subsurface geologic structures that might harbor hydrocarbons, it has proven more effective to cluster seismographs close to each other. The yardstick by which seismographs are determined to be 'close together' or 'far apart' is the wavelength of a seismic wave of interest. In this paper we will use the terms 'distributed array' and 'dense array' to refer to groups of instruments whose inter-station spacings are much larger or smaller, respectively, than a seismic wavelength of interest.

The primary reason that dense array data are useful is that when ground motions are recorded on a sufficiently dense array, it is then possible to resolve the ground motion into any of a number of types of constituent waves. For example, the so-called 'frequency-wavenumber' ( $f - k$ ) analysis, such as the procedure of Capon [1969], decomposes the wave field into its constituent monochromatic plane waves, each having its own propagation slowness (1/velocity) across the array and its own direction of travel. Once the wave field is broken into plane waves, various plane waves can be identified as body or surface waves incident from differing directions. In the geophysics industry, the process of migration is roughly equivalent to decomposing the wave field into a sum of spherical waves (to a first approximation) centered on various points within the earth. Each of these spherical waves can then be identified as a wave scattered from some point heterogeneity in the earth.

Regardless of the type of decomposition, once the wave field is resolved into constituents each having a physical interpretation, the experimenter can sensibly partition the component waves into those that are of interest and those that are not. Furthermore, the experimenter can filter out the uninteresting waves by reassembling the wave field without the uninteresting components, thereby eliminating scattered waves or surface waves from the seismograms.

Although dense arrays have been used for decades in teleseismic seismology and in seismic reflection profiling, their use for studying high-frequency ( $> 1 \text{ Hz}$ ) ground motions from local earthquakes is quite recent. McLaughlin

## 286 OBSERVATIONS OF EARTHQUAKE RUPTURE DYNAMICS

[1983] recorded microearthquake seismograms on a temporary dense array near the San Andreas fault and, using  $f - k$  analysis, found that lateral variations in seismic velocity structure near the fault were large enough to bend microearthquake  $P$ -waves into paths that travelled toward the fault. McLaughlin et al. [1983] measured ground accelerations 6 km from a nuclear blast and found that most of the energy recorded at frequencies above 5 Hz was scattered rather than direct energy. McMechan et al. [1985] recorded microearthquakes at Mammoth Lakes, California, on a 120-element linear array and used a technique borrowed from the exploration industry, wave field extrapolation [McMechan, 1982], to produce an image of the microearthquake source within a 2-D slice of the earth. This application of wave field extrapolation to dense array data from earthquakes is a highly promising approach for both studies of the earthquake source and scatterers within the earth.

Dense accelerograph arrays, for the study of strong ground motions from large local earthquakes, have been deployed primarily to study the strains that the ground undergoes during earthquakes. The magnitudes of these strains are relevant to the damage that long structures such as bridges and underground pipelines sustain during earthquakes. A vigorous program of engineering-oriented dense array studies is being conducted in Japan using both 2-D arrays on the surface and downhole instrument arrays extending as deeply as 950 m [Narahashi et al., 1984; Omote et al., 1984]. The most ambitious of these Japanese arrays is that at Chiba [Katayama et al., 1984], which consists of 36 3-component digital accelerometers, 11 of which are at ground level and 25 of which are buried as deeply as 40 m. The maximum spatial separation of array elements in the Chiba array is about 200 m. Similar to the Chiba array but spatially larger is the SMART-1 array in Taiwan [Bolt et al., 1982, 1984], which is comprised of 37 digital surface accelerometers arranged in three concentric rings of radius 200 m, 1 km, and 2 km. This array recorded an event of  $M_L = 6.7$  on 29 January 1981 that occurred 30 km away and had a rupture length of about 19 km. Abrahamson [1985] was able to observe rupture propagation during this event by using a time-dependent  $f - k$  analysis, and he estimated that rupture velocity varied between 2.1 and 4.9 km/s during the event, with a mean of 3.1 km/s. Abrahamson's analysis was impeded by geometric considerations; because of the short rupture length and the fault orientation relative to the array, the propagation direction of body waves impinging on the array changed by only about  $30^\circ$  due to rupture propagation.

The most successful dense array observation of rupture dynamics thus far was made by Spudich and Cranswick [1984], who used recordings of the 1979 Imperial Valley earthquake made on the 5-element El Centro differential array. This array was strategically located only 5.6 km from the surface trace of the fault, and the 30 km rupture length of the event caused the propagation direction of waves impinging upon the array to change by about  $150^\circ$  during the event, a huge azimuthal signal. Spudich

and Cranswick were able to track the progress of the rupture front along the entire length of the fault, and observed changes in rupture velocity, including a possibly brief period of super-shear rupture velocity, consistent with the low-frequency modeling studies of Olson and Apsel [1982] and Archuleta [1984]. The major impediments to Spudich and Cranswick's work were the linearity of their array and its short length (213 m).

## Capabilities and Limitations of Dense Arrays

Given that the dense arrays now in place will continue to record earthquake data, and that more dense arrays are likely to be installed due to their high engineering importance [Iwan, 1978, 1981], it is worthwhile to explore their capabilities and limitations.

Dense arrays are foremost a powerful tool for studying the composition of strong ground motions at a particular site. The ground motions that a simple microearthquake causes at a particular site are composed of body and surface waves that travel directly from the source to the observer as well as body and surface waves that are scattered off geological heterogeneities. Close to large earthquakes the ground motions are even more complicated because both direct and scattered energy from many different points on the source can arrive at the observer simultaneously. Liu and Heaton [1984] show that ground motions observed in the Los Angeles basin and San Fernando Valley during the 1971 San Fernando earthquake were composed of body waves coming directly from the rupture surface and surface waves generated at the edges of the basins. Had these waves been observed on a dense array, it would have been possible not only to identify their velocities and propagation directions, but also to apply velocity filtering to reject unwanted waves. This technique could be used to retain only body waves travelling directly from the source, permitting for example, more accurate measurement of the earthquake source spectrum, the faulting duration, the *rms* acceleration, and other quantities whose measurements are degraded by contamination from scattered waves and surface waves. In addition, such filtered seismograms would be more amenable for waveform modeling due to the removal of waves that cannot be calculated accurately using current synthetic seismogram methods.

Because all the array elements are essentially at the same site, however, the picture of the earthquake source derived from the array data is necessarily biased by the array location. Clearly there is no place on the fault for which the array gives good azimuthal coverage, and the array data are much more sensitive to the behavior of the nearby parts of the fault than to the distant parts. The distorted picture of the fault derivable from dense array data can be easily appreciated using the isochrone formulation of Bernard and Madariaga [1984] and Spudich and Frazer [1984].

An Example: Array Studies  
of a Hypothetical Parkfield Earthquake

Moderate-sized earthquakes ( $M \sim 6.0$ ) have occurred on the San Andreas fault at Parkfield, California, in 1857,

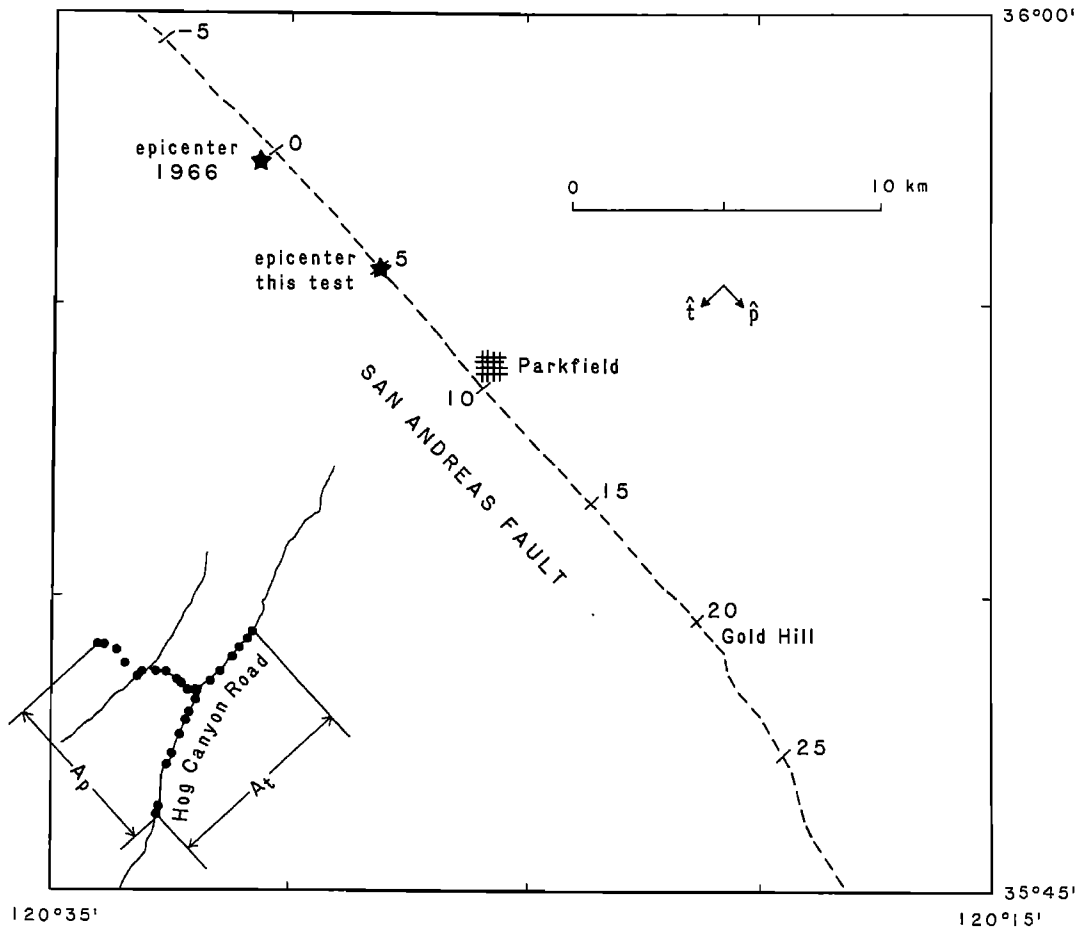


Fig. 1. Map of the Parkfield region of the San Andreas fault. Numbers along fault are a horizontal coordinate system measuring distance in km from the epicenter of the 1966 earthquake, which ruptured at least as far as Gold Hill. The hypothetical array elements are shown by heavy dots. Rupture in our simulated earthquake extends from -5 to 25 km. The parallel and transverse components of motion are indicated by the  $\hat{p}$  and  $\hat{t}$  unit vectors.

1901, 1922, 1934, and 1966 [Bakun and McEvilly, 1984]. The last three events had very similar moments (within 20% of each other) and rupture lengths (20–30 km). Given the high probability of another such event occurring there in the near future, what might be observed by a dense array located in the Parkfield region in such an event? To answer this question we will first calculate synthetic seismograms for this event at a hypothetical dense array, and we will then perform frequency-wavenumber analysis on the synthetic seismograms to determine whether rupture behavior can be observed. In the process we will additionally be able to demonstrate a number of claims made earlier in the paper.

Our hypothetical earthquake occurs upon a vertical plane simulating the San Andreas fault at Parkfield, with its epicenter lying midway between the epicenter of the 1966 shock and the town of Parkfield (Figure 1). Rupture is initially bilateral, progressing as far northwest as

$u = -5$  km and to  $u = 25$  km to the southeast, where  $u$  is a coordinate parallel to the fault strike. Rupture occurs between depths of 1 and 13 km. The mechanism of the hypothetical event is purely strike-slip, with the amplitude of slip being uniform over the fault. The rupture velocity is approximately 0.75 of the shear velocity, with some random local variations of rupture time added to generate additional high frequency motions (Figure 2). The seismic velocity model used in these calculations (Figure 3) is a smoothed version of the southeast structure of Eaton [1967]. Our postulated array consists of 26 elements laid out roughly in the shape of a 'T' (Figure 1). Using the isochrone method, we calculated synthetic ground velocities at each array element (Figure 4), using only S-waves and assuming that the slip function at each point on the fault was a ramp function. The omission of surface waves and scattered waves is not as grave as it might seem; for the most part these waves will occur in different parts of

## 288 OBSERVATIONS OF EARTHQUAKE RUPTURE DYNAMICS

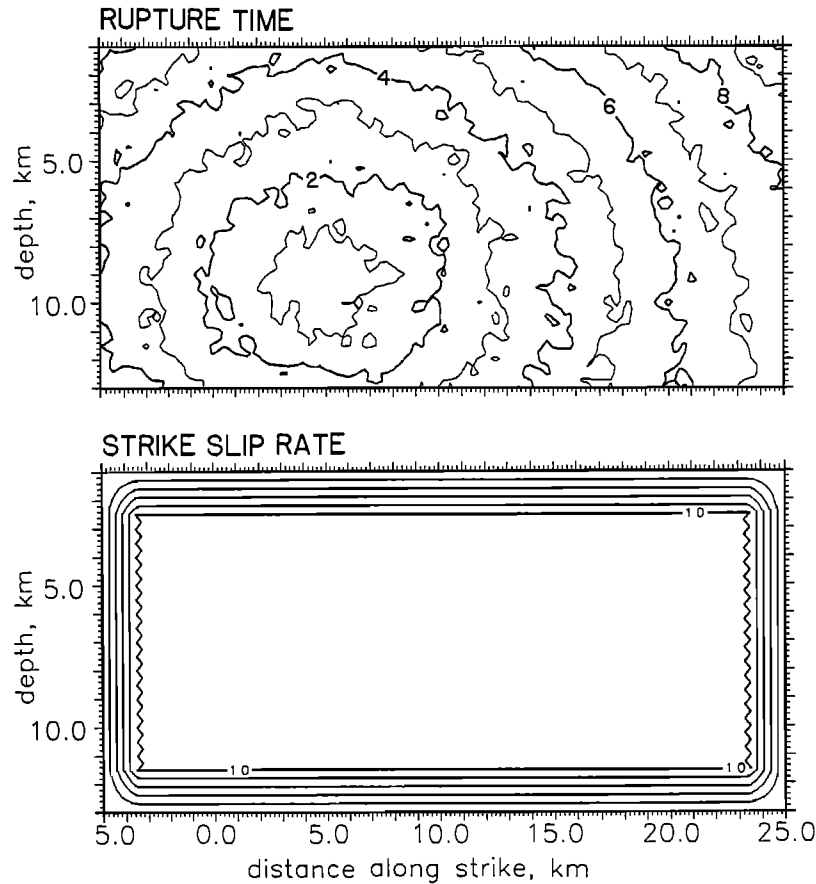


Fig. 2. Contours of rupture time (upper panel) and strike-slip dislocation rate (lower panel) on the San Andreas fault plane for our simulated event. Average rupture velocity is 0.75 of the local shear wave velocity, and some randomness has been added to rupture time to cause the irregular rupture expansion. Units of slip velocity are arbitrary.

the  $f - k$  domain than will the direct body waves, and hence will be discriminable. Shaking occurs at the array from 6 to 18 s after the earthquake origin time, but the motions are not strong at the array during the last 5 s owing to radiation pattern nodes, to the large distance between the array and the rupture front, and to the propagation of the rupture away from the array. The isochrone formalism provides a very simple way to depict this phenomenon graphically.

If  $\mathbf{x}$  is the observer location and  $\mathbf{y}$  is a point on the fault, the  $\hat{\mathbf{a}}$ -component of ground velocity due to  $S$ -waves is

$$\dot{u}_a^*(\mathbf{x}, t) = \tilde{f}_r(t) * \int_{\mathbf{y}(t, \mathbf{x})} \mathbf{s}_r(\mathbf{y}) \cdot \mathbf{G}_a^*(\mathbf{y}, \mathbf{x}) c(\mathbf{y}, \mathbf{x}) dl , \quad (1)$$

where  $\mathbf{y}(t, \mathbf{x})$  is the isochrone or path of integration on the fault corresponding to time  $t$  at observer  $\mathbf{x}$ ,  $l$  is length along the isochrone,  $c$  is the isochrone velocity, which contains the seismic directivity effect, and  $\mathbf{G}_a^*(\mathbf{y}, \mathbf{x})$  is the vector amplitude of the traction caused at  $\mathbf{y}$  by an  $S$ -wave generated at  $\mathbf{x}$  by a point force in the  $\hat{\mathbf{a}}$  direction. The  $\mathbf{G}$

term contains the geometric spreading and the free-surface amplification effects.  $\mathbf{s}_r$  and  $f_r$  are the amplitude and time dependence of the dislocation  $\mathbf{d}(\mathbf{y}, t)$  on the fault,

$$\mathbf{d}(\mathbf{y}, t) = \mathbf{s}_r(\mathbf{y}) f_r(t - t_r(\mathbf{y})) \quad (2)$$

where  $t_r(\mathbf{y})$  is the time that point  $\mathbf{y}$  ruptures. In our example  $f_r(t)$  is a linear ramp function commencing at  $t = 0$ . Consequently  $\dot{f}_r = \delta(t)$ , and we will ignore it henceforth. The double-couple radiation pattern is a result of the dot product  $\mathbf{s} \cdot \mathbf{G}_a$  in (1); radiation pattern nodes lie at the places on the fault where the dislocation vector  $\mathbf{s}$  is perpendicular to the traction  $\mathbf{G}_a$ .

We can determine how much energy each part of the fault radiates to the observer  $\mathbf{x}$  by plotting the integrand of (1) as a function of position on the fault. If we let  $\hat{\mathbf{p}}$ ,  $\hat{\mathbf{t}}$ , and  $\hat{\mathbf{d}}$  be unit vectors oriented parallel to the fault strike, transverse to the strike, and downward (Figure 1), the integrand corresponding to the  $\hat{\mathbf{p}}$  component of motion at the observer is

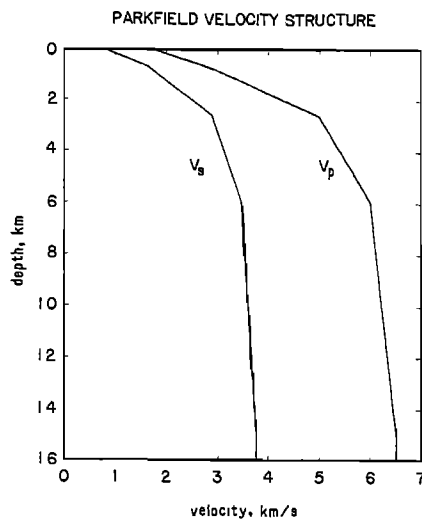


Fig. 3.  $P$  and  $S$ -wave velocity structures used for the calculations.  $S$ -wave velocity is derived assuming a Poisson solid.

$$I_p(\mathbf{y}, \mathbf{x}) = \mathbf{s}(\mathbf{y}) \cdot \mathbf{G}_p^*(\mathbf{y}, \mathbf{x}) \mathbf{c}(\mathbf{y}, \mathbf{x}), \quad (3)$$

with  $I_t$  and  $I_d$  defined similarly. For simplicity we first consider integrands calculated for our hypothetical example without random variations of rupture time. These integrands are shown in Figure 5. Their interpretation is straightforward;  $I_p(\mathbf{y}, \mathbf{x})$  shows the amplitude of the parallel component of ground motion at  $\mathbf{x}$  that comes from point  $\mathbf{y}$  on the fault.  $I_p$ ,  $I_t$ , and  $I_d$  all have radiation pattern nodes, shown by heavy lines, that cross the fault at differing places for each component of motion. Slip at the point denoted by a star in Figure 5 will cause no vertical or transverse motion at the array, but fairly large parallel motion. It can now be seen from the plot of  $I_p$  that the reason the  $\hat{\mathbf{p}}$ -component of ground motion is so small in Figure 4 after 13 s is due primarily to a radiation pattern node.

Despite the uniformity of slip over the entire fault surface, these plots show that the radiation arriving at a particular observer is radiated nonuniformly from the fault. This observation was previously noted by Archuleta and Hartzell [1981]. Now consider this observation in the context of the inverse problem. Observations of the  $\hat{\mathbf{a}}$ -component of motion at any point  $\mathbf{x}$  will be highly sensitive to slip on some parts of the fault, and completely insensitive to slip on other parts. With a distributed array, stations can be scattered around the fault in such a way that no part of the fault is nodal for all stations. Observations made with a dense array, however, cannot avoid this situation.

Having generated synthetic seismograms at our array elements, we now proceed to analyze them. As mentioned earlier, the wave field extrapolation technique of McMechan [1982] holds considerable promise for these types of problems, but to implement it for high-frequency  $S$ -waves and a

2-D fault would necessitate use of a 3-D finite difference solution of the elastic wave equation (McMechan performed his calculations for a 2-D geometry with the acoustic wave equation). For computational expedience we choose a simpler alternative. We break our seismograms into 7 1.6-s-long frames (Figure 4), and perform the high-resolution frequency-wavenumber ( $f - k$ ) analysis of Capon [1969] on each frame individually.

Given some observed wave field  $\mathbf{u}(\mathbf{x}, t)$ , the goal of  $f - k$  analysis is to find some optimal estimate of  $\bar{\mathbf{u}}(\mathbf{k}, \omega)$ , the spatial and temporal Fourier transform of  $\mathbf{u}(\mathbf{x}, t)$ , where  $\mathbf{k}$  is wavenumber. McLaughlin [1983] gives a lucid discussion of both conventional and high-resolution  $f - k$  analysis. Because a plane wave propagating with wave vector  $\mathbf{k}_o$  and frequency  $\omega_o$  will have an  $f - k$  spectrum  $\bar{\mathbf{u}}(\mathbf{k}, \omega) = \delta(\mathbf{k} - \mathbf{k}_o) \delta(\omega - \omega_o)$ , taking the  $f - k$  spectrum of a wave field is equivalent to expressing the wave field as a sum of plane waves, with  $\bar{\mathbf{u}}(\mathbf{k}, \omega)$  being the amplitude of the plane wave with propagation vector  $\mathbf{k}$  and frequency  $\omega$ . We have added one improvement to the usual procedure: since we wish to analyze only the body waves from the earthquake, and since body waves, being essentially non-dispersive, have the same slowness vector (or ray parameter)  $\mathbf{S} = \mathbf{k}/\omega$  for all frequencies, we perform  $f - k$

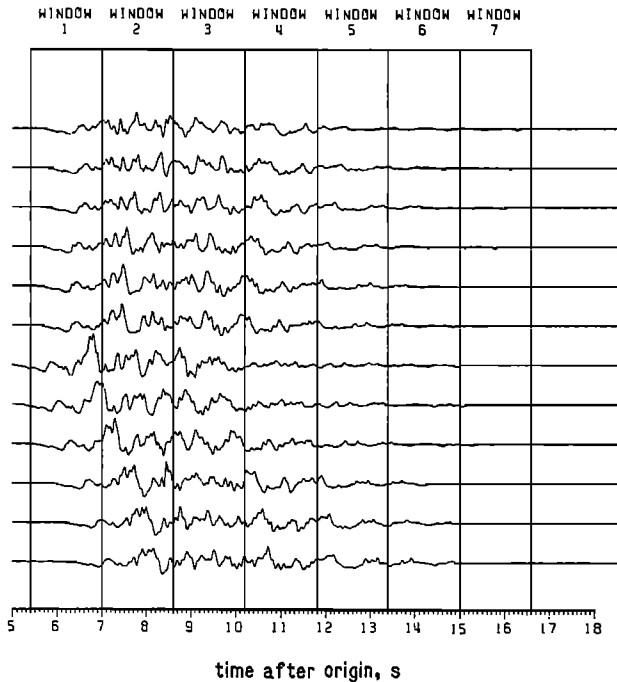
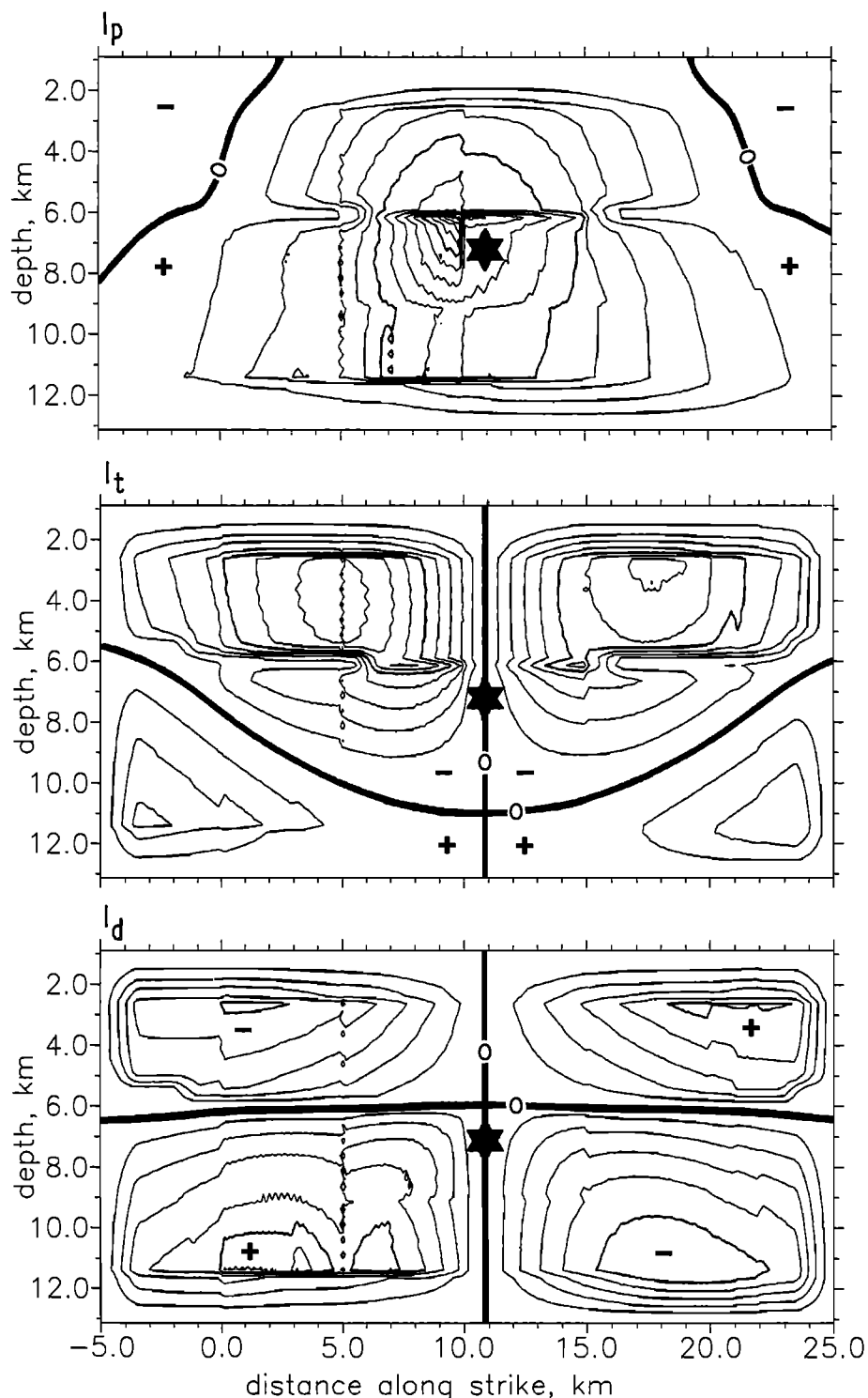


Fig. 4. Synthetic ground velocity seismograms ( $\hat{\mathbf{p}}$ -component) calculated at alternating array elements (Figure 1), resulting from the rupture model in Figure 2. Seismograms are bandpass filtered from 1.5 to 8.5 Hz. The top six seismograms are for array elements going from NW to SE on the NW arm of the array, and the bottom six are from elements running from NE to SW on Hog Canyon Road. Time windows used in subsequent analysis are shown.

## 290 OBSERVATIONS OF EARTHQUAKE RUPTURE DYNAMICS



**Fig. 5.** Contour plots of the integrand of (1) for the parallel, transverse, and downward components of motion. These show how much ground motion is caused at the array by the rupturing of any point on the fault. For example, when the point (star) ruptures, it causes significant motion on the parallel component, and none on the downward and transverse components. Heavy lines are nodes of the radiation pattern. Plus and minus signs show polarity of regions.

analysis for many frequencies and stack the results in the slowness domain. More specifically, for a set of slownesses  $\{S_j\}$ , we calculate

$$\tilde{P}(S_j) = \sum_i P(k_{ij}, \omega_i) ; \quad k_{ij} = S_j \omega_i \quad (4)$$

where  $P(k, \omega_i)$  is Capon's maximum likelihood estimate of power for frequency  $\omega_i$ .

Stacking in the slowness domain is not equivalent to the commonly used procedure of averaging the cross-spectral matrix over frequency. The latter procedure destroys arrivals having constant slownesses [McLaughlin, 1983]. Since each slowness vector  $S$  corresponds to a plane wave arriving at the array with known ray parameter and azimuth of approach, we then use seismic ray tracing to trace this ray back to its point of origin on the fault (Figure 6). The ray tracing establishes a mapping of power in the slowness plane onto radiated power on the fault plane. For example, Figure 7 shows  $P(S)$  observed at the array for a point source of energy at the center of the fault plane, and it shows this power projected on the fault plane. In this case  $P(S)$  is the beam pattern of the array, and its size is inversely proportional to frequency.

To improve the accuracy of the  $f - k$  analysis, Capon [1969] suggests that the results be averaged over adjacent time frames. Since our time series are not stationary, we instead calculate and average the results for the  $\hat{p}$  and  $\hat{t}$  components of motion and for two horizontal components of motion rotated  $45^\circ$  from  $\hat{p}$  and  $\hat{t}$ . This procedure improves the accuracy of the image and also removes some of the biases caused by radiation patterns, since points on the fault that are nodal for  $\hat{p}$  motion are generally not for  $\hat{t}$  motion (Figure 5). By averaging over four horizontal components of motion, the power radiated from any point on the fault is no longer proportional to only  $I_p^2$  or  $I_t^2$ . Rather, it is proportional to  $I_p^2 + I_t^2$ , which is shown in Figure 8 for rupture lacking and having random variations in rupture time.

The addition of a random component to the rupture time causes the integrand to become quite rough, thereby adding considerable high-frequency energy to the seismograms. The roughness of the integrand (3) is caused by variations in isochrone velocity  $c$ , where

$$c = |\nabla_s t_a|^{-1} , \quad (5a)$$

$$t_a(y, x) = t_r(y) + t^s(y, x) . \quad (5b)$$

Here  $t_r(y)$  is the time  $y$  ruptures,  $t^s$  is the  $S$ -wave travel time from  $y$  to  $x$ , and  $\nabla_s$  is the surface gradient operator. Irregular variation of  $t_r$  on the fault surface can cause  $\nabla_s t_a$  to be small or zero, leading to large or singular values in the integrand. These are the 'critical points' discussed by Farra et al. [1986]. Physically they occur at points of supershear rupture velocity, such as those points where the rupture

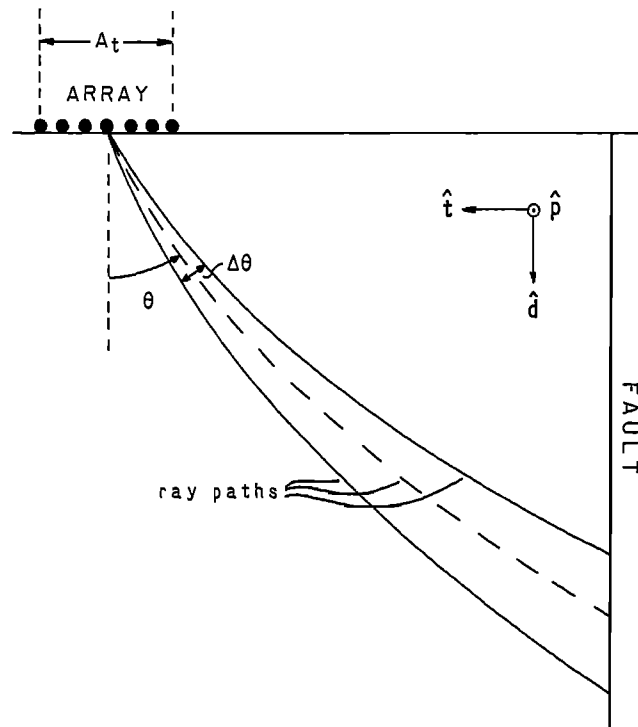


Fig. 6. Cross section of the earth viewed parallel to the fault. Seismic ray paths with incidence angles of  $\theta - \Delta\theta/2$ ,  $\theta$ , and  $\theta + \Delta\theta/2$  at the array, corresponding to observed slownesses at the array  $S - \Delta S/2$ ,  $S$ , and  $S + \Delta S/2$ , respectively, can be projected onto the fault plane using seismic ray tracing to find the ray paths in the local velocity structure (Figure 3). This procedure establishes the mapping from the slowness plane to the fault plane. When  $\Delta\theta$  is the angular spread corresponding to the width of the central peak of the beam pattern,  $\Delta S_t$ , the ray tracing shows the corresponding size of the peak on the fault plane.

jumps ahead of itself discontinuously. The sensitivity of  $c$  to variations in rupture time explains the observation of Archuleta [1984] that synthetic seismograms calculated for the 1979 Imperial Valley earthquake were more dependent upon rupture time than on slip amplitude.

The results of performing  $f - k$  analysis on each time frame of synthetic data (Figure 4) and projecting  $P(S)$  onto the fault are shown in Figure 9. For comparison with the observed power distribution we plot the isochrone corresponding to the center of each window with a dashed line, and we plot the total range of isochrones associated with the entire time window as a stippled region. The stippled region may be viewed roughly as the true answer and the plotted power distribution is our estimate of it, although it must be recalled that the true radiated power is proportional to the lower panel of Figure 8. Note that our analysis procedure produces images of isochrones rather than the rupture front since we are examining waves with a specified arrival time at the array.

## 292 OBSERVATIONS OF EARTHQUAKE RUPTURE DYNAMICS

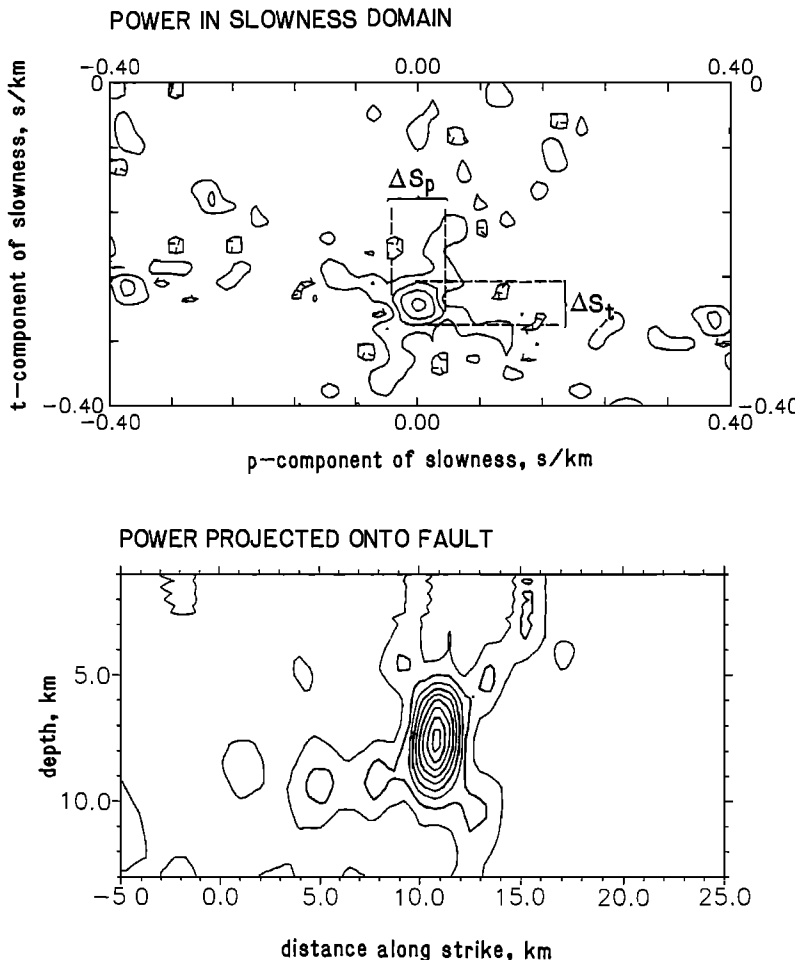


Fig. 7. Upper panel: Beam pattern of the array plotted in the slowness plane for an incident 5 Hz plane wave. Power is contoured in 3dB intervals. The width of the central peak scales inversely with frequency. Lower panel: the beam pattern power distribution projected onto the San Andreas fault, using ray-tracing in the local velocity structure (Figure 3). Contours are linear in power in the lower panel.

The basic features of the bilateral rupture propagation can be seen in the sequence of frames of Figure 9. The processing seems to recover the vertically oriented parts of the rupture better than the horizontal, probably because the beam pattern is somewhat elongated vertically (Figure 7). This elongation could be alleviated by increasing the aperture of the array in the direction perpendicular to the fault, as will be shown below. The images for times 7.8, 9.4 and 11.0 tend to be asymmetric and in some cases systematically displaced from their true position. For the 11.0 s frame the asymmetry is probably related to the low amount of energy radiated from the region of the fault for  $-5$  to  $0$  km along strike compared with the region around  $15$  km along strike (Figure 8). The cause of the other discrepancies is yet unknown to us.

When attempting to understand the discrepancies between the expected and observed results, it should be noted

that there are two separate sources of indeterminacy that must be considered when using a dense array and  $f - k$  analysis. The first is the array's limited ability to define the incoming wave field uniquely. Although an exact analysis of the resolving power of stacked high-resolution  $f - k$  spectra is beyond the scope of this paper, an approximate analysis can be done using Cox's [1973] observation that when multiple interfering waves are present, as would be expected in the near-source region of a large earthquake, the resolving power of the high-resolution technique is similar to that of the conventional  $f - k$  analysis, in which the observed  $f - k$  spectrum is a convolution of the true spectrum with a beam pattern (Figure 7). If  $\Delta S_t$  and  $\Delta S_p$  are the widths in the  $t$  and  $p$  directions of the central peak of the beam pattern in the slowness domain (Figure 7), we have  $\Delta S_t \propto (\omega A_t)^{-1}$  and  $\Delta S_p \propto (\omega A_p)^{-1}$ , where  $A_t$  and  $A_p$  are the maximum extent (aperture) of the array in the

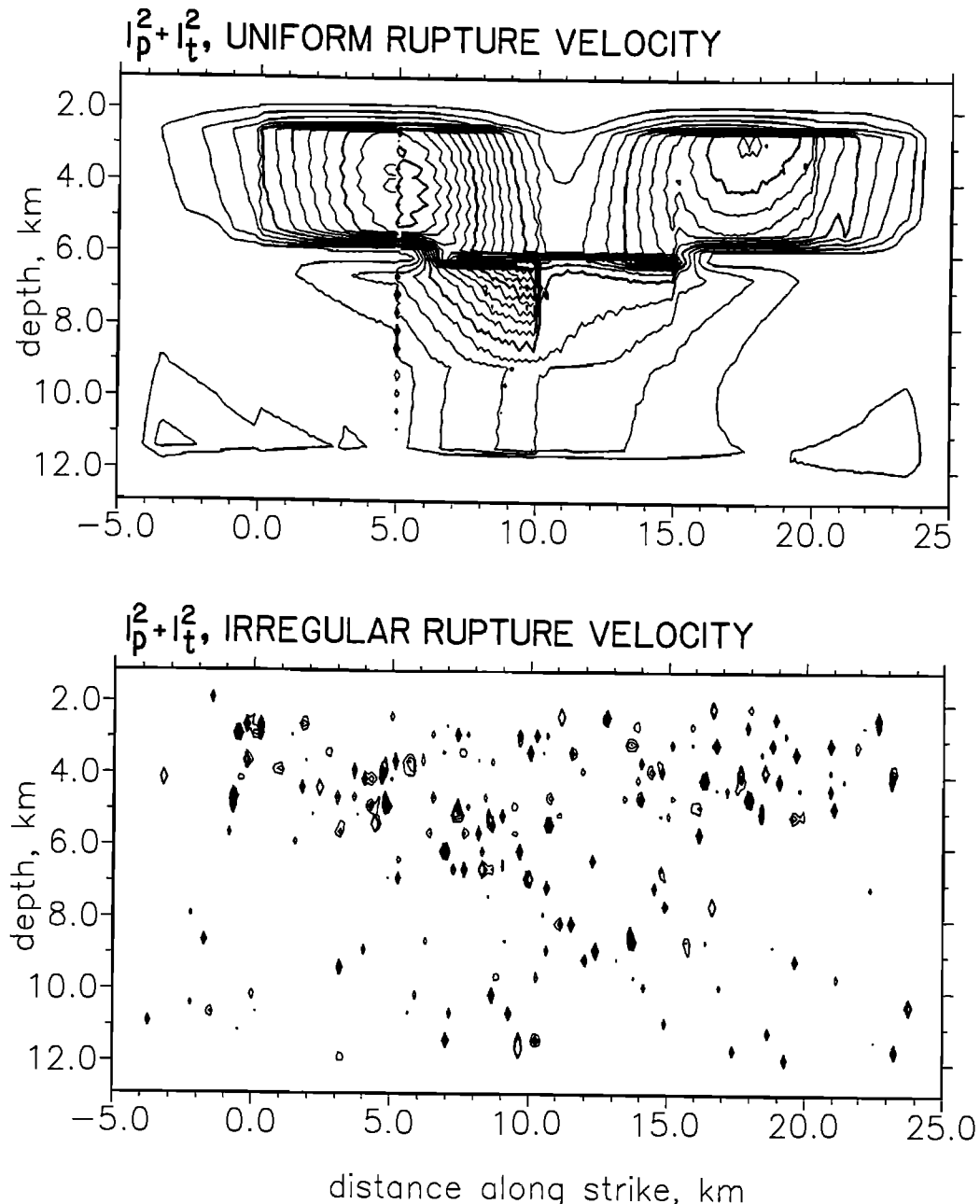


Fig. 8.  $I_p^2 + I_t^2$  is proportional to the power observed in the average of the four horizontal components of motion (see text). Upper panel: power radiated from the fault for the case of smooth rupture propagation at 0.75 of the shear velocity  $v_s$ . Lower panel:  $I_p^2 + I_t^2$  for the case of irregular rupture propagation with average rupture velocity of 0.75  $v_s$  (case illustrated in Figure 2, upper panel). The radiated power is dominated by singularities in isochrone velocity  $c$ , although the overall pattern is modulated by the power distribution for smooth rupture (upper panel).

$t$  and  $p$  directions (Figure 1). Snell's law,  $S = v^{-1} \sin \theta$ , can be used to relate an observed slowness  $S$  to incidence angle  $\theta$  at the array (Figure 6), where  $v$  is the seismic velocity at the array. We then find that the beam width  $\Delta\theta$

in a vertical plane varies with array aperture and incidence angle  $\theta$  (Figure 9) like

$$\Delta\theta \propto \frac{v \Delta S_t}{\cos \theta} = \frac{v}{w A_t \cos \theta}$$

## 294 OBSERVATIONS OF EARTHQUAKE RUPTURE DYNAMICS

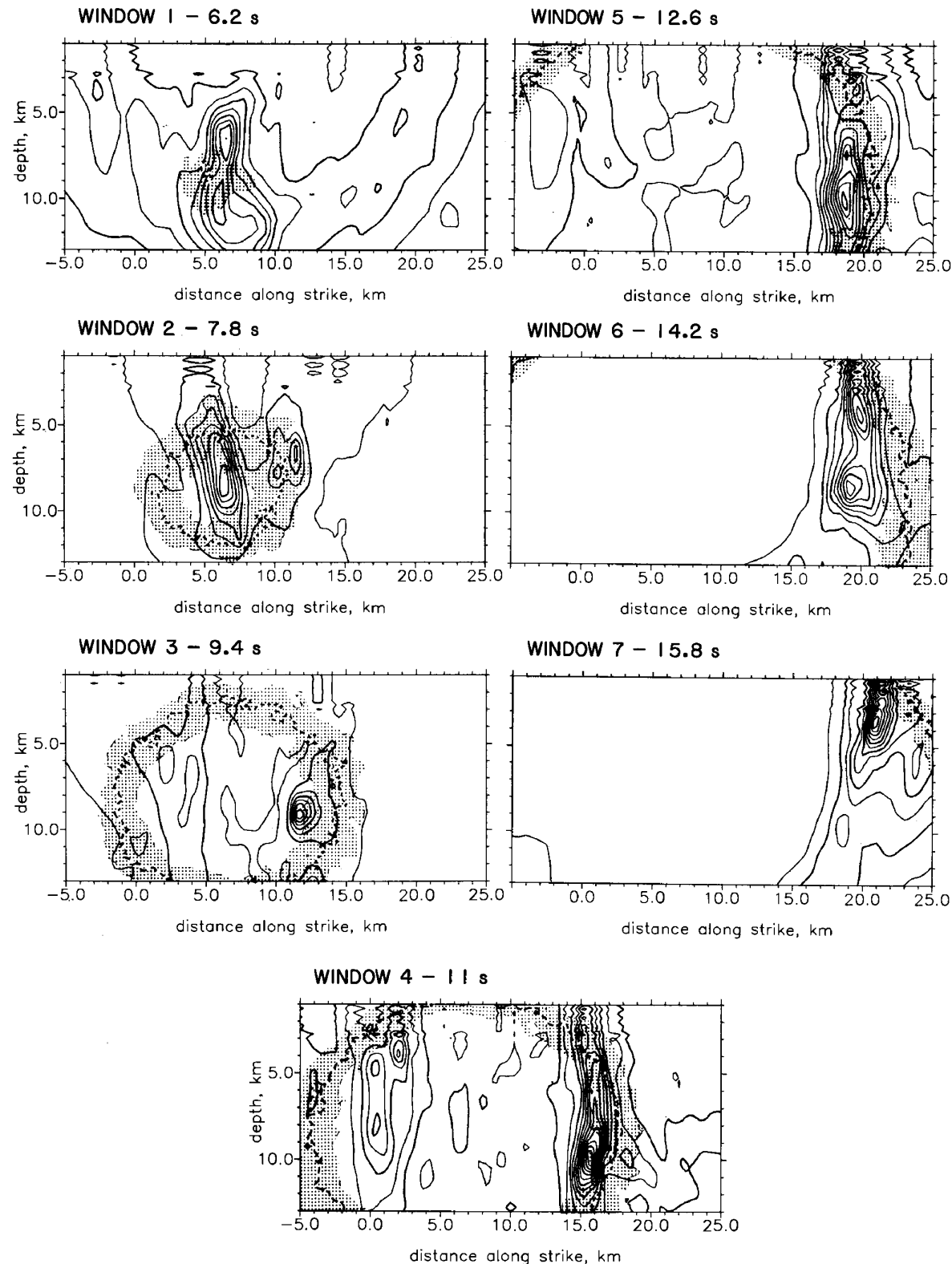


**Fig. 9.** Contour plots of power, projected on the fault, resulting from  $f-k$  analysis of the time windows shown in Figure 4. The dashed line is the isochrone for the time of the center of each time window (shown above each plot), and the stippled region corresponds to the total region of the fault contributing to each time window. Ideally, the inferred power (contours) should peak above the stippled regions. The basic bilateral nature of the event is resolved. See text for additional explanations.

This expression shows that the resolution of a 2-D array is best for waves incident normally to the array and worst for waves incident edge-on. The addition of a downhole string of seismometers can remedy the latter problem. Even if the array were able to determine the input wave field exactly, the second source of indeterminacy is the one mentioned earlier, namely, that we can only observe  $I_p^2$ ,  $I_t^2$ , and  $I_d^2$  (3), not s. A fuller understanding of both sources of indeterminacy can be obtained by using the resolution analysis of Spudich [1980].

Despite the discrepancies in our computed example, we note that with a modest amount of computing (about 2.5 hours on a VAX-11/780) we have analyzed ground motions with frequencies up to 10 Hz and have derived a reasonable picture of the rupture mechanism. To put this into a context, studies of the 1979 Imperial Valley earthquake by Olson and Apsel [1982], Hartzell and Heaton [1983], and Archuleta [1984] required massive amounts of computing to derive rupture mechanisms with approximately equal spatial resolution, and their studies were limited to the 0–1 Hz band. Equivalent massive computer time used by more sophisticated methods of array analysis such as migration or wave field extrapolation may result in correspondingly better images from such high-frequency dense array data.

#### References

- Abrahamson, N. A., Estimation of seismic wave coherency and rupture velocity using the SMART 1 strong motion array recordings, Ph.D. thesis, 122 pp., University of California, Berkeley, 1985.
- Archuleta, R. J., A faulting model for the 1979 Imperial Valley earthquake, *J. Geophys. Res.*, **89**, 4559–4585, 1984.
- Archuleta, R. J., and S. Hartzell, Effects of fault finiteness on near-source ground motions, *Bull. Seismol. Soc. Am.*, **71**, 939–957, 1981.
- Bakun, W., and T. McEvilly, Recurrence models and Parkfield, California, earthquakes, *J. Geophys. Res.*, **89**, 3051–3058, 1984.
- Bernard, P., and R. Madariaga, A new asymptotic method for the modeling of near field accelerograms, *Bull. Seismol. Soc. Am.*, **74**, 539–558, 1984.
- Bolt, B. A., Y. Tsai, K. Yeh, and M. Hsu, Earthquake strong motions recorded by a large near-source array of digital seismographs, *Earthquake Engineering Structural Dynamics*, **10**, 561–573, 1982.
- Bolt, B. A., N. Abrahamson, and Y. T. Yeh, The variation of strong ground motion over short distances, *Proc. Eighth World Conf. Earthquake Eng.*, II, San Francisco, Ca., Prentice-Hall, Englewood Cliffs, N.J., 183–189, 1984.
- Capon, J., High resolution frequency-wavenumber spectral analysis, *Proc. IEEE*, **57**, 1408–1418, 1969.
- Cox, H., Resolving power and sensitivity to mismatch of optimum array processors, *J. Acoust. Soc. Am.*, **54**, 771–785, 1973.
- Eaton, J. P., Instrumental seismic studies, the Parkfield-Cholame, California, earthquakes of June–August 1966, U.S. Geol. Surv. Prof. Pap., **579**, 57–65, 1967.
- Farra, V., P. Bernard, and R. Madariaga, Fast near source evaluation of strong ground motion for source models with complex rupture propagation, *this volume*, 1986.
- Hartzell, S. H., and T. H. Heaton, Inversion of strong ground motion and teleseismic waveform data for the fault rupture history of the 1979 Imperial Valley, California, earthquake, *Bull. Seismol. Soc. Am.*, **73**, 1553–1584, 1983.
- Iwan, W. D. Ed., Strong motion earthquake instrument arrays, *Proceedings of the International Workshop on Strong Motion Earthquake Instrument Arrays*, May 1978, Honolulu, Hawaii, National Science Foundation, Washington, D.C., 1978.
- Iwan, W. D. Ed., U.S. strong motion earthquake instrumentation, *Proceedings of the U.S. National Workshop on Strong-Motion Earthquake Instrumentation*, April 1981, Santa Barbara, California, National Science Foundation, Washington, D.C., 1981.
- Katayama, T., J. Farjoodi, and N. Sato, Measurement of seismic ground strain by a dense seismograph array, *Proc. Eighth World Conf. Earthquake Eng.*, II, San Francisco, Ca., Prentice-Hall, Englewood Cliffs, N.J., 207–214, 1984.
- Liu, H.-L., and T. Heaton, Array analysis of the ground velocities and accelerations from the 1971 San Fernando, California, earthquake, *Bull. Seismol. Soc. Am.*, **74**, 1951–1968, 1984.
- McLaughlin, K. L., Spatial coherency of seismic waveforms, Ph.D. thesis, 138 pp., University of California, Berkeley, 1983.
- McLaughlin, K. L., L. Johnson, and T. McEvilly, Two-dimensional array measurements of near source ground accelerations, *Bull. Seismol. Soc. Am.*, **73**, 349–375, 1983.
- McMechan, G. A., Determination of source parameters by wavefield extrapolation, *Geophys. J. R. Astron. Soc.*, **71**, 613–628, 1982.
- McMechan, G. A., J. H. Luetgert, and W. D. Mooney, Imaging of earthquake sources in Long Valley Caldera, California, 1983, *Bull. Seismol. Soc. Am.*, **75**, 1005–1020, 1985.
- Narahashi, H., S. Omote, J. Maeda, and M. Watakabe, Spatial correlations of the ground motion recorded by the strong motion earthquakes instrument array, *Proc. Eighth World Conf. Earthquake Eng.*, II, San Francisco, Ca., Prentice-Hall, Englewood Cliffs, N.J., 239–246, 1984.
- Olson, A. H., and R. J. Apsel, Finite faults and inverse theory with applications to the 1979 Imperial Valley earthquake, *Bull. Seismol. Soc. Am.*, **72**, 1969–2002, 1982.
- Omote, S., Y. Ohsawa, B. Ohmura, S. Iizuka, T. Ohta, and K. Takahashi, Observation of earthquake strong motion with deep boreholes, *Proc. Eighth World Conf. Earthquake Eng.*, II, San Francisco, Cal., Prentice-Hall, Englewood Cliffs, N.J., 247–254, 1984.
- Spudich, P., The deHoop-Knopoff representation theorem

## 296 OBSERVATIONS OF EARTHQUAKE RUPTURE DYNAMICS

as a linear inverse problem, Geophys. Res. Lett., **7**, 717–720, 1980.

Spudich, P., and E. Cranswick, Direct observation of rupture propagation during the 1979 Imperial Valley, California, earthquake using a short-baseline accelerometer

array, Bull. Seismol. Soc. Am., **74**, 2083–2114, 1984.

Spudich, P., and L. N. Frazer, Use of ray theory to calculate high-frequency radiation from earthquake sources having spatially variable rupture velocity and stress drop, Bull. Seismol. Soc. Am., **74**, 2061–2082, 1984.

## A STUDY OF STRONG MOTIONS FROM ITALY AND YUGOSLAVIA IN TERMS OF GROSS SOURCE PROPERTIES

Ezio Faccioli

Department of Structural Engineering, Politecnico, Piazza L. da Vinci 32, Milano, Italy

**Abstract.** A  $\omega$ -cube spectral model is shown to provide predictions of peak ground acceleration and velocity in good agreement with a large body of data from recent earthquakes in Italy and Yugoslavia. The model is characterized by two corner frequencies  $f_2$  and  $f_1$ , the seismic moment as a scaling parameter, and a Q-factor varying linearly with frequency. The lowest corner frequency  $f_2$  is regarded as a gross measure of the size of dominant subevent, whereas  $f_1$  is a high-frequency rolloff limit which may be caused by either site or source effects. The dependence of  $f_2$  and  $f_1$  on  $M_0$  is obtained by empirical regressions, which show that  $f_2$  is always higher than the corner frequency of the Brune model (for  $M_0 > 10^{22}$  dyne cm) and does not scale self-similarly. For a given Q=Q(f) relation, the predictions of peak acceleration and velocity are obtained as a function of  $M_0$  only. It is found that the dependence of the previous quantities on  $M_0$  is somewhat stronger than predicted by the  $\omega$ -square model with constant stress drop and fixed high-frequency limit. The performance of the model with respect to a set of data from thrust and normal events of the Western U.S. is also illustrated.

## Introduction

The strong dependence of the high-frequency seismic radiation on strength and stress heterogeneities along the fault zone is today an accepted fact [e.g., Boatwright, 1982; Papageorgiou and Aki, 1983a, b]. At the same time, a simple model which uses a constant stress parameter and the  $\omega$ -square spectrum of Brune [1970] with a fixed high-frequency limit, has been shown to provide satisfactory overall predictions of ground motions from moderate and strong California earthquakes in the 1–10 Hz frequency range [Hanks and McGuire, 1981; Boore, 1983]. For the sake of brevity only, I will refer to this model as band-limited white noise (BLWN). Its most recent version is presented in this volume [Boore, 1986]. In the context of the BLWN description, much attention is currently focused on the physical causes of  $f_{\max}$ , i.e., of the high-frequency cutoff observed in real spectra, and the contrast between site-dependent and

source-dependent interpretations of  $f_{\max}$  does not appear to be resolved as yet [Aki, 1986; Anderson, 1986]. Although frequencies beyond  $\sim 10$  Hz are of interest only in special cases in seismic hazard studies, the role played by  $f_{\max}$  in the interpretation of the scaling of peak motions in small earthquakes appears to be crucial [McGarr, 1986]. Leaving the issue of  $f_{\max}$  temporarily aside, one can ask whether the BLWN model, shown to be satisfactory for California events, works equally well in different seismotectonic settings (e.g., in subduction zones), or for different source mechanisms and depths even within the same region. Actually, one of the motivations for this work stemmed from the observation that several acceleration spectra from recent earthquakes of Italy and of the April 15, 1979, Montenegro event exhibit a  $f^{-\gamma}$  decay, with  $\gamma$  close to 1, in the range from 1–2 Hz to 10 or more Hz and a distinct corner frequency at 0.5–1 Hz (see Figure 1). For the larger earthquakes, this frequency is considerably higher than the corner frequency of the Brune model. The spectra of Figure 1 were calculated without any filtering from the uncorrected data obtained by digitization at constant  $\Delta t = 0.01$  s of standard SMA-1 accelerograph recordings [Petrovski et al., 1980]. Only a 10% cosine bell was used for tapering the sample prior to computing the Fourier transform. The insufficient bandwidth of the data does not allow resolution of the Brune corner frequency at about 0.1 Hz. Similar peculiarities are also found in spectra of the Coalinga, California earthquake sequence including the main shock of May 2, 1983 (see Figure 2). As shown in Figure 1, these properties reflect the presence in the time histories of bursts of strong acceleration, suggesting that the high frequency is dominated by the radiation from one, or a few compact subsources. It is therefore of interest to resort to more complex spectral models, which contain BLWN as a particular case and can account for irregularities of the source process in the high-frequency range [Boatwright, 1982; Faccioli, 1983].

The aim of this paper is to report on the applicability of one such model, calibrated with a set of strong-motion records mainly from recent events of Italy and Yugoslavia and developed

## 298 STRONG MOTIONS STUDY

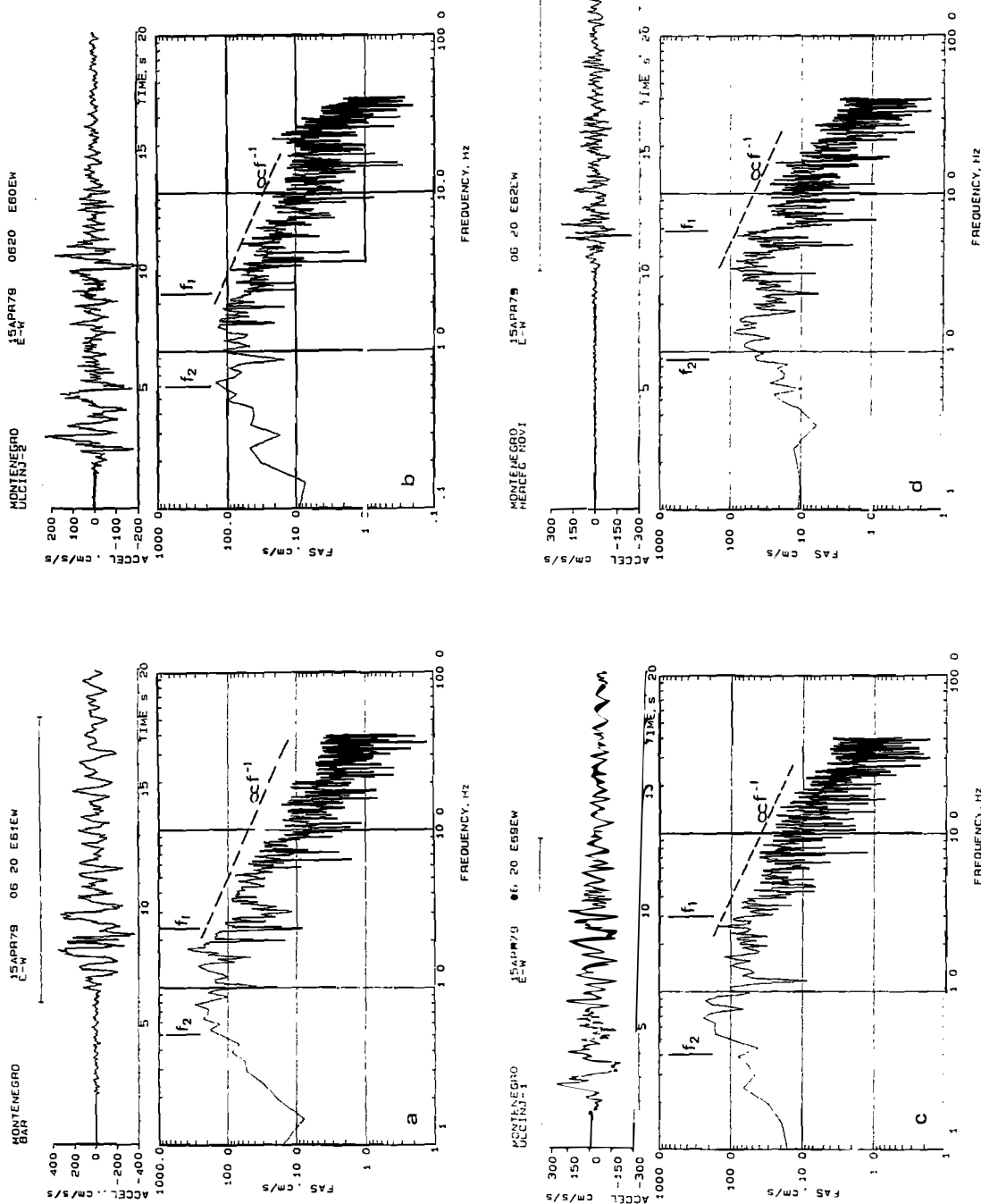


Fig. 1. Fourier amplitude spectra (FAS) of representative horizontal acceleration components of the 1979 Montenegro earthquake, with characteristic frequencies  $f_2$  and  $f_1$  indicated by vertical bars. Focal distances of recording stations vary between about 15 km (Ulcinj) and 70 km (Herceg-Novi), but source distances could be significantly less in some cases (see text).

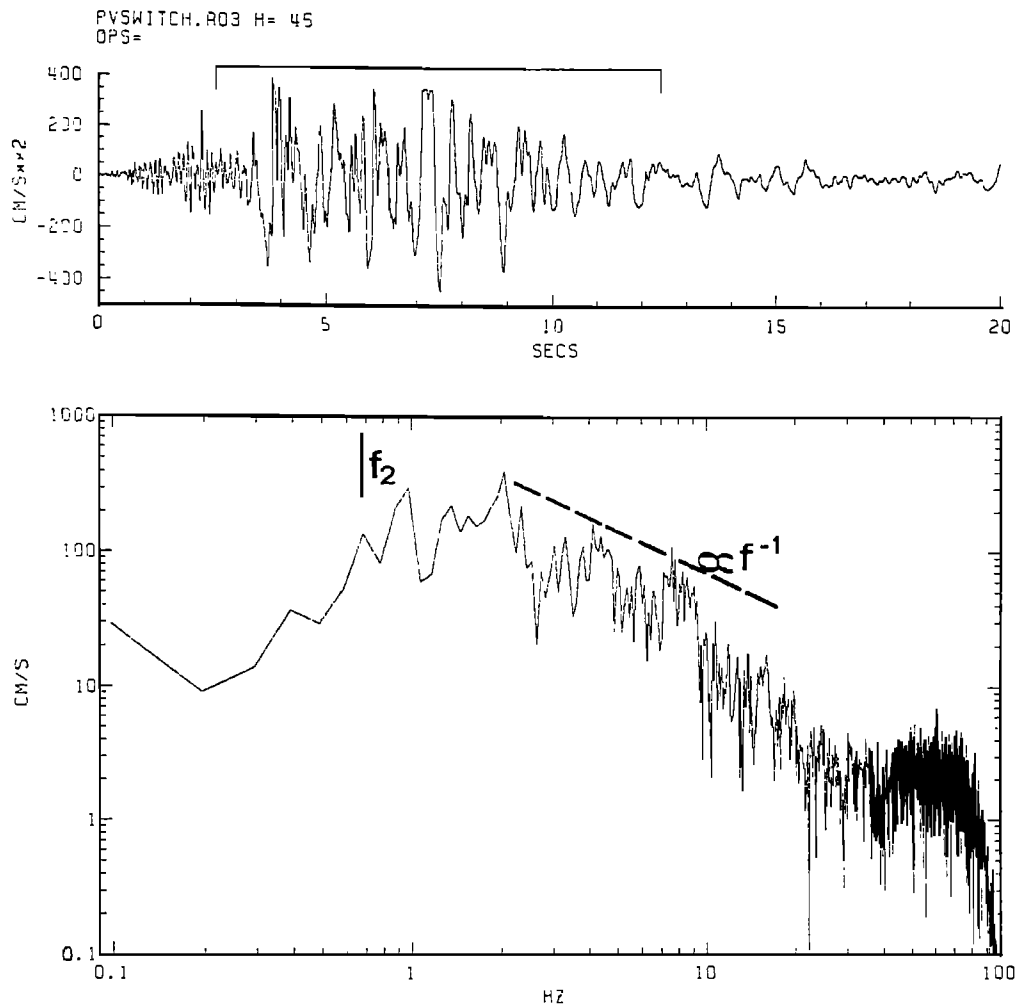


Fig. 2. Horizontal acceleration component and spectrum of the Pleasant Valley Switchyard recording of the May 2, 1983 Coalinga main shock, with characteristic frequency  $f_2$ .

by the writer on the basis of the Haskell [1966] stochastic description of the source spectrum [Faccioli, 1983; Faccioli et al., 1984]. The proposed formulation yields closed form expressions for the Arias intensity, the root mean square (rms) acceleration, and other parameters, which makes it attractive for engineering applications and allows a direct estimation of the source parameters from the data. The present work is focused on the scaling and prediction of peak ground motions. In the following sections, after presenting the data used for parameter estimation, and summarizing some relevant analytical expressions derived from the assumed source model, I shall discuss its performance with respect to the observations.

#### The Strong-Motion Data

The main body of data for this study includes 110 strong-motion horizontal acceleration compo-

nents from 15 events with local magnitude  $M_L$  in the range 4.4–6.7 and seismic moment  $M_0$  in the range  $3 \cdot 10^{22}$ – $10^{26}$  dyne cm.

The earthquakes belong to two bordering tectonic regions (Figure 3); one including Friuli and Montenegro (Eastern and Dinaric Alps), with predominant thrust faulting, and the other including the Apennines where normal faulting is instead prevalent. Friuli, Irpinia and Montenegro were the strongest earthquakes occurring in Italy and Yugoslavia during the last few decades. When seismological determinations of seismic moment were available I have used the 10 to 20 s body-wave values, consistent with the assumption that the theoretical acceleration spectrum (given in the next section) only accounts for the direct S waves from the source. For Irpinia and Montenegro the body wave  $M_0$  is roughly one-fourth of the 256 s surface wave value whereas for the strongest events of the Friuli sequence the short-period  $M_0$  values

## 300 STRONG MOTIONS STUDY



Fig. 3. Location of events providing the main body of data for this study: 1. Ancona, 1972; 2. Friuli, 1976-1977; 3. Valnerina, 1979; 4. Montenegro, 1979; 5. Irpinia, 1980-81.

mostly agree with the long-period ones [Lyon-Caen, 1980]. Focal depths are between 5 and 10 km, except for the Irpinia main shock (18 km). The depth of the Montenegro event, apparently characterized by a multiple source process, is rather uncertain. I have tentatively assumed 15 km based on Boore et al. [1981] and Console and Favali [1981].

About 80% of the data are from stations located within 30 km focal distance, since the emphasis is presently on the scaling of ground motions versus source strength. For some stations recording the Montenegro earthquake, such as Bar and Herceg Novi in Figure 1, the source distance is significantly less than focal distance since the causative fault ruptured parallel to the coast (Figure 3) over 40-50 km and the stations were mostly in coastal towns. I chose the focal distance for consistency with the S-minus-trigger time (about 10 s for Herceg Novi in Figure 1) and the interpretation that distance in the Haskell model is measured from the initiation of rupture. Representative uncorrected acceleration histories with their Fourier Amplitude Spectrum (FAS) for the Montenegro earthquake are illustrated in Figure 1. A recently redigitized version at constant  $\Delta t \approx 0.004$  s, resulting in visi-

bile reduction of long-period noise, was used for the Irpinia recordings.

The examples of Figure 1 show that the intermediate portion of the FAS is bounded by a lower and an upper characteristic frequency called  $f_2$  and  $f_1$ , respectively. These frequencies are taken to be the same as the corner frequencies of the theoretical spectrum discussed in the next section. Whereas  $f_2$  can generally be interpreted as a subevent corner frequency and, hence, as a source property, there is evidence (discussed below) suggesting that in some cases the origin of  $f_1$  is associated with propagation or site effects. In the case of the Montenegro earthquake, the Brune corner frequency corresponding to a 256 s surface wave seismic moment of  $4.6 \times 10^{26}$  dyne cm is  $f_c = 0.13$  Hz, whereas the observed  $f_2$  values are between 0.5 and 0.8 Hz.

The values of  $f_1$ ,  $f_2$  were picked directly on the spectra in all cases in which a relatively clear choice could be made; they are shown by vertical bars in Figure 1. My visual choice of  $f_2$  is in most cases close to the frequency,  $f_{0.05}$ , for which the cumulative squared spectral acceleration equals 5% of its value for  $f \rightarrow \infty$ , and this can be used as a more objective criterion for identifying  $f_2$ . The mean value of  $f_2$  for each event is plotted against  $M_0$  in Figure 4a and the least-squares fit through these data is given by:

$$f_2 = 3.54 \times 10^5 M_0^{-0.23} \quad (1)$$

with  $f_2$  in Hz and  $M_0$  in dyne cm, and a standard deviation of the exponent of 0.04. Also plotted in Figure 4a is the Brune corner frequency

$$f_c = 4.9 \times 10^6 \beta (\Delta\sigma/M_0)^{1/3} \quad (2)$$

with  $\beta = 3.5$  km/s, for two values of the stress parameter  $\Delta\sigma$ , namely 100 bars [Boore, 1983] and 800 bars, which seems roughly compatible with the data in the figure. Estimates of subevent stress drops are available for the Friuli earthquakes and are always less than 300 bars [Cipar, 1981].

Interpreting the  $f_2$  data of Figure 4a through the Brune model would thus seem to require values of  $\Delta\sigma$  not supported by independent evidence. Equation (1) means that, at least for the present data,  $M_0 f_2^4 \approx \text{const}$  as opposed to  $M_0 f_0^3 \approx \text{const}$  of (2), and implies that the "local" stress drop associated with the breaking of the asperities which radiate the high frequencies, increases with seismic moment. Subevent corner frequencies from Japan Sea earthquakes display a trend quite similar to that of the present  $f_2$  values [Aki, 1986].

Regressing in a similar way the average values of  $f_1$  (Figure 4b) yields:

$$f_1 = 7.31 \times 10^3 M_0^{-0.12} \quad (3)$$

with a standard deviation of the exponent of 0.02. The average  $f_1$  value from the Irpinia main

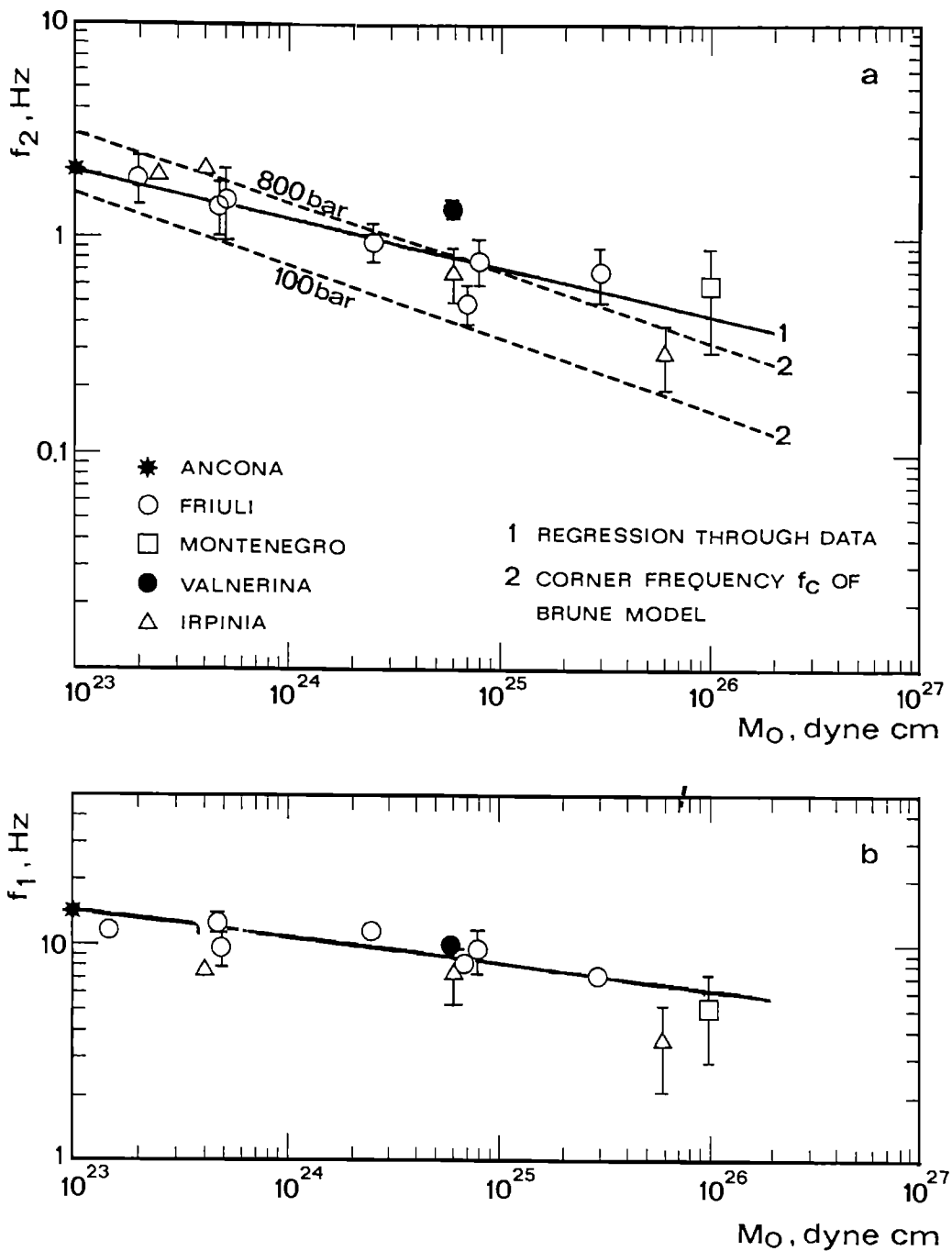


Fig. 4. Observed dependence of characteristic frequencies  $f_2$  (a) and  $f_1$  (b) on seismic moment. Vertical bars denote 1 standard deviation intervals. The corner frequencies of the Brune model are from equation (2).

shock (3.7 Hz) seems anomalously low, and was not used in the regression. For most of the data for  $M_L \lesssim 6$  the frequency  $f_1$  can be identified with the  $f_{\max}$  discussed in the introduction, and for the Friuli stations the observed  $f_{\max}$  values

( $\sim 10$  Hz) are probably related to site effects occurring within a few hundred meters from the surface. This is mainly inferred from the recordings of the Somplago-D station, located in a cavity housing an underground power plant

## 302 STRONG MOTIONS STUDY

260 m deep into massive limestone, which exhibit a flat acceleration spectrum extending up to the high-frequency filter rolloff around 25 Hz. Figure 5 shows typical  $f_1$  values as a function of local magnitude for a number of accelerograph stations in Friuli, and the difference between the values observed at the underground Somplago-D station and those observed at the surface stations is apparent. The curve gives the estimate of  $f_{\max}$  by Anderson [1986] using an  $\omega$ -square model and a high-frequency spectral decay of the type  $\exp(-\pi k f)$  with a decay parameter  $k = 0.05$  s, which represents typical attenuation for California. The fact that the observed values of  $f_1$  at the surface are in good agreement with this prediction, and at the same time substantially smaller than those recorded underground suggest that site effects had a dominant influence on the high-frequency cutoff in the Friuli spectra. On the other hand, for the largest events like Irpinia and Montenegro  $f_1$  lies mostly between 2 and 6 Hz, in agreement with Papageorgiou and Aki [1983b] who found  $f_{\max} = 2.5\text{--}5.0$  Hz for California earthquakes of comparable size. Since some of the stations recording the Irpinia and Montenegro earthquakes were several tens of kilometers from the source, scattering and structural complexities could be contributing to give a low estimate for  $f_1$ . However, in the Montenegro spectra the decay beyond  $f_1$  is characteristically close to  $f^{-1}$  up to 10–15 Hz (Figure 1) suggesting that source effects such as progressive stopping of rupture could be important in this frequency range. Note that the spectra in Figure 1 can be regarded as accurate below about 25 Hz.

## Theory

Following the format suggested by Boore [1983], I express the shear wave, far-field Fourier amplitude spectrum of acceleration as:

$$A(f) = \frac{C M_o}{R} S(f, f_1, f_2) \exp(-\pi f R/2Q\beta) \quad (4)$$

where  $C$  is a constant,  $M_o$  is the seismic moment,  $R$  is the focal distance,  $S(f, f_1, f_2)$  is the source spectrum. The exponential term describes the attenuation effect, and

$$C = F S \bar{R}_{\theta, \phi} V_p / (4\pi\rho\beta^3) \quad (5)$$

where  $F S$  is the free-surface correction,  $\bar{R}_{\theta, \phi}$  is the rms value of the shear wave radiation pattern,  $V_p$  is a vectorial partition factor, and  $\rho$  and  $\beta$  are the density and S-wave velocity of the medium, respectively. The values  $F S = 2$ ,  $\bar{R}_{\theta, \phi} = 0.63$  and  $V_p = 1/\sqrt{2}$  will be used in the sequel. I describe the seismic source by means of the statistically inhomogeneous model proposed by Haskell [1966], where the slip acceleration is characterized by an autocorrelation function which ensures that most of the radiated energy

is associated with small spatial and temporal lags. Fault rupture, although irregular in detail, is assumed to occur unilaterally at a constant mean speed  $c$  and to be governed by two independent parameters, namely the rupture correlation length (or coherent length)  $k_L^{-1}$ , and the correlation time  $k_T^{-1}$ . The quantity  $k_L^{-1}$  is regarded as a fraction of the total fault length  $L$ , and  $k_T^{-1}$  as a fraction of the total rupture duration  $T_r$ . More generally, I regard  $k_L^{-1}$  and  $k_T^{-1}$  as parameters related to the scale of the inhomogeneities of the source process. For instance,  $k_T^{-1}$  and  $k_L^{-1}$  could be taken as measures of the size of the dominant and of the minimum source subevents, respectively, although for the latter a site-related origin is also possible.

The Haskell source spectrum can be expressed as:

$$S(f, f_1, f_2) = \frac{4\pi^2 f^2}{[1 + (f/f_1)^2]^{1/2} [1 + (f/f_2)^2]} \quad (6)$$

where  $f_1$  and  $f_2$  are two corner frequencies, given by:

$$f_1 = ck_L/[2\pi(1 - m \cos\theta)] \quad \text{and} \quad f_2 = k_T/2\pi \quad (7)$$

In (7)  $m = c/\beta$  and  $\theta$  is the angle between the seismic ray and the direction of the faulting. Note that neither  $f_1$  nor  $f_2$  depend on the whole fault length, in contrast to the corner frequency of the Brune model, defined as  $f_c = c/L$ . By introducing the directivity factor  $\lambda$ :

$$\lambda = 1 - m \cos \theta \quad (8)$$

and a spectral bandwidth parameter  $\xi$ :

$$\xi = f_2/f_1 = \lambda \frac{k_L^{-1}}{c k_T^{-1}} \quad (9)$$

Equation (6) can also be written in the form:

$$S(f, f_2, \xi) = \frac{4\pi^2 f^2}{[1 + (\xi f/f_2)^2]^{1/2} [1 + (f/f_2)^2]} \quad (10)$$

The limiting case  $\xi \rightarrow 0$  corresponds to a spatially uncorrelated rupture process with  $k_L^{-1} \rightarrow 0$ . If, in addition, we make  $k_T^{-1} \rightarrow T_r/2\pi$ , equation (10) reduces to the spectrum of the Brune model with corner frequency  $f_c = f_2$ . The acceleration spectrum described by (6) or (10) decays as  $f^{-1}$  for  $f > \max(f_1, f_2)$ . As to the attenuation term in (4), for seismic  $Q$  in a range up to 100 km from the focus I assume the frequency-dependent relationship:

$$Q(f) = Q_0 f \quad (11)$$

which seems to be peculiar for the Mediterranean regions [Console and Rovelli, 1981; Rovelli, 1982, 1983, 1984]. Introducing (11) the attenua-

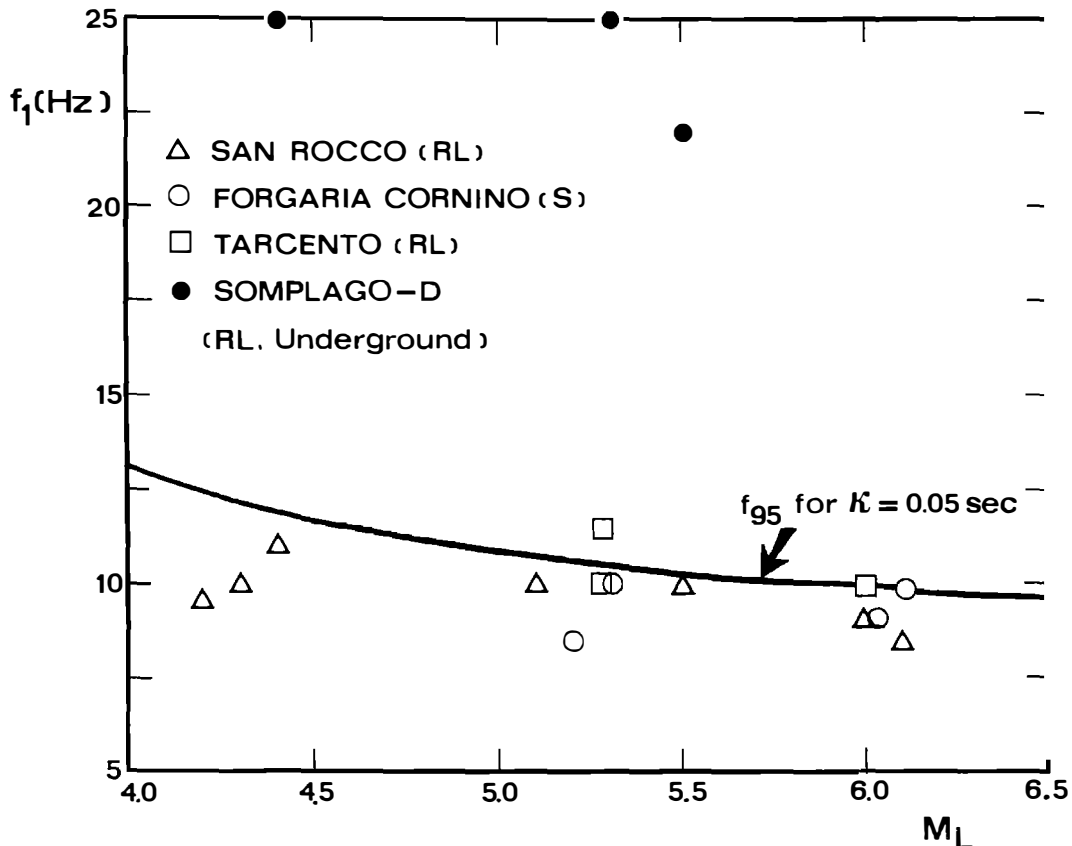


Fig. 5. Values of upper characteristic frequency  $f_1$  as a function of local magnitude  $M_L$  observed in the 1976 Friuli sequence at accelerograph stations located within 20 km focal distance (RL = rocklike, S = soil). The high  $f_1$  values of the underground Somplago-D station are very close to the rolloff of filter used for high-frequency correction. Continuous line shows the estimate of  $f_{\max}$  associated with typical California attenuation [Anderson, 1986].

tion correction reduces to  $\exp(-qR)$ , where:

$$q = \frac{\pi}{Q_o \beta} \quad (12)$$

Relations (11) and (12) imply that the distance affects the source spectrum only through a scaling factor, without changing its shape. As long as the distance range is limited to a hundred kilometers from the source, this peculiarity is reasonably well verified by the spectral attenuation trends of the strong-motion data. Moreover, estimates of seismic Q obtained by using coda wave decay of seismometric data from small earthquakes show a very similar frequency dependence [Rovelli, 1982].

The cumulative squared acceleration, velocity, and displacement can be evaluated in closed form from the previous expressions through Parseval's equality, under the assumption that the only significant contribution to ground motion comes from the S waves directly radiated from the source. The expression for the squared acceleration is:

$$I_a = \int_0^{T_o} a^2(t) dt = \frac{C}{4} M_o^2 \frac{e^{-2qR}}{R^2} k_T^5 D_a(\xi) \quad (13)$$

where  $a(t)$  denotes acceleration as a function of time  $t$ ,  $T_o$  is the total duration of motion, and:

$$D_a(\xi) = \frac{2 + \xi}{\xi(1 + \xi)^2} \quad (14)$$

is a factor accounting for spectral bandwidth and directivity.

A further quantity of interest is the rms acceleration  $\bar{a}$  over the time interval  $T$  carrying the S waves, defined as:

$$\bar{a}(T) = \left[ \frac{1}{T} \int_{t_s}^{t_s+T} a^2(t) dt \right]^{1/2} \quad 0 < t_s + T < T_o \quad (15)$$

where  $t_s = R/\beta$  is the instant of the S wave arrival. Using the faulting duration  $T_f$  as an estimate of  $T$  and substituting (13) in (15) yields a convenient approximate expression for  $\bar{a}(T)$ .

## 304 STRONG MOTIONS STUDY

However, if the spectral cutoff at  $f_{\max}$  is introduced, it can be shown that by virtue of Parseval's equality and (15):

$$\bar{a} = B_a M_o \frac{e^{-qR}}{R} \frac{f_2^3}{\sqrt{f_2 T_r}} G(f_2, f_{\max}) \quad (16)$$

where:

$$B_a = (2\pi)^{5/2} C/2.$$

It is useful for later applications to give the expression of the function  $G(f_2, f_{\max})$  for two limiting cases, both valid if  $(f_2/f_{\max}) \ll 1$ , namely

$$G(f_2, f_{\max}) \approx \left[ \frac{(1-3\xi)}{\xi} + \frac{8\xi}{\pi} \right]^{1/2} \quad f_2 < f_1 = f_{\max} \quad (17)$$

$$G(f_2, f_{\max}) \approx \left[ \left( \frac{3}{4} - \frac{4}{\pi} \frac{f_2}{f_{\max}} \right)^{1/2} \quad f_2 = f_1 < f_{\max} \quad (18)$$

Equation (17) corresponds to the case of small  $\xi$ , i.e., to a relatively flat spectrum. If in (17) we make  $\xi$  small with respect to unity, and also take  $f_2 = f_c = T_r^{-1}$  equation (16) reduces to:

$$\bar{a} = B_a M_o \frac{e^{-qR}}{R} f_c^3 (f_{\max}/f_c)^{1/2} \quad (19)$$

Aside from the propagation term, this is the expression of rms acceleration yielded by the BLWN model [Boore, 1983].

As shown by Hanks and McGuire [1981] and by Boore [1983], random vibration concepts can be profitably employed to estimate peak values of ground acceleration and velocity in terms of their respective rms values. Specifically, if

$$\tilde{N} = 2 f T \quad (20)$$

is the number of zero-crossings in a time interval  $T$ , in which  $f$  is the predominant frequency of motion, we can use the asymptotic approximation for large  $N$ :

$$\tilde{r}_a = \frac{E[a_{\max}]}{\bar{a}} = (2 \ln N)^{1/2} + \frac{0.577}{(2 \ln N)^{1/2}} \quad (21)$$

where  $E[a_{\max}]$  is the expected value of the largest acceleration extremum. Under the assumption  $f_{\max}/f_2 \gg 1$ , one obtains for the predominant frequency of acceleration  $\tilde{f}_a$  the expression

$$\tilde{f}_a \approx \left[ \left( \frac{4}{\pi} - 1 \right)^{1/2} f_{\max} \quad f_2 < f_1 = f_{\max} \quad (22) \right.$$

$$\left. 4(f_2 f_{\max}/3\pi)^{1/2} \quad f_2 = f_1 < f_{\max} \quad (23) \right]$$

The predominant frequency given by (22) is one-half of the value  $\tilde{f}_a = f_{\max}$  calculated from the spectrum of the BLWN model under the same approximations [Boore, 1983, equation A7a].

We can use the same treatment to obtain the analogous estimates for ground velocity. Thus, the rms velocity  $\bar{v}$  is expressed as:

$$\bar{v} = B_v M_o \frac{e^{-qR}}{R} \frac{f_2^2}{\sqrt{f_2 T_r}} \frac{1}{1+\xi}; \quad (B_v = B_a / 2\pi) \quad (24)$$

valid for  $(f_2/f_{\max})^2 \ll 1$ . Again, for  $\xi \rightarrow 0$  and  $f_2 = f_c = T_r^{-1}$ , equation (24) reduces to the equivalent expression for the BLWN model [Boore, 1983, equation A6b]. It is noteworthy that the rms velocity is independent of  $f_{\max}$ . The ratio  $E[v_{\max}] / \bar{v}$  can be estimated through the right-hand member of (21) and (20), but the predominant frequency of ground velocity (calculated without introducing the cutoff at  $f_{\max}$ ) is:

$$\tilde{f}_v = f_2 (1 + 2/\xi)^{1/2} \quad (25)$$

If we take  $f_c = f_2 \ll f_1 = f_{\max}$ , so that  $\xi \ll 1$ , equation (25) yields:

$$\tilde{f}_v = \sqrt{2} (f_{\max}/f_c)^{1/2} f_c \quad (26)$$

## Model Performance

The performance of the proposed model is illustrated by comparing the predicted peak motions with the observed ones. Crucial to the accuracy of theoretical predictions are the empirical correlations (1) and (3), which are substituted in the appropriate expressions of the previous section. As a result, these become a function of the single source parameter  $M_o$ . It should be emphasized that (1) and (3) are independent of the spectral model adopted; the basic assumption is that the observed values of  $f_1$  and  $f_2$  coincide with the corner frequencies (7) of the source spectrum (6).

The predicted value of horizontal peak acceleration,  $E[a_{\max}]$ , is obtained by introducing (16) and (20) into (21). The resulting expressions are plotted as solid curves labeled 1 and 2 in Figure 6a. In deriving the expression for curve 1, use is made of (17) and (22), whereas curve 3 corresponds to (18) and (23) with  $f_2$  and  $f_1$ , both given by (1) and  $f_{\max} = 10$  Hz. The predicted  $a_{\max}$  is normalized with respect to the distance term, and the data points are represented by plotting for each event the average of  $a_{\max} R / \exp(-qR)$  over all the stations used for that event,  $a_{\max}$  being the largest of the two peak values at each station. In agreement with the findings of the cited studies, the single value  $Q_0=80$  has been used for computing  $q$  from (12). Curve 1 in Figure 6a roughly corresponds to  $a_{\max} \propto M_o^{0.37}$  and curve 2 to  $a_{\max} \propto M_o^{0.52}$ ; note that they provide close upper and lower bounds to the data. This suggests that the  $f_1$  estimates of (3), when used in the context of the proposed model, are somewhat on the high side, and that the best-fitting values of  $f_1$  are intermediate between those given by (1) and (3). Curve 3 in Figure 6a is the random-vibration prediction of  $R_{a_{\max}}$  yielded by the BLWN model

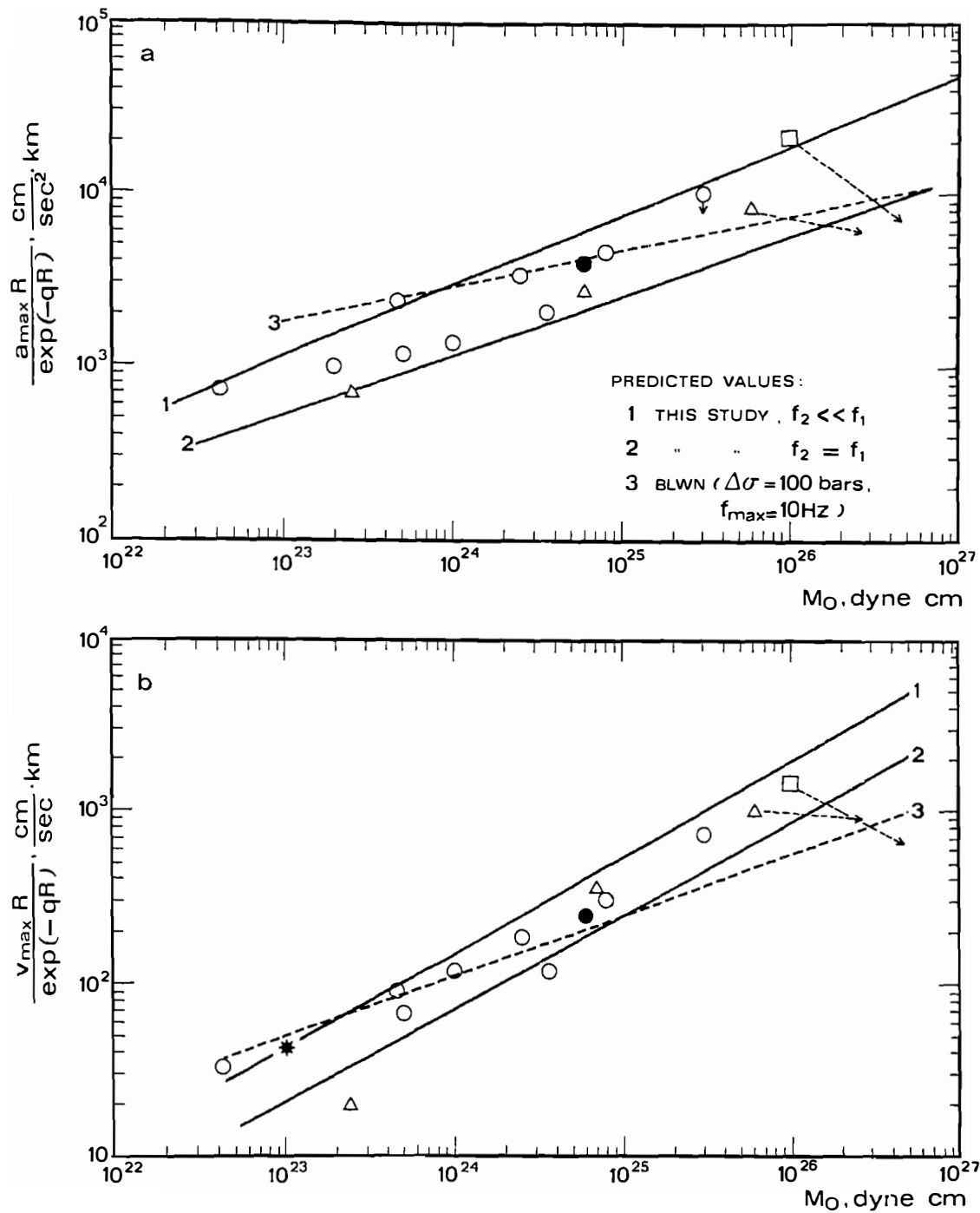


Fig. 6. Comparison of predicted and observed peak accelerations (a) and velocities (b) corrected for focal distance and Q-factor. All predictions shown are based on the random vibration approach. The data symbols are as in Figure 4a.

[Boore, 1983, equations (5) and (A8a)] with  $f_c$  given by (2),  $f_{\max} = 10$  Hz and  $\Delta\sigma = 100$  bars. The values  $\beta = 3.2$  km/s and  $\rho = 2.7$  gr/cm<sup>3</sup> were used in all calculations. Both the observations

and curves 1 and 2 show that  $a_{\max}$  increases with  $M_0$  according to a power  $\approx 1/3$ , as opposed to a power  $\approx 1/5$  predicted by the BLWN model. If the Q-correction is neglected and the surface wave

## 306 STRONG MOTIONS STUDY

(256 s) values of  $M_0$  are used, for consistency with the BLWN model in which the corner frequency  $f_c$  is related to overall fault size, the points for the main shocks of Friuli, Irpinia, and Montenegro change their positions as shown by the arrows in Figure 6a. This improves the fit of curve 3, and shows that the comparative performance of the two models considerably depends on the criteria adopted for representing the data. The analytical predictions obtained from the random vibration approach both for the present and the BLWN model are applicable in reality only to sufficiently large earthquakes, since they were developed mainly for scaling purposes. For  $M_0 \lesssim 10^{23}$  dyne cm it is therefore preferable to determine the scaling of  $a_{\max}$  and  $v_{\max}$  by direct numerical simulations [Boore, 1983]. Figure 6b displays the data points and the prediction curves for peak velocity, using the same criteria of peak acceleration, so that the predicted values are the result of introducing (24) and (20) into (21), and curves 1 and 2 correspond to the previous alternative hypotheses on spectral bandwidth. Curve 3 is for the BLWN model [Boore, 1983, equations (5) and (A8b)]. Note again the character of upper and lower bound apparently inherent in the two predictions of the present model, and also that they are less sensitive than predicted accelerations to the spectral bandwidth. The fitting provided by the BLWN curve is better than for peak acceleration, especially if the Irpinia and Montenegro data are plotted as a function of the surface-wave  $M_0$ , as shown by the arrows. The distribution of observations about curve 3 suggests that focal depth and crustal environment effects may not be as significant as it was found by McGarr [1984] for the Western U.S. In fact, since the rather uniform depth (6–8 km) and type of mechanism (thrust) make the Friuli data plot close to curve 3 in Figure 6b, we would expect, on the basis of McGarr's study, the Montenegro data ( $h \approx 15$  km, thrust fault) to be well above curve 3, in contrast to the position shown by the arrow. By the same reasoning, if the scaling of curve 3 in Figure 6a were correct, it would be difficult to explain why several of the Friuli data are so far from it despite the fact that most of the events have the same focal depth and mechanism. The previous observations are aptly summarized by saying that for the present set of data the BLWN model provides slightly less satisfactory simultaneous predictions of  $a_{\max}$  and  $v_{\max}$  than the present model.

Additional tests are obviously desirable concerning different sets of strong-motion data from other seismic regions. As a representative example, I have taken from McGarr [1984, Table 1] a number of strong-motion observations from the Western U.S. relative to events with the same range of focal depths and the same mechanism (thrust and normal) as those previously discussed. To cover a larger range for seismic moment, I have additionally considered U.S. Geo-

logical Survey recordings of numerous aftershocks of the 1983 Coalinga earthquake. The average  $Ra_{\max}$  and  $Rv_{\max}$  values for all these events are displayed in Figure 7a and b, respectively, where prediction curves 1 and 2 of Figure 6 are also plotted. Curves 3 in Figure 7a and b correspond to the numerical simulation predictions given by Boore [1983, Figure 11] for the BLWN model with  $f_{\max} \approx 11$  Hz which are more appropriate than those of Figure 6 for small events. The present predictions tend again to provide upper and lower bounds to the data, especially for  $Rv_{\max}$ , and it is remarkable that even the Shumagin Islands data, associated with a focal depth of 40 km, are within the bounds. On the other hand, the predictions of the BLWN model seem to underestimate somewhat the dependence of peak values on  $M_0$ .

Extrapolation of curves 1 and 2 below the limits of Figure 7 is not feasible because my predictions strongly depend on correlations (1) and (3), which are only valid in the range shown in Figure 4. However, if at  $M_0 \approx 10^{22}$  dyne cm the subevent corner frequencies ( $f_2$ ) merge with the event corner frequencies  $f_c$  given by (2), one should expect a transition in the peak motions scaling for the smaller events. The strength of the scaling in the lower  $M_0$  range would then depend on the relation between  $f_c$  and  $M_0$ . If, for instance, the dependence of source radius and, hence, of  $f_c$  on  $M_0$  becomes very weak, then  $Ra_{\max}$  and  $Rv_{\max}$  would tend to scale as  $M_0^{\delta}$  with  $\delta$  close to 1. In support of this interpretation I note that the transition in scaling found by McGarr [1986] for several California earthquake sequences occurs typically around  $M_0 = 10^{21}-10^{22}$  dyne cm, and that for  $Rv_{\max}$  the value of the scaling exponent is remarkably stable and between 0.7 and 0.8.

## Summary and Conclusions

I have illustrated a spectral acceleration model characterized by two corner frequencies  $f_2$  and  $f_1$ , by the body-wave seismic moment as a scaling parameter, and by a Q-factor linearly depending on frequency. The model, developed in previous studies on the basis of Haskell's [1966] "statistical" source model, is extended here for the first time to the prediction of peak ground acceleration and velocity. Analysis of a large set of strong-motion recordings from thrust and normal events of Italy and Yugoslavia has shown that the observed peak motion values versus  $M_0$  are better predicted by the present model than by an  $\omega^2$ -square model with constant stress drop and fixed high-frequency limit. In particular, the latter tends to underestimate somewhat the dependence of  $a_{\max}$  and  $v_{\max}$  on seismic moment for  $M_0 > 10^{23}$  dyne cm. However, the comparative performance of the two models may depend to a considerable extent on the seismic moment values and attenuation corrections used for representing the data.

Two characteristic frequencies are identified

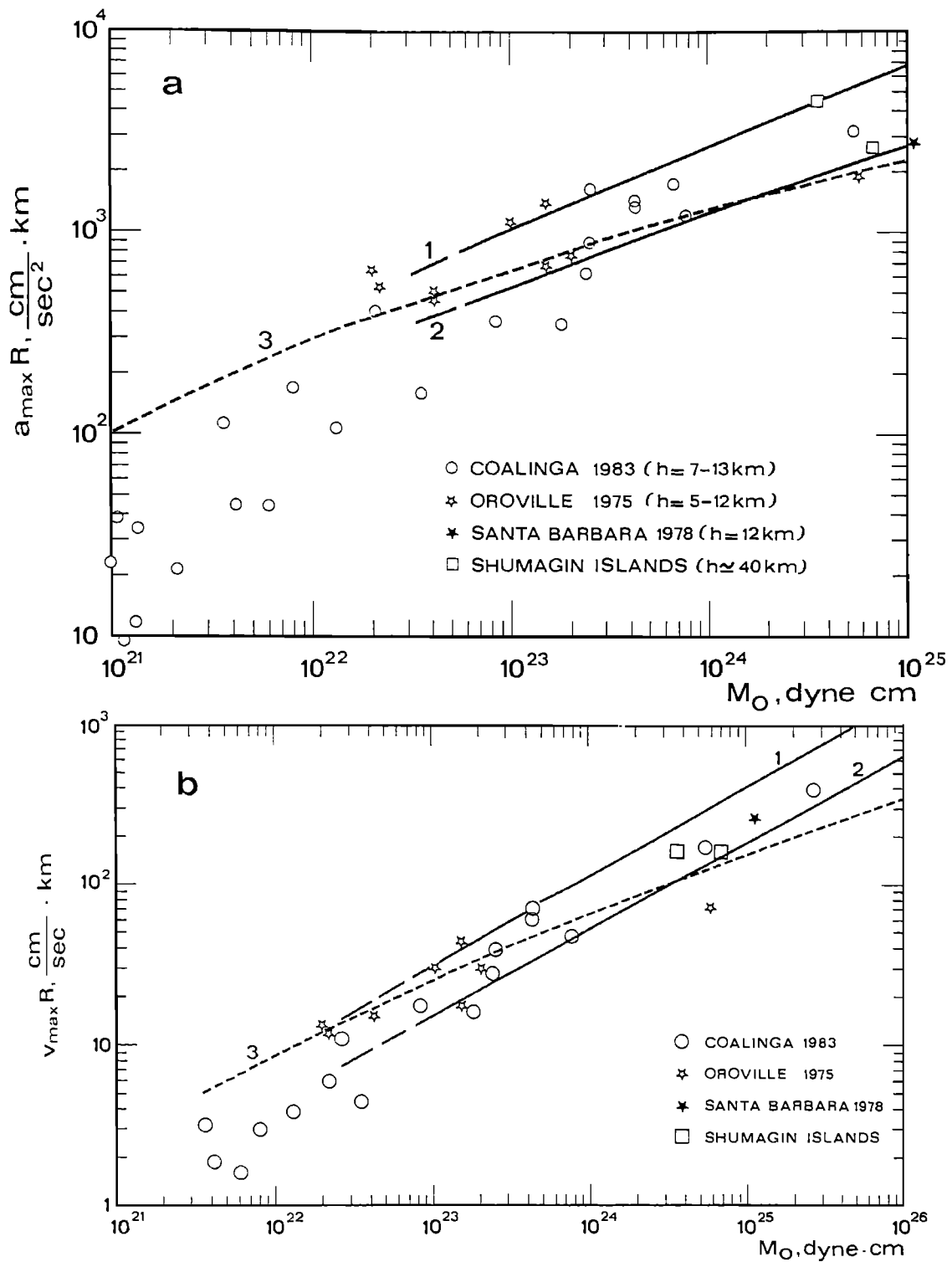


Fig. 7. Comparison of observed peak accelerations (a) and velocities (b) from thrust and normal events of Western U.S. (corrected for focal distance) with theoretical predictions. Curves 1 and 2 have the same meaning as in Figure 6a, except that  $f_{\max} = 10 \text{ Hz}$  was used. Curve 3 directly reproduces the numerical simulation results by Boore [1983, Figure 11], with  $f_{\max} \approx 11 \text{ Hz}$ .

## 308 STRONG MOTIONS STUDY

in most of the observed acceleration spectra, which bound the region where the high-frequency energy is concentrated, and these are assumed to coincide with the corner frequencies of the theoretical spectrum. The lowest characteristic frequency,  $f_2$ , is higher than the corner frequency of the Brune model for the set of events considered and is assumed to depend on the size of dominant subevents. The observed scaling relation  $f_2 \propto M_0^{1/4}$  indicates that the "local" stress drop associated with such subevents should increase with seismic moment. The highest observed characteristic frequency,  $f_1$ , is interpreted as a source effect for relatively large events such as Montenegro, and as a site-effect for smaller earthquakes of the 1976 Friuli sequence.

The predictions obtained herein are also in agreement with peak ground motion data from thrust and normal events of the Western U.S. including the strongest aftershocks of the 1983 Coalinga sequence, although they cannot be presently extrapolated in the range of  $M_0 < 10^{23}$  dyne cm where a much stronger dependence of the peak motion values on seismic moment is observed. The observed sharp transition in scaling for the small events could be explained by a dependence of source size on seismic moment substantially weaker than predicted by the self-similarity, constant stress drop assumption, as in the case of the characteristic frequency  $f_2$  used herein (Figure 4a). An additional point of interest, deserving further study, is that the body-wave seismic moment, although not as physically significant as the dynamic stress drop, is possibly a better scaling factor for high-frequency ground motions.

**Acknowledgments.** This work is supported by the National Research Council (C.N.R.) of Italy. I am grateful to A. Rovelli for this cooperation, to M. Basili for supplying the new version of the digitized data of the Irpinia earthquake, and to J. Boatwright for supplying data of the Coalinga earthquake sequence. Finally, I am indebted to the Studio Geotecnico Italiano for typing the manuscript and for drafting the figures.

## References

- Aki, K., Origin of  $f_{\max}$ , this volume, 1986.
- Anderson, J., Implication of attenuation for studies of the earthquake source, this volume, 1986.
- Boatwright, J., A dynamic model for far-field acceleration, *Bull. Seismol. Soc. Am.*, 72, 1049-1068, 1982.
- Boore, D.M., Stochastic simulation of high-frequency ground motions based on seismological models of the radiated spectra, *Bull. Seismol. Soc. Am.*, 73, 1865-1994, 1983.
- Boore, D.M., The effect of finite bandwidth on seismic scaling relationships, this volume, 1986.
- Boore, D.M., J.D. Sims, H. Kanamori, and S. Hard, The Montenegro-Yugoslavia, earthquake of April 15, 1979: source orientation and strength, *Phys. Earth Planet. Inter.* 27, 133-142, 1981.
- Brune, J.N., Tectonic stress and the spectra of seismic shear waves from earthquakes, *J. Geophys. Res.* 75, 4997-5009, 1970.
- Cipar, J., Broadband time domain modeling of earthquakes from Friuli, Italy, *Bull. Seismol. Soc. Am.*, 71, 1215-1231, 1981.
- Console, R., and P. Favali, Study of Montenegro earthquake sequence (March-July 1979), *Bull. Seismol. Soc. Am.*, 71, 1233-1248, 1981.
- Console, R., and A. Rovelli, Attenuation parameters from Friuli region from strong-motion accelerograms spectra, *Bull. Seismol. Soc. Am.*, 71, 1981-1991, 1981.
- Faccioli, E., Measures of strong ground motion derived from a stochastic source model, *Soil Dynamics Earthquake Eng.*, 2, 135-149, 1983.
- Faccioli, E., A. Rovelli, and R. Fregonese, A study of the spectral characteristics of accelerograms from recent earthquakes of Italy and nearby regions, *Proc. of the Eighth World Conf. on Earthquake Eng.*, convened San Francisco, Calif., July 21-28, 1984, 2, 361-368, 1984.
- Hanks, T.C., and R.K. McGuire, The character of high frequency strong motion, *Bull. Seismol. Soc. Am.*, 71, 2071-2095, 1981.
- Haskell, N.A., Total energy and energy spectral density of elastic wave radiation from propagating faults. Part 2. A statistical source model, *Bull. Seismol. Soc. Am.*, 56, 125-140, 1966.
- Lyon-Caen, H., Séismes du Frioul (1976): modèles de source à l'aide de sismogrammes synthétiques d'ondes de volume, Ph.D. Dissertation, Université Paris VII, Paris, France, 1980.
- McGarr, A., Scaling of ground motion parameters, state of stress and focal depth, *J. Geophys. Res.* 89, 6969-6979, 1984.
- McGarr, A., Some observations indicating complications in the nature of earthquake scaling, this volume, 1986.
- Papageorgiou, A.S., and K. Aki, A specific barrier model for the quantitative description of strong ground motion, I. Description of the model, *Bull. Seismol. Soc. Am.*, 73, 693-722, 1983a.
- Papageorgiou, A.S., and K. Aki, A specific barrier model for the quantitative description of strong ground motion, II. Applications of the model, *Bull. Seismol. Soc. Am.*, 73, 953-978, 1983b.
- Petrovski, D., Naumovsky, N., Zelenovic, V., and S. Stamatvska, Strong motion earthquake accelerograms, Vol. II, Part E, *Inst. Earthquake Eng. and Eng. Seismol.*, Skopje, Yugoslavia, Publication No. 67, 1980.
- Rovelli, A., On the frequency dependence of Q in Friuli from short-period digital records, *Bull. Seismol. Soc. Am.*, 72, 2369-2372, 1982.

Rovelli, A., 1983, Frequency relationship for seismic Q of Central-Southern Italy from accelerograms of the Irpinia earthquake, 1980, *Phys. Earth Planet. Inter.* 32, 209-217, 1983.

Rovelli A., 1984. Seismic Q for the lithosphere of the Montenegro region, Yugoslavia: frequency, depth and time windowing effects *Phys. Earth Planet. Inter.* 34, 159-172, 1984.

## IMPLICATION OF ATTENUATION FOR STUDIES OF THE EARTHQUAKE SOURCE

John G. Anderson

Institute of Geophysics and Planetary Physics, Scripps Institution of Oceanography,  
University of California, San Diego, La Jolla, California 92093

**Abstract.** This paper assumes that the spectral decay at high frequencies, as recognized by Anderson and Hough (1984) on large magnitude events, is an effect of attenuation. This attenuation effect is then applied to hypothetical spectra for small magnitude earthquakes. The result is that the assumed attenuation has an important to dominant effect on inferences of corner frequency for small earthquakes, and may affect inferences about the magnitude dependence of stress drop for magnitudes up to 6. The interaction of the corner frequency and attenuation causes a magnitude dependence on "f<sub>max</sub>" (Hanks, 1982). When "f<sub>max</sub>" is a factor of ten or more larger than what appears to be the corner frequency on an acceleration spectrum, then it is reasonably safe to conclude that this apparent corner frequency approximates the true corner frequency caused by the earthquake source.

## Introduction

From the study of accelerograms for  $M > 5$  earthquakes, Anderson and Hough [1984] suggested that the shape of the acceleration spectrum  $A(f)$  at high frequency,  $f$ , is typically described by exponential decay:

$$A(f) \sim A_0 e^{-\pi \kappa f} \quad f > f_E \quad (1)$$

In (1),  $\kappa$  is the spectral decay parameter. The frequency  $f_E$  was introduced to describe the point above which this asymptotic form is reached. For the larger earthquakes considered by Anderson and Hough [1984],  $f_E$  was typically 2 to 5 Hz, and therefore distinctly greater than the earthquake corner frequency. The spectral decay parameter appeared to be a function of distance,  $\kappa(R)$ . The function  $\kappa(R)$  increased slowly from a finite intercept. A linear approximation would be

$$\kappa(R) = \kappa_0 + mR, \quad (2)$$

but a linear approximation is not a definitive shape for  $\kappa(R)$ .

The spectral decay parameter  $\kappa$  is strictly an observational parameter. Anderson and Hough [1984] presented the case that the physical phenomenon which controls  $\kappa$  is attenuation within the earth, based on the observed behavior of  $\kappa(R)$ . Anderson and Hough [1984] suggest that the intercept,  $\kappa(0)$ , represents a site effect due to attenuation in the weathered layer and that the slow increase with distance measured by the slope  $d\kappa/dR$  is a regional effect which describes whole path attenuation during lateral propagation. An  $\omega$ -square source model and  $Q$  which is independent of frequency but increasing with depth would explain the results. In this explanation, the attenuation acts at all frequencies, deviations of the spectrum from (1) at  $f < f_E$  are

caused by deviations of the source displacement spectrum from an  $\omega^{-2}$  asymptote at low frequencies, and  $f_E$  is a magnitude-dependent parameter.

However, several studies have found a frequency dependence to  $Q$  [e.g., Aki, 1980]. To the extent that  $Q(f, z)$  can be approximated by

$$\frac{1}{Q(f, z)} = \frac{1}{Q_0(z)} + \frac{1}{A(z)f} \quad (3)$$

only the term in  $Q_0(z)$  contributes to the parameter  $\kappa$ . As an example, for  $Q(f, z) = Q_1 f^\alpha$ , and for  $0 \leq \alpha \leq 1$ ,  $Q_0$  and  $A$  in (3) can be chosen such that the approximation in (3) is good to within 10% over the frequency range 5 Hz to 50 Hz. Thus data on attenuation which are fit by a form  $Q_1 f^\alpha$  could be fit equally well by (3) in most, if not all, cases. Thus the spectral shape observations which are described by (1) and the approximation in (2) may be the result of an  $\omega$ -square source model, and attenuation along the path due to a frequency-independent contribution to the total attenuation.

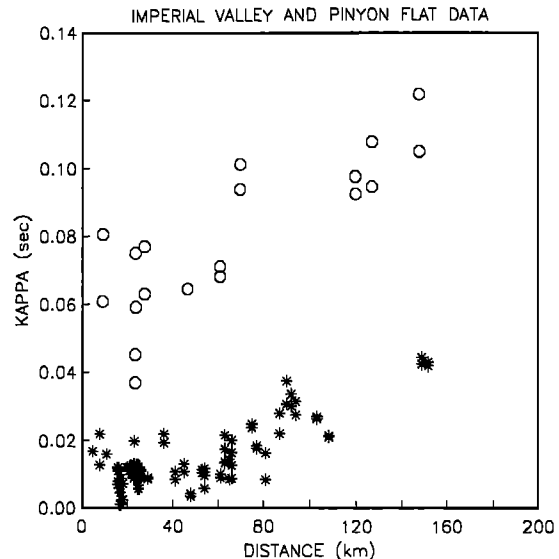


Fig. 1. Spectral decay parameter,  $\kappa$ , from earthquakes recorded at El Centro (open circles) and Pinyon Flat (asterisk). El Centro data are from Anderson and Hough [1984]. The Pinyon Flat data was obtained by S. Hough as part of her dissertation research.

## 312 IMPLICATION OF ATTENUATION FOR SOURCE STUDIES

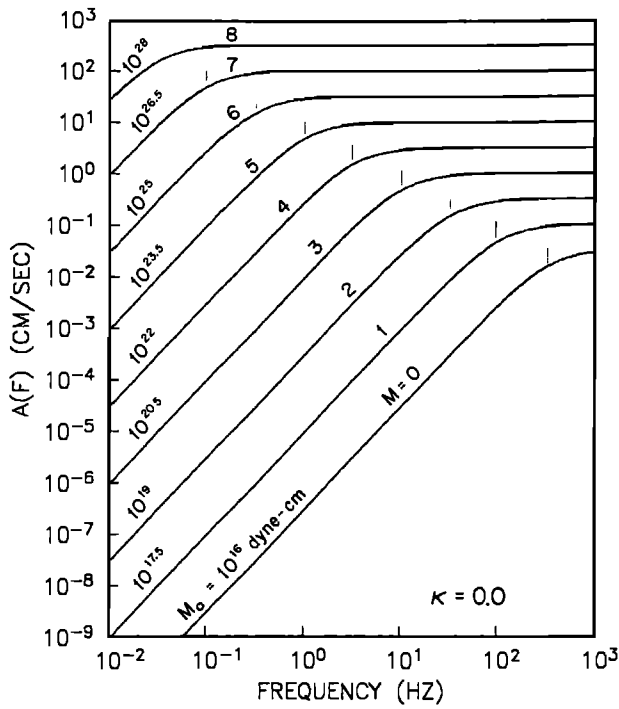


Fig. 2. Brune [1970] acceleration spectra (6) generated for seismic moments of  $10^{16}$  to  $10^{28}$  dyne cm. Other parameters are  $\rho = 2.8 \text{ gm cm}^{-3}$ ,  $R = 10 \text{ km}$ , and  $\beta = 3.2 \text{ km s}^{-1}$ , and  $\Delta\sigma = 100 \text{ bars}$ . The corner frequency is denoted by vertical bar.

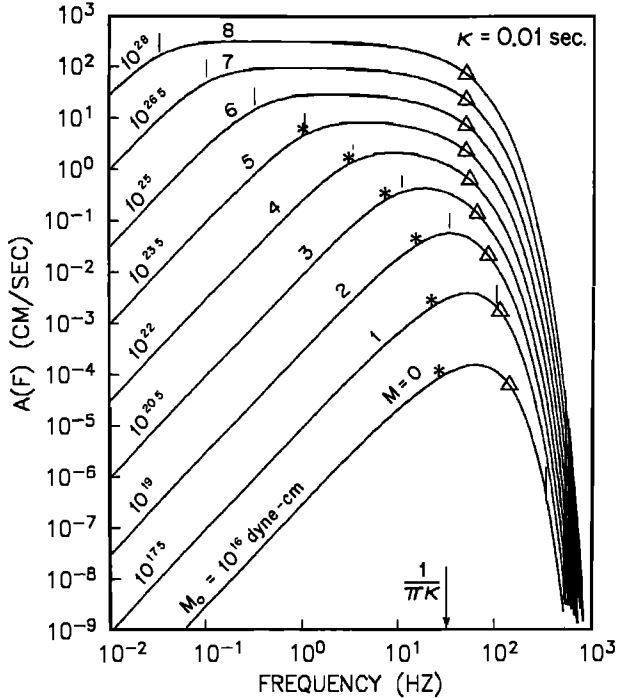


Fig. 3. Spectra from Figure 2, modified by an attenuation function corresponding to  $\kappa = 0.01 \text{ s}$  (8). The corner frequency is denoted by a vertical bar, apparent corner frequency (see text) is denoted by an asterisk, and  $f_{95}(10)$  by a triangle.

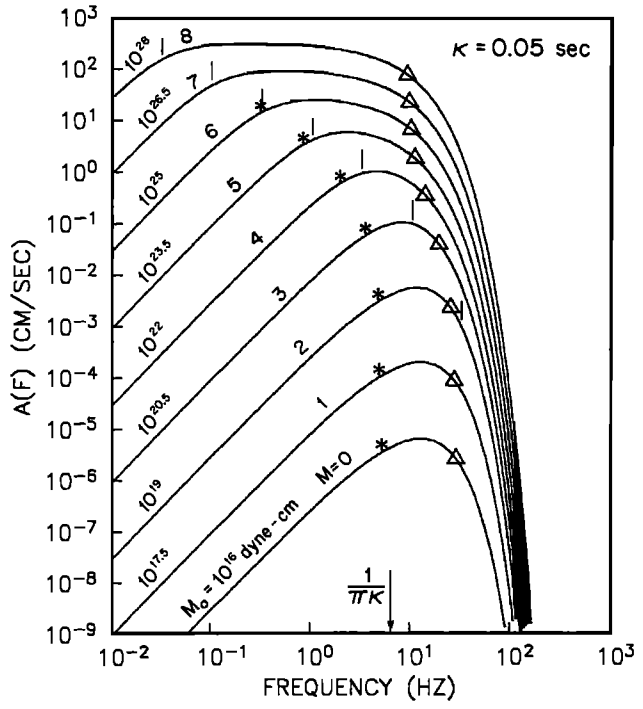


Fig. 4. Equivalent of Figure 3 for  $\kappa = 0.05 \text{ s}$ .

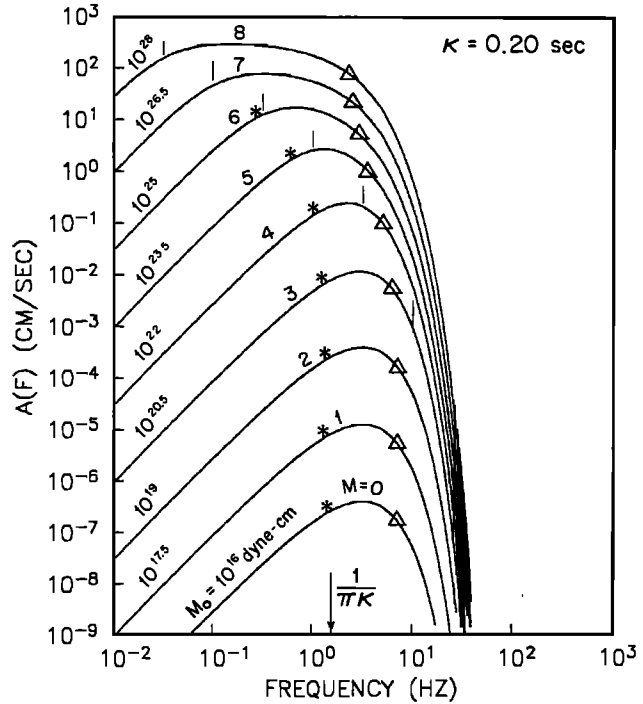


Fig. 5. Equivalent of Figure 3 for  $\kappa = 0.20 \text{ s}$ .

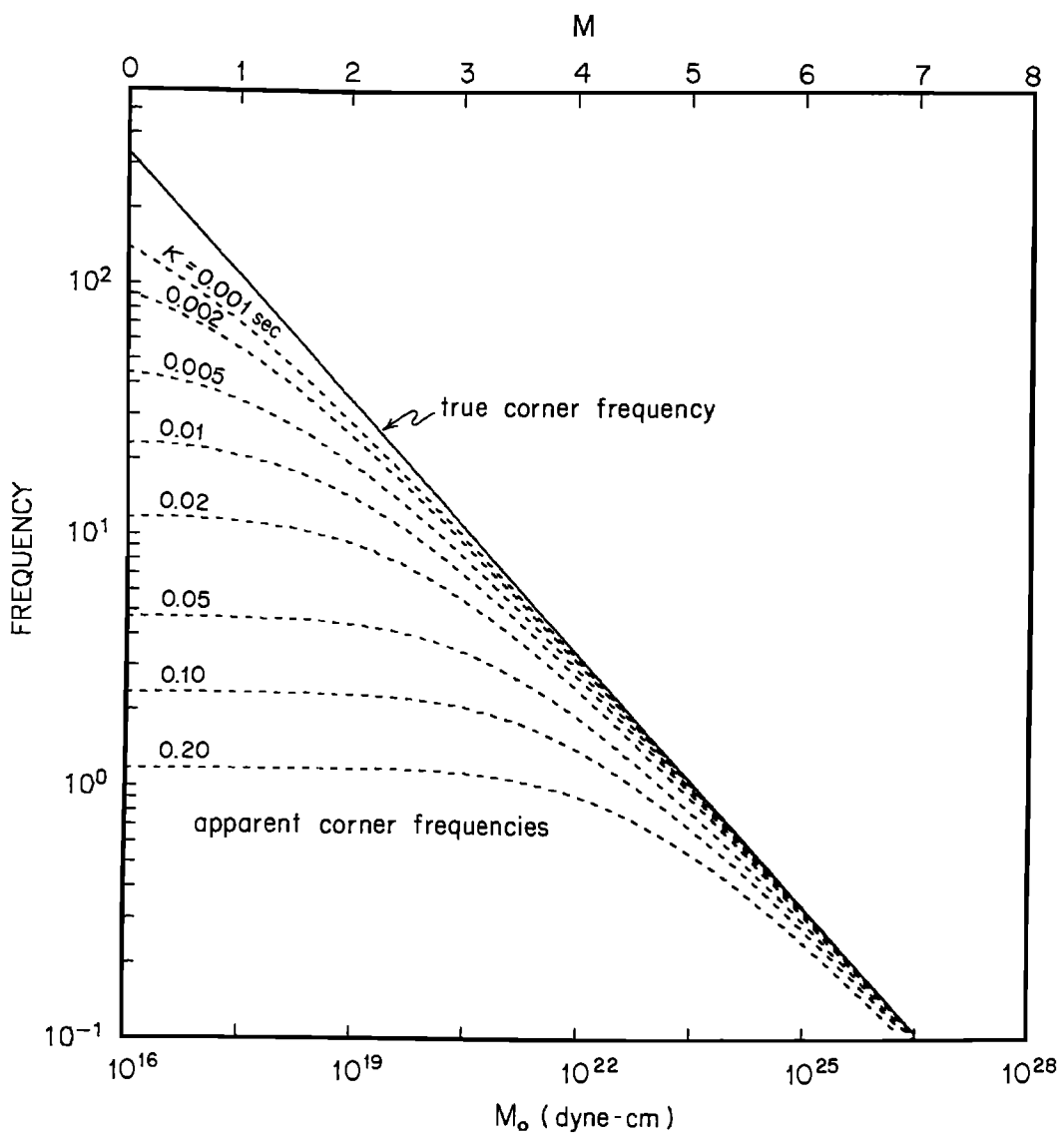


Fig. 6. Apparent corner frequencies for the spectra in Figures 3–5 and for two additional values of the spectral decay parameters.

These results in Anderson and Hough [1984] were anticipated by Hasegawa [1974]. He modeled the high-frequency acceleration spectrum as an  $\omega^2$  model and frequency-independent attenuation, and suggested that the most appropriate value for  $Q$  increases as distance increases. If one makes the association:

$$\kappa(R) = \frac{R}{Q_0 \beta} \quad (4)$$

then the values of  $\overline{Q}_0$  for various distances suggested by Hasegawa [1974] are consistent with values of  $\kappa(R)$  found by Anderson and Hough [1984] for accelerograms which were recorded in the Imperial Valley and from the San Fernando earthquake in southern California. McGuire and Hanks [1980] modeled the high-

frequency spectrum in the same manner as Hasegawa, but did not discuss the most appropriate values for  $Q$ .

Some additional research has now been carried out on this phenomenon using the digital seismic network at Anza, California [Berger et al., 1984]. This network consists of ten stations; each station detects three components of motion on velocity transducers with a natural frequency of 2 Hz, and the seismograms are transmitted via 16-bit digital telemetry to the recording station at a rate of 250 samples/s.

Figure 1 shows the distance dependence of the spectral decay parameter for one of the stations, PFO, in the Anza array. These data have been prepared by S. Hough (personal communication, 1985), who is studying them to infer  $Q_0(z)$  as part of her thesis research. These data show that  $\kappa(R)$  has a more complex func-

## 314 IMPLICATION OF ATTENUATION FOR SOURCE STUDIES

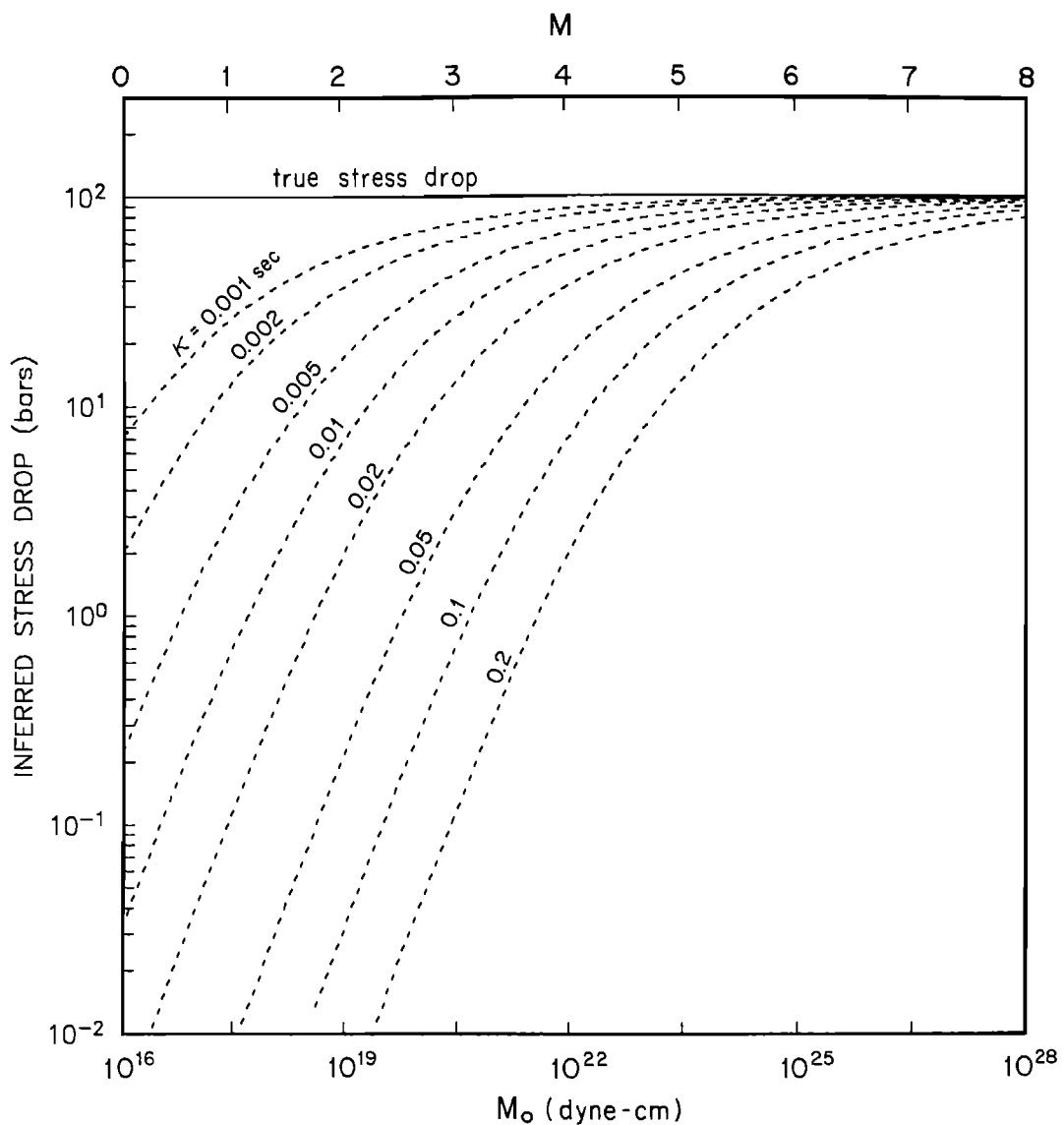


Fig. 7 Inferences of stress drop from apparent corner frequency. Models were generated with true stress drop parameter of 100 bars.

tional dependence on  $R$  than the linear approximation in (2). Figure 1 also shows the dependence of  $\kappa(R)$  which was obtained by Anderson and Hough [1984] for strong motion data from El Centro in the Imperial Valley, 120 km to the southeast of PFO. The higher quality data from PFO has less scatter than observed at El Centro.

The striking feature of Figure 1 is that the decay parameter,  $\kappa(R)$ , is much smaller at PFO than at El Centro. However, within the scatter of the data, the trend at El Centro appears to approximately equal the trend at PFO plus a constant offset:

$$\kappa(R)_{\text{El Centro}} = \kappa(R)_{\text{PFO}} + \Delta\kappa \quad (5)$$

At El Centro the weathered layer consists of at least 4 km of sediments, in which low velocity and low  $Q$  cause the intercept of about 0.05 sec, while at PFO the station is situated on slightly weathered granite, in which both the shear velocity and  $Q$  are

higher; thus it is expected that there should be less attenuation in the vicinity of the PFO site. The upper kilometer of the earth, even in plutonic rock such as at PFO, will inevitably have some cracks, implying attenuation, due to decompression, and thus surface sites in southern California which are significantly better than PFO may be rare. In any case the similarity of trends, except for the offset  $\Delta\kappa$ , argues strongly for the hypothesis that  $\kappa$  is an attenuation parameter which receives contributions both from the weathered layer and along the entire propagation path. A contribution from more severe attenuation in the fault zone is also possible.

#### Implication for Spectra of Small Earthquakes

For this section I assume that the exponential decay which is observed on spectra of large earthquakes is an attenuation effect

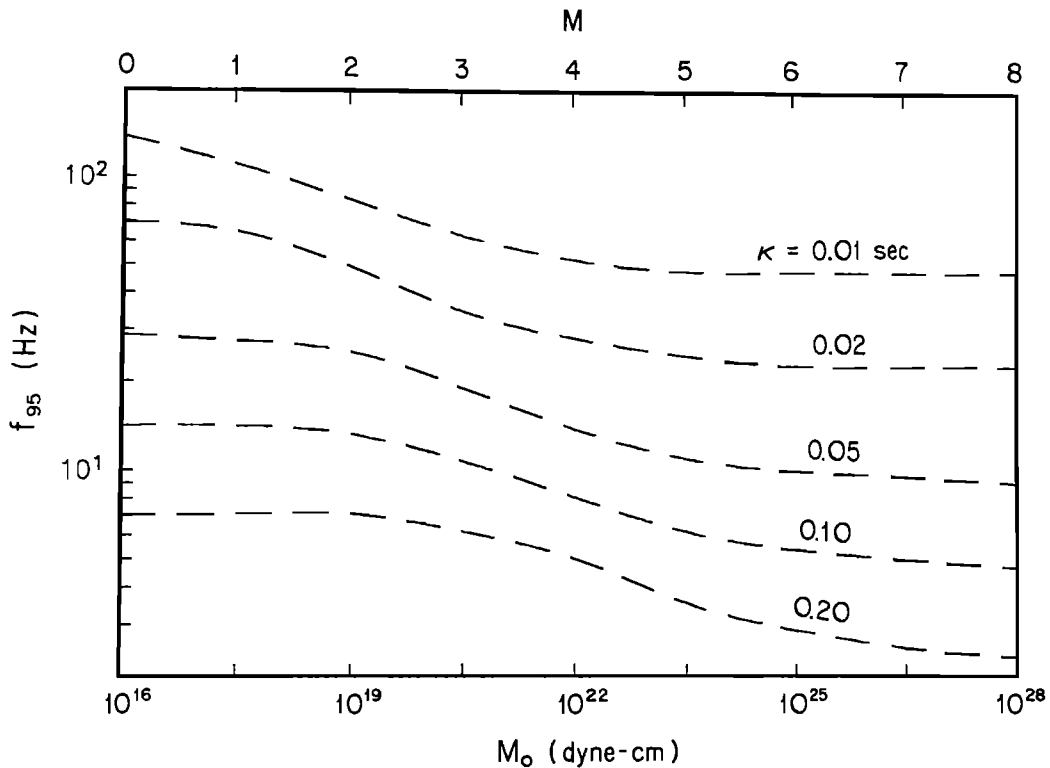


Fig. 8. Values of  $f_{95}$  (10) derived from spectra in Figures 3–5 and for two additional values of the spectral decay parameter.

and consider the consequences for small earthquakes. To illustrate this effect, I assume a shape for the spectrum consistent with an  $\omega$ -square source scaling [Hanks, 1979]. The details of this shape,  $S(f)$ , are not particularly important for the present purpose. I assume after Brune [1970] that  $S(f)$  takes the form

$$S(f) = \frac{0.84M_0}{4\pi\rho\beta^3 R} \frac{(2\pi f)^2}{\left[1 + \left(\frac{f}{f_0}\right)^2\right]} \quad (6)$$

where the corner frequency,  $f_0$ , is

$$f_0 = 0.49 \left[ \frac{\Delta\sigma}{M_0} \right]^{1/3} \beta \quad (7)$$

Thus  $S(f)$  accounts for the corner frequency and for geometrical spreading in an approximate way. There are known limitations to (6) but for the purposes of this paper they are not important. Also in (6),  $M_0$  is the moment of the earthquake. In this paper the magnitude  $M$  is treated as a charge of variables from seismic moment by [Hanks and Kanamori, 1979]

$$\log M_0 = 16 + 1.5M. \quad (8)$$

By the assumption that the exponential decay is caused by attenuation which acts in the same way on all magnitude earthquakes, the observed spectrum becomes

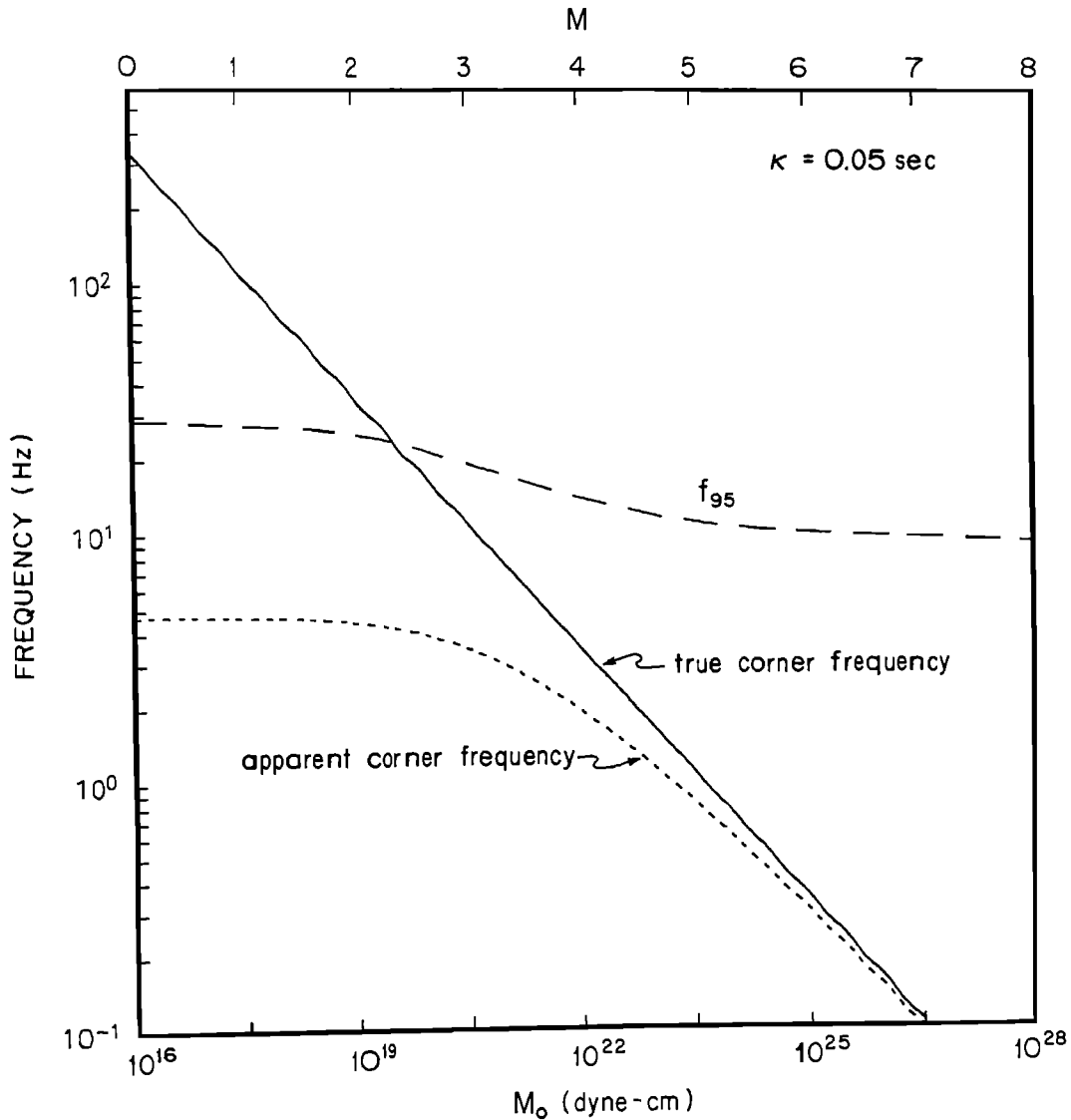
$$A(f) = S(f) e^{-\pi\kappa f} \quad (9)$$

Figure 2 shows numerical evaluations of (9) for  $M = 0$  through 8, and for  $\kappa = 0.0$ . Other parameters employed to obtain Figure 2 are hypocenter distance  $R = 10$  km, stress drop parameter  $\Delta\sigma = 100$

bars, density  $\rho = 2.8 \text{ gm cm}^{-3}$ , and shear velocity  $\beta = 3.2 \text{ km s}^{-1}$ . Figure 3 is the equivalent for  $\kappa = 0.01 \text{ s}$ , Figure 4 employs  $\kappa = 0.05 \text{ s}$ , and Figure 5 employs  $\kappa = 0.20 \text{ s}$ . The values of  $\kappa = 0.01$ ,  $0.05$ , and  $0.20$  represent cases of an unusually small spectral decay parameter, a typical spectral decay parameter, and an unusually large spectral decay parameter for stations on the surface of the earth. Typical values for  $\kappa$  for strong motion accelerograms in California are between 0.05 seconds and 0.10 seconds. The shapes, which are the primary interest in this paper, are independent of  $R$ ; the choice  $R = 10 \text{ km}$  is not meant to imply that the extremely small or extremely large values of  $\kappa$  have been observed at that particular distance. Figures 2–5 employ log-log axes. Semi-log axes are of course ideal for the recognition and measurement of the spectral decay parameter,  $\kappa$ , but the log-log axes are more suited for the purposes of this paper, namely recognition of the effect of attenuation on the corner frequency and on  $f_{\max}$ .

We first consider the corner frequencies on these spectra. These are marked by a vertical tick. For the case of no attenuation (Figure 2), a line which is asymptotic to the spectrum at low frequencies has a slope of +2 on the log-log axes and a line which is asymptotic to the spectrum at high frequencies has a slope of zero. These asymptotes intersect at the corner frequency,  $f_0$ , which ranges from 0.034 Hz for the  $M = 8$  spectrum to 340 Hz for the  $M = 0$  spectrum. As soon as the attenuation is introduced, however, the corner frequency becomes unrecognizable at the smallest magnitudes. In the limit of small seismic moments and consequent high corner frequencies, the corner frequency has no effect on the shape of the spectrum. All spectra have the same shape, with the level controlled by the seismic moment. Thus in

## 316 IMPLICATION OF ATTENUATION FOR SOURCE STUDIES

Fig. 9. Relationship of true corner frequency, apparent corner frequency and  $f_{95}$  for  $\kappa = 0.05$  s.

this limit all amplitude parameters of the seismogram (e.g., peak acceleration, peak velocity, magnitude, etc.) scale the same in proportion to seismic moment.

Now I consider the effect of picking corner frequencies from the uncorrected spectra. For the case of small attenuation (Figure 3), the corner frequency picked from the spectra shown here would underestimate the true corner when magnitude is less than 2. For moderate attenuation (Figure 4), the corner frequency would be underestimated for earthquakes with  $M < 3$ . For severe attenuation (Figure 5), the corner frequency would be underestimated for  $M < 4$ . From equation (7), an underestimate of the corner frequency would lead to an underestimate of the stress drop for these small earthquakes. This could be confused with a trend for smaller earthquakes to show smaller stress drops. Chouet et al. [1978] and Archuleta et al. [1982] have identified a tendency for the corner frequency of earthquakes with small moments (e.g.,

less than  $10^{21}$  dyne-cm, or  $M \sim 3$ ) to become constant or to increase much less rapidly with decreasing moment than predicted by (5) for constant stress drop. It is possible that effects similar to those operating in Figures 2–4 are present in some of their data. The test suggested by this paper is to determine the spectral decay parameter for each station from the largest available earthquakes, which should be large enough for the corner frequency scaling given by (5) to be valid. Then one can determine which of the smaller earthquake spectra might be dominated by this effect.

The tendency to underestimate the corner frequency can be quantified, and for the spectra in Figures 3–5 it is possible to define an apparent corner frequency,  $f_0(\text{apparent})$ , from the intersection of the low-frequency asymptote and the tangent to the spectrum with zero slope. These apparent corners are marked by asterisks on Figures 3–5, and are always smaller than  $f_0$ . In the limit of high moments,  $f_0(\text{apparent})$  asymptotically approaches

$f_0$ ; in the limit of small moments,  $f_0(\text{apparent})$  approaches an upper bound equal to  $2(\pi\kappa e)^{-1}$ . Figure 6 illustrates the behavior of  $f_0(\text{apparent})$ , compared to  $f_0$ , for eight values of the spectral decay parameter ranging from extremely small (0.001 s) to extremely large (0.20 s). For  $\kappa = 0.01$  s,  $f_0(\text{apparent})$  is a factor of 2 less than  $f_0$  for magnitudes less than about 2½; for  $\kappa = 0.10$  the same discrepancy appears at magnitudes less than about 4. Differing values of the stress drop parameter  $\Delta\sigma$  lead to some adjustments of these curves, of course. Also, Archuleta et al. [1982] pointed out that under cases of uncorrected attenuation, one may be prone to choose a steeper slope for the high frequencies, resulting in a higher corner frequency than  $f_0(\text{apparent})$  as defined here. I have not attempted to quantify this effect, which may partially relieve the tendency shown here to seriously underestimate the corner frequency at magnitudes typical of microearthquake studies.

Figure 7 shows the result of employing  $f_0(\text{apparent})$  in the place of  $f_0$  to derive the stress drop parameter in equation (7). Inferred values of stress drop decrease rapidly at small magnitudes due to the third power relationship with the corner frequency. A notable feature of Figure 7 is that the subtle effects of spectral decay on the apparent corner frequencies causes an increase in the inferred stress drop with magnitude in the intermediate magnitude range ( $M$  4 to 6). This emphasizes the importance of making every effort to understand the effects of attenuation thoroughly before attempting to infer these source parameters for earthquakes of all sizes.

From equations (6–9) the effect of a different stress parameter can be described. For example, the shape of a magnitude  $M$  spectrum with  $\Delta\sigma = 100$  bars is the same as the shape of a magnitude  $M-1$  spectrum with  $\Delta\sigma = 3.2$  bars, except for a multiplication constant. Thus for sources with a 3-bar stress drop, the corner frequency will be underestimated when  $M < 3$  in the case of low attenuation (Figure 3), when  $M < 4$  in the case of moderate attenuation (Figure 4), and when  $M < 5$  in the case of severe attenuation (Figure 5). For small magnitudes it is important to discriminate between corners caused by the earthquake source and corners caused by attenuation.

We next define a parameter  $f_{95}$  as follows

$$\frac{\int_0^{f_{95}} |a(f)|^2 df}{\int_0^{\infty} |a(f)|^2 df} = 0.95 \quad (10)$$

This parameter is shown as a triangle on Figures 3–5. The parameter  $f_{95}$  is introduced as a quantitative equivalent to  $f_{\max}$ .

This usage for  $f_{95}$  is not identical to many previous usages of  $f_{\max}$ , but the concept of describing "the high-frequency band-limitation of the radiated field of earthquakes" Hanks [1982] is preserved. This qualitative concept has been quantified in several distinct ways. Hanks [1979] defined  $f_{\max}$  such that the integral of a constant approximately equal to the maximum level of the spectrum from 0 to  $f_{\max}$  implied the same root-mean-square acceleration as the actual spectrum. Hanks and McGuire [1981] define  $f_{\max} = Q\beta/(\pi R)$ , so that in that usage, with (4),  $f_{\max} = (\pi\kappa)^{-1}$ . Hanks [1982] employed  $f_{\max}$  as a parameter which is picked visually from the acceleration spectrum where the spectrum begins to fall off rapidly. Papageorgiou and Aki [1983a,b] pick  $f_{\max}$  visually from an inferred source spectrum after correcting for whole path attenuation. (However, if the Anderson and Hough [1984] hypothesis is correct, then the attenuation correction employed by Papageorgiou and Aki [1983a,b] does not remove the site effects represented by  $\kappa(0)$ ). Boore [1983] introduces a low-pass filter

with a corner at  $f_{\max}$  for computation of synthetic seismograms. Considering Figures 3–5, we can see that the values of  $f_{95}$  derived from (10) are consistent with the concept  $f_{\max}$  is intended to represent. The quantity  $(\pi\kappa)^{-1}$  is indicated on the abscissa of Figures 3–5; for small moments it is clear that this is a poor estimate for  $f_{\max}$ .

This author considers it unfortunate that the terminology " $f_{\max}$ " has become established in the literature, because the subscript "maximum" carries a connotation that higher-frequency ground motion is not important. That is not the case. Spectral levels at higher frequencies are significantly above the noise level, so  $f_{\max}$  is not a true maximum. Even though frequencies above  $f_{\max}$  carry only a small fraction of the total energy, in a large earthquake these high-frequency ground motions can be strong enough to cause damage.

Figure 8 shows the values of  $f_{95}$  as defined by (10), as a function of magnitude, for the five values of  $\kappa$ . This figure shows  $f_{95}$  decreasing slowly with increasing magnitude. This decrease is entirely a result of the interaction of the assumed shape for  $S(f)$  and the attenuation. From data analysis, Papageorgiou and Aki [1983b], Aki [this volume] and Faccioli [this volume] suggested a "slight trend" for  $f_{\max}$  to decrease with earthquake magnitude. The specific barrier model of Papageorgiou and Aki [1983a] attributes that decrease to an earthquake source effect. Under the model which generated Figures 3–8, a similar trend results when attenuation is not corrected, or when the attenuation correction is not complete.

Finally, Figure 9 was drawn to provide guidance for recognizing when the corner frequency and  $f_{\max}$  are too close together. At low magnitudes, where attenuation dominates,  $f_{95}$  is about 29 Hz, while  $f_0$  (apparent) is about 4.7 Hz; the difference is a multiplicative factor of about 6. This figure suggests that a conservative criterion to trust the corner frequency is when  $f_{\max}$  is an order of magnitude larger than the corner frequency. In Figure 9 this criterion is satisfied for magnitudes greater than 4.5.

### Conclusions

It is necessary to correct for attenuation before attempting to make inferences about the earthquake source. That correction must include the effect of vertical propagation through the weathered layer. A simple correction procedure is available when the spectral decay parameter is known; it will be successful for the limited range of the corner frequency which allows sufficient signal at higher frequencies to be above the noise level in the data. When the correction is omitted or is not complete, the source corner frequency may be confused with the attenuation corner on the spectrum, and a magnitude dependency to  $f_{\max}$  may appear. These results were derived for a Brune [1970] spectrum model; alternative models will only modify the numerical details.

**Acknowledgments.** I thank S. Hough for the Anza data shown in Figure 1, and for helpful discussions. This research was supported by the Electric Power Research Institute project RP2556-2 and National Science Foundation grants EAR84-08429 and CEE83-19620.

### References

- Aki, K., Attenuation of shear-waves in the lithosphere for frequencies from 0.05 to 25 Hz, *Phys. Earth Planet. Inter.* 21, 50–60, 1980.
- Aki, K., Origin of  $f_{\max}$ , this volume.

## 318 IMPLICATION OF ATTENUATION FOR SOURCE STUDIES

- Anderson, J. G., and S. Hough, A model for the shape of the Fourier amplitude spectrum of acceleration at high frequencies, *Bull. Seismol. Soc. Am.*, 74, 1969–1994, 1984.
- Archuleta, R. J., E. Cranswick, C. Mueller, and P. Spudich, Source parameters of the 1980 Mammoth Lakes, California, earthquake sequence, *J. Geophys. Res.*, 87, 4595–4607, 1982.
- Berger, J., L. N. Baker, J. N. Brune, J. B. Fletcher, T. C. Hanks, and F. L. Vernon, The Anza array: a high dynamic-range, broad-band, digitally radio-telemetered seismic array, *Bull. Seismol. Soc. Am.*, 74, 1469–1682, 1984.
- Boore, D. M., Stochastic simulation of high frequency ground motions based on seismological models of the radiated spectra, *Bull. Seismol. Soc. Am.*, 73, 1865–1894, 1983.
- Brune, J. N., Tectonic stress and the spectra of seismic shear waves from earthquakes, *Bull. Seismol. Soc. Am.*, 60, 4997–5009, 1970.
- Chouet, B., K. Aki, and M. Tsujiura, Regional variation of the scaling law of earthquake source spectra, *Bull. Seismol. Soc. Am.*, 68, 49–79, 1978.
- Faccioli, E., A study of spectra and peak values of strong ground motion accelerograms from Italy and Yugoslavia in terms of gross source properties, this volume.
- Hanks, T. C.,  $b$ -values and  $\omega^{-\gamma}$  seismic source models: implications for tectonic stress variations along active crustal fault zones and the estimation of high-frequency strong ground motion, *J. Geophys. Res.*, 84, 2235–2242, 1979.
- Hanks, T. C.,  $f_{\max}$  *Bull. Seismol. Soc. Am.*, 72, 1867–1880, 1982.
- Hanks, T. C., and H. Kanamori, A moment magnitude scale, *J. Geophys. Res.*, 84, 2348–2350, 1979.
- Hanks, T. C., and R. K. McGuire, The character of high frequency strong ground motion, *Bull. Seismol. Soc. Am.*, 71, 2071–2096, 1981.
- Hasegawa, H. S., Theoretical synthesis and analysis of strong motion spectra of earthquakes, *Can. Geotech. J.* 11, 278–297, 1974.
- McGuire, R. K., and T. C. Hanks, RMS accelerations and spectral amplitudes of strong ground motion during the San Fernando, California, earthquake, *Bull. Seismol. Soc. Am.*, 70, 1907–1919, 1980.
- Papageorgiou, A. S., and K. Aki, A specific barrier model for the quantitative description of inhomogeneous faulting and the prediction of strong ground motion. Part I. Description of the model, *Bull. Seismol. Soc. Am.*, 73:4, 693–722, 1983a.
- Papageorgiou, A. S. and K. Aki, A specific barrier model for the quantitative description of inhomogeneous faulting and the prediction of strong ground motion. Part II. Application of the model, *Bull. Seismol. Soc. Am.*, 73:4, 953–978, 1983b.

## DOWNHOLE RECORDINGS OF SEISMIC RADIATION

Ralph J. Archuleta

Department of Geological Sciences, University of California at Santa Barbara, Santa Barbara, California 93106

**Abstract.** At McGee Creek in the Mammoth Lakes, California region, we have put 3-component accelerometers and velocity transducers at depths of 166.5 m, 35.0 m, and 0.0 m. The glacial moraine in the region extends to a depth of 30.5 m. We have simultaneously recorded eight microearthquakes  $1.0 \leq M_D \leq 3.0$  with S - P times from 0.5 s to 2.8 s. Two larger earthquakes  $M_L 5.7$  and  $4.9$  have also been recorded on all 9 channels of acceleration. Analysis of the microearthquakes shows that the glacial moraine generally increases the amplitude and duration of the signal recorded at depth. However, corner frequencies of S-waves measured at depth and of the surface are very nearly the same. Based on this data we infer that the local site effect due to the glacial moraine is not the cause of the nearly constant source radius, i.e.,  $f_{\max}$ , observed for earthquakes in the region.

## Introduction

If there is any characteristic of seismic ground motion measurements, it is that nearly all measurements have been made with instruments at the earth's free surface. Consequently these measurements of seismic radiation are continuously subjected to criticisms. What is the effect of near surface sediments? What is the effect of the water table? What is the effect of the obvious joints and other cracks? What about the nonlinear behavior of soils? Is it true that an increase in amplitude due to a low modulus of rigidity trades off with greater attenuation in unconsolidated sediments? These and others are valid questions concerning the measurements. Because of the uncertainty as to the magnitude of these effects, they become even more critical when we try to infer the nature of the seismic source.

For linear response of the medium the observed ground motion is a convolution of the responses of the source and the propagation path, which includes the local site characteristics. Any inference about properties of the source requires knowledge and/or assumptions about the propagation path. The tradeoff between source effect and path effect is the central argument for explanations of the well-documented nearly constant source radius for earthquakes with seismic moments less than about  $10^{21}$  dyne cm, [Tucker and Brune, 1973; Fletcher, 1980; Bakun et al., 1976; Archuleta et al., 1982; Frankel, 1982]. Although the papers by Tucker and Brune, Fletcher, Bakun et al. provided the first evidence of this effect, it was analysis of the aftershocks of the 1980 Mammoth Lakes, California, earthquakes by Archuleta et al. [1982] that showed the transition from a monotonically decreasing source radius to a nearly constant source radius as seismic moment monotonically decreased (Figure 1). A similar transition was observed for the Coalinga aftershocks [Andrews et al., 1984]. The data sets from Mammoth Lakes and Coalinga were able to document this transition because both sets span at least 5 orders of magnitude in seismic moment. The result that seismic moment decreases while the source radius remains fixed implies that the stress drop is decreasing along with the seismic moment. If so, the supposition that the mechanics of microearthquakes are similar to moderate or major earthquakes is invalid because similarity depends on their being a constant stress drop for all earthquakes [Aki, 1967].

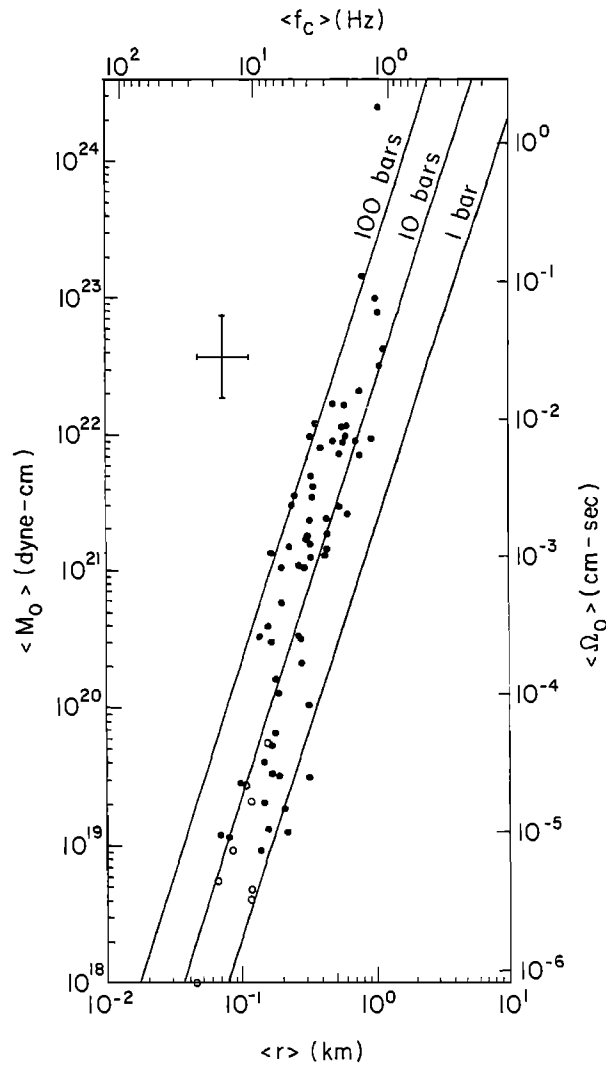


Fig. 1. Plot of seismic moment ( $M_0$ ) versus corner frequency ( $f_c$ ) source radius ( $r$ ) for the 1980 Mammoth Lakes aftershocks [Archuleta et al., 1982]. Data are shown as solid dots. Open circles show eight events recorded at the McGee Creek downhole site. The data change their trend for seismic moments less than about  $10^{23}$  dyne-cm and scatter about a nearly vertical line, a constant source radius.

## 320 DOWNHOLE RECORDINGS OF SEISMIC RADIATION

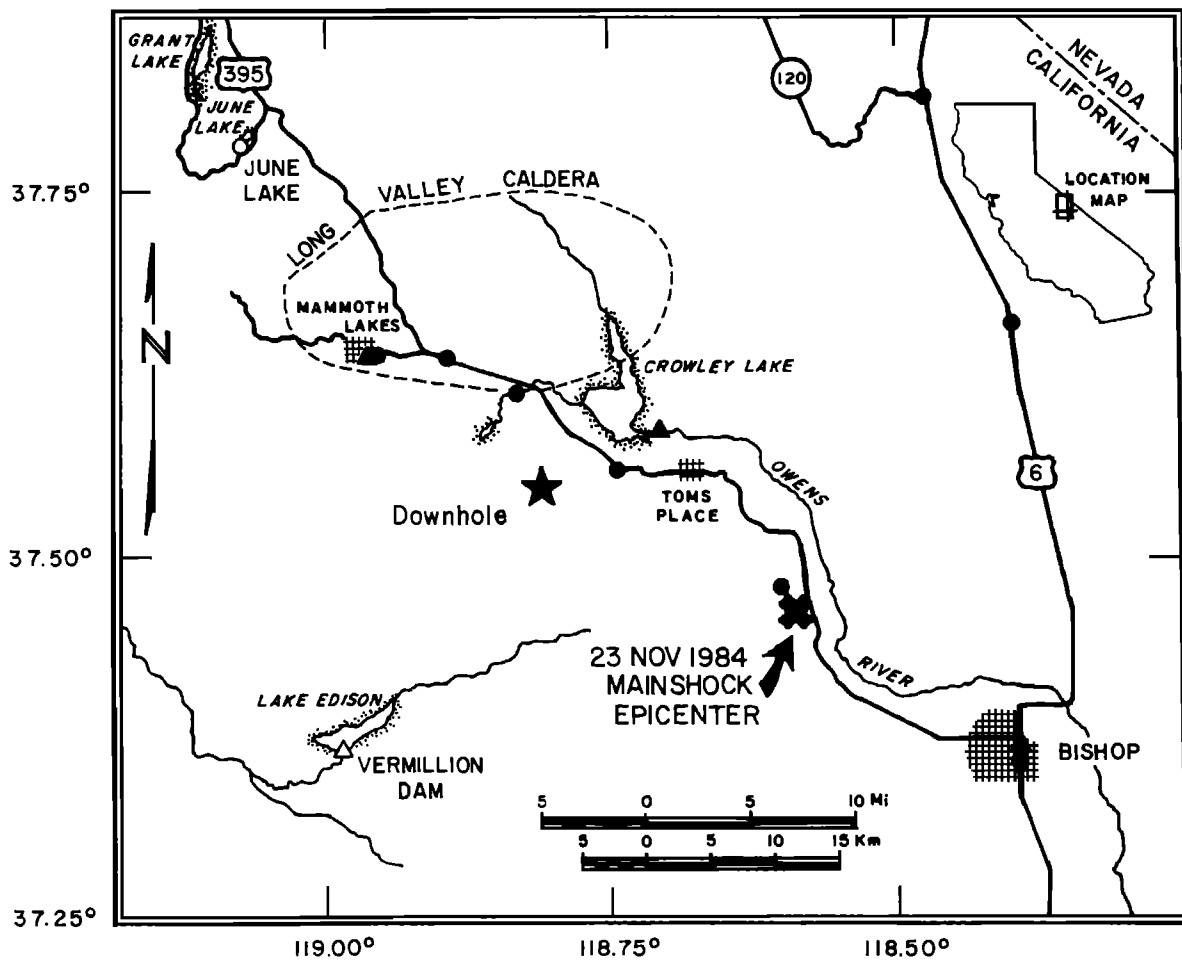


Fig. 2. Areal map showing the location of the Mammoth Lakes region with respect to California and the location of the McGee Creek downhole site, shown by the star, with respect to geological and cultural features in the region. This map also points out the location of the  $M_L$  5.7 earthquake for which we recorded accelerations at all three depths plus the locations, shown by solid dots, of other accelerographs operated by the California Division of Mines and Geology.

Because the nearly constant source radius is associated with a nearly constant frequency, Hanks [1982] succinctly refers to this question as “ $f_{\max}$ ”, i.e., there is a limiting frequency  $f_{\max}$  independent of corner frequency  $f_c$  such that  $f_{\max}$  will mask the true corner frequency whenever  $f_c > f_{\max}$ . Such arguments presuppose that there exists a  $f_c > f_{\max}$ . Anderson and Hough [1984] and Anderson (this volume) present a straightforward model of attenuation that would explain how  $f_{\max}$  might arise. Although this model shows how attenuation would lead to an  $f_{\max}$  effect, it does not explain the often overlooked, but critical, observation that the displacement amplitude spectrum decays proportional to frequency raised to a constant power (Amplitude  $\propto f^b$  where  $b$  is a constant, generally around 4). Attenuation caused by an exponential transfer function, e.g.  $\exp(-\pi fR/Q\beta)$  where  $f$  is frequency,  $R$  is hypocentral distance,  $\beta$  is shear wave velocity, and  $Q$  is attenuation parameter, produces, on a log amplitude versus log frequency plot, a continuously steeper curve (see, for example, Anderson [this volume]). However, as one can see in the Mammoth Lakes spectra this is not the case.

If a local site condition is responsible for strongly attenuating the frequencies above some specified  $f_{\max}$  as suggested by Hanks [1982], then

it is possible to isolate the effect by measuring the seismic radiation before and after it passes through the near surface material. Conceptually it is a simple matter of drilling through the near surface material and into, presumably, the more competent, homogeneous, and less attenuative bedrock and putting seismometers into the bedrock and at the earth's surface. Simultaneous measurements of the seismic radiation provide a direct answer as to whether or not the near surface material is responsible for the nearly constant source radius. In the case of earthquakes recorded at McGee Creek, the near surface glacial moraine is not responsible for the nearly constant source radius.

#### Location and Instrumentation

We selected the McGee Creek site (Figure 2) for several reasons: (1) it is centrally located with respect to the seismicity of area (Figure 3); (2) it was estimated, and confirmed by drilling, that the glacial moraine was only about 30.5 m thick thus facilitating drilling into bedrock; and (3) McGee creek is close to a site of the same name used during the 1980 recording of aftershocks.

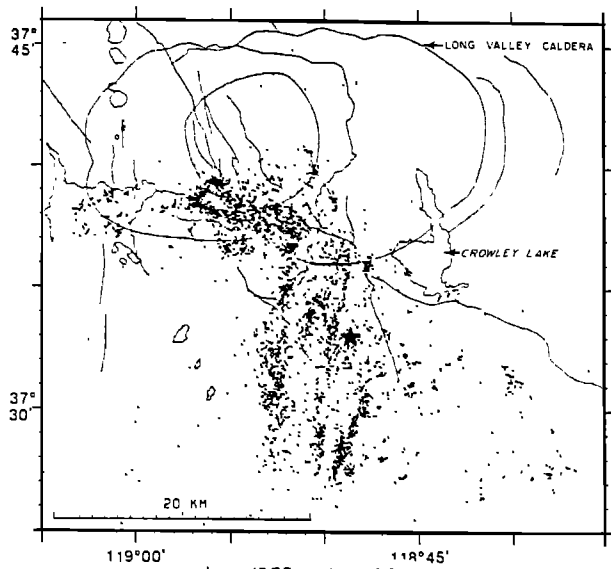


Fig. 3. The downhole site indicated by a star, is shown in relation to the epicenters of more than 13,000 earthquakes located in the Mammoth Lakes area during the period June 1982 to July 1984. [Cockerham and Pitt, 1984].

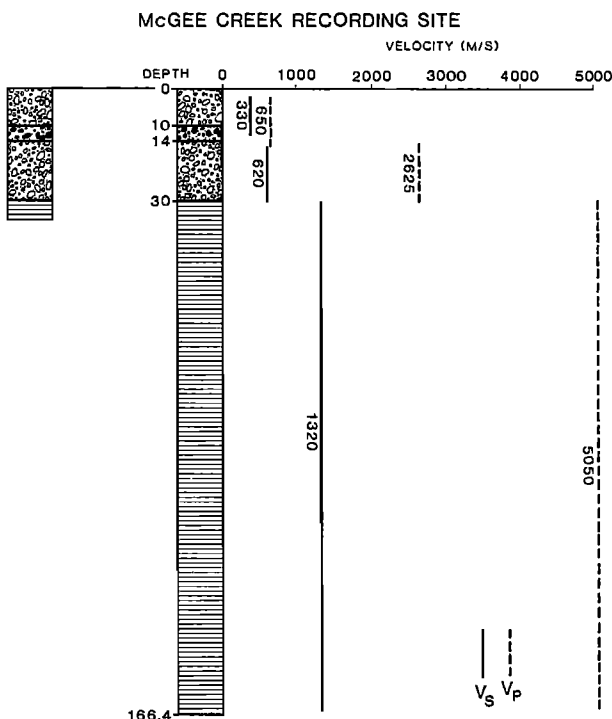


Fig. 4. A schematic drawing of the two drill holes. At the bottom of each is placed an instrument package consisting of a 3-component accelerometer and a 3-component velocity transducer. Horizontal shading below 30 m indicates the medium is hornfels; the material above 30 m indicates the medium is hornfels; the material above 30 m is glacial till except for a small region of alluvial fan deposits (10-14 m) from a metamorphic source. Also shown are the velocity profiles for P and S waves as determined from downhole logs [Fumal et al., 1985].

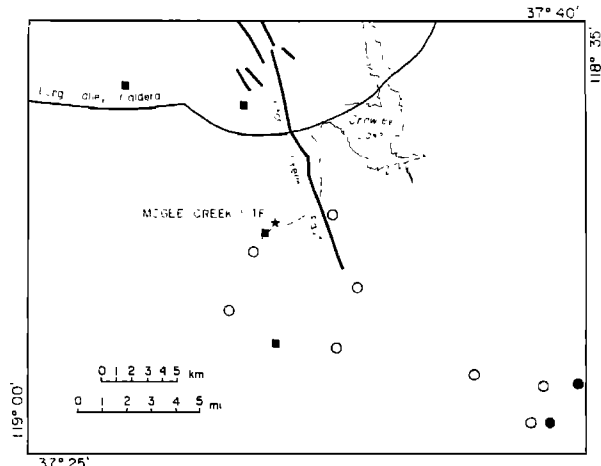


Fig. 5. An enlarged map view showing the downhole site, (a star), the location of eight microearthquakes (open circles) numbered in correspondence with Table 1 of the text, location of the  $M_L$  5.7 and 4.9 earthquakes (solid circles) recorded by the downhole accelerometers, and the location of the  $4 M_L > 6.0$  earthquakes solid squares of May 1980.

We drilled two holes 3 m apart. The shallow one goes to 35 m depth, 4.5 m into the bedrock, hornfels [Fumal et al., 1985]. The deep hole goes to a depth of 166.5 m, 136 m into bedrock. The shallow hole is cased with PVC to a depth of 33 m; the deep hole is cased to a depth of 31 m. The shallow hole is not cased to 35 m so that our instrument package would be directly coupled to the surrounding bedrock. The deep hole was logged for temperature, shear wave velocity, and compressional wave velocity. The basic nature of the S-wave velocity is a nearly constant velocity of 330 m/s in the upper 12 m, a velocity of 620 m/s between 12 m and 30.5 m and a velocity of 1320 m/s between 30.5 to 166.5 m (Figure 4) [Fumal et al., 1985].

In each hole we placed a 3-component force balanced accelerometer (FBA) and a 3-component velocity transducer. The velocity transducer is a downhole Mark Products L 22 with a response to particle velocity that is uniform from 2.0 Hz to 100 Hz. The FBA is a Kinematics 2 g ( $g$  is acceleration due to gravity) downhole package which has a response to acceleration that is uniform from 0.0 Hz to 100 Hz. We had the FBA's response extended from a nominal 35 Hz to 100 Hz in anticipation of higher frequencies. Because the holes tilted more than 3° with respect to the local vertical, we have only one working horizontal channel on each of the downhole velocity transducers. All six downhole components of acceleration are operational. At the surface we installed a Mark Products L 22 and 3 single component FBA's (Kinematics F 11) and a Kinematics SMA 1. The surface instruments are oriented with positive ground motion up, due North (0 degrees) and due East (90 degrees). The orientation of the downhole horizontal channels is not known at this time. Based on waveform similarity the operational horizontal velocity transducer at 35 m is closely aligned with 90° surface instrument. For the purposes of this paper the exact orientation of the horizontal components is not critical.

The acceleration channels along with time from WWVB and an internal clock are recorded on a CRA-1 film recorder. These instruments are part of our permanent instrument package which was installed November 10, 1984, by personnel from the U.S. Geological Survey Branch of Engineering Seismology and Geology. At various times since the instruments were deployed we have used GEOS [Borchardt et al., 1985] recorders to record the output of the velocity and acceleration channels for microearthquakes. GEOS records using a 16 bit analog to digital chip with 96 dB gain and

## 322 DOWNHOLE RECORDINGS OF SEISMIC RADIATION

TABLE 1. Earthquakes Recorded at McGee Creek Downhole

No.	Yr	Mo	Day	Hr	Min	Event	M <sub>D</sub>	Lat. (37°N)	Long. (118°W)	S-P(s)
1	84	12	9	8	32	3420832	1.14	31.90'	49.90'	0.5
2	84	12	7	22	05	3422205	3.0	26.02'	37.45'	2.8
3	84	12	8	7	02	3430702	1.71	28.67'	46.15'	1.10
4	84	12	8	11	15	3431115	1.55	30.72'	45.28'	1.07
5	84	12	8	15	57	3431557	1.48	33.28'	46.39'	0.65
6	84	12	9	5	20	3440520	2.14	29.57'	50.92'	1.10
7	84	12	9	12	21	3441221	2.10	27.70'	40.03'	~2.13
8	85	1	9	17	30	0091730	2.97	27.33'	36.96'	2.65

Locations and magnitudes are courtesy of R. Cockerham, U.S.G.S.

a sampling rate as high as 1200 samples per second. In our use of GEOS the sampling rate was 200 samples per second per channel.

#### Data

On November 23, 1984, a magnitude 5.8 earthquake occurred at 37°27.48' N, 118° 35.32'W at a depth of 12.0 km and origin time of 18 hr 18 min 20.30 s UTC. All nine channels of acceleration were successfully recorded on film. The data clearly show that the amplitude of the acceleration at the earth's surface is both larger and more complex than that recorded at either 35 m or 166 m depths [Archuleta, 1985]. This difference can be attributed to the variation in material properties as we shall see later. Importantly the accelerograms at depth do not show an obviously greater amount of high frequencies. This is verified by examining spectral ratios.

Having recorded the accelerations from a moderate earthquake we had to question whether or not the apparent effect of the near surface glacial moraine was real for microearthquakes ( $M < 3.0$ ). In fact, it is the difference in the spectra between moderate earthquakes and microearthquakes that led Archuleta et al. [1982] to speculate that the similarity principle for earthquakes was violated, i.e., stress drop is not

constant but depends on seismic moment for earthquakes with  $M_o < 1 \times 10^{21}$  dyn-cm. Eight microearthquakes (Table 1; figure 5), have been recorded at the downhole site. All of the events were recorded by GEOS [Borchert et al., 1985]. Only one, event 0091730 (January 9, 1985, 17:30) was recorded at all three levels. All of the other events were recorded at 35 m and 0 m. These events confirm that the glacial moraine is responsible for the complexity of the surface recordings.

As we shall see next the recordings at depth do not have a significantly greater spectral content at high frequencies ( $f > 10$  Hz) than the surface records. Moreover, the spectral amplitudes are almost entirely accounted for by the variation in the properties of the glacial moraine versus those of the hornfels that underlie the glacial moraine.

#### Data Analysis

Using the spectral analysis of Brune [1970], we determined the seismic moment and the source radius for each event (Table 2). There are several particulars that should be noted. Rather than taking the square root of the sum of squares of the surface moments we decided to use only that surface component (90° on which the surface seismogram most closely resembles the seismogram recorded at 35 m). This was done for all the events recorded

TABLE 2. Source Parameters

Event	* $\Omega_o(0)$ Cm-s x 10 <sup>-6</sup>	* $\Omega_o(35)$ Cm-s x 10 <sup>-6</sup>	$M_o(0)$ dyn-cm	$M_o(35)$ dyn-cm	$f_c(0)$ Hz	$f_c(35)$ Hz
3420832	1.4 (0.37) +	0.8			27.3	20.
3422205	61.0 (16.4)	12.2	$9.3 \times 10^{17}$	$2.0 \times 10^{11}$	11.0	11.3
3430702	14.0 (3.7)	2.0	$4.1 \times 10^{19}$	$3.1 \times 10^{19}$	14.1	16.5
3431115	8.1 (2.2)	0.9	$9.3 \times 10^{18}$	$5.0 \times 10^{10}$	19.2	21.1
3431557	7.2 (1.9)	1.0	$5.5 \times 10^{18}$	$2.3 \times 10^{18}$	10.7	13.6
3440520	41.0 (11.0)	9.0	$4.8 \times 10^{18}$	$2.5 \times 10^{18}$	12.0	15.5
3441221	31.0 (8.3)	3.6	$2.8 \times 10^{19}$	$2.3 \times 10^{19}$	10.8	10.7
0091730	85.0 (22.8)	45.0	$2.1 \times 10^{19}$	$9.1 \times 10^{18}$	8.0	10.7

\*  $\Omega_o$  has been normalized to a S-P time of 1.2 s, corresponding to a hypocentral distance of 10 km using a shear wave speed of 3.5 km/s and a P-wave speed of 6.0 km/s.

+ Value in parentheses is after dividing by 3.72 which accounts for impedance of glacial moraine and free surface.

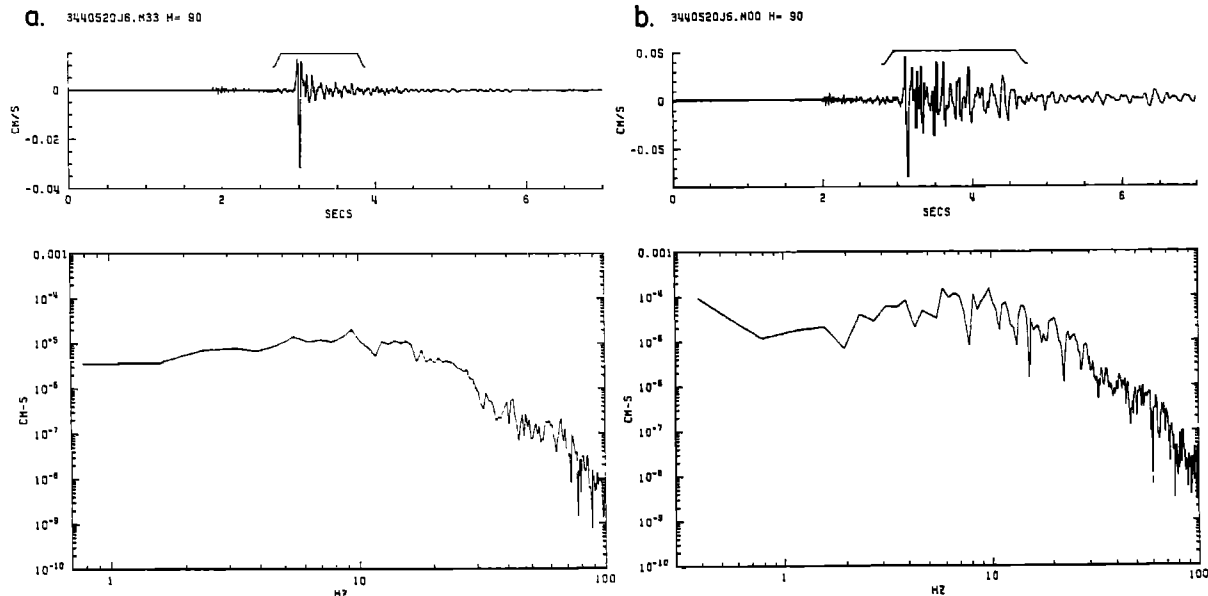


Fig. 6. (a) The horizontal particle velocity time series for event 3440520 recorded at 35 m depth and its corresponding displacement amplitude spectrum for the windowed portion of the time series. The window is shown by the line above the appropriate part of the time series and includes a 10% taper at each end. Duration magnitude  $M_D$  is 2.14. (b) Event 3440520 recorded at 0 m.

in 1984. Brune's approach is strictly valid only for SH waves. However, because we lack a second horizontal component at depth, we did not rotate the components to SH. Rather than simply multiply by  $\sqrt{2}$  (which assumes equal SH amplitude on both horizontal components) we chose to compare the spectra of individual components of motion.

The corrections we made to the surface seismogram's spectral amplitude include dividing by 0.6, for an average SH radiation factor, dividing by 2 for the free surface amplification and dividing by a factor of 1.86

(assuming normal incidence) for the amplification due to the glacial moraine. With these corrections we computed the seismic moment  $M_0 = 4\pi \rho B^3 R \Omega_0 / (0.6)(2.0)(1.86)$ , where  $R$ , the hypocentral distance, was based on S minus P times assuming an S-wave velocity of 3.5 km/s and a P-wave velocity of 6.0 km/s. We assumed  $\rho = 3.0 \text{ gm/cm}^3$  in the source region. The results for these eight events have been plotted along with the events from 1980 aftershocks in Figure 1. The results from these earthquakes are not noticeably different from the 1980 aftershocks.

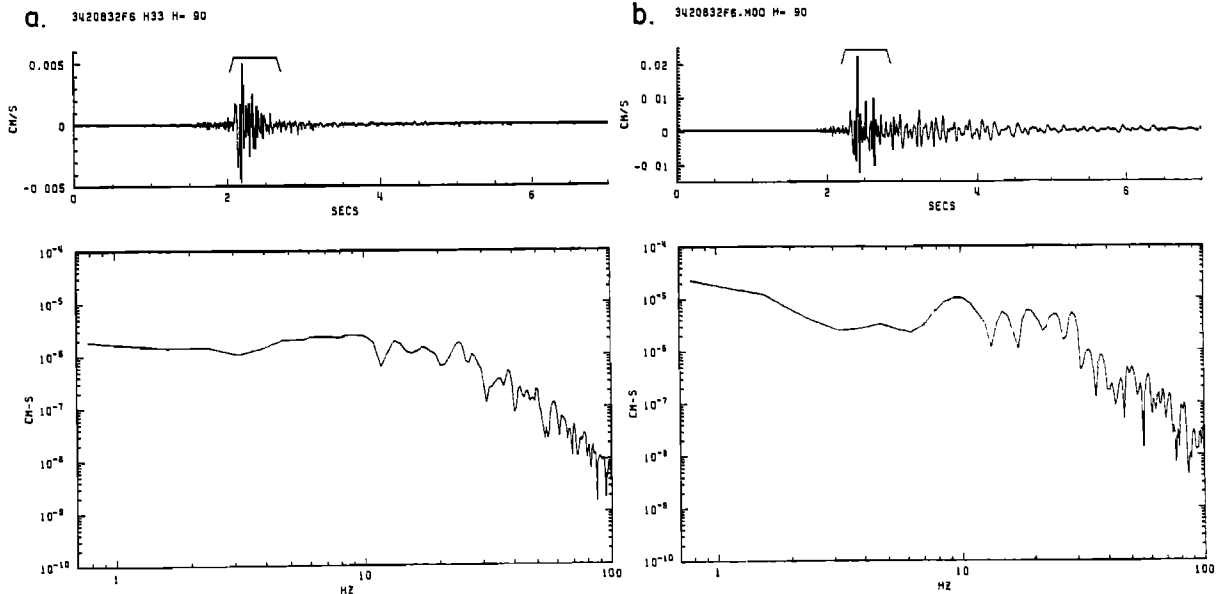


Fig. 7. (a)Event 3420832 recorded at 35 m.  $M_D = 1.14$ . (b) Event 3420832 recorded at 0 m. See caption of Figure 6 for details

## 324 DOWNHOLE RECORDINGS OF SEISMIC RADIATION

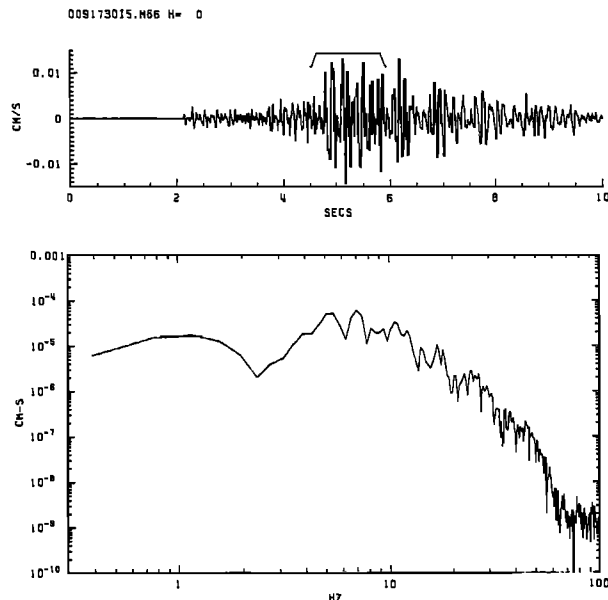


Fig. 8. Event 0091730 recorded at 166 m.  $M_D = 2.97$ . See caption of Figure 6 for details.

However, the primary thrust of this paper is to compare the earthquake records at the surface with those at depth. The obvious difference between a recording at depth and one at the surface is seen in Figure 6. This earthquake has a duration magnitude 2.1 and an S-P time of 1.10 s ( $R \cong 8.8$  km). The two obvious differences between the recording at 0 m and 35 m are the larger amplitude and the longer duration of the surface record. However, one can see that the initial S-wave on the surface seismograms has almost the same shape as the S-wave at 35 m. In both cases the Fourier transform of the S-wave packet produces a well-defined displacement

amplitude spectrum from which we have selected a corner frequency and a low-frequency asymptote (Table 2).

Because of the nearly single pulse at 35 m depth (Figure 6a), one might be suspicious that not every pulse would be so ideal. That is true. In figure 7, we show the seismograms for our closest earthquake: S - P time of 0.5 s ( $R \cong 2.4$  km) and duration magnitude  $M_D 1.1$ . Although the pulse at 35 m is not nearly so clean as we saw previously, the seismogram at 0 m maintains the same characteristics: (1) it has a larger amplitude; and (2) it has a longer duration.

Regardless of the complexity or simplicity of the waveform at 35 m the surface seismograms all show a larger amplitude and equal or longer duration. In terms of spectral content there is no obvious diminution of the spectral amplitudes at frequencies greater than the corner frequency determined from the spectra of S waves recorded at 35 m depth.

Fortunately we have recorded one event,  $M_D 3.0$  and an S-P time of 2.65 s ( $r \cong 20.3$  km) at all three depths, (Figures 8 and 9). The striking feature of these records is the similarity of the waveforms at 35 m and 166 m. Comparing the record at 0 m and that at 166 m, one can easily see a lower-frequency content in the surface record. However, this appearance may be due to an enrichment of frequencies in the 5-10 Hz range for the deeper instruments. The spectra of the 166 m and 35 m recordings are somewhat peaked in the 5-10 Hz range. Our selection of the corner frequency and low-frequency asymptote was made more difficult because of this. Nonetheless we did not find any major discrepancy in the choice of a corner frequency at 0 m compared to that at 166 m (Table 2).

To see if there were any systematic differences between the seismograms recorded at the surface and those recorded at depth we plotted corner frequency at 35 m versus corner frequency at 0 m and similarly the logarithm of the low-frequency asymptote  $\Omega_0$  at 35 m versus the logarithm of  $\Omega_0$  at 0 m (Figure 10). The low-frequency asymptotes were normalized to 10 km hypocentral distance, and  $\Omega$  at 0 m was corrected by the factor of 3.72 to account for the free surface and impedance contrast. A least squares fit to the data indicates that the corner frequencies are nearly one to one. Similarly, the low-frequency asymptotes, used to determine seismic moment, are nearly the same after corrections are made for the free surface and impedance contrast.

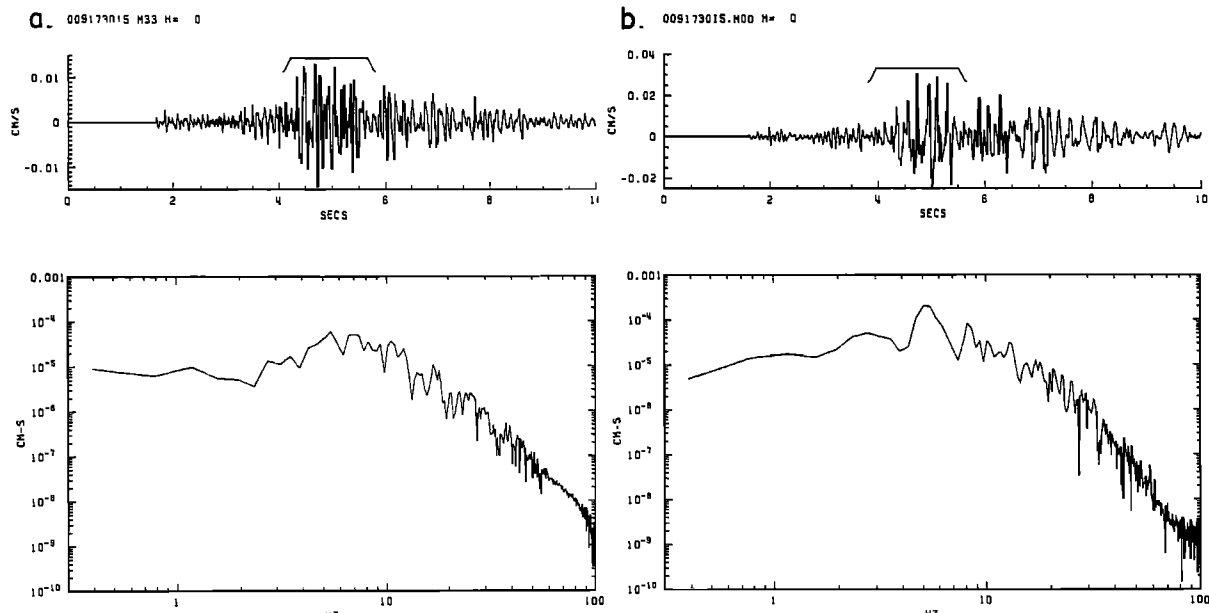


Fig. 9. (a) Event 0091730 recorded at 35 m. (b) Event 0091730 recorded at 0 m.

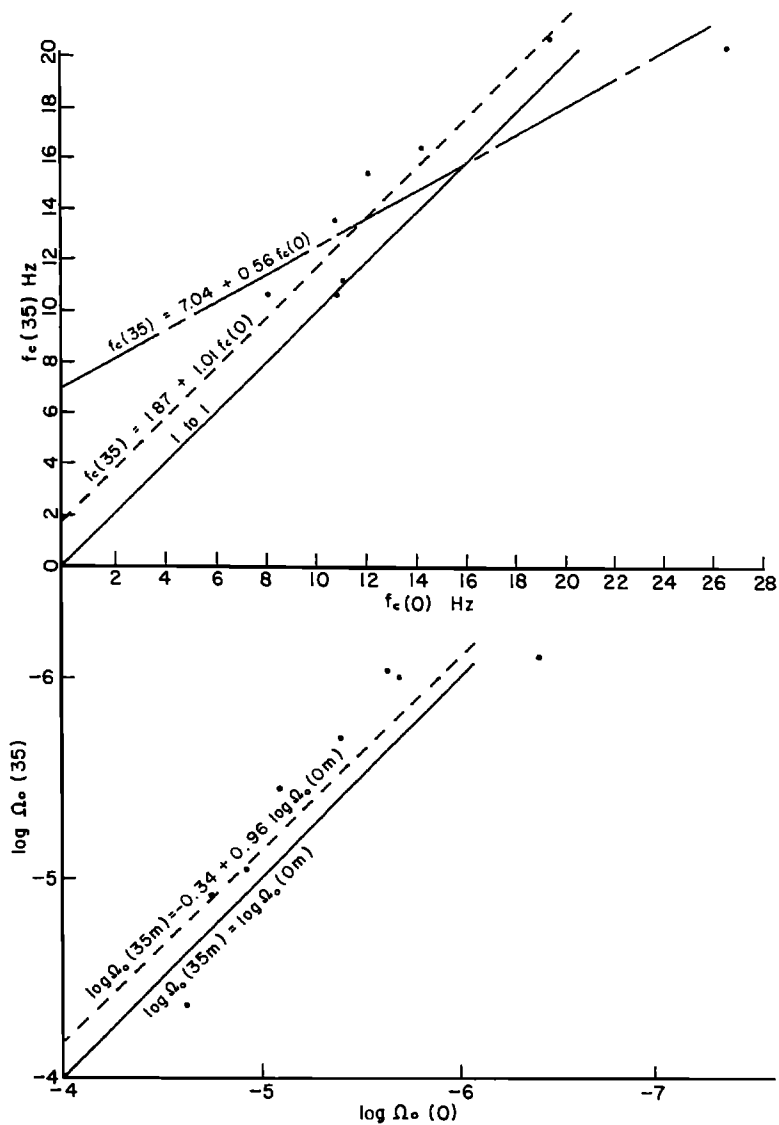


Fig. 10. In the upper part of the corner frequency determined at 35 m is plotted against the corner frequency at 0 m. There are two least squares regression curves. The long-short dashed line uses all eight data points; the short dashed line ignores the one datum  $f_c(0) = 27.3$  Hz. Of the two regression lines, the line  $f_c(35) = 1.87 - 1.01 f_c(0)$  is preferred. In the lower figure the logarithm of the low-frequency spectral amplitude asymptote at 35 m is plotted against the logarithm of the low-frequency spectral amplitude asymptote at 0 m.  $\Omega_0(0)$  has been corrected for amplification at the free surface and the impedance of the glacial till. The solid line shows a one-to-one fit; the dashed line shows the least squares regression fit to the data.

The effect of the glacial moraine on the entire spectrum can be most easily seen by taking spectral ratios. Although we are uncertain about the orientation of the downhole seismometers, the similarity of the waveforms suggests that we are comparing like signals. In Figures 11 and 12, we show spectral ratios for two of the previously discussed earthquakes. First consider the spectral ratio for the radiation recorded at 166 m and that at 35 m (Figure 13). The spectral ratio is almost 1 for the entire frequency band of 2.0 - 50.0 Hz. Considering the near equality of the two signals in the time domain, this result is not surprising. It does, however, lend credence to our use of spectral ratios between the surface records and those at 35 m to show that the primary influence on the surface records comes from the glacial moraine. Looking at Figures 14, 15, and 16, we see that

the spectral ratio, on average, is between 2.0 and 4.0 for the entire frequency band. Assuming normal incidence for S-waves, using the observed S-wave velocity structure and allowing for a factor of 2 at the free surface, the glacial moraine would amplify the surface records by about 3.7. More important than the absolute amplification due to the glacial moraine is the fact that above the corner frequencies, in the range 10-15 Hz, there is no obvious decrease in the spectral ratio.

#### Discussion

The simultaneous measurements of S-wave radiation at the surface and downhole contradict the supposition that near surface material is

## 326 DOWNHOLE RECORDINGS OF SEISMIC RADIATION

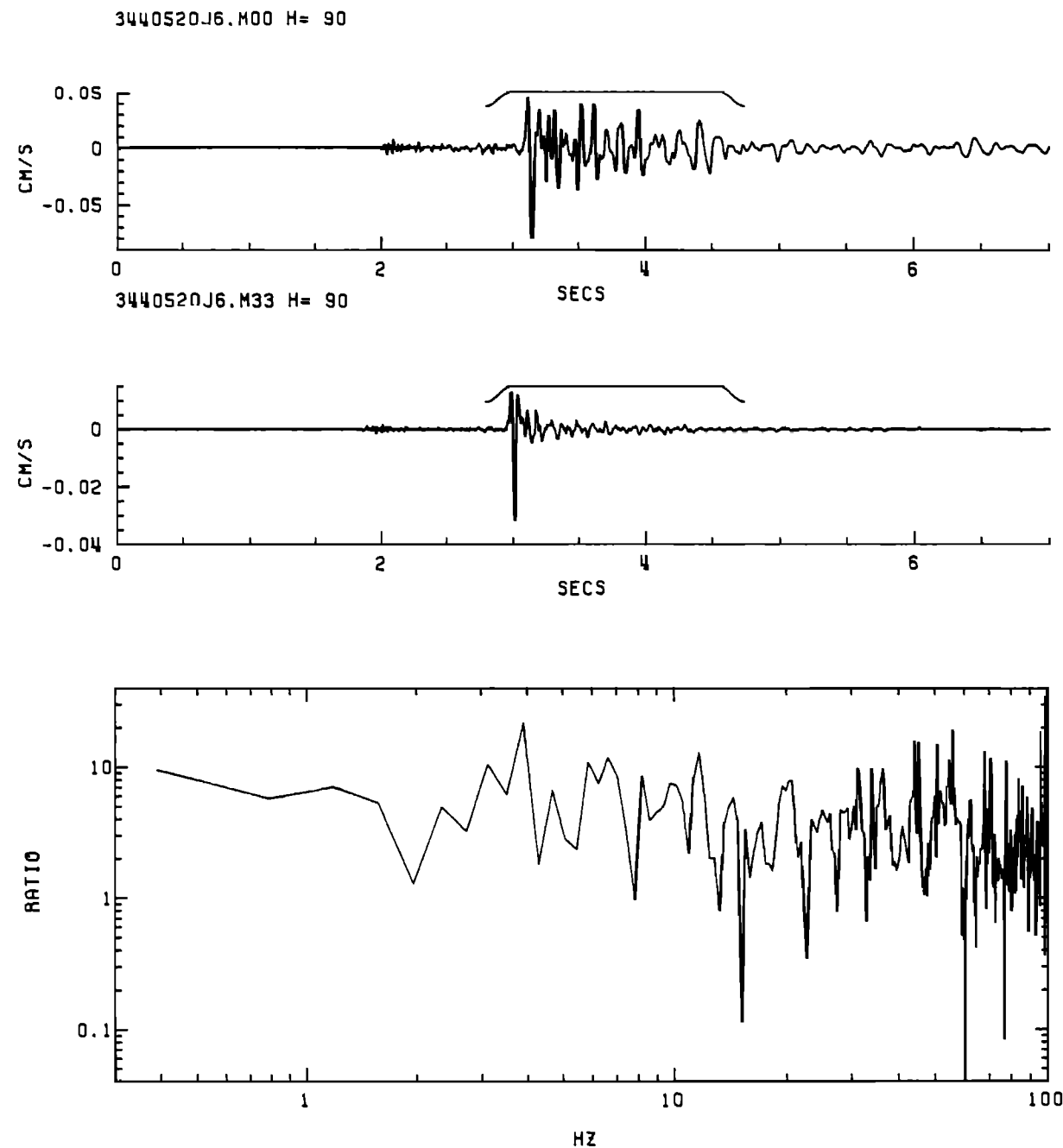


Fig. 11. The spectrum of each windowed time series, upper two graphs, is computed. The ratio is computed by dividing the spectrum of the upper windowed time series (0 m) by the spectrum of the lower windowed time series (35 m). The average spectral ratio for event 3440520 across the frequency band 2.0-50.0 Hz is approximately 4.0. The impedance and free surface correction gives a value of 3.7.

responsible for the nearly constant source radius observed for earthquakes near Mammoth Lakes [Archuleta et al., 1982]. The corner frequencies measured at depth (Figure 10) do not show a systematic difference from those measured at the surface. The spectral ratios of surface recordings to those at depth do not show any obvious decrease for frequencies greater than the corner frequency. The spectral ratios do reflect the impedance

contrast between the glacial moraine and the basement rock. Moreover, by comparing records at 0 m, 35 m, and 166 m shows that the extra complexity of the surface records is due to the glacial moraine and not to the material between 166 m and 35 m.

Although our data are limited to 11 earthquakes (two larger events  $M_L$  4.9 recorded on the film recorder but have only recently been processed

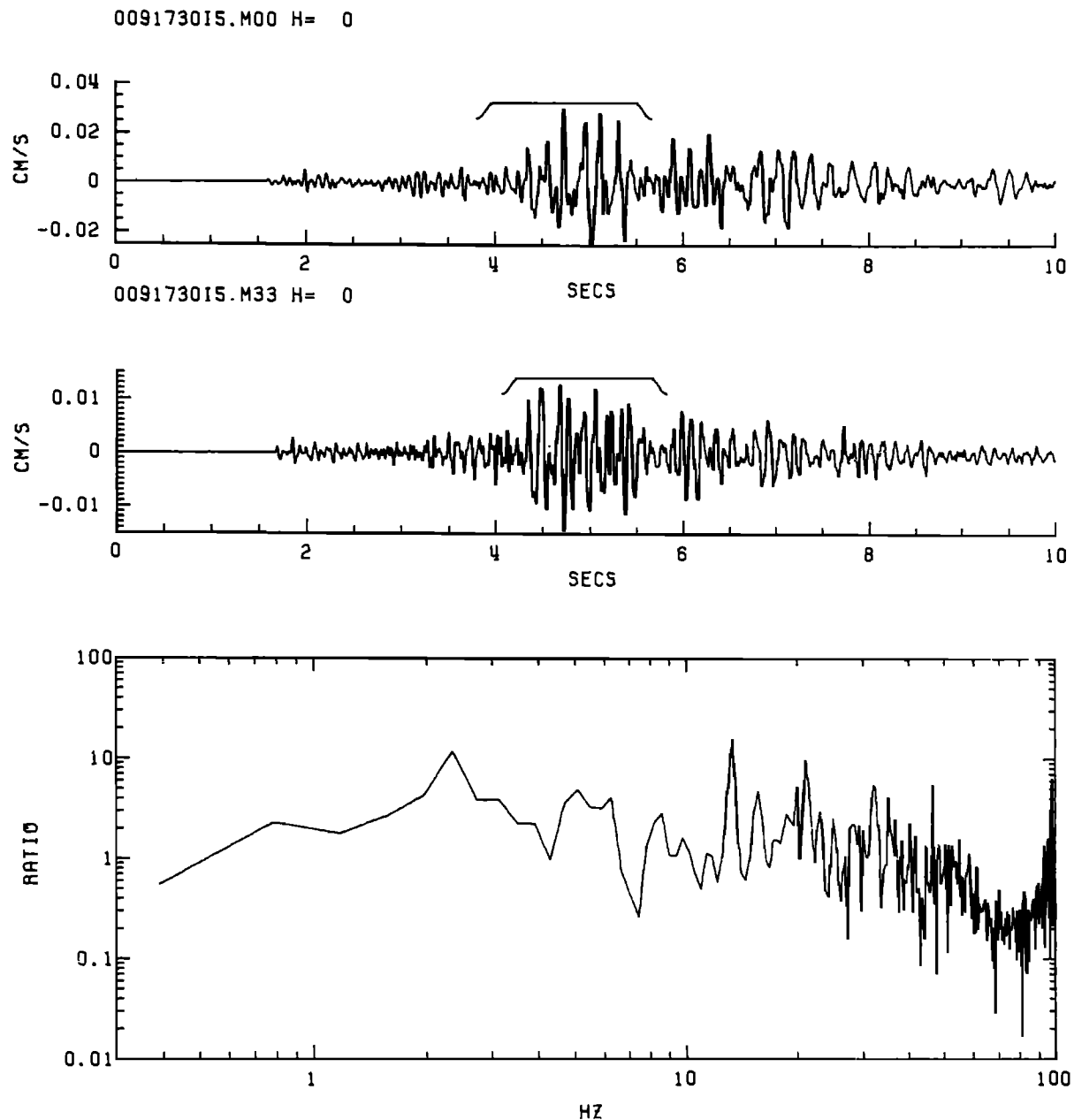


Fig. 12. Spectral ratio for event 0091730. Average spectral ratio is approximately 2.0 for frequency band 2.0-50.0 Hz. See caption of Figure 11 for details.

and not fully analyzed [Archuleta, 1985]), the inference supported by the available data is that the nearly constant source radius is a source effect. There is a caveat, or course. The medium between 166 m and 35 m has a large Poisson ration, 0.46, which indicates that there are many open cracks in the hornfels (T. Fumal, personal communication, 1985). Thus the possibility exists that the high frequencies are lost before they reach the deepest recorder. At the same time one must consider that at only 166 m the P-wave velocity is nearly equal to its value of crustal depths and the S-wave velocity is one-third of its value. The P-wave velocity suggests that spectral analysis of the P-waves may yield a constraint on

where the high frequencies are attenuated if they exist.

As we record more earthquakes, it may become possible to differentiate between source and path effects. However, with the present data we are fairly sure that the cause of the nearly constant source radius ( $f_{max}$ ) is not due to material properties of the glacial moraine at McGee Creek. Archuleta et al. [1982] showed that whole path  $Q_B$  values of 250 did not demonstrably affect the choice of either the corner frequency or the low-frequency asymptote. Unless it can be demonstrated that the medium in which our downhole instruments reside has special attenuative properties, the most likely cause of  $f_{max}$  is the earthquake source itself.

## 328 DOWNHOLE RECORDINGS OF SEISMIC RADIATION

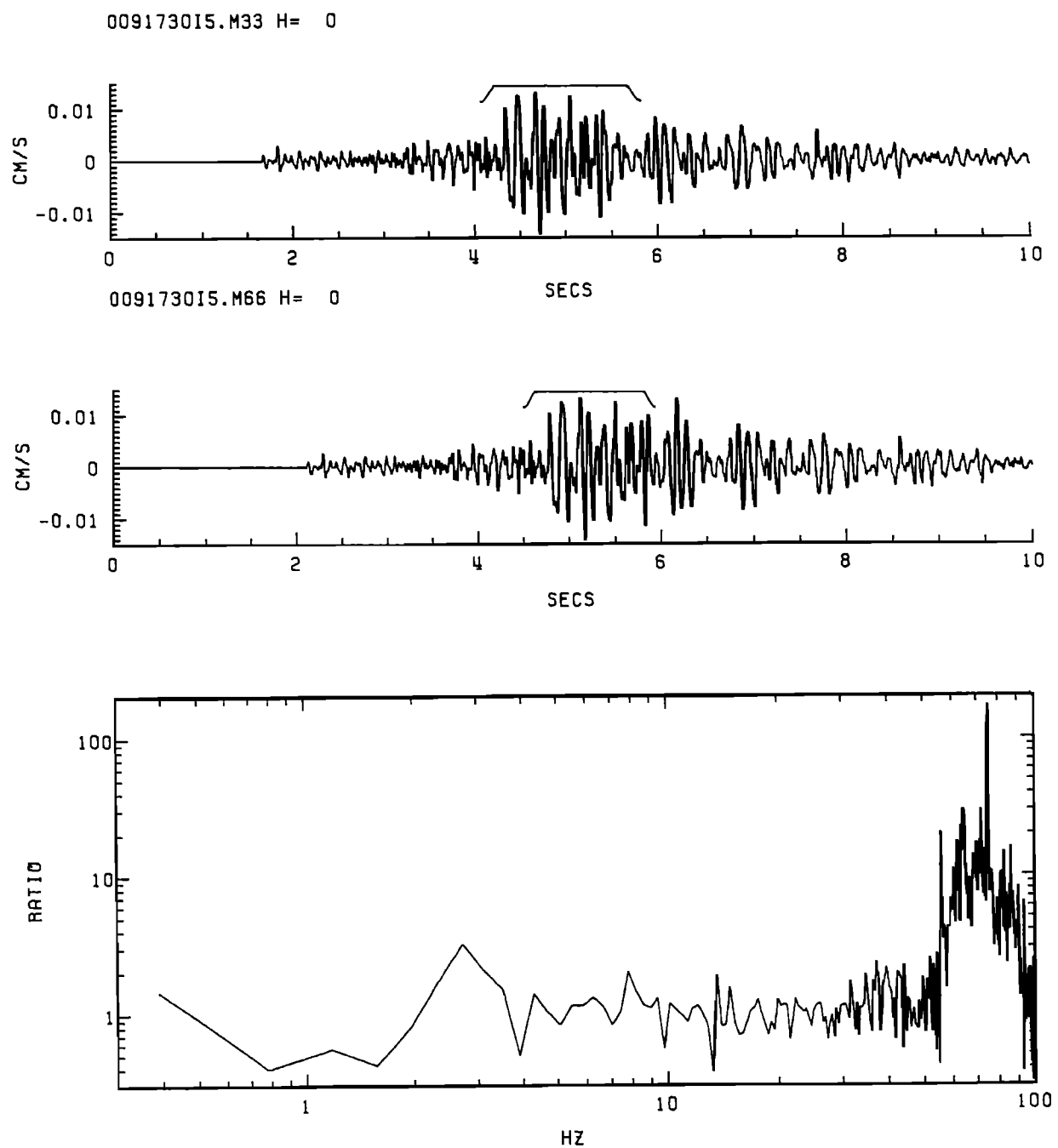


Fig. 13. Spectral ratio for event 0091730 where the spectrum at 35 m is divided by the spectrum at 166 m. Spectral ratio is very close to 1.0 for the frequency band 2.0-50.0 Hz. See caption of Figure 14 for details.

**Acknowledgements.** There are many people who have participated during the initial phase of this project which began while I was at the U.S. Geol. Survey in Menlo Park, California. Collectively I wish to thank the U.S. Geological Survey Branch of Engineering Seismology and Geology. In particular, I want to thank R. Fumal who has done most of the work on the geologic and seismic velocity logs of the boreholes. For instrumentation I am grateful for the expert assistance of E. Etheridge and R. Warrick. The data presented was collected through the dedicated efforts of J. Gibbs and J. Sena and initially processed by J. Watson and C. Mueller. The success of this project is due, in large part, to the support and advice of R. Borcherdt. R. Cockerham provided locations and magnitudes for these events. I thank the U.S. Forest Service for allowing us to put our instruments in such an excellent location. This research is supported by the Office of Nuclear Regulatory Research, U.S. Nuclear Regulatory Commission, Grant Number NRC-G-04-85-004.

#### References

- Aki, K., Scaling law of seismic spectrum, *J. Geophys. Res.*, 72, 1217-1231, 1967.
- Anderson, J. G. and S. E. Hough, A model shape of the Fourier amplitude spectrum of acceleration at high frequencies, *Bull. Seismol. Soc. Am.*, 74, 1969-1993, 1984.
- Andrews, M. C., C. S. Mueller, and A. McGarr, Moment-dependent source and peak ground motion parameters of the Coalinga, California, aftershock sequence, *EOS*, 65, 1005, 1984.
- Archuleta, R. J., Strong ground motion recorded downhole, *EOS, Trans. AGU*, 66, 976, 1985.
- Archuleta, R. J., E. Cranswick, C. Mueller, and P. Spudich, Source parameters of the 1980 Mammoth Lakes, California, earthquake sequence, *J. Geophys. Res.*, 87, 4595-4607, 1982.
- Bakun, W. H., C. G. Bufe, and R. M. Stewart, Body wave spectra of central California earthquakes, *Bull. Seismol. Soc. Am.*, 66, 439-459, 1976.
- Borcherdt, R., J. B. Fletcher, E. G. Jensen, G. L. Maxwell, J. R. VanSchaack, R. E. Warrick, E. Cranswick, M. J. S. Johnston, and R. McClearn, A General Earthquake Observations System (GEOS), *Bull. Seismol. Soc. Am.*, 75, 1783-1825, 1985.
- Brune, J. N., Tectonic stress and the spectra of seismic shear waves from earthquakes, *J. Geophys. Res.*, 75, 4997-5009, 1970. (Correction, *J. Geophys. Res.*, 76, 5002, 1971.)
- Cockerham, R. S. and A. M. Pitt, Seismic activity in Long Valley, eastern California: June 1982 through July 1984, Proceedings on active tectonics and magmatic processes beneath Long Valley caldera, eastern California, *U.S. Geol. Sur.*, Open File Report 84-939, 493-526, 1984.
- Cranswick, E., R. Wetmiller, and J. Boatwright, High-frequency observations and source parameters of microearthquakes recorded at hard rock sites, *Bull. Seismol. Soc. Am.*, 75, 1535-1567, 1985.
- Fletcher, J. B., Spectra from high-dynamic range digital recordings of Oroville, California, aftershocks and their source parameters, *Bull. Seismol. Soc. Am.*, 70, 735-755, 1980.
- Frankel, A., The effects of attenuation and site response on the spectra of microearthquakes in northeastern Caribbean, *Bull. Seismol. Soc. Am.*, 72, 1379-1402, 1982.
- Fumal, T. E., R. E. Warrick, E. C. Etheridge, and R. J. Archuleta, Downhole geology, seismic velocity structure and instrumentation at the McGee Creek, California, recording site, *Earthquake Notes*, 55, 5, 1985.
- Hanks, T. C.,  $f_{\max}$ , *Bull. Seismol. Soc. Am.*, 72, 1867-1879, 1982.
- Papageorgiou, A. S., and K. Aki, A specific barrier model for the quantitative description of inhomogeneous faulting and the prediction of strong ground motions. Part II. Applications of the model, *Bull. Seismol. Soc. Am.*, 73, 953-978, 1983.
- Tucker, B. E., and J. N. Brune, S-wave spectra and source parameters for aftershocks of the San Fernando earthquake of February 9, 1971, in *Geological and Geophysical Studies*, vol. 3, pp. San Fernando Earthquake of February 9, 1971, NOAA, Washington, D.C., 1973.

**THE EFFECTS OF ATTENUATION ON THE SCALING OF SOURCE PARAMETERS  
FOR EARTHQUAKES AT ANZA, CALIFORNIA**

J. B. Fletcher<sup>1</sup>, L. C. Haar<sup>1</sup>, F. L. Vernon<sup>2</sup>, J. N. Brune<sup>2</sup>, T. C. Hanks<sup>1</sup>, and J. Berger<sup>2</sup>

<sup>1</sup>U.S. Geological Survey, Menlo Park, California 94025

<sup>2</sup>Institute of Physics and Planetary Physics, University of California, San Diego, La Jolla, California 92093

**Abstract.** Source radii for Anza earthquakes calculated from spectral corner frequencies are surprisingly constant over 4 orders of magnitude in moment. This apparent constancy leads to a strong dependence of stress drop on moment: the largest events ( $10^{21}$  dyne-cm) have stress drops of about 100 bars, whereas events with moment of  $10^{18}$  dyne-cm or less have stress drops of a bar or less. However, displacement spectra used for corner frequency picks were not corrected for attenuation. In this paper we explore two arguments which suggest that an attenuation correction would alter, but not eliminate the small stress drops. Spectral ratios calculated for three events strongly support a linear frequency-dependent  $Q$ . The dependence  $Q = 12.9 + 11.8 f$  was obtained from one ratio for which the effect of ( $f \lesssim 60$  Hz) site resonances appeared to be at a minimum. Above 60 Hz the spectra would require an exponentially increasing  $Q$ . Alternatively, this could be due to their being contaminated by excessive noise above 60 Hz. The high  $Q$ /low attenuation at higher frequencies suggests that corner frequencies would not change drastically as a result of this attenuation correction. This method, however, does not differentiate where along the ray path attenuation is occurring or attenuation that may be common to all of the recording sites.

$f_{\max}$ , the intercept of the level part of acceleration spectra with high-frequency decay, can be interpreted as a site-specific attenuation parameter. Anza stations to the north and east tend to have a high  $f_{\max}$  ( $\geq 30$  Hz) compared to stations near the trifurcation of the San Jacinto-Buck Ridge-Coyote Creek faults, and to the southwest. Most of the corner frequencies at a specific station will tend to be lower than the  $f_{\max}$  for that station, thus attenuation does limit the upper range of corner frequencies. Source radii were recomputed using data only from just those stations with  $f_{\max} \geq 20$  Hz and again from those with  $f_{\max} \geq 30$  Hz. Recomputed source radii for some events did shift to smaller values, but the overall range of stress drops stayed about the same. We conclude that some events with high corner frequencies were affected by

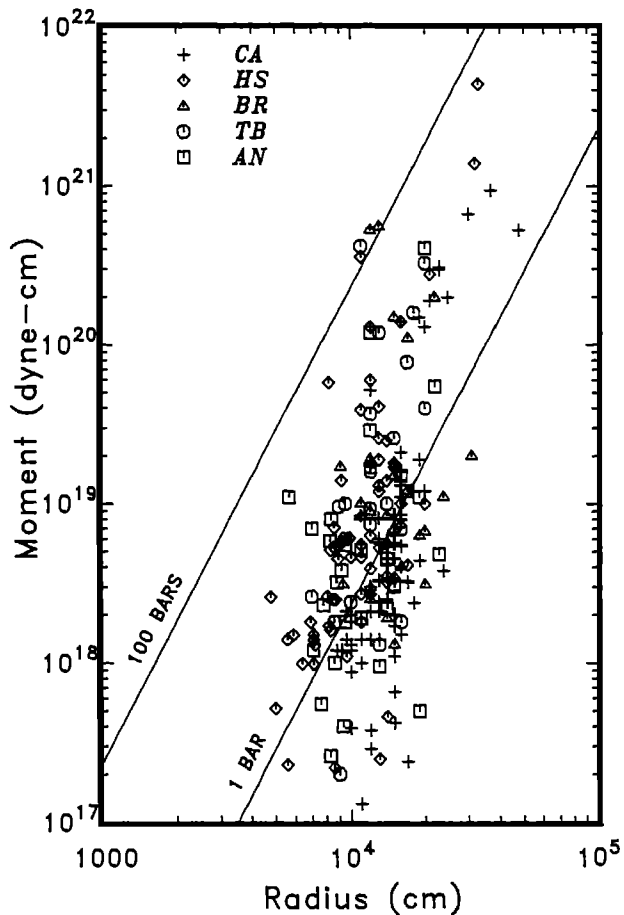


Fig. 1. Source radii plotted versus moment for Anza earthquakes. Straight lines that cut diagonally across plot are contours of stress drop. Data has been plotted by source region. Refer to Figure 3 for identification of source regions. Note that stress drops tend to range from greater than 100 bars to less than 1 bar.

## 332 SEISMIC ATTENUATION AT ANZA, CALIFORNIA

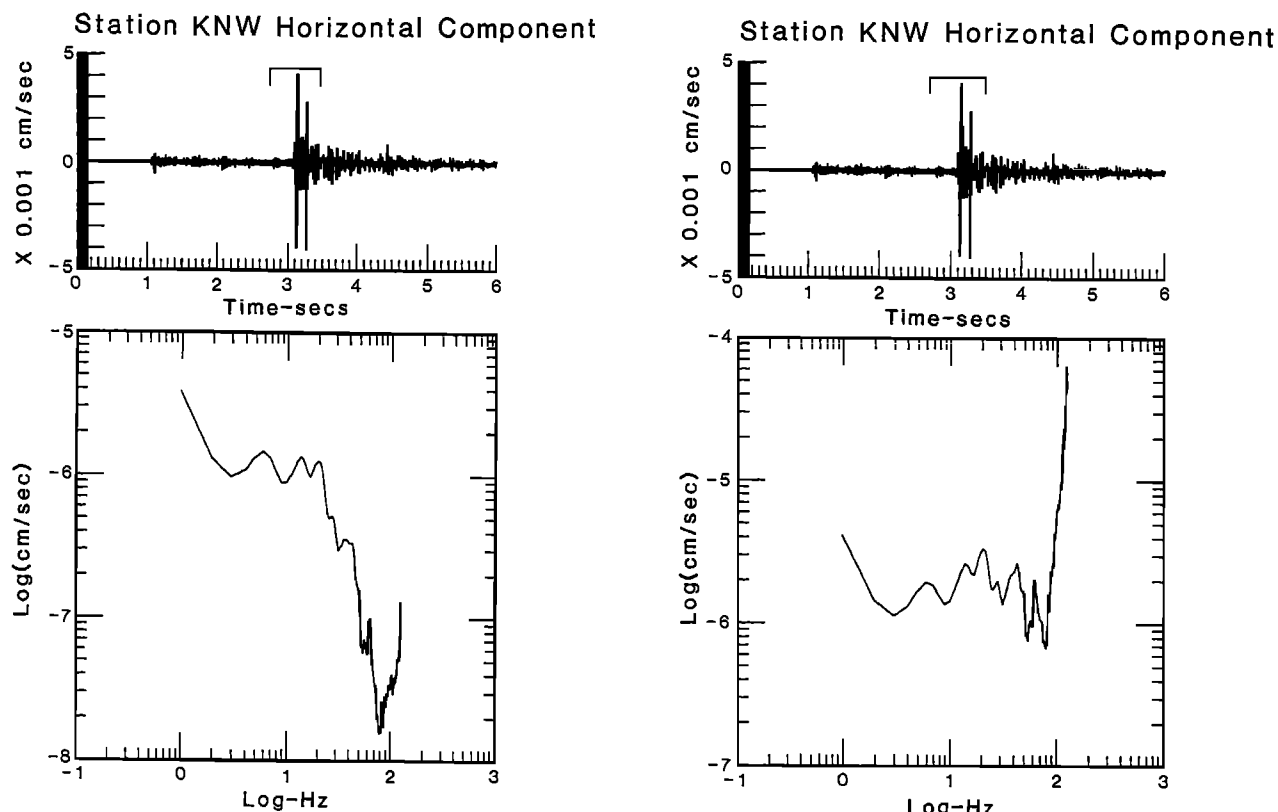


Fig. 2. Effect of attenuation correction on small event at Anza. In frame on the left no correction was applied. In the right a correction with a constant  $Q$  of 300 was applied, giving a  $t^*$  of 0.015 s.

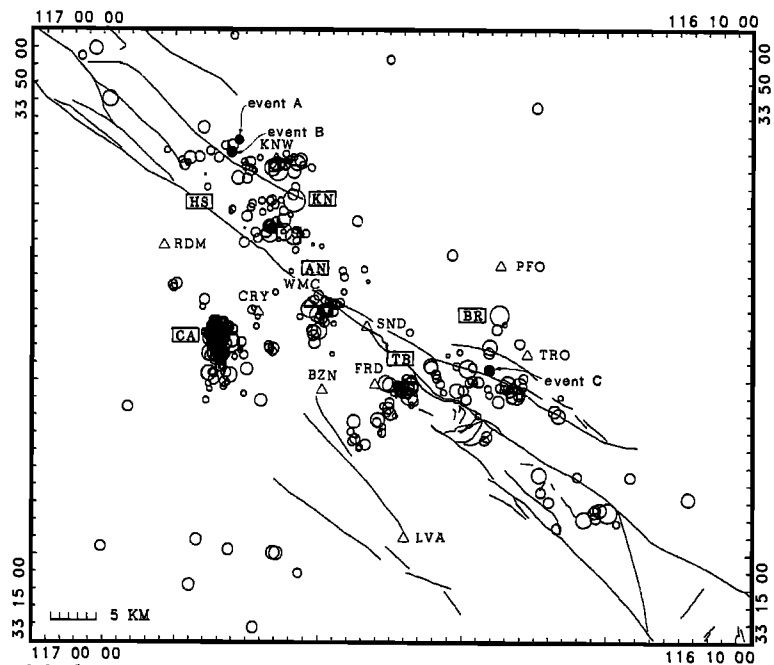


Fig. 3. Map of faults, stations, and epicenters near Anza. Source regions are given by two-letter identification: KN = Keencamp, HS = Hot Springs, CA = Cahuilla, AN = Anza, TB = Table Mtn., and BR = Buck Ridge. Events used in calculating spectral ratios have been labeled *a*, *b*, and *c*.

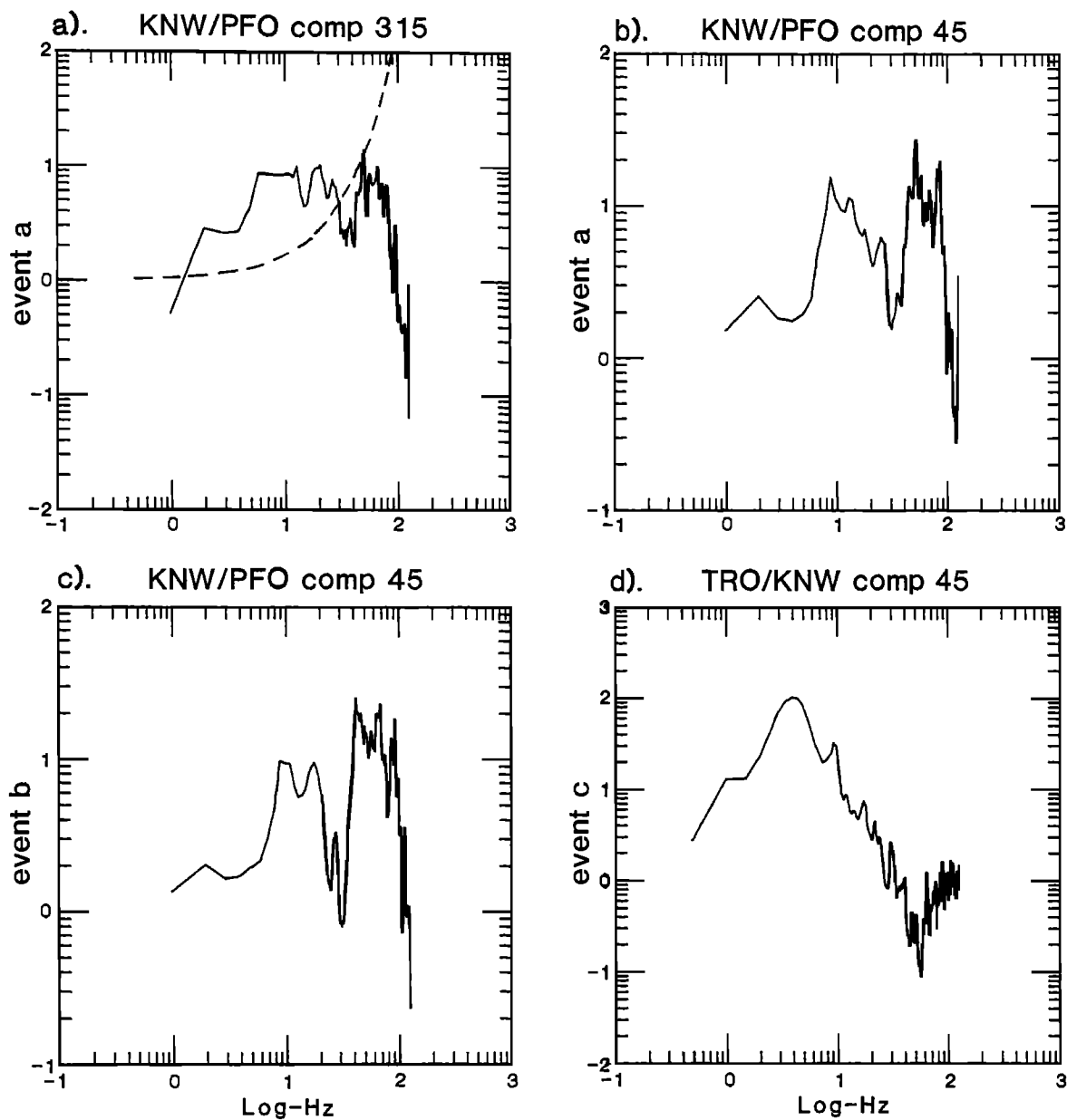


Fig. 4. Spectral ratios for four events plotted as logarithm of the amplitude ratio versus logarithm of frequency. In each case an  $S$ -wave spectrum for a near station is divided by that from a far station. The dotted line in 4a shows the spectral ratio expected if the apparent attenuation was due to a constant  $Q$  of 300. Note the dissimilarity of the two curves.

attenuation at the low  $f_{\max}$  sites, but that on the average, this is not a severe effect.

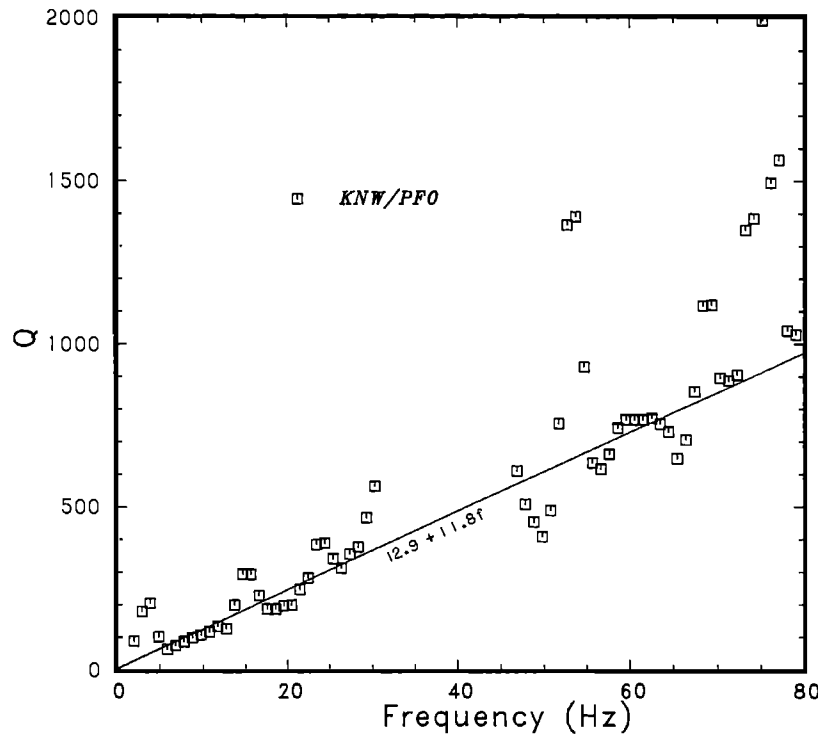
#### Introduction

Source parameters of small earthquakes obtained from near-source arrays of digital and analog instrumentation all show a strong dependence of stress drop on moment [Tucker and Brune, 1973; Spottiswoode and McGarr, 1975, Bakun et al., 1976; Fletcher, 1980; Archuleta et al., 1982;

and McGarr et al., 1984]. More recent results from the digital array at Anza [Fletcher et al., 1985; Figure 1] show a similar trend for inferred source radii and moments calculated for 292 events recorded over a 2-year period.

The Anza array was constructed with digital data acquisition components to provide wide-bandwidth and high-resolution data. This equipment has a bandwidth far beyond that needed to measure corner frequencies of microearthquakes. Thus, the possibility that there could be

## 334 SEISMIC ATTENUATION AT ANZA, CALIFORNIA

Fig. 5.  $Q_s$  necessary to predict spectral ratio in Figure 4a.

an instrumental cause of the stress-drop dependence on moment is remote. Furthermore, we chose Anza as the site for this array because we expected the granite and tonalites of the Southern California Batholith to transmit high frequencies more efficiently than other possible locations in California. In spite of these precautions, an apparent moment dependence of stress drop for small events is readily observed and therefore must be either a source or wave propagation effect.

Previous analysis of the Anza data set [Fletcher et al., 1985] largely assumed attenuation was not severely affecting the shape of the displacement spectra; no attenuation correction was applied before spectral parameters were picked. Anderson [1986], however, pointed out that very small  $t^*$ 's (0.01 to 0.015 s) in the attenuation correction:

$$A(\omega) = A_0(\omega) e^{\frac{\omega t^*}{2}}, \quad (1)$$

would move the corner frequencies of many of the smaller events to much higher values; the implication of this is that attenuation is limiting the corner frequencies and causing the dependence of stress drop on moment (see Figure 2). If this is true, then stress drops of smaller events are larger than the sub-bar values shown in Figure 1, and the overall width of the distribution of stress drops much less.

We calculated spectral ratios to measure  $Q$  and in particular to test the assumption of a frequency-independent  $Q$ . We found  $Q$  to be strongly frequency dependent for the whole-path differencing technique used. We have also

correlated corner frequencies with  $f_{\max}$  at each station and found that  $f_{\max}$  is an approximate upper limit to the observed corner frequencies at the station. However most corner frequencies are well below  $f_{\max}$  suggesting that attenuation probably does not affect the picking of corner frequencies of all or even most of the smaller earthquakes.

#### Spectral Ratios

We divide  $S$ -wave spectra from the same earthquake recorded at different hypocentral distances to obtain the effects of wave propagation. Differences caused by radiation pattern effects would still be present because the rays to each station do not leave the same point on the focal sphere. However, the connection between high-frequency amplitudes and the double-couple radiation pattern is notoriously tenuous [Fletcher et al., 1984; Hanks and McGuire, 1981]. Figure 3 shows the stations and epicenters used in calculating spectral ratios. Four spectral ratios are shown in Figure 4. Each ratio is calculated by dividing the  $S$ -wave velocity spectrum from a nearby station by that from a more distant station. Spectra are determined over 0.5- to 1.0-second windows and smoothed with a five-point running-mean average. The signal-to-noise ratio of body-wave spectra is usually about 1 at both the high- and low-frequency limits [e.g., Tucker and Brune, 1977]. Hence spectral ratios are also near 1 at the high- and low-frequency limits. Between these limits ratios are mostly positive although most ratios show the effect of site res-

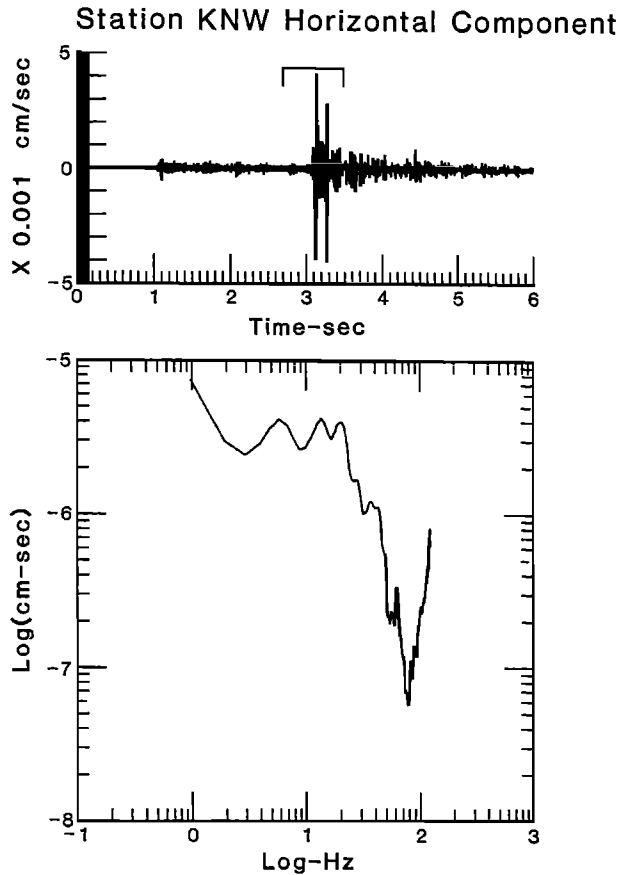


Fig. 6. Body wave spectra shown in Figure 2 corrected with a frequency-dependent  $Q$  determined from spectral ratio.

onances. For example, 4a, b, and c have a notch in the ratio between 20 and 30 Hz due to a site resonance in this frequency band at station PFO.

To calculate  $Q$  from a spectral ratio, we first correct for spherical spreading

$$r_n A_n = A_0(\omega) e^{-\frac{\omega r_n}{2Q\beta}} \quad \text{and} \quad r_f A_f = A_0(\omega) e^{-\frac{\omega r_f}{2Q\beta}} \quad (2)$$

where  $A$  is the measured spectral amplitude at a particular site,  $n = \text{near}$  and  $f = \text{far}$ ,  $A_0$  is the source excitation, assumed to be the same for both recordings,  $Q$  is the attenuation factor, and where  $r_n$  and  $r_f$  are the hypocentral distances to the near and far stations, respectively. Taking the logarithm of the ratio  $\frac{A_n}{A_f}$  yields

$$\ln \frac{r_f}{r_n} - \ln \frac{A_n}{A_f} = \frac{\omega}{2Q\beta} [r_n - r_f] . \quad (3)$$

Solving for  $Q$ ,

$$Q = \frac{\pi f}{\beta} \frac{r_n - r_f}{\ln \frac{r_f}{r_n} - \ln \frac{A_n}{A_f}} \quad (4)$$

We applied (4) to the ratio shown in Fig. 4a, the simplest-looking curve in Figure 4, to estimate the frequency dependence of  $Q$  (Figure 5). Our lack of radiation pattern corrections contributes to the error in these estimates. These errors would represent a constant shift in our spectral ratios and change the absolute values of the calculated  $Q(f)$ , but could not render them independent of frequency.

The data in Figure 5 were fit by a weighted least-squares line yielding  $Q = (12.9 \pm 52.) + (11.8 \pm 1.1) f$ . This straight line, however, does not fit the very high-frequency data ( $\geq 60$  Hz). At frequencies close to the Nyquist frequency of 125 Hz, the spectra appear to be composed mostly of digitizer noise, which we would expect to give a spectral ratio of about 1, and equivalent very large  $Q$ s. The frequency at which the data become significantly contaminated by instrument noise is not well known at present. On the other hand, if the  $Q$  values at 60 to 80 Hz are valid, then an exponential curve would be a better fit to all of the  $Q$  values for the frequency range plotted in Figure 5.

We can now use this frequency-dependent  $Q$  to correct spectra for the effects of attenuation. Figure 6 shows a horizontal component seismogram and its corrected spectrum from station KNW for a  $M = 1.1$  event that is located at the KN cluster. (An uncorrected spectrum and one corrected with a  $Q$  of 300 for the same station and event are shown in Figure 2.) Only slight differences are apparent between Figures 2a and 6. A corner frequency picked by eye would be approximately the same place in both Figures 2a and 6.

This brief analysis of specific attenuation models suggests a frequency-independent  $Q$  is not appropriate for the Anza region. A quantitative estimate of this frequency dependence yields relatively high values of  $Q$  and a low attenuation at frequencies of 20 Hz or higher at the average hypocentral distances encountered at Anza. The above method which uses spectral ratios to estimate  $Q$  does not take into account an attenuation that would be common to all sites nor does it separate out intrinsic anelastic losses from losses caused by scattering.

#### $f_{\max}$ at the Anza Array

A compilation of corner frequencies by station at the Anza array shows that some stations, such as SND, tended to have consistently lower corner frequencies than other stations, such as KNW. This site-specific attenuation can be parameterized by  $f_{\max}$ , which is the intersection of the flat and high-frequency decay sections of acceleration spectra [Hanks, 1982]. In this interpretation,  $f_{\max}$  represents the frequency above which attenuation is significant: stations with low-velocity sediment and high attenuation will transmit fewer high frequencies and exhibit a relatively low  $f_{\max}$ . Corner frequencies are compiled by station in Figure 7. Values of  $f_{\max}$  shown are averages of 5 to 10 values

## 336 SEISMIC ATTENUATION AT ANZA, CALIFORNIA

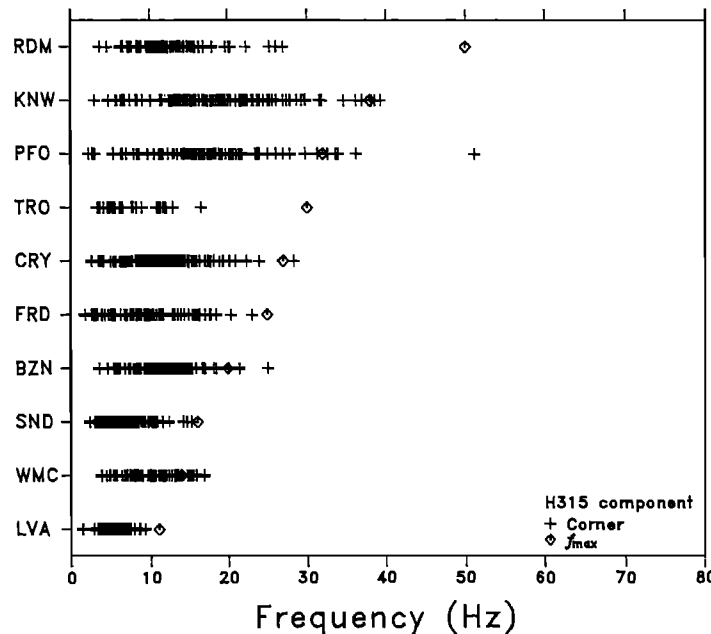


Fig. 7. Corner frequencies (+) for about 1/2 of all of the source parameters at Anza and  $f_{\max}$  ( $\diamond$ ) plotted for each station at Anza for one of the horizontal components. Note that corner frequencies are generally less than  $f_{\max}$ .

measured from acceleration spectra calculated from the observed ground velocity.

It is apparent in Figure 7 that  $f_{\max}$  does tend to act as an upper limit to corner frequencies measured. Stations LVA, WMC, and SND, which have particularly low  $f_{\max}$ s, have a range in corner frequencies that is 1/2 to 1/3 less than that of stations RDM, PFO, and KNW. The corner frequency from many different earthquakes are plotted in Figure 2, suggesting that this attenuation seems to be site-specific.

$f_{\max}$  values can be correlated with station locations and site geology. With the exception of LVA which is located well off the fault most of the low  $f_{\max}$  stations are located near the trifurcation point of the San Jacinto-Buck Ridge-Coyote Creek faults, or just to the west of these. Shallow deposits of recent alluvium are contained within the fault or near many of these sites. All of the high  $f_{\max}$  sites are located to the north or east of the array center.

Since attenuation only removes seismic energy we assume that the higher  $f_{\max}$  stations must be closest to representing the true source excitation, whereas low  $f_{\max}$  stations must be contributing erroneously low corner-frequency data to at least some ensemble of earthquakes (i.e., those earthquakes that have corner frequencies above the  $f_{\max}$ s of the low  $f_{\max}$  stations—shown by those data at the high  $f_{\max}$  stations). The source radii and stress drops are presently being biased to low values by the inclusion of data from low  $f_{\max}$  stations.

To correct for this effect, source parameters were recalculated for the Anza data after deleting the data from the low  $f_{\max}$  stations. This was done twice; once with all sta-

tions with  $f_{\max}$  less than 20 Hz deleted, and again with all stations whose  $f_{\max}$  is less than 30 Hz deleted. The moment and source radius are replotted in Figures 8a and 8b. In comparison to Figure 1, the overall distribution of stress drops has not changed: there still are numerous events with stress drops less than 1 bar. On the other hand, there has been an overall shift of the data with small moments to move toward smaller source dimensions, confirming the bias of the original data set caused by the data from the low  $f_{\max}$  stations.

It is certainly possible that the remaining data ( $f_{\max} \geq 30$  Hz) could still be suffering some attenuation. If this is true then it is likely that all surface recorded data would be at least as attenuated, as are the Anza stations which are situated on or within a few meters of competent rock. It is worth noting that most of the corner frequencies at the high  $f_{\max}$  stations are between 10 and 22 Hz. This is well below 30 Hz, which suggests that if stations with  $f_{\max}$  lower than 40 Hz or so were paired out of the data set, the source radii would not continue to illustrate the change found between Figures 1 and 8.

In this model of acceleration spectra,  $f_{\max}$  is assumed to be the lower limit in frequency of the effect of attenuation. It is possible, however, that attenuation is not as well behaved as implied by (1). Resonant peaks or valleys associated with particular rock compositions or grain geometries could produce attenuation curves that could affect the picking of corner frequencies below  $f_{\max}$ . Nevertheless, we are not aware of any examples of this form of attenuation and we therefore disregard it until further evidence of its existence is available.

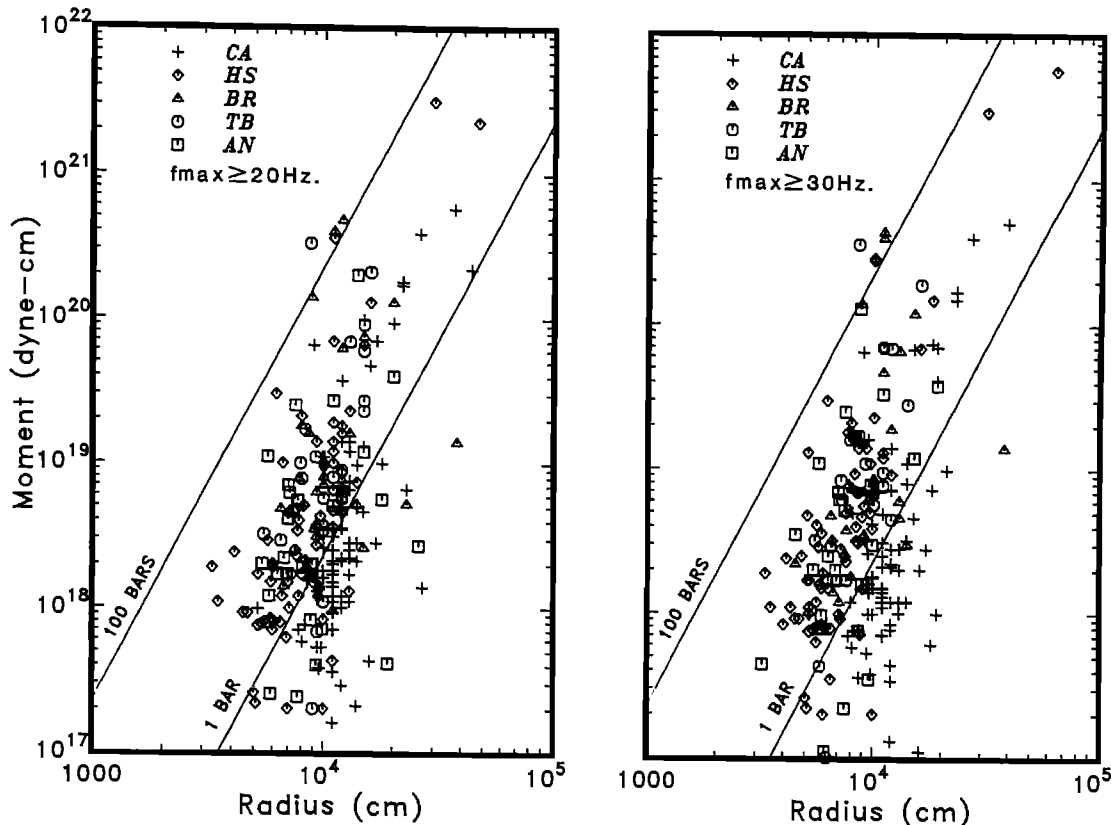


Fig. 8. Source parameters of Figure 1 recalculated with spectra from stations with  $f_{\max} \geq 20$  Hz (a) and  $f_{\max} \geq 30$  Hz (b).

### Conclusions

1. Body-wave spectra from Anza are sensitive to the attenuation correction. A correction based on a  $t^*$  of 0.01 to 0.015 s would raise the high frequencies such that many of the corner frequencies for the smaller events would be much higher.
2. Spectral ratios suggest a frequency-independent  $Q$  model is not valid. A  $Q$  of  $12.9 + 11.8 f$  is valid to a frequency of about 65 Hz. Most corner frequencies would not change dramatically with a correction based on this  $Q$ .
3.  $f_{\max}$  for Anza stations ranges from 10 to 50 Hz. The original source dimensions are biased by corner-frequency data from the low  $f_{\max}$  stations. Data recalculated with this data deleted has a general trend toward smaller source radii for the smallest events, but the overall distribution of stress drops has not changed dramatically; there still exist many events with stress drops less than 1 bar.

### References

- Anderson, J. G., Implications of attenuation for studies of the earthquake source, *this volume*, 1986.  
 Archuleta, R. J., Cranswick, E., Mueller, C., and Spudich, P., Some parameters of the 1980 Mammoth Lakes, Cal-ifornia earthquake sequence, *J. Geophys. Res.*, **87**, 4595-4607, 1982.  
 Bakun, W. H., Bufe, C. G., and Stewart, R. M., Body-wave spectra of central California earthquakes, *Bull. Seismol. Soc. Am.*, **66**, 439-459, 1976.  
 Fletcher, J. B., Spectra from high-dynamic range digital recordings of Oroville, California, aftershocks and their source parameters, *Bull. Seismol. Soc. Am.*, **70**, 735-755, 1980.  
 Fletcher, J., Boatwright, J., Haar, L., Hanks, T., and McGarr, A., Source parameters for aftershocks of the Oroville California earthquake, *Bull. Seismol. Soc. Am.*, **74**, 1101-1123, 1984.  
 Fletcher, J., Haar, L., Hanks, T., Vernon, F., Berger, J., and Brune, J., The digital array at Anza, California: Processing and initial interpretations of source parameters: Paper presented at 5th Ewing Symposium on Earthquake Source Mechanics, Harriman, N.Y., May 20-24, 1985.  
 Hanks, T. C.,  $f_{\max}$ , *Bull. Seismol. Soc. Am.*, **72**, Part A, 1867-1880, 1982.  
 Hanks, T. C., and McGuire, R. K., The character of high frequency strong ground motion, *Bull. Seismol. Soc. Am.*, **71**, 2071-2095, 1981.  
 McGarr, A., Mueller, C. S., Fletcher, J. B., and Andrews, M. C., Ground motion parameters of the 1983 Coalinga,

## 338 SEISMIC ATTENUATION AT ANZA, CALIFORNIA

- California earthquake: Implications for crustal strength, Proceedings of Workshop XXVII Mechanics of the May 2, 1983 Coalinga Earthquake, U.S. Geol. Surv. Open-File Rep., 85-44, 254-275, 1985.
- Spottiswoode, S. M., and McGarr, A., Source parameters of tremors in a deep-level gold mine, Bull. Seismol. Soc. Am., 65, 93-112, 1975.
- Tucker, B. E., and Brune, J. N., S-wave spectra and source parameters for aftershocks of the San Fernando earthquake of February 9, 1971 in San Fernando earthquake of February 9, 1971, Geological and Geophysical Studies, vol. 3, Washington, D.C., 1973.
- Tucker, B. E., and Brune, J. N., Source mechanism and  $m_o - M$ , analysis of aftershocks of the San Fernando earthquake, Geophys. J. R. Astron. Soc., 49, 371-426, 1977.

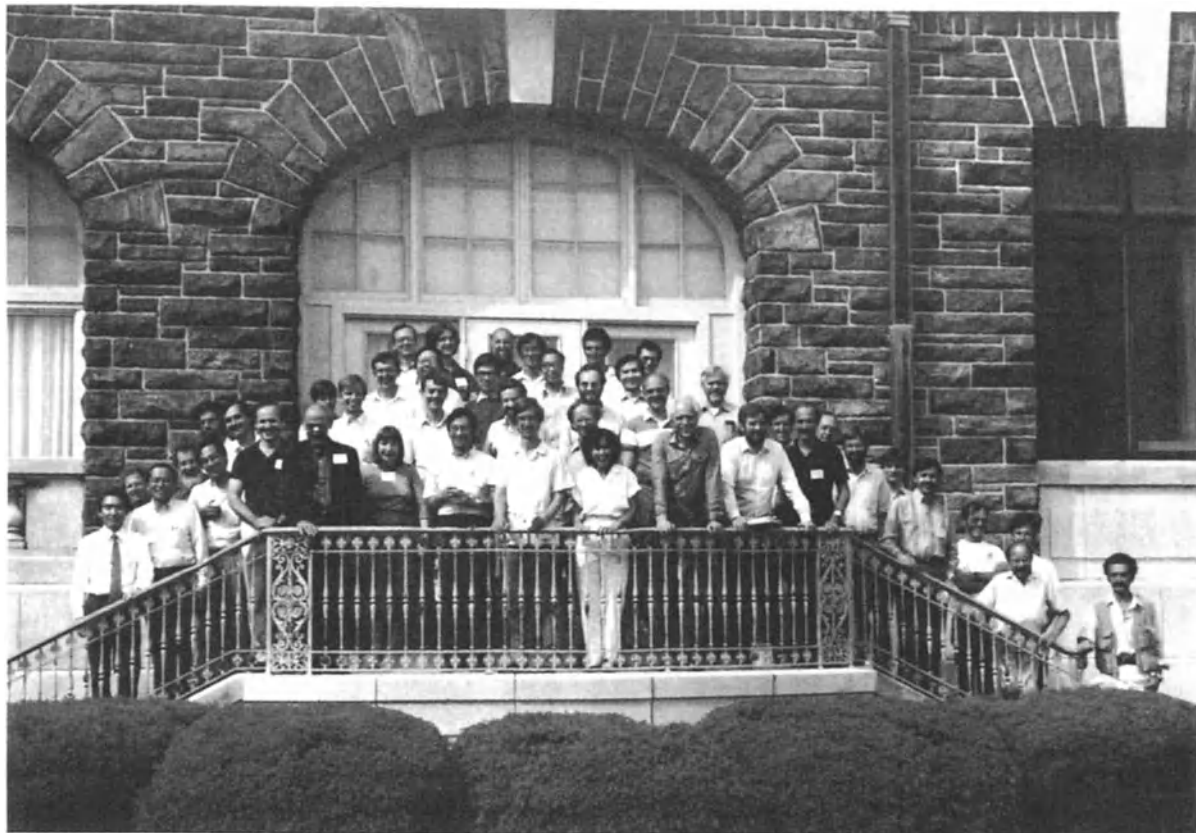
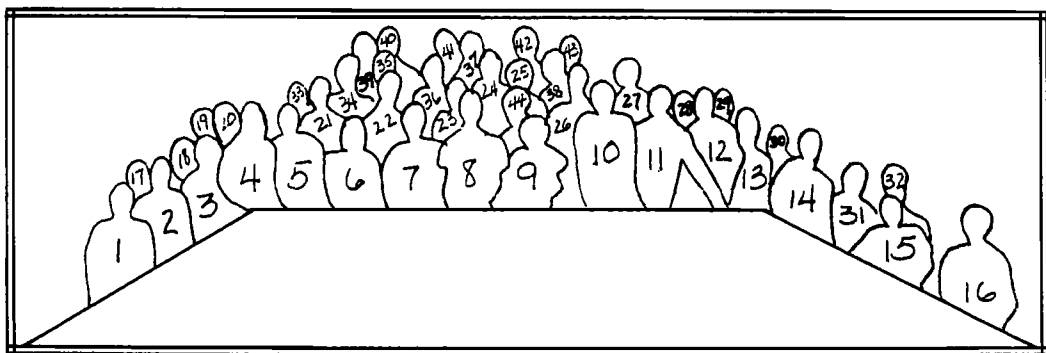


Photo courtesy of K. Mogi



## KEY TO SYMPOSIUM PARTICIPANTS

- |                 |                  |                     |                   |
|-----------------|------------------|---------------------|-------------------|
| 1. K. Mogi      | 12. J. Andrews   | 23. J. Logan        | 34. D. Boore      |
| 2. K. Aki       | 13. H. Quin      | 24. Q. Deng         | 35. T.-F. Wong    |
| 3. R. Madariaga | 14. R. Archuleta | 25. A. Papageorgiou | 36. T. Cao        |
| 4. J. Dieterich | 15. P. Spudich   | 26. W. Bakun        | 37. P. Okubo      |
| 5. W. Joyner    | 16. L. Seeber    | 27. J. Brune        | 38. M. Ohnaka     |
| 6. R. Dmowska   | 17. A. McGarr    | 28. J. Fletcher     | 39. J. Armburster |
| 7. H. Kanamori  | 18. K. Jacob     | 29. S. Gibowicz     | 40. L. Ruff       |
| 8. C. Scholz    | 19. A. Ruina     | 30. J. Strehlau     | 41. W. Thatcher   |
| 9. S. Das       | 20. E. Faccioli  | 31. R. Sibson       | 42. P. Bernard    |
| 10. B. Kostrov  | 21. J. Anderson  | 32. J. Boatwright   | 43. B. Freund     |
| 11. G. King     | 22. T. Tullis    | 33. C. Nicholson    | 44. J. Byerlee    |

We would like to thank the following people for their critical review of papers which appear in this volume. They are:

Aki, K.	Madariaga, R.
Allen, C. R.	Madden, T. R.
Anderson, J.	McGarr, A.
Andrews, D. J.	Nabelek, J.
Archuleta, R. J.	Papageorgiou, A.
Bakun, W.	Plafker, G.
Boore, D. M.	Reasenberg, P.
Brune, J. N.	Rice, J. R.
Byerlee, J. D.	Roeloffs, E.
Cifuentes, I.	Rudnicki, J. W.
Cox, S.	Ruff, L. J.
Cranswick, E.	Ruina, A. L.
Day, S. M.	Savage, J. C.
Dmowska, R.	Shimazaki, K.
Doornbus, D. J.	Sibson, R. H.
Faccioli, E.	Silver, P.
Frazer, L. N.	Spence, W.
Freund, L. B.	Spudich, P. K.
Hanks, T. C.	Stein, R.
Hartzell, S.	Stump, B.
Heaton, T.	Sykes, L. R.
Helmberger, D.	Thatcher, W.
Hobbs, B.	Tullis, T. E.
Irikura, K.	Turcotte, D. L.
Jacob, K. H.	Wong, T.-F.
Joyner, W. B.	Wyss, M.
Kanamori, H. H.	Yamashita, T.
King, G.	

The Editors